Poro-Elastic Theory with Applications to Transport in Porous Media

Dong-Sheng Jeng and Lin Cui

CRC Press
Taylor & Francis Group

Poro-Elastic Theory with Applications to Transport in Porous Media

This book treats the subject of porous flow and its applications in three engineering and scientific problems. The first major part of the book is devoted to solute transport in unsaturated porous media. Dynamic hydraulic conductivity and degree of saturation associate with pore pressures are also included in the consolidation-induced solute transport process. The second part of this book focuses on tidal dynamics in coastal aquifers, including shallow water expansion for sloping beaches, two-dimensional problem in estuarine zone and leaky confined aquifers. The final part of the book summarizes the recent development of porous model in the field of liquefaction around marine infrastructures including fundamental mechanisms of momentary and residual seabed liquefaction, two-dimensional and three-dimensional porous models for fluid-seabed interactions around breakwaters, pipelines and piled foundations in marine environments.

The authors' aim is to describe in detail the applications of porous models for several engineering problems. This book will provide academic researchers and industry an overview of recent development in the field of porous models and the applications.

Dong-Sheng Jeng is a professor of Civil Engineering at Qingdao University of Technology, China.

Lin Cui is a lecturer of Civil Engineering at Qingdao University of Technology, China.

Taylor & Francis
Taylor & Francis Group
http://taylorandfrancis.com

Poro-Elastic Theory with Applications to Transport in Porous Media

Dong-Sheng Jeng
Lin Cui

CRC Press
Taylor & Francis Group
Boca Raton London New York

CRC Press is an imprint of the
Taylor & Francis Group, an **informa** business

First edition published 2023
by CRC Press
6000 Broken Sound Parkway NW, Suite 300, Boca Raton, FL 33487-2742

and by CRC Press
4 Park Square, Milton Park, Abingdon, Oxon, OX14 4RN

CRC Press is an imprint of Taylor & Francis Group, LLC

Library of Congress Cataloging-in-Publication Data

Names: Jeng, Dong-Sheng, author. | Cui, Lin (Civil engineering teacher) author.
Title: Poro-elastic theory with applications to transport in porous media / Dong-Sheng Jeng and Lin Cui.
Description: First edition. | Boca Raton : CRC Press, 2023. | Includes bibliographical references and index.
Identifiers: LCCN 2022052277 | ISBN 9781032311913 (hbk) | ISBN 9781032311920 (pbk) | ISBN 9781003308539 (ebk)
Subjects: LCSH: Multiphase flow. | Porous materials--Fluid dynamics. | Elastic analysis (Engineering) | Transport theory. | Ocean bottom. | Soil-structure interaction. | Offshore structures--Anchorage.
Classification: LCC TA357.5.M84 J46 2023 | DDC 620.1/16--dc23/eng/20230110
LC record available at https://lccn.loc.gov/2022052277

ISBN: 978-1-032-31191-3 (hbk)
ISBN: 978-1-032-31192-0 (pbk)
ISBN: 978-1-003-30853-9 (ebk)

DOI: 10.1201/9781003308539

Typeset in Nimbus font
by KnowledgeWorks Global Ltd.

Publisher's note: This book has been prepared from camera-ready copy provided by the authors.

Contents

Taylor & Francis
Taylor & Francis Group
http://taylorandfrancis.com

Preface

Poro-elastic theory has been widely applied in numerous engineering and scientific problem involved in multi-phase media. For environmental science and civil related engineering fields, we are interested in static and dynamic response of porous media subject to environmental loading as well as other type of forces, such as those of thermal and chemical origin. These are generally known as poromechanics, which was first created from the Biot Conference on Poromechanics.

This book consists of three sections with fourteen chapters. They are: (1) Solution transport in porous media; (2) Tidal dynamics in coastal aquifers and (3) Fluid-seabed-structures interactions. In Chapter 1, three main streams covered in this book are discussed briefly and some future research scopes are highlighted for readers.

Chapter 2 discusses the one-dimensional model for solute transport in an unsaturated porous medium, based on the assumption of small strain. Both consolidation and solute transport models will be coupled through the pore pressures in the porous medium. The governing equations are derived and further applied to a liner landfill system. Based on the scaling analysis, importance of each term will be examined. Within the framework, the 1D model will be further extended to an unsaturated layered soil system with detailed parametric study.

Chapter 3 outlines the finite strain model for solute transport in an unsaturated porous medium. Variations of key parameters in the consolidation-induced solute transport process will be discussed. The finite strain model will be further applied to a landfill liner with a detailed parametric study.

Chapter 4 considers a porous medium with dynamic compressibility (associated with degree of saturation) and hydraulic conductivity. In this model, both compressibility of pore fluid and hydraulic conductivity (i.e., soil permeability) vary with dynamic pore pressures. With the new model, the effects of dynamic compressibility and hydraulic conductivity on the solute transport in an unsaturated porous medium will be discussed.

Based on the finite strain model, a porous model for non-isothermal, multi-phase moisture and volatile organic contamination (VOC) transport (in solid, liquid and gas phases) for unsaturated soil is presented in Chapter 5. A detailed derivation of the new model will be presented. A parametric study for volatile organic contamination transport in an unsaturated porous medium is carried out.

Chapter 6 outlines the shallow water expansion for the tidal dynamic in a coastal aquifer with a sloping beach, a classic free surface flow in porous media. In this chapter, we discuss the limitation of previous technique used in the shallow water expansion for a sloping beach, and propose a new technique to overcome the limitation of the previous models. Based on this new technique, the analytical solutions up to the second-order are presented and discussed. Within the same framework, a numerical technique is introduced to automatically generate the

perturbation solution for the tidal dynamic in a coastal aquifer. Up to 24th-order solution is presented and discuss the effects of the high-order solution.

Chapter 7 focuses on the capillarity effects on tide-induced groundwater fluctuations in a coastal aquifer. First, based on the definition proposed by Parlange and Brutsaert (1987), an analytical solution up to the second order shallow expansion for a sloping beach is presented. Second, a new definition of capillarity fringe is proposed and a new solution is presented.

Chapter 8 further discusses the tidal dynamic in a coastal aquifer in estuarine zone with two-dimensional model. Again, shallow water expansion is adopted to explore the mechanics of tide-induced groundwater table fluctuations in a coastal aquifer and effects of rhythmic shorelines. Capillarity effect is included in the second part of this chapter.

In addition to the above generalised problem, several problems have been further considered in Chapter 9. For example, the steepness expansion is proposed to further extend the applicable range of shallow water expansion; the analytical solution for tidal dynamics in leaky confined aquifers is derived; and springer-neap tide-induced beach water table fluctuations in sloping coastal aquifers is examined.

Chapter 11 discusses two recent developments for wave-seabed interactions. First, we introduce the concept of dynamic permeability, in which soil permeability is a function of pore pressures. The impact of dynamic permeability on the seabed response will be explored. Second, we introduce the non-Darcy flow model into the wave-seabed interactions, which overcomes the limitation of the conventional Darcy flow model.

In Chapter 12, a recent numerical model, PORO-FSSI-FOAM, based on OpenFOAM, is introduced. This chapter will focus on the applications to different breakwaters, including composite breakwaters, submerged breakwaters as well as three-dimensional model for the cases around breakwater heads and offshore detached breakwaters.

Chapter 13 focuses on the offshore pipelines. Two common protection techniques commonly used in offshore pipeline projects will be examined through theoretical studies. These include trench layer and articulated concrete mattresses (ACMs). In addition to theoretical study, possible design methods for seabed protection of the pipeline are suggested.

Finally, Chapter 14 discusses the applications of the porous model to liquefaction around pile-typed foundations. First, we examine the wave (current)-induced momentary seabed response around a single piled foundation, based on PORO-FSSI-FOAM. Second, a group of piles will be discussed. Third, the seabed liquefaction around a jacket support structure is examined.

This book provides a starting point for junior researchers who are interested in the field of porous flow. There are more research tasks can be further studied in the future.

Dong-Sheng Jeng & Lin Cui

Acknowledgments

It has been over ten years since the publisher approached the first author regarding publishing a book in the field of porous flow. The initial idea of this book was only the second part of the final version. As more PhD students projects reached completion, this resulted in the expansion of the research field. The scope of this book has been expanded three times of the initial idea. It is not easy to keep going when the writing scopes have been expanding.

In preparing this book, numerous PhD students and co-workers have made contribution, even though they are not listed as co-authors. This includes: Dr. Huijie Zhang (Jiansu University, China), Dr. Sheng (Sherry) Wu (GHD consultant, Brisbane) have contributed to the first part of this book during their PhD study; while Professor Andrew Barry (EPFL, Switzerland), Professor Brian Seymour (UBC, Canada) and Professor Ling Li (Westlake University, China) contribute to the theoretical development of the second part of the book. The third part of the book includes the fundamental study during my PhD project, and numerous PhD student projects and Postdoctoral projects, including Professors Jisheng Zhang and Hongyi (David) Zhao (Hohai University, China), Professor Fuping Gao, Professor Jianhong Ye, Dr. Wengang Qi (Chinese Academy of Science, China), Professor Mouzhen Zhou (Beijing Jiaotong University, China) and Dr. Zuodong Liang (Guanxi University, China). Without these collaborations, this book will not be able to completed successfully.

Finally, the authors are grateful for the support from the following funding scheme during preparing this book: Qingdao University of Technology Academic Monograph Publication Funding, Qingdao University of Technology Scientific Research Start-up Funding (C2019-195), Shandong Provincial Overseas High-level Talent Workstation and National Natural Science Foundation of China (52271281).

Dong-Sheng Jeng & Lin Cui
October 2022

Taylor & Francis
Taylor & Francis Group
http://taylorandfrancis.com

1 Introduction

1.1 PORO-ELASTIC THEORY

Porous materials can be found in many different places in nature, for example, soil, sand and rocks, and plant tissue as living bodies, etc. Porous materials take many shapes and forms. They can be granular materials or porous solids such as sand, clay or silt, which are commonly discussed in soil mechanics. They could be volcanic rock and sandstones, which contain pores of millimeter or even centimeter size. These are geomaterials occurring in nature. Porous materials can also be manufactured, such as concrete and polyurethane foam, etc. For porous materials, pore space comes in various sizes, which could even be as small as nano size.

Poro-elastic theory has been widely applied in numerous engineering and scientific problems involved in multi-phase media (Cheng, 2016). For environmental science and civil-related engineering fields, we are interested in static and dynamic responses of porous media subject to environmental loading as well as other types of forces, such as those of thermal and chemical origin. These are generally known as poromechanics, which was first created from the Biot Conference on Poromechanics (Thimus et al., 1998).

This book will provide basic mechanics of poro-elastic theory and its applications in three main disciplines of porous flow, including (1) solute and contaminant transport in a deformable porous medium; (2) tidal dynamics in coastal aquifers for various aquifer conditions; and (3) basic seabed mechanics under dynamic loading, and applications to marine engineering infrastructures. This book will provide scientific researchers and industry and government agents with updated knowledge in these fields with applications to porous flow. In the following sections, we will discuss the above three disciplines and highlight possible future scopes.

More detailed fundamental knowledge of linear poro-elastic theory can be found in Wang (2000), while the applications of poro-elasticity to various problems can be found in Cheng (2016).

1.2 SOLUTE TRANSPORT IN A POROUS MEDIUM

Solute transport in a porous medium is one of the key problems in environmental science and engineering, due to development of urban areas and growth of industry activities. Various environmental situations are typically investigated using solutions of the solute transport equations considering the porous medium to be rigid (Bear, 1972; Barry and Sposito, 1989; Barry, 1990, 1992). Since the mid-twentieth century, numerous researchers have worked on the advection-dispersion equation (ADE) through analytical approximations (Wang and Zhan, 2015), numerical simulations (Craig and Rabideau, 2006; Boso et al., 2013) and laboratory experiments (Rolle et al., 2012) in fully saturated soil environments. Furthermore, solute transport in an unsaturated soil matrix has been studied by several researchers. For example,

Fityus et al. (1999) focused on the effects of the degree of saturation and presented pollutant migration in a steady-state unsaturated soil liner under a landfill. In such cases, no volume change occurs during the transport process; therefore, the advection is then determined solely by the hydraulic gradient. However, deformation of the porous media may lead to unsteady advective flow. Examples include solute transport through a clay liner during waste-filling operations, dredged contaminated sediment after placement in a confined disposal facility, consolidation of contaminated sediments due to overburden of capping material, and solute transport in cartilage under mechanical load (Smith, 2000; Arega and Hayter, 2008; Zhang and Szeri, 2005). In these cases, the deformation of porous media and solute transport processes occur simultaneously, and coupled effects should be considered.

Modeling of contaminant transport through deformable porous media has received attention during the last two decades. Potter et al. (1994) presented a model for dissolved phase advection-dispersion transport using Terzaghi's consolidation theory. Smith (2000) derived a one-dimensional (1D) theory of contaminant migration based on a small strain analysis of a consolidating soil. The equations were recast in a material coordinate system for problems involving large deformation or a moving boundary. Later, Peters and Smith (2002) further extended their previous model of Smith (2000) for transient solute transport within a deformable porous medium. Moo-Young et al. (2003) presented experimental results of contaminant transport in soil specimens undergoing consolidation induced by a centrifuge in which consolidation was observed to accelerate solute migration. Based on the Terzaghi consolidation and ADE (advection-dispersion equation), Alshawabkeh et al. (2005) and Alshawabkeh and Rahbar (2006) calculated the contaminant mass flux that was enhanced by the capping load-induced sediment consolidation and concluded that advection caused by consolidation would accelerate the breakthrough of the contaminant through the cap. Arega and Hayter (2008) used a 1D large strain consolidation and contaminant transport model to simulate capping consolidating contaminated sediment based on reduced coordinates.

In addition to the approaches for small strain, Lewis et al. (2009) generalized the finite strain consolidation and solute transport model of Peters and Smith (2002) by incorporating self-weight in the consolidation process, and included more general constitutive functions for consolidation and transport coefficients. Fox and his co-workers Fox (2007*a*,*b*); Fox and Lee (2008) adopted a piecewise linear approach to handle coupled 1D large strain consolidation and two-dimensional (2D) solute transport in a confined disposal facility for dredged contaminated sediments. In real environments, unsaturated porous media are common (Fityus et al., 1999). For example, the groundwater table is located some distance below a landfill geomembrane, in which case the soil beneath the landfill will be partially saturated (Fityus et al., 1999).

Recently, adopting Biot's consolidation theory (Biot, 1941), Zhang et al. (2012*a*) further developed the small strain model proposed by Peters and Smith (2002) to account for the degree of saturation and fluid compressibility. When soil deformation increases, large strain models are required, as reported in Fox (2007*a*,*b*) and Zhang et al. (2013*b*).

Benefiting from the simplicity of the traditional ADE, the conventional model enjoys vast applicability, including in the modeling of solute transport, especially of purely diffusive flows in a heterogeneous soil matrix. For example, field measurement (Ellsworth and Jury, 1991) and soil column experimental evaluations have been conducted to examine the solute behavior in layered soil (Sharma et al., 2014). Satisfying the solute mass conservation principle at soil interfaces, Leij and Van Genuchten (1995) derived an analytical solution for solute transport in two-layer porous media with the technique of Laplace transformation. Liu et al. (1998) provided an analytical solution with an arbitrary initial condition and inlet boundary condition. Later, Li and Cleall (2011) extended previous studies to incorporate different combinations of fixed concentration, zero flux, and fixed flux conditions at inlet and outlet boundaries. However, to date, the effect of soil deformation on the solute transport within a layered soil has not been fully studied. The only attempt, for a coupled solute transport and consolidation model in multi-layer soil, was made by Pu and Fox (2016, 2015) using the piecewise method. They compared the numerical modeling results of two-layer soil and homogeneous soil to highlight the impact of layered soil in a fully saturated soil matrix undergoing significant deformation. However, for an unsaturated layered soil, relevant studies had not been available in the literature until Wu and Jeng (2017).

Section I focuses on the solute transport in an unsaturated deformed porous medium. This section consists of four chapters. Chapter 2 will discuss the 1D model for solute transport in an unsaturated porous medium, based on the assumption of small strain. Both consolidation and solute transport models will be coupled through the pore pressures in the porous medium. The governing equations are derived and further applied to a liner landfill system (Zhang et al., 2012*a*). Based on the scaling analysis, the importance of each term will be examined. Within the framework, the 1D model will be further extended to an unsaturated layered soil system (Wu and Jeng, 2017) with detailed parametric study.

Chapter 3 outlines the finite strain model for solute transport in an unsaturated porous medium (Zhang et al., 2013*b*). Variations of key parameters in the consolidation-induced solute transport process will be discussed. The finite strain model will be further applied to a landfill liner with a detailed parametric study.

Chapter 4 considers a porous medium with variable compressibility (associated with degree of saturation) and hydraulic conductivity (Wu et al., 2020). In this model, both compressibility of pore fluid and hydraulic conductivity (i.e., soil permeability) vary with dynamic pore pressures. With the new model, the effects of dynamic compressibility and hydraulic conductivity on the solute transport in an unsaturated porous medium will be discussed.

Based on the finite strain model, a porous model for non-isothermal, multi-phase moisture and volatile organic contamination (VOC) transport (in solid, liquid and gas phases) for unsaturated soil will be presented in Chapter 5. A detailed derivation of the new model will be presented. A parametric study for VOC transport in an unsaturated porous medium will be carried out.

There are a few future scopes in the field of solute transport in porous media:

- The finite strain model for solute transport in porous media is only limited to 1D. Following the similar framework in Chapter 3, this could be further extended to 2D and 3D cases.
- Similarly, the concept of dynamic compressibility of pore fluid and hydraulic conductivity can first be extended to 2D and 3D cases, as well as finite strain models.
- Contaminant transport in marine environments is one of the important problems for marine pollution. The existing models for consolidation-induced solute transport in porous media can be further applied to the problem by introducing the hydrodynamic loading instead of static loading.

1.3 TIDAL DYNAMICS IN COASTAL AQUIFERS

Groundwater dynamics within a sandy beach influences erosion control (Grant, 1948), saltwater intrusion (Dagan and Zeitoun, 1998), chemical transformation (Trefry, 1999) and biological activities (McArdle and McLachan, 1991; Pollock and Hummon, 1971). In particular, accurate prediction of dynamic groundwater hydraulics in coastal zones is required to improve coastal management.

Most studies of coastal aquifers are based on the Boussinesq equation together with the Dupuit–Forchheimer assumption (Bear, 1972; Dagan, 1967). The nonlinear governing equation was derived by Dagan (1967) and subsequently approximated by expanding in terms of a perturbation parameter representing the shallow water approximation. Dagan (1967) showed that higher-order approximations are significant for fine sand with lower hydraulic conductivity. These solutions are only applicable when the amplitude of the motion is small compared to the mean water depth. Parlange et al. (1984) extended the work of Dagan (1967) to a higher-order solution to describe the free surface elevation of the groundwater flow.

In the early stage, to simplify the problem, most previous investigations for water table fluctuations in coastal aquifers have considered the case of a vertical beach instead of the more realistic case of a sloping beach. Nielsen (1990) was the first to derive an analytical solution where the assumption of a fixed location of the shoreline boundary condition is relaxed. Later, numerous high-order analytical approximations for tidal dynamics in a sloping beach were proposed to improve the limitation of Nielsen (1990)'s model (Li et al., 2000*b*; Teo et al., 2003; Stojsavljevic et al., 2012).

In the conventional approach to describing tidal fluctuations in coastal aquifers, it is often assumed that the upper free surface is a sharp boundary between saturated and dry aquifer material. This assumption is an oversimplification in many situations, as the upper boundary is not abrupt but a diffuse transition zone of partially unsaturated material. Parlange and Brutsaert (1987) proposed a capillarity correction to describe the effect of the diffuse transition zone based on the Boussinesq equation. Later, Barry et al. (1996) extended Parlange and Brutsaert (1987)'s work to order $O(\alpha^2)$, and concluded that the capillarity correction is important at high frequencies. Based on Parlange and Brutsaert (1987), Li et al. (1997*a*) further examined the

capillarity on the groundwater fluctuation due to run up through numerical modeling. Jeng et al. (2005*c*) proposed a new definition of capillarity effects and derived a new analytical solution.

The aforementioned solutions have been limited to 1D in the cross-shore direction, in which case the alongshore variability of the coastline cannot be examined. Some researchers have considered the shape of the coastline through 2D models. Among these, Sun (1997) developed a 2D analytical solution for tidal fluctuation in aquifers adjacent to estuaries. However, the boundary condition in his model ignored the effects of oceanic tides, as pointed out by Li et al. (2000*a*). To overcome the problem, Li et al. (2000*a*) developed another analytical solution for the case of an L-shaped coastline using the Green's function approach. Their solution demonstrated the significant influence of the interaction of estuarine and oceanic tides on water table fluctuations. Later, Li et al. (2002*b*) derived an approximate analytical solution for tide-induced water table fluctuations in a coastal aquifer bounded by rhythmic shorelines. In their model, both sinusoidal and natural coastlines were considered. However, only the first-order approximation was derived. Higher-order approximations for tided-induced groundwater fluctuation in a sloping beach with rhythmic shorelines were further developed in Jeng et al. (2005*a*,*e*).

Section II mainly focuses on the tidal dynamics in coastal aquifers. This section consists of four chapters. Chapter 6 outlines the shallow water expansionfor tidal dynamics in coastal aquifers with a sloping beach, a classic free surface flow in porous media. In this chapter, we discuss the limitation of previous techniques used in the shallow water expansion for a sloping beach, and propose a new technique to overcome the limitation of the previous models (Nielsen, 1990; Li et al., 2000*b*). Based on this new technique, the analytical solutions up to the second-order are presented and discussed (Teo et al., 2003). With the same framework, a numerical technique is introduced to automatically generate the perturbation solution for tidal dynamics in coastal aquifers. Up to the 24th-order solution is presented, and the effects of the high-order solution are discussed(Stojsavljevic et al., 2012).

Chapter 7 focuses on the capillarity effects on tide-induced groundwater fluctuations in a coastal aquifer. First, based on the definition proposed by Parlange and Brutsaert (1987), an analytical solution up to the second-order shallow expansion for a sloping beach is presented Jeng et al. (2005*c*). Second, a new definition of capillarity fringe is proposed and a new solution is presented.

Chapter 8 further discusses the tidal dynamic in a coastal aquifer in estuarine zone with a 2D model. Again, shallow water expansion is adopted to explore the mechanics of tide-induced groundwater table fluctuations in coastal aquifers and effects of rhythmic shorelines (Jeng et al., 2005*a*). Discussion of the capillarity effect is included in the second part of this chapter (Jeng et al., 2005*e*).

In addition to the above generalised problem, several problems have been further considered in Chapter 9. For example, the steepness expansion was proposed to further extend the applicable range of shallow water expansion (Jeng et al., 2005*d*); the analytical solution for tidal dynamics in leaky confined aquiferswas derived (Jeng et al., 2002); and springer-neap tide-induced beach water table fluctuations in sloping coastal aquifers (Jeng et al., 2005*b*).

The following scientific topics could be further considered in the field of tidal dynamics in coastal aquifers:

- Tide-induced groundwater fluctuations in coastal aquifers will directly affect the horizontal loading acting on the support structures, for example, pile foundations for civil engineering structures in coastal zones, such as Surface Paradise, Gold Coast, Australia. The models outlined in this book could be further linked with geotechnical design for the pile foundation in this region.
- The perturbation technique introduced in Chapter 6 could be further applied to leaky confined aquifers with a sloping aquifer. The impact of higher-order solutions can then be examined and used to clarify the applicable range of different solutions.
- Coastal aquifers are normally not homogeneous porous media. How the non-homogeneous porous media affect the tide-induced groundwater fluctuation is a topic worth exploring in the future.

1.4 POROUS MODELS FOR FLUID-SEABED INTERACTIONS AROUND MARINE STRUCTURES

Poro-elastic theory has been commonly adopted to investigate the mechanics of the wave-induced soil response in a porous seabed since the 1970s. In the past few decades, considerable efforts have been devoted to the problem of the wave–seabed interactions around marine structures. The major reason for the growing interest is that a few marine infrastructures have been damaged by the wave-induced seabed instability and its association with the failure of the infrastructure rather than construction deficiencies (Christian et al., 1974; Lundgren et al., 1989). Another applications of the poro-elastic theories for wave-soil interactions are for field measurements, such as the determination of the wave surface profiles using measured pore pressure in marine sediments Raubenheimer et al. (1998), determination of the shear modulus of soil (Yamamoto and Trevorrow, 1991), the directional spectra of ocean surface waves (Nye and Yamamoto, 1994), and acoustic wave propagating through porous media (Yamamoto and Turgut, 1988).

Two mechanisms of the wave-induced soil response have been reported in the literature, based on the observations in the laboratory and field measurements (Zen and Yamazaki, 1990*a*; Nago et al., 1993; Sumer and Fredsoe, 2002). The first mechanism resulted from the *transient* or *oscillatory* excess pore pressure and is accompanied by attenuation of the amplitude and phase lag in the pore pressure changes (Yamamoto et al., 1978; Madsen, 1978). This is particularly important for small-amplitude waves and it could only liquefy momentarily in the seabed under wave troughs (Jeng, 2012). The second mechanism is termed as the *residual* pore pressure, which is the buildup of excess pore pressure caused by contraction of the soil under the action of cyclic loading (Seed and Rahman, 1978; Sumer and Fredsoe, 2002). As reported in Jeng (2012), the residual mechanism is more important for large wave loading.

Basic mechanics for the wave-seabed interactions have been intensively studied since Yamamoto et al. (1978); Madsen (1978); Seed and Rahman (1978) with two different streams. One is for oscillatory mechanism (Yamamoto et al., 1978; Madsen, 1978) and the other is for residual mechanism (Seed and Rahman, 1978). However, these two mechanisms have not been considered together in one model, although Jeng and Ou (2010) tried to use both mechanisms for the assessment of seabed liquefaction.

For the transient soil response and associated momentary seabed liquefaction, based on Biot's poro-elastic theory (Biot, 1941), analytical approximations for an isotropic homogeneous seabed have been adopted at the early stage. Yamamoto et al. (1978) and Madsen (1978) are two classic solutions and have been commonly cited in the literature. Based on the mixture theory, Mei and Foda (1981) proposed the boundary-layer approximation with a simple form. Okusa (1985) investigated the effects of degree of saturation on the soil response and phase lags between pore pressures and dynamic wave pressures. Later, this framework (Yamamoto-Madsen Model) has been further extended to 3D short-crested wave system (Hsu et al., 1993; Hsu and Jeng, 1994), a layered seabed (Yamamoto, 1981; Rahman et al., 1994; Hsu et al., 1995), cross-anisotropic seabed (Jeng, 1997*a*), or variable permeability (Jeng and Seymour, 1997; Kitano and Mase, 2001). Numerical modeling has also been adopted for more complicated problems with marine infrastructure (Gatmiri, 1990, 1992; Jeng and Lin, 1996, 2000*a*; Jeng et al., 2000; Jeng and Lin, 2000*b*; Lin and Jeng, 2000).

Regarding pore pressure accumulation (buildup) and the associated residual seabed liquefaction, based on Seed and Rahman (1978), numerous analytical solutions have been proposed (McDougal et al., 1989; Cheng et al., 2001; Sumer and Fredsoe, 2002; Jeng and Seymour, 2007; Jeng et al., 2007). Later, Jeng and Zhao (2015) proposed a new definition of the source term in the governing equation for the residual pore pressures with the concept of instant shear stresses. This framework has been further applied for different marine infrastructures(Zhao et al., 2014, 2015; Zhao and Jeng, 2016; Zhao et al., 2022).

In addition to the above quasi-static model, partial dynamic and full dynamic soil behaviours have been included in the models for wave-seabed interactions around marine structures. Jeng et al. (1999) was the first attempt for the partial dynamic model ($u-p$ approximation) in an infinite seabed without a structure. Later, this model was further extended to a seabed with finite thickness (Jeng and Rahman, 2000) and marine infrastructures (Jeng et al., 2013; Ye et al., 2013). In addition to the $u-p$ approximation, Jeng and Cha (2003) further derived an analytical solution for the wave-seabed interactions with full dynamic soil behaviour and clarified the applicable range between Biot's consolidation model and full dynamic model. Later, Ulker et al. (2009) proposed a similar solution and provided a more precise applicable range for three different approaches, quasi-static, partial dynamic and full dynamic models. These results (Jeng and Cha, 2003; Ulker et al., 2009) are particularly important for numerical modeling in the industry and helps them decide which model they should adopt.

An EU program during 2002–2004, LIMAS (Liquefaction around Marine Structures), specifically focused on the seabed liquefaction around various marine infrastructures such as caisson-type breakwaters, pipelines and mono-piles. The program was led by led by Professor B. M. Sumer at DTU, and ten research institutes and industries in Europe were involved with this program. The research outcomes of this program were published in two special issues of an ASCE journal (Sumer, 2006, 2007) and a book (Sumer, 2014).

Section III will focus on the recent developments in the wave-seabed interactions around marine infrastructures. This section consists of five chapters. Among these, Chapter 10 will discuss the basic mechanisms of the wave-seabed interactions in a porous seabed. Most previous models for both oscillatory and residual mechanisms will be summarised and discussed. A few mistakes in the previous study for the residual liquefaction (Jeng and Seymour, 2007) will be corrected. A new concept of the two-way coupling model (Zhai and Jeng, 2022) will be introduced.

Chapter 11 discusses two recent developments for wave-seabed interactions. First, we introduce the concept of dynamic permeability, in which soil permeability is function of pore pressures (Zhou et al., 2021*a*). The impact of dynamic permeability on the seabed response will be explored. Second, we introduce the non-Darcy flow model into the wave-seabed interactions, which overcomes the limitation of the conventional Darcy flow model.

Chapters 12-14 will discuss seabed liquefaction around marine structures. In Chapter 12, a recent numerical model, PORO-FSSI-FOAM(Liang et al., 2020), based on OpenFOAM, will be introduced. This chapter will focus on the applications of different breakwaters, including composite breakwaters, submerged breakwaters as well as a 3D model for the cases around breakwater heads and offshore detached breakwaters.

Chapter 13 focuses on the offshore pipelines. Two common protection techniques commonly used in offshore pipeline projects will be examined through theoretical studies. These include trench layer and articulated concrete mattresses (ACMs). In addition to theoretical study, possible design methods for seabed protection of the pipeline are suggested.

Chapter 14 discusses the applications of the porous model to liquefaction around pile-typed foundations. First, we examine the wave (current)-induced momentary seabed response around a single piled foundation, based on PORO-FSSI-FOAM. Second, a group of piles will be discussed. Third, the seabed liquefaction around a jacket support structure is examined.

Since offshore geotechnics is a new research topic that has attracted great attention among coastal and geotechnical engineers, numerous challenges still exist in the engineering design. We outlined the following future scopes for readers:

- The concept of two-way coupling for wave-seabed interactions can be further applied to the problem of wave-seabed-structure interactions. The porous seabed models can be further linked with the conventional scour model to provide more precised prediction of local scour around marine

structures. This will not only integrate two different seabed failure models, but also provide a better understanding of the physical process.

- The idea of dynamic permeability and non-Darcy flow models can be developed for wave-seabed interactions around marine infrastructures.
- Marine energy has become one of the hottest research topics in offshore industry due to the growing development of offshore activity. The seabed stability of the support structures, such as offshore wind turbine system, is one of the important tasks. The models outlined in this book could be further developed for these marine energy facilities.
- From the scientific aspect, the existing models for wave-induced residual seabed response have been limited to the quasi-static model, which is insufficient for some engineering problems such as the rocking of structures. A new model for residual liquefaction with partial dynamic or full dynamic soil behaviour is desired, but it has been not available in the literature yet.

Taylor & Francis
Taylor & Francis Group
http://taylorandfrancis.com

Section I

Solute Transport in Porous Media

Taylor & Francis
Taylor & Francis Group
http://taylorandfrancis.com

2 Solute Transport in a Porous Medium: 1D Small Strain Model

2.1 INTRODUCTION

Contaminant mass transport through porous media is usually described by well-established conventional advection dispersion transport models (Bear, 1972; Barry, 1992) with the ability to account for advection, dispersion, and sorption. Since the mid-20th century, numerous researchers have worked on the advection-dispersion equation (ADE) through analytical approximations (Wang and Zhan, 2015), numerical simulations (Craig and Rabideau, 2006; Boso et al., 2013) and laboratory experiments (Rolle et al., 2012) in fully saturated soil environments. Furthermore, solute transport in an unsaturated soil matrix has been studied by several researchers. For example, Fityus et al. (1999) focused on the effects of the degree of saturation and presented pollutant migration in a steady-state unsaturated soil liner under a landfill, and Kumar and Dodagoudar (2010) proposed a stable and convergent 2D numerical model using the mesh-free technique.

All the aforementioned studies were based on the assumption of rigid porous media, that the volume of the porous media does not change and advective flow is only induced by an external hydraulic gradient. In fact, soil volume change (i.e., soil consolidation) occurs simultaneously with solute transport in many cases. For example, it occurs where the field is under an applied load (self-weight, fill placement, finite size loading, etc.) or experiencing changes in the groundwater table (pumping, artesian wells, etc.). In such cases, the coupled effect of soil deformation and solute transport needs to be considered. Alshawabkeh et al. (2004) showed that the excess pore pressure dissipation produced a transient advective flux of contaminants, which had a strong influence on overall flux.

Modeling of contaminant transport through deformable porous media has received attention during the last two decades. Potter et al. (1994) presented a model for dissolved phase advection-dispersion transport using Terzaghi's consolidation theory. Smith (2000) derived a 1D theory of contaminant migration based on a small strain analysis of a consolidating soil. The equations were recast in a material coordinate system for problems involving large deformation or a moving boundary. Peters and Smith (2002) extended the previous model of Smith (2000) for transient solute transport within a deformable porous medium for both small and large deformations. Moo-Young et al. (2003) presented experimental results of contaminant transport in soil specimens undergoing consolidation induced by a centrifuge.

With the coupled Terzaghi's consolidation and ADE equation, Alshawabkeh et al. (2005) calculated the contaminant mass flux that was enhanced by the capping load-induced sediment consolidation. They concluded that advection caused by consolidation will accelerate the breakthrough of the contaminant through the cap (Alshawabkeh et al., 2005). Arega and Hayter (2008) used a 1D large strain consolidation and contaminant transport model to simulate capping consolidating contaminated sediment based on reduced coordinates.

In real environments, unsaturated porous media are common (Okusa, 1985; Fityus et al., 1999). For example, marine sediments are often unsaturated due to gas produced in biochemical processes. Another case is where the groundwater table is located some distance below a landfill geomembrane, in which case the soil beneath the landfill will be partially saturated (Fityus et al., 1999). Recently, adopting Biot (1941)'s consolidation theory, Zhang et al. (2012*b*) further developed the small strain model (Peters and Smith, 2002) to account for the degree of saturation and fluid compressibility. When soil deformation increases, large strain models are required, as reported in Fox (2007*a*,*b*) and Zhang et al. (2013*b*). In this chapter, we only used a small strain model as the first approximation.

Benefiting from the simplicity of the traditional ADE, the conventional model enjoys vast applicability, including in the modeling of solute transport, especially of purely diffusive flows in a heterogeneous soil matrix. For example, field measurement (Ellsworth and Jury, 1991) and soil column experimental evaluations have been conducted to examine the solute behavior in layered soil (Sharma et al., 2014). Satisfying the solute mass conservation principle at soil interfaces, Leij and Van Genuchten (1995) derived an analytical solution for solute transport in two-layer porous media with the technique of Laplace transformation. Liu et al. (1998) provided an analytical solution with an arbitrary initial condition and inlet boundary condition. Later, Li and Cleall (2011) extended previous studies to incorporate different combinations of fixed concentration, zero flux, and fixed flux conditions at inlet and outlet boundaries. However, to date, the effect of soil deformation on the solute transport within a layered soil has not been fully studied. The only attempt, for a coupled solute transport and consolidation model in multi-layer soil, was made by Pu and Fox (2016, 2015) using the piecewise method. They compared the numerical modeling results of two-layer soil and homogeneous soil to highlight the impact of layered soil in a fully saturated soil matrix undergoing significant deformation. However, for an unsaturated layered soil, relevant studies have not been not available in the literature until Wu and Jeng (2017).

In this chapter, the consolidation-induced solute transport in an unsaturated porous media will be investigated. The case of a landfill liner is considered, for which a 1D Biot's consolidation equation (Biot, 1941) is used to describe flow in an unsaturated porous medium incorporating the self-weight of the liner. The situation considered is that of compressible pore-water at a fixed saturation. The ADE that is typically used to describe solute transport through a rigid porous medium (Bear, 1972) is modified to include partial saturation, CPW (compressible pore-water), SVP (spatial variation of porosity) and longitudinal dispersivity. The equations are non-dimensionalized, identifying nine important parameters. The importance of

these parameters is discussed for a range of physical conditions. A hypothetical engineered landfill liner is used as an illustrative example, demonstrating the influence of partial saturation and the loading process on contaminant migration. The model will be further applied to the case of layered soil.

2.2 THEORETICAL MODEL

In this section, the governing equations for 1D consolidation and solute transport problems will be outlined and integrated to understand the effects of soil deformation on the solute transport. The detailed mathematical derivations can be referred to Appendix 2.6.

2.2.1 CONSOLIDATION EQUATION

Here we state the basic equations linking flow velocity with excess pore pressure. The 1D unsaturated fluid storage (the mathematical derivation is given in Appendix 2.6) and the 1D Biot equations (Tsai et al., 2006) are expressed as

$$S_r n\beta \frac{\partial p^e}{\partial t} + S_r \frac{\partial^2 u}{\partial t \partial z} = \frac{1}{\rho_w g} \frac{\partial}{\partial z}\left(K \frac{\partial p^e}{\partial z}\right), \tag{2.1a}$$

$$G\frac{2(1-\nu)}{(1-2\nu)} \frac{\partial^2 u}{\partial z^2} + \left(1-n^0\right)\left(\rho_s - \rho_w\right) g \frac{\partial u}{\partial z} = \frac{\partial p^e}{\partial z}, \tag{2.1b}$$

where p^e is excess pore pressure; u is soil displacement; S_r represents the degree of saturation; n is current porosity; n^0 is initial porosity; K is hydraulic conductivity; G is shear modulus; ν is Poisson's ratio; ρ_w is the density of pore-water and ρ_s is the density of solid materials. Note that a compressive effective normal stress is negative here.

In this study, density of both components of soil are independent of the dilute solute concentration (Klett et al., 2005). When the sorption occurs, the mass of a unit volume of solid grains (i.e., density) ρ_s becomes $\rho_s(1 + K_d c_f)$, where K_d is the partitioning of the contaminant. Using the clay liner as an example, the measured VOC concentration in the landfill leachate ranges from 10 to 10^4 μg/l (Klett et al., 2005). Lewis et al. (2009) adopted the distribution coefficient $K_d = 1$ mg/l, leading to a change of the density of solids due to sorption of less than 0.001%, which is negligible. Consequently, it is reasonable to assume that ρ_s is independent of the solute mass concentration. Therefore, the assumption of volume-preserving deformation of the solid phase embedded in the derivation (see Appendix 2.6) can be ensured, i.e., $\nabla \cdot \vec{v}_s = 0$ (Bear and Cheng, 2010).

The compressibility of pore fluid in clay, β, depends on the degree of saturation, S_r, the amount of dissolved air in pore-water and absolute air pressure. It can be

estimated by (Fredlund and Rahardjo, 1993):

$$\beta = \frac{S_r}{K_{w0}} + \frac{1 - S_r + r_h S_r}{P_a + P_{atm}}, \tag{2.2}$$

where K_{w0} is the bulk modulus of pore-water, which is taken as 1.95×10^9 N/m^2 (Yamamoto et al., 1978); r_h denotes volumetric fraction of dissolved air within pore-water; P_a denotes gauge air pressure and P_{atm} represents the atmosphere pressure. In the high saturation limit, when $r_h = 0.02$, $S_r = 0.8 \sim 1.0$ and β falls into the range of $2 \times 10^{-6} \sim 2 \times 10^{-7}$ Pa^{-1}.

2.2.2 SOLUTE TRANSPORT EQUATION

Following Peters and Smith (2002), the solute transport equation in a 1D deforming porous medium is

$$\frac{\partial \left(nS_r c_f\right)}{\partial t} + \frac{\partial \left[(1-n)\, c_s\right]}{\partial t} = -\frac{\partial}{\partial z}\left[nS_r\left(-D\frac{\partial c_f}{\partial z} + v_f c_f\right) + (1-n)\, v_s c_s\right], \tag{2.3}$$

where c_f and c_s are the concentration of the solute in the fluid and solid phase, respectively; D represents the hydrodynamic dispersion coefficient, which is the sum of the effective molecular diffusion (D_m) and dispersion ($\alpha_L(v_f - v_s)$), where v_f denotes the average fluid velocity and v_s is the velocity of the solid. Herein, the effective molecular diffusion tensor, mechanical dispersion tensor and consequently the hydrodynamic dispersion tensor reduce to scalar for the 1D isotropic soil.

By definition the concentration of the contaminant in the solid phase is

$$c_s = \rho_s S = \rho_s F(c_f, t), \tag{2.4}$$

where S is the mass of contaminant sorbed onto the solid phase per unit mass of solid phase, and F is a function describing the relationship. If sorption is an equilibrium linear reversible process, then, S in (2.4) can be expressed as (Smith, 2000)

$$S = K_d c_f, \tag{2.5}$$

in which K_d describes the partitioning of the contaminant.

Based on the mass balance equations for the fluid, (2.27), and solid phases, (2.34) (see Appendix 2.6), and considering the solid particles as incompressible (i.e., ρ_s is constant), (2.3) becomes

$$\begin{aligned} S_r n\frac{\partial c_f}{\partial t} + (1-n)\frac{\partial c_s}{\partial t} = &\frac{\partial}{\partial z}\left(S_r n D\frac{\partial c_f}{\partial z}\right) - S_r n v_f \frac{\partial c_f}{\partial z} - (1-n)\, v_s \frac{\partial c_s}{\partial z} \\ &+ S_r n \beta\left(\frac{\partial p^e}{\partial t} + v_f \frac{\partial p^e}{\partial z}\right) c_f. \end{aligned} \tag{2.6}$$

Assuming the linear sorption relationship described by (2.4) and (2.5), and using (2.49) in Appendix 2.6, then, (2.6) becomes

$$\begin{aligned}[S_r n+(1-n)\rho_s K_d]\frac{\partial c_f}{\partial t} &= S_r n D_m \frac{\partial^2 c_f}{\partial z^2} - \alpha_L \frac{K}{\rho_w g}\frac{\partial p^e}{\partial z}\frac{\partial^2 c_f}{\partial z^2} \\ &+ \frac{\partial c_f}{\partial z}\left\{-\alpha_L S_r n\beta \frac{\partial p^e}{\partial t} - \alpha_L S_r \frac{\partial^2 u}{\partial z \partial t}\right. \\ &+ \frac{\alpha_L \beta K}{\rho_w g}\left(\frac{\partial p}{\partial z}\right)^2 + S_r D_m \frac{(1-n)^2}{1-n^0}\frac{\partial^2 u}{\partial z^2} \\ &\left.+ \frac{K}{\rho_w g}\frac{\partial p^e}{\partial z} - [S_r n+(1-n)\rho_s K_d]\frac{\partial u}{\partial t}\right\} \\ &+ S_r n\beta \frac{\partial p^e}{\partial t}c_f - \beta \frac{K}{\rho_w g}\left(\frac{\partial p^e}{\partial z}\right)^2 c_f \\ &+ S_r n\beta \frac{\partial u}{\partial t}\frac{\partial p^e}{\partial z}c_f.\end{aligned} \tag{2.7}$$

Details of the mathematical derivation are given in Appendix 2.6.

It is worthwhile to compare the above equation, (2.6), with the transport equation proposed by Peters and Smith (2002) (Eq. (30) in their paper). In the present notation, their equation (Peters and Smith, 2002) is

$$n\frac{\partial c_f}{\partial t} + (1-n)\frac{\partial c_s}{\partial t} = \frac{\partial}{\partial z}\left(nD\frac{\partial c_f}{\partial z}\right) - nv_f\frac{\partial c_f}{\partial z} - (1-n)v_s\frac{\partial c_s}{\partial z}. \tag{2.8}$$

Comparing (2.6) and (2.8), it is clear that (2.8) is a special case of (2.6) with $S_r = 1$, i.e., $\beta \approx 0$, while new terms due to the compressibility of the pore-water are contained in our equation.

Using the relationship between n and n^0 proposed by Tsai et al. (2006), i.e.,

$$n = n^0 + \left(1-n^0\right)\frac{\partial u}{\partial z}, \tag{2.9}$$

the equations become considerably more complex. However, our main focus is on the effect of unsaturation and compressibility of pore-water. If the deformation is relatively small, the volume strain, i.e., $\partial u/\partial z$ herein is consequently small, therefore n in (2.1a) and (2.7) will not differ appreciably from n^0 (Peters and Smith, 2002). On the other hand, although the reducing porosity can narrow the aqueous solute transport path, it tends to result in a bigger intrinsic pore-water velocity and in turn the advective flux. Therefore, it is a reasonable approximation of constant n employed in the following non-dimensional analysis. This approach has been used in the numerous investigations (Peters and Smith, 2002; Alshawabkeh et al., 2005; Zhang et al., 2012*a*).

Keeping temporal and spatial variations of porosity, the governing equations (2.1a), (2.1b) and (2.7) become

$$S_r n^0 \beta \frac{\partial p^e}{\partial t} + S_r \frac{\partial^2 u}{\partial t \partial z} = \frac{1}{\rho_w g} \frac{\partial}{\partial z} \left(K \frac{\partial p^e}{\partial z} \right), \tag{2.10a}$$

$$G \frac{2(1-\nu)}{(1-2\nu)} \frac{\partial^2 u}{\partial z^2} + (\rho_s - \rho_w) g \frac{\partial u}{\partial z} = \frac{\partial p^e}{\partial z}, \tag{2.10b}$$

and

$$\begin{aligned} \left[S_r n^0 + \left(1-n^0\right) \rho_s K_d \right] \frac{\partial c_f}{\partial t} &= S_r n^0 D_m \frac{\partial^2 c_f}{\partial z^2} - \alpha_L \frac{K}{\rho_w g} \frac{\partial p^e}{\partial z} \frac{\partial^2 c_f}{\partial z^2} \\ &+ \frac{\partial c_f}{\partial z} \left\{ -\alpha_L S_r n^0 \beta \frac{\partial p^e}{\partial t} - \alpha_L S_r \frac{\partial^2 u}{\partial z \partial t} \right. \\ &+ \frac{\alpha_L \beta K}{\rho_w g} \left(\frac{\partial p}{\partial z} \right)^2 + S_r D_m \left(1-n^0\right) \frac{\partial^2 u}{\partial z^2} \\ &\left. + \frac{K}{\rho_w g} \frac{\partial p^e}{\partial z} - \left[S_r n^0 + \left(1-n^0\right) \rho_s K_d \right] \frac{\partial u}{\partial t} \right\} \\ &+ S_r n^0 \beta \frac{\partial p^e}{\partial t} c_f - \beta \frac{K}{\rho_w g} \left(\frac{\partial p^e}{\partial z} \right)^2 c_f \\ &+ S_r n^0 \beta \frac{\partial u}{\partial t} \frac{\partial p^e}{\partial z} c_f. \end{aligned} \tag{2.10c}$$

The above equations are the governing equations for the consolidation-induced solute transport in a porous medium in 1D.

2.2.3 NON-DIMENSIONAL ANALYSIS OF COUPLED EQUATIONS

To understand the influence of each term in the governing equations, here the variables are non-dimensionalized and the order of each term is considered with a scaled quantity relative to a characteristic unit:

$$p^* = \frac{p^e}{p_c},\ t^* = \frac{t}{t_c},\ z^* = \frac{z}{l_c},\ u^* = \frac{u}{u_c},\ c^* = \frac{c_f}{c_0}, \tag{2.11a}$$

$$t_c = \frac{(1-2\nu) L^2 S_r \rho_w g}{2(1-\nu) G K}, \tag{2.11b}$$

$$p_c = \frac{2(1-\nu) G \left[S_r n^0 + \left(1-n^0\right) \rho_s K_d \right]}{(1-2\nu) S_r}, \tag{2.11c}$$

$$u_c = \frac{L\left[S_r n^0 + \left(1-n^0\right)\rho_s K_d\right]}{S_r}, \tag{2.11d}$$

where the characteristic unit for length; l_c, is the thickness of the soil layer; and c_0 is the reference solute mass concentration.

Herein, t_c is similar to the consolidation time factor T_v in Terzaghi consolidation theory (Terzaghi, 1925). However, t_c incorporates the degree of saturation rather than L^2/c_v ($c_v = [2(1-\nu)GK]/[\rho_w g(1-2\nu)]$, is the coefficient of consolidation). Both p_c (related to the soil shear modulus) and u_c reflect the influence of unsaturation and solute retardation due to sorption.

Table 2.1
Coefficients $A_1 - A_8$ used in the governing equations (2.12).

Coefficient	Expression	Physical meaning
A_1	$\frac{2G(1-\nu)n^0\beta}{1-2\nu}$	Ratio of skeleton modulus to that of pore fluid
A_2	$\frac{\left(1-n^0\right)(\rho_s-\rho_w)gL(1-2\nu)}{2G(1-\nu)}$	Body force effect on consolidation
A_3	$\frac{S_r^2 n^0 D_m \rho_w g(1-2\nu)}{2\left[S_r n^0+\left(1-n^0\right)\rho_s K_d\right]G(1-\nu)K}$	Reciprocal of Péclet number with modification for retardation and unsaturation
A_4	α_L/L	Longitudinal dispersivity per unit length
A_5	$\frac{A_1 A_4 A_7}{n^0}$	-
A_6	$\frac{A_3 A_7\left(1-n^0\right)}{n^0}$	-
A_7	$\frac{S_r n^0+\left(1-n^0\right)\rho_s K_d}{S_r}$	Modified retardation factor
A_8	$\frac{A_1 A_7}{n^0}$	-

With the coefficients A_i given in Table 2.1, the non-dimensional governing equations are

$$A_1 \frac{\partial p^*}{\partial t^*} + \frac{\partial^2 u^*}{\partial t^* \partial z^*} = \frac{\partial^2 p^*}{\partial z^{*2}}, \tag{2.12a}$$

$$\frac{\partial^2 u^*}{\partial z^{*2}} + A_2 \frac{\partial u^*}{\partial z^*} = \frac{\partial p^*}{\partial z^*}, \tag{2.12b}$$

$$\begin{aligned} \frac{\partial c^*}{\partial t^*} &= A_3 \frac{\partial^2 c^*}{\partial z^{*2}} - A_4 \frac{\partial p^*}{\partial z^*} \frac{\partial^2 c^*}{\partial z^{*2}} \\ &+ \frac{\partial c^*}{\partial z^*} \left(-A_1 A_4 \frac{\partial p^*}{\partial t^*} - A_4 \frac{\partial^2 u^*}{\partial z^* \partial t^*} + A_5 \frac{\partial p^*}{\partial z^*} \frac{\partial p^*}{\partial z^*} \right. \\ &\left. + A_6 \frac{\partial^2 u^*}{\partial z^{*2}} + \frac{\partial p^*}{\partial z^*} - A_7 \frac{\partial u^*}{\partial t^*} \right) \\ &+ A_1 \frac{\partial p^*}{\partial t^*} c^* - A_8 \left(\frac{\partial p^*}{\partial z^*} \right)^2 c^* + A_1 A_7 \frac{\partial u^*}{\partial t^*} \frac{\partial p^*}{\partial z^*} c^*. \end{aligned} \tag{2.12c}$$

We interpret the coefficients in (2.12a)–(2.12c) as follows. A_1 represents the ratio of skeleton modulus to that of pore fluid, which becomes notable for an unsaturated stiff porous medium. A_2 represents the body force effect on consolidation, and is analogous to the "body force number" in Tsai et al. (2006). When it is negligible, the effect of self-weight can be ignored. $A_3 = \left(t_c S_r \left(n^0\right)^2 D_m\right) / \left([S_r n^0 + (1-n^0)\rho_s K_d] L^2\right)$ can be seen as the reciprocal of Péclet number with the modifications of retardation and unsaturation. A_4 is longitudinal dispersivity per unit length. A_7 is the modified retardation factor including unsaturation.

2.3 APPLICATION TO A SINGLE-LAYER LANDFILL SYSTEM

2.3.1 PROBLEM CONSIDERED

The landfill liner system is similar to the operational liner investigated previously Peters and Smith (2002), as depicted in Figure 2.1. It includes a primary leachate collection system (PLCS), a geomembrane overlying a compacted clay liner (CCL), and a secondary leachate collection system (SLCS) (Figure 2.1). The origin of the vertical axis is located on the top of the CCL.

The landfill is assumed to fill with waste at a fixed loading rate until it reaches its capacity. At the top boundary, the impermeable geomembrane prevents Darcy flow, and the total vertical stress equals the surcharge loading, i.e.,

$$q(0,t) = -\frac{K}{\rho_w g} \frac{\partial p^e(0,t)}{\partial z} = 0, \tag{2.13}$$

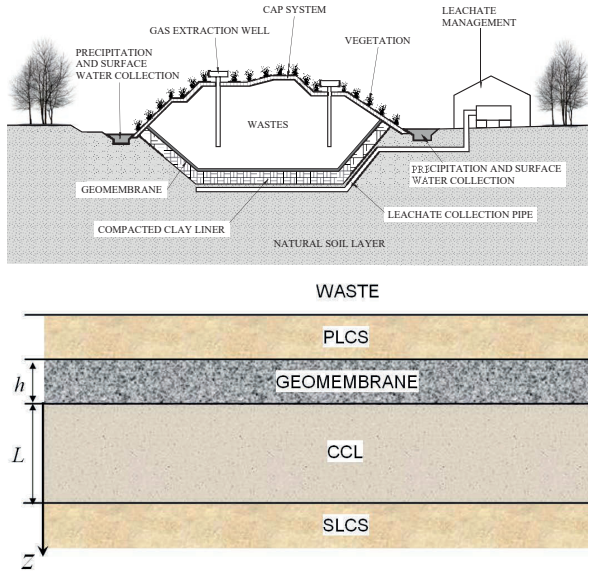

Figure 2.1 A schematic of an engineered landfill liner.

$$G\frac{2(1-\nu)}{(1-2\nu)}\frac{\partial u(0,t)}{\partial z} = -Q(t) + p^e. \tag{2.14}$$

The volatile organic compounds diffuse through the thin (relative to CCL) geomembrane at the top boundary, and the solute flux can be approximated as

$$f(0^-,t) = -D_G\frac{c_f(0^+,t) - c_0}{h}, \tag{2.15}$$

while the flux in the CCL at the interface is

$$f(0^+,t) = -nD\frac{\partial c_f}{\partial z}(0^+,t). \tag{2.16}$$

Equating (2.15) and (2.16) (Peters and Smith, 2002), we have

$$\frac{\partial c_f}{\partial z}(0,t) - \frac{D_G}{n(0^+,t)hD}c_f(0,t) = -\frac{D_G}{n(0^+,t)hD}c_0. \tag{2.17}$$

Here, the zero Darcy flow but non-zero contaminant solute flux makes it impossible to utilize analytical solutions. Some analytical solutions for solute transport in porous

media without a geomembrane are available (Rowe and Booker, 1985; Guerrero and Skaggs, 2010; Li and Cleall, 2011).

At the lower fixed boundary of the clay liner, the pore fluid is assumed to drain freely, and the gradient of solute concentration is assumed to be zero (Danckwert's boundary condition, Danckwerts (1953)), although different interpretations of this condition are possible (e.g., Barry and Sposito (1988)):

$$p^e(L,t)=0, \quad u(L,t)=0, \quad \frac{\partial c_f}{\partial z}(L,t)=0. \tag{2.18}$$

The initial excess pore-water pressure, soil displacement and solute concentration in the clay liner are zero. That is

$$p^e(z,0)=0, \;\; u(z,0)=0, \;\; c_f(z,0)=0. \tag{2.19}$$

2.3.2 VALIDATION OF THE PRESENT MODEL

FEM codes for various models were constructed using the multiphysics modeling software package COMSOL 3.5a (COMSOL, 2010). These involve solution of consolidation under ramp surcharge and the solute transport equation. Since there are no models or experimental data considering the present case, it is only possible to reduce the present model to previously reported special cases (i.e., full saturation, $S_r = 1$, $\beta = 0$). When A_1, A_2, $A_4 \sim A_6$ and A_8 are zero, the present model reduces to the small deformation model of Peters and Smith (2002). In the FEM analysis, the system was discretized into unstructured Lagrange-linear elements with a maximum global element size of 10^{-2} m, and maximum local element size at the end boundaries (where the most rapid changes occur) of 10^{-4} m. Temporally, the sub-time step was 10^{-2} year. As shown in Figure 2.2, the present model agrees well with earlier results (Peters and Smith, 2002).

2.3.3 DIMENSIONLESS ANALYSIS

In this section, we discuss the significance of each term in the governing equations. Based on the numerical examples used in Peters and Smith (2002) and Lewis et al. (2009), the input data or parameters adopted in the landfill clay barrier system are listed in Table 2.2. It should be noted that inter-relationships exist among the various A_is. Further, $(2G(1-\nu)K)/(1-2\nu)$ in A_3 should be restricted to a reasonable range of c_v. In addition, given the assumption on porosity, the choice of parameters should ensure that the non-dimensional soil deformation is relatively small, e.g., less than 20%. Assuming $S_r = 0.8 \sim 1.0$, $\alpha_L = 0.1$ m, $\nu = 0.33$, we focus on variations of $S_r(\beta)$, D_m, K, G and present the magnitude of each coefficient as in Table 2.3. The characteristic parameters are, $t_c = 4.97 \times 10^7$ s (1.576 y), $p_c = 6.50 \times 10^5$ Pa, $u_c = 0.33$ m for case 1 and $t_c = 3.98 \times 10^6$ s (0.126 y), $p_c = 6.50 \times 10^6$ Pa, $u_c = 0.33$m for case 2.

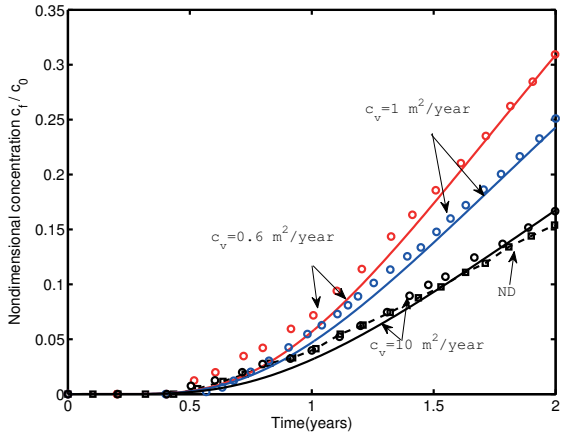

Figure 2.2 Comparison with previous work (Peters and Smith, 2002). The present model: lines; results from Peters and Smith (2002): circles; result of the no-deformation model (ND) from Peters and Smith (2002): dashed line with square symbol. $L = 0.914$ m, $n^0 = 0.25$, $D_m = 0.1$ m^2/y ($S_r = 1$ and $\beta = 0$).

Table 2.2
Typical parameter values for a landfill clay barrier system.

Parameter	Value
Waste loading, $Q(t)$	ramp loading, 2×10^5 Pa/y $\times$ 2 y
Thickness of geomembrane, h	0.0015 m
Thickness of CCL, L	$0.914 \sim 1.22$ m
Mass transfer coefficient of geomembrane, D_G	10^{-4} m^2/y
Partitioning coefficient, K_d	0
Effective coefficient of molecular diffusion in the clay, D_m	$5 \times 10^{-10} \sim 5 \times 10^{-9}$ m^2/s
Coefficient of consolidation in clay, c_v	$0.6 \sim 10$ m^2/y
Shear modulus, G	$5 \times 10^5 \sim 5 \times 10^6$ Pa
Hydraulic conductivity of clay, K	$10^{-10} \sim 1.5 \times 10^{-10}$ m/s
Initial porosity of clay, n^0	0.33
Acceleration due to gravity, g	9.8 m/s^2
Initial density of the pore fluid, ρ_w	10^3 kg/m^3
Density of the solid phase, ρ_s	2.6×10^3 kg/m^3

Table 2.3
Magnitude of coefficients $A_1 - A_8$ used in the landfill case and simulation cases.

Coefficient	range	Case 1	Case 2
A_1	$0.13 \sim 14.05$	0.13	14.05
A_2	$5.33 \times 10^{-4} \sim 10^{-3}$	5.33×10^{-3}	5.33×10^{-4}
A_3	$1.65 \times 10^{-3} \sim 0.248$	0.248	1.99×10^{-3}
A_4	0.1	0.1	0.1
A_5	$1.30 \times 10^{-2} \sim 1.4$	1.3×10^{-2}	1.4
A_6	$1.11 \times 10^{-3} \sim 0.166$	0.166	1.33×10^{-3}
A_7	0.33	0.33	0.33
A_8	$0.13 \sim 14.05$	0.13	14.05

The corresponding non-dimensional form for the boundary conditions (BCs) and initial conditions (ICs) are

$$\frac{\partial p^*(0,t^*)}{\partial z^*} = 0, \quad p^*(1,t^*) = 0, \quad p^*(z^*,0) = 0; \tag{2.20a}$$

$$\begin{aligned} &\frac{\partial u^*(0,t^*)}{\partial z^*} = \frac{(1-2\nu)Lp_c}{2G(1-\nu)u_c}\left[\frac{-Q(t^*t_c)}{p_c} + p^*\right] = \frac{-Q(t^*t_c)}{p_c} + p^*, \\ &u^*(1,t^*) = 0, \quad u^*(z^*,0) = 0; \end{aligned} \tag{2.20b}$$

$$\begin{aligned} \frac{\partial c^*(0,t^*)}{\partial z^*} &= \frac{D_G L}{n^0 h D_m}(C^* - 1) = A_9(C^* - 1), \\ \frac{\partial c^*(1,t^*)}{\partial z^*} &= 0, \quad C^*(z^*,0) = 0; \end{aligned} \tag{2.20c}$$

where the ratio of the mass transfer coefficients of geomembrane and clay is specified as $D_G/D_m = 10^{-3}$, then $A_9 = 2.02$.

2.3.4 SIMPLIFICATION ANALYSIS

Peters and Smith (2002) and Lewis et al. (2009) performed a small deformation analysis using a spatial coordinate system. In their models (Peters and Smith, 2002; Lewis et al., 2009), the spatial variation of porosity, self-weight of the clay liner and longitudinal dispersivity were not considered (Peters and Smith, 2002; Lewis et al., 2009). That is because they emphasized mechanical consolidation-induced advective solute transport and the differences made by geometric and material non-linearity

compared with linear models. A useful metric is the "breakthrough time", which is defined as the time for the contaminant concentration in the SLCS to reach a predetermined concentration, say 0.1 times that of concentration in landfill, i.e., $c^* = 0.1$ in the present non-dimensional analysis.

At the bottom boundary, there is only an advective contaminant flux component because of the zero gradient in c_f. Besides the breakthrough time, the advective emission, i.e., the cumulative contaminant mass outflow per unit area from the barrier system due to advective flow, is also important to evaluate the influence of deformation and the potential environmental risk. Provided the fixed bottom boundary, the non-dimensional advective emission can be taken as

$$E^*_{adv} = \int_0^{t^*} -\frac{\partial p^*(\tau)}{\partial z^*} c^*(\tau) d\tau. \tag{2.21}$$

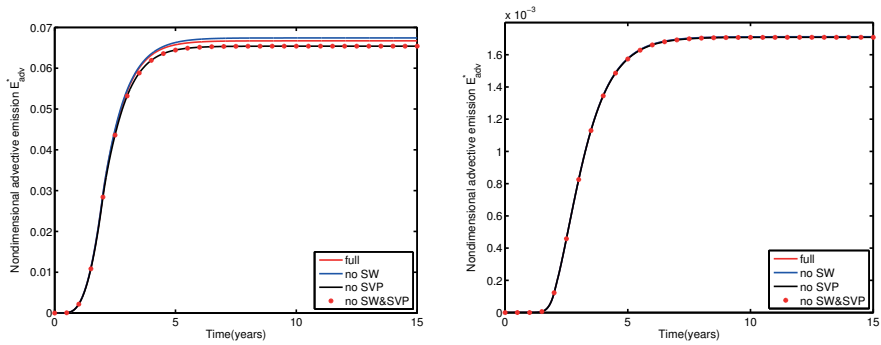

(a) Case 1 (b) Case 2

Figure 2.3 Influence of self-weight (SW) and spatial variation of porosity (SVP) on advective emission.

Based on the present model, the effect of SW, SVP, CPW and longitudinal dispersion on solute transport in terms of advective solute emission at the exit boundary is examined. For Cases 1 and 2, results are given in Figures 2.3–2.5, and the details for model A-G are tabulated in Table 2.4. As shown in Table 2.3, A_2, A_3 and A_6 are relatively small. However, A_3 represents molecular diffusion mechanism, which is the main contaminant transport mechanism in the post-consolidation period. Therefore, A_3 is kept in the present model. Figure 2.3 shows that the effect of SW and SVP are negligible for case 1; both can be omitted without inducing a discernible difference. Regarding case 2, the differences due to SW and SVP are even smaller because of the smaller values of A_3 and A_6 than in case 1.

When $A_1 = 0$, the compressibility of pore-water is ignored in the consolidation and transport equations. In the latter, the CPW gives rise to three terms similar to sources/sinks, and also terms that couple with dispersivity. Figure 2.4 shows that the influence of CPW is increasingly important in case 2 (the advective emission (or

flux) increases approximately four times for the case including CPW). Furthermore, results of mode C are close to that of the full model, which indicates that the terms arising due to CPW in the transport equations matter little, while the terms due to CPW in the consolidation equation alter the flows and dominate the emission flux.

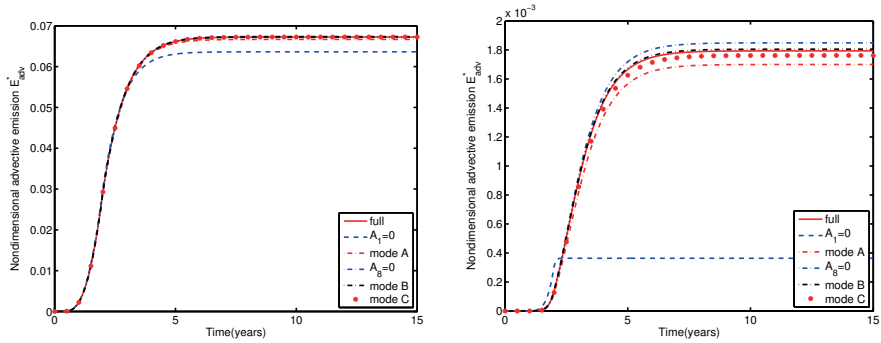

(a) Case 1 (b) Case 2

Figure 2.4 Influence of compressibility of pore-water (CPW) on advective emission.

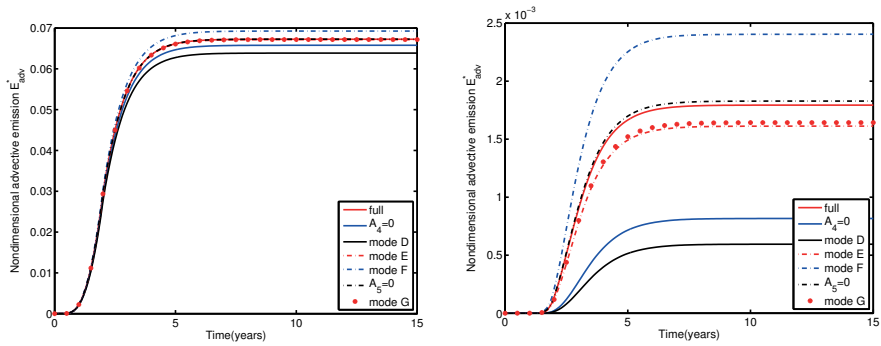

(a) Case 1 (b) Case 2

Figure 2.5 Influence of longitudinal dispersivity on advective emission.

Figure 2.5 shows that the effect of longitudinal dispersivity increases when D_m decreases. In case 2, the advective emission predicted by the model with longitudinal dispersivity is twice that of the model without longitudinal dispersivity. Among these four longitudinal dispersivity terms, the influence of $(\partial p^*/\partial z^*)(\partial^2 c^*/\partial z^{*2})$ and $(\partial^2 u^*/\partial z^* \partial t^*)(\partial c^*/\partial z^*)$ are much greater than that of $(\partial p^*/\partial t^*)(\partial c^*/\partial z^*)$ and $(\partial p^*/\partial z^*)\partial c^*/\partial z^*$. Therefore, it is reasonable to retain only the former two terms as in mode G.

Table 2.4
Details of each model.

Model	Details
Mode A	$A_1 \frac{\partial p^*}{\partial t^*} c^*$ is omitted
Mode B	$A_1 A_7 \frac{\partial u^*}{\partial t^*} \frac{\partial p^*}{\partial z^*} c^*$ is omitted
Mode C	$A_8 = 0$, $A_1 \frac{\partial p^*}{\partial t^*} c^*$ and $A_1 A_7 \frac{\partial u^*}{\partial t^*} \frac{\partial p^*}{\partial z^*} c^*$ are omitted
Mode D	$A_4 \frac{\partial p^*}{\partial z^*} \frac{\partial^2 c^*}{\partial z^{*2}}$ is omitted
Mode E	$A_1 A_4 \frac{\partial p^*}{\partial t^*} \frac{\partial c^*}{\partial z^*}$ is omitted
Mode F	$A_4 \frac{\partial^2 u^*}{\partial z^* \partial t^*} \frac{\partial c^*}{\partial z^*}$ is omitted
Mode G	$A_5 = 0$ and $A_1 A_4 \frac{\partial p^*}{\partial t^*} \frac{\partial c^*}{\partial z^*}$ are omitted

Based on the above analysis, the complete model can be simplified as

$$\frac{2G(1-\nu)n^0\beta}{1-2\nu}\frac{\partial p^*}{\partial t^*} + \frac{\partial^2 u^*}{\partial t^* \partial z^*} = \frac{\partial^2 p^*}{\partial z^{*2}}, \tag{2.22a}$$

$$\frac{\partial^2 u^*}{\partial z^{*2}} = \frac{\partial p^*}{\partial z^*}, \tag{2.22b}$$

$$\begin{aligned}\frac{\partial c^*}{\partial t^*} = {} & \frac{S_r^2 n^0 D_m \rho_w g(1-2\nu)}{2\left[S_r n^0 + (1-n^0)\rho_s K_d\right] G(1-\nu)K}\frac{\partial^2 c^*}{\partial z^{*2}} - \frac{\alpha_L}{L}\frac{\partial p^*}{\partial z^*}\frac{\partial^2 c^*}{\partial z^{*2}} \\ & + \frac{\partial c^*}{\partial z^*}\left\{-\frac{\alpha_L}{L}\frac{\partial^2 u^*}{\partial z^* \partial t^*} + \frac{\partial p^*}{\partial z^*} - \frac{\left[S_r n^0 + (1-n^0)\rho_s K_d\right]}{S_r}\frac{\partial u^*}{\partial t^*}\right\}.\end{aligned} \tag{2.22c}$$

As shown in Figure 2.6, the proposed model gives a reasonable approximation to the full model.

2.4 SOLUTE TRANSPORT IN LAYERED POROUS MEDIA

Based on the fundamental construction method of a landfill site, an unsaturated multi-layer soil matrix subjected to a vertical ramp load on the top of the field

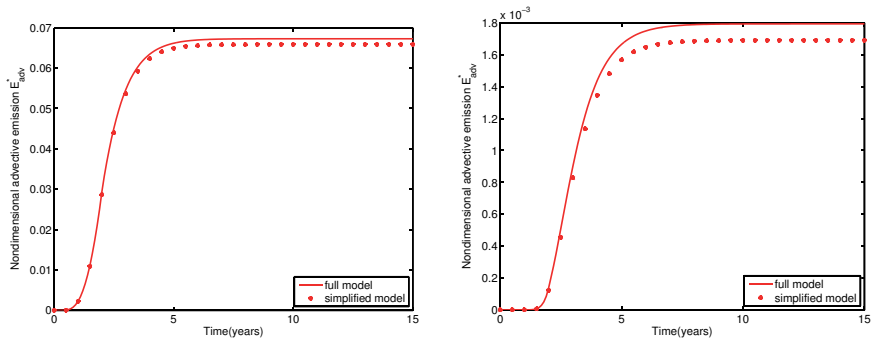

(a) Case 1 (b) Case 2

Figure 2.6 Comparison of advective emission between the simplified and complete full models.

was assumed, as shown in Figure 2.7, where P1 through P7 are the points used in the parametric study. Since the soil is deformable, it will produce excess pore pressure when an external ramp load is applied and the excess pore pressure will dissipate gradually when the load becomes constant (the post-loading state). The excess pore pressure will generate a transient advective flow, which carries the non-active contaminant migrating downward. Furthermore, the width of the landfill site was assumed to be larger than the thickness of each soil layer, and the load on the top surface was assumed to be uniform. Therefore, a 1D model was used, with its positive z-axis pointing downward. In contrast to the previous study of Zhang et al. (2012*a*), this section focused on a multi-layer structure and ran simulations in a dimensional form.

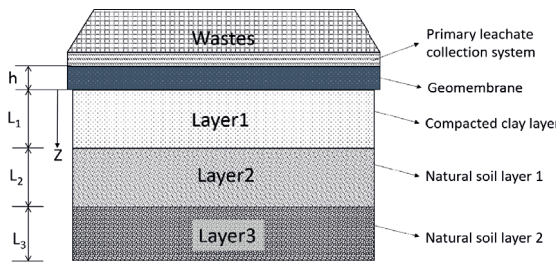

Figure 2.7 A schematic diagram of a simplified three-layer landfill.

2.4.1 BOUNDARY CONDITIONS AND INITIAL CONDITIONS

Herein, a landfill with one leachate collection system was assumed to be constructed on the top of a compacted clay layer and two natural soil layers (Figure 2.7). The contaminant migration through the three soil layers beneath the landfill was

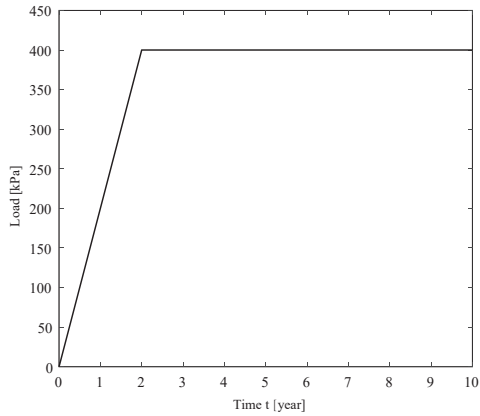

Figure 2.8 Ramp load for a layered porous medium.

evaluated. The governing equation for solute transport in layered porous media are the same as that in a single-layer, i.e., (2.1a), (2.1b) and (2.10c). The following boundary and initial conditions are employed:

- At the top boundary ($z = 0$), the impermeable geomembrane layer prevented Darcy's flow. Therefore, a zero excess pore pressure gradient was postulated, i.e., (2.13) & (2.14).
- Furthermore, as the waste was disposed to landfill gradually until reaching its capacity, a ramp load was assumed with a constant increasing rate. As shown in Figure 2.8, the external load (Q) keeps increasing in a rate of 200 kPa annually for two years and remains constant of 400 kPa until the end of simulation period.
- To derive the top boundary condition for soil deformation, an elastic deformation was taken into account, and a vertical force balance relationship was applied. This led to the soil deformation at the top boundary to be (2.14).
- According to Zhang et al. (2012*a*), considering the volatile organic compounds that diffuse through the geomembrane layer and dissolve into the pore-water, the top boundary condition for the solute concentration was (2.17).
- At the two interfaces ($z = Z_1 = L_1$ and $z = Z_2 = L_1 + L_2$), boundary conditions of continuity were applied to the pore pressure, soil deformation, and solute concentration fields, and the continuity of the pore fluid flux and solute mass flux were incorporated:

$$\begin{cases} p^e(Z_i^-,t) = p^e(Z_i^+,t) \\ w(Z_i^-,t) = w(Z_i^+,t) \\ c_f(Z_i^-,t) = c_f(Z_i^+,t) \end{cases} \quad \text{for } i = 1,2, \tag{2.23a}$$

$$K_i \frac{\partial p^e(Z_i^-,t)}{\partial z} = K_{i+1} \frac{\partial p^e(Z_i^+,t)}{\partial z} \quad \text{for } i = 1,2, \tag{2.23b}$$

$$S_{ri} n_{0i} D_i \frac{\partial c_f(Z_i^-,t)}{\partial z} = S_{ri+1} n_{0i+1} D_{i+1} \frac{\partial c_f(Z_i^+,t)}{\partial z} \quad \text{for } i = 1,2, \tag{2.23c}$$

where D_i is the coefficient of hydrodynamic dispersion that describes the joint effects of molecular diffusion and longitudinal dispersion at the i-th interface, and Z_i^- and Z_i^+ refer to the positions right above and below the i-th interface, respectively.

- At the exit boundary ($z = L_e = L_1 + L_2 + L_3$), a free drainage condition was considered, which implied a zero pore pressure, and no deformation was allowed at that point. In addition, the concentration gradient was assumed to be zero. Hence, only advective flow occurred at the outlet boundary. The lower boundary conditions were given in (2.18).
- To simplify the model, all initial values for pore pressure field, soil deformation and solute transport are set to zeros, i.e., (2.19).

The major differences between single-layer and multiple-layer soils are the matching boundary conditions, i.e., (2.23).

2.4.2 INPUT PARAMETERS

First of all, a single-layer (SL) model was simulated as the reference group. Table 2.5 summarizes the parameter input for the SL model.

A parametric study was conducted to investigate the multi-layer effects by varying certain parameters for each layer while keeping the rest of the parameters the same as those in the SL model. A summary of the varied parameters were summarized in Table 2.4.2. Note that the parameters used in the SL model were consistent with the middle-layer parameters in the three-layer model, most of which were the average values of the varied parameters for each layer. A combination of the parameters was selected to ensure that the coefficient of consolidation (c_v) stayed within the range of 1×10^{-8} to 3×10^{-7} m^2/s (Sivakugan, 1990; Wallace and Otto, 1964). The coefficient of consolidation (c_v) can be expressed as:

$$c_v = \frac{2GK(1-\nu)}{\rho_w g(1-2\nu)}. \tag{2.24}$$

Additionally, while making selection of the parameters, soil deformation was kept less than 20% to satisfy the small deformation assumption.

The finite element method is implied to solve the complicated coupled partial differential equations using the multiphysics modeling software package COMSOL 5.0. In the finite element method analysis, the system was discretized

Table 2.5
Parameters for the single-layer model (SL).

Parameter	Value	Description
$Q(t)$	See Table 2.2	Waste loading
h	0.0015 m	Thickness of geomembrane
$^*L$	1 m	Thickness of each layer
$^*S_r$	0.90	Degree of saturation
n^0	0.33	Initial porosity
$^*G$	2.75×10^6 Pa	Shear modulus
$^*\nu$	0.33	Poisson's ratio
$^*K$	1.5×10^{-10} m/s	Hydraulic conductivity
α_L	0.1 m	Longitudianl dispersion factor
ρ_w	1×10^3 kg/m^3	Initial density of the pore fluid, varied due to fluid compressibility
ρ_s	2.6×10^3 kg/m^3	Density of the solid phase
K_d	0	Partitioning coefficient
r_h	0.02 m	Volumetric fraction of dissolved air within pore-water
D_G	1×10^{-4} m^2/y	Mass transfer coefficient of geomembrane
$^*D_m$	2.75×10^{-9} m^2/s	Molecular diffusion coefficient in the clay
c_0	0.1 kg/m^3	Reference solute concentration
g	9.8 m/s^2	Gravity acceleration

Note that the parameters with * are used in the parametric study.

into unstructured Lagrange-linear elements. The maximum global element size is controlled to be 0.01 m, and local element size at each boundary (where is the most sensitive to any changes) was controlled to be finer than 10^{-4} m. Temporally, the time step was 0.01 year and each model in the parametric study was simulated for 80 years.

2.4.3 COMPARISON WITH A SINGLE-LAYER MODEL

soil deformation and solute concentration distributions along the soil depth for different years, the solute concentration at some points (P_1, P_4, and P_7 in Figure 2.1), and the advective emission (E_{adv}) at the outlet, obtained with the present three-layer model and the full SL model in Zhang et al. (2012*a*), were first compared, as shown in Figure 2.9. Before making any comparison to the three-layer model, all dimensionless results presented in Zhang et al. (2012*a*) were converted to a dimensional form. Figure 2.9 shows that the three-layer model agrees with the previous SL model (Zhang et al., 2012*b*).

Table 2.6
Parametric study cases setup.

Model	Varied Parameter Values	Unit	Description
A	K_1= 1.5×10^{-11}; K_2=1.5×10^{-10}; K_3=2.85×10^{-10}	m/s	Varied hydraulic conductivity
B	$G_1 = 5 \times 10^5$; $G_2 = 2.75 \times 10^6$; $G_3 = 5 \times 10^6$	Pa	Varied shear modulus
C	$D_{m1} = 5 \times 10^{-10}$; $D_{m2} = 2.75 \times 10^{-9}$; $D_{m3} = 5 \times 10^{-9}$	m^2/s	Varied molecular diffusion coefficient
D	$S_{r1} = 0.8$; $S_{r2} = 0.9$; $S_{r3} = 0.98$		varied degree of saturation
E	$\nu_1 = 0.2$; $\nu_2 = 0.33$; $\nu_3 = 0.4$		Varied Poisson's ratio
F	$G_1 = 5 \times 10^6$; $G_2 = 2.75 \times 10^6$; $G_3 = 5 \times 10^5$	Pa	Varied shear modulus with reverse of order compare to Model B
G	$L_1 = 0.5$; $L_2 = 1$; $L_3 = 1.5$; $D_{m1} = 5 \times 10^{-10}$; $D_{m2} = 2.75 \times 10^{-9}$; $D_{m3} = 5 \times 10^{-9}$	m m^2/s	Varied thickness of each layer and feature to varied molecular diffusion coefficient

Utilizing the piecewise function, the ramp load can be applied with different smoothing methods at the turning point. Here, a continuous second derivative was adopted and applied for a period of half a year. This smoothing method can be understood as follows: when the landfill site is about to reach capacity, less waste is disposed into this field, and more waste delivered to a new site. Therefore, the loading rate decreases.

Adopting the parameters listed in Table 2.5, the three-layer model was first used for a simulation of 80 years to mimic a single-layer situation, and the results are shown in Figure 2.10. The consolidation progress can be observed in Figure 2.10(a) and Figure 2.10(b). For the first two years, when the external load keeps rising at a constant increasing rate of 200 kPa/year, the excess pore pressure dramatically increases and reaches its maximum. The soil also shows noticeable deformation during the period because the pore fluid is expelled from the soil matrix. However, during the post-loading period, the excess pore pressure dissipates and leads to an increment of the effective stress, which contributes to further soil deformation. Figure 2.10(a) indicates that the excess pore pressure will fully dissipate in 20 years, with the soil deformation reaching its maximum (soil deforms less than 4%) around the same time (Figure 2.10(b)).

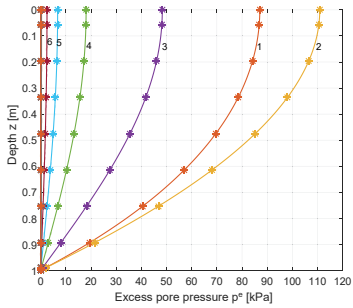

(a) Excess pore pressure distribution

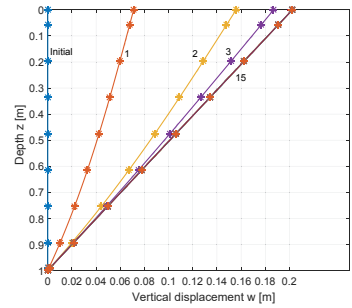

(b) Soil deformation

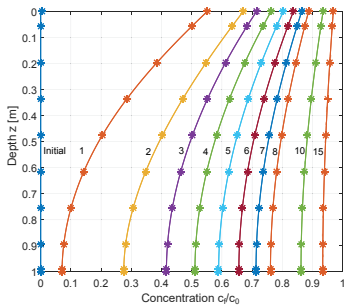

(c) Solute concentration distribution

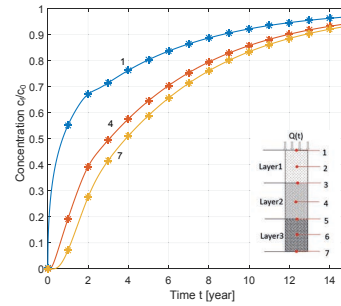

(d) Solution concentration at each cutpoint

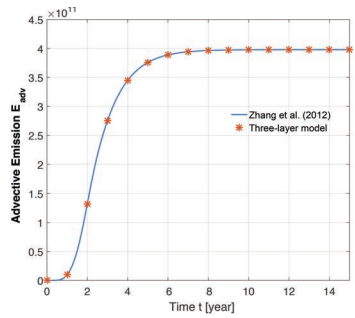

(e) Advective emission at outlet

Figure 2.9 The comparison of the present three-layer modeling result ($*$) with Zhang et al. (2012*a*) (solid line). Note: $S_r = 1$, $L = 1m$, $G = 500kPa$, $K = 1e-10m/s$, $D_m = 5e-9m^2/s$.

Additionally, Figure 2.10(c) illustrates the distribution of the normalized solute concentration. After one year, the contaminant migrates to a depth of $1m$; after 10 years, the contaminant reaches the bottom boundary. Although the excess pore pressure has fully dissipated at the twentieth year, due to the molecular diffusion, the contaminant keeps spreading until the whole site is polluted. Figure 2.10(d) shows the revolution of the solute concentration at the top, middle, and bottom of each layer. From this figure, the breakthrough time, which is the time taken for the contaminant concentration to reach a certain pollution level, can be read. For example, it takes

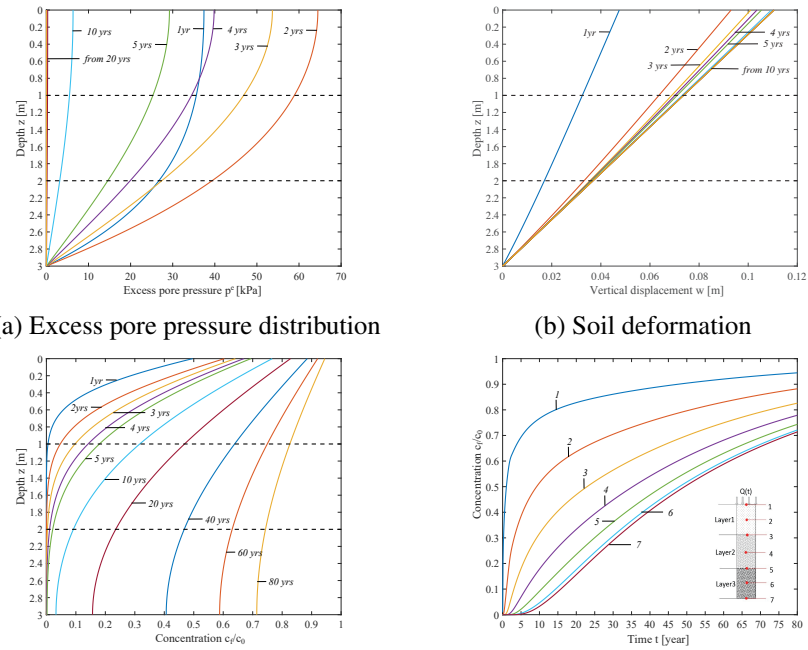

(a) Excess pore pressure distribution

(b) Soil deformation

(c) Solute concentration distribution

(d) Breakthrough diagram

Figure 2.10 Results of the single-layer model (SL).

15 years for the contaminant level at the outlet boundary (P_7) to reach 10% of the concentration in the landfill. It is an important metric for the evaluation of the contaminant transport, and an earlier breakthrough time implies that the site may be polluted more easily. The results of the SL model were used as the reference group in the parametric study described below. Figures 2.11–2.15 provide the results from models A through G, respectively, with the critical results from the SL model plotted against them in dashed lines. When there is no significant difference, the result from the SL model is not presented.

2.4.4 EFFECTS OF HYDRAULIC CONDUCTIVITY

Figure 2.11 illustrates the soil stratification effect of the hydraulic conductivity K, solid lines are the results from Model A and dashed lines plot the SL model simulation results. For model A, While the middle layer has the hydraulic conductivity as same as in SL model, the first layer is less permeable and the bottom layer is assumed with larger hydraulic conductivity permeability. As the excess pore pressure distribution figure (Figure 2.11(a)) shown, when the hydraulic conductivity varies suddenly at the contact surfaces of each layer, a turning point can be observed at each time step. This is consistent with the boundary conditions of the interface, ensuring the continuity of the pore fluid flux (2.23b). The first layer with a K value

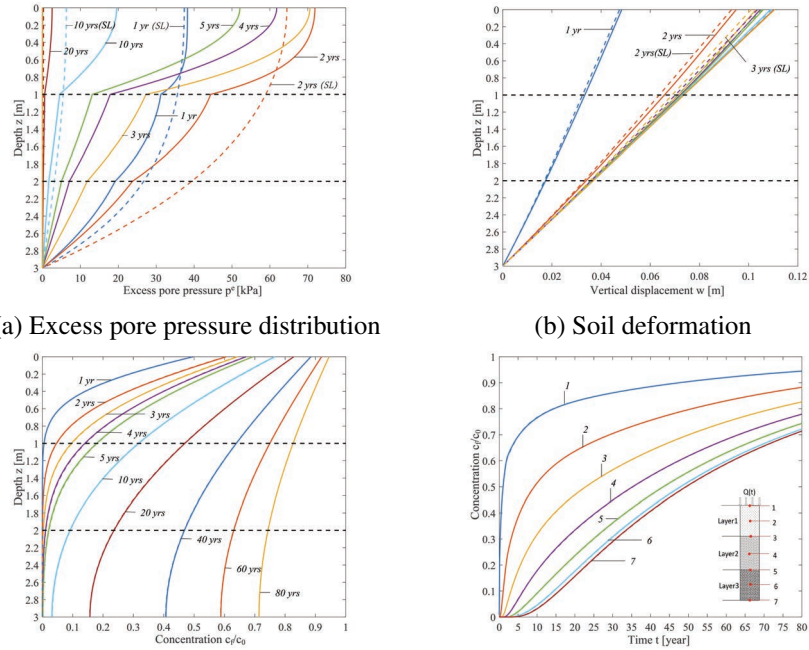

(a) Excess pore pressure distribution

(b) Soil deformation

(c) Solute concentration distribution

(d) Breakthrough diagram

Figure 2.11 Results of the Model A which hydraulic conductivity are varied for each layer.

(1.5×10^{-11} m/s) smaller than that in the SL model experiences a faster excess pore pressure buildup during the loading period, and a higher peak excess pore pressure (more than $70kPa$) that occurs at the top surface. Furthermore, the first layer also shows a slower dissipation process after the load becomes constant. after 20 years, while the excess pore pressure has been fully dissipated in the SL model, Model A results shows a remaining of 5 kPa. However, the impact of slower dissipation from first layer are made up by the third layer with larger K values. Specifically, a larger hydraulic conductivity implies that the pore fluid is easier travelling through the voids, hence the bottom layer leads to a faster excess pore pressure dissipation. This trend can be shown from Figure 2.11(a) that the pore pressure for Model A in the bottom layer is smaller than that in SL model at all time steps.

It is interesting to see the joint effect from the middle layer that shares the same parameter settings as the SL model. It is obvious that the middle layer shows a less excess pore pressure buildup as well as a quicker excess pore pressure dissipation than a homogeneous situation. This trend reveals that the hydraulic conductivity at the bottom layer dominates the soil stratification effects especially for the soil response of excess pore pressure. It is because that for this study case assumes relatively thin layers and the transient flow is only allowed to be drained from the bottom. In addition, the soil deforms slower than SL model as a result of less pore pressure buildup and quicker dissipation. However, at the end of the

simulation time, same level of deformation can be observed because the hydraulic conductivity is only related to the speed of consolidation but has no impact on the final deformation level (Figure 2.11(b)). In terms of the solute transport, it seems that the soil stratification effect of hydraulic conductivity is not obvious for this proposed case (Figure 2.11(c&d)).

2.4.5 EFFECTS OF SHEAR MODULUS

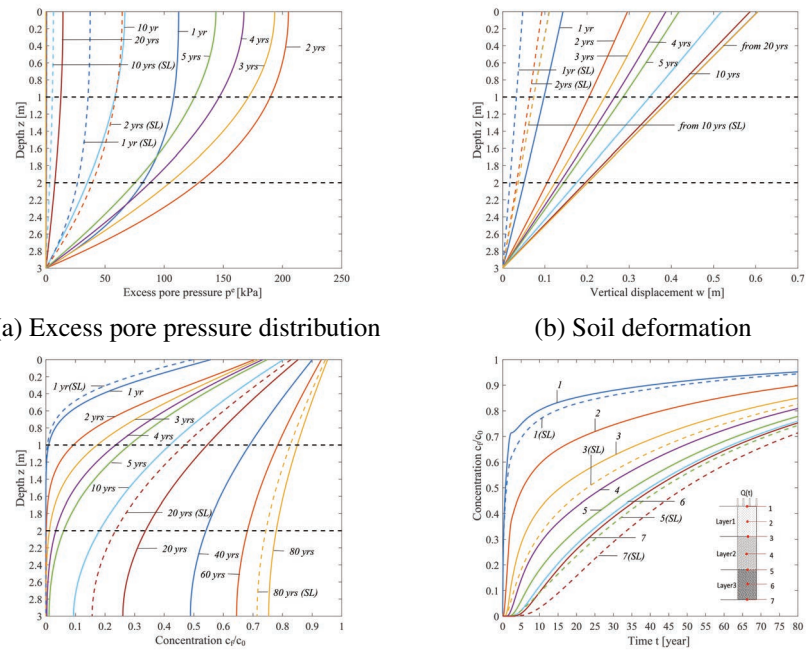

(a) Excess pore pressure distribution

(b) Soil deformation

(c) Solute concentration distribution

(d) Breakthrough diagram

Figure 2.12 Results of the Model B which the shear modulus are varied for each layer.

The effect of soil stratification from the variation of the shear modulus G was studied and the results are presented in Figure 2.12. It is well known that the shear modulus plays an important role in soil consolidation and consequently affects the solute transport process. For model B, the shear modulus values in the three layers from top to bottom are 5×10^5, 2.75×10^6, 5×10^6 Pa, soft to stiff. Due to a relatively small G in the top layer, the final deformation (around 20%) at the end of the simulation period is about six times larger than that in the SL model (Figure 2.12(b)). As for the excess pore pressure, its peak value at the inlet boundary increases to more than 200 kPa, and a longer time is required for the excess pore pressure to fully dissipate. Specifically, at the end of 20 years, the excess pore pressure fully dissipates in the SL model, while a residual excess pore pressure of more than 10 kPa still exists at the top boundary in model B simulation results (Figure 2.12(a)).

This is understandable considering a porous media that is more easily deformed under a load, but in which a relatively low hydraulic conductivity limits the rate of fluid expulsion. Therefore, the pore pressure increases. Finally, due to the high pore pressure and the slow dissipation process, the contaminant migrates at a faster rate, and an earlier breakthrough is detected (Figure 2.12(c) and Figure 2.12(d)).

It seems that the soil properties of the top layer play a more important role in the layered soil behavior and solute transport. To verify this, model F was designed in a reverse order of G for each layer compared to model B, with the soil being most rigid on the top, and the results are shown in Figure 2.13. Compared to the SL model, the excess pore pressure dissipates more rapidly and less soil deformation is detected. Moreover, during the post-loading stage, the excess pore pressure in model F dissipates and leads to an increment of normal stress, and the top layer is too rigid to show any noticeable deformation. On the other hand, the soil in the bottom layer is soft. Therefore, little deformation is observed (Figure 2.13(a) and Figure 2.13(b)). As for the contaminant transport, no significant effect is detected (Figure 2.13(c) and Figure 2.13(d)). In general, results of model F shows no consistency with those of model B (Figure 2.12). Hence, a conclusion can be drawn that the order of parameter values for each layer will also significantly alter the simulation result. Furthermore, the soil properties of the top layer seem to have a more noticeable effect on the soil response and solute transport process.

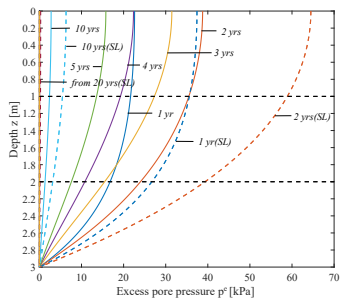

(a) Excess pore pressure distribution

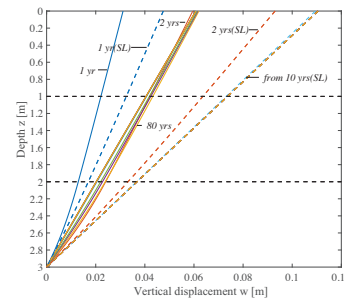

(b) Soil deformation

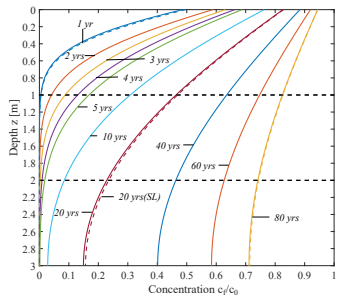

(c) Solute concentration distribution

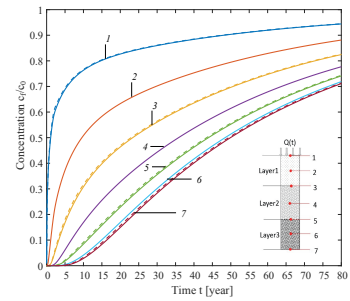

(d) Breakthrough diagram

Figure 2.13 Results of the Model F with various shear modulus for each layer and in a reversed order to Model B.

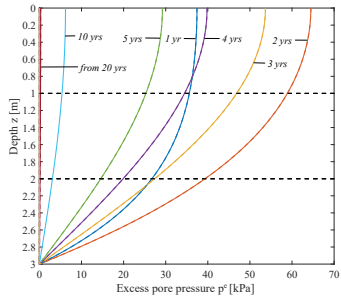

(a) Excess pore pressure distribution

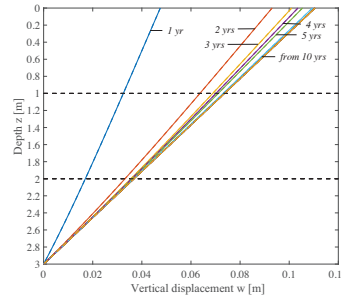

(b) Soil deformation

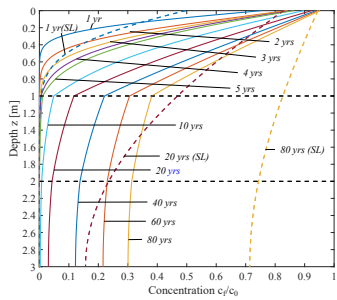

(c) Solute concentration distribution

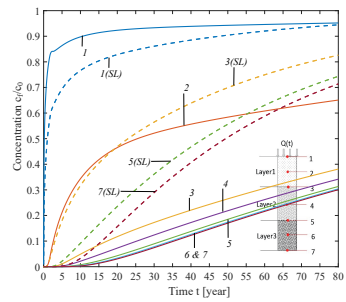

(d) Breakthrough diagram

Figure 2.14 Results of the Model C with various molecular diffusion coefficients for each layer.

2.4.6 EFFECTS OF MOLECULAR DIFFUSION COEFFICIENT

In this study, the contaminant transport was considered to be the joint effect of hydrodynamic dispersion and contaminants carried by transient advective flow due to consolidation. In particular, the molecular diffusion (controlled by D_m), one component of the hydrodynamic dispersion, is mainly manifested as particles move from an area of high concentration to an area of low concentration. Compared to the longitudinal dispersion (controlled by α_L), in a relatively slow advective flow, the molecular diffusion dominates. The stratified D_m effect is demonstrated in model C. Figure 2.14(a) and Figure 2.14(b) illustrate no differences in the consolidation process and transient flow from those in the SL model. This is consistent with the semi-coupled computing scheme introduced in section 2.3.4. However, the stratified D_m contributes to a noticeable deceleration of solute transport even though the concentration at the inlet is greater than that in the SL model. Specifically, with a smaller D_m in the top soil layer, a greater concentration gradient is obtained according to the top boundary condition of contaminant concentration, which is related to the nature of volatile pollutants diffusing through the geomembrane layer. Even with a larger solute concentration at inlet, a significantly slowdown solute spread is shown in model C than in the SL model, especially in the top layer.

Although the differences are narrowed by the larger D_m in the bottom layer, a later breakthrough time and smaller concentration in model C are shown in Figure 2.14(c) and Figure 2.14(d). For example after 20 years, the differences of c/c_0 between Model C and SL model is 0.4 at $z = 1$m, and the difference has been reduces to 0.15 at $z = 2$m. For the breakthrough time, it takes around 15 years for the SL model to reach solute concentration of 0.01kg/m^3 ($c/c_0 = 0.1$) at the outlet, while for Model C, it takes nearly 30 years. These findings are consistent with the conclusion in section 2.4.5 that the factors of the top layer are more critical than those of the lower soil layers with the same layer thickness. Furthermore, it is also obvious to see a chance of solute concentration gradient at interfaces for Model C, that is due to the sudden change of molecular diffusion coefficients and meanwhile ensure the solute flux continuity at each interfaces. In model A (section 2.4.4) a similar trend of discontinuous excess pore pressure gradient can be found.

2.4.7 EFFECTS OF THICKNESS OF EACH LAYER

The soil stratification effect in terms of the thickness of each layer was also tested. Model G utilized the same parameter setting as model C but adjusted the thickness for each layer so that they were 0.5 m, 1.0 m, and 1.5 m, respectively. As a result, for Model G, the discontinous solute concentration gradient occurs at interfaces where $z = 0.5$m and $z = 1.5$m. As discussed in section 2.4.6, the molecular diffusion coefficient does not influence the consolidation process. Therefore, model G and the SL model show no differences in terms of the excess pore pressure and soil vertical deformation (Figure 2.15(a) and Figure 2.15(b)). In general, assuming a thicker bottom layer with larger molecular diffusion coefficient would reduce the gap with the SL model in certain extend but it does not accelerate the solute transport too much (Compared to result of Model C). As shown in Figure 2.15(c), except for the soils near inlet, Model G reveals less contaminant migrating through the whole layers than the SL model even with the bottom layer (larger D_m) three times thicker than the top layer (Smaller D_m). Moreover, the breakthrough time for outlet to reach concentration of 0.01kg/m^3 is now around 20 years. The breakthrough time has been shortened for 10 years compared to Model C (30 years), but it is still greatly longer than that in the SL model (15 years). As a result, a conclusion can be drawn that altering the thickness would has certain effects to solute transport but not significant, and D_m at the top layer still play a key role in consolidation-induced solute transport.

2.4.8 EFFECTS OF DEGREE OF SATURATION AND POISSON'S RATIO

Figure 2.16 summarises the soil stratification effects in terms of different degree of saturation in each layer. The top layer is less saturated while the bottom layer is almost fully saturated. The excess pore pressure distribution diagram indicates that the peak excess pore pressure occurs after 2 years is smaller than that in the SL model, and it takes a little longer for the excess pore pressure to be fully dissipated. Generally speaking, with the variance of S_r in each layer, the fluid compressibility varies. Smaller S_r at the top layer means the pore fluid is easier to be compressed

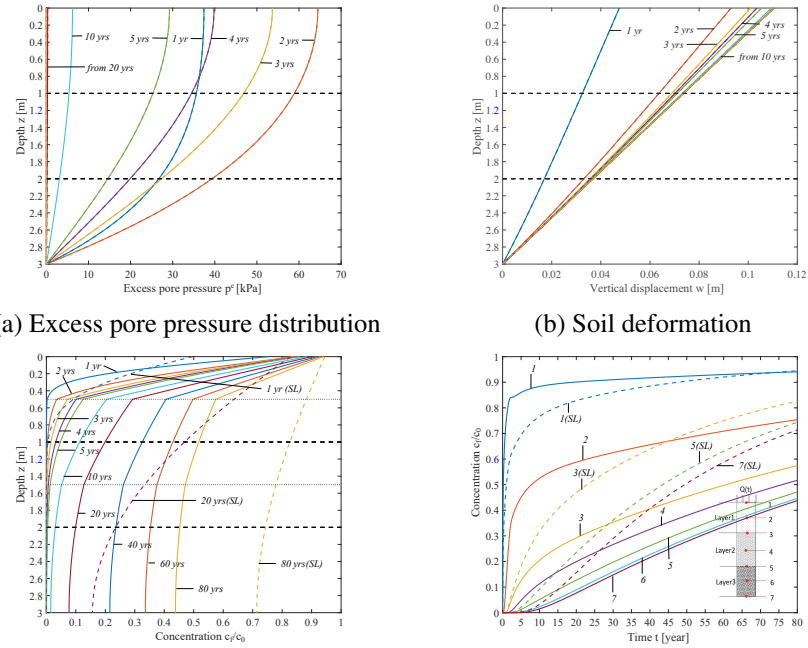

(a) Excess pore pressure distribution

(b) Soil deformation

(c) Solute concentration distribution

(d) Breakthrough diagram

Figure 2.15 Results of the Model G with various layer thickness and the molecular diffusion coefficient are varied for each layer.

and further leads to the smaller excess pore pressure buildup. As a results, though it is not obvious, the soil deforms slightly quicker than in the SL model, while remains the same level of deformation at the end of simulation (Figure 2.16(b)). Moreover, the varied degree of saturation contributed to slower contaminant migration. Figure 2.16(d) illustrates that after 80 years, the contaminant concentration is less than $0.07 kg/m^3$ which is less than that in the SL model.

Like the shear modulus, Poisson's ratio ν is an important factor in the soil deformation. To be specific, ν is a measurement of the material expansion that is perpendicular to the direction of compression. Compared to the SL model, a smaller Poisson's ratio in the top layer in model E allows less transverse expansion. According to Figure 2.17, for a stratified ν distribution, greater excess pore pressure and soil deformation are observed. The solute transport however is less affected.

2.4.9 ADVECTIVE EMISSION AND AVERAGE FLOW VELOCITY

To further examine the consolidation-induced advective flow, the average flow velocity at the bottom boundary for each model is plotted in Figure 2.18(a). It can be

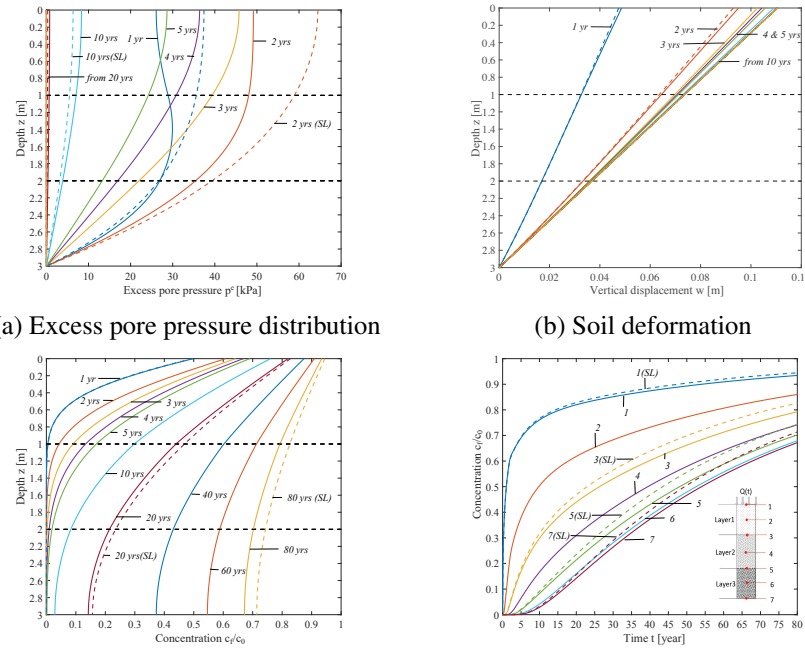

(a) Excess pore pressure distribution

(b) Soil deformation

(c) Solute concentration distribution

(d) Breakthrough diagram

Figure 2.16 Results of the Model D with various degrees of saturation are varied for each layer.

calculated as the summation of Darcy's velocity and the solid phase velocity:

$$v_f = -\frac{K}{S_r n^0 \rho_w g}\frac{\partial p^e}{\partial z} + \frac{\partial w}{\partial t}. \tag{2.25}$$

The v_f values for the SL model, model C and model G are the same, because the variation of D_m only affects solute transport but has no impact on soil consolidation. The peak v_f for all models occurs at around two years, when the post-loading stage is about to begin. Model B, with the varied shear modulus, shows a faster transient advective flow, with a peak flow velocity more than twice as large as that of the SL model. Moreover, the transient excess flow lasts longest (around 35 years) in model B while all other models need less than 16 years to fully dissipate the excess pore pressure. This is consistent with the results in Figure 2.12, in which a residual excess pore pressure of around 20 kPa remains after 20 years. These transient excess flows triggered by soil consolidation show considerable influence on the solute transport. The effects can be observed from the advective emission (E_{adv}) as summarized in

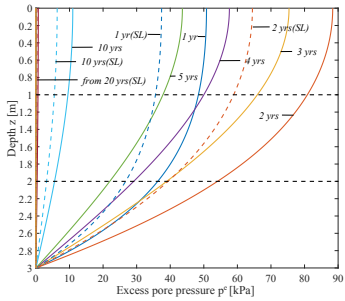

(a) Excess pore pressure distribution

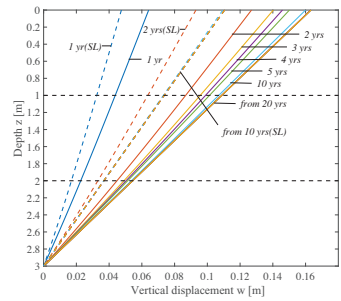

(b) Soil deformation

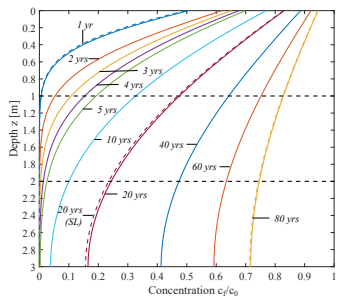

(c) Solute concentration distribution

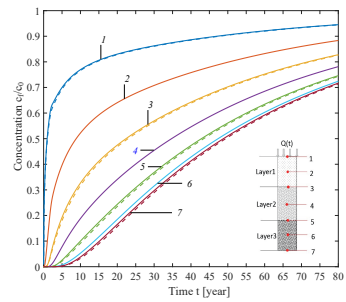

(d) Breakthrough diagram

Figure 2.17 Results of the Model E with various Poisson's ratio for each layer.

Figure 2.18(b). E_{adv} can be calculated as (Zhang et al., 2012*b*)

$$E_{adv} = \int_0^t -\frac{\partial p^e(\tau)}{\partial z} c_f(\tau) d\tau, \tag{2.26}$$

where τ is the independent variable of integration.

When a zero concentration gradient is assumed at the bottom outlet, no diffusion takes place and only advective flow occurs. Thus, the advective emission at each bottom boundary refers to the cumulative contaminant mass outflow, particularly due to the advective flow. Figure 2.18(b) presents the advective emission at each bottom boundary. As previously discussed, for some models (A, E, and F), the controlled parameters seem to have no discernible effects on the transit time needed for the contaminant to migrate through the soil layers or the solute breakthrough time. However, the advective emissions reflect noticeable differences compared to an averaged homogeneous single-layer situation. According to Figure 2.18(a), a faster advective transient flow may lead to a greater emission flux. After the consolidation process ends (at around 35 years for model B and 15 years for the others), E_{adv} reaches its maximum and remains constant. As for the SL model and models C and G, although the transient active flow shows no differences, the emission flux varies due to the individual molecular diffusion process. Specifically, with a smaller

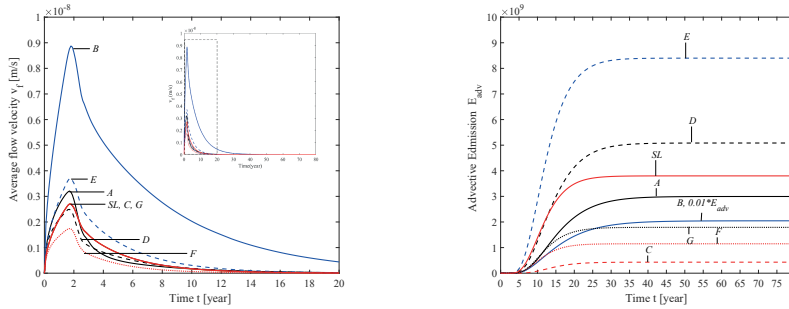

(a) Average flow velocity (b) Advective emission

Figure 2.18 The advective emission and the averaged flow velocity for all models.

molecular diffusion coefficient in the first layer, Model C shows the least advective emission which is less than 0.5×10^9. On the other hand, the largest advective emission occurs in model B, mainly due to its long-lasting consolidation process and higher excess pore pressure within voids.

2.5 SUMMARY

In this chapter, a theoretical model for the solute transport in a deformable unsaturated porous medium is developed. In this 1D model, small strain soil deformation is considered. The model is applied to a single landfill system and validated with the previous model (Peters and Smith, 2002). Based on dimensional analysis, a simplified model is proposed.

Based on the single-layer model, the multi-layer model was developed. With the new model, we further examined the multi-layer effects on the solute transport through a parametric study. Based on the numerical examples presented, the importance of correct modeling of a multi-layer soil matrix instead of simplified model for homogeneous situation with averaged soil profiles was highlighted. The guidance for designing a landfill site subject to a multi-layer soil environment was provided. In addition, selection of the appropriate construction site or proper treatment (such as field compaction) of the natural soil, especially the top layer, may reduce costs and better control the contaminated degree.

The parametric study presented in this chapter has treated the soil parameters' heterogeneity as varied in each layer, but within the same layer, the soil is still treated as homogeneous and constant over time. However, it is of interested to see how soil parameters' heterogeneity affects the consolidation-induced solute transport when the parameters such as hydraulic conductivity is varied with respect to pore pressure. Therefore, some of the parameters are dynamic and coupled with pore pressure.

2.6 APPENDIX: DERIVATION OF FLUID STORAGE AND SOLUTE TRANSPORT EQUATIONS FOR 1D CASES WITH SMALL STRAIN

The macroscopic mass conservative equation for pore-water in a general form is (Bear and Cheng, 2010)

$$\frac{\partial}{\partial t}\left(\theta\rho_w\right) = -\nabla\cdot\left(\rho_w\theta\overrightarrow{\mathbf{v}_f}\right), \tag{2.27}$$

where the volume fraction θ is related to porosity n and degree of saturation S_r by $\theta = S_r n$, ρ_w is density of pore water, $\overrightarrow{\mathbf{v}_f}$ denotes the average fluid velocity vector, which can be related to specific discharge relative to solid, $\overrightarrow{\mathbf{q}_r}$ based on Darcy's law by

$$\overrightarrow{\mathbf{q}_r} = \theta\left(\overrightarrow{\mathbf{v}_f} - \overrightarrow{\mathbf{v}_s}\right) = -\frac{K}{\rho_w g}\nabla p^e, \tag{2.28}$$

where $\overrightarrow{\mathbf{v}_s}$ is velocity of the solid.

Assuming ρ_w depends only on p, and with the definition of coefficient of compressibility β $(= (1/\rho_w)d\rho_w/dp)$, (2.27) yields

$$\frac{\partial S_r n}{\partial t} + \nabla\cdot\left(S_r n\overrightarrow{\mathbf{v}_f}\right) = -S_r n\beta\left(\frac{\partial p^e}{\partial t} + \overrightarrow{\mathbf{v}_f}\cdot\nabla p^e\right). \tag{2.29}$$

In view of Darcy's law, it becomes

$$\frac{\partial S_r n}{\partial t} + S_r\nabla\cdot\left(n\overrightarrow{\mathbf{v}_s}\right) - \nabla\cdot\left(\frac{K}{\rho_w g}\nabla p^e\right) = -S_r n\beta\left(\frac{\partial p^e}{\partial t} + \overrightarrow{\mathbf{v}_f}\cdot\nabla p^e\right). \tag{2.30}$$

Using the chain rule, we have

$$\nabla\cdot\left(\frac{K}{\rho_w g}\nabla p^e\right) = \frac{1}{\rho_w g}\nabla\cdot\left(K\nabla p^e\right) - \frac{K}{\rho_w g}\beta\nabla p^e\cdot\nabla p^e. \tag{2.31}$$

Substituting this expression and (2.28) into (2.30) gives

$$\begin{aligned}\frac{\partial S_r n}{\partial t} + S_r\nabla\cdot\left(n\overrightarrow{\mathbf{v}_s}\right) - \frac{1}{\rho_w g}\nabla\cdot\left(K\nabla p^e\right) - S_r n\beta\left(\overrightarrow{\mathbf{v}_f} - \overrightarrow{\mathbf{v}_s}\right)\cdot\nabla p^e \\ = -S_r n\beta\left(\frac{\partial p^e}{\partial t} + \overrightarrow{\mathbf{v}_f}\cdot\nabla p^e\right).\end{aligned} \tag{2.32}$$

Rearranging,

$$\frac{\partial S_r n}{\partial t} + S_r\nabla\cdot\left(n\overrightarrow{\mathbf{v}_s}\right) - \frac{1}{\rho_w g}\nabla\cdot\left(K\nabla p^e\right) = -S_r n\beta\left(\frac{\partial p^e}{\partial t} + \overrightarrow{\mathbf{v}_s}\cdot\nabla p^e\right). \tag{2.33}$$

Regarding the solid phase, its mass conservation equation is given by

$$\frac{\partial}{\partial t}\left[(1-n)\rho_s\right] = -\nabla\cdot\left((1-n)\rho_s\overrightarrow{\mathbf{v}_s}\right). \tag{2.34}$$

Since the deformation modulus of soil particles is relatively large under usual loading, deformation of the solid phase is assumed to be volume preserving, i.e., $D_s\rho_s/Dt = 0$ (where D_s/Dt is the material derivation), hence,

$$\frac{\partial n}{\partial t} = (1-n)\nabla\cdot\overrightarrow{\mathbf{v}_s} - \overrightarrow{\mathbf{v}_s}\cdot\nabla n = \nabla\cdot\overrightarrow{\mathbf{v}_s} - \nabla\cdot(n\overrightarrow{\mathbf{v}_s}). \tag{2.35}$$

Therefore, (2.33) becomes

$$S_r\nabla\cdot\overrightarrow{\mathbf{v}_s} - \frac{1}{\rho_w g}\nabla\cdot(K\nabla p^e) = -S_r n\beta\left(\frac{\partial p^e}{\partial t} + \overrightarrow{\mathbf{v}_s}\cdot\nabla p^e\right). \tag{2.36}$$

In case of relatively small deformations, it is reasonable to make the assumption that the advective component variation of p^e can be ignored Bear and Cheng (2010), i.e.,

$$\left|\frac{\partial p^e}{\partial t}\right| \gg |\overrightarrow{\mathbf{v}_s}\cdot\nabla p^e|, \tag{2.37}$$

thus,

$$S_r n\beta\frac{\partial p^e}{\partial t} + S_r\nabla\cdot\overrightarrow{\mathbf{v}_s} = \frac{1}{\rho_w g}\nabla\cdot(K\nabla p^e). \tag{2.38}$$

When $S_r = 1$, it leads to

$$n\beta\frac{\partial p^e}{\partial t} + \nabla\cdot\overrightarrow{\mathbf{v}_s} = \frac{1}{\rho_w g}\nabla\cdot(K\nabla p^e), \tag{2.39}$$

which is equivalent to the well-known storage equation of Verruijt (1969).

Consideration of solute mass in the fluid phase for a fixed representative element volume (REV) leads to

$$\frac{\partial\left(nS_r c_f\right)}{\partial t} + s = -\frac{\partial}{\partial z}\left[nS_r\left(-D\frac{\partial c_f}{\partial z} + v_f c_f\right)\right], \tag{2.40}$$

where, s is the rate of solute mass source per unit volume. The rate of solute loss by sorption onto the solid phase is equal to the rate of the solute gain by the solid phase from the fluid phase. It is noted that the amount and identity of matter in the REV may change with time, while the shape and position of this volume remain fixed. However, for the deformable porous medium considered in this study, the porosity n is time-dependent, and the macroscopic velocity of the solid matrix is not zero.

Conservation of solute mass for the solid phase is given by

$$\frac{\partial[(1-n)c_s]}{\partial t} - s = -\frac{\partial}{\partial z}\left[(1-n)v_s c_s\right]. \tag{2.41}$$

Finally, the transport equation for a solute in a deforming porous medium is expressed by combination of (2.40) and (2.41),

$$\frac{\partial\left(nS_r c_f\right)}{\partial t} + \frac{\partial[(1-n)c_s]}{\partial t} = -\frac{\partial}{\partial z}\left[nS_r\left(-D\frac{\partial c_f}{\partial z} + v_f c_f\right) + (1-n)v_s c_s\right]. \tag{2.42}$$

By the use of the mass balance equations for the fluid phase, (2.29), and solid phases, (2.34), and keeping in mind that ρ_s is constant, (2.42) can be simplified to

$$\begin{aligned} S_r n\frac{\partial c_f}{\partial t}+(1-n)\frac{\partial c_s}{\partial t} =& \frac{\partial}{\partial z}\left(S_r n D\frac{\partial c_f}{\partial z}\right)-S_r n v_f\frac{\partial c_f}{\partial z} \\ &-(1-n)v_s\frac{\partial c_s}{\partial z}+S_r n\beta\left(\frac{\partial p^e}{\partial t}+v_f\frac{\partial p^e}{\partial z}\right)c_f. \end{aligned} \tag{2.43}$$

Assuming the linear sorption relationship as described by (2.4) and (2.5), expanding (2.43) leads to

$$\begin{aligned} [S_r n+(1-n)\rho_s K_d]\frac{\partial c_f}{\partial t} =& S_r n D\frac{\partial^2 c_f}{\partial z^2}+\frac{\partial c_f}{\partial z}\left(S_r n\frac{\partial D}{\partial z}+S_r D\frac{\partial n}{\partial z}+\frac{K}{\rho_w g}\frac{\partial p^e}{\partial z}\right. \\ &\left.-[S_r n+(1-n)\rho_s K_d]\frac{\partial u}{\partial t}\right)+S_r n\beta\frac{\partial p^e}{\partial t}c_f \\ &-\beta\frac{K}{\rho_w g}\left(\frac{\partial p^e}{\partial z}\right)^2 c_f+S_r n\beta\frac{\partial u}{\partial t}\frac{\partial p^e}{\partial z}c_f. \end{aligned} \tag{2.44}$$

It is noted that the spatial derivative of porosity exists in (2.44). Volume conservation of the solid phase in soil can be utilized to develop its expression. For an incompressible solid:

$$U_s = U_m(1-n) = \text{constant}, \tag{2.45}$$

where U_s, U_m denote solid particle volume and the porous medium volume in the representive volume element, respectively. We separate U_m into the initial volume U_{m0} and incremental volume U_m^e, (2.45) becomes

$$U_s = (U_{m0}+U_m^e)(1-n). \tag{2.46}$$

By definition, volumetric strain $\varepsilon_v = U_m^e/U_{m0}$. Dividing both sides of (2.46) by U_{m0} obtains

$$1-n^0 = (1+\varepsilon_v)(1-n). \tag{2.47}$$

Therefore,

$$\nabla\left((1+\varepsilon_v)(1-n)\right) = 0. \tag{2.48}$$

Correspondingly,

$$\nabla n = \frac{(1-n)}{1+\varepsilon_v}\nabla\varepsilon_v = \frac{(1-n)^2}{1-n^0}\nabla\varepsilon_v. \tag{2.49}$$

In the analysis of Peters and Smith (2002), the spatial variation of n was neglected. Here, this can be accommodated by use of (2.49). Therefore, (2.44)

becomes

$$\begin{aligned}[S_r n+(1-n)\rho_s K_d]\frac{\partial c_f}{\partial t} &= S_r n D\frac{\partial^2 c_f}{\partial z^2}+\frac{\partial c_f}{\partial z}\left(S_r n\frac{\partial D}{\partial z}+S_r D\frac{(1-n)^2}{1-n^0}\frac{\partial^2 u}{\partial z^2}\right.\\ &\quad\left.+\frac{K}{\rho_w g}\frac{\partial p^e}{\partial z}-[S_r n+(1-n)\rho_s K_d]\frac{\partial u}{\partial t}\right)\\ &\quad+S_r n\beta\frac{\partial p^e}{\partial t}c_f-\beta\frac{K}{\rho_w g}\left(\frac{\partial p^e}{\partial z}\right)^2 c_f\\ &\quad+S_r n\beta\frac{\partial u}{\partial t}\frac{\partial p^e}{\partial z}c_f.\end{aligned} \tag{2.50}$$

Taking into account the constant longitudinal dispersivity, (2.50) changes to

$$\begin{aligned}[S_r n+(1-n)\rho_s K_d]\frac{\partial c_f}{\partial t} &= S_r n D_m\frac{\partial^2 c_f}{\partial z^2}+S_r n\alpha_L(v_f-v_s)\frac{\partial^2 c_f}{\partial z^2}\\ &\quad+\frac{\partial c_f}{\partial z}\left\{S_r\alpha_L n\frac{\partial(v_f-v_s)}{\partial z}+S_r D_m\frac{(1-n)^2}{1-n^0}\frac{\partial^2 u}{\partial z^2}\right.\\ &\quad+S_r\alpha_L(v_f-v_s)\frac{\partial n}{\partial z}+\frac{K}{\rho_w g}\frac{\partial p^e}{\partial z}\\ &\quad\left.-[S_r n+(1-n)\rho_s K_d]\frac{\partial u}{\partial t}\right\}\\ &\quad+S_r n\beta\frac{\partial p^e}{\partial t}c_f-\beta\frac{K}{\rho_w g}\left(\frac{\partial p^e}{\partial z}\right)^2 c_f\\ &\quad+S_r n\beta\frac{\partial u}{\partial t}\frac{\partial p^e}{\partial z}c_f.\end{aligned} \tag{2.51}$$

Recall the chain rule,

$$\begin{aligned}S_r\alpha_L n\frac{\partial\left(v_f-v_s\right)}{\partial z}+S_r\alpha_L\left(v_f-v_s\right)\frac{\partial n}{\partial z} &= \alpha_L\frac{\partial\left[S_r n\left(v_f-v_s\right)\right]}{\partial z}\\ &= -\alpha_L\frac{\partial\left(\frac{K}{\rho_w g}\frac{\partial p^e}{\partial z}\right)}{\partial z},\end{aligned} \tag{2.52}$$

and employing (2.31) and (2.38)), (2.51) becomes

$$
\begin{aligned}
[S_r n + (1-n)\rho_s K_d]\frac{\partial c_f}{\partial t} &= S_r n D_m \frac{\partial^2 c_f}{\partial z^2} - \alpha_L \frac{K}{\rho_w g}\frac{\partial p^e}{\partial z}\frac{\partial^2 c_f}{\partial z^2} \\
&+ \frac{\partial c_f}{\partial z}\left\{-\alpha_L S_r n\beta \frac{\partial p^e}{\partial t} - \alpha_L S_r \frac{\partial^2 u}{\partial z \partial t}\right. \\
&+ \frac{\alpha_L \beta K}{\rho_w g}\left(\frac{\partial p^e}{\partial z}\right)^2 + S_r D_m \frac{(1-n)^2}{1-n^0}\frac{\partial^2 u}{\partial z^2} \\
&\left.+ \frac{K}{\rho_w g}\frac{\partial p^e}{\partial z} - [S_r n + (1-n)\rho_s K_d]\frac{\partial u}{\partial t}\right\} \\
&+ S_r n\beta \frac{\partial p^e}{\partial t} c_f - \beta \frac{K}{\rho_w g}\left(\frac{\partial p^e}{\partial z}\right)^2 c_f + S_r n\beta \frac{\partial u}{\partial t}\frac{\partial p^e}{\partial z} c_f .
\end{aligned}
\tag{2.53}
$$

which is (2.7) in Section §2.2.

3 Coupled Consolidation and Solute Transport Model: 1D Finite Deformation

3.1 INTRODUCTION

Land-based containment facilities are commonly used for the disposal of municipal solid waste and contaminated dredged material (Liu, 2007). In modern landfills, liner systems are designed to isolate the landfill contents from the surrounding environment to protect the groundwater from pollution. For well-constructed composite liners, the geo-membrane typically has few defects, so restricting advection through it (Giroud and Bonaparte, 1989; Foose et al., 2002). However, volatile organic compounds (VOCs) can diffuse through membranes with magnitude four to six orders greater than the possible advection. Therefore, diffusion of VOCs in composite liners is viewed as a critical issue in the design of landfill liners (Foose, 2002).

The VOC transit time was traditionally estimated using the diffusion equation (Rowe and Badv, 1996; Fityus et al., 1999; Foose, 2002). However, several field tests have reported that the transit of VOCs is much earlier than theoretical predictions (Workman, 1993; Othman et al., 1997). Many researchers attribute this to consolidation and associated advective transport. Several theoretical models coupling mechanical consolidation with solute transport were constructed in recent years (Smith, 2000; Fox, 2007*b*; Lewis et al., 2009).

Based on the 1D Biot consolidation theory, Zhang et al. (2012*a*) proposed an advection-diffusion equation that incorporates the degree of saturation, compressibility of the pore fluid (CPW) and dispersivity of the solute transport in a nearly saturated deforming porous medium. Both CPW and dispersivity were found to influence solute migration within the CCL, significantly so in some circumstances. However, Zhang et al. (2012*a*) considered an infinitesimal strain, (i.e., small deformation) model. Additionally, they did not consider the material and geometric nonlinearity, factors that could be important in some circumstances (Lewis et al., 2009). Financial constraints sometimes limit deployment of the relatively costly CCLs. Natural clay deposits (sometimes with relatively high compressibility) are used as substitutes. Since the soft clayey soil generally provides a good contact adhesion with a geomemebrane, high effectiveness is a priori expected. However, the finite deformation caused by the emplacement of waste cannot be neglected.

In this chapter, the small deformation model for solute transport in a nearly saturated medium (Zhang et al., 2012*a*) will be further extended to finite deformations. This allows us to clarify the influence of consolidation in the progress

of solute transport (using a time-dependent boundary in terms of void ratio at the CCL base). The influence of the degree of saturation on the VOC transit time in clay barriers will also be examined. To account for the geometric non-linearity, a material coordinate system is used. Both CPW and dispersivity are considered in the new model. Further, our approach incorporates nonlinearity of the constitutive properties related to soil compressibility, the hydraulic conductivity and decreasing effective diffusion coefficient. A parametric study is carried out to examine the influence of several dominant parameters on the process of solute transport in porous medium.

3.2 MODEL FORMULATION

Lewis et al. (2009) and Peters and Smith (2002) developed a model coupling finite strain consolidation and solute transport in a fully saturated soil. Below, the CPW and dispersion in a nearly saturated soil is included.

3.2.1 FINITE STRAIN CONSOLIDATION

A Lagrangian coordinate system (z, t) is employed to derive the flow and transport equations. We define $\xi(z,t)$ as the particle displacement with $\xi(z,0) = z$. The relationship between Lagrangian and Eulerian (ξ,t) coordinate systems then implies that for any variable $F(z,t) = f(\xi(z,t),t)$:

$$\frac{\partial F}{\partial z} = \frac{\partial f}{\partial \xi}\frac{\partial \xi}{\partial z}, \quad \frac{\partial F}{\partial t} = \frac{\partial f}{\partial \xi}\frac{\partial \xi}{\partial t} + \frac{\partial f}{\partial t} = \frac{\partial f}{\partial \xi}v_s + \frac{\partial f}{\partial t}, \tag{3.1}$$

where $v_s = \partial\xi/\partial t$ is the solid velocity.

The equation describing changes in void ratio, $e(z,t)$, are derived from the continuity equations for the solid and fluid phases together with Darcy's law. The mass balance equation of the solid phase in differential form is

$$\frac{\partial}{\partial t}\left[\rho_s(1-n)\frac{\partial \xi}{\partial z}\right] = 0, \tag{3.2}$$

where ρ_s is the soil grain density, $n = e/(1+e)$ is the current porosity, and $n_0 = n(z,0)$ is the initial porosity. Note that, for constant ρ_s, the Jacobian, M, for the coordinate transformation is

$$M = \frac{\partial \xi}{\partial z} = \frac{1-n_0}{1-n} = \frac{1+e}{1+e_0}, \tag{3.3}$$

where e_0 is the initial void ratio.

The continuity equation for the fluid phase (i.e., pore-water) is

$$\frac{\partial}{\partial t}\left(nS_r\rho_f\frac{\partial \xi}{\partial z}\right) = -\frac{\partial}{\partial z}(\rho_f q), \tag{3.4}$$

where ρ_f is the pore fluid density.

According to Darcy's Law, the fluid flux is given by

$$q = -\frac{k_v}{\rho_f g}\frac{\partial p}{\partial \xi}, \tag{3.5}$$

where k_v is hydraulic conductivity and p is excess pore pressure. If the hydraulic gradient is constant, the Darcy equation in terms of total pressure can be transformed to this form (Peters and Smith, 2002).

Assuming ρ_f varies with pore pressure as $\partial \rho_f / \partial p = \beta \rho_f$ (Barry et al., 2007), substituting (3.5) into (3.4), then the continuity equation for the fluid phase becomes:

$$nS_r\beta\frac{\partial \xi}{\partial z}\frac{\partial p}{\partial t} + \frac{\partial}{\partial t}\left(S_r\frac{\partial \xi}{\partial z}\right) = \frac{1}{\rho_f g}\frac{\partial}{\partial z}\left(k_v\frac{\partial p}{\partial z}\frac{\partial z}{\partial \xi}\right), \tag{3.6}$$

where the compressibility of pore fluid (β) is defined in (2.2).

Because n and n_0 (implicitly embedded in $\partial \xi / \partial z$) appear simultaneously, and n is unknown, (3.6) can not be directly solved in terms of p. In the following derivation, it turns out that once the relationship between the derivative of p (with respect to t and a) and the corresponding derivative of e is known, it is straightforward to convert (3.6) to an equation in terms of e.

Assuming self-weight is negligible due to the relatively small thickness of the CCL (Zhang et al., 2012*a*), the vertical force equilibrium is

$$\frac{\partial \sigma}{\partial z} = 0, \tag{3.7}$$

where σ (now a function of t only) is the total normal stress of the soil and the z coordinate is vertically upwards. Assuming the compressive normal stress is positive, i.e., $\sigma = \sigma' + p$ (σ' is the effective normal stress), (3.7) leads to:

$$\frac{\partial p}{\partial \xi} = \frac{\partial}{\partial z}\left(-\sigma' + \sigma\right)\frac{\partial z}{\partial \xi} = \frac{1+e_0}{1+e}\frac{1}{\alpha_v}\frac{\partial e}{\partial z}, \tag{3.8}$$

where $\alpha_v = -de/d\sigma'$ is the coefficient of soil compressibility.

In the absence of self-weight, the rate of change of total stress at an arbitrary location equals that of the external top loading,

$$\frac{\partial \sigma}{\partial t} = \frac{\partial Q}{\partial t}, \tag{3.9}$$

where Q is the external load. The rate of change of the excess pore water pressure in the time domain is

$$\frac{\partial p}{\partial t} = \frac{\partial}{\partial t}(\sigma - \sigma') = \frac{\partial Q}{\partial t} + \frac{1}{\alpha_v}\frac{\partial e}{\partial t}. \tag{3.10}$$

Substituting (3.3), (3.8), (3.10) into (3.6) yields:

$$\left(\frac{eS_r\beta}{(1+e_0)\alpha_v} + \frac{S_r}{1+e_0}\right)\frac{\partial e}{\partial t} - \frac{1+e_0}{\rho_f g}\frac{\partial}{\partial z}\left(\frac{k_v}{\alpha_v(1+e)}\frac{\partial e}{\partial z}\right) = -\frac{S_r\beta e}{1+e_0}\frac{\partial Q}{\partial t}. \tag{3.11}$$

For the fully saturated case and when the CPW is neglected, i.e., $\beta = 0$, (3.11) reduces to:

$$\frac{1}{1+e_0}\frac{\partial e}{\partial t} = \frac{1+e_0}{\rho_f g}\frac{\partial}{\partial z}\left(\frac{k_v}{\alpha_v(1+e)}\frac{\partial e}{\partial z}\right), \tag{3.12}$$

which is identical to Eq. (1) of Lewis et al. (2009).

3.2.2 SOLUTE TRANSPORT EQUATIONS

Solute transport occurs in both solid and fluid phases. Here, for the nearly saturated soil, the mixture of pore-water and entrapped air is taken as a homogeneous fluid. Due to the discrete air bubbles, VOC transport by gas diffusion can be neglected in a nearly-saturated soil. Therefore, the mass conservation equation for the solute in the solid phase is

$$\frac{\partial}{\partial t}\left[(1-n)\rho_s S\frac{\partial \xi}{\partial z}\right] = f'_{a\to s}, \tag{3.13}$$

where S is the mass of solute sorbed on or within the solid phase per unit mass of the solid phase and $f'_{a\to s}$ denotes rate of solute loss in the water phase by solid phase sorption.

The mass conservation equation for solute in the fluid phase is

$$\frac{\partial}{\partial t}\left(nS_r c_f\frac{\partial \xi}{\partial z}\right) = -\frac{\partial J_f}{\partial z} - f'_{a\to s}, \tag{3.14}$$

where c_f is the concentration of the solute in the pore fluid. In (3.14), the term $\partial\xi/\partial z$ comes from the volumetric change (Peters and Smith, 2002) and J_f represents solute flux in the fluid phase, which is described by (Peters and Smith, 2002):

$$J_f(z,t) = nS_r(v_f - v_s)c_f - \frac{nS_r D}{M}\frac{\partial c_f}{\partial z}, \tag{3.15}$$

where D is the hydrodynamic dispersion coefficient. It is given by the sum of the effective diffusion coefficient (D_e) and the coefficient of mechanical dispersion (D_m):

$$D_m = \alpha_L\left(v_f - v_s\right), \tag{3.16}$$

where α_L is dispersion coefficient, v_f is the pore fluid velocity and $v_f - v_s$ denotes the relative velocity of the pore fluid.

Based on (3.13)–(3.15), we have:

$$\frac{\partial}{\partial t}\left\{\left[nS_r c_f + (1-n)\rho_s S\right]\frac{\partial \xi}{\partial z}\right\} = \frac{\partial}{\partial z}\left(\frac{nS_r D}{M}\frac{\partial c_f}{\partial z}\right) - \frac{\partial}{\partial z}\left[nS_r(v_f - v_s)c_f\right]. \tag{3.17}$$

The above equation can be further simplified with Darcy's Law, (3.5), and the mass balance equations for both solid and fluid phases, (3.2) and (3.4), respectively. (3.17) can then be expressed as:

$$nS_r\frac{\partial\xi}{\partial z}\frac{\partial c_f}{\partial t}+(1-n)\rho_s\frac{\partial\xi}{\partial z}\frac{\partial S}{\partial t}=\frac{\partial}{\partial z}\left(\frac{nS_rD}{M}\frac{\partial c_f}{\partial z}\right)+\frac{k_v}{\rho_f g}\frac{\partial p}{\partial\xi}\frac{\partial c_f}{\partial z}+\left(nS_r\beta\frac{\partial\xi}{\partial z}\frac{\partial p}{\partial t}-\frac{\beta k_v}{\rho_f g}\frac{\partial p}{\partial\xi}\frac{\partial p}{\partial z}\right)c_f. \tag{3.18}$$

Substituting (3.8) and (3.10) into (3.18) results in:

$$\begin{aligned}\left(S_r\frac{e}{1+e_0}+\frac{\rho_sK_d}{1+e_0}\right)\frac{\partial c_f}{\partial t}&=S_r\frac{\partial}{\partial z}\left(\frac{e(1+e_0)}{(1+e)^2}D\frac{\partial c_f}{\partial z}\right)\\&+\frac{k_v}{\rho_f g}\frac{1+e_0}{\alpha_v(1+e)}\frac{\partial e}{\partial z}\frac{\partial c_f}{\partial z}\\&+\beta\left[S_r\frac{e}{1+e_0}\left(\frac{\partial Q}{\partial t}+\frac{1}{\alpha_v}\frac{\partial e}{\partial t}\right)\right.\\&\left.-\frac{k_v}{\rho_f g\alpha_v^2}\frac{1+e_0}{1+e}\left(\frac{\partial e}{\partial z}\right)^2\right]c_f,\end{aligned} \tag{3.19}$$

where K_d describes the partitioning coefficient.

3.2.3 SPECIAL CASES

In this section, three special cases of the present model are outlined.

A. Saturated soil with finite deformation

For a saturated soil, where $S_r=1$, and incompressible pore fluid, i.e., $\beta=0$, (3.19) reduces to:

$$\left(\frac{e}{1+e_0}+\frac{\rho_sK_d}{1+e_0}\right)\frac{\partial c_f}{\partial t}=\frac{\partial}{\partial z}\left(\frac{e(1+e_0)}{(1+e)^2}D\frac{\partial c_f}{\partial z}\right)+\frac{k_v}{\rho_f g}\frac{1+e_0}{\alpha_v(1+e)}\frac{\partial e}{\partial z}\frac{\partial c_f}{\partial z}, \tag{3.20}$$

which is identical to Eq. (4) of Lewis et al. (2009) and Eq. (44) in Peters and Smith (2002).

B. Small deformation model

Under the assumptions of negligible self-weight and small deformation (constant porosity, i.e., $n=n_0$), the coupled deformation model can be expressed the following, which is identical to that of Zhang et al. (2012*a*):

$$S_rn_0\beta\frac{\partial p}{\partial t}+S_r\frac{\partial^2u}{\partial t\partial\xi}=\frac{1}{\rho_w g}\frac{\partial}{\partial\xi}\left(k_v\frac{\partial p}{\partial\xi}\right), \tag{3.21a}$$

$$G\frac{2(1-\nu)}{(1-2\nu)}\frac{\partial^2 u}{\partial \xi^2}=\frac{\partial p}{\partial \xi}, \tag{3.21b}$$

and

$$\begin{aligned}[S_r n_0+(1-n_0)\rho_s K_d]\frac{\partial c_f}{\partial t}&=S_r n_0 D_e\frac{\partial^2 c_f}{\partial \xi^2}-\alpha_L\frac{k_v}{\rho_w g}\frac{\partial p}{\partial \xi}\frac{\partial^2 c_f}{\partial \xi^2}\\&+\frac{\partial c_f}{\partial \xi}\left\{-\alpha_L S_r n_0\beta\frac{\partial p}{\partial t}-\alpha_L S_r\frac{\partial^2 u}{\partial \xi\partial t}\right.\\&+\frac{\alpha_L\beta k_v}{\rho_w g}\left(\frac{\partial p}{\partial \xi}\right)^2+S_r D_e(1-n_0)\frac{\partial^2 u}{\partial \xi^2}\\&\left.+\frac{k_v}{\rho_w g}\frac{\partial p}{\partial \xi}-[S_r n_0+(1-n_0)\rho_s K_d]\frac{\partial u}{\partial t}\right\}\\&+S_r n_0\beta\frac{\partial p}{\partial t}c_f-\beta\frac{k_v}{\rho_w g}\left(\frac{\partial p}{\partial \xi}\right)^2 c_f\\&+S_r n_0\beta\frac{\partial u}{\partial t}\frac{\partial p}{\partial \xi}c_f,\end{aligned} \tag{3.21c}$$

where u is the soil displacement, G is the shear modulus and ν is Poisson's ratio. The constant material coefficients can be described as:

$$\begin{aligned}G&=\frac{c_v\rho_f g(1-2\nu)}{2k_v(1-\nu)}=\frac{(1+e_p)(1-2\nu)}{2(1-\nu)\alpha_{vp}},\\k_v&=k_p,\quad D_e=D_{e0},\end{aligned} \tag{3.22}$$

where c_v is the consolidation coefficient; k_s and k_p the saturated hydraulic conductivity and hydraulic conductivity of the soil corresponding to e_p (the void ratio corresponding to pre-consolidation stress), respectively.

C. Nearly saturated soil with no deformation

For the partially saturated no deformation model, i.e., $e=e_0$, $\xi=z$, the overloading, Q, does not affect solute transport. In the spatial coordinate system (ξ, t), (3.19) reduces to the linear diffusion equation:

$$\frac{\partial c_f}{\partial t}=D\left(1+\frac{\rho_s K_d}{S_r e_0}\right)^{-1}\frac{\partial^2 c_f}{\partial \xi^2}. \tag{3.23}$$

3.3 VARIATIONS OF PARAMETERS IN CONSOLIDATION AND SOLUTE TRANSPORT PROCESSES

The finite deformation model allows consideration of the effects of variations in the coefficients of consolidation and transport (such as the coefficient of compressibility,

α_v, hydraulic conductivity, k_v and hydrodynamic dispersion, D) on solute transport process. Lewis et al. (2009) utilized void ratio-dependent functions for the related coefficients while Li and Liu (2006) used a fractal pore-space theory to develop fractal models of water flow and solute diffusion in rigid unsaturated soils. Their approach allowed comparison of these coefficients between the fully saturated and unsaturated cases. Here, a combination of both models is employed so that the hydraulic conductivity and the effective diffusion depend on both the void ratio and the degree of saturation. Linear, reversible solute sorption is assumed in this study. however, the approach can be adapted for other sorption models.

3.3.1 SOIL COMPRESSIBILITY

The soil layer is assumed to be over-consolidated, and compression of the soil layer commences when the applied stress exceeds the pre-consolidation stress, i.e., deformation due to re-compression is neglected. In this case, the void ratio is idealized as a linear function of the logarithm of the effective stress (Means and JV., 1964):

$$e = e_p - C_c \log\left(\frac{\sigma'}{\sigma'_p}\right), \tag{3.24}$$

where σ' is effective stress, σ'_p denotes the pre-consolidation stress and C_c is the compression index of the soil (defined by the absolute value of the slope of the idealized virgin compression line).

For a nearly saturated soil, the degree of saturation is sufficiently high so that the air phase exists in the form of occluded bubbles. Vaughan (2003) claimed that the presence of occluded air bubbles is unlikely to affect soil effective stresses. Therefore, (3.24) is employed to describe the volumetric change of a nearly saturated soil.

The coefficient of compressibility in terms of void ratio can be obtained by differentiation of (3.24) with respect to effective normal stress (Lewis et al., 2009):

$$\alpha_v = \alpha_{vp} \exp\left[\ln 10\left(\frac{e - e_p}{C_c}\right)\right], \tag{3.25}$$

where α_{vp} is the coefficient of compressibility corresponding to σ'_p, i.e.,

$$\alpha_{vp} = \frac{C_c}{\sigma'_p \ln 10}. \tag{3.26}$$

3.3.2 HYDRAULIC CHARACTERISTICS

For hydraulic conductivity, an empirical relationship describing its variation with void ratio in saturated clay soils is given as (Mitchelll, 1993):

$$k_s = k_p \exp\left[\ln(10)\left(\frac{e - e_p}{C_k}\right)\right], \tag{3.27}$$

where C_k is the hydraulic conductivity index.

The power law relationship equation for hydraulic conductivity versus water content θ ($= S_r n$) is (Li and Liu, 2006):

$$k_v = k_s \left(\frac{\theta}{\theta_s} \right)^{\alpha}, \tag{3.28}$$

where θ_s is saturated water content, and α falls in the range of 2.68 to 2.78 for clay loam.

3.3.3 DISPERSION COEFFICIENT

In a saturated soil, the effective solute diffusion coefficient is defined as the product of the free diffusion coefficient of the solute in the pore fluid (D_f) and the tortuosity factor (t_f), which accounts for the irregular path that diffusing molecules must take through the pore space (Acar and Haider, 1990). Lewis et al. (2009) claimed that it is rational to take D_e as constant, because uncertainty of the range of τ_f can be the same order of consolidation-induced change of D_e. Alternatively, the reduction of D_e can be expressed with a hypothetical relationship associated with the overall void ratio change as (Lewis et al., 2009; Morel-Seytour et al., 1996):

$$D_e = \left(\frac{e_0 - e}{3(e_0 - e_f)} + \frac{e - e_f}{e_0 - e_f} \right) D_{e_0}, \tag{3.29}$$

where e_f denotes the final void ratio, and D_{e0} is the initial effective dispersion coefficient.

In variably saturated soils, the effective diffusion coefficient, D_e, depends on soil water content, bulk density, and soil type for soils with different textures. Regarding the water content, there is a threshold value under which solute diffusivity vanishes (Hunt and Ewing, 2003; Hamamoto et al., 2009). The impedance factor (Porter et al., 1960) (i.e., the ratio of solute diffusion coefficient in soil to product of solute diffusion coefficient in free water and volumetric soil water content), decreased with increasing bulk density for each soil type, but the effect of the overall bulk density on the impedance factor is minor compared with the effect of soil water content and soil type (Hamamoto et al., 2009).

The effective diffusion coefficient was found to decrease with decreasing saturation in laboratory experiments (Barbour et al., 1996). The decrease was found to be quite rapid initially, followed by a near-linear decline for degree of saturation below 60%. Here, the soil diffusion coefficient is expressed as (Li and Liu, 2006):

$$D_e = 1.1 D_f \theta (\theta - \theta_t), \tag{3.30}$$

where θ_t denotes threshold water content, which was observed to become higher with increasing clay content and varies between 3% and 20% for clay soil.

3.3.4 SORPTION

It has been reported that the effect of the degree of saturation on the adsorption coefficient is insignificant from full saturation to a degree of saturation of 10%

(Barbour et al., 1996). A significant decrease in the adsorption coefficient only occurs in cases with a low degree of saturation. In this study the degree of saturation varies from 1 to 0.8, i.e., the effect on sorption can be neglected. Therefore, the concentration of solute in the solid phase, S, is expressed as:

$$S = K_d c_f. \tag{3.31}$$

This assumption of a linear sorption is valid at the relatively low concentrations that are usually found in the municipal waste disposal sites (Mathur and Jayawardena, 2008).

3.4 APPLICATION TO A LANDFILL LINER

As the schematic in Figure 2.1 shows, the composite landfill liner beneath a primary leachate collect system (PLCS) consists of an impermeable (to diffusion of inorganic solute) geomembrane, an underlying engineered compacted clay layer (CCL), and a second leachate collecting system (SLCS).

The model parameters employed in the following analyses are based on those used in recent studies of solute transport in composite liners (Foose, 2002; Lewis et al., 2009). Because of the unavailability of consolidation data in the literature, hypothetical values of the applied stress, pre-consolidation stress, compression index, hydraulic conductivity index, threshold moisture content and other parameters in calculating the D_e and k_v are used. As a primary parameter, the compression index covers a large range to account for the high-compressibility soil considered (Lewis et al., 2009). However, the related applied stress was selected to avoid negative and unrealistically low void ratios. The parameters used are given in Table 3.1.

3.4.1 BOUNDARY CONDITIONS FOR CONSOLIDATION

The following boundary conditions are introduced. Assuming there are no defects in the geomembrane, the top boundary ($z = 0$) is assumed to be impermeable, i.e., $q = 0$. Therefore, from (3.5) and (3.8),

$$\frac{\partial e}{\partial z} = 0 \text{ at } z = 0. \tag{3.32}$$

At the bottom drainage boundary ($z = L$), the excess pore pressure is zero and a Dirichlet-type boundary condition for void ratio (e) can be derived from the effective stress–void ratio equilibrium relationship, (3.24):

$$e = e_p - C_c \log\left(\frac{\sigma'_L}{\sigma'_p}\right), \tag{3.33}$$

where σ'_L denotes the effective stress at bottom.

The excess pore pressure vanishes at the bottom boundary, so $\sigma'_L = \sigma_a$, where σ_a is a time-varying stress due to the external overburden. Note that σ_a is the maximum

Table 3.1
Values of input parameters.

Parameter	Value
Maximum applied stress (ramp loading for 2 years), σ_a	450 kPa
Preconsolidation stress, σ_p'	50 kPa
Compression index, C_c	0.2, 0.8
Preconsolidation hydraulic conductivity, k_p	10^{-9}, 2×10^{-10} m/s
Constant, α	2.7
Hydraulic conductivity index, C_k	0.585
Thickness of geomembrane, h	0.0015 m
Thickness of CCL, L	1.22 m
Mass transfer coefficient of geomembrane, P_G	4×10^{-11}m^2/s
Initial effective diffusion coefficient, D_{e0}	2×10^{-10} m^2/s
Free diffusion coefficient in the pore fluid, D_f	10^{-9} m^2/s
Threshold moisture content, θ_t	0.05
Partitioning coefficient, K_d	0, 0.2, 1 ml/g
Dispersion, α_L	0, 0.1 m
Initial void ratio, e_0 (= e_p)	1.17
Acceleration due to gravity, g	9.81 m/s^2
Initial density of pore-water, ρ_f	10^3 kg/m^3
Density of the solid phase, ρ_s	2.7×10^3 kg/m^3
Degree of saturation of clay, S_r	1, 0.9, 0.8

loading in the model of Lewis et al. (2009). The void ratio rapidly approaches a steady value, which consequently leads to a spurious higher fluid velocity and faster solute transport. To distinguish the cases, we label the present boundary condition at the CCL bottom as 'BCC' and 'BCL', i.e., the boundary conditions used by Lewis et al. (2009).

3.4.2 BOUNDARY CONDITIONS FOR SOLUTE TRANSPORT

At the top of the CCL, VOC diffusion through the geo-membrane is described by Fick's law (Booker et al., 1997), so the concentration gradient is proportional to the difference in concentrations on each side of the (sufficiently thin) geomembrane. In the material coordinate system, the boundary condition is (Lewis et al., 2009):

$$\frac{\partial c_f}{\partial z}(0,t) = \frac{(1+e(0,t))^2}{e_0(1+e_0)}\frac{P_G}{hD_e}\left(c_f(0,t) - C_{f0}\right), \tag{3.34}$$

where C_{f0} is the (constant) solute concentration at the top surface of the geo-membrane with the assumption that the landfill waste volume is large (Peters and

Smith, 2002); h and P_G are, respectively, the thickness and the permeation coefficient for the solute in the geo-membrane.

The lower boundary condition for the solute concentration (c_f) is (Peters and Smith, 2001):

$$\frac{\partial c_f}{\partial z} = 0, \quad \text{at } z = L, \tag{3.35}$$

which assumes negligible diffusion below the CCL base (Barry and Sposito, 1988).

3.4.3 MODEL VERIFICATION

Since there are no experimental data available in the literature, the present model was reduced to the full-saturation case using the same boundary condition at the CCL bottom for e as used by Lewis et al. (2009), i.e., σ_a is taken as the maximum loading; and $K_d = 0$, $\alpha_L = 0$, $C_c = 0.8$, $k_p = 10^{-9}$ m/s. A comparison between the present and previous models is illustrated in Figure 3.1. In the figure, the results of the finite deformation with constant and decreasing hydrodynamic dispersion, 3.29, small deformation model (Zhang et al., 2012*a*) and the pure diffusion model (i.e., no deformation model) are included. Both consolidation (i.e., void ratio, e, distribution) and relative concentration obtained from the present model are in excellent agreement with results of Lewis et al. (2009). As shown in Figure 3.1, with the constant effective diffusion coefficient, the small deformation model (Zhang et al., 2012*a*) predicts a slower solute migration than the corresponding finite deformation model.

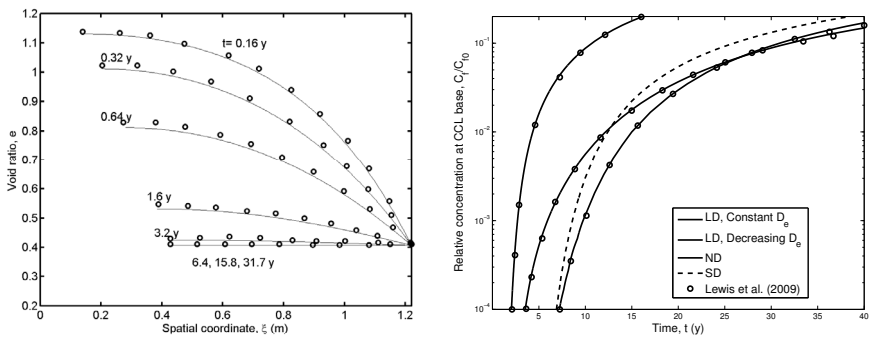

(a) Void ratio evolution (b) Breakthrough curves

Figure 3.1 Comparison of (a) void ratio evolution and (b) breakthrough curves between the present model (solid line) and Lewis et al. (2009) (circle). Notations: FD: finite deformation model, SD: small deformation model, ND: no deformation model.

3.4.4 CORRECTNESS OF THE BOUNDARY CONDITION AT CCL BASE

The differences due to the different boundary conditions, 'BCL' (used by Lewis et al. (2009)) and 'BCC' (used in the present model), are presented in Figure 3.2, where

$C_c = 0.8$ and $k_p = 10^{-9}$ m/s. A comparison of Figure 3.2(a) (BCC) and 3.1(a) (BCL) shows that taking σ_a as the maximum loading leads to a greater void ratio gradient and a faster consolidation process, although the final value of e is very close. This initially speeds up the solute transit slightly, and then slows it down in the long-term (Figure 3.2(b)). The reason the trend reverses after the consolidation completes for the 'BCL' case is that the higher solute concentration level during the consolidation phase of 'BCC' occurs later resulting in an increased advective flux. The separation is more obvious for the relatively soft and higher permeablility cases. In the following sections all numerical results are based on the boundary condition 'BCC'.

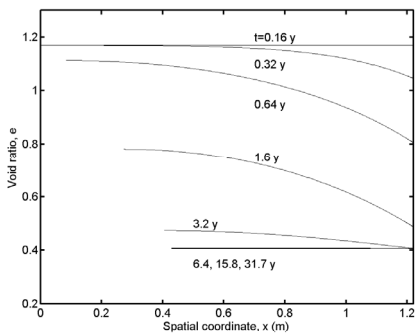

(a) Void ratio evolution (BCC only)

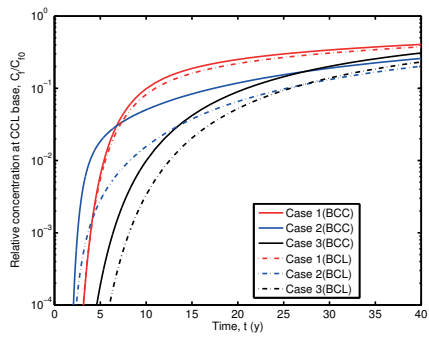

(b) Breakthrough curves (BCC and BCL)

Figure 3.2 Influence of Boundary condition of void ratio (e) at CCL base (a) void ratio evolution (BCC only) and (b) breakthrough curves ($S_r = 1$, $\beta = 0$, $\alpha_L = 0$, constant D_e). In (b), solid line for 'BCC', and dash-dot line for 'BCL'. Case 1: $k_p = 2 \times 10^{-10}$ m/s, C_c =0.8; Case 2: $k_p = 10^{-9}$ m/s, C_c =0.8; and Case 3: $k_p = 10^{-9}$ m/s, C_c =0.2.

3.5 NUMERICAL RESULTS AND DISCUSSIONS

A numerical solution was constructed using COMSOL 3.5a (COMSOL, 2010). It discretized the domain into unstructured Lagrange-linear elements with a maximum global element size of 10^{-2} m, and maximum local element size at the end boundaries (where the most rapid changes occur) of 10^{-4} m. Temporally, the sub-time step was 10^{-2} y. To be easily interpreted, solution curves were plotted in the spatial coordinate x:

$$x = z + \int_z^L \frac{e_0 - e(\zeta)}{1 + e_0} d\zeta. \tag{3.36}$$

Thus, the first-order PDE,

$$\frac{\partial x}{\partial z} = 1 - \frac{e_0 - e(z)}{1 + e_0}, \tag{3.37}$$

with boundary conditions $x(0,t) = S_{mt}$ and $x(L,t) = L$ was constructed to find x, where the settlement S_{mt} is given by:

$$S_{mt} = \int_0^L \frac{e_0 - e(\zeta)}{1+e_0} d\zeta. \tag{3.38}$$

3.5.1 EFFECT OF CONSOLIDATION

On basis of the 'BCL' boundary condition, Lewis et al. (2009) observed that there is no noticeable solute concentration at the CCL base when consolidation of the liner is completed even for the case of very high compressibility ($C_c = 0.8$). They thus concluded that transport can be simulated using the pure diffusion model with the final void ratio value. However, during consolidation the distribution of solute concentration changes, which is the initial condition of what follows. Thus, advective transport due to consolidation may not be negligible.

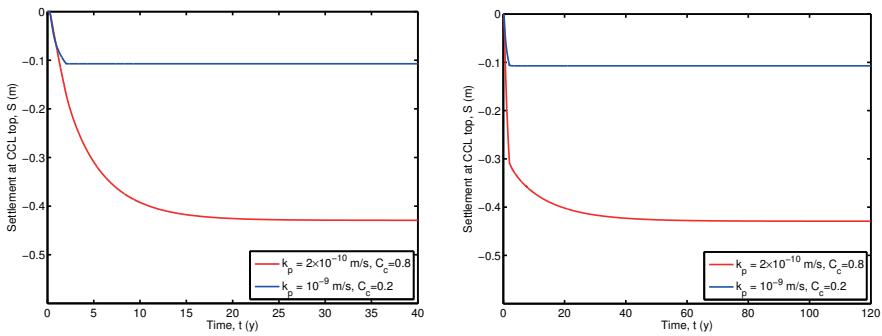

Figure 3.3 Consolidation settlements in a (a) saturated soil ($S_r = 1$) and (b) partially saturated soils ($S_r = 0.8$).

Figures 3.3(a) and 3.4(a) illustrate the consolidation processes and solute transport in a saturated soil for two cases with different compression indices (C_c) and hydraulic conductivities (k_v). Consolidation lasts 2.2 and 34.5 y for $C_c = 0.2$ and $C_c = 0.8$, respectively. For the 'soft' case, a noticeable concentration difference from the no deformation model appears at the CCL base during consolidation, as shown in Figure 3.4(a). The difference decreases with higher levels of sorption (Figure 3.4(a)). The effect of consolidation on transport exists during both the consolidation and post-consolidation stages, which is consistent with Fox (2007*b*). Since the advection results in a notable concentration level at the CCL base, simplifying assumptions such as instant deformation, pure diffusion and finite deformation without advection modeling are not appropriate. The magnitude of solute concentration C_f in Figure 3.4(a) is an order greater than that in Figure 3.4(a) . Here, the influence of sorption is noticeable as it drastically retards the solute transport.

Figures 3.3(b) and 3.4(b) present the results for a nearly saturated soil. We see again that soft clay consolidation has a noticeable effect on solute transport (Figure

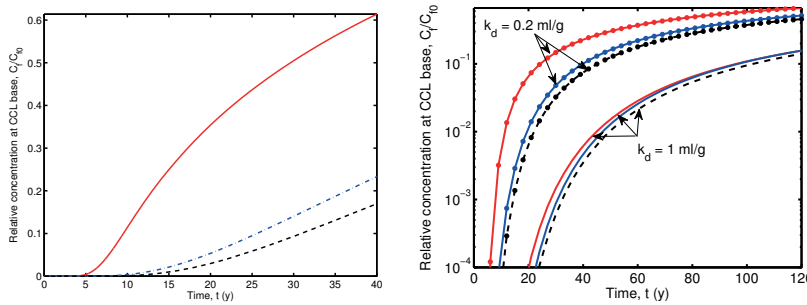

$K_d = 0$ $K_d \neq 0$

(a) saturated soil (S_r=1)

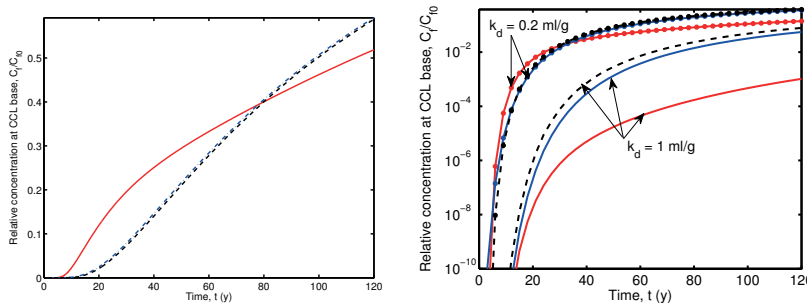

$K_d = 0$ $K_d \neq 0$

(b) partially saturated soils ($S_r = 0.8$)

Figure 3.4 Effect of consolidation on relative concentration C_f/C_{f0} in a (a) saturated soil ($S_r = 1$, , $\alpha_L = 0$, constant D_e) and (b) partially saturated soils ($S_r = 0.8$, with CPW, $\alpha_L = 0.1$ m, varying D_e as in (3.30)) with two cases ($K_d = 0$ and (b) $K_d \neq 0$) . Notations: solid line (FD, finite deformation model): $C_c = 0.8$, $k_p = 2 \times 10^{-10}$ m/s; dash-dot line (FD, finite deformation model): $C_c = 0.2$, $k_p = 10^{-9}$ m/s; and dashed line: no deformation model (ND).

3.3(b)). However, since the effective diffusion (D_e) reduces with deformation, concentrations for the pure diffusion model surpass those of coupled models, as is obvious for the case of $K_d = 1$ ml/g.

Consolidation effects are composed of the variation of void ratio and the occurrence of pore-water flow, which in turn causes the advective transport flux. As mentioned previously, Lewis et al. (2009) claimed the advection component can be ignored as long as the variation of void ratio is considered. Here, we included in Figure 3.5 the case of finite deformation without advection, i.e., advection is removed from (3.19). Exclusion of advection underestimates the concentration level and consequently leads to a longer transit time. In the absence of sorption, at the nominal 10% breakthrough, a nearly twofold change occurs in the transit time; this change increases when sorption is included.

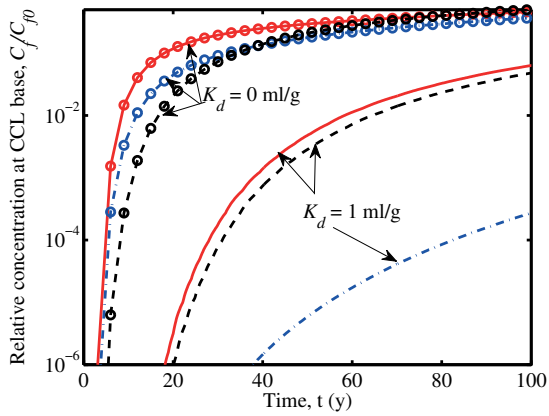

Figure 3.5 Effect of advection flux on concentration level at CCL base for partially saturated cases ($S_r = 0.8$, with CPW, $\alpha_L = 0.1$ m, varying D_e as in (3.30)). For finite deformation model, solid line: $C_c = 0.8$, $k_p = 2 \times 10^{-10}$ m/s; dash-dot line: without advection flux in transport, (3.19); dashed line: No deformation model.

3.5.2 EFFECT OF DEGREE OF SATURATION

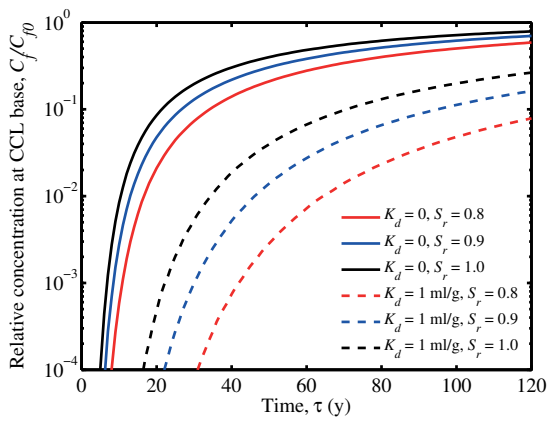

Figure 3.6 Effect of saturation S_r on transport for no-deformation model.

Figure 3.6 demonstrates that the higher saturation of the no-deformation (ND) model results in faster solute transport due to the saturation (S_r)-dependent effective diffusion; the gap is larger in the presence of sorption. Concentrations predicted by the coupled finite deformation and solute transport model are shown in Figure 3.7. For cases with parameters $C_c = 0.8$ and $k_p = 10^{-9}$ m/s, consolidation lasts for approximately 12.8 y. Higher saturation results in faster solute transport because of

greater effective diffusion, regardless of the sorption. For decreasing D_e, the transit time increases, as shown in Figure 3.7(a). With sorption, finite deformation with $S_r = 0.8$ and constant D_e leads to almost the same concentration as for the ND model (Figure 3.7(b)). Again, this demonstrates that the effect of unsaturation is more apparent in the presence of sorption. Interestingly, with both sorption and decreasing D_e taken into account, finite deformation (FD) models will not always produce faster solute transport (Figure 3.7(a)). During consolidation and in the early post-consolidation stage, the FD models have a faster transit, but then are surpassed by the ND model because the effective diffusion is reduced due to compaction. However, the decreasing D_e with compaction is inevitable. In the field, VOC has been shown to appear earlier than predicted by the pure diffusion model has been observed (Peters and Smith, 2002). Possible explanations are: (1) the constitutive relationships for soil parameters are not accurate enough; or (2) other factors, such as heat transfer, should be also included in the model.

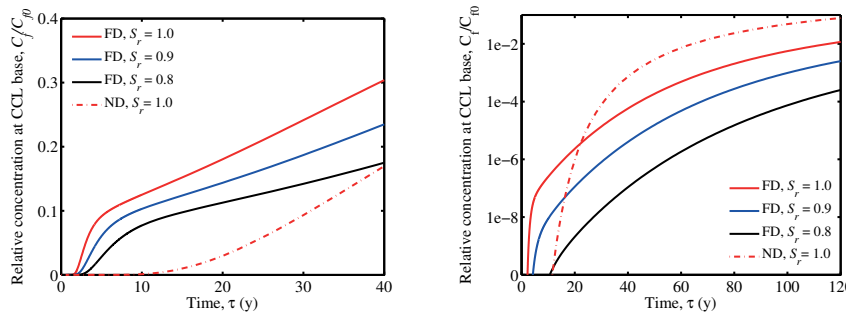

$K_d = 0$ $K_d = 1$ ml/g

(a) The case with decreasing D_e

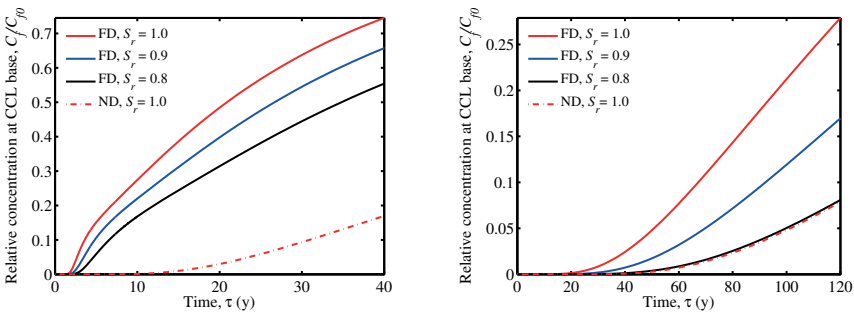

$K_d = 0$ $K_d = 1$ ml/g

(b) The case with a constant D_e

Figure 3.7 Concentration level at CCL base for partially saturated cases with decreasing D_e. ($C_c = 0.8$, $k_p = 10^{-9}$ m/s). Notation: FD: finite deformation model and ND: no deformation model.

3.5.3 EFFECT OF COMPRESSIBILITY OF PORE-WATER (CPW)

As shown in Figure 3.8, the effect of compressibility of pore-water (CPW) is related to the soil consolidation coefficient. The influence of CPW on the relative concentration at the CCL becomes more significant for the cases with smaller consolidation coefficients. When the soil is relatively soft ($C_c = 0.8$ and $k_p = 2 \times 10^{-10}$ m/s), CPW causes twofold longer transit times for the nominal 10% breakthrough. However, at the early consolidation stage, the retarding effect of CPW is more pronounced for 'stiffer' soils and then the trend reverses (Figure 3.8) after consolidation completes. These graphs are not shown as the numerical values are too small to present in the same figure. This can be explained by the slowing fluid flow and longer consolidation time due to CPW. Since the separation of curves at a relatively higher concentration level, i.e., absolute concentration difference, is of interest, it follows that the influence of CPW is more significant in softer soil.

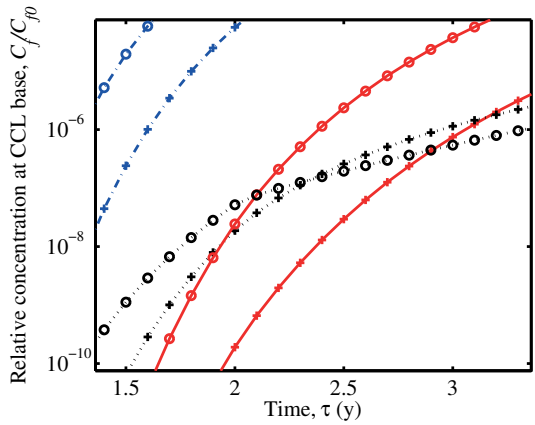

Figure 3.8 Effect of CPW on concentration level at CCL base for partially saturated cases ($S_r = 0.8$) with varying D_e and without sorption ($K_d = 0$). Solid lines: $C_c = 0.8$, $k_p = 2 \times 10^{-10}$ m/s; Dashdot lines: $C_c = 0.8$, $k_p = 10^{-9}$ m/s; Dotted lines: $C_c = 0.2$, $k_p = 10^{-9}$ m/s. Cross symbol: with CPW; circle symbol: without CPW ($\beta = 0$).

To investigate further the influence of CPW, three models examining the three terms containing β are considered here.

- Model A: eliminate $\frac{eS_r\beta}{(1+e_0)\alpha_v}\frac{\partial e}{\partial t}$ from (3.11);
- Model B: eliminate $-\frac{S_r\beta e}{1+e_0}\frac{\partial Q}{\partial t}$ from (3.11);
- Model C: eliminate the term involving β from (3.19).

As shown in Figure 3.9, each of the missing terms leads to a large deviation from the full model, so all terms involving β should be retained for the cases considered.

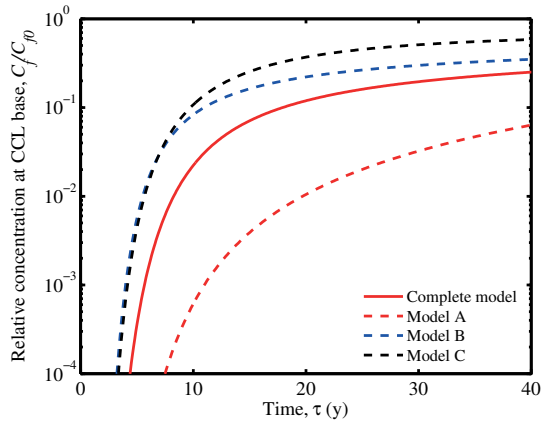

Figure 3.9 Significance of each term involving β on concentration level at CCL base for partially saturated cases ($S_r = 0.8, C_c = 0.8, k_p = 2 \times 10^{-10}$ m/s) with varying D_e and without sorption ($K_d = 0$).

3.5.4 EFFECT OF DISPERSION

Lewis et al. (2009) neglected mechanical dispersion on the assumption that the pore fluid velocity in fine-grain soil is less than 10^{-6} m^2/s. However, as shown in Figure 3.10, its influence cannot be neglected when the clay is relatively soft, even when the maximum fluid average linear velocity is approximately 4.5×10^{-9} m/s for the case $C_c = 0.8$ and $k_p = 2 \times 10^{-10}$ m/s. Its influence becomes more significant as the hydraulic conductivity increases with the same soil compressibility, C_c. This is because decreasing D_e increases the Péclet number (ratio of the rate of advection to the rate of diffusion). Therefore, a rough estimate using pore fluid velocity alone as proposed by Lewis et al. (2009) is not always definitive.

Figure 3.11 illustrates the individual influence of decreasing D_e, dispersion and CPW. The effect of reducing D_e causes slower transport, while dispersion a faster transit. Although the influence of CPW is not as significant as decreasing D_e and dispersion, it is not negligible, as shown in Figure 3.11.

3.5.5 EFFECT OF FINITE DEFORMATION

For the soil without sorption (see Figures 3.1(b), 3.7(a), 3.7(b), 3.11(a)), the ND model always leads to a longer transit time than the finite deformation model. In the presence of sorption (as shown in Figure 3.7(b)), the difference between the ND model and the finite deformation model is negligibly small. However, when the decrease of the effective diffusion coefficient due to deformation is also considered (Figure 3.7(a) and 3.11(b)), the results of the two models differ.

Compared with the finite deformation model, the small deformation model can overestimate the contaminant transit time in a liner undergoing large consolidation

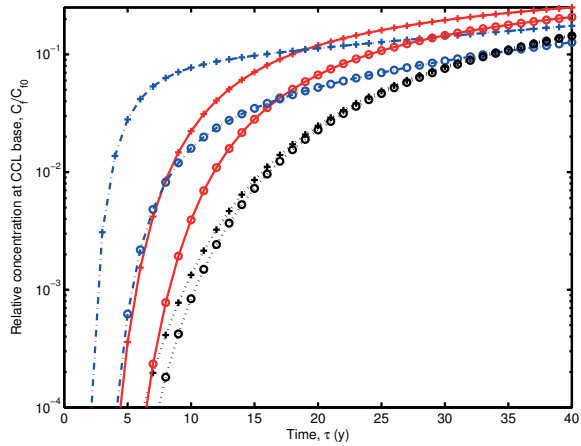

Figure 3.10 Effect of dispersion on concentration level at CCL base for partially saturated cases ($S_r = 0.8$) with varying D_e and without sorption ($K_d = 0$). Solid lines: $C_c = 0.8$, $k_p = 2 \times 10^{-10}$ m/s; Dashdot lines: $C_c = 0.8$, $k_p = 10^{-9}$ m/s; Dotted lines: $C_c = 0.2$, $k_p = 10^{-9}$ m/s. Cross symbol: $\alpha_L = 0.1$ m; circle symbol: $\alpha_L = 0$ (no dispersion).

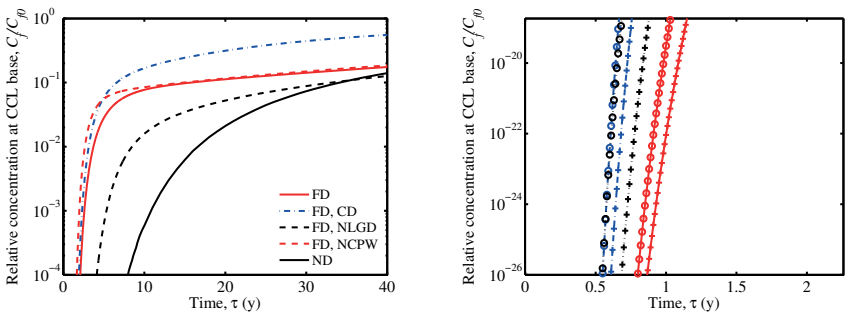

Figure 3.11 Comparison of the concentration level at CCL base for various variable associative in partially saturation soils ($S_r = 0.8, C_c = 0.8, k_p = 10^{-9}$ m/s). Notation: FD: finite deformation model; CD: constant D_e; NLGD: excluding the dispersion; NCPW: excluding the CPW; ND: no deformation model.

(Figure 3.1(b)). This demonstrates that the significance of geometric nonlinearity is noticeable for relatively soft soil. This finding is consistent with that of Peters and Smith (2002) and Lewis et al. (2009). Regarding the consolidation, the small deformation model can predict settlement that is non-physical for soft soil (i.e., larger than the total soil thickness). Therefore, for a relatively compressible soil, where the consolidation effect is more significant, a finite deformation consolidation is necessary when being coupled with the solute transport.

3.6 SUMMARY

In this chapter, a finite deformation model for coupling consolidation and solute transport processes in partially saturated soil has been presented. It was applied to predict the VOC breakthrough in a landfill clay liner. CPW, dispersion, the nonlinear variation of soil compaction, hydraulic conductivity and effective diffusion are included in the model. Based on the numerical simulation results, the following conclusions can be drawn.

(1) Consolidation-induced advection has a lasting effect on solute transport during and after the deformation for relatively compressible soil regardless of the sorption level, though the sorption can dramatically slow the solute transport process rate.
(2) After an initial acceleration effect on transport, the finite-deformation coupled model with decreasing effective diffusion and sorption produces a lower concentration at the CCL base than the pure diffusion model.
(3) A lower degree of saturation leads to a slower pore fluid flow and solute transport(since larger pores drain preferentially with decreasing saturation). The CPW associated with unsaturated conditions cannot be ignored when the consolidation is required to be coupled with solute transport. In the model, CPW terms exist in both the consolidation and transport equations, none of which can be neglected for simplification. Effective diffusion decreases during consolidation and consequently the relative importance of mechanical dispersion becomes profound. For a long-term prediction, mechanical dispersion could cause significant solute transport. Therefore, it should be included in modeling efforts.
(4) Generally speaking, reducing soil compressibility and improving sorption levels of clay are the most effective ways to retard contaminant migration. At the same level of stiffness and sorption, the lower hydraulic conductivity and lower degree of saturation can lengthen the time for contaminants to break through the protective liner.

4 Solute Transport with Dynamic Hydraulic Conductivity and Compressibility of Pore Fluid

4.1 INTRODUCTION

Previous studies for solute transport in a porous medium have treated the hydraulic conductivity and the degree of saturation as constant in the entire soil layer. However, hydraulic conductivity has been reported to be a function of void ratio (e) (Tavenas et al., 1983; Al-Tabbaa and Wood, 1987; Chapuis, 2004). Furthermore, pore-water pressure also affects the hydraulic conductivity (Bird, 1994; Civan et al., 2011; Gardner, 1958). Changes in pore-water pressure lead to changes in stresses and in turn soil deformation. Since the hydraulic properties of the soil, such as porosity, hydraulic conductivity and water storage capacity are affected by the changes in stresses. This coupled effect highlights the strong correlation between flow and stress-deformation, and the connection to the effects of pore pressure related hydraulic conductivity and the degree of saturation to the consolidation-induced solute transportation. Different expressions for the constitutive relationships of dynamic hydraulic conductivity and degree of saturation were available such as presented in Gardner (1958); Wu and Zhang (2009); Gallipoli et al. (2003).

Wu et al. (2020) may be the first attempt to include dynamic hydraulic conductivity and degree of saturation in the model for solute transport in unsaturated deformable porous media. In this chapter, based on Wu et al. (2020)'s work, we discuss the effects of dynamic hydraulic conductivity and the degree of saturation on consolidation-induced solute transport in unsaturated deformable porous media. First, these effects are introduced when there is positive pore pressure, then new non-linear governing equations for the pore pressure field and solute concentration field are derived. Then, parametric studies for solute transport in an unsaturated soil layer are conducted to investigate the influence of dynamic parameters on the consolidation-induced solute transport.

4.2 DYNAMIC HYDRAULIC CONDUCTIVITY AND DEGREE OF SATURATION

Dynamic hydraulic conductivity and degree of saturation are considered to be functions of pore pressures in order to investigate the consolidation-induced solute transport in a deformable medium. Herein, some key previous theories are outlined and the modified forms of this dependence are proposed.

4.2.1 DYNAMIC HYDRAULIC CONDUCTIVITY

Several different forms of the dependence of hydraulic conductivity ($K(p)$) on the pore pressure p (or equivalently suction s) have been proposed. Gardner (1958) considered two forms for hydraulic conductivity, a power law of the form:

$$K(s) = \frac{a}{s^d + b}, \tag{4.1}$$

for various d, and an exponential law:

$$K(s) = ae^{-fs}, \text{ or } K(p) = ae^{fp}. \tag{4.2}$$

where a,b,d and$f$ are constants and s is the suction.

Wu and Zhang (2009) used the version of exponential relationship and extended into the form:

$$K(p) = \begin{cases} K_s & |p| \le |\psi_{ae}|, \\ K_s e^{\alpha\psi_{ae}+\alpha p} & |p| > |\psi_{ae}|, \end{cases} \tag{4.3}$$

where $K(p)$ [m/s] is the dynamic hydraulic conductivity, K_s [m/s] is the coefficient of conductivity at full saturation and α [1/kPa] is the de-saturation coefficient, which is related to the grain size distribution of a soil (Philip, 1969). Generally speaking, the greater the clay content, the lower the de-saturation rate, i.e., the smaller the value of α (Zhan and Ng, 2004). For a fully saturated soil, α is set as zero, hence the hydraulic conductivity is a constant K_s. ψ_{ae} [kPa] is the air-entry constant that is determined by the radius of the largest pore of a specific soil type. A smaller pore size (such as for clay) produces a relatively larger air-entry value. The typical values of these parameters for several soil types are listed in Table 4.1.

4.2.2 DYNAMIC DEGREE OF SATURATION

For the degree of saturation, Gallipoli et al. (2003), using experimental data, proposed a model of the form:

$$S_r(s) = \left(\frac{1}{1+(\gamma s)^{m_1}}\right)^{m_2}, \tag{4.4}$$

in which γ, m_1 and m_2 are soil constants.

Table 4.1
Coefficient of hydraulic conductivity at full saturation (K_s), air-entry value (ψ_{ae}) and de-saturation coefficient (α) for classic soils.

Soil type	k_s (m/s)	ψ_{ae} (kPa)	α (kPa^{-1})
Clay	10^{-10}—10^{-8}	20–39	0.016 for Beit Netofa clay
Silt	10^{-8}—10^{-6}	7–155	0.043 for a silt loam
Sand	10^{-5}—10^{-3}	1–3	0.106 for a fine sand
Gravel	10^{-2}—10^{-1}	Nil	0.081 for Hpgiene sandstone

Ref: Genuchten (1980); Hillel (1998); Hills et al. (1989)

Wu and Zhang (2009) proposed an exponential relationship between degree of saturation and pore pressure in the same format as they used for hydraulic conductivity. The dynamic degree of saturation was determined with respect to suction:

$$S_r(s) = \begin{cases} 1 & |s| \le |\psi_{ae}|, \\ e^{\alpha\psi_{ae}+\alpha p} & |s| > |\psi_{ae}|, \end{cases} \tag{4.5}$$

With loads acting on the soil matrix, air bubbles may be expelled out from the pore fluid, leading to an increase in the degree of saturation. However, $S_r(p)$ cannot exceed unity. To incorporate the positive pore pressure, the constitutive relationship for dynamic degree of saturation is proposed as:

$$S_r(p) = \begin{cases} S_r^0 & |p| \le |\psi_{ae}|, \\ -e^{\alpha\psi_{ae}-\alpha p}+1+S_r^0 & |\psi_{ae}| < |p| \le |P_{Sr=1}|, \\ 1 & |p| > |P_{Sr=1}|. \end{cases} \tag{4.6}$$

The degree of saturation ($S_r(p)$) is again picked to be related to the air-entry value ψ_{ae} [kPa] and the de-saturation value α [1/kPa]; S_r^0 refers to the initial degree of saturation (or commonly known as the residual saturation) before a load acts on the soil. Figure 4.1(a) illustrates the relationship between dynamic degree of saturation and the pore pressure (4.6), but not to scale. In the figure, another important parameter $P_{Sr=1}$ is defined as that pore pressure at which S_r reaches unity. Beyond this point, S_r will stop increasing; i.e., the soil matrix remains fully saturated.

When S_r is dynamic, it will vary both spatially and temporally. The variation of degree of saturation is particular important in deriving the consolidation-induced solute transport theory. Herein, the partial derivative of S_r with respect to p will be used and is firstly introduced here:

$$\frac{dS_r(p)}{dp} = \begin{cases} 0 & |p| \le |\psi_{ae}|, \\ \alpha e^{\alpha\psi_{ae}-\alpha p} & |\psi_{ae}| < |p| \le |P_{Sr=1}|, \\ 0 & |p| > |P_{Sr=1}|. \end{cases} \tag{4.7}$$

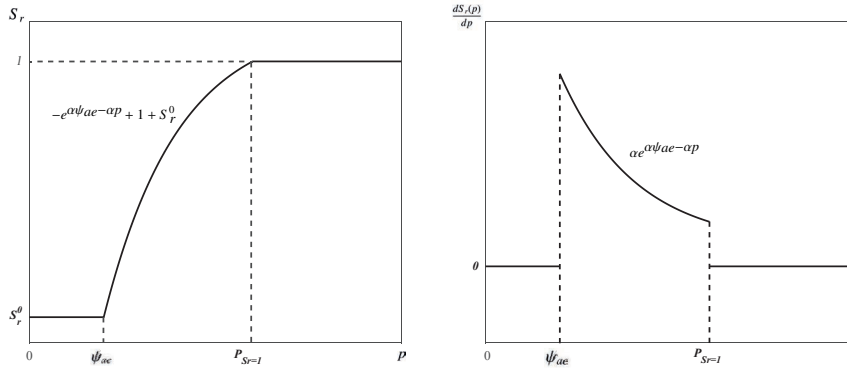

(a1) Dynamic degree of saturation (a2) gradient of degree of saturation

(a) Type 1

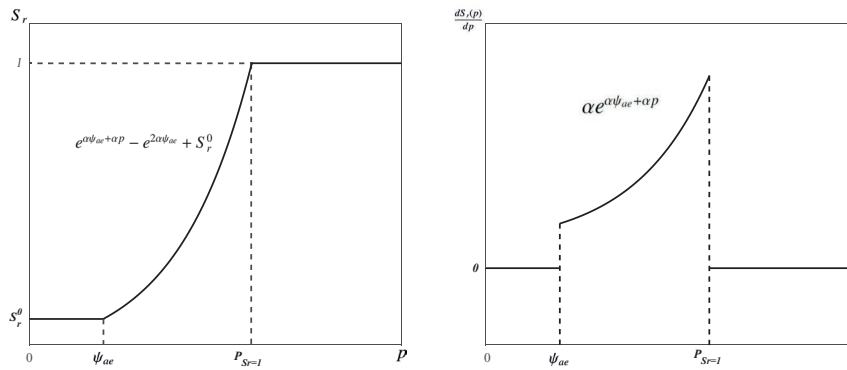

(b1) Dynamic degree of saturation (b2) gradient of degree of saturation

(b) Type 2

Figure 4.1 Relationship between the dynamic degree of saturation and pore pressure (a) Type 1 and (b) Type 2.

As shown in Figure 4.1(a2), the partial differentiation of degree of saturation function is discontinuous. Before pore pressure reaches ψ_{ae} or exceeds the value of $P_{S_r=1}$, $\frac{dS_r(p)}{dp}$ equals to 0 because S_r is constant. Note that the details of the shape of $S_r(p)$ in Figure 4.1(a1) is a proposed shape only. The curve is concave and we designate it as a Type 1 shape.

In order to study the effects of the concavity of the dynamic degree of saturation function, an alternative convex-shape formulation is proposed and named as 'Type 2':

$$S_r(p) = \begin{cases} S_r^0 & |p| \le |\psi_{ae}|, \\ e^{\alpha\psi_{ae}+\alpha p} - e^{2\alpha\psi_{ae}} + S_r^0 & |\psi_{ae}| < |p| \le |P_{Sr=1}|, \\ 1 & |p| > |P_{Sr=1}|. \end{cases} \tag{4.8}$$

and the co-responding derivative of S_r with respect to p becomes:

$$\frac{dS_r(p)}{dp} = \begin{cases} 0 & |p| \leq |\psi_{ae}|, \\ \alpha e^{\alpha\psi_{ae}+\alpha p} & |\psi_{ae}| < |p| \leq |P_{Sr=1}|, \\ 0 & |p| > |P_{Sr=1}|. \end{cases} \tag{4.9}$$

The diagram for the dynamic degree of saturation relationship with pore pressure for Type 2 is shown in Figure 4.1(b). As for Type 1, the degree of saturation increases from 0.85 to unity as the pore pressure increases. For Type 2 the S_r versus p curve is convex, which results in a increasing function $dS_r(p)/dp$.

4.3 THEORETICAL MODELS

4.3.1 MODEL CONFIGURATION

When an external load is applied to a deformable soil matrix, an excess pore pressure is generated. Under draining conditions, the excess pore pressures will gradually dissipate after the load stops increasing (post-loading stage). When there is a source of non-active pollution, the contaminants are carried by the transient advective flow (triggered by the excess pore pressure) and finally spread and cause pollution. To model this process, three governing equations are required to calculate the excess pore pressure, soil displacement and solute concentration fields.

In this study, four models are considered, with summary shown in Table 4.2. Note that, for both Model Srp and Model Kp+Srp, dynamic degree of saturation formulation Type 1 is used. The following sections explain the theories of the conventional model and modified dynamic models.

Here the work of Zhang et al. (2012*a*) is extended to consider the effects of dynamic hydraulic conductivity and degree of saturation. Although the original equilibrium equation is directly applicable to all dynamic models, the governing equations for both the excess pore pressures and concentration fields need to be updated. This section will only present the final governing equations for each model while the detailed derivation is in Appendixes 4.7.1 & 4.7.2.

According to Zhang et al. (2012*a*), the force balance equation is:

$$G\frac{2(1-\nu)}{(1-2\nu)}\frac{\partial^2 u}{\partial z^2} + \left(1-n^0\right)\left(\rho_s - S_r\rho_w\right)g\frac{\partial u}{\partial z} = \frac{\partial p}{\partial z}; \tag{4.10}$$

where u [m] is the vertical displacement, p [Pa] is the excess pore pressure, G [Pa] is the shear modulus and assumed to be constant in this study, ν is the Poisson's ratio, and ρ_w [kg/m^3] & ρ_s [kg/m^3] denote the densities of the pore fluid and solid particles.

4.3.2 DYNAMIC MODEL (KP+SRP)

The spatial derivative of hydraulic conductivity for $|p| > |\psi_{ae}|$ is:

$$\frac{\partial K}{\partial z} = \frac{dK}{dp}\frac{\partial p}{\partial z} = \alpha K_s e^{\alpha\psi_{ae}+\alpha p}\frac{\partial p}{\partial z} = \alpha K\frac{\partial p}{\partial z}. \tag{4.11a}$$

Table 4.2
Summary of models.

Name in paper	Label	Description
Conventional model	CON	Coupled consolidation-transport model, with constant K and S_r.
Dynamic K model	Kp	Coupled consolidation-transport model, with constitutive law for $K(p)$, (4.3), and constant S_r
Dynamic S_r model	Srp	Coupled consolidation-transport model, with constitutive law for $S_r(p)$(Type 1, (4.6)) and constant K
Dynamic $K\&S_r$ model	Kp+Srp	Coupled consolidation-transport model, with constitutive laws for $K(p)$, (4.3) and $S_r(p)$(Type 1, (4.6))

Similarly, the temporal and spatial derivations of degree of saturation (Type 1) are, for $|\psi_{ae}| < |p| \leq |P_{Sr=1}|$:

$$\frac{\partial S_r}{\partial t} = \frac{dS_r}{dp}\frac{\partial p}{\partial t} = \alpha e^{\alpha\psi_{ae}-\alpha p}\frac{\partial p}{\partial t}, \tag{4.11b}$$

and

$$\frac{\partial S_r}{\partial z} = \frac{dS_r}{dp}\frac{\partial p}{\partial z} = \alpha e^{\alpha\psi_{ae}-\alpha p}\frac{\partial p}{\partial z}. \tag{4.11c}$$

It is important to point out that, by using product law, the term $\frac{\partial K}{\partial t}$, $\frac{\partial S_r}{\partial t}$, $\frac{\partial S_r}{\partial z}$ could be solved as long as $\frac{dK}{dp}$ and $\frac{dS_r}{dp}$ are known. Therefore, other forms of dynamic constitutive relationships are also applicable.

Substitute (4.11a)-(4.11c) into (4.35), and replace porosity n with its initial value n^0 (Zhang et al., 2012*a*), then the governing equations for excess pore pressure are summarised as:

- for $|p| \leq |\psi_{ae}|$,

$$S_r n^0 \beta \frac{\partial p}{\partial t} + S_r \frac{\partial^2 u}{\partial z \partial t} = \frac{K}{\rho_w g} \left(\frac{\partial^2 p}{\partial z^2} \right), \tag{4.12a}$$

  where β is the fluid compressibility as defined in (4.29) (Fredlund and Rahardjo, 1993).
- for $|\psi_{ae}| < |p| \leq |P_{Sr=1}|$,

$$\begin{aligned} \left(S_r n^0 \beta + n^0 \alpha e^{\alpha(\psi_{ae} - \alpha p)} \right) \frac{\partial p}{\partial t} + S_r \frac{\partial^2 u}{\partial z \partial t} \\ = \frac{K}{\rho_w g} \left(\frac{\partial^2 p}{\partial z^2} \right) + \frac{\alpha K}{\rho_w g} \left(\frac{\partial p}{\partial z} \right)^2 \\ - n^0 \alpha e^{\alpha(\psi_{ae} - \alpha p)} \frac{\partial u}{\partial t} \frac{\partial p}{\partial z}, \end{aligned} \tag{4.12b}$$

- for $|p| > |P_{Sr=1}|$,

$$S_r n^0 \beta \frac{\partial p}{\partial t} + S_r \frac{\partial^2 u}{\partial z \partial t} = \frac{K}{\rho_w g} \left(\frac{\partial^2 p}{\partial z^2} \right) + \frac{\alpha K}{\rho_w g} \left(\frac{\partial p}{\partial z} \right)^2. \tag{4.12c}$$

The governing equations for solute transport with dynamic hydraulic conductivity and degree of saturation are given below, with the detailed derivations provided in Appendix 4.7.2.

- for $|p| \leq |\psi_{ae}|$ or $|p| > |P_{Sr=1}|$,

$$\begin{aligned} \left[S_r n^0 + \left(1 - n^0\right) \rho_s K_d \right] \frac{\partial c}{\partial t} = \frac{\partial^2 c}{\partial z^2} \left(S_r n^0 D_m - \alpha_L \frac{K}{\rho_w g} \frac{\partial p}{\partial z} \right) \\ + \frac{\partial c}{\partial z} \left\{ -\alpha_L S_r n^0 \beta \frac{\partial p}{\partial t} - \alpha_L S_r \frac{\partial^2 u}{\partial z \partial t} \right. \\ + \frac{\alpha_L \beta K}{\rho_w g} \left(\frac{\partial p}{\partial z} \right)^2 + S_r D_m \left(1 - n^0\right) \frac{\partial^2 u}{\partial z^2} \\ \left. + \frac{K}{\rho_w g} \frac{\partial p}{\partial z} - \left[S_r n^0 + \left(1 - n^0\right) \rho_s K_d \right] \frac{\partial u}{\partial t} \right\} \\ + c \left[S_r n^0 \beta \frac{\partial p}{\partial t} - \beta \frac{K}{\rho_w g} \left(\frac{\partial p}{\partial z} \right)^2 + S_r n^0 \beta \frac{\partial u}{\partial t} \frac{\partial p}{\partial z} \right], \end{aligned} \tag{4.13a}$$

- for $|\psi_{ae}| < |p| \leq |P_{Sr=1}|$,

$$\begin{aligned}\left[S_r n^0 + \left(1-n^0\right)\rho_s K_d\right]\frac{\partial c}{\partial t} &= \frac{\partial^2 c}{\partial z^2}\left(S_r n^0 D_m - \alpha_L \frac{K}{\rho_w g}\frac{\partial p}{\partial z}\right)\\ &+ \frac{\partial c}{\partial z}\left\{n^0 \alpha e^{\alpha\psi_{ae}-\alpha p}\left(D_m\frac{\partial p}{\partial z} - \alpha_L\frac{\partial p}{\partial t} - \alpha_L\frac{\partial u}{\partial t}\frac{\partial p}{\partial z}\right)\right.\\ &- \alpha_L S_r n^0 \beta\frac{\partial p}{\partial t} - \alpha_L S_r\frac{\partial^2 u}{\partial z\partial t} + \frac{\alpha_L\beta K}{\rho_w g}\left(\frac{\partial p}{\partial z}\right)^2\\ &+ \frac{K}{\rho_w g}\frac{\partial p}{\partial z} + S_r D_m\left(1-n^0\right)\frac{\partial^2 u}{\partial z^2}\\ &\left.- \left[S_r n^0 + \left(1-n^0\right)\rho_s K_d\right]\frac{\partial u}{\partial t}\right\}\\ &+ c\left[S_r n^0\beta\frac{\partial p}{\partial t} - \beta\frac{K}{\rho_w g}\left(\frac{\partial p}{\partial z}\right)^2 + S_r n^0\beta\frac{\partial u}{\partial t}\frac{\partial p}{\partial z}\right].\end{aligned} \tag{4.13b}$$

4.3.3 DYNAMIC MODEL (SRP)

When the degree of saturation is dynamic (Type 1) and the hydraulic conductivity is constant, the governing equations for excess pore pressure field are:

- for $|p| \leq |\psi_{ae}|$ or $|p| > |P_{Sr=1}|$, same as (4.12a),
- for $|\psi_{ae}| < |p| \leq |P_{Sr=1}|$,

$$\begin{aligned}\left(S_r n^0\beta + n^0\alpha e^{\alpha(\psi_{ae}-\alpha p)}\right)\frac{\partial p}{\partial t} + S_r\frac{\partial^2 u}{\partial z\partial t} &= \frac{K}{\rho_w g}\left(\frac{\partial^2 p}{\partial z^2}\right)\\ &- n^0\alpha e^{\alpha(\psi_{ae}-\alpha p)}\frac{\partial u}{\partial t}\frac{\partial p}{\partial z}.\end{aligned} \tag{4.14}$$

The updated solute transport equations are:

- for $|p| \leq |\psi_{ae}|$ or $|p| > |P_{Sr=1}|$, same as (4.13a)
- for $|\psi_{ae}| < |p| \leq |P_{Sr=1}|$, same as (4.13b)

4.3.4 DYNAMIC MODEL (KP)

Under the assumption of dynamic hydraulic conductivity but constant degree of saturation, the governing equations for excess pore pressure are:

- for $|p| \leq |\psi_{ae}|$, same as (4.12a),
- for $|p| > |\psi_{ae}|$, same as (4.12c).

Although the hydraulic conductivity is dynamic, the solute transport equation is the same as (4.13a). This is because the dynamic hydraulic conductivity term is only introduced into the solute transport equation when replacing the velocity terms. A detailed explanation is given in Appendix 4.7.2.

4.3.5 THE CONVENTIONAL MODEL WITH CONSTANT K AND S_R

When both the hydraulic conductivity and degree of saturation are constant, the governing equation for excess pore pressure is the same as (4.12a), and for solute concentration field, it is written as the form of (4.13a). It is important to point out that these two equations are the same as presented in Zhang et al. (2012*a*).

Since no experimental data for solute transport in a deformable porous medium with dynamic hydraulic conductivity and degree of saturation is available in the literature, a possible validation of the present model is to compare with the previous models with constant soil properties (Peters and Smith, 2002; Zhang et al., 2012*a*). To compare with those results, the new dynamic model (with both K & S_r dynamic) was run with a very high ψ_{ae} value (1000 kPa). Then, pore pressure will never exceed the air-entry value. That is, the dynamic model was actually calculating the conventional study case where both K and S_r remains unchanged. Furthermore, utilizing the piecewise function, the ramp load can be applied with different smoothing methods at the turning point. Here, a continuous second derivative was adopted and applied for a period of half a year. This smoothing method can be explained as follows: when the landfill site is about to reach capacity, less waste is disposed into this field, and more waste delivered to a new site. Therefore, the loading rate decreases. Figure 4.2 presents the validation of the newly added smoothing methods. Two sets of results were compared with the control of c_v calculated from (4.20). Results in red and blue are for the coefficient of consolidation equals 0.6 m^2/s and 1.0 m^2/s respectively. It is clear that the dynamic model with the smoothing method (solid lines) is a good fit to both Zhang et al. (2012*a*) (dotted lines) and Peters and Smith (2002) (circled points).

4.4 NUMERICAL MODEL FOR A LANDFILL SYSTEM

4.4.1 BOUNDARY CONDITIONS AND INITIAL CONDITIONS

As an application, a landfill with one leachate collection system is assumed to be constructed on the bottom of a compacted clay layer (Figure 2.1). The contaminant migration through the clay layer beneath the landfill is evaluated. The width of the landfill site is considered to be larger than the thickness of soil layer, and the load on the top surface is assumed to be uniform, therefore, 1D model will be applied with z-axis positive pointing downwards.

At the top boundary ($z = 0$), the impermeable geomembrane layer prevents Darcy's flow. Therefore, a zero excess pore pressure gradient can be postulated, as follows:

$$\frac{\partial p}{\partial z}(0,t) = 0. \tag{4.15}$$

Furthermore, as the wastes is disposed to landfill gradually until reaching its capacity, a ramp load is proposed with a constant increasing rate. As shown in Figure 4.3, the external load (Q) keeps increasing in a rate of 200 kPa annually for two years and remains constant of 400 kPa until the end of simulation period.

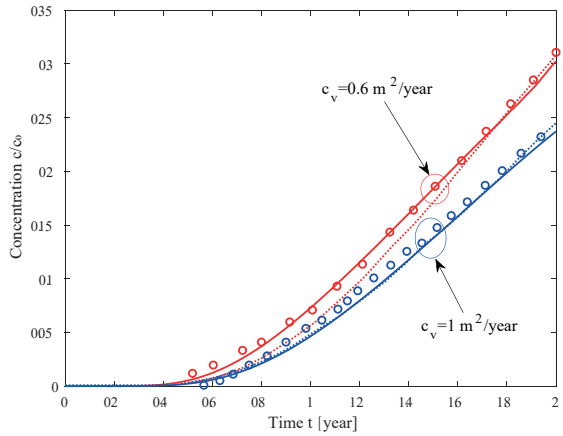

Figure 4.2 The comparison of the present dynamic model (solid lines) with Zhang et al. (2012*a*) (dotted lines) and Peters and Smith (2002) (circled points). Note: case 1 (red) is presented for c_v = 0.6 m^2/s, case 2 (blue) is presented for c_v = 1 m^2/s.

To derive the top boundary condition for soil deformation, an elastic deformation is taken into account, and a vertical force balance relationship is applied. This leads to the soil deformation at the top boundary to be (Zhang et al., 2012*a*):

$$\frac{\partial u}{\partial z}(0,t) = \frac{1-2\nu}{2G(1-\nu)}[-Q(t)+p]. \tag{4.16}$$

According to Zhang et al. (2012*a*), considering the volatile organic compounds that diffuse through the geomembrane layer and dissolve into the pore-water, the top boundary condition for the solute concentration is expressed as:

$$\frac{\partial c}{\partial z}(0,t) = \frac{D_G}{n^0 h D_m}(c-c_0), \tag{4.17}$$

where D_G is the mass transfer coefficient of geomembrane, and c_0 is the reference solute concentration in the waste.

At the exit boundary ($z = L$), with a leachate collection system, a free drainage condition is considered, which implies a zero pore pressure, and no deformation is allowed at that point. In addition, the concentration gradient is assumed to be zero. Hence, only advective flow occurs at the outlet boundary. The lower boundary conditions can be expressed as:

$$p(L,t) = 0, \quad u(L,t) = 0, \quad \frac{\partial c}{\partial z}(L,t) = 0. \tag{4.18}$$

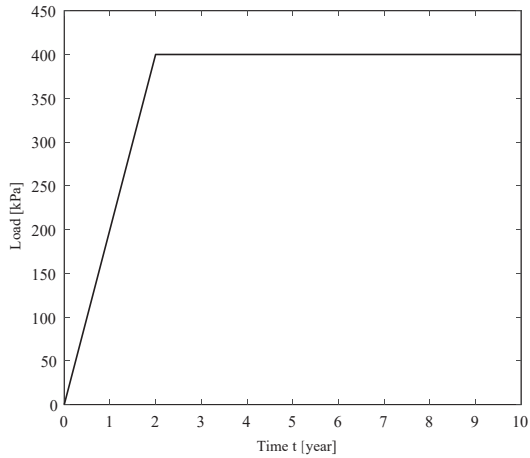

Figure 4.3 Ramp load (Q) at the top boundary.

To simplify the model, all initial values for pore pressure field, soil deformation and solute transport are set to zero, i.e.,

$$p(z,0) = 0, \quad u(z,0) = 0, \quad c(z,0) = 0. \tag{4.19}$$

The initial values of dynamic hydraulic conductivity and degree of saturation are also critical in this study, and the initial values (K_s & S_r^0) will be introduced in the following section along with other input parameters.

4.4.2 INPUT PARAMETERS

In this study, all models simulates the same landfill case but with different considerations of the hydraulic conductivity and degree of saturation. Table 4.3 summarises all parameters used in Model CON and parameters only used in the dynamic models.

The combination of the parameters is selected to ensure that the coefficient of consolidation (c_v) stays within the range of 1×10^{-8} to 3×10^{-7} m^2/s (Sivakugan, 1990; Wallace and Otto, 1964). The coefficient of consolidation (c_v) can be calculated as

$$c_v = \frac{2GK(1-\nu)}{\rho_w g(1-2\nu)}. \tag{4.20}$$

Additionally, while making selection of the parameters, soil deformation was kept less than 20% to satisfy the small deformation assumption.
Note that in the conventional model, S_r is assumed to be equal to S_r^0 and K is set to be equal to K_s through the whole simulation.

Table 4.3
Input parameters for numerical examples.

Parameters for Model CON		
Parameter	Value	Description
$Q(t)$	see Table 2.2	Waste loading
h	0.0015 m	Thickness of geomembrane
L	3 m	Thickness of clay layer
S_r^0	0.85	Initial degree of saturation
n^0	0.33	Initial porosity
G	5×10^5 Pa	Shear modulus
ν	0.33	Poisson's ratio
K_s	1×10^{-9} m/s	Initial hydraulic conductivity
α_L	0.1 m	Longitudianl dispersion factor
ρ_w	1×10^3 kg/m^3	Initial density of the pore fluid, varied due to fluid compressibility
ρ_s	2.6×10^3 kg/m^3	Density of the solid phase
K_d	0	Partitioning coefficient
r_h	0.02 m	Volumetric fraction of dissolved air within pore-water
D_G	1.5×10^{-4} m^2/y	Mass transfer coefficient of geomembrane
D_m	5×10^{-9} m^2/s	Molecular diffusion coefficient in the clay
c_0	0.1 kg/m^3	Reference solute concentration
g	9.8 m/s^2	Gravity acceleration
Parameters for Model Kp, Srp & Kp+Srp		
ψ_{ae}	30 kPa	Air-entry value for clay
α	0.016 kPa^{-1}	De-saturation coefficient for clay

4.5 RESULTS AND DISCUSSIONS

In this section, the results from the dynamic Models Kp, Srp and $Kp + Srp$ are presented together with the conventional model, CON. Section 4.5.4 then summarizes the averaged flow velocity and the advective emission for all models. The results in Sections 4.5.1–4.5.4 are all for the Type 1 $S_r(p)$ shape. A comparison for the Type 2 $S_r(p)$ shape is given in Section 4.5.5

4.5.1 DYNAMIC HYDRAULIC CONDUCTIVITY MODEL (MODEL KP)

The results presented in this section are from the dynamic hydraulic conductivity model while keeping the degree of saturation as a constant value.

The most important result of Model Kp is the form of the evolution of the dynamic conductivity (K). Figure 4.4 shows changes in K at different locations. At

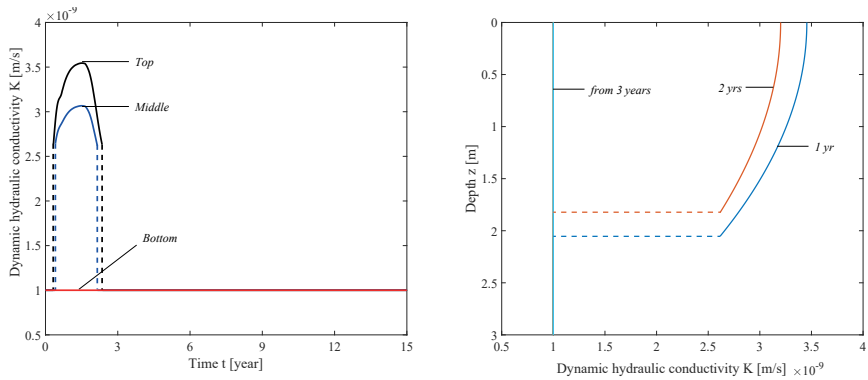

Figure 4.4 Distribution of dynamic hydraulic conductivity vs time and depth for Model Kp.

the bottom (the contaminant outlet in the clay layer) K is constant and always equal to K_s. This is attributed to the zero pore pressure at that point allowing for the pore fluid to flow freely into the leachate collection pipe, since the pore pressure at the outlet will never exceed the air entry value. However, the values of K at both the top point (the contaminant inlet in the clay layer) and the middle point (where $z = L/2$ in the clay layer) experience increasing and then decreasing periods. The excess pore pressure increases as the ramp load is gradually applied to the clay layer, when the pore fluid does not have time to drain out. Once the pore pressure rises up to the air entry level, K starts to increase. After the load reaches the post-loading period (load stops increasing) in around 2 years, the excess pore pressure starts to dissipate with the pore fluid gradually expelling out from soil matrix. According to the dynamic conductivity model, the pore pressure recovers to the air-entry level, when K then maintains the level of K_s. The largest K value of around $3.5 \times 10^{-9} m/s$ occurs at the inlet in 1.5 years. The dynamic conductivity curve at the top point is higher than that at the middle point, implying that the pore pressure is generally a maximum at the top. Figure 4.4 also shows the distributions of K along the clay layer were plotted at different times. The dark blue line labelled $'1yr'$ indicates values after 1 year of loading. K curves for 1 year and 2 years confirm the maximum increase at the upper layer, where the pore pressure is harder to dissipate compared to the lower layer. After 3 years, K returns to initial value of K_s and remains unchanged through the whole layer to the end of the simulation.

Spatial and temporal changes in K affect the corresponding excess pore pressure (p), as indicated in Figure 4.5(a). The solid lines describe the results of Model Kp while the dashed lines are the results of Model CON, where $K = K_s$. Comparing the two models, some similar trends can be found. For example, p in the upper layer is higher than in the lower layer; p rises rapidly during the loading period then drops gradually after entering the post-loading stage. However, their increasing/dissipation rate and amount are all affected by dynamic K. The peak excess pore pressures for Model Kp at the top point and middle point are 50 kPa & 40 kPa respectively, while for Model CON, the highest p is almost double (100 kPa & 75 kPa) at the two

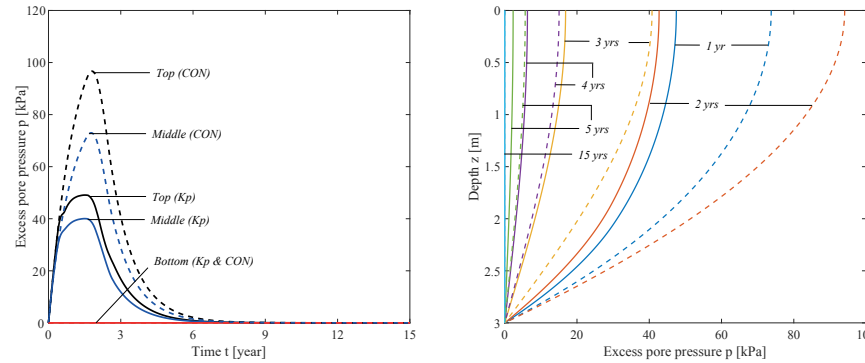

(a) Excess pore pressure

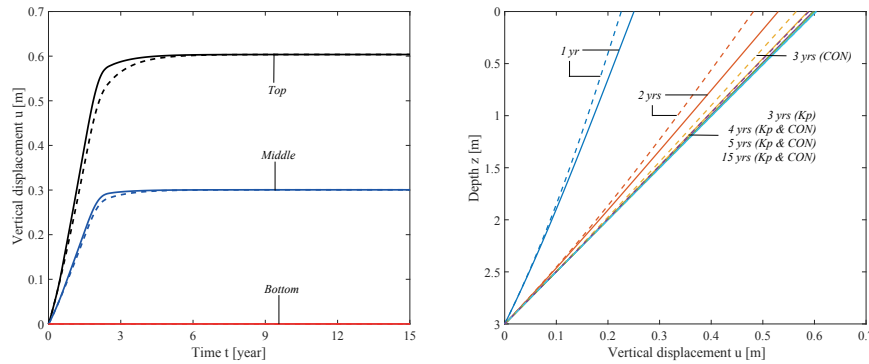

(b) Vertical displacement

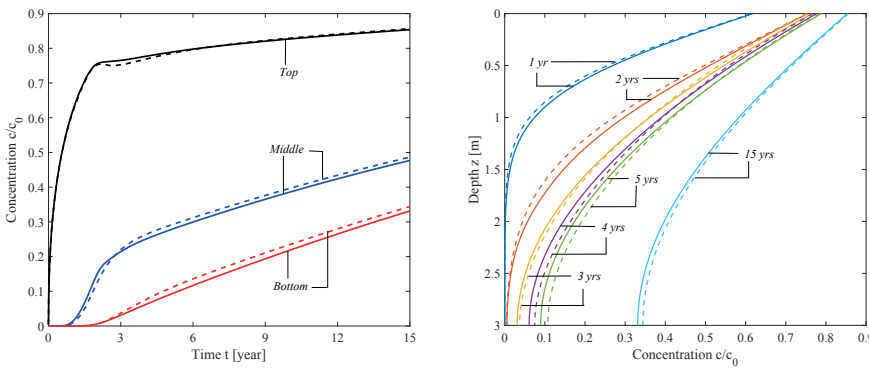

(c) Solute concentration

Figure 4.5 Distribution of (a) excess pore pressure, (b) vertical displacement and (c) solute transport vs time and depth for Model Kp and Model CON.

locations. Moreover, the dynamic conductivity also influences the dissipation rate during the post-loading period. At the top boundary of the clay layer, p has been nearly fully dissipated after 5 years for Model Kp while a remainder of around 8 kPa exists for the conventional model. These features can be explained by the definition of hydraulic conductivity ; a larger K means the pore fluid is easier to travel within the void, hence accelerates the drainage at the outlet. The dynamic hydraulic conductivity and pore pressure relationship that results in a higher K on the top layer, further leads to a smaller excess pore pressure build up and quicker dissipation.

Compared to the pore pressure, the vertical soil deformation (u) was less influenced by the dynamic conductivity and the final level of soil deformation is not affected at all. The displacement versus time figure (Figure 4.5(b)) shows that the largest vertical displacement is 0.6 m measured from the top and 0.3 m at the middle point for both Model Kp and Model CON. The bottom point is assumed to be rigid so no vertical displacement is allowed. However, the rate of soil deformation is affected when K becomes dynamic. The displacement versus depth figure indicates that after 2 years, the top surface has sunk 0.53 m with dynamic conductivity. However, the conventional model only shows a 0.48 m downward settlement. Furthermore, the Model Kp predicts that the top surface reaches its final deformation level after 3 years, but Model CON is still 5 cm short of its final value at that time.

For the volatile pollutant to spread in the soil matrix, part of the solute dissolves in the transient advective flow, which is produced from the soil consolidation process. Meanwhile, hydrodynamic dispersion, which is a combined process of molecular diffusion and longitudinal dispersion, takes place. Molecular diffusion is mainly manifested as particles move from an area of high concentration to an area of low concentration and longitudinal diffusion refers to the process whereby solutes are mechanically mixed by velocity variations. Generally speaking, in relatively low speed environments, molecular diffusion dominates the process. For the numerical examples considered here, during the loading period, there is no significant difference at the top point (due to the boundary condition constrain) or the bottom point (since the contaminants have not reached bottom). Nevertheless, a faster contaminant migration can be discovered at the middle point (Figure 4.5(c)). Detailed results can be seen from the plot of concentration (c/c_0) versus depth. After 2 years, at a depth of $1.7m$ the contaminant level has reached 10% $(c/c_0 = 0.1)$ for Model Kp, while for Model CON, the same contaminant level was reached 10 cm higher. On the post-loading stage, K recovers to its initial value and the transient excess flow carrying contaminants continues spreading. Due to pore pressure dissipation, the rate of solute transportation reduces in both models. After the pore pressure is fully dissipated, only hydrodynamic dispersion contributes to contaminant transportation. Moreover, according to the outlet boundary condition, the contaminant cannot escape the soil layer, which results in an accumulation at the bottom. Compared to Model CON, Figure 4.5(c) reveals that a dynamic K will eventually reduce pollution. For example, the breakthrough time, the time required for the solute concentration to reach 10% of the referenced concentration at the outlet, takes half a year longer with dynamic conductivity.

4.5.2 DYNAMIC DEGREE OF SATURATION MODEL (MODEL SRP)

Here we vary the dynamic degree of saturation (Model Srp), but keep the hydraulic conductivity constant.

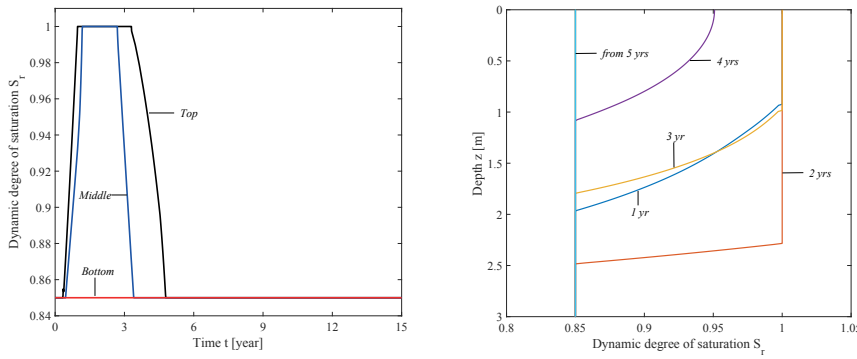

(a) Dynamic degree of saturation vs time (b) Dynamic degree of saturation distribution

Figure 4.6 Distribution of dynamic degree of saturation vs time and depth for Model Srp (Type 1).

Figure 4.6 shows that the degree of saturation (S_r) varies between S_r^0 (0.85) and 1. The dynamic S_r happens mainly during the loading period and in the upper layer. As the load acts on the soil layer, the air bubbles are expelled out from the pore fluid and result in a change in the degree of saturation. Figure 4.6(a) presents the evolution of S_r in the three cut points. Except for the bottom point, degree of saturation at both top point and middle point are greatly changed. Specifically, soil has became fully saturated for nearly 3 years at the top and around 2 years at middle point. Due to the constrain of pore pressure at the 0utlet S_r remains unchanged at the level of S_r^0. After 3 years, with the excess pore pressure gradually dissipating, S_r reduced. Moreover, Figure 4.6(b) shows the vertical distribution of the dynamic S_r with different colour lines indicating each time step. After 2 years, the fully saturation zone has reached 2.4 m down, however after 4 years, the whole clay layer returns to unsaturated status.

The effect of dynamic degree of saturation on the excess pore pressure is plotted in Figure 4.7(a), and it is very different from Model Kp. With Model Srp the peak excess pore pressure shows almost no differences compared with Model CON at both top and middle points. However, both excess pore pressure accumulation rate and dissipation rate are affected especially during the period when S_r is experiencing either sudden rise (0.5 year– 1 year) and drop (3 years - 6 years). This implies that although the change of S_r magnitude is small (from 0.85 to 1), the rate of change (the additional terms in excess pore pressure governing equations due to $\frac{\partial S_r}{\partial t}$) contributes to the consolidation process to a certain extent. For Model CON, the excess pore pressure is almost fully dissipated after 6 years, while due to dynamic S_r, a residue of 10 kPa exits at the middle point. With excess pore pressure expelled out of the soil matrix, the soil deforms.

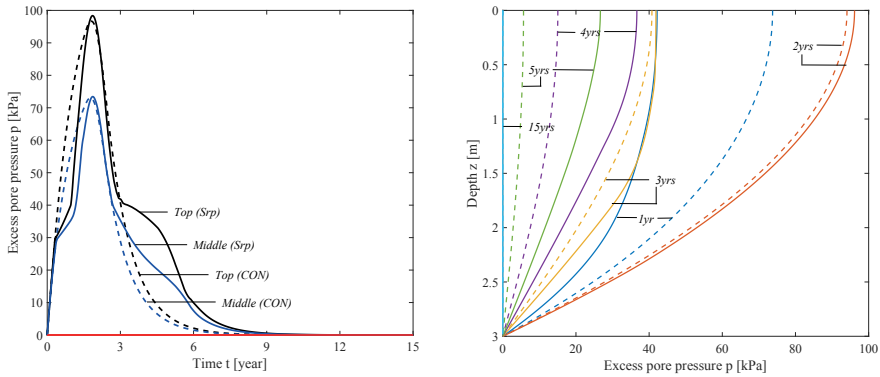

(a) Excess pore pressure

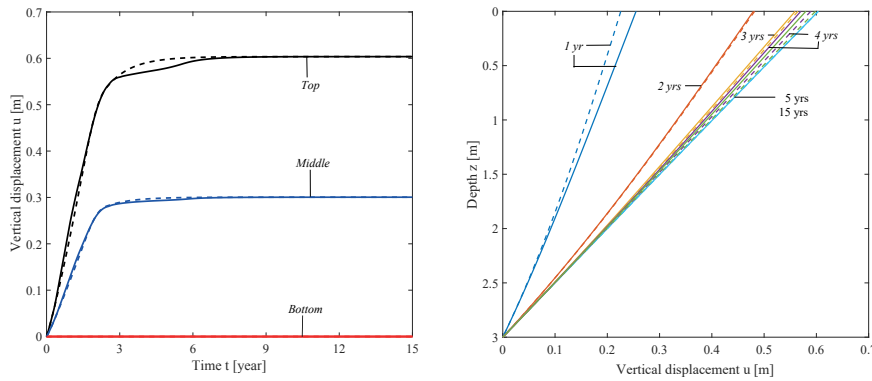

(b) Vertical displacement

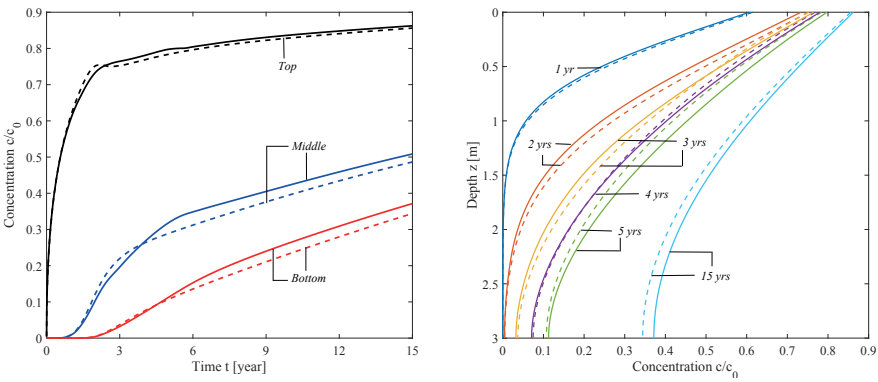

(c) solute concentration

Figure 4.7 Distribution of (a) excess pore pressure, (b) vertical displacement and (c) solute transport vs time and depth for Model Srp and Model CON.

Similar to Model Kp, dynamic S_r does not affect the final deformation, but the inlet will eventually drop 0.6m (Figure 4.7(b)). Due to the reduction of excess pore pressure dissipation rate during Year 3 to Year 6, the soil deforms slightly slower at the this period. For the solute transport, the Model Srp results in a slightly slower solute transport during the loading period and a faster spreading on the post-loading stage. Eventually, higher solute concentration can be observed. According to Figure 4.7(c), it takes 7.5 years for the outlet to be 20% contaminated for Model Srp, while with constant S_r it takes 1.5 years longer to reach the same contaminated level. At the end of 15 years, the outlet has been polluted to 38% with dynamic S_r, while Model CON suggests the final contamination level to be lower than 35%.

4.5.3 DYNAMIC HYDRAULIC CONDUCTIVITY AND DEGREE OF SATURATION MODEL (MODEL KP+SRP)

In the dynamic hydraulic conductivity and degree of saturation model (Model Kp+Srp), both hydraulic conductivity and dynamic degree of saturation vary with pore pressure. Figure 4.8 presents Model Kp+Srp results for dynamic conductivity and dynamic degree of saturation versus time and depth. According to the dynamic theory, K, p and S_r are mutually interacting. As a result, although the same parameters were used in Model Kp+Srp, Model Kp and Model Srp, the evolution of both K and S_r are quite different from the previous two dynamic models. Specifically, the peak value of K for the current model is greater than the maximum K (3.5×10^{-9}m/s) in Model Kp. Moreover, the dynamic S_r evolution shows several differences compared with Model Srp, For instance, the fully saturated condition lasts shorter at both top and middle points; after 2 years the fully saturated zone shrinks to 1.5m while Model Sp obtained a 2.4m saturated zone; when S_r recovers back to the level of S_r^0 after 3 years, the top point in Model Srp remains fully saturated.

The dynamic effects of K and S_r have been discussed separately in previous sections. Under the dynamic effects of both, compared with Model CON, a reduction of excess pore pressure (Figure 4.9(a)) and a slightly faster soil deformation (Figure 4.9(b)) can be observed. This is reasonable since the dynamic S_r effect is less significant than the dynamic K in term of the soil consolidation process. However, since dynamic K results in a slower solute transport while dynamic S_r accelerates the contaminant migration process, for our numerical study case, concentration results for Model$Kp+Srp$ eventually shows limited differences with Model CON (Figure 4.9(c)).

4.5.4 AVERAGE FLOW VELOCITY AND ADVECTIVE EMISSION

Here the average flow velocity (v_f) and the advective emission (E_{adv}) for all models are compared to examine the effects of dynamic K and dynamic S_r on the consolidation-induced solute transport model.

The average flow velocity at the bottom boundary for each model is plotted in Figure 4.10(a). The average flow velocity can be calculated as the sum of Darcy's

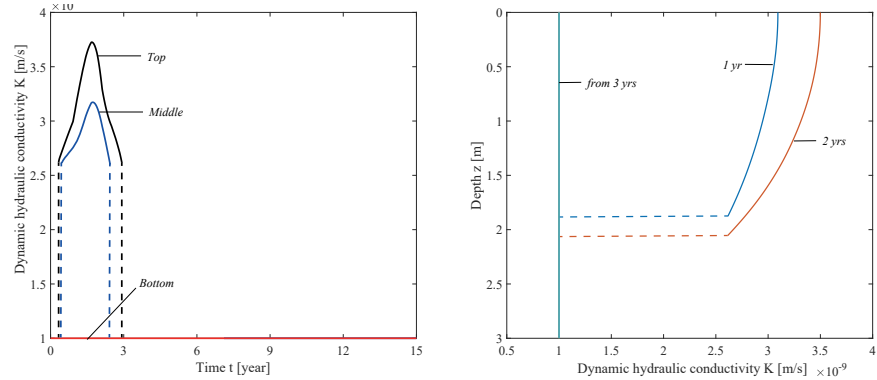

(a) Dynamic hydraulic conductivity

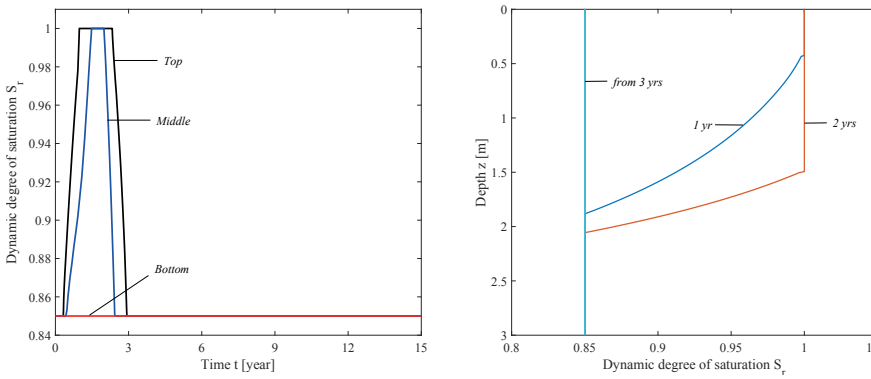

(b) Dynamic degree of saturation

Figure 4.8 Distribution of (a) dynamic hydraulic conductivity and (b) dynamic degree of saturation vs time and depth for Model Kp+Srp.

velocity and the solid phase velocity:

$$v_f = -\frac{K}{S_r n^0 \rho_w g}\frac{\partial p}{\partial z} + \frac{\partial u}{\partial t}. \tag{4.21}$$

The peak v_f for all models occurs at around two years, when the post-loading stage begins. The conventional model and dynamic degree of saturation model shows faster transient advective flow, with a peak flow velocity to be around 2.5×10^{-8}m/s (Figure 4.10(a)). Further, the v_f curve for Model Kp+Srp does not show much difference to the dynamic K model, but is considerable lower than the other two models. Meanwhile, Model Srp and Model CON generate similar V_f trends. Hence, the transient flow reduces speed with the dynamic K, however, the varying degree of saturation has less influence on the average advective flow velocity.

Transient excess flows triggered by soil consolidation shows considerable influence on the solute transport. This effect can be observed from the advective

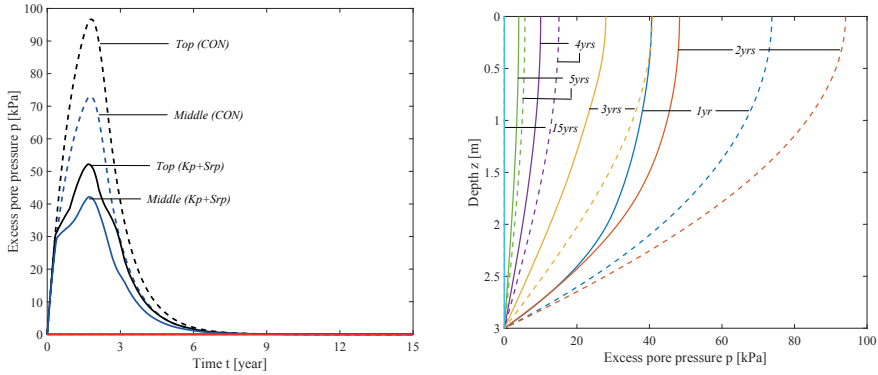

(a) Excess pore pressure

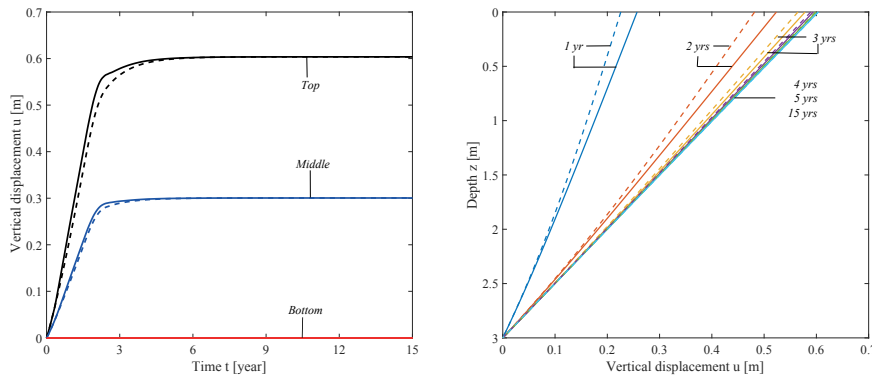

(b) Vertical displacement

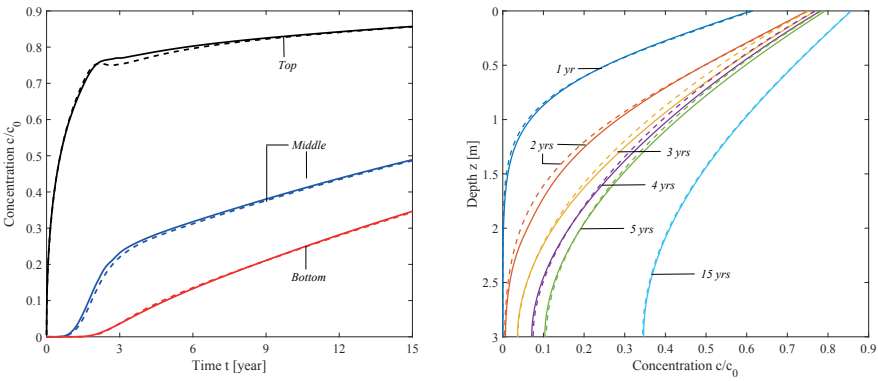

(c) solute concentration

Figure 4.9 Distribution of (a) excess pore pressure, (b) vertical displacement and (c) solute transport vs time and depth for Model Kp+Srp and Model CON.

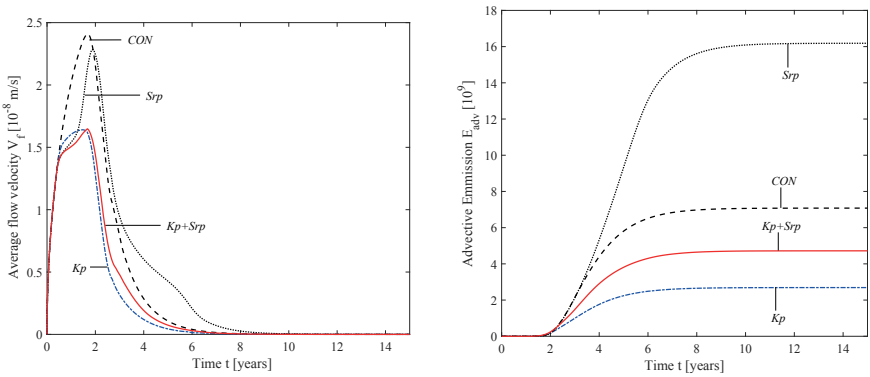

(a) Average flow velocity (b) Advective emission

Figure 4.10 The advective emission and the averaged flow velocity for all models.

emission (E_{adv}) as summarized in Figure 4.10(b). E_{adv} can be calculated as (Zhang et al., 2012*a*)

$$E_{adv} = \int_0^t -\frac{\partial p(\tau)}{\partial z} c(\tau) d\tau, \tag{4.22}$$

where τ is the independent variable of integration.

With the assumption of zero concentration gradient at the outlet, no diffusion takes place and only advective flow is allowed. Thus, the advective emission at the bottom boundary refers to the cumulative contaminant mass outflow. Figure 4.10(b) presents the advective emission at the bottom boundary for each model. Clearly the advective emissions are significantly different for each dynamic model compared to the conventional model. Specifically, dynamic hydraulic conductivity reduces the advective emission while dynamic degree of saturation tends to increase the emission by a larger amount. However, considering dynamic K and S_r simultaneously, Model Kp+Srp model suggest a mitigation of E_{adv}. This feature reveals a coupled effect of dynamic conductivity and degree of saturation so that their effects cannot be simply added. Further, the largest advective emission occurs in Model Srp, which is consistent with the solute concentration result and averaged flow velocity result, that dynamic S_r produces a faster solute transport while keeping a relatively fast transient flow rate.

4.5.5 CONCAVITY OF DYNAMIC DEGREE OF SATURATION FUNCTION

In Section 4.2.2, two expressions were proposed to describe the relationship between dynamic degree of saturation and pore pressure. For both expressions, the degree of saturation increases from S_r^0 to 1 as pore pressure increased. The only difference is that Type 1 function is concave downwards while the Type 2 function is concave up. To study the effect of the concavity to consolidation-induced solute transport,

assuming constant hydraulic conductivity, a modified dynamic S_r model is used and compared with previous Model Srp.

Using the definition (4.8), the modified storage equation for dynamic S_r Type 2 becomes:

- for $|p| \leq |\psi_{ae}|$ or $|p| > |P_{Sr=1}|$, same as (4.12a),
- for $|\psi_{ae}| < |p| \leq |P_{Sr=1}|$,

$$\begin{aligned}\left(S_r n^0 \beta + n^0 \alpha e^{\alpha \psi_{ae} + \alpha p}\right) \frac{\partial p}{\partial t} + S_r \frac{\partial^2 u}{\partial z \partial t} = & \frac{K}{\rho_w g} \left(\frac{\partial^2 p}{\partial z^2}\right) \\ & - n^0 \alpha e^{\alpha \psi_{ae} + \alpha p} \frac{\partial u}{\partial t} \frac{\partial p}{\partial z}.\end{aligned} \tag{4.23}$$

The modified solute transport equation are:

- for $|p| \leq |\psi_{ae}|$ or $|p| > |P_{Sr=1}|$, same as (4.13a)
- for $|\psi_{ae}| < |p| \leq |P_{Sr=1}|$,

$$\begin{aligned}\left[S_r n^0 + \left(1 - n^0\right) \rho_s K_d\right] \frac{\partial c}{\partial t} = & \frac{\partial^2 c}{\partial z^2} \left(S_r n^0 D_m - \alpha_L \frac{K}{\rho_w g} \frac{\partial p}{\partial z}\right) \\ & + \frac{\partial c}{\partial z} \left\{ n^0 \alpha e^{\alpha \psi_{ae} + \alpha p} \left(D_m \frac{\partial p}{\partial z} - \alpha_L \frac{\partial p}{\partial t} - \alpha_L \frac{\partial u}{\partial t} \frac{\partial p}{\partial z}\right) \right. \\ & - \alpha_L S_r n^0 \beta \frac{\partial p}{\partial t} - \alpha_L S_r \frac{\partial^2 u}{\partial z \partial t} \\ & + \frac{\alpha_L \beta K}{\rho_w g} \left(\frac{\partial p}{\partial z}\right)^2 + S_r D_m \left(1 - n^0\right) \frac{\partial^2 u}{\partial z^2} \\ & \left. + \frac{K}{\rho_w g} \frac{\partial p}{\partial z} - \left[S_r n^0 + \left(1 - n^0\right) \rho_s K_d\right] \frac{\partial u}{\partial t} \right\} \\ & + c \left[S_r n^0 \beta \frac{\partial p}{\partial t} - \beta \frac{K}{\rho_w g} \left(\frac{\partial p}{\partial z}\right)^2 + S_r n^0 \beta \frac{\partial u}{\partial t} \frac{\partial p}{\partial z} \right],\end{aligned} \tag{4.24}$$

Note that the force balance equation remains the same as previous models.

The distribution of dynamic degree of saturation versus time and depth are shown in Figure 4.11. Solid lines indicate dynamic S_r Type 2 results while dashed lines are from the previous Model Srp (Type 1 dynamic S_r theory). In generally, the Type 2 shows a more pronounced change in degree of saturation dynamics. Specifically, as shown in Figure 4.11(b), at year 5, the whole soil layer returns the original S_r level of 0.85 for Type 1, while Type 2 shows a higher S_r in the upper layer (around $z = 0.3m$). The fully saturated zone extents deeper with dynamic S_r Type 2, so that, for example, the fully saturated zone is nearly half meter thicker in year 2 and 1 meter thicker in year 3. Moreover, Type 2 dynamic S_r results in a slightly longer fully-saturated period at both top and middle points.

Figure 4.12 (a) indicates that, while the Type 2 model has an impact on pore pressure distribution for a short period (during year 5 to year 9), there are no

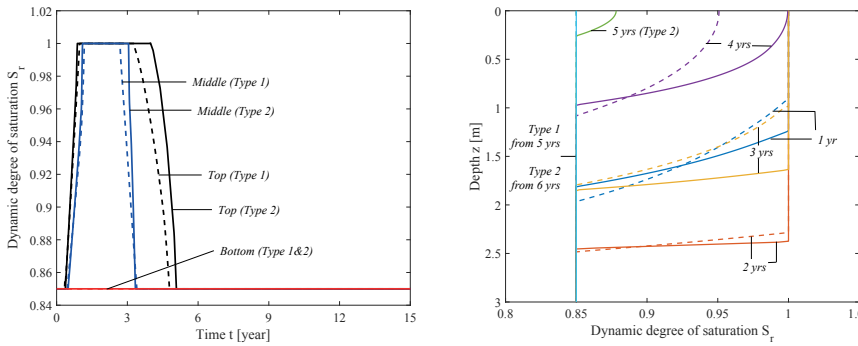

(a) Dynamic S_r vs time (b) Dynamic S_r distribution

Figure 4.11 Distribution of dynamic degree of saturation vs time and depth for Model Srp, comparison between Type 1(dashed lines) and Type 2(solid line).

significant differences on the peak pore pressure values. Regardless of the path how S_r reaches unity, it takes 9 years for pore pressure to be fully dissipated for both models. Further, Figure 4.12(b) indicates similar vertical displacement distribution for the two models showing that the soil deformation is hardly influenced by the concavity of dynamic S_r formulation. Consequently, the effect of concavity of dynamic S_r on solute concentration is limited (Figure 4.12(c)).

4.5.6 PARAMETRIC STUDY FOR VARIOUS AIR-ENTRY

As discussed in Section 4.3, the air-entry value (ψ_{ae}) is an important parameter of the criterion for judging whether hydraulic conductivity and degree of saturation are dynamic. Only in the situation where excess pore pressure is greater than the air-entry value, K and S_r are considered to be varying with respect to the pore pressure. Consequently, the effects of varied ψ_{ae} to the consolidation-induced solute transport is particularly of interest and presented in this section. Figures 4.13-4.15 show the parametric study results for Model Kp, Model Srp and Model Kp+Srp respectively. In each figure, solid lines, dashed lines and dotted lines denote the simulation results when ψ_{ae} equals 20kPa, 30kPa and 39kPa assuming a clayey type of soil.

In general, ψ_{ae} alters the time when K and S_r become dynamic and affects the magnitudes of these parameters. Smaller ψ_{ae} implies that pore pressure is more easier to excess the air-entry value, so that the longer dynamic period can be observed. For Model Kp, with smaller ψ_{ae} (20 kPa), Figure 4.13(a) indicates the hydraulic conductivity starts to increasing from 0.25 year, and the dynamic period ends at 3.5 year at the top point and 2.5 year at the middle point. With the largest air entry value of 39 kPa, the hydraulic conductivity dynamic period is shorten to around 1.8 years for middle point and around 2 years at top. It is important to point out that, the outlet boundary (bottom) is assumed to allow free drainage of the excess pore fluid ($p^e = 0$) so that pore pressure will never exceed the air entry value, and

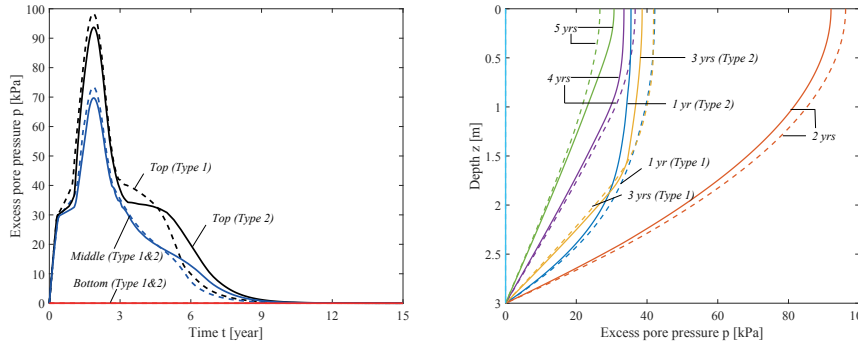

(a) Excess pore pressure

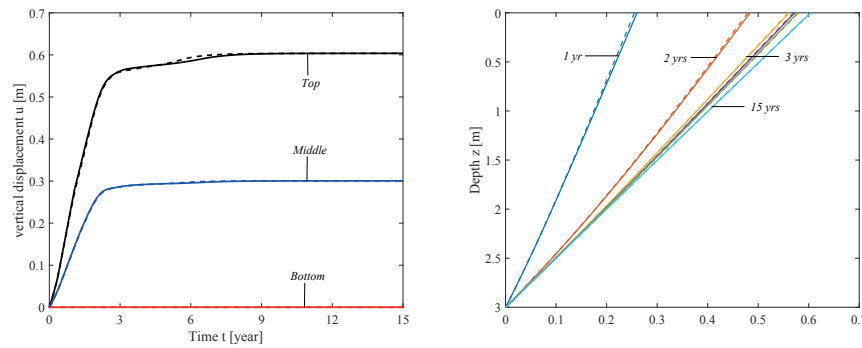

(b) Vertical displacement

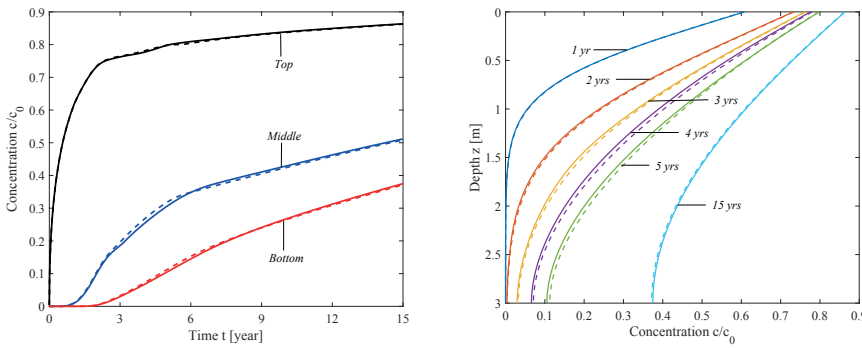

(c) Solute concentration

Figure 4.12 Distribution of (a) excess pore pressure, (b) vertical displacement and (c) solute transport vs time and depth for Model Srp, comparison between Type 1(dashed lines) and Type 2(solid line).

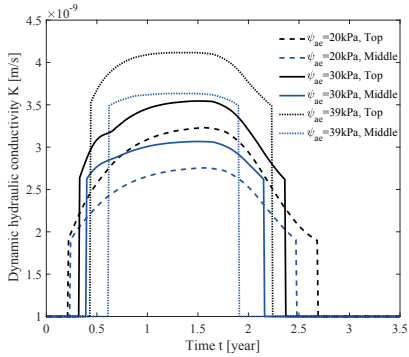

(a) Dynamic K vs time

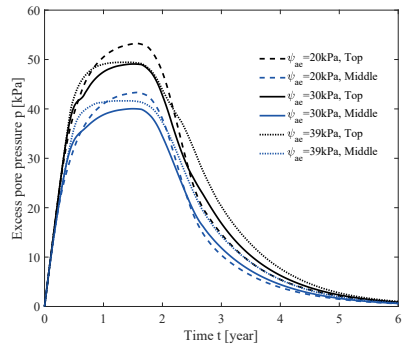

(b) Excess pore pressure vs time

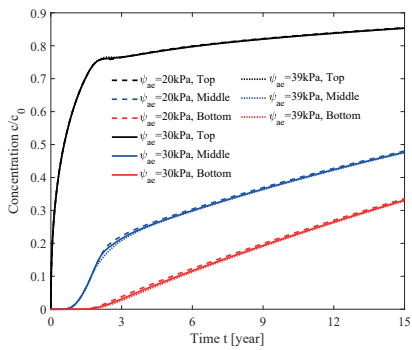

(c) Solute concentration vs time

Figure 4.13 Distribution of (a) dynamic hydraulic conductivity (b) excess pore pressure and (c) solute concentration vs time for Model Kp with various ψ_{ae}.

this feature further leads to constant K and S_r at bottom through out the whole simulation time. In addition to the influence of dynamic period, another impact on the magnitude of the dynamic K can be conclude that larger ψ_{ae} results in lower K at both top and middle points. With the combined effects of both, the excess pore pressure distribution (Figure 4.13(b)) shows the lowest peak value occurs when $\psi_{ae} = 30$kPa, which is neither the smallest not largest air-entry value. This interesting finding highlights the importance of numerically conducting dynamic model rather than qualitative analysis. Further more, according to Figure 4.13(c) for Model Kp, the solute concentration is less affected by air-entry value. It is also contributed by the joint effects that with increased ψ_{ae}, K shows shorter dynamic period but larger magnitude.

Figure 4.14 presents the dynamic degree of saturation, excess pore pressure and solute concentration distribution for Model Srp with varied ψ_{ae}. When conducting the parametric study, the value $P_{Sr=1}$ needs to be adjusted for each air-entry value ($P_{Sr=1}$=30kPa & 49kPa for ψ_{ae}=20kPa & 39kPa). Although the starting point of

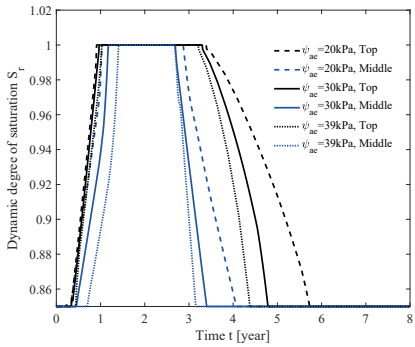

(a) Dynamic S_r vs time

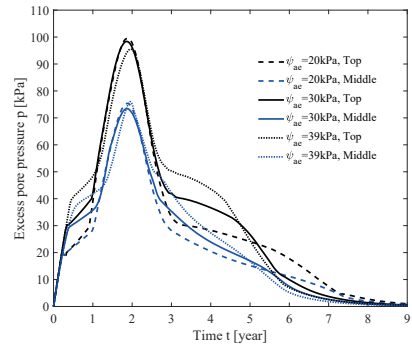

(b) Excess pore pressure vs time

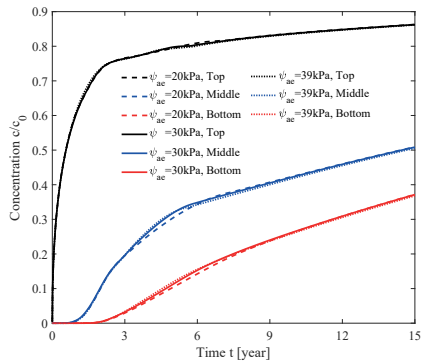

(c)Solute concentration vs time

Figure 4.14 Distribution of (a) dynamic degree of saturation (b) excess pore pressure and (c) solute concentration vs time for Model Srp with various ψ_{ae}.

dynamic degree of saturation is less affected, longer dynamic period as well as longer fully saturated period can be observed from Figure 4.14(a). Specifically, the dynamic period for largest air-entry value is 1.5 years shorter than the result with $\psi_{ae} = 20kPa$. Further more, different from the trending of Model Kp, the peak value for S_r is not affected. As a result, conclusion can be drawn that compared with Model Kp, Model Srp is less influenced by the air-entry value.

In addition, the parametric study is also conducted for Model Kp+Srp, parameter $P_{Sr=1}$ is set to be as same as listed in parametric study of Model Srp. As shown in Figure 4.15(a)&(b), dynamic period for both hydraulic conductivity and degree of saturation is reduced compared to Model Kp and Model Srp. The peak values of K are similar as in Model Kp, while compared to Model Srp, differences can be observed. For example, at the middle point when ψ_{ae}=39kPa, the peak degree of saturation only reaches 0.88, while in previous dynamic degree of saturation model, a 1.5 year fully saturation period exists at the same location. The lowest excess pore pressure occurs when ψ_{ae}=39kPa, and the peak value exists when ψ_{ae}=39kPa at

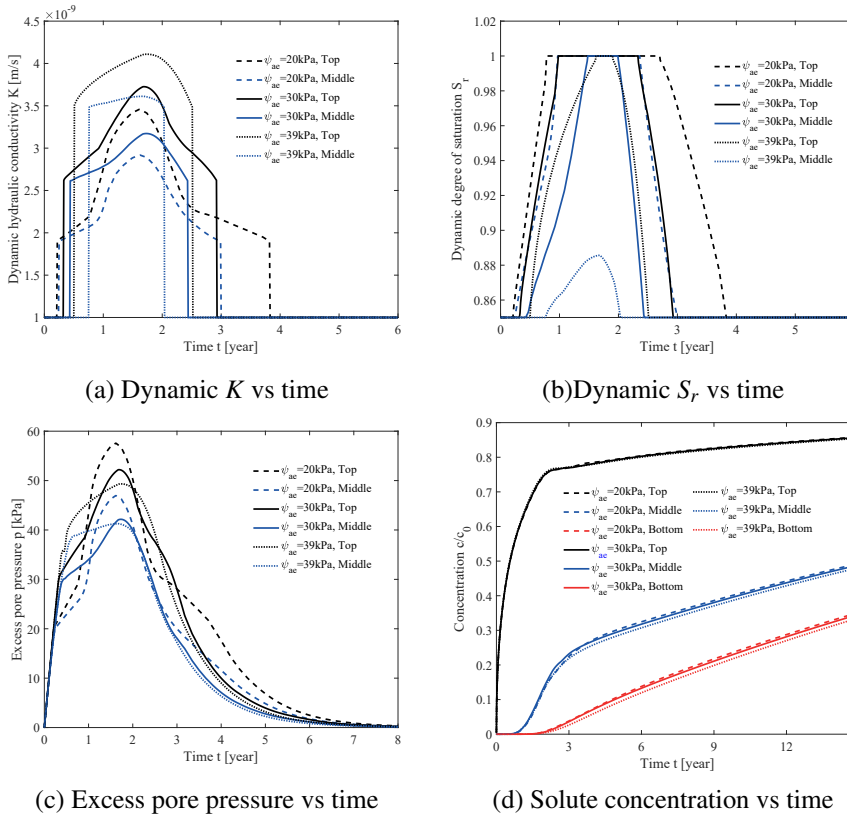

(a) Dynamic K vs time

(b)Dynamic S_r vs time

(c) Excess pore pressure vs time

(d) Solute concentration vs time

Figure 4.15 Distribution of (a) dynamic hydraulic conductivity (b) dynamic degree of saturation (c) excess pore pressure and (d) solute concentration vs time for Model Kp+Srp with various ψ_{ae}.

around 60kPa (Figure 4.15(c)). This peak excess pore pressure is slightly higher than Model Kp and much lower than peak p^e in Model Srp, which implies that the hydraulic conductivity plays a more significant role in governing the excess pore pressure dissipation compared with degree of saturation. Lastly, according to Figure 4.15(d), larger air-entry value generally contributes to a slower contaminant migration and leads to a later break through time. Recall that both Model Kp and Model Srp show limited impact on solute concentration, the fully dynamic model finally demonstrates the effects of varied air-entry value to the consolidation-induced solute migration.

4.6 SUMMARY

In this chapter, three dynamic models were established, one for dynamic hydraulic conductivity (Model Kp), one for dynamic degree of saturation (Model Srp) and

the third dynamic model for both (Model Kp+Srp). Due to the lack of field measurements and experimental data, model validation was conducted between previous numerical studies (Peters and Smith, 2002; Zhang et al., 2012*a*). The present dynamic model controls the excess pore pressure to be always less than air entry value. The dynamic model results were compared with the conventional model to see the dynamic effects on the consolidation-induced solute transport. Following that, an alternative dynamic S_r model is proposed and compared with Model Srp to study the effects of the concavity of pore pressure related dynamic degree of saturation function on consolidation-induced solute transport. Additionally, parametric study was performed to investigate the model sensitivity to the air-entry value.

In general, the consideration of dynamic hydraulic conductivity greatly affects the consolidation process and slightly reduces the consolidation-induced solute transport speed. the dynamic degree of saturation, on the other hand, results in an acceleration of contaminant migration. It is important to include the dynamic soil parameters especially when pore pressure is large and the air-entry value is low. This chapter introduces novel ideas by considering dynamic changes of soil parameters. By extending the conventional solute transport in deformable unsaturated porous media, the fully dynamic model now is able to incorporate the fluid compressibility, dynamic fluid density, dynamic soil porosity, dynamic hydraulic conductivity as well as the dynamic degree of saturation. The application of incorporating dynamic soil parameters in soil response is not limited to the landfill case as presented in this study, more examples could be made such as seabed response or marine structure stability (Wu and Jeng, 2019).

4.7 APPENDIX: DERIVATION OF CONSOLIDATION-INDUCED SOLUTE TRANSPORT WITH DYNAMIC HYDRAULIC CONDUCTIVITY AND DEGREE OF SATURATION

4.7.1 DERIVATION OF FLUID STORAGE EQUATION WITH DYNAMIC HYDRAULIC CONDUCTIVITY AND DEGREE OF SATURATION

Mass conservation for pore fluid is presented as:

$$\frac{\partial}{\partial t}(S_r n \rho_w) = -\frac{\partial}{\partial z}(S_r n \rho_w v_f). \tag{4.25}$$

in which S_r refers degree of saturation, n is the porosity, v_f denotes the flow velocity in the voids and ρ_w is the density of pore fluid.

The well known Darcy's Law can be written as:

$$S_r n \left(v_f - v_s\right) = -\frac{K}{\rho_w g}\frac{\partial p}{\partial z} \tag{4.26}$$

where p represents the excess pore pressure K indicates hydraulic conductivity and v_s refers to the velocity of the solid.

Keeping in mind that K, S_r and ρ_w are all dynamic and substituting (4.26) into (4.25) gives the relationship shown as:

$$\rho_w \frac{\partial S_r n}{\partial t} + S_r n \frac{\partial \rho_w}{\partial t} = -\frac{\partial}{\partial z}\left[\rho_w\left(-\frac{K}{\rho_w g}\frac{\partial p}{\partial z} + S_r n v_s\right)\right] \tag{4.27}$$

Expending (4.27) leads to:

$$\rho_w \frac{\partial S_r n}{\partial t} + S_r n \frac{\partial \rho_w}{\partial t} = \frac{1}{g}\frac{\partial}{\partial z}\left(K\frac{\partial p}{\partial z}\right) - S_r n v_s \frac{\partial \rho_w}{\partial z} - \rho_w \frac{\partial}{\partial z}\left(S_r n v_s\right). \tag{4.28}$$

Although the soil is partially saturated, the degree of saturation is assumed to be relatively high, so that the air is embedded in pore-water in the form of bubbles. The fluid compressibility (β) can then be expressed interns of degree of saturation as (Fredlund and Rahardjo, 1993):

$$\beta = \frac{S_r}{K_{w0}} + \frac{1 - S_r + r_h S_r}{P_a + P_0}, \tag{4.29}$$

in which K_{w0} is the pore-water bulk modulus (1000 MPa), r_h is the volumetric fraction of dissolved air within pore-water (0.02), P_a and P_0 are the gauge air pressure and the atmosphere pressure ($P_a + P_0 = 100$ kPa).

The fluid density(ρ_w) is considered to be changing with pore pressure, which implies the spatial and time variation of fluid density as:

$$\frac{\partial \rho_w}{\partial t} = \beta \rho_w \frac{\partial p}{\partial t}, \tag{4.30}$$

$$\frac{\partial \rho_w}{\partial z} = \beta \rho_w \frac{\partial p}{\partial z}. \tag{4.31}$$

Hence, (4.28) becomes to:

$$\begin{aligned} S_r \frac{\partial n}{\partial t} + n\frac{\partial S_r}{\partial t} + S_r n\beta\left(\frac{\partial p}{\partial t} + v_s \frac{\partial p}{\partial z}\right) = \frac{1}{\rho_w g}\frac{\partial}{\partial z}\left(K\frac{\partial p}{\partial z}\right) \\ - S_r \frac{\partial n v_s}{\partial z} - n v_s \frac{\partial S_r}{\partial z}. \end{aligned} \tag{4.32}$$

Considering the mass conservation of solid phase, the temporal derivative of porosity can be expressed as (Zhang et al., 2012*a*):

$$\frac{\partial n}{\partial t} = \frac{\partial v_s}{\partial z} - \frac{\partial n v_s}{\partial z}. \tag{4.33}$$

Further, the assumption of relatively small deformation implies the relationship that:

$$\left|\frac{\partial p}{\partial t}\right| \gg \left|v_s \frac{\partial p}{\partial z}\right|, \tag{4.34}$$

where the velocity of solid phase can be calculated as $\frac{\partial u}{\partial t}$.

Combining (4.32), (4.33) and (4.34), the governing equation for excess pore pressure field that is applicable to the condition of dynamic hydraulic conductivity and dynamic degree of saturation is proposed as:

$$n\frac{\partial S_r}{\partial t}+S_r n\beta\frac{\partial p}{\partial t}+S_r\frac{\partial^2 u}{\partial z\partial t}=\frac{K}{\rho_w g}\left(\frac{\partial^2 p}{\partial z^2}\right)+\frac{1}{\rho_w g}\frac{\partial K}{\partial z}\frac{\partial p}{\partial z}-n\frac{\partial u}{\partial t}\frac{\partial S_r}{\partial z}. \quad (4.35)$$

4.7.2 DERIVATION OF SOLUTE TRANSPORT EQUATION WITH DYNAMIC HYDRAULIC CONDUCTIVITY AND DEGREE OF SATURATION

For the governing equation of solute concentration field, conservation of solute mass in fluid and solid phase were considered, so that the solute transport equation can be written as:

$$\frac{\partial}{\partial t}\left(S_r nc\right)+\frac{\partial}{\partial t}\left[(1-n)c_s\right]=-\frac{\partial}{\partial z}\left[S_r n\left(-D\frac{\partial c}{\partial z}+v_f c\right)+(1-n)v_s c_s\right], \quad (4.36)$$

where c and c_s refer to the solute concentration in fluid and solid phase, respectively, and D denotes the hydrodynamic dispersion coefficient.

Under the assumption of compressible fluid and incompressible soil particle and combining with mass conservation of pore fluid and soil particles, Zhang et al. (2012*a*) suggested the transport equation to be written as:

$$\begin{aligned}S_r n\frac{\partial c}{\partial t}+(1-n)\frac{\partial c_s}{\partial t}=&\frac{\partial}{\partial z}\left(S_r nD\frac{\partial c}{\partial z}\right)-S_r nv_f\frac{\partial c}{\partial z}\\&-(1-n)v_s\frac{\partial c_s}{\partial z}+S_r n\beta\left(\frac{\partial p}{\partial t}+v_f\frac{\partial p}{\partial z}\right)c.\end{aligned} \quad (4.37)$$

By considering linear sorption:

$$c_s=\rho_s K_d c, \quad (4.38)$$

in which K_d describes the partitioning of the contaminant, and substitute v_f and v_s as introduced in Appendix 4.7.1 into (4.37), the governing equation can be expressed as:

$$\begin{aligned}&\left[S_r n+(1-n)\rho_s K_d\right]\frac{\partial c}{\partial t}=S_r nD\frac{\partial^2 c}{\partial z^2}\\&+\frac{\partial c}{\partial z}\left[\frac{\partial}{\partial z}\left(S_r nD\right)+\frac{K}{\rho_w g}\frac{\partial p}{\partial z}-S_r n\frac{\partial u}{\partial t}-(1-n)\rho_s K_d\frac{\partial u}{\partial t}\right]\\&+c\left[S_r n\beta\frac{\partial p}{\partial t}-\beta\frac{K}{\rho_w g}\left(\frac{\partial p}{\partial z}\right)^2+S_r n\beta\frac{\partial u}{\partial t}\frac{\partial p}{\partial z}\right].\end{aligned} \quad (4.39)$$

To incorporate the dynamic degree of saturation in the derivation process, chain rule is applied so that:

$$\frac{\partial}{\partial z}\left(S_r n D\right) = S_r n \frac{\partial D}{\partial z} + S_r D \frac{\partial n}{\partial z} + D n \frac{\partial S_r}{\partial z}. \tag{4.40}$$

The hydrodynamic dispersion coefficient (D) can be calculated as the summation of molecular diffusion coefficient (D_m) and longitudinal dispersion(α_L). i.e.,

$$D = D_m + \alpha_L \left(v_f - v_s\right). \tag{4.41}$$

Furthermore,the spatial variation can be calculated as Zhang et al. (2012*a*) :

$$\frac{\partial n}{\partial z} = \frac{(1-n)^2}{1-n^0}\frac{\partial^2 u}{\partial z^2}, \tag{4.42}$$

where n^0 refers to the initial soil porosity.

Substituting (4.40), (4.41) and (4.42) into (4.39), the governing equation becomes to:

$$\begin{aligned}\left[S_r n + (1-n)\rho_s K_d\right]\frac{\partial c}{\partial t} &= S_r n D_m \frac{\partial^2 c}{\partial z^2} + S_r n \alpha_L \left(v_f - v_s\right)\frac{\partial^2 c}{\partial z^2} \\ &+ \frac{\partial c}{\partial z}\left\{ S_r n \alpha_L \frac{\partial\left(v_f - v_s\right)}{\partial z} + S_r D_m \frac{(1-n)^2}{1-n^0}\frac{\partial^2 u}{\partial z^2}\right. \\ &+ S_r \alpha_L \left(v_f - v_s\right)\frac{\partial n}{\partial z} + D_m n \frac{\partial S_r}{\partial z} + n\alpha_L\left(v_f - v_s\right)\frac{\partial S_r}{\partial z} \\ &\left.+ \frac{K}{\rho_w g}\frac{\partial p}{\partial z} - \left[S_r n + (1-n)\rho_s K_d\right]\frac{\partial u}{\partial t}\right\} \\ &+ c\left[S_r n \beta \frac{\partial p}{\partial t} - \beta \frac{K}{\rho_w g}\left(\frac{\partial p}{\partial z}\right)^2 + S_r n \beta \frac{\partial u}{\partial t}\frac{\partial p}{\partial z}\right].\end{aligned} \tag{4.43}$$

Utilising the produce rule, the following relationship can be obtained, i.e.,

$$S_r n \frac{\partial\left(v_f - v_s\right)}{\partial z} + S_r\left(v_f - v_s\right)\frac{\partial n}{\partial z} = \frac{\partial}{\partial z}\left[S_r n\left(v_f - v_s\right)\right] - n\left(v_f - v_s\right)\frac{\partial S_r}{\partial z}. \tag{4.44}$$

Combining with Darcy's law (4.26), (4.43) now becomes:

$$\begin{aligned}\left[S_r n + (1-n)\rho_s K_d\right]\frac{\partial c}{\partial t} &= \frac{\partial^2 c}{\partial z^2}\left(S_r n D_m - \alpha_L \frac{K}{\rho_w g}\frac{\partial p}{\partial z}\right) \\ &+ \frac{\partial c}{\partial z}\left\{\alpha_L \frac{\partial}{\partial z}\left(-\frac{K}{\rho_w g}\frac{\partial p}{\partial z}\right) + S_r D_m \frac{(1-n)^2}{1-n^0}\frac{\partial^2 u}{\partial z^2}\right. \\ &\left.+ D_m n \frac{\partial S_r}{\partial z} + \frac{K}{\rho_w g}\frac{\partial p}{\partial z} - \left[S_r n + (1-n)\rho_s K_d\right]\frac{\partial u}{\partial t}\right\} \\ &+ c\left[S_r n \beta \frac{\partial p}{\partial t} - \beta \frac{K}{\rho_w g}\left(\frac{\partial p}{\partial z}\right)^2 + S_r n \beta \frac{\partial u}{\partial t}\frac{\partial p}{\partial z}\right].\end{aligned} \tag{4.45}$$

Now, recall the updated storage equation (4.35) and apply the product rule, the only term which might be affected by the dynamic hydraulic conductivity can be replaced as:

$$\begin{aligned}\frac{\partial}{\partial z}\left(-\frac{K}{\rho_w g}\frac{\partial p}{\partial z}\right) &= -\frac{1}{\rho_w g}\frac{\partial}{\partial z}\left(K\frac{\partial p}{\partial z}\right)+K\frac{\partial p}{\partial z}\left[\frac{\partial}{\partial z}\left(-\frac{1}{\rho_w g}\right)\right]\\ &= -S_r\frac{\partial^2 u}{\partial z\partial t}-n\frac{\partial S_r}{\partial t}-S_r n\beta\frac{\partial p}{\partial t}\\ &\quad -n\frac{\partial u}{\partial t}\frac{\partial S_r}{\partial z}+\beta\frac{K}{\rho_w g}\left(\frac{\partial p}{\partial z}\right)^2.\end{aligned} \tag{4.46}$$

Moreover, based on the discussion in Zhang et al. (2012*a*), it is reasonable to approximate n to a constant initial soil porosity (n^0) at this stage. Hence, the final governing equation for solute concentration field is presented as:

$$\begin{aligned}\left[S_r n^0+\left(1-n^0\right)\rho_s K_d\right]\frac{\partial c}{\partial t} &= \frac{\partial^2 c}{\partial z^2}\left(S_r n^0 D_m-\alpha_L\frac{K}{\rho_w g}\frac{\partial p}{\partial z}\right)\\ &\quad+\frac{\partial c}{\partial z}\left\{-n^0\alpha_L\frac{\partial S_r}{\partial t}-n^0\alpha_L\frac{\partial u}{\partial t}\frac{\partial S_r}{\partial z}+D_m n^0\frac{\partial S_r}{\partial z}\right.\\ &\quad-\alpha_L S_r n^0\beta\frac{\partial p}{\partial t}-S_r\alpha_L\frac{\partial^2 u}{\partial z\partial t}+S_r D_m(1-n^0)\frac{\partial^2 u}{\partial z^2}\\ &\quad\left.+\frac{\alpha_L\beta K}{\rho_w g}\left(\frac{\partial p}{\partial z}\right)^2+\frac{K}{\rho_w g}\frac{\partial p}{\partial z}-\left[S_r n^0+\left(1-n^0\right)\rho_s K_d\right]\frac{\partial u}{\partial t}\right\}\\ &\quad+c\left[S_r n^0\beta\frac{\partial p}{\partial t}-\beta\frac{K}{\rho_w g}\left(\frac{\partial p}{\partial z}\right)^2+S_r n^0\beta\frac{\partial u}{\partial t}\frac{\partial p}{\partial z}\right].\end{aligned} \tag{4.47}$$

5 Volatile Organic Contamination through Deforming Clay Liner

5.1 INTRODUCTION

Solid waste landfills can pose major environmental threats to the quality of groundwater resources. Unlike inorganic compounds, Volatile organic contamination (VOCs) can diffuse through the geomembrane, then breakthrough the underlying barrier and contaminate the surrounding groundwater. Understanding the progress and minimizing the migration of VOCs in landfill liners aids both barrier design and analysis of existing landfills.

Most research in the area has focused on the transport of the liquid phase. For example, Kim (1997) modeled VOC solute transport through a leachate drainage layer overlying a geomembrane and the compacted soil layer underneath. The leaked leachate was approximated as uniform flow over the whole surface area of soil liner. The seepage velocity was evaluated by an equivalent hydraulic gradient, which depends on the height of the leachate level accumulated on the geomembrane. The medium was considered to be fully saturated with dissolved VOC due to aqueous phase advection and diffusion. Nguyen et al. (2011) compared the performance of different composite liner systems based on the diffusion of VOCs in the liquid phase through a fully saturated liner. In reality, the basal soil liner is always unsaturated (Fityus et al., 1999). Fityus et al. (1999) employed a steady-state unsaturated moisture distribution to model the mass transfer through a partially saturated soil liner incorporating only the liquid phase. However, VOCs can reside in the gas phase in addition to the solid and liquid phases (Jury et al., 1990). Therefore, gas-phase motion in the pores of an unsaturated soil liner and its contribution to VOC migration should be investigated to ascertain its contribution to VOC transport in landfills.

Moisture transport in unsaturated soils is affected by temperature gradients, which, for example, can cause liquid-to-vapour phase changes and vice versa, as well as vapour phase transport. A series of laboratory experiments were carried out by Nassar et al. (1999) to investigate heat, water, potassium chloride, and benzene transport in unsaturated soils under isothermal and non-isothermal conditions. They concluded that the effect of temperature and temperature gradients should be included to describe the movement of volatile chemicals in soils.

Although the temperature generated by the breakdown of solid waste in a landfill is not in general extremely high (between 30 °C and 60 °C (Rowe, 2005)), the transport of volatile organics can be influenced by different factors:

- The temperature gradient can act as a driving force in moisture transport.

Especially for unsaturated soil with a connected pore air phase, the moisture flow caused by water vapour density variations can play an important role (Philip and de Vries, 1957). In this case, multi-phase flow modeling is necessary.

- Further, a rising temperature influences the contaminant transport due to its effect on the gaseous mixture of water vapour, dry air and VOC gas. Therefore, generally speaking, non-isothermal multi-phase moisture flow should be included in modeling VOC transport within an unsaturated landfill clay liner with inter-connected pore air.

An analytical solution is available for volatile organic contamination (VOC) transport in a porous medium (Shan and Stephens, 1995). Not surprisingly, it includes several assumptions and does not account for transient fluid and gas velocities induced by consolidation and temperature gradients. For such phenomena, numerical models are essential. Some progress has been made using numerical solutions to couple non-isothermal moisture flow with solute or toxic gas transport in unsaturated soils. For example, Nassar and Horton (1997) included three fully-coupled partial differential equations connecting the heat, water, and solute transfer to describe their simultaneous transfer in a rigid unsaturated soil. Thomas and Ferguson (1999) developed a fully coupled heat and mass transfer model describing the migration of liquid water, heat, air, and contaminant gas through an engineered clay liner, but without including deformations.

Small soil deformations were incorporated for non-isothermal moisture transport in an unsaturated landfill liner (Thomas and He, 1997; Zhou and Rowe, 2005). However, small-deformation models could overestimate the transit time of contaminants across a landfill liner with increasing discrepancies for increasing compressibility of the liner (Peters and Smith, 2002). Therefore, finite deformation formulations should generally be utilized to address the geometric non-linearity (Lewis et al., 2009; Zhang et al., 2013*b*).

There is increasingly more interest in VOC emissions through the landfill cover (Bogner et al., 2010; Scheutz et al., 2008; Schuetz et al., 2003), because the landfill emissions are regulated based on emissions of non-methane organic compounds rather than methane in some countries (for instance, in the US). Landfills generally have three types of covers: daily, intermediate, and final. Many daily covers are approximately 30cm thick exposed layers of clay soil over refuse. Therefore, there is a strong desire to model VOC through soils experiencing temperature gradients with variable water saturation.

To overcome these restrictions, Zhang et al. (2013*a*) proposed a mathematical model for non-isothermal, multi-phase moisture and VOC transport (in solid, liquid and gas phases) for unsaturated soil, incorporating finite deformations. The model is benchmarked against an example of isothermal moisture transport in a soil column and an analytical solution describing multi-phase VOC transport in unsaturated soil. In this chapter, the work of Zhang et al. (2013*a*) will be summarized.

5.2 MODEL FORMULATION

The main processes considered are mechanical consolidation, and moisture, VOC and heat transport. Correspondingly, the model consists of an equilibrium of forces for the solid phase, mass balances for moisture, gas and VOC, and balance of energy. The primary variables selected are the capillary pressure, p_c, pore air pressure, p_a, increase of absolute temperature, T, and the liquid VOC mass concentration, c_l.

In deriving the basic equations, the following assumptions are made:

- The pore fluid flow in both the liquid and gas phases are driven by pressure, viscous and gravity forces. Knudsen diffusion, which may become pronounced when the gas molecules collide primarily with the pore walls rather than with other molecules (Sleep, 1998), is not accounted for in this work, because the gas permeability coefficient of CCL considered is 10^{-12} m^2 and thus much greater than the threshold value of 10^{-14} m^2(Fen et al., 2011). Also, data associated with the Knudsen diffusion coefficient and its variation with water content and temperature are not available for CCL experiments.
- Diffusion and convection drive the movement of the water vapour. To model the multicomponent gas mixtures, the dusty gas model including the Knudsen diffusion is frequently used (Sleep, 1998). An alternative approach (Nassar and Horton, 1997), which is used in this chapter, can be used when Knudsen diffusion can be neglected. Their approach (Nassar and Horton, 1997) accounts for partial pressure gradients and binary gas-phase diffusion, which are important factors for multi-components gas.
- Heat flow occurs by conduction and convection and boiling, freezing, and thawing are not considered (Nassar and Horton, 1997). The approximation of local thermal equilibrium is used which means all phases within a representative element volume (REV) of soil have the same temperature. This assumption is acceptable as the energy exchange between the phases is significantly faster than the energy transport within a phase. This is valid for small grain sizes and their linked large specific soil surface area between the phases (Geiges, 2009).
- The soil liner is intact, namely there is no presence of inorganic pollutant or the associated chemical reactions with soil liner. Sorption is assumed not to change the soil porosity.

5.2.1 COORDINATE SYSTEMS

A Lagrangian coordinate system (z,t) is used with $\xi(z,t)$ as the particle displacement and $\xi(z,0)=z$. The relation between the Lagrangian and Eulerian (ξ,t) coordinate systems then implies that for any variable $F(z,t)=f(\xi(z,t),t)$:

$$\frac{\partial F}{\partial z}=\frac{\partial f}{\partial \xi}\frac{\partial \xi}{\partial z},\quad \frac{\partial F}{\partial t}=\frac{\partial f}{\partial \xi}\frac{\partial \xi}{\partial t}+\frac{\partial f}{\partial t}=\frac{\partial f}{\partial \xi}v_s+\frac{\partial f}{\partial t}, \tag{5.1}$$

where $v_s=\partial\xi/\partial t$ is the solid velocity.

Since the same amount of solid remains in each soil representative elementary volume (REV), the continuity equation for the solid phase takes the form:

$$\rho_s(z,0)(1-n_0)\Delta z = \rho_s(1-n)\Delta\xi, \tag{5.2}$$

where ρ_s is the soil grain density, $n = e/(1+e)$ is the current porosity, and $n_0 = n(z,0)$ is the initial porosity. The Jacobian, M, for the coordinate transformation is:

$$M = \frac{\partial\xi}{\partial z} = \frac{1-n_0}{1-n} = \frac{1+e}{1+e_0}, \tag{5.3}$$

where e_0 is the initial void ratio.

5.2.2 FORCE EQUILIBRIUM

The lateral soil pressure, σ_l is related to the vertical pressure, σ_v by the earth pressure coefficient at rest, K_0 (Boyd and Sivakumar, 2011; Fredlund and Rahardjo, 1993; Ishihara, 1993):

$$\sigma_l + p_a = K_0(\sigma_v + p_a). \tag{5.4}$$

Hence, the net mean stress is:

$$\sigma^* = \frac{\sigma_v + 2\sigma_l}{3} + p_a = \frac{1+2K_0}{3}\sigma_v + p_a. \tag{5.5}$$

Here, the tension stresses are taken as positive and p_a is the pore air gauge pressure.

For the compaction-induced soil lateral pressure, the value of K_0 increases rapidly with the degree of saturation around the optimum water content, and may exceed 0.9 when the water content is above the optimum (Ishihara, 1993). In engineering practice, the landfill clay liner is required to be compacted with the water content usually above the optimum (Edil, 2003). Therefore, K_0 is taken as 0.9 in this study.

The force equilibrium of the soil is described in terms of vertical soil stress σ_v by:

$$\frac{\partial\sigma_v}{\partial z} - b\frac{\partial\xi}{\partial z} = 0, \tag{5.6}$$

where b denotes the body force:

$$b = \{[\theta\rho_l + (1-n)\rho_s] - [\theta_0\rho_l + (1-n_0)\rho_s]\}\, g_i. \tag{5.7}$$

Herein, θ and θ_0 represent the current and initial water volume fractions, respectively, ρ_l denotes the density of liquid water, g_i is the gravitational vector taken with positive being upwards (and equals the acceleration due to gravity g, when the vertical coordinate, z, is opposite the direction of gravity; otherwise, $g_i = -g$). The masses of dry air and water vapour are negligibly small and are ignored.

5.2.3 MOISTURE AND HEAT ENERGY TRANSFER IN THE SPATIAL COORDINATE SYSTEM (ξ, T)

5.2.3.1 Mass balance for water

The liquid water and water vapour flux in an unsaturated media can be written as:

$$q_l = \rho_l \theta v_{li} - \rho_l D_T \frac{\partial t}{\partial \xi}, \tag{5.8a}$$

$$q_v = -D^* \frac{\partial \rho_v}{\partial \xi} + \rho_v (n - \theta) v_{ai}. \tag{5.8b}$$

The second term on the right-hand side (RHS) of (5.8a) represents the water flux due to the thermal gradient; D_T is a phenomenological coefficient relating the water flux to the temperature gradient, T is the absolute temperature increase, and D^* describes the effective molecular diffusivity of the water vapour.

According to Darcy's law, the intrinsic or linear average velocity of each individual liquid phase in soil is:

$$v_{li} = -\frac{k_l}{\theta} \frac{\partial}{\partial \xi} (p_c + p_a + \rho_l g_i \xi) + v_s, \tag{5.9a}$$

$$v_{ai} = -\frac{k_a}{n - \theta} \frac{\partial p_a}{\partial \xi} + v_s, \tag{5.9b}$$

where k_l and k_a are the mobility coefficients for the liquid pore-water and continuous air phases, respectively, $k_l = K_l/(\rho_l g)$, in which K_l is the hydraulic conductivity of the soil medium and v_{li} and v_{ai} denote the intrinsic phase average velocity with respect to a fixed coordinate system (Bear and Cheng, 2010) for liquid and vapour water, respectively. The gravitational contribution to v_{ai} is neglected because the density of air ρ_a is negligibly small (Zhou and Rajapakse, 1998).

The importance of the compressibility of pore-water was demonstrated in the prediction of solute breakthrough curves from partially saturated landfill liners (Zhang et al., 2012*a*). The solute was assumed to exist in the solid and liquid phases. For the multi-phase VOC transport model in this study, the density of both liquid and vapour water are taken as functions of temperature and capillary pressure:

$$\rho_l = \rho_{l0} [1 + \beta_l (p_c + p_a) - \alpha_l T], \tag{5.10}$$

where the initial density of liquid water is $\rho_{l0} = 998$ kg/m^3, the pore-water compressibility coefficient $\beta_l = 3.3 \times 10^9$ Pa^{-1}, and $\alpha_l = 3.0 \times 10^{-4}$ K^{-1} (Zhou and Rajapakse, 1998),

$$\rho_v = \rho_0 h = \rho_0 \exp\left[\frac{p_c}{\rho_l R_v (T + T_0)}\right], \tag{5.11}$$

in which h is relative humidity and ρ_0 is the density of vapour at saturation given by (Thomas et al., 1996):

$$\rho_0 = \frac{1}{194.4}\exp\left[a_0 T' + b_0 \left(T'\right)^2\right], \tag{5.12}$$

where $a_0 = 0.06374$, $b_0 = -0.1634 \times 10^{-3}$, $T' = T + T_0 - 273$, and T_0 is the initial temperature (K assumed).

In earlier non-isothermal moisture transport models (Azad et al., 2012; Thomas et al., 1996; Thomas and He, 1997; Zhou and Rajapakse, 1998; Zhou and Rowe, 2005), the solid velocity was not included in the expression for the water flux in deformable media. Here, the solid velocity is incorporated in both the mass and heat fluxes, and also in the liquid linear average velocity. When converted to the material coordinate system in the next section, all terms involving v_s are found to disappear and no extra complexity in the formulas is introduced.

The mass conservation equation for the moisture in a deformable unsaturated soil is:

$$\frac{\partial}{\partial t}\left[\rho_l \theta + \rho_v (n-\theta)\right] = -\frac{\partial}{\partial \xi}\left(q_l + q_v\right). \tag{5.13}$$

Zhou and Rajapakse (1998) took D_T as 2.4×10^{-10} m^2/(s K) in their example of a non-isothermal unsaturated soil column, while other researchers have attributed the influence of the temperature on the liquid water flux to its effect on the capillary potential head, expressed as (Nassar and Horton, 1997; Philip and de Vries, 1957):

$$D_T = k_l \rho_l g \frac{\partial \Psi}{\partial t}. \tag{5.14}$$

The temperature-corrected potential head, assumed to be a function of the capillary potential head, Ψ, and the temperature, is given by (Milly, 1984):

$$\Psi = \frac{p_c}{\rho_l g}\exp(-C_\psi T), \tag{5.15}$$

where C_ψ= -0.0068 K^{-1}is the temperature coefficient of water retention (Scanlon and Milly, 1994; Zhou and Rowe, 2003).

Considering a gaseous mixture of dry air and water vapour, the effective molecular diffusivity of the water vapour, D^*, can be expressed as (Philip and de Vries, 1957; Zhou and Rajapakse, 1998):

$$D^* = D_{atm} \nu_m \tau (n-\theta), \tag{5.16}$$

where τ is the dimensionless tortuosity factor to account for complexities in the pore geometry and the boundary conditions that influence the vapour transport at the microscopic scale. Its typical value is less than unity for intact soil, and it is temperature dependent (Zhou and Rajapakse, 1998). The mass flow factor is defined as $\nu_m = p_a/(p_a - p_v)$. D_{atm} is the molecular diffusion coefficient of water vapour in

air (m^2/s), and is expressed in terms of absolute temperature and air pressure (here, p_a is in units of Pa) (Thomas et al., 1996):

$$D_{atm} = 5.893 \times 10^{-6} \frac{(T + T_0)^{2.3}}{p_a}. \tag{5.17}$$

Alternatively, the diffusion flux of vapour, which is assumed to be driven by the vapour density gradient (Thomas and He, 1997), can be described by an extended vapour velocity equation (Thomas and King, 1994):

$$D^* \frac{\partial \rho_v}{\partial \xi} = n D_{atm} \nu_m \left[\frac{\partial \rho_v}{\partial p_c} \frac{\partial p_c}{\partial \xi} + \frac{(\nabla T)_a}{\nabla T} \frac{\partial \rho_v}{\partial t} \frac{\partial t}{\partial \xi} \right], \tag{5.18}$$

where $(\nabla T)_a / \nabla T$ is the ratio of the microscopic to the macroscopic temperature gradient. It is introduced since the microscopic temperature gradients in the fluid-filled pores are much higher than the macroscopic gradients across the sample as a whole. Thomas and Ferguson (Thomas and Ferguson, 1999) employed (5.18) to describe the water vapour diffusivity even in the presence of VOC gas.

When the concentration of the VOCs in the liquid phase increases to a critical level, its effect on Ψ cannot be neglected. It is considered via the surface tension model (Smith and Gillham, 1994):

$$\Psi = \Psi(T_r)(\gamma_m / \gamma_w), \tag{5.19}$$

where T_r is an arbitrary reference temperature, $\Psi(T_r)$ is the capillary pressure head at the reference temperature, γ_w is the surface tension of a free-water system at the reference temperature (J/m^2), and γ_m is the surface tension (J/m^2) at a VOC concentration of c_l. In view of (5.15), the capillary pressure head can be expressed as:

$$\Psi = \frac{p_c \gamma_m}{\rho_l g \gamma_w} \exp(-C_\psi T), \tag{5.20}$$

The effect of organic chemical concentrations on the surface tension, γ_m / γ_w, can be calculated for a nonionized organic solute by (Nassar and Horton, 1999; Reid et al., 1987):

$$\frac{\gamma_m}{\gamma_w} = \left[\Gamma_w + \Gamma_0 (\gamma_0 / \gamma_w)^{1/4} \right]^4, \tag{5.21}$$

where γ_0 is the surface tension of the VOCs (J/m^2), Γ_w and Γ_0 represent the superficial volume fraction of water and VOCs in the surface layer, for which data are rare in literature. Therefore, the effect of the VOCs on the surface tension of a mixed liquid is included by specifying a constant reduction factor for γ_m / γ_w. In contrast to inorganic species, organic compounds typically decrease the surface tension of water. The reduction factor falls within the range of 0.6 to 1 for organic concentrations lower than 10 mg/ml or less than 10^{-3} mol/ml (Tuckermann, 2007; Tuckermann and Cammenga, 2004).

In the case of a gaseous mixture composed of water vapour, dry air, and VOC vapour, the water vapour diffusion may be influenced by the presence of the VOC vapour especially when its mole fraction is relatively large. It can be described by (Nassar and Horton, 1999; Welty et al., 1984):

$$D^* = D_{wm}(n-\theta)^{5/3}, \tag{5.22}$$

where the molecular diffusivity of water vapour in a gas mixture (m^2/s), D_{wm} is:

$$D_{wm} = \left(y_2'/D_{i-2} + y_3'/D_{i-3} + \ldots + y_n'/D_{i-n}\right)^{-1}, \tag{5.23}$$

in which D_{i-n} denotes the molecular diffusivity for the binary pair, i.e., water vapour diffusing through components n. y_n' is the mole fraction of component n in the gas mixture evaluated on a component-water-vapour-free basis, that is,

$$y_2' = \frac{y_2}{y_2 + y_3 + \ldots + y_n}. \tag{5.24}$$

For a gaseous mixture that obeys the ideal gas law, the mole fraction equals the ratio of the corresponding partial pressures (Welty et al., 1984).

5.2.3.2 Mass balance for dry air

Air flow occurs as a bulk flow and as a diffusive flow of dry air and the dissolved air within the pore-water. Assuming that the diffusive flux of the dry air is very small relative to the bulk flow and can be ignored (Thomas and He, 1997; Zhou and Rajapakse, 1998), the mass balance for air in a deformable unsaturated soil can be written as:

$$\frac{\partial}{\partial t}\left\{\rho_{da}\left[n-(1-H)\theta\right]\right\} = -\frac{\partial q_{da}}{\partial \xi}, \tag{5.25}$$

where ρ_{da} is the density of dry air and H is the dimensionless coefficient of solubility defined by Henry's law (Thomas and Sansom, 1995). The dry air flux, q_{da}, is described by:

$$q_{da} = H\rho_{da}\left(\theta v_{li} - D_T\frac{\partial t}{\partial \xi}\right) + \rho_{da}(n-\theta)v_{ai}. \tag{5.26}$$

Since the variation of the pore air pressure from the atmosphere pressure in this study is far less than 1 bar, except when the degree of saturation exceeds 0.985, and the temperature falls in the range of 283-333 K, the background condition is close to STP (standard temperature and pressure). It is then reasonable to assume that the gas mixture obeys the ideal gas law and Dalton's law (Thomas and Sansom, 1995; Thomas and He, 1997). Therefore, we have:

$$\rho_{da} = \frac{p_{da}}{R_{da}(T+T_0)}, \tag{5.27a}$$

$$p_v = \rho_v R_v (T + T_0), \tag{5.27b}$$

where $R_i (i = da, v)$ is the specific gas constant (the ideal gas constant divided by the molecular weight).

When the volume fraction of VOC in the gas phase is sufficiently small (Challa et al., 1997; Hodgson et al., 1992; Soltani-Ahmadi, 2000), it can be assumed that the presence of the VOCs does not significantly alter the density and pressure of the dry air and the water vapour. Applying Dalton's law to the pore air mixture, the pore air pressure p_a is the sum of the dry air pressure p_{da} and the vapour pressure p_v:

$$p_a = p_{da} + p_v. \tag{5.28}$$

Substituting (5.27b) and (5.28) into (5.27a) leads to:

$$\rho_{da} = \frac{p_a}{R_{da}(T + T_0)} - \frac{R_v}{R_{da}}\rho_v, \tag{5.29}$$

where the specific gas constant, $R_{da} = 287.1$ J/kg K, $R_v = 461.5$ J/kg K.

The above approach is applicable to the case with a relatively large VOC mole fraction in the gas mixture. Since the density of the VOC vapour (ρ_{VOC}) can be expressed in terms of the adsorption coefficient H and the liquid concentration of the VOCs, c_l, by $\rho_{VOC} = Hc_l$, this additional compound does not add an extra unknown. Using Dalton's law of partial pressure yields

$$p_{VOC} = \rho_{VOC} R_{VOC} (T + T_0), \tag{5.30a}$$

$$p_a = p_{da} + p_v + p_{VOC}, \tag{5.30b}$$

and

$$\rho_{da} = \frac{p_a}{R_{da}(T + T_0)} - \frac{R_v}{R_{da}}\rho_v - -\frac{R_{VOC}}{R_{da}}\rho_{VOC}, \tag{5.30c}$$

where R_{VOC} is the specific gas constant for the VOC.

5.2.3.3 Heat energy balance

For a unit volume of a deformable unsaturated medium, conservation of heat energy can be written as:

$$\frac{\partial \Phi}{\partial t} = -\frac{\partial q_T}{\partial \xi}, \tag{5.31}$$

where Φ and q_T are the heat capacity of the soil and the total heat flux per unit volume, respectively.

Besides the heat content in an individual phase, considering the contributions of the latent heat of vapourization and exothermic process of wetting of the porous medium, Φ can be written as (Zhou and Rajapakse, 1998):

$$\begin{aligned}\Phi = &[\rho_s(1-n)C_s + \rho_l\theta C_l + \rho_v(n-\theta)C_v + \rho_{da}(n-(1-H)\theta)C_{da}]T \\ &+ L_0\rho_v(n-\theta) + \rho_l\theta W,\end{aligned} \tag{5.32}$$

where C_i $(i = s, l, v, da)$ is the specific heat capacity of each constituent in the soil, L_0 is the latent heat of vapourization, and W (J/kg) is the differential heat of wetting given by (Milly, 1984):

$$W = \frac{H_w}{\rho_l\delta}\exp\left(-\frac{\theta}{\delta S'}\right), \tag{5.33}$$

in which $S' = 10^7$ m^{-1} is the specific surface of the material and the material constant values are H_w=1 J/m^2, $\delta = 10^{-9}$ m in accordance with Zhou and Rajapakse (1998).

Heat transfer mechanisms in our model include conduction, convection, the vapourization of heat, the gradient of the water potential, and the differential heat of the wetting flux. When expressing the gradient of the differential heat of wetting flux as the liquid water flux multiplied by the coefficient of the differential heat of wetting (W), q_T can be written as (Prunty, 2002):

$$\begin{aligned}q_T = &-\lambda\frac{\partial t}{\partial\xi} + (\rho_s(1-n)v_sC_s + q_lC_l + q_vC_v + q_{da}C_{da})T + q_lW \\ &+ L_0q_v - D_c^*\frac{\partial}{\partial\xi}(p_c + p_a + \rho_l g\xi_i),\end{aligned} \tag{5.34}$$

where $\lambda = (1-S_l)\lambda_{dry} + S_l\lambda_{sat}$ is the thermal conductivity (where the degree of saturation $S_l = \theta/n$, $\lambda_{dry} = 0.5$ J/(s m K), and $\lambda_{sat} = 2$ J/(s m K) (Zhou and Rajapakse, 1998)). $D_c^* = (T+T_0)D_T$ relates the water potential gradient to the heat flux (Kay and Groenevelt, 1974; Milly, 1982). For the case where there is a relatively large VOC concentration in all three phases, the heat transfer parameters employed should be measured specifically to incorporate the effect of the VOCs.

5.2.3.4 Organic solute transfer

VOCs may reside in the soil in a liquid, gaseous, or a solid phase (Jury et al., 1990), and their transport can be due to diffusion and advection in both the liquid and vapour phases. Ignoring the degradation of the VOCs in the soil, their mass conservation is expressed as:

$$\frac{\partial c_{mt}}{\partial t} = -\frac{\partial q_{ct}}{\partial\xi}, \tag{5.35}$$

where c_{mt} denotes the mass of the contaminants per unit volume of the soil matrix, and q_{ct} represents the total VOC flux. In accordance with Nassar and Horton (1999), we have:

$$c_{mt} = (1-n)\rho_sS + \theta c_l + (n-\theta)c_g, \tag{5.36}$$

where S is the adsorbed concentration (mass per mass soil) and can be divided into two parts (Poulsen et al., 1998), which is that sorbed from the water phase and from the air phase. Local chemical equilibrium is assumed between each phase, i.e., the concentration of the VOCs in one phase can be evaluated from that in another phase. Assuming a linear partitioning coefficient between the soil phases i and j, H_{ij} (Nassar and Horton, 1999; Nassar et al., 1999), we have

$$S = H_{sl}c_l + H_{sg}c_g, \qquad c_g = H_{gl}c_l, \tag{5.37}$$

where c_i $(i = l, g)$ denotes the mass of the VOCs per unit volume of the liquid and gas phases, respectively. They are related by $H_{ij}(i, j = s, l, g)$, the linear partitioning coefficients between the individual soil phases. Nassar et al. (1999) found that the liquid–solid partitioning coefficient, $H_{sl} = 0.343 \times 10^{-3}\text{m}^3/\text{kg}$ (which depends on the water mass content, kg water per kg soil), and the dimensionless Henry's constant, $H_{gl} = 0.2$ (which depends on the temperature and the relative humidity).

The sorption of VOC from the vapour phase onto soil minerals, namely, H_{sg}, is strongly dependent upon the pore-water content, the soil type, and the chemical properties of the sorbing VOC (Nassar et al., 1999; Petersen et al., 1995). It can be around 1,000 times the H_{sl} for dry soil (Ong, 2006). H_{gl} for benzene is taken as 0.191 (Staudinger and Roberts, 2001). The partitioning coefficients are assumed to be functions of σ^*, p_c, p_a, and T for the sake of generality in the derivation of the related equations and coefficients. The linear sorption relationship employed here is valid because the concentrations of the VOCs in a landfill liner are normally very low (Poulsen et al., 1996, 1998).

For the VOC transport mechanism, advection is caused by moisture transport (liquid and vapour) and by the solid grain motion for the deformable porous medium considered, while dispersion is caused by mechanical dispersion and molecular diffusion:

$$\begin{aligned} q_{ct} = &-\theta D_{lc}\frac{\partial c_l}{\partial \xi} - (n-\theta)D_{gc}\frac{\partial c_g}{\partial \xi} + \rho_s v_s S + \frac{q_l}{\rho_l}c_l \\ &+ (n-\theta)(v_{ai} + v_g)c_g, \end{aligned} \tag{5.38}$$

where D_{ic} $(i = l, g)$ is the hydrodynamic dispersion coefficient and the thermal diffusion effect is represented through the temperature-dependent diffusion coefficient in each phase. Here, the VOC advective flux in the gas phase has two parts: v_{ai} is driven by the air pressure gradient and the equivalent vapour diffusion velocity, and v_g is due to the water vapour density gradient. In previous studies, Thomas and Ferguson (1999) took into account the first part, while Nassar and Horton (1999) considered the second part. However, in general both of them should be incorporated, by analogy with the derivation of the water vapour transport equation.

When defining the total concentration of the VOCs (5.36) and their flux (5.38), the bulk density of the soil, ρ_{sb}, is often used to express the solute mass sorbed onto the solid phase (Nassar and Horton, 1999; Shan and Stephens, 1995). However, ρ_{sb} varies with porosity changes. Therefore, ρ_s is employed here, for convenience in explicitly describing the varying porosity.

The hydrodynamic dispersion coefficient for VOCs in the liquid phase, D_{lc}, is given by (Nassar and Horton, 1999):

$$D_{lc} = 0.001 D_0 \frac{e^{10\theta}}{\theta} + D_{hw}, \tag{5.39}$$

where $D_{hw} = \alpha_{Lw}|v_{li}|$ ($\alpha_{Lw} = 0.004$ m (Yong et al., 1992) is the longitudinal dispersivity) is the mechanical dispersion coefficient of the VOC. D_0 is the mass diffusivity of the organic chemical through water, and can be expressed through the Wilke–Chang equation (Welty et al., 1984), which is also quoted by (Nassar and Horton, 1999):

$$D_0 = \frac{7 \times 10^{-12} \sqrt{\phi M_w}\,(T + T_0)}{\mu_w V_i^{0.6}}, \tag{5.40}$$

where ϕ is the dimensionless association factor of the solvent (2.6 for water (Nassar and Horton, 1999)), M_w is the molecular weight of water, and V_i is the molal volume of organic solute at the normal boiling point, which can be estimated from additive methods (Reid et al., 1987) as 224 cm^3/mol and 98 cm^3/mol for toluene and benzene, respectively.

The dynamic viscosity of water, μ_w (mPa s), is (Zhou and Rajapakse, 1998):

$$\mu_w = 661.2\,(T + T_0 - 229)^{-1.562}. \tag{5.41}$$

Liquid state theories for calculating diffusion coefficients are quite idealized and none can be considered as universally satisfactory for calculations (Reid et al., 1987). Equation (5.40), which has an error around 10% (Reid et al., 1987) is one of the estimation methods for the binary liquid diffusion coefficient of a liquid at infinite dilution. .

The hydrodynamic dispersion coefficient for VOCs in the gas phase, D_{gc}, is (Nassar and Horton, 1999):

$$D_{gc} = \Omega D_{gm} + D_{hg}, \tag{5.42}$$

where $D_{hg} = \alpha_{Lg}|v_{ai}|$ (α_{Lg} is the dispersivity and is taken to be 1 cm (Cann et al., 2004) in this chapter) is the dispersion coefficient of the VOC in the gas phase. The molecular-diffusion coefficient of an organic compound in a gaseous mixture (water vapour, air and VOC), D_{gm}, can be calculated via (5.23), while $\Omega = (n - \theta)^{2/3}$ is a factor representing the tortuosity.

The binary diffusion diffusivity (m^2/s) for gas i through gas n in the vapour phase can be calculated from (Fuller et al., 1966; Welty et al., 1984; Reid et al., 1987):

$$D_{i-n} = \frac{1.43 \times 10^{-7}\,(T + T_0)^{1.75}}{P\,(M_{i-n})^{1/2}\left[(\Sigma_v)_i^{1/3} + (\Sigma_v)_n^{1/3}\right]^2}, \tag{5.43}$$

where $M_{i-n} = 2\,(1/m_i + 1/m_n)^{-1}$, $m_j (j = i, n)$ (g/mol) is the molecular weight for the gases ($j = i, n$), Σ_v (no units) is the sum of the atomic diffusion volumes for each

gas component (Reid et al., 1987) (18 for water vapour, 19.7 for dry air, 90.96 for benzene) and P is the air pressure ($= p_a$) with units in bar.

Since each VOC compound has a different specific gas constant (due to its unique molecular weight) and partitioning coefficient, one mass conservation equation can be written for each individual component when the VOCs are a multicomponent mixture. There is no extra theoretical complexity except that more computational effort is required. Herein, only a single compound is considered.

5.2.4 MOISTURE AND HEAT ENERGY TRANSFER IN THE MATERIAL COORDINATE SYSTEM (Z, T)

The mass balance equation for moisture is:

$$\frac{\partial}{\partial t}\left\{\left[\rho_l\theta+\rho_v(n-\theta)\right]M\right\}=-\frac{\partial}{\partial z}\left[-\rho_l k_l\frac{\partial}{\partial\xi}(p_c+p_a+\rho_l g\xi_i)-\rho_l D_T\frac{\partial t}{\partial\xi}-D^*\frac{\partial\rho_v}{\partial\xi}-\rho_v k_a\frac{\partial p_a}{\partial\xi}\right], \tag{5.44}$$

where M on the left hand side (LHS) accounts for deformation of a representative element volume (REV) relative to the spatial grid. The spatial gradient involved in the water flux on the right-hand side is implemented by transforming to the material coordinate system, i.e., $\partial(\cdot)/\partial\xi = M^{-1}\partial(\cdot)/\partial z$.

The mass balance equation for dry air is:

$$\frac{\partial}{\partial t}\left\{\rho_{da}\left[n-(1-H)\,\theta\right]M\right\}=-\frac{\partial}{\partial z}\left\{H\rho_{da}\left[-k_l\frac{\partial}{\partial\xi}(p_c+p_a+\rho_l g\xi_i)-D_T\frac{\partial t}{\partial\xi}\right]+\rho_{da}\left(-k_a\frac{\partial p_a}{\partial\xi}\right)\right\}. \tag{5.45}$$

Heat energy conservation gives:

$$\begin{aligned}\frac{\partial}{\partial t}(\Phi M)=-\frac{\partial}{\partial z}\Bigg\{&-\lambda\frac{\partial t}{\partial\xi}+\left[\left(-D^*\frac{\partial\rho_v}{\partial\xi}-\rho_v k_a\frac{\partial p_a}{\partial\xi}\right)C_v\right.\\&+\left(-\rho_l k_l\frac{\partial}{\partial\xi}(p_c+p_a+\rho_l g\xi_i)-\rho_l D_T\frac{\partial t}{\partial\xi}\right)C_l\\&+\left(H\rho_{da}\left[-k_l\frac{\partial}{\partial\xi}(p_c+p_a+\rho_l g\xi_i)-D_T\frac{\partial t}{\partial\xi}\right]\right.\\&\left.\left.+\rho_{da}\left(-k_a\frac{\partial p_a}{\partial\xi}\right)\right)C_{da}\right]T\\&+\left[-\rho_l k_l\frac{\partial}{\partial\xi}(p_c+p_a+\rho_l g\xi_i)-\rho_l D_T\frac{\partial t}{\partial\xi}\right]W\end{aligned}$$

$$+L_0\left(-D^*\frac{\partial\rho_v}{\partial\xi}-\rho_v k_a\frac{\partial p_a}{\partial\xi}\right)-D_c^*\frac{\partial}{\partial\xi}\left(p_c+p_a+\rho_l g\xi_i\right)\Bigg\}. \tag{5.46}$$

Mass conservation for the VOCs is given by:

$$\begin{aligned}\frac{\partial}{\partial t}\left(c_{mt}M\right)=-\frac{\partial}{\partial z}\Bigg\{&-\theta D_{lc}\frac{\partial c_l}{\partial\xi}-\left(n-\theta\right)D_{gc}\frac{\partial c_g}{\partial\xi}\\&-\left[k_l\frac{\partial}{\partial\xi}\left(p_c+p_a+\rho_l g\xi_i\right)+D_T\frac{\partial t}{\partial\xi}\right]c_l\\&-k_a\frac{\partial p_a}{\partial\xi}c_g+\frac{D^*}{\rho_v}\frac{\partial\rho_v}{\partial\xi}c_g\Bigg\}.\end{aligned} \tag{5.47}$$

Expanding the terms on the left-hand-side of each equation yields:

$$\begin{aligned}&E_{11}\frac{\partial\sigma_v}{\partial t}+E_{12}\frac{\partial p_c}{\partial t}+E_{13}\frac{\partial p_a}{\partial t}+E_{14}\frac{\partial t}{\partial t}\\&\quad=-\frac{\partial}{\partial z}\Bigg[-\rho_l k_l\frac{\partial}{\partial\xi}\left(p_c+p_a+\rho_l g\xi_i\right)-\rho_l D_T\frac{\partial t}{\partial\xi}\\&\qquad-D^*\frac{\partial\rho_v}{\partial\xi}-\rho_v k_a\frac{\partial p_a}{\partial\xi}\Bigg],\end{aligned} \tag{5.48}$$

$$\begin{aligned}&E_{21}\frac{\partial\sigma_v}{\partial t}+E_{22}\frac{\partial p_c}{\partial t}+E_{23}\frac{\partial p_a}{\partial t}+E_{24}\frac{\partial t}{\partial t}\\&\quad-\frac{\partial}{\partial z}\Bigg\{H\rho_{da}\left[-k_l\frac{\partial}{\partial\xi}\left(p_c+p_a+\rho_l g\xi_i\right)-D_T\frac{\partial t}{\partial\xi}\right]\\&\qquad+\rho_{da}\left(-k_a\frac{\partial p_a}{\partial\xi}\right)\Bigg\},\end{aligned} \tag{5.49}$$

$$\begin{aligned}&E_{31}\frac{\partial\sigma_v}{\partial t}+E_{32}\frac{\partial p_c}{\partial t}+E_{33}\frac{\partial p_a}{\partial t}+E_{34}\frac{\partial t}{\partial t}\\&\quad=-\frac{\partial}{\partial z}\Bigg\{-\lambda\frac{\partial t}{\partial\xi}+\left(-D^*\frac{\partial\rho_v}{\partial\xi}-\rho_v k_a\frac{\partial p_a}{\partial\xi}\right)C_v T\\&\quad+\left[-\rho_l k_l\frac{\partial}{\partial\xi}\left(p_c+p_a+\rho_l g\xi_i\right)-\rho_l D_T\frac{\partial t}{\partial\xi}\right]C_l T\\&\quad+H\rho_{da}\left[-k_l\frac{\partial}{\partial\xi}\left(p_c+p_a+\rho_l g\xi_i\right)-D_T\frac{\partial t}{\partial\xi}\right]C_{da}T\\&\qquad+\rho_{da}\left(-k_a\frac{\partial p_a}{\partial\xi}\right)C_{da}T\end{aligned}$$

$$+\left[-\rho_l k_l \frac{\partial}{\partial \xi}\left(p_c + p_a + \rho_l g \xi_i\right) - \rho_l D_T \frac{\partial t}{\partial \xi}\right] W$$
$$+ L_0 \left(-D^* \frac{\partial \rho_v}{\partial \xi} - \rho_v k_a \frac{\partial p_a}{\partial \xi}\right) - D_c^* \frac{\partial}{\partial \xi}\left(p_c + p_a + \rho_l g \xi_i\right)\Bigg\}, \tag{5.50}$$

and

$$\begin{aligned} E_{41} c_l \frac{\partial \sigma_v}{\partial t} + E_{42} c_l \frac{\partial p_c}{\partial t} + E_{43} c_l \frac{\partial p_a}{\partial t} + E_{44} c_l \frac{\partial t}{\partial t} + E_{45} \frac{\partial c_l}{\partial t} \\ = -\frac{\partial}{\partial z}\Bigg\{ \left[\theta D_{lc} + (n-\theta) D_{gc} H_{gl}\right] \frac{\partial c_l}{\partial \xi} - (n-\theta) D_{gc} \frac{\partial H_{gl}}{\partial \xi} c_l \\ - \left[k_l \frac{\partial}{\partial \xi}\left(p_c + p_a + \rho_l g \xi_i\right) + D_T \frac{\partial t}{\partial \xi}\right] c_l \\ - k_a \frac{\partial p_a}{\partial \xi} H_{gl} c_l - \frac{D^*}{\rho_v} \frac{\partial \rho_v}{\partial \xi} + H_{gl} c_l \Bigg\}. \end{aligned} \tag{5.51}$$

The coefficients E_{ij} ($i = 1-4$, $j = 1-5$) used in (5.48)–(5.51) are formulated in detail in Appendix 5.7. The spatial coordinate ξ is determined by:

$$\xi = z + \int_z^L \frac{e_0 - e(\zeta)}{1 + e_0} d\zeta. \tag{5.52}$$

Thus, the first-order PDE:

$$\frac{\partial \xi}{\partial z} = 1 + \frac{e_0 - e(z)}{1 + e_0}, \tag{5.53}$$

with boundary conditions $\xi(L,t) = L$ was constructed to find ξ.

5.2.5 CONSTITUTIVE RELATIONSHIPS

A non-linear elastic soil model is used here. Generally, both state surfaces for the void ratio and the liquid water content can be postulated as (Zhou and Rajapakse, 1998):

$$e = f_e(\sigma^*, p_c, T), \tag{5.54a}$$

$$\theta = f_\theta(\sigma^*, p_c, T). \tag{5.54b}$$

Considering (5.5), e and θ actually depend on the four primary variables. Thus, we have:

$$e = f_e(\sigma_v, p_c, p_a, T), \tag{5.55a}$$

$$\theta = f_\theta(\sigma_v, p_c, p_a, T). \tag{5.55b}$$

Lloret and Alonso (1985) give an extensive review of a number of forms of state surfaces and concluded that the following formulation gives the best description of the soil behavior (also employed in Zhou and Rowe (2005)):

$$e = a + b\ln(-\sigma^*) + c\ln(-p_c) + d\ln(-\sigma^*)\ln(-p_c) + (1+e_0)\alpha_T T, \tag{5.56}$$

where a, b, c, and d are model parameters. The thermal coefficient of volume change, α_T, can be expressed by (Thomas et al., 1996):

$$\alpha_T = \alpha_0 + \alpha_2 T + (\alpha_1 + \alpha_3 T)\ln\left(\frac{\sigma^*}{\sigma_0^*}\right). \tag{5.57}$$

Here, σ_0^* is the reference net mean stress and α_i $(i = 0, 1, 2, 3)$ are the model parameters.

The water retention curve and the hydraulic conductivity for a clay liner at a reference temperature of T_r can be described by Lloret and Alonso (1985) (employed in (Azad et al., 2012)):

$$\theta = \{a' - [1 - \exp(-b' p_c)](c' - d'\sigma^*)\}\frac{e}{1+e}, \tag{5.58}$$

where a', b', c', and d' are model parameters.

The unsaturated hydraulic conductivity of a deformable soil under isothermal conditions, K_l, is given by (Alonso et al., 1988):

$$K_l = k_l \rho_l g = A\left(\frac{S_l - S_{lu}}{1 - S_{lu}}\right)^3 10^{\alpha_k e}, \tag{5.59}$$

where S_l is the degree of saturation and A, S_{lu}, and α_k are the related constants. The mobility coefficient of the continuous air phase, k_a, is (Alonso et al., 1988):

$$k_a = \frac{B}{\mu_a}\left[e\,(1 - S_l)\right]^\beta, \tag{5.60}$$

where μ_a is the dynamic viscosity of the pore air and B and β are model constants.

The governing equations are solved using the multiphysics modeling software package COMSOL 3.5a (COMSOL, 2010). In the model, the spatial domains were discretized into unstructured Lagrange-linear elements with a maximum global element size of 10^{-2} m, and maximum local element size at the end boundaries of 10^{-3} m. The sub-time steps were set to 1 hour and 1 day in the two benchmark problems, respectively. The corresponding solutions have been confirmed to be independent on the sizes of time-steps and meshes.

5.3 VERIFICATION OF THE PROPOSED MODEL

In this section, the model just presented is reduced in order to be validated against benchmark problems in the literature. The governing equations are solved using the multiphysics modeling software package COMSOL 3.5a (COMSOL, 2010). In the model, the spatial domains were discretized into unstructured Lagrange-linear elements with a maximum global element size of 10^{-2} m, and maximum local element size at the end boundaries of 10^{-3} m. The sub-time steps were set to 1 hour and 1 day in the two benchmark problems, respectively. The corresponding solutions have been confirmed to be independent on the sizes of time-steps and meshes.

To verify the present model, the model was reduced in order to be validated against benchmark problems in the literature. The first example is for the Isothermal moisture transport in a deformable soil column (Zhou and Rajapakse, 1998), while the second example is for the multi-phase VOC transport (Shan and Stephens, 1995). The compersions between the reduction from present model and the previous analytical solutions show an excellent agreement.

5.3.1 ISOTHERMAL MOISTURE TRANSPORT IN A DEFORMABLE SOIL COLUMN

The infiltration of an unsaturated soil column 1-m high is considered in Zhou and Rajapakse (1998). The initial conditions of the soil are a uniform capillary pressure p_{c0}= -200 kPa, uniform air pressure p_{a0}= 1 bar, and zero temperature increase, $T(t = 0)$= 0 K with a uniform background temperature of T_0= 293 K. At the top ($z = 0$) of the soil column, a constant capillary pressure increase of 150 kPa was applied. The soil was free to deform and both the air pressure and temperature were kept constant. At the fixed bottom (z= 1 m), each quantity was held fixed at its initial state. The comparison results are shown in Figure 5.1, which is an excellent agreement.

5.3.2 MULTI-PHASE VOC TRANSPORT

Here, an analytical solution of the multi-phase VOC transport in Shan and Stephens (1995) is adopted as a benchmark case. Consider the problem of Trichloroethylene (TCE) transport in a vadose zone with a thickness of 10 m. Initially, there is a uniform concentration of 100 μg/cm^3 between 700 and 710 cm. The boundary conditions are zero concentration at the soil surface and zero concentration gradient at the bottom. The effects of mechanical dispersion and biodegradation are neglected and the gas advection velocity was assumed to be zero. As shown in Figure 5.2, the present model accurately reproduces the analytical solution.

5.4 APPLICATION: VOC TRANSPORT THROUGH AN INTACT CCL

The liner system investigated here is of a type widely used in waste impoundments and is assumed to be of sufficiently large extent to justify a 1D analysis. As schematically shown in Figure 2.1, the composite landfill consists of an impermeable geomembrane impervious to the diffusion of an inorganic solute, an underlying

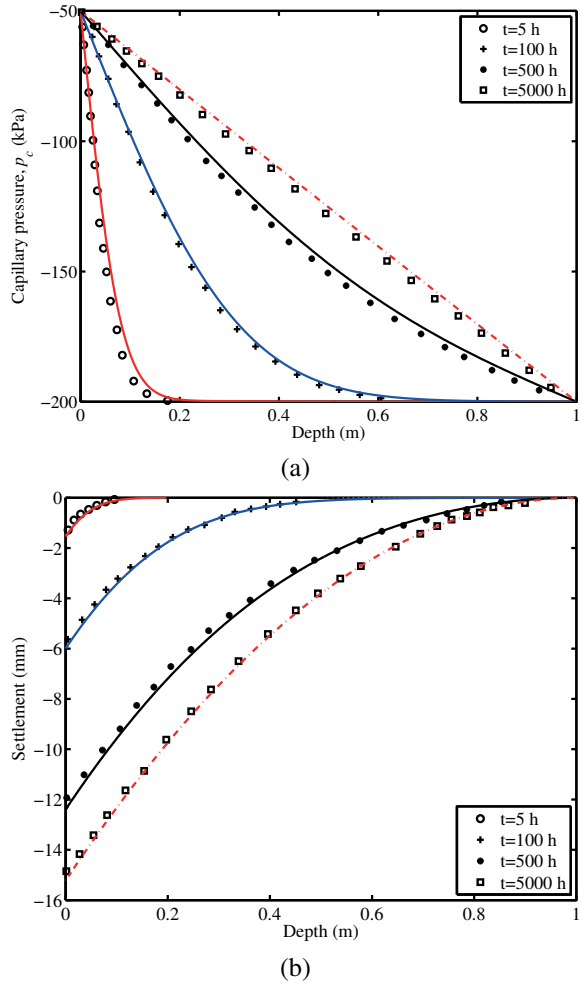

Figure 5.1 Comparison of capillary pressure and displacement due to infiltration: symbols are for results in Zhou and Rajapakse (1998) and the solid and dashed-dotted lines are for the present model.

clay soil layer such as an engineered compacted clay layer, and a second leachate collecting system. In this chapter, only the CCL is modeled, the effects of the overlying geomembrane and the second leachate collecting system below CCL on the porous flow and VOCs transport are represented with proper boundary (Peters and Smith, 2002). The CCL is assumed to be intact during the VOC breakthrough.

Initially, the VOC-free CCL has a uniform pore air pressure (1 bar) and temperature of T_0. To account for the initial steady liquid distribution with gravity, a

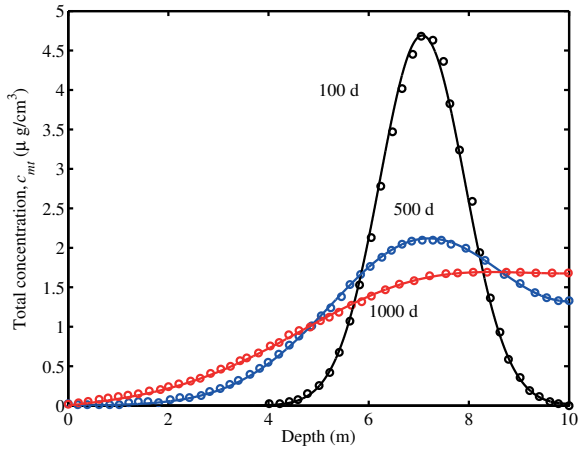

Figure 5.2 Comparison of total concentration distribution at three times (100, 500, 1000 d): circles are for results in Zhou and Rajapakse (1998) and solid lines are for the present model.

linear variation of the pore-water pressure is assumed as in (Thomas et al., 1996):

$$p_c(z,t=0) = p_{cr} + \rho_{l0} g_i (L - z). \tag{5.61}$$

Here, p_{cr} is the reference capillary pressure and L is the thickness of the CCL. The initial uniform net mean stress is σ_0^*.

At the top of the CCL, a time-dependent temperature increase is imposed. It increases rapidly to a fixed value, and then decreases gradually to zero.

$$T(z=0,t) = \begin{cases} t/t_1 \Delta T, & 0 \le t \le t_1 \\ \Delta T, & t_1 \le t \le t_2 \\ [1-(t-t_2)/(t_3-t_2)]\Delta T, & t_2 \le t \le t_3 \\ 0, & t \ge t_3 \end{cases}. \tag{5.62}$$

Here, ΔT is the maximum temperature increase and t_i $(i = 1,2,3)$ are the times at which the temperature changes due to waste degradation.

The waste filling process is approximated by a linear ramp loading (Peters and Smith, 2002):

$$\sigma_v(z=0,t) = \begin{cases} t/t' \Delta Q, & 0 \le t \le t' \\ \Delta Q. & t \ge t' \end{cases}, \tag{5.63}$$

where ΔQ is the maximum surcharge and t' is the time taken by the landfill to reach its full capacity.

The impervious geomembrane means that the liquid water mass flux equals zero, $q_l(z=0,t) = 0$, and the pore air pressure gradient vanishes, i.e., $\partial p_a(z=0,t)/\partial z = 0$.

VOC vapour can permeate through a non-porous geomembrane at the molecular level. The process occurs in three steps (Pierson and Barroso, 2002; Stark and Choi, 2005). First, the permeant dissolves and partitions at the geomembrane surface. Second, it diffuses through the geomembrane in the direction of lower chemical potential. Finally, it evapourates or desorbs onto the ambient receiving medium. The VOCs diffuse through the thin (relative to the CCL) geomembrane at the top boundary, with a flux given by:

$$f(0^-,t) = -P_G \frac{c_l(0^+,t) - c_0}{h}, \tag{5.64}$$

where c_0 is the concentration of the VOCs in the liquid phase at the top side of the geomembrane, which has a thickness of h_{GM}. P_G is the product of the diffusion coefficient for the solute in the geomembrane (D_G) and the partitioning coefficient of the solute between the geomembrane and the adjacent fluid (S_G) (Lewis et al., 2009). A good contact between the geomembrane and the CCL is assumed, and consequently $c_l(0^+,t)$ is the same as the concentration at the bottom surface of the geomembrane. Then, the flux in the CCL at the interface is:

$$f(0^+,t) = -\theta D_{lc} \frac{\partial c_l}{\partial z}(0^+,t). \tag{5.65}$$

Equating (5.64) and (5.65) (Peters and Smith, 2002), a Neumann boundary condition for the solute concentration is obtained:

$$\frac{\partial c_l}{\partial z}(0,t) - \frac{P_G}{\theta(0^+,t) h D_{lc}} c_f(0,t) = -\frac{P_G}{\theta(0^+,t) h D_{lc}} c_0. \tag{5.66}$$

At the bottom of the CCL, the second leachate collecting system is often made of gravel material with a high hydraulic conductivity. Therefore, the flow of pore-water contained in the CCL driven by the capillary pressure and temperature gradients is assumed to drain freely and the gradient of the solute concentration is assumed to be zero (Danckwert's boundary condition, Danckwerts (1953)), although different interpretations of this condition are possible (e.g., Barry and Sposito (1988)):

$$\begin{aligned} &p_c(z=L,t) = p_c(z=L,t=0), \\ &p_a(z=L,t) = 1 \text{ bar}, \\ &T(z=L,t) = T_0, \\ &\frac{\partial c_l}{\partial z} = 0. \end{aligned} \tag{5.67}$$

The model parameters employed in the following analyses are based on recent studies of solute transport in clay liners (Foose, 2002; Lewis et al., 2009). The values of the parameters used are shown in Tables 5.1–5.4 unless stated otherwise.

The coupled non-linear equations are solved using the multiphysics modeling software package COMSOL 3.5a, which solves Equations (5.6), (5.48)–(5.51), and (5.53) simultaneously. Consequently, the two-way coupling of the moisture and

Table 5.1
Soil parameters employed in numerical simulations.

Parameter	Value
Initial concentration in the landfill, c_0	100 mg/dm^3
Maximum waste loading, ΔQ	2×10^5 Pa
Loading period, t'	2 y
Geomembrane thickness, h_{GM} (Lewis et al., 2009)	0.0015 m
Mass transfer coefficient of geomembrane, P_G (Lewis et al., 2009)	4×10^{-11}m^2/s
CCL thickness, L	1 m
Magnitude of acceleration due to gravity, g	9.81 m/s^2
Initial compressive stress, σ_{v0} (Zhou and Rowe, 2005)	-200 kPa
Reference capillary pressure, p_{cr} (Zhou and Rowe, 2005)	-2.8 kPa
Earth pressure coefficient at rest, K_0	0.9
Temperature coefficient of water retention, C_ψ (Scanlon and Milly, 1994)	-0.0068 K^{-1}
Temperature increase at the top boundary, ΔT	30 K
Initial temperature in the liner, T_0	288 K
Temperature changes parameters, t_i $(i = 1,2,3)$	1 y, 10 y and 10 y respectively

the VOC transport is implemented. In the model, the system was discretized into unstructured Lagrange-linear elements with a maximum global element size of 10^{-2} m, and maximum local element size at the end boundaries (where the most rapid changes occur) of 10^{-3} m. The setting of sub-step size along the lines is corresponding to the waste filling process. The external loading increases from zero to its maximum in the first 2 y and then keeps steady. The sub-time step was set to 10^{-2} y in the simulation of the first 2 year, after which it was increased to 1 y in the following simulation period. All aforementioned time-steps and meshes have been checked through a convergence tests and then used in the following numerical examples.

Table 5.2
Soil components properties.

Parameter	Value
Soil solids	
Density of the solid phase, ρ_s	2.7×10^3 kg/m^3
Specific heat capacity, $C_{p,s}$ (Lewis et al., 2009)	800 J kg^{-1} K^{-1}
Soil liquid water	
Initial pore-water density, ρ_{l0} (Lewis et al., 2009)	0.998×10^3 kg/m^3
Phenomenological coefficient relating liquid flux to temperature, D_T (Zhou and Rajapakse, 1998)	2.7×10^{-10} m^2/(s K)
Reduction factor of surface tension due to VOC, γ_m/γ_w	0.8
Specific heat capacity, $C_{p,f}$ (Lewis et al., 2009)	4180 J kg^{-1} K^{-1}
Soil air	
Henry's solubility coefficient for air, H (Lewis et al., 2009)	0.02
VOC transport	
Specific gas constant for VOC, R_{VOC}	8.3144621/MW J/(kg K)[1]
Partitioning coefficient, H_{sg}	1.8×10^{-3} m^3/kg
Longitudinal mechanical dispersion coefficient for liquid phase, α_{Lw}	0.004 m

[1] MW is molar weight of VOC (78.114 g/mol for Benzene)

Table 5.3
State surface functions for unsaturated soil (Zhou and Rowe, 2005).

Void ratio	a	b	c	d	α_T (K^{-1})
	5.5	-0.4	-0.25	0.02	2.5×10^{-4}
Volumetric water content	a'	b'	c'	d'	
	0.9	-0.8	-10^{-8}	10^{-5}	

Table 5.4
Liquid mobility in unsaturated soil (Zhou and Rowe, 2005).

Hydraulic conductivity	A (m/s)	S_{lu}	α_k
	6×10^{-14}	0.05	5
Conductivity of air	B (Pa m/s)	μ_a (N s/m^2)	β_k
	1.8×10^{-12}	1.0×10^{-5}	4

5.5 RESULTS AND DISCUSSIONS

5.5.1 GEOMETRIC NON-LINEARITY AND SOIL VELOCITY

One of the important features of the finite deformation model (FD) is that it accounts for the finite deformation of the CCL, namely, the geometric non-linearity. In addition, the soil velocity is included. Two other models were constructed for comparison. The first one is a small deformation model (SD1), which does not incorporate the soil velocity occurrence in both the mass flux and the linear average velocity of the liquid phase v_{li} and v_{ai}. The second (SD2) is also a small deformation model, the difference with SD1 being that it considers the soil velocity.

As illustrated in Figure 5.3, the small deformation model underestimates the transit of the contaminant. Relative to the finite deformation model (FD), the small deformation models SD1 and SD2 assume that the thickness of the soil is constant even though consolidation causes soil contraction. As a result, it takes the VOCs longer to breakthrough the CCL. In previous research on non-isothermal moisture transport in deformable soil, the solid velocity was neglected based on the assumption that it is relatively small. However, Figure 5.3 demonstrates that including soil mobility can accelerate the transport of VOCs. It is noted that even with a small solid velocity, the capacity of the solid to transport solute ($(1-n)\rho_s v_s S$) may become non-negligible because of a relatively large solid density. Therefore, the FD model not only is theoretically consistent by considering the soil velocity but also accommodates the geometric non-linearity.

Since there is a significant advective VOC flux (the advective flux is approximately 50 times the diffusive flux, especially when the temperature increases, ΔT is higher), the VOC concentration level at the exiting boundary may exceed that in its vicinity. With a temperature decrease, and an advective flux gradually vanishing, the VOC concentration at the bottom boundary gradually decreases due to the dispersion of mass to the adjacent zone, until steady state is reached.

5.5.2 TWO-WAY COUPLING COEFFICIENT D^* AND ρ_{DA}

The water vapour diffusivity, D^*, can be calculated using (5.22), (5.23), (5.43), which we refer to as method WVD1. This approach requires two-way coupling of the moisture, heat, and the VOC transport to provide real-time values of the concentration of the VOCs when determining D^*. Alternatively, D^* can be

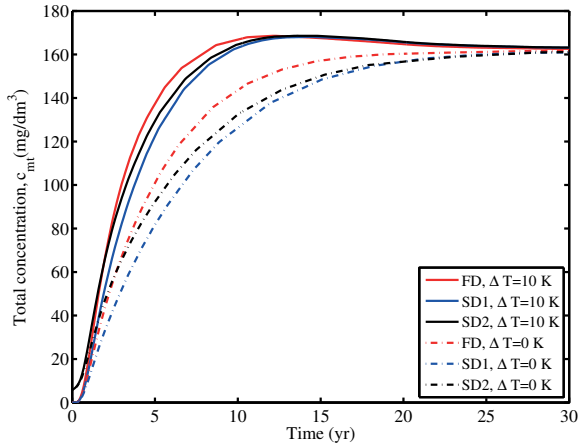

Figure 5.3 Effect of geometric non-linearity and soil velocity on VOCs breakthrough.

approximated by (5.16) and (5.17) (method WVD2), so that the solution of the VOC transport can be decoupled and calculated sequentially after solving for the moisture and heat transport. However, Figure 5.4 demonstrates that WVD2 overestimates the water vapour diffusivity and predicts a faster contaminant migration as a result. For either WVD1 or WVD2, the final levels of the total VOC concentration are identical, regardless of the temperature gradient. As explained in the last section, the concentration level at the exit boundary undergoes a decrease, especially for a greater temperature gradient. This is probably caused by the relatively larger ratio of advection to the effective dispersion in the advection–dispersion equation. On the other hand, whether considering VOCs or not when calculating the density of dry air, ρ_{da} does not make a discernible difference on the VOC transport progress (results not shown).

5.5.3 TOTAL CONSTITUTION OF THE CONCENTRATION OF THE VOCS

In the literature, there is no consensus on an expression for the total concentration of VOCs in unsaturated soil. While Thomas and Ferguson (Thomas and Ferguson, 1999) only focused on retention of VOCs in the aqueous and gaseous phases, most researchers consider that the VOCs also reside in the solid phase, due to sorption. However, different description are used. For example, some have described the sorbed concentration as being from either the aqueous or gaseous phases (Lin and Hildemann, 1995; Nassar and Horton, 1999), but others have included adsorption from both fluid phases (Poulsen et al., 1998; Shan and Stephens, 1995).

Figure 5.5 illustrates the liquid phase concentration and the total concentration level at the bottom boundary. 'ExpCtoti' represents three kinds of model: with the expression for the total concentration used in the present model ($i = 1$), excluding any contribution of adsorption from the gas phase ($i = 2$), and no adsorption onto

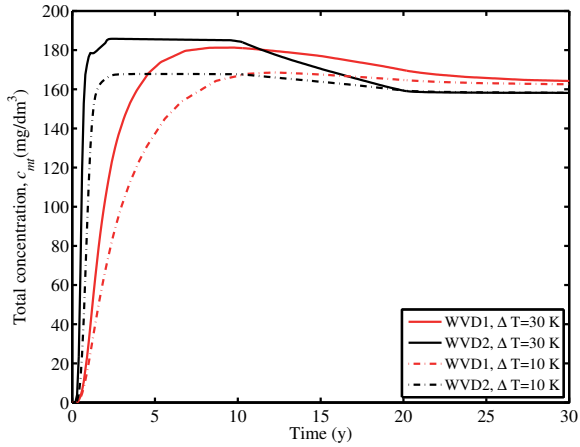

Figure 5.4 Effect of different methods for estimations of water vapour diffusivity on VOCs breakthrough.

the solid phase ($i = 3$). Although the liquid and gas phases are assumed to be in equilibrium in this study, it means that the transfer kinetic comes to a steady state, namely the concentration of the VOCs in one phase can be evaluated from that in another phase. However, the concentration in liquid and gas phases are not necessary to be identical. Therefore, the sorption was separated from both the liquid and gas phases.

As expected, the more complete adsorption mechanism results in slower VOC transport due to retardation. The difference of the final total concentrations in Figure 5.5(b) caused by their different constitutions are significant. Therefore, more experiments are needed to clarify which expression of the adsorption is appropriate. A higher temperature increase at the top boundary leads to a larger carrying capacity of both the liquid and gas phases. Consequently, the migration of the VOCs is accelerated.

5.5.4 LONGITUDINAL MECHANICAL DISPERSION (D_{HW} AND D_{HG})

Based on the assumption that the pore-water flow velocity in fine-grained soils due to mechanical consolidation is low (less than 10^{-6} m/s), mechanical dispersion can be neglected (Acar and Haider, 1990; Lewis et al., 2009). However, Zhang et al. (2012*a*) confirmed that the mechanical dispersion could double the final advective emission at the bottom of a partially saturated CCL when the molecular diffusion coefficient decreases within a practical range. In this section, the effect of mechanical dispersion on VOC transport is reexamined in a multi-phase context.

The mechanical dispersivity is often obtained by fitting measured breakthrough curves with analytical solutions of the advection–dispersion equation. However, there is the so-called dispersion-scale effect, namely, the dispersivity changes with the distance over which the contaminants travel. A good first approximation is to use

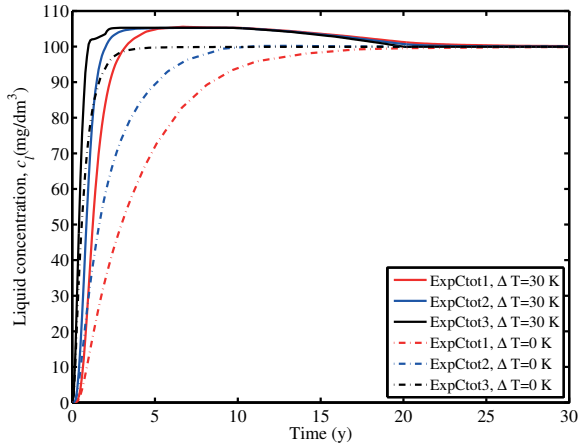

(a)

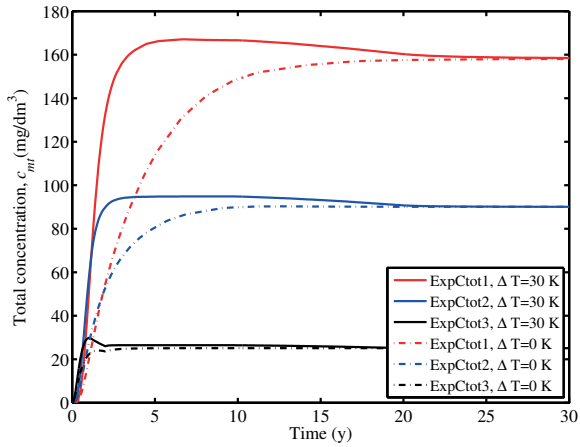

(b)

Figure 5.5 Comparison of the different expressions for the total VOC concentration on the predicted breakthrough.

a value of one-tenth of the transport distance for the longitudinal dispersivity if there is not enough information (Anderson, 1984). In this section, $\alpha_{Lw} = 0.1$ m (Yule and Gardner, 1978) was used to examine the effect of mechanical dispersion.

Figure 5.6 illustrates the distribution of the VOCs' dispersive flux in both the aqueous and gaseous phases. For the unsaturated soil considered here, the gas molecular diffusive flux is over four orders greater than the gas mechanical dispersivity flux, so the mechanical dispersive flux is small compared with the dominant diffusive flux through the gas phase (which is at the scale of 10^{-6} g/(m^2 s)). Therefore, the mechanical dispersion in unsaturated CCL in the considered cases can be neglected (as shown in Figure 5.7).

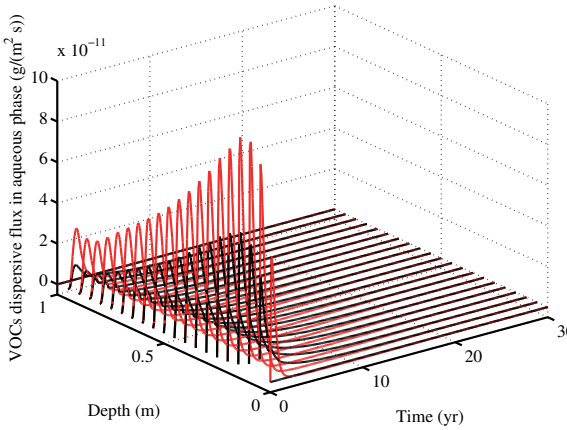

(a) Aqueous phase flux

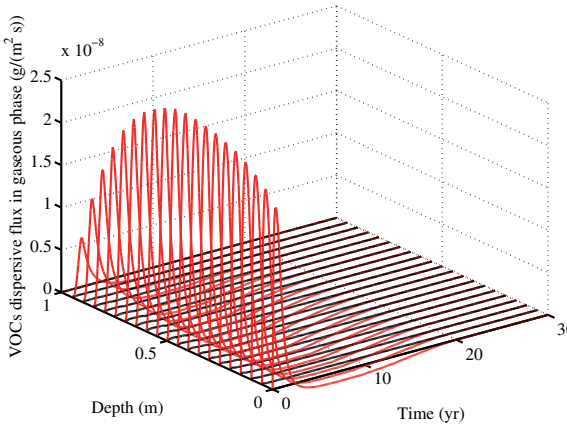

(b) Gaseous phase flux

Figure 5.6 Distribution of VOCs' dispersive flux ($\alpha_{Lw} = 0.1$ m): red curves for $T = 30$ K and black curves for $T = 0$ K.

5.5.5 MECHANICAL CONSOLIDATION AND TEMPERATURE INCREASE

When the waste is added at the top boundary, the clay liner undergoes mechanical consolidation, which can cause advective porous flow and thus is expected to help accelerate VOC transit. To investigate the contribution of mechanical consolidation in an unsaturated CCL, the present model was reduced to 'NoSV', which does not include variation of the vertical stress. A comparison was made between it and the present model (Model Cpt). Figure 5.8(a) and the case with $\Delta T = 30$ K in Figure 5.8b demonstrate that including the vertical compressive stress, namely, the mechanical consolidation, seems to predict a slower transport of the VOCs, which is contrary to the conclusion for their transport (in the solid and liquid phases) within a saturated or partially saturated CCL. This is due to two effects: First, the gas phase diffusion

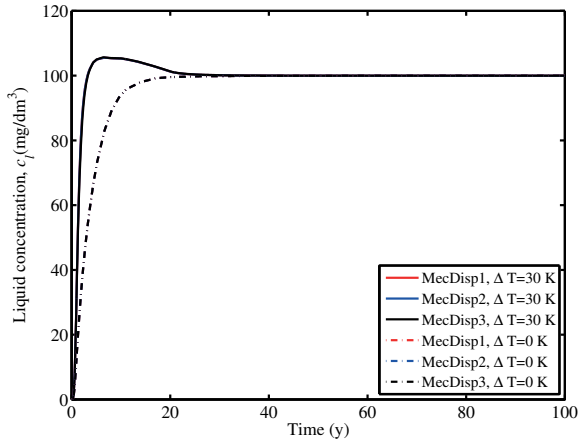

Figure 5.7 Effect of mechanical dispersion on VOC breakthrough ($\alpha_{Lw} = 0.1$ m).

dominates the transport progress for unsaturated soil instead of the advective flux in the liquid phase for saturated soil; second, the mechanical consolidation compacts the CCL and reduces the effective gas diffusion due to the lower void ratio. For the cases with larger temperature gradients, the effect of soil contraction due to mechanical consolidation is balanced by the swelling due to heating. Thus, the influence of mechanical consolidation on the movement of the VOCs is limited. Furthermore, both the liquid phase concentration and the total concentration of the VOCs at higher temperature gradients have higher peak values than at lower temperature gradients. This phenomenon is a result of the advective transport due the higher temperature gradient. Gradually, the concentration level decreases with decreasing advective fluxes of the VOCs.

In Figure 5.8(b), the total concentration for 'Model Cpt' surpasses that of 'Model NoSV' for cases with $\Delta T = 0$ K after a certain period. This is because the total sorptive capacity of a unit volume of solid is greater than that of a unit volume of pore fluid. When the soil is compressed and the void fluid is expelled, a unit volume of soil can carry more VOCs. Therefore, mechanical consolidation does not always lead to a faster transit of multi-phase VOCs within an unsaturated soil.

Figure 5.9 indicates that the lower pre-consolidation stress and the consequent larger initial void can speed the migration of the VOCs. Three pre-consolidation stress levels are considered here: PS1 with $\sigma_{v0} = -200$ kPa, PS2 with $\sigma_{v0} = -100$ kPa, and PS3 with $\sigma_{v0} = -50$ kPa. The values of the corresponding initial void ratio are 0.628 (0.646), 0.775 (0.815) and 0.920 (0.980), respectively. The values in brackets are the void ratios at the CCL bottom (the void ratio increases linearly from top to bottom due to the distribution of the initial capillary pressure).

A higher temperature increase at the top boundary was observed to shorten significantly the time required for breakthrough. This is because the gas phase VOC diffusion increases rapidly with increasing temperature and dominates the migration progress.

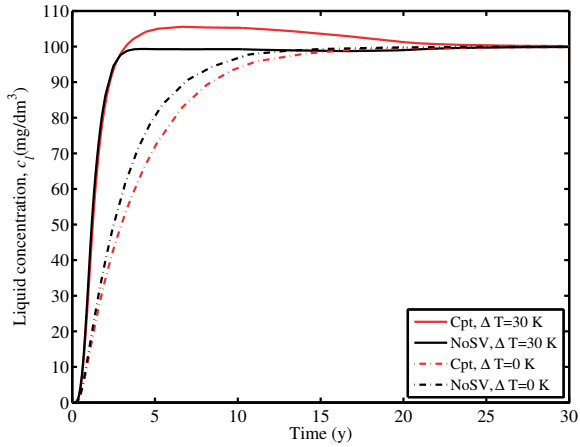

(a)

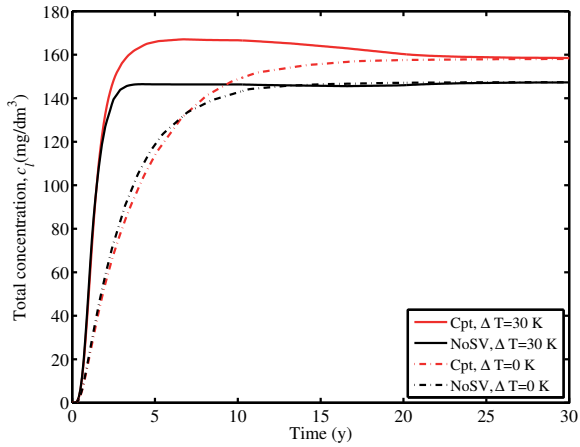

(b)

Figure 5.8 Effect of mechanical consolidation and temperature increase on VOC breakthrough.

5.5.6 CONTRIBUTION OF THE GASEOUS PHASE

In this section, a model (NoGas) without VOC flux in the gas phase is setup by letting $H_{gl} = H_{sg} = 0$ in the present model. As illustrated in Figure 5.10, incorporating the gas phase can dramatically speed up the migration of VOCs for both non-isothermal and isothermal soils. This is attributed to the greater magnitude of the diffusion coefficient (around 10^{-7} m^2/s) for the gas phase relative to that for the fluid phase (around 10^{-10} m^2/s).

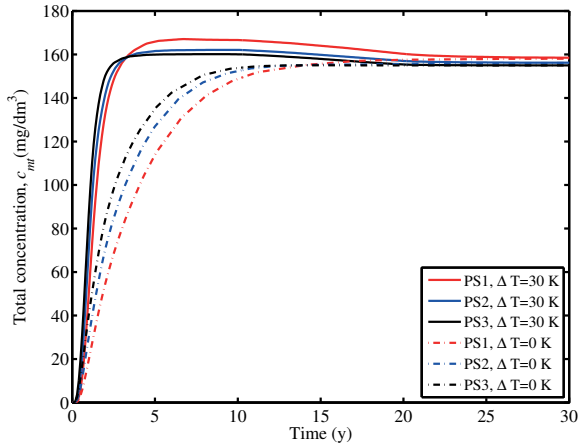

Figure 5.9 Effect of pre-consolidation stress (σ_{v0}) and temperature increase on VOC breakthrough ($a' = 0.9$).

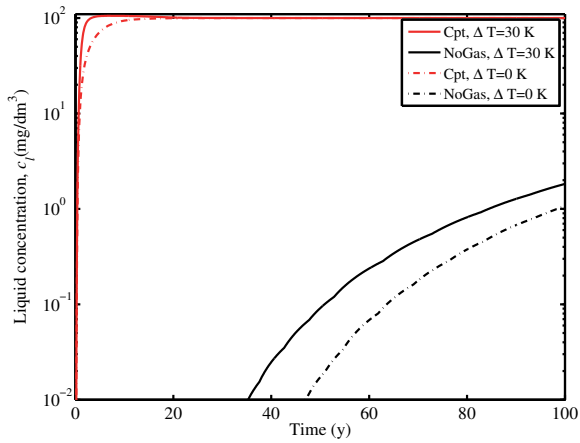

Figure 5.10 Contribution of the gas phase to VOC breakthrough ($a' = 0.9$).

Since gas phase diffusion depends on the gas saturation, $S_g = 1 - \theta/n$, a parametric study on the initial volume water content, θ, was performed to examine the influence of the degree of saturation on VOC migration. Figure 5.11 shows that lower water content leads to faster VOC migration in unsaturated soil, predicted by three-phase transport model, which is in the opposite direction to the trend for the two-phase (aqueous and solid phases) model (NoGas). In the former model, a lower water content means a larger gas saturation and a larger gas flow pathway. In contrast, it results in a smaller pore-water fraction, which impedes the VOC transit according to the model NoGas.

Therefore, gas phase transport plays a crucial role in the VOC transport within

unsaturated soil. As reported in the literature, some researchers attributed the observed faster VOCs breakthrough than the estimation of the pure-diffusion model to the mechanical consolidation of soil liner (Peters and Smith, 2002, 2004). However, other researchers (Lewis et al., 2009; Zhang et al., 2013*b*) suggested that the influence of mechanical consolidation on solute transport was not important, especially when the compressibility is low and decreasing of hydrodynamic dispersion due to soil compression is significant. The present results redirect our attention to examine whether the soil liner is fully saturated. If it is not, the gaseous phase VOCs transport could be a primary reason for accelerated VOC transport.

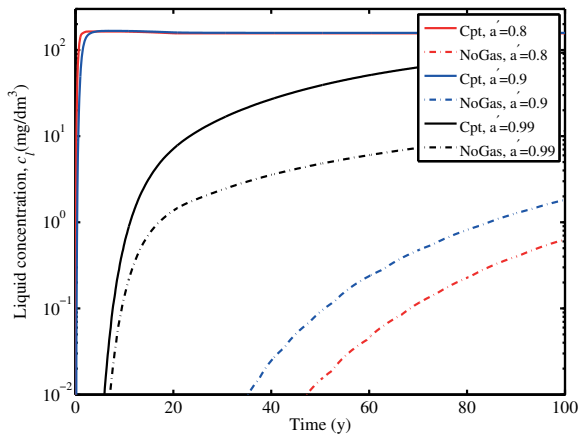

Figure 5.11 Effect of water content on VOC breakthrough: Solid line is the present model and dash-dot line is for the NoGas model.

5.6 SUMMARY

A 1D non-isothermal multi-phase (solid, liquid, and gas phases) moisture and VOC transport model for a non-linear elastic porous medium was developed. The model proposed in this study is theoretically consistent for a deformable soil column by including the soil velocity in the linear average pore fluid (liquid and gas) velocities and taking into account the mass flux due to the motion of the soil. Based on the finite deformation model, benzene migration in a solid waste landfill CCL under top surcharge and temperature gradient conditions was investigated. Mainly, the following conclusions can be drawn:

1. The assumption of small deformations (neglecting changes of the soil column) and ignoring the motion of the soil underestimates the transit of the VOCs. A two-way coupling approach is essential to get an accurate determination of the water vapour diffusion coefficient in the presence of VOC vapour.
2. Taking into account the adsorption of the VOCs from both the gas and fluid phases in the composition of the total concentration can considerably

slow down the migration progress predicted by the model. The mechanical dispersion of the fluid phase can be neglected because the related VOC dispersion fluxes are several orders of magnitude less than the diffusive flux in the gas phase.

3. The shrinking of the pores in the soil due to mechanical consolidation helps to prevent VOC breakthrough, but a higher environmental temperature increases the VOC gas phase diffusion, which plays a predominant role in an unsaturated soil liner. Furthermore, the deviation of saturation from the fully saturated state can significantly speed up the motion of VOCs. Therefore, a non-isothermal multi-phase moisture and VOC transport model is essential to obtain a reliable prediction of the migration of VOCs in an unsaturated soil liner exposed to heating and compression.

5.7 APPENDIX: COEFFICIENTS FOR VOC THROUGH DEFORMING CLAY LINER

The coefficients E_{ij} ($i = 1-4$, $j = 1-5$) used in (5.48)–(5.51) are given as follows.

For the case of a finite deformation, i.e., $M \neq 1$,

$$E_{11} = \frac{1+2K_0}{3}\left[\frac{1+e}{1+e_0}(\rho_l - \rho_v)\frac{\partial\theta}{\partial\sigma^*} + \frac{1}{1+e_0}(\rho_l\theta + \rho_v - \rho_v\theta)\frac{\partial e}{\partial\sigma^*}\right], \quad (5.68a)$$

$$\begin{aligned} E_{12} = {} & \theta\frac{1+e}{1+e_0}\frac{\partial\rho_l}{\partial p_c} + \left(\frac{e}{1+e_0} - \theta\frac{1+e}{1+e_0}\right)\frac{\partial\rho_v}{\partial p_c} \\ & + \frac{1+e}{1+e_0}(\rho_l - \rho_v)\frac{\partial\theta}{\partial p_c} + \frac{1}{1+e_0}(\rho_l\theta + \rho_v - \rho_v\theta)\frac{\partial e}{\partial p_c}, \end{aligned} \quad (5.68b)$$

$$E_{13} = \theta\frac{1+e}{1+e_0}\frac{\partial\rho_l}{\partial p_a} + \left(\frac{e}{1+e_0} - \theta\frac{1+e}{1+e_0}\right)\frac{\partial\rho_v}{\partial p_a} + E_{11}\frac{3}{1+2K_0}, \quad (5.68c)$$

$$\begin{aligned} E_{14} = {} & \theta\frac{1+e}{1+e_0}\frac{\partial\rho_l}{\partial t} + \left(\frac{e}{1+e_0} - \theta\frac{1+e}{1+e_0}\right)\frac{\partial\rho_v}{\partial t} \\ & + \frac{1+e}{1+e_0}(\rho_l - \rho_v)\frac{\partial\theta}{\partial t} + \frac{1}{1+e_0}(\rho_l\theta + \rho_v - \rho_v\theta)\frac{\partial e}{\partial t}, \end{aligned} \quad (5.68d)$$

$$E_{21} = \frac{1+2K_0}{3}\left(-(1-H)\rho_{da}\frac{1+e}{1+e_0}\frac{\partial\theta}{\partial\sigma^*} + \frac{\rho_{da}}{1+e_0}[1-(1-H)\theta]\frac{\partial e}{\partial\sigma^*}\right), \quad (5.69a)$$

$$\begin{aligned} E_{22} = {} & \left[\frac{e}{1+e_0} - (1-H)\theta\frac{1+e}{1+e_0}\right]\frac{\partial\rho_{da}}{\partial p_c} - (1-H)\rho_{da}\frac{1+e}{1+e_0}\frac{\partial\theta}{\partial p_c} \\ & + \frac{\rho_{da}}{1+e_0}[1-(1-H)\theta]\frac{\partial e}{\partial p_c}, \end{aligned} \quad (5.69b)$$

$$E_{23} = \left[\frac{e}{1+e_0} - (1-H)\,\theta\frac{1+e}{1+e_0}\right]\frac{\partial \rho_{da}}{\partial p_a} + E_{21}\frac{3}{1+2K_0}, \tag{5.69c}$$

$$\begin{aligned} E_{24} = &\left[\frac{e}{1+e_0} - (1-H)\,\theta\frac{1+e}{1+e_0}\right]\frac{\partial \rho_{da}}{\partial t} - (1-H)\,\rho_{da}\frac{1+e}{1+e_0}\frac{\partial \theta}{\partial t} \\ &+ \frac{\rho_{da}}{1+e_0}\left[1-(1-H)\,\theta\right]\frac{\partial e}{\partial t}, \end{aligned} \tag{5.69d}$$

$$E_{31} = \frac{1+2K_0}{3}\left(E_{311}\frac{\partial e}{\partial \sigma^*} + E_{312}\frac{\partial \theta}{\partial \sigma^*}\right), \tag{5.70a}$$

$$\begin{aligned} E_{311} = &L_0\frac{\rho_v}{1+e_0} - L_0\frac{\rho_v\theta}{1+e_0} + W\rho_l\frac{\theta}{1+e_0} + C_lT\rho_l\frac{\theta}{1+e_0} \\ &+ C_vT\frac{\rho_v}{1+e_0} - C_vT\frac{\rho_v\theta}{1+e_0} + C_{da}T\frac{\rho_{da}}{1+e_0}[1-(1-H)\theta], \end{aligned} \tag{5.70b}$$

$$\begin{aligned} E_{312} = &-L_0\frac{\rho_v(1+e)}{1+e_0} + W\rho_l\frac{1+e}{1+e_0} + C_lT\rho_l\frac{1+e}{1+e_0} \\ &- C_vT\frac{\rho_v(1+e)}{1+e_0} - C_{da}T(1-H)\rho_{da}\frac{1+e}{1+e_0} \\ &+ \rho_l\theta\frac{1+e}{1+e_0}\frac{\partial W}{\partial \theta}, \end{aligned} \tag{5.70c}$$

$$\begin{aligned} E_{32} = &E_{321}\frac{\partial \rho_v}{\partial p_c} + E_{322}\frac{\partial \rho_l}{\partial p_c} + C_{da}T\left[\frac{e}{1+e_0} - (1-H)\theta\frac{1+e}{1+e_0}\right]\frac{\partial \rho_{da}}{\partial p_c} \\ &+ E_{311}\frac{\partial e}{\partial p_c} + E_{312}\frac{\partial \theta}{\partial p_c}, \end{aligned} \tag{5.70d}$$

$$E_{321} = L_0\frac{e}{1+e_0} - L_0\frac{(1+e)\theta}{1+e_0} + C_vT\frac{e}{1+e_0} - C_vT\frac{(1+e)\theta}{1+e_0}, \tag{5.70e}$$

$$E_{322} = W\frac{(1+e)\theta}{1+e_0} + C_lT\frac{(1+e)\theta}{1+e_0} + \rho_l\theta\frac{1+e}{1+e_0}\frac{\partial W}{\partial \rho_l}, \tag{5.70f}$$

$$\begin{aligned} E_{33} = &E_{321}\frac{\partial \rho_v}{\partial p_a} + E_{322}\frac{\partial \rho_l}{\partial p_a} + C_{da}T\left[\frac{e}{1+e_0} - (1-H)\theta\frac{1+e}{1+e_0}\right]\frac{\partial \rho_{da}}{\partial p_a} \\ &+ E_{31}\frac{3}{1+2K_0}, \end{aligned} \tag{5.70g}$$

$$\begin{aligned}E_{34} =& E_{321}\frac{\partial \rho_v}{\partial t} + E_{322}\frac{\partial \rho_l}{\partial t} + C_{da}T\left[\frac{e}{1+e_0} - (1-H)\theta\frac{1+e}{1+e_0}\right]\frac{\partial \rho_{da}}{\partial t} \\ &+ E_{311}\frac{\partial e}{\partial t} + E_{312}\frac{\partial \theta}{\partial t} + C_s\frac{\rho_s}{1+e_0} \\ &+ \left[C_l\rho_l\theta\frac{1+e}{1+e_0} + C_v\rho_v\left(\frac{e}{1+e_0} - \theta\frac{1+e}{1+e_0}\right)\right] \\ &+ C_{da}\frac{\rho_{da}}{1+e_0}[e-(1-H)\theta(1+e)],\end{aligned} \tag{5.70h}$$

and

$$\begin{aligned}E_{41} =& \frac{1+2K_0}{3}\left[E_{411}\frac{\partial e}{\partial \sigma^*} + E_{412}\frac{\partial \theta}{\partial \sigma^*} + \frac{\rho_s}{1+e_0}c_l\frac{\partial H_{sl}}{\partial \sigma^*}\right. \\ &\left. + \frac{1}{1+e_0}\rho_s c_l\frac{\partial\left(H_{sg}H_{gl}\right)}{\partial \sigma^*} + \frac{\partial \xi}{\partial z}(n-\theta)c_l\frac{\partial H_{gl}}{\partial \sigma^*}\right],\end{aligned} \tag{5.71a}$$

where

$$E_{411} = \frac{\theta}{1+e_0}c_l + H_{gl}c_l\frac{1-\theta}{1+e_0}, \tag{5.71b}$$

$$E_{412} = \frac{\partial \xi}{\partial z}c_l - H_{gl}c_l\frac{\partial \xi}{\partial z}, \tag{5.71c}$$

$$\begin{aligned}E_{42} =& E_{411}\frac{\partial e}{\partial p_c} + E_{412}\frac{\partial \theta}{\partial p_c} + \frac{\rho_s}{1+e_0}c_l\frac{\partial H_{sl}}{\partial p_c} \\ &+ \frac{\rho_s}{1+e_0}c_l\frac{\partial\left(H_{sg}H_{gl}\right)}{\partial p_c} + \frac{\partial \xi}{\partial z}(n-\theta)c_l\frac{\partial H_{gl}}{\partial p_c},\end{aligned} \tag{5.71d}$$

$$E_{43} = \frac{3}{1+2K_0}E_{41}, \tag{5.71e}$$

$$\begin{aligned}E_{44} =& E_{411}\frac{\partial e}{\partial t} + E_{412}\frac{\partial \theta}{\partial t} + \frac{\rho_s}{1+e_0}c_l\frac{\partial H_{sl}}{\partial t} \\ &+ \frac{\rho_s}{1+e_0}c_l\frac{\partial\left(H_{sg}H_{gl}\right)}{\partial t} + \frac{\partial \xi}{\partial z}(n-\theta)c_l\frac{\partial H_{gl}}{\partial t}\end{aligned} \tag{5.71f}$$

and

$$E_{45} = \frac{\rho_s}{1+e_0}\left(H_{sl} + H_{sg}H_{gl}\right) + \theta\frac{\partial \xi}{\partial z} + (n-\theta)\frac{\partial \xi}{\partial z}H_{gl}. \tag{5.71g}$$

For small strain deformations, i.e., $M = 1$,

$$E'_{11} = \frac{1+2K_0}{3}\left[(\rho_l - \rho_v)\frac{\partial\theta}{\partial\sigma^*} + \rho_v(1+e)^{-2}\frac{\partial e}{\partial\sigma^*}\right], \tag{5.72a}$$

$$E'_{12} = \theta\frac{\partial\rho_l}{\partial p_c} + (n-\theta)\frac{\partial\rho_v}{\partial p_c} + (\rho_l - \rho_v)\frac{\partial\theta}{\partial p_c} + \rho_v(1+e)^{-2}\frac{\partial e}{\partial p_c}, \tag{5.72b}$$

$$E'_{13} = \theta\frac{\partial\rho_l}{\partial p_a} + (n-\theta)\frac{\partial\rho_v}{\partial p_a} + E'_{11}\frac{3}{1+2K_0}, \tag{5.72c}$$

$$E'_{14} = \theta\frac{\partial\rho_l}{\partial t} + (n-\theta)\frac{\partial\rho_v}{\partial t} + (\rho_l - \rho_v)\frac{\partial\theta}{\partial t} + \rho_v(1+e)^{-2}\frac{\partial e}{\partial t}, \tag{5.72d}$$

$$E'_{21} = \frac{1+2K_0}{3}\left[-(1-H)\rho_{da}\frac{\partial\theta}{\partial\sigma^*} + \rho_{da}(1+e)^{-2}\frac{\partial e}{\partial\sigma^*}\right], \tag{5.73a}$$

$$E'_{22} = [n-(1-H)\theta]\frac{\partial\rho_{da}}{\partial p_c} - (1-H)\rho_{da}\frac{\partial\theta}{\partial p_c} + \rho_{da}(1+e)^{-2}\frac{\partial e}{\partial p_c}, \tag{5.73b}$$

$$E'_{23} = [n-(1-H)\theta]\frac{\partial\rho_{da}}{\partial p_a} + E'_{21}\frac{3}{1+2K_0}, \tag{5.73c}$$

$$E'_{24} = [n-(1-H)\theta]\frac{\partial\rho_{da}}{\partial t} - (1-H)\rho_{da}\frac{\partial\theta}{\partial t} + \rho_{da}(1+e)^{-2}\frac{\partial e}{\partial t}, \tag{5.73d}$$

$$E'_{31} = \frac{1+2K_0}{3}\left(E'_{311}\frac{\partial e}{\partial\sigma^*} + E'_{312}\frac{\partial\theta}{\partial\sigma^*}\right), \tag{5.74a}$$

$$E'_{311} = T(1+e)^{-2}(\rho_v C_v + \rho_{da}C_{da}) + L_0\rho_v(1+e)^{-2}, \tag{5.74b}$$

$$E'_{312} = T[\rho_l C_l - \rho_v C_v - \rho_{da}C_{da}(1-H)] - L_0\rho_v + W\rho_l + \rho_l\theta\frac{\partial W}{\partial\theta} \tag{5.74c}$$

and

$$\begin{aligned} E'_{32} =& E'_{321}\frac{\partial\rho_v}{\partial p_c} + E'_{322}\frac{\partial\rho_l}{\partial p_c} + C_{da}T[n-(1-H)\theta]\frac{\partial\rho_{da}}{\partial p_c} \\ &+ E'_{311}\frac{\partial e}{\partial p_c} + E'_{312}\frac{\partial\theta}{\partial p_c}, \end{aligned} \tag{5.74d}$$

where

$$E'_{321} = (n-\theta)(L_0 + C_v T), \tag{5.74e}$$

$$E'_{322} = (W + TC_l)\theta + \rho_l \theta \frac{\partial W}{\partial \rho_l}, \tag{5.74f}$$

$$\begin{aligned} E'_{33} =& E'_{321}\frac{\partial \rho_v}{\partial p_a} + E'_{322}\frac{\partial \rho_l}{\partial p_a} + C_{da}T\left[n-(1-H)\theta\right]\frac{\partial \rho_{da}}{\partial p_a} \\ &+ E'_{31}\frac{3}{1+2K_0}, \end{aligned} \tag{5.74g}$$

$$\begin{aligned} E'_{34} =& E'_{321}\frac{\partial \rho_v}{\partial t} + E'_{322}\frac{\partial \rho_l}{\partial t} + C_{da}T\left[n-(1-H)\theta\right]\frac{\partial \rho_{da}}{\partial t} \\ &+ E'_{311}\frac{\partial e}{\partial t} + E'_{312}\frac{\partial \theta}{\partial t} + C_s\rho_s(1-n) \\ &+ C_l\rho_l\theta + C_v\rho_v(n-\theta) + C_{da}\rho_{da}\left[n-(1-H)\theta\right], \end{aligned} \tag{5.74h}$$

and

$$\begin{aligned} E'_{41} =& \frac{1+2K_0}{3}\left[E'_{411}\frac{\partial e}{\partial \sigma^*} + E'_{412}\frac{\partial \theta}{\partial \sigma^*} + E'_{413}\frac{\partial H_{sl}}{\partial \sigma^*}\right. \\ &\left. + E'_{413}\frac{\partial\left(H_{sg}H_{gl}\right)}{\partial \sigma^*} + E'_{414}\frac{\partial H_{gl}}{\partial \sigma^*}\right], \end{aligned} \tag{5.75a}$$

where

$$E'_{411} = c_l(1+e)^{-2}\left[\rho_s\left(H_{sl} + H_{sg}H_{gl}\right) + H_{gl}\right], \tag{5.75b}$$

$$E'_{412} = c_l\left(1-H_{gl}\right), \tag{5.75c}$$

$$E'_{413} = c_l(1-n)\rho_s, \tag{5.75d}$$

$$E'_{414} = c_l(n-\theta), \tag{5.75e}$$

$$E'_{42} = E'_{411}\frac{\partial e}{\partial p_c} + E'_{412}\frac{\partial \theta}{\partial p_c} + E'_{413}\frac{\partial H_{sl}}{\partial p_c} + E'_{413}\frac{\partial\left(H_{sg}H_{gl}\right)}{\partial p_c} + E'_{414}\frac{\partial H_{gl}}{\partial p_c}, \tag{5.75f}$$

$$E'_{43} = \frac{3}{1+2K_0} E'_{41}, \tag{5.75g}$$

$$E'_{44} = E'_{411}\frac{\partial e}{\partial t} + E'_{412}\frac{\partial \theta}{\partial t} + E'_{413}\frac{\partial H_{sl}}{\partial t} + E'_{413}\frac{\partial \left(H_{sg}H_{gl}\right)}{\partial t} + E'_{414}\frac{\partial H_{gl}}{\partial t} \tag{5.75h}$$

and

$$E'_{45} = (1-n)\,\rho_s\left(H_{sl} + H_{sg}H_{gl}\right) + \theta + (n-\theta)\,H_{gl}. \tag{5.75i}$$

5.8 APPENDIX: COORDINATE CONVERSION FOR THE GOVERNING EQUATIONS

As an example, consider the transformation of the moisture mass balance equation (5.13) from (ξ, t) coordinates to (z, t) coordinates. Inserting (5.8a)–(5.9b) into (5.13) yields

$$\begin{aligned}\frac{\partial}{\partial t}\left[\rho_l\theta + \rho_v(n-\theta)\right] = -\frac{\partial}{\partial \xi}\Bigg[&-\rho_l k_l \frac{\partial}{\partial \xi}\left(p_c + p_a + \rho_l g \xi_i\right) \\ &- \rho_l D_T \frac{\partial t}{\partial \xi} + \rho_l \theta v_s \\ &- D^* \frac{\partial \rho_v}{\partial \xi} - \rho_v k_a \frac{\partial p_a}{\partial \xi} + \rho_v (n-\theta) v_s\Bigg].\end{aligned} \tag{5.76}$$

Apply the transformation formula (5.1) and multiply both sides by M to get

$$\begin{aligned}\frac{\partial \xi}{\partial z}\frac{\partial}{\partial t}\Bigg[\rho_l\theta + \rho_v(n-\theta)\Bigg] - v_s \frac{\partial}{\partial \xi}\left[\rho_l\theta + \rho_v(n-\theta)\right]\frac{\partial \xi}{\partial z} \\ = -\frac{\partial}{\partial z}\Bigg[-\rho_l k_l \frac{\partial}{\partial \xi}\left(p_c + p_a + \rho_l g \xi_i\right) - \rho_l D_T \frac{\partial t}{\partial \xi} \\ - D^* \frac{\partial \rho_v}{\partial \xi} - \rho_v k_a \frac{\partial p_a}{\partial \xi}\Bigg] - \left[\rho_l\theta + \rho_v(n-\theta)\right]\frac{\partial v_s}{\partial z} \\ - v_s \frac{\partial}{\partial z}\left[\rho_l\theta + \rho_v(n-\theta)\right].\end{aligned} \tag{5.77}$$

The first term on the LHS and the second term on the right-hand side can be simplified using the product rule of differentiation,

$$\begin{aligned}\frac{\partial}{\partial t}\left[\rho_l\theta + \rho_v(n-\theta)\frac{\partial \xi}{\partial z}\right] = -\frac{\partial}{\partial z}\Bigg[&-\rho_l k_l \frac{\partial}{\partial \xi}\left(p_c + p_a + \rho_l g \xi_i\right) - \rho_l D_T \frac{\partial t}{\partial \xi} \\ &- D^* \frac{\partial \rho_v}{\partial \xi} - \rho_v k_a \frac{\partial p_a}{\partial \xi}\Bigg],\end{aligned} \tag{5.78}$$

which is with the same as (5.44).

Taylor & Francis
Taylor & Francis Group
http://taylorandfrancis.com

Section II

Tidal Dynamics in Coastal Aquifers

Taylor & Francis
Taylor & Francis Group
http://taylorandfrancis.com

6 Free Surface Flow in Coastal Aquifers: Shallow Water Expansion

6.1 INTRODUCTION

Groundwater dynamics within a sandy beach influence erosion control (Li et al., 2000*b*), saltwater intrusion (Dagan and Zeitoun, 1998), chemical transformation and biological activities (Pollock and Hummon, 1971; McArdle and McLachan, 1991). In particular, accurate prediction of dynamic groundwater hydraulics in coastal zones is required to improve coastal management. Most studies of coastal aquifers are based on the Boussinesq equation together with the Dupuit assumption (Dagan, 1967; Bear, 1972). The non-linear governing equation was derived by Dagan (1967) and subsequently approximated by expanding in terms of a perturbation parameter representing the shallow water approximation. Dagan (1967) showed that higher-order approximations are significant for fine sand with lower hydraulic conductivity. These solutions are only applicable when the amplitude of the motion is small compared to the mean water depth. Parlange et al. (1984) extended the work of Dagan (1967) to a higher-order solution to describe the free surface elevation of the groundwater flow.

To simplify the problem, most previous investigations for water table fluctuations in coastal aquifers have considered the case of a vertical beach instead of the more realistic case of a sloping beach. Nielsen (1990) was the first to derive an analytical solution where the assumption of a fixed location of the shoreline boundary condition is relaxed. However, his solution contains only an approximation to the boundary condition at the intersection of the beach and the ocean. Later, Li et al. (2000*b*) proposed the concept of a moving boundary to reexamine the problem using the same perturbation parameter as Nielsen (1990). The model proposed by Li et al. (2000*b*) overcame the inconsistency of the boundary condition in Nielsen's model (Nielsen, 1990). However, in both models (Nielsen, 1990; Li et al., 2000*b*), the slope of the beach was included in the perturbation parameter, limiting the applicability of their models to a certain range of the beach slope. In addition, both models only provided incomplete solutions of the second harmonic oscillations. Only the zeroth-order boundary value problem(i.e., the Boussinesq equation) has been solved for a sloping beach until Teo et al. (2003). It was demonstrated that the second-order correction to the linear solution will be particularly important under certain combination of wave and soil characteristics in coastal aquifers (Teo et al., 2003). With the same framework (Teo et al., 2003), Stojsavljevic et al. (2012) further

developed a semi-analytical solution for the higher-order problem with numerical perturbation technique.

In this chapter, we will present a higher-order solution for the tide-induced water table fluctuations in coastal aquifers adjacent to a sloping beach using a perturbation technique. The boundary value problem for tidal dynamics in coast aquifer will be outlined in Section §6.2. Then, the shallow water expansion is used to derive the higher-order boundary value problems (Section §6.3). The previous solutions for the zero-order shallow water expansion will be outlined and discuss their limitations in Section §6.4. A complete analytical solution is derived through two perturbation parameters (shallow water parameter ε and amplitude parameter α) in Section §6.5. A comprehensive comparison with previous solutions is made, and the effects of the second-order components and beach slope are examined in the section. With similar framework, a numerical perturbation approximation for the tidal dynamics in coast aquifer is presented in Section §6.6. Finally, a summary and discussion about the possible limitation of the present solution will be discussed in Section §6.7.

6.2 BOUNDARY VALUE PROBLEM FOR FREE SURFACE FLOW IN COASTAL AQUIFERS

The flow is assumed to be homogeneous, isothermal and incompressible in a rigid porous medium. The configuration of the tidal forced dynamic groundwater flow is shown below.

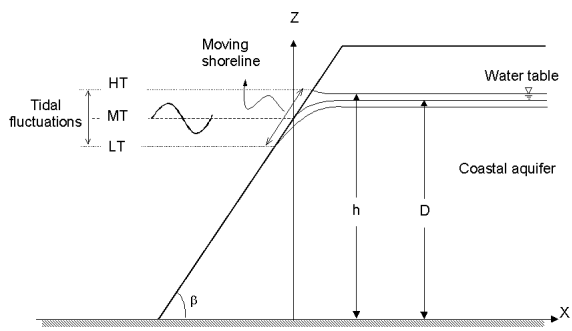

Figure 6.1 Schematic diagram of tidal water table fluctuations in a coastal aquifer.

In Figure 6.1, $h(x,t)$ is the total tide-induced water table height and D is the still water table height. The condition that the water table heights at the boundary of the ocean and coast (i.e., $x = x_0(t)$) are equal to the specified tidal variation, is

$$h(x_0(t),t) = D + A\cos\omega t = D(1+\alpha\cos\omega t), \tag{6.1}$$

where $\alpha = A/D$ is a dimensionless *amplitude parameter*, representing the ratio of the maximum tidal variation, A, to the average height of the water table, D. Note that we have neglected the seepage face.

If β is the slope of the beach, the horizontal extent of the tidal variation is

$$x_0(t) = A\cot\beta\cos\omega t. \tag{6.2}$$

For an incompressible and inviscid fluid, the potential head $\phi(x,z,t)(=z+p/\rho g)$ satisfies Laplace's equation (Bear, 1972),

$$\phi_{xx}+\phi_{zz}=0, \qquad -D\le z\le h(x,t). \tag{6.3}$$

Equation (6.3) is to be solved subject to (6.1) and the following boundary conditions,

$$\phi_z=0, \qquad z=0, \tag{6.4a}$$

$$\phi=h, \qquad z=h, \tag{6.4b}$$

$$n_e\frac{\partial\phi}{\partial t}=K\left[\left(\frac{\partial\phi}{\partial x}\right)^2+\left(\frac{\partial\phi}{\partial z}\right)^2\right]-K\frac{\partial\phi}{\partial z}, \qquad z=h, \tag{6.4c}$$

$$\frac{\partial\phi}{\partial x}=0, \qquad z\to\infty. \tag{6.4d}$$

The soil properties are defined by the two constants n_e, the soil porosity, and K, the hydraulic conductivity.

6.3 SHALLOW WATER EXPANSION

6.3.1 NON-DIMENSIONAL EQUATIONS

The standard linear solution to (6.3) to (6.4d) has a decay length, L, the length scale for significant variations in the x- direction, defined by (Nielsen, 1990)

$$L=\sqrt{\frac{2KD}{n_e\omega}}, \tag{6.5}$$

Here we consider shallow water flows and hence define the *shallow water parameter*, ε, as

$$\varepsilon=\frac{D}{L}=\sqrt{\frac{n_e\omega D}{2K}}. \tag{6.6}$$

This represents the ratio of the water table height to the linear decay length. Note that ε is entirely controlled by the material constants and the prescribed boundary condition, (6.1), and for shallow water flows, $\varepsilon << 1$. Thus, there are three independent parameters defined by the material and the boundary conditions: the shallow water parameter, ε, the amplitude parameter α, and the beach slope β. We construct solutions valid for small ε and α and a large range of β ($\pi/2\ge\beta>0$).

In general, the hydraulic conductivity (K) for coastal aquifers varies between 50 and 1000 m/day (fine sand to gravel beach, Bear (1972)), tidal wave frequency $\omega = 4\pi$ /day (=$2\pi/(0.5$ day)), and aquifer depth D varies between 5 and 10 m. These lead to the shallow water parameter, ε, varies between 0.1 and 0.6 (extreme case). The tidal amplitude (A) varies between 1 and 2 m, which leads to the amplitude parameter (α) varies between 0.1 and 0.4. Thus, both ε and α are usually small in real environments.

For perturbation approximation, it is convenient to rewrite the governing equations in dimensionless form. The following non-dimensional and perturbation parameters are used in this study:

$$X = \frac{x}{L} = \frac{\varepsilon x}{D}, \quad Z = \frac{z}{D}, \quad H = \frac{h}{D}, \quad \Phi = \frac{\phi}{D},$$
$$T = \omega t, \quad \varepsilon = \frac{D}{L}, \quad L = \sqrt{\frac{2KD}{n_e \omega}}. \tag{6.7}$$

Hence the governing equation, (6.3), becomes:

$$\Phi_{ZZ} = -\varepsilon^2 \Phi_{XX}. \tag{6.8}$$

and the non-linear boundary condition, (6.4c), leads to

$$2\Phi_T = \Phi_X^2 + \frac{1}{\varepsilon^2}\Phi_Z^2 - \frac{1}{\varepsilon^2}\Phi_Z. \tag{6.9}$$

The boundary condition, (6.1), becomes:

$$H(X_0(T), T) = 1 + \alpha \cos(T) \quad \text{on} \quad X_0(T) = \alpha\varepsilon \cot\beta \cos(T), \tag{6.10}$$

where $\alpha = A/D$.

Since (6.10) represents a boundary condition on a moving boundary, we change variables to put the condition at a fixed point (Li et al., 2000*b*), defining

$$X_1 = X - X_0(T), \text{and } T_1 = T, \tag{6.11}$$

then

$$\frac{\partial f}{\partial T} = \frac{\partial f}{\partial T_1} + \frac{\partial f}{\partial X_1}\frac{\partial X_1}{\partial T_1} = \frac{\partial f}{\partial T_1} + \alpha\varepsilon \cot\beta \sin(T_1)\frac{\partial f}{\partial X_1}. \tag{6.12}$$

where f is a dependent variable such as ϕ and H.

Note that the above concept of moving boundary was first proposed by Li et al. (2000*b*) to overcome the limitation of the previous solution for a sloping beach proposed by Nielsen (1990).

6.3.2 EXPANSION WITH THE SHALLOW WATER PARAMETER (ε)

Following Teo et al. (2003), the potential head (ϕ) and water table level (H) can be expanded in powers of ε:

$$\Phi = \sum_{n=0}^{\infty} \varepsilon^n \Phi_n, \quad \text{and} \quad H = \sum_{n=0}^{\infty} \varepsilon^n H_n. \tag{6.13}$$

The governing equation (6.8) leads to

$$\Phi_0 = C_0(Y,T), \tag{6.14a}$$
$$\Phi_1 = C_1(Y,T), \tag{6.14b}$$
$$\Phi_2 = C_2(Y,T) - \frac{Z^2}{2}\Phi_{0XX}, \tag{6.14c}$$
$$\Phi_3 = C_3(Y,T) - \frac{Z^2}{2}\Phi_{1XX}, \tag{6.14d}$$
$$\Phi_4 = C_4(Y,T) - \frac{Z^2}{2}C_{2XX} + \frac{Z^4}{24}\Phi_{0XXXX}. \tag{6.14e}$$

With boundary condition of (6.4b) in non-dimensional form, $\Phi = H$, we have

$$\Phi_0 = H_0, \quad \Phi_1 = H_1, \quad \Phi_2 = H_2, \quad \Phi_3 = H_3, \quad \Phi_4 = H_4, \tag{6.15}$$

which leads to

$$C_0(X_1,T) = H_0, \tag{6.16a}$$

$$C_1(X_1,T) = H_1, \tag{6.16b}$$

$$C_2(X_1,T) = H_2 + \frac{H^2}{2}\Phi_{0X_1X_1}, \tag{6.16c}$$

$$\begin{aligned} C_{2X_1} &= H_{2X_1} + \frac{1}{2}\left(H^2\Phi_{0X_1X_1}\right)_{X_1} \\ &= H_{2X_1} + \frac{1}{2}(2HH_{X_1}\Phi_{0X_1X_1} + H^2\Phi_{0X_1X_1X_1}), \end{aligned} \tag{6.16d}$$

$$\begin{aligned} C_{2X_1X_1} =& H_{2X_1X_1} + \frac{1}{2}\left(H^2\Phi_{0X_1X_1}\right)_{X_1X_1} \\ =& H_{2X_1X_1} + H_{X_1}^2\Phi_{0X_1X_1} + HH_{X_1X_1}\Phi_{0X_1X_1} + 2HH_{X_1}\Phi_{0X_1X_1X_1} \\ &+ \frac{1}{2}H^2\Phi_{0X_1X_1X_1}. \end{aligned} \tag{6.16e}$$

With the above relations, we have

$$\begin{aligned} (\Phi_{X_1}|_H)^2 &= \left[\Phi_{0X_1} + \varepsilon\Phi_{1X_1} + \varepsilon^2\left(C_{2X_1} - \frac{1}{2}(H^2\Phi_{0X_1X_1})_{X_1}\right)\right]^2 \\ &= \left[H_{0X_1} + \varepsilon H_{1X_1} + \varepsilon^2\left(H_{2X_1} + H_0H_{0X_1}H_{0X_1X_1}\right)\right]^2 \\ &= H_{0X_1}^2 + +2\varepsilon H_{0X_1}H_{1X_1} + \varepsilon^2[H_{1X_1}^2 + 2H_{0X_1} \\ &\quad (H_{2X_1} + H_0H_{0X_1}H_{0X_1X_1})], \end{aligned} \tag{6.17a}$$

$$\begin{aligned}\Phi_Z|_H =& \left\{-\varepsilon^2 Z\Phi_{0X_1X_1} - \varepsilon^3 Z\Phi_{1X_1X_1}\right.\\ &\left.-\varepsilon^4\left(ZC_{2X_1X_1} - \frac{1}{6}H^3\Phi_{0X_1X_1X_1X_1}\right)\right\}\Bigg|_H\\ =&-\varepsilon^2 HH_{0X_1X_1} - \varepsilon^3 HH_{1X_1X_1} - \varepsilon^4\left(HC_{2X_1X_1} - \frac{1}{6}H^3H_{0X_1X_1X_1X_1}\right) \qquad (6.17b)\\ =&-\varepsilon^2 H_0H_{0X_1X_1} - \varepsilon^3(H_1H_{0X_1X_1} + H_0H_{1X_1X_1})\\ &-\varepsilon^4 H_2H_{0X_1X_1} + H_1H_{1X_1X_1} + H_0H_{2X_1X_1} + H_0^2H_{0X_1X_1}^2\\ &+H_{0X_1}^2H_{0X_1X_1}H_0 + 2H_0^2H_{0X_1}H_{0X_1X_1X_1} + \frac{1}{3}H_0^3H_{0X_1X_1X_1X_1},\end{aligned}$$

$$(\Phi_Z|_H)^2 = \varepsilon^4 H_0^2 H_{0X_1X_1}^2, \qquad (6.17c)$$

$$\begin{aligned}\Phi_T|_H =& H_{0T_1} + \varepsilon(H_{1T_1} + \alpha\sin(T_1)\cot(\beta)H_{0X_1})\\ &+\varepsilon^2\left[H_{2T_1} + H_0H_{0T_1}H_{0X_1X_1} + \alpha\sin(T_1)\cot(\beta)H_{1X_1}\right].\end{aligned} \qquad (6.17d)$$

Then, from (6.9), we have the governing equation for each order as

$$O(1) \quad : \quad 2H_{0T_1} = (H_0H_{0X_1})_{X_1}, \qquad (6.18a)$$

$$O(\varepsilon) \quad : \quad 2[H_{1T_1} + \alpha\sin(T_1)\cot(\beta)H_{0X_1}] = (H_0H_1)_{X_1X_1}, \qquad (6.18b)$$

$$\begin{aligned}O(\varepsilon^2) \quad : \quad & 2\left[H_{2T_1} + \alpha\sin(T_1)\cot(\beta)H_{1X_1}\right] = \frac{1}{2}(H_1^2)_{X_1X_1}\\ &+(H_0H_2)_{X_1X_1} + \frac{1}{3}(H_0^3H_{0X_1X_1})_{X_1X_1}, \qquad (6.18c)\end{aligned}$$

It is noted that the above governing equations for each order of ε are non-linear partial differential equations. To solve the groundwater table fluctuation, we need another perturbation process with an additional small parameter to transform the above non-linear equation to a set of linear equations, which will be discussed in Section §6.5.

6.4 PREVIOUS SOLUTIONS

As shown in the last section, each order of governing equations, (6.18), are still in non-linear form. Therefore, another perturbation parameter is required to develop a completed solution. The amplitude parameter, $\alpha = A/D$, has been used for this problem. In general, the ratio of the amplitude of tide-induced groundwater fluctuation to the thickness of aquifer is small. Therefore, this parameter (α) is an appropriate perturbation parameter here.

Most previous studies for tide-induced groundwater table fluctuation in coastal aquifers were based on the zeroth-order shallow water expansion or partially first-order shallow water expansion. For example, Parlange et al. (1984) was based on the zeroth-order shallow water expansion for a vertical beach, while Nielsen (1990) and Li et al. (2000*b*) were partially the zeroth-order and first-order shallow water expansion with different way for a sloping beach. In this section, we outlined these solution and comment on their approaches.

6.4.1 PREVIOUS SOLUTIONS FOR A VERTICAL BEACH

For an aquifer with a vertical beach, Parlange et al. (1984), derived the second-order solution with the amplitude parameter ($\alpha = A/D$). His solution is re-organised in non-dimensional form here:

$$H_{Parlange} = 1+\alpha e^{-X}\cos(T-X)+\alpha^2\left\{\frac{1}{4}(1-e^{-2X})\right. \\ \left.+\frac{1}{2}\left[e^{-\sqrt{2}X}\cos(2T-\sqrt{2}X)-e^{-2X}\cos(2(T-X)\right]\right\}. \tag{6.19}$$

Note that the above solution is the zeroth-order shallow water expansion with the second-order approximation with the amplitude parameter (α), as presented in Section §6.5. furthermore, (6.19) is only for a vertical beach.

Based on the first-order approximation with O(α), Trefry (1999) considered a composite aquifer, which have multiple horizontal layer aquifers with different hydraulic conductivity. In his study, three different boundary conditions and the corresponding solutions were presented. They are: Dirichlet (prescribed head), Neumann (prescribed flux) and Cauchy (mixed) conditions. Note that only Dirichlet (prescribed head) boundary condition is considered in this chapter.

6.4.2 PREVIOUS SOLUTIONS FOR A SLOPING BEACH

Nielsen (1990) presented the first analytical investigation where the assumption of a fixed location of the shoreline boundary condition is relaxed. His solution is re-organised in non-dimensional form here:

$$H_{Nielsen} = 1+\alpha e^{-X}\cos(T-X)+\alpha\varepsilon_N[\frac{1}{2}+\frac{\sqrt{2}}{2}e^{-\sqrt{2}X}\cos(2T-\sqrt{2}X+\frac{\pi}{4})], \tag{6.20}$$

where $\varepsilon_N = \alpha\varepsilon\cot(\beta)$ is a perturbation parameter for a sloping beach.

Using the same perturbation parameter, ε_N, Li et al. (2000*b*) applied the concept of a moving boundary to Nielsen's approach (Nielsen, 1990). Their solution is re-organised in non-dimensional form as:

$$H_{Li} = 1+\alpha e^{-X}\cos(T-X)+\frac{1}{\sqrt{2}}\alpha\varepsilon_N[\frac{1}{\sqrt{2}}-e^{-X_1}\cos\left(X_1-\frac{1}{4}\pi\right) \\ +e^{-\sqrt{2}X_1}\cos(2T-\sqrt{2}X_1+\frac{1}{4}\pi)-e^{-X_1}\cos(2T-X_1+\frac{1}{4}\pi)]. \tag{6.21}$$

Note that this solution is in terms of $X_1(X,T)$.

We first comment on some shortcomings in the previous solutions (Nielsen, 1990; Li et al., 2000*b*).

(1) *The perturbation parameter (ε_N)*: Nielsen (1990) includes the slope of the beach (β) in the perturbation parameter, limiting the range of applicability of the solution. As ε_N is a perturbation parameter, assumed to be small compared with unity, the slope of the beach (β) is restricted by $\tan^{-1}(\alpha\varepsilon) \approx \alpha\varepsilon << \beta \leq \pi/2$. For example when $\alpha\varepsilon = 0.05$, $15^o < \beta \leq 90^o$, while for $\alpha\varepsilon = 0.2$, $25^o < \beta \leq 90^o$.

(2) *Incomplete solution for higher-order components*: It is observed that Nielsen's solution is only part of the present solution up to $O(\varepsilon\alpha^2)$ and Li's solution contains terms of $O(\alpha)$ and $O(\varepsilon\alpha^2)$. Their solutions do not include the higher-order term, $O(\alpha^2)$. This is because their models were based on the Boussinesq equation.

(3) *Incomplete solution for $\beta = 90^o$*. When $\beta = 90^o$, $\varepsilon_N = 0$ and both Nielsen (1990)'s and Li et al. (2000*b*)'s solutions reduce to the simple linear solution and contain no higher-order terms.

(4) *Boundary condition at $X_1 = 0$* (i.e., $X = X_0$). It is clear that Nielsen's solution, i.e., (6.20) (Nielsen, 1990) does not satisfy (6.10). In fact, Nielsen (1990)'s solution will only satisfy the boundary condition when all terms of the perturbation expansion are included. This has been overcome by Li et al. (2000*b*).

6.5 SECOND-ORDER SHALLOW WATER EXPANSION

The major shortcoming of Nielsen (1990) and Li et al. (2000*b*) arises from the use of $\varepsilon_N = \alpha\varepsilon\cot(\beta)$ as a perturbation parameter. In fact, it is unnecessary to include the slope of the beach in the perturbation parameter, and as $\cot(\beta)$ becomes large for small β, ε_N may become $O(1)$. Here only the perturbation parameters ε and α, which are always small compared to unity, are used in the formulation of the sloping beach problem, avoiding the shortcomings of the previous solutions (Nielsen, 1990; Li et al., 2000*b*).

6.5.1 ZEROTH-ORDER APPROXIMATION

Boundary value problem

Based on Section §6.3, we have the governing equation for the zeroth-order approximation as,

$$2H_{0T_1} = \left(H_0 H_{0X_1}\right)_{X_1}. \tag{6.22}$$

It is noted that (6.22) is a non-linear partial differential equation. Here, we need another small perturbation parameter to further transform the non-linear differential equation to a set of linear differential equations. The ratio of amplitude of

groundwater fluctuations (A) to the thickness of aquifer (D) is normally less than one, which has been used as the perturbation parameter in the previous studies (Parlange et al., 1984). Now, we introduce

$$H_0 = 1 + \alpha H_{01} + \alpha^2 H_{02} + O(\alpha^3). \tag{6.23}$$

Then, we have the governing equation, (6.22), sorting out as

$$O(\alpha): \quad 2H_{01T_1} = H_{01X_1X_1}, \tag{6.24a}$$

$$O(\alpha^2): \quad 2H_{02T_1} = H_{02X_1X_1} + \left(H_{01}H_{01X_1}\right)_{X_1}. \tag{6.24b}$$

Solution of O(α)

The boundary value problem for O(α) is

$$\begin{aligned} 2H_{01T_1} &= H_{01X_1X_1}, && (6.25a)\\ H_{01}(0,T_1) &= \cos(T_1), && (6.25b)\\ H_{01X_1}(\infty,T_1) &= 0. && (6.25c) \end{aligned}$$

The solution of (6.25a)–(6.25c) is

$$H_{01}(X_1,T_1) = \exp(-X_1)\cos(T_1 - X_1). \tag{6.26}$$

Solution of O(α^2)

The boundary value problem for O(α^2) is

$$\begin{aligned} 2H_{02T_1} &= H_{02X_1X_1} + \left(H_{01}H_{01X_1}\right)_{X_1}, && (6.27a)\\ H_{02}(0,T_1) &= 0, && (6.27b)\\ H_{02X_1}(\infty,T_1) &= 0. && (6.27c) \end{aligned}$$

Now, check right-hand-side of (6.27a) term by term:

$$\begin{aligned} \left(H_{01}H_{01X_1}\right)_{X_1} &= \frac{1}{2}\left(H_{01}^2\right)_{X_1X_1}\\ &= \frac{1}{4}\left(e^{-2X_1}\right)_{X_1X_1} + \frac{1}{4}\left[e^{-2X_1}\cos 2(T_1 - X_1)\right]_{X_1X_1}\\ &= \exp(-2X_1) - 2\exp(-2X_1)\sin 2(T_1 - X_1). \end{aligned} \tag{6.28}$$

Thus, we have

$$2H_{02T_1} - H_{02X_1X_1} = \exp(-2X_1) - 2\exp(-X_1)\sin 2(T_1 - X_1). \tag{6.29}$$

For the time-independent term on the RHS of (6.29), we have the solution in the form as

$$H_{02a} = -\frac{1}{4}\exp(-2X_1) + C_1X_1 + C_2. \tag{6.30}$$

To satisfy the boundary condition, (6.27c), $C_1 = 0$. In addition, to satisfy the boundary condition, (6.27b), $C_2 = 1/4$.

For the time-depending term, the homogeneous solution of (6.29) is

$$H_{02hom} = \left[A\exp(-\sqrt{2}X_1) + B\exp(\sqrt{2}X_1)\right]\ \cos(2T_1 - \sqrt{2}X_1), \tag{6.31}$$

with the boundary condition, (6.27c), $B = 0$. Then, we have the homogeneous solution as

$$H_{02hom} = A\exp(-\sqrt{2}X_1)\ \cos(2T_1 - \sqrt{2}X_1). \tag{6.32}$$

Now, we have the particular solution as,

$$H_{02par} = -\frac{1}{2}\exp(-2X_1)\cos 2(T_1 - X_1). \tag{6.33}$$

To satisfy the boundary condition, (6.27b), $A = 1/2$.

Then, the solution of $O(\alpha^2)$ can be written as

$$\begin{aligned} H_{02} =& \frac{1}{4}\left(1 - e^{-2X_1}\right) \\ &+ \frac{1}{2}\left[e^{-\sqrt{2}X_1}\cos(2T_1 - \sqrt{2}X_1) - ^{-2X_1}\cos 2(T_1 - X_1)\right]. \end{aligned} \tag{6.34}$$

6.5.2 FIRST-ORDER APPROXIMATION

Boundary value problem

Based on Section §6.3, the governing equation for the first-order approximation is,

$$2[H_{1T_1} + \alpha\sin(T_1)\cot(\beta)H_{0X_1}] = (H_o H_1)_{X_1X_1}, \tag{6.35}$$

Now, we introduce

$$H_1 = \alpha H_{11} + \alpha^2 H_{12} + O(\alpha^3). \tag{6.36}$$

Then, we have the governing equations sorting out as

$$O(\varepsilon\alpha): \quad 2H_{11T_1} = H_{11X_1X_1}, \tag{6.37a}$$

$$O(\varepsilon\alpha^2): \quad 2H_{12T_1} + 2\sin(T_1)\cot(\beta)H_{01X_1} = H_{12X_1X_1} + (H_{01}H_{11})_{X_1X_1}. \tag{6.37b}$$

Solution of O($\varepsilon\alpha$)

The boundary value problem for O($\varepsilon\alpha$) is

$$2H_{11T_1} = H_{11X_1X_1}, \tag{6.38a}$$

$$H_{11}(0, T_1) = 0, \tag{6.38b}$$

$$H_{11X_1}(\infty, T_1) = 0. \tag{6.38c}$$

The solution of the above equations, (6.38a)–(6.38c), is

$$H_{11}(X_1, T_1) = 0. \tag{6.39}$$

Solution of O($\varepsilon\alpha^2$)

The boundary value problem for O($\varepsilon\alpha^2$) is

$$\begin{aligned} 2H_{12T_1} + 2\sin(T_1)\cot(\beta)H_{01X_1} &= H_{12X_1X_1}, && \text{(6.40a)} \\ H_{12}(0,T_1) &= 0, && \text{(6.40b)} \\ H_{12X_1}(\infty,T_1) &= 0. && \text{(6.40c)} \end{aligned}$$

Here, the second term of left-hand-side of (6.40a) can be further simplified as

$$\begin{aligned} 2\sin(T_1)\cot(\beta)H_{01X_1} =& 2\sin(T_1)\cot(\beta)[\sin(T_1-X_1)-\cos(T_1-X_1)]e^{-X_1} \\ =& \cot(\beta)[-\sin(2T_1-X_1)-\sin(X_1) \\ & -\cos(2T_1-X_1)+\cos(X_1)]e^{-X_1} \\ =& \sqrt{2}\cot(\beta)e^{-X_1}[\cos(X_1+\frac{\pi}{4})-\cos(2T_1-X_1-\frac{\pi}{4})], \end{aligned} \tag{6.41}$$

Thus, we have

$$2H_{12T_1} - H_{12X_1X_1} = -\sqrt{2}\cot(\beta)e^{-X_1}\left[\cos(X_1+\frac{\pi}{4})-\cos(2T_1-X_1-\frac{\pi}{4})\right], \tag{6.42}$$

For the non-oscillating term in the time domain, we have

$$H_{12P1} = \frac{1}{\sqrt{2}}\cot(\beta)[\frac{1}{\sqrt{2}} - \exp(-X_1)\cos\left(X_1-\frac{1}{4}\pi\right)].$$

For the oscillating term in time domain, we have

$$\begin{aligned} H_{12H} &= C\exp(-\sqrt{2}(1+i)X_1)\exp(2iT_1), \\ H_{12P2} &= -\frac{\sqrt{2}}{2}\cot(\beta)\exp(-(1+i)X_1)\exp(2iT_1+\frac{\pi i}{4}). \end{aligned}$$

Then, we have

$$C = \frac{\sqrt{2}}{2}\cot(\beta)\exp(\frac{\pi i}{4}).$$

The solution of $O(\varepsilon\alpha^2)$ is

$$\begin{aligned} H_{12} =& \frac{1}{\sqrt{2}}\cot(\beta)\left[\frac{1}{\sqrt{2}} - e^{-X_1}\cos\left(X_1-\frac{\pi}{4}\right)\right] \\ &+ \frac{1}{\sqrt{2}}\cot(\beta)\left[e^{-\sqrt{2}X_1}\cos(2T_1-\sqrt{2}X_1+\frac{\pi}{4})\right. \\ & \left. -e^{-X_1}\cos(2T_1-X_1+\frac{\pi}{4})\right]. \end{aligned} \tag{6.43}$$

6.5.3 SECOND-ORDER APPROXIMATION

Perturbation approximation

Based on Section §6.3, the governing equation for the second-order problem is given by

$$\begin{aligned} 2\left[H_{2T_1}+\alpha\sin(T_1)\cot(\beta)H_{1X_1}\right] =& \frac{1}{2}\left(H_1^2\right)_{X_1X_1}+\left(H_0H_2\right)_{X_1X_1} \\ &+\frac{1}{3}\left(H_0^3H_{0X_1X_1}\right)_{X_1X_1}, \end{aligned} \tag{6.44}$$

with

$$H_o=1+\sum_{n=1}^{\infty}\alpha^nH_{0n}, \quad \text{and} \quad H_m=\sum_{n=1}^{\infty}\alpha^nH_{mn}, \quad m\geq 2. \tag{6.45}$$

Then, (6.44) can be sorted out as

$$\begin{aligned} H_1^2 &= \alpha^2H_{11}^2+O(\alpha^3)+\ldots=0, \\ H_0H_2 &= \alpha H_{21}+\alpha^2\left(H_{01}H_{21}+H_{22}\right)+\ldots, \\ H_0^3H_{0X_1X_1} &= \alpha H_{01X_1X_1}+\alpha^2\left(3H_{01}H_{01X_1X_1}+H_{02X_1X_1}\right)+\ldots. \end{aligned}$$

The second-order governing equation becomes

$$O(\varepsilon^2\alpha): \quad 2H_{21T_1}=H_{21X_1X_1}+\frac{1}{3}H_{01X_1X_1X_1X_1}, \tag{6.46a}$$

$$\begin{aligned} O(\varepsilon^2\alpha^2): \quad 2H_{22T_1} =& H_{22X_1X_1}+\left(H_{01}H_{21}\right)_{X_1X_1} \\ &+\left(H_{01}H_{01X_1X_1}+\frac{1}{3}H_{02X_1X_1}\right)_{X_1X_1}. \end{aligned} \tag{6.46b}$$

Solution of O($\varepsilon^2\alpha$)

The boundary value problem of $O(\varepsilon^2\alpha)$ is

$$2H_{21T_1}=H_{21X_1X_1}+\frac{1}{3}H_{01X_1X_1X_1X_1}, \tag{6.47a}$$

$$H_{21}(0,T_1)=0, \tag{6.47b}$$

$$H_{21X_1}(\infty,T_1)=0, \tag{6.47c}$$

which is similar to the case of vertical beach. Thus, we have

$$H_{21}=-\frac{\sqrt{2}}{3}X_1\exp(-X_1)\cos(T_1-X_1-\frac{\pi}{4}). \tag{6.48}$$

Solution of $O(\varepsilon^2\alpha^2)$

The boundary value problem of $O(\varepsilon^2\alpha^2)$ is

$$2H_{22T_1} = H_{22X_1X_1} + (HH_{21})_{X_1X_1} + \left(H_{01}H_{01X_1X_1} + \frac{1}{3}H_{02X_1X_1}\right)_{X_1X_1}, \tag{6.49a}$$

$$H_{21}(0,T_1) = 0, \tag{6.49b}$$

$$H_{21X_1}(\infty,T_1) = 0. \tag{6.49c}$$

Following the same procedure as other orders, we have

$$\begin{aligned} H_{22} = &-\frac{1}{3} + \frac{1}{6}(2+X_1)\exp(-2X_1) \\ &- \frac{2}{3}X_1 e^{-\sqrt{2}X_1}\cos(2T_1 - \sqrt{2}X_1 - \frac{\pi}{4}) + \frac{1}{3}e^{-\sqrt{2}X_1}\sin(2T_1 - \sqrt{2}X_1) \\ &+ \frac{\sqrt{2}}{3}X_1 e^{-2X_1}\cos(2T_1 - 2X_1 - \frac{\pi}{4}) - \frac{1}{3}e^{-2X_1}\sin(2T_1 - 2X_1). \end{aligned} \tag{6.50}$$

6.5.4 SPECIAL CASE: A VERTICAL BEACH

In summary, the solution of tide-induced water table fluctuations in a sloping beach can be written as

$$\begin{aligned} H = &1 + \alpha e^{-X_1}\cos(\theta_1) \\ &+ \alpha^2[\frac{1}{4}(1-e^{-2X_1}) + \frac{1}{2}e^{-\sqrt{2}X_1}\cos(\theta_2) - \frac{1}{2}e^{-2X_1}\cos(2\theta_1)] \\ &+ \frac{1}{\sqrt{2}}\cot(\beta)\varepsilon\alpha^2[\frac{1}{\sqrt{2}} - e^{-X_1}\cos(X_1 - \frac{1}{4}\pi) \\ &+ e^{-\sqrt{2}X_1}\cos(\theta_2 + \frac{1}{4}\pi) - e^{-X_1}\cos(\theta_3 + \frac{1}{4}\pi)] \\ &- \frac{\sqrt{2}}{3}\varepsilon^2\alpha X_1 e^{-X_1}\cos(\theta_1 - \frac{\pi}{4}) \\ &+ \frac{1}{3}\varepsilon^2\alpha^2\{-1 + (1+\frac{X_1}{2})e^{-2X_1} - 2X_1 e^{-\sqrt{2}X_1}\cos(\theta_2 - \frac{\pi}{4}) \\ &+ e^{-\sqrt{2}X_1}\sin(\theta_2) + \sqrt{2}X_1 e^{-2X_1}\cos(2\theta_1 - \frac{\pi}{4}) - e^{-2X_1}\sin(2\theta_1)\}, \end{aligned} \tag{6.51}$$

where

$$\theta_1 = T_1 - X_1,\ \theta_2 = 2T_1 - \sqrt{2}X_1, \text{ and } \theta_3 = 2T_1 - X_1.$$

For the special case of a vertical beach, $\beta = 90^o$, when $X_1 = X$, $T_1 = T$ and

$\cot\beta = 0$, then, (6.51) becomes

$$\begin{aligned} H =& 1 + \alpha e^{-X}\cos(\theta_1) + \alpha^2\Big\{\frac{1}{4}(1-e^{-2X}) \\ &+ \frac{1}{2}[e^{-\sqrt{2}X}\cos(\theta_2) - e^{-2X}\cos(2\theta_1)]\Big\} \\ &- \frac{\sqrt{2}}{3}\varepsilon^2\alpha X e^{-X}\cos(\theta_1 - \frac{\pi}{4}) \\ &+ \frac{1}{3}\varepsilon^2\alpha^2\Big\{-1 + (1+\frac{X}{2})e^{-2X} - 2Xe^{-\sqrt{2}X}\cos(\theta_2 - \frac{\pi}{4}) \\ &+ e^{-\sqrt{2}X}\sin(\theta_2) + \sqrt{2}Xe^{-2X}\cos(2\theta_1 - \frac{\pi}{4}) - e^{-2X}\sin(2\theta_1)\Big\}. \end{aligned} \tag{6.52}$$

Note that (6.52) to the solution of $O(\alpha^2)$ for a vertical beach is identical to Parlange et al. (1984), while the solution of $O(\varepsilon^2\alpha^2)$ is a new higher-order approximation.

6.5.5 COMPARISONS WITH PREVIOUS SOLUTIONS

To investigate the difference between the previous solutions (Nielsen, 1990; Li et al., 2000*b*) and the present solution, graphs of water table fluctuations for various beach slopes are illustrated in Figure 6.2. In general, the results of Nielsen (1990) and Li et al. (2000*b*) lie between the linear solution (α) and the second-order solution ($\varepsilon\alpha^2$). This is because the previous solutions only contain part of the higher-order components. As shown in the figure, Nielsen's solution (Nielsen, 1990) does not match the boundary condition at $X = X_0(t)$ with $\beta = 10^o$ and 15^o, while both Li et al. (2000*b*) and the present solutions satisfy the boundary condition. Significant differences between the previous solutions (Nielsen, 1990; Li et al., 2000*b*) and the present solution are observed in Figure 6.2, especially for smaller beach slopes. This results from the use of the inappropriate perturbation parameter used in the previous models.

Figure 6.2 also indicates a major difference of the over-height between the previous solutions (Nielsen, 1990; Li et al., 2000*b*) and the present solution. Comparing (6.20), (6.21) and (6.51), it is clear that both previous solutions excluded the non-oscillating terms in the $O(\alpha^2)$ components, such as $\frac{1}{4}(1-e^{-X_1})$. It is also observed that Nielsen's solution (Nielsen, 1990) and Li's solution (Li et al., 2000*b*) are identical to the linear solution of $O(\alpha)$ for a vertical beach (i.e., $\beta = 90^o$). This is because the governing equation used in their models was only the zeroth-order governing equation, $O(1)$.

To further investigate the difference between Li et al. (2000*b*) and the present solutions, i.e. (6.21) and (6.51), the water table level (H) versus the horizontal inland distance (X) for different time intervals are plotted in Figure 6.3. The figure shows that the maximum difference between the two solutions occurs at $T = 2n\pi$ ($n = 0, 1, 2...$).

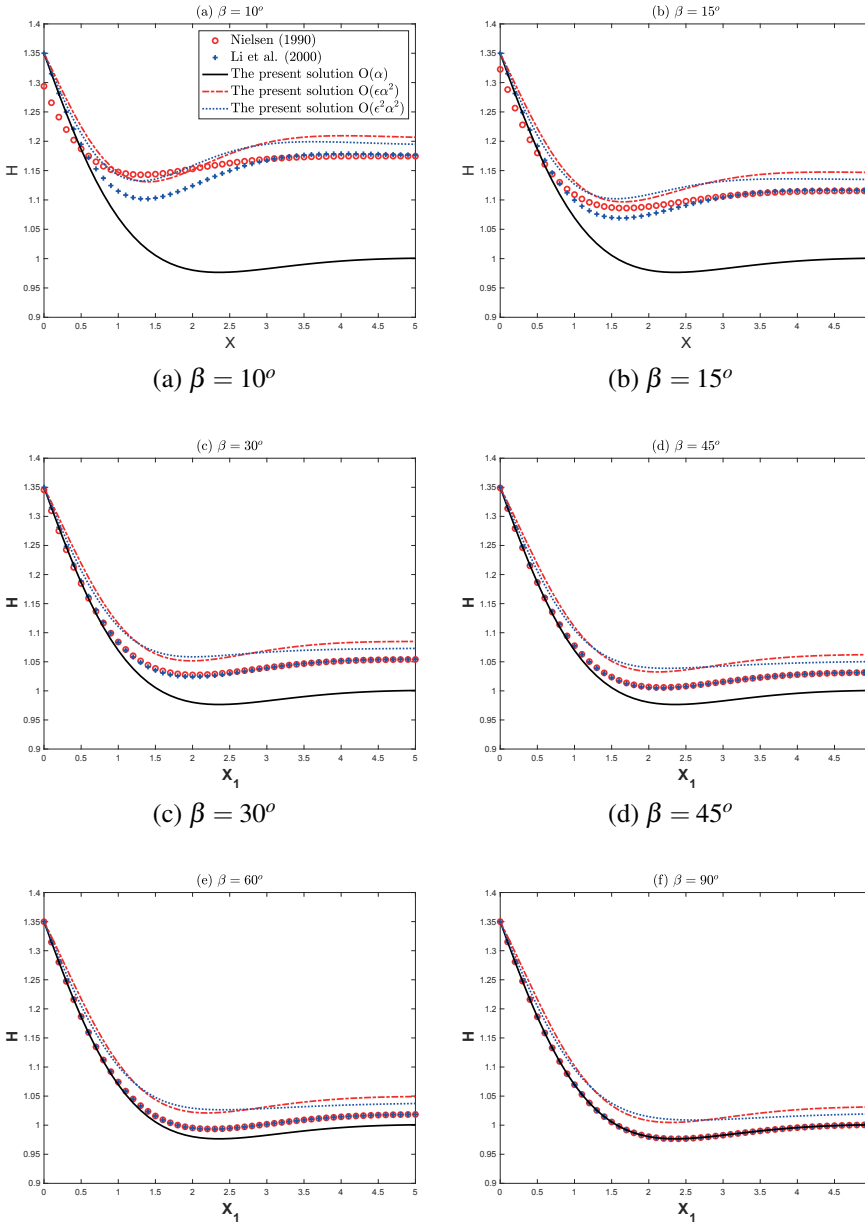

Figure 6.2 Comparisons of tide-induced water table fluctuations in a sloping beach ($\varepsilon = 0.5$, $\alpha = 0.35$, $T = 0$). '◇' for (Nielsen, 1990), '-○-' for Li et al. (2000*b*), '—' for the present solution $O(\varepsilon^2\alpha^2)$, '- -' for $O(\varepsilon\alpha^2)$ and '$\cdots$' for $O(\alpha)$.

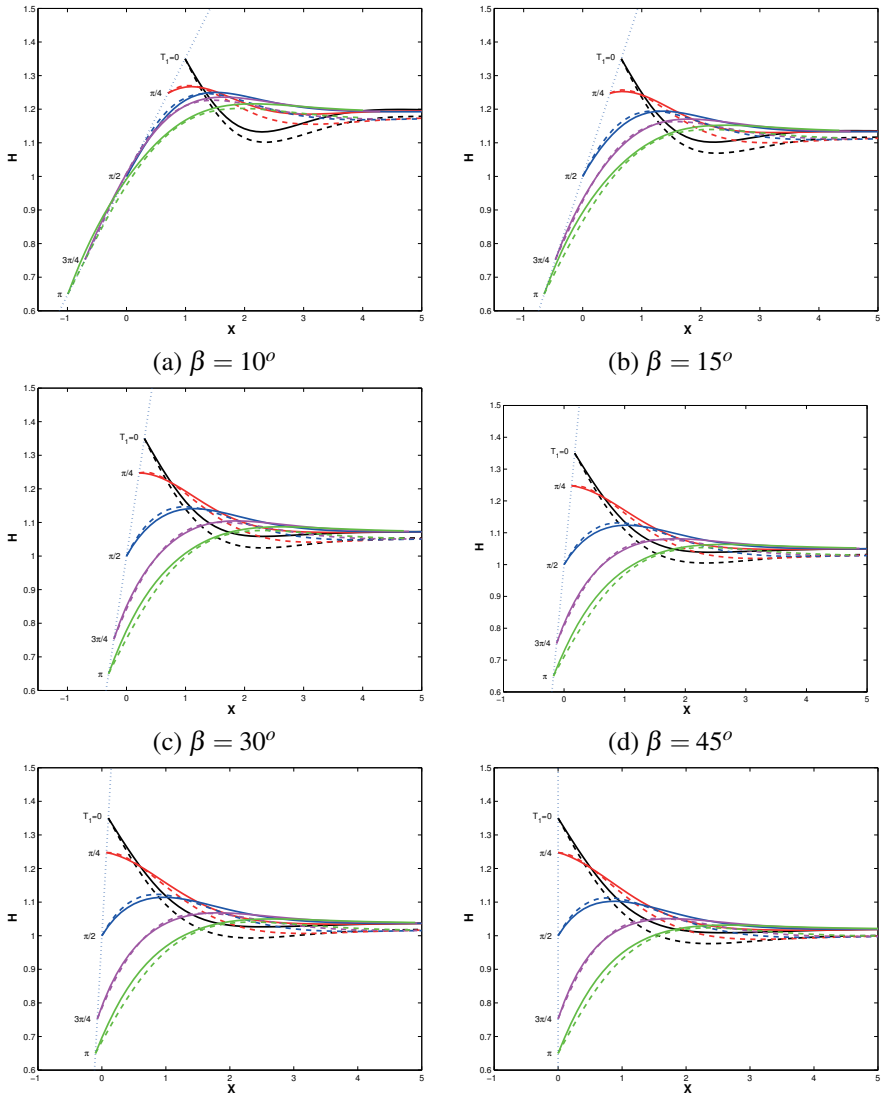

(a) $\beta = 10^o$ (b) $\beta = 15^o$

(c) $\beta = 30^o$ (d) $\beta = 45^o$

(e) $\beta = 60^o$ (f) $\beta = 90^o$

Figure 6.3 Comparisons of tide-induced water table fluctuations in a sloping beach ($\varepsilon = 0.5$, $\alpha = 0.35$, $T = 0$). '- -' for Li et al. (2000*b*), and '—' for the present solution $O(\varepsilon^2\alpha^2)$.

6.5.6 EFFECTS OF THE SECOND-ORDER COMPONENT

Since the higher-order solution in (6.51) is new, it is necessary to examine the effects of the higher-order components on the water table fluctuations at a sloping beach. The distribution of water table level (H) versus time $(T/2\pi)$ for various order solutions are illustrated in Figure 6.4. In the figure the results of Li's solution (Li et al., 2000*b*) are included for comparison. It is observed that the results of Li et al. (2000*b*) are close to the zeroth-order solution (α), except for the case of $\alpha = 0.4$ and $\varepsilon = 0.5$. Significant difference between the zeroth-order (α) and higher-order solutions $(\varepsilon^2\alpha^2)$ are observed for larger values of α and ε.

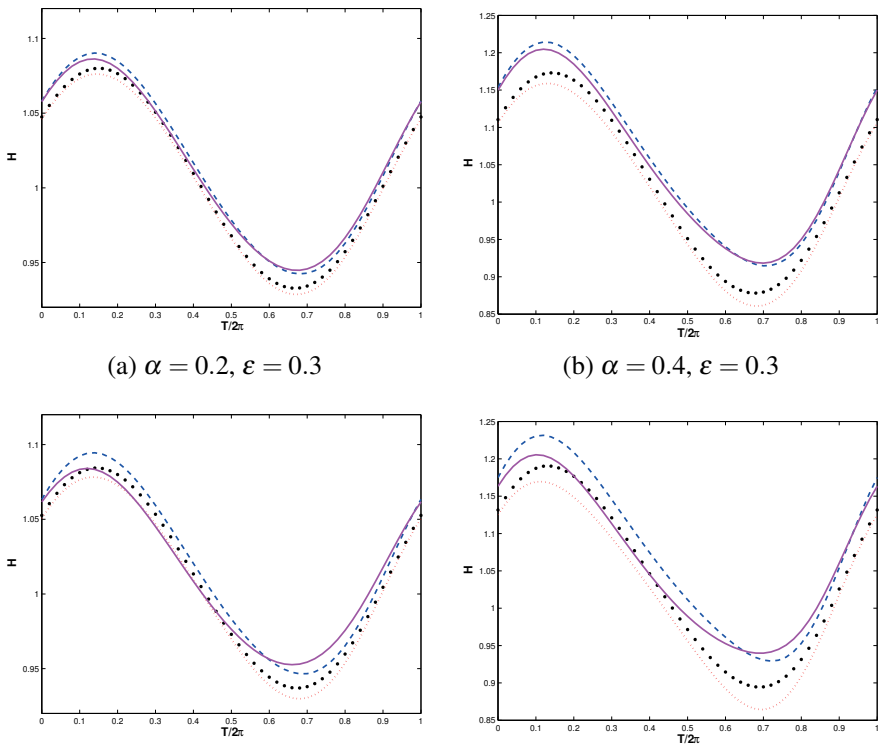

(a) $\alpha = 0.2, \varepsilon = 0.3$ (b) $\alpha = 0.4, \varepsilon = 0.3$

(c) $\alpha = 0.2, \varepsilon = 0.5$ (d) $\alpha = 0.4, \varepsilon = 0.5$

Figure 6.4 Distribution of water table level (H) versus time $(T/2\pi)$ in a sloping beach ($\beta = 45^o$, $X = 1$). '$\circ$' for Li et al. (2000*b*), '—' for the present solution $O(\varepsilon^2\alpha^2)$, '- -' for $O(\varepsilon\alpha^2)$ and '$\cdots$' for $O(\alpha^2)$.

To further examine the effects of the higher-order components, the distribution of water table level versus horizontal inland distance is plotted in Figure 6.5. A significant difference between $O(\alpha)$ and $(\varepsilon^2\alpha^2)$ is observed for the case $\alpha = 0.4$

and $\varepsilon = 0.5$. This difference of over-height comes from the non-oscillating terms in (6.51).

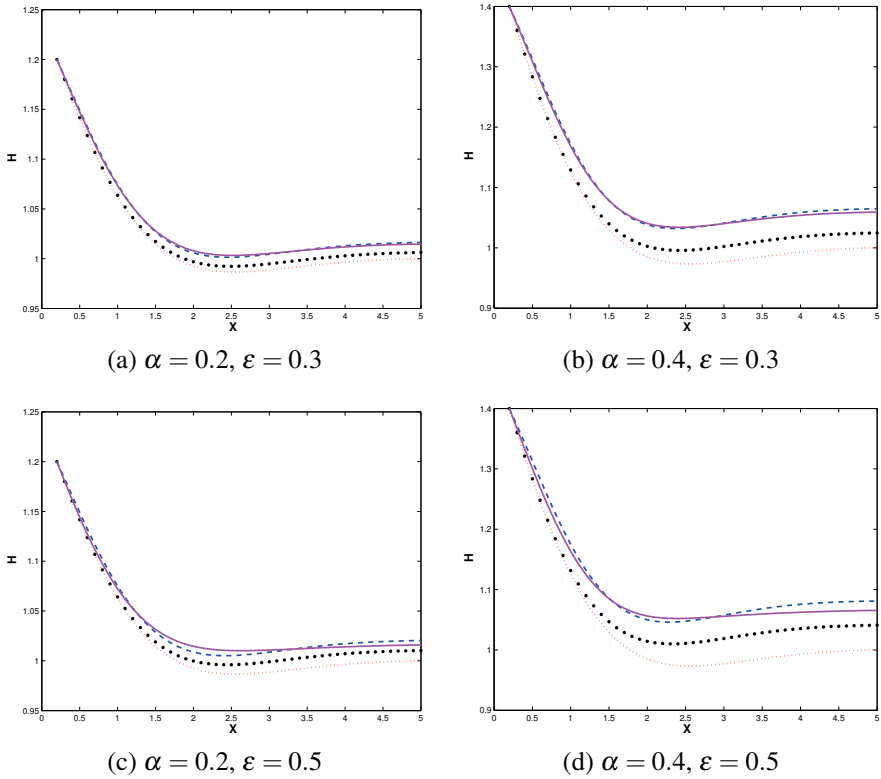

(a) $\alpha = 0.2, \varepsilon = 0.3$ (b) $\alpha = 0.4, \varepsilon = 0.3$

(c) $\alpha = 0.2, \varepsilon = 0.5$ (d) $\alpha = 0.4, \varepsilon = 0.5$

Figure 6.5 Distribution of water table level (H) versus horizontal distance (X) in a sloping beach ($\beta = 45^o$, $T = 0$). '$\circ$' for Li et al. (2000*b*), '—' for the present solution $O(\varepsilon^2\alpha^2)$, '- -' for $O(\varepsilon\alpha^2)$ and '$\cdots$' for $O(\alpha^2)$.

6.5.7 EFFECTS OF BEACH SLOPES (β)

Figure 6.2 indicates some effects of beach slope (β) on the water table fluctuations at a sloping beach. To further examine the influence of the beach slope, we plot the distribution of water table level for various beach slopes in Figure 6.6. As shown in the figure, the beach slope (β) significantly affects the water table fluctuations; in general, H increases as β decreases. This influence arises from the component of $O(\varepsilon\alpha^2)$ since a factor of $\cot(\beta)$ appears in this term.

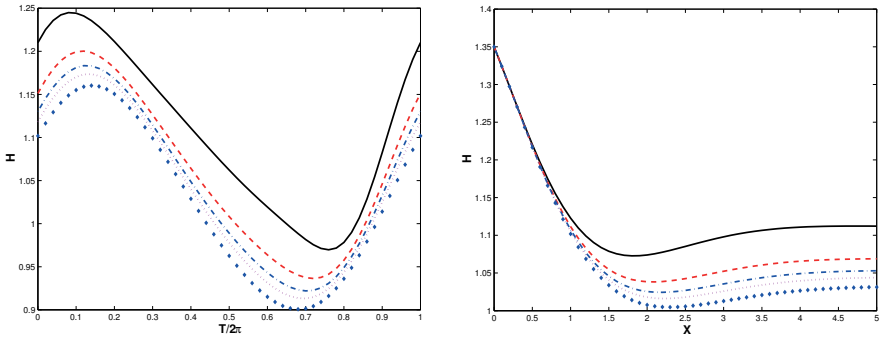

(a) H versus $T/2\pi$ ($X = 1$) (b) H versus X ($T = 0$)

Figure 6.6 Effect of slope (β) on the tide-induced water table fluctuations in a sloping beach. ($\alpha = \varepsilon = 0.35$). '—' for $\beta = 15^o$, '- -' $\beta = 30^o$, '- .' for $\beta = 45^o$, '$\cdots$' $\beta = 60^o$ and '$\Diamond$' for $\beta = 90^o$.

6.6 HIGHER-ORDER SHALLOW WATER EXPANSION

The objective of this section is to develop an effective algorithm for the generation of higher-order solutions for the tide-induced groundwater fluctuations in coastal aquifers, based on the model and methods used by Teo et al. (2003), which was outlined in previous sections. The work was first published in Stojsavljevic et al. (2012).

6.6.1 GENERAL FORMS OF BOUNDARY VALUE PROBLEMS FOR ZEROTH AND FIRST-ORDER PROBLEM

Based on the analytical solution of Teo et al. (2003), we have the zeroth-order boundary value problem as

$$O(\alpha) : 2H_{01T_1} - H_{01X_1X_1} = 0, \tag{6.53a}$$

$$O(\alpha^2) : 2H_{02T_1} - H_{02X_1X_1} = \frac{1}{2}\left(H_{01}^2\right)_{X_1X_1}, \tag{6.53b}$$

$$O(\alpha^3) : 2H_{03T_1} - H_{03X_1X_1} = (H_{01}H_{02})_{X_1X_1}, \tag{6.53c}$$

$$\vdots \qquad\qquad \vdots \qquad\qquad \vdots$$

$$O(\alpha^n) : 2H_{0nT_1} - H_{0nX_1X_1} = \frac{1}{2}\sum_{a=1}^{n-1}\left(H_{0a}H_{0(n-a)}\right)_{X_1X_1}, \tag{6.53d}$$

with the following adapted boundary conditions,

$$O(\alpha) : H_{01} = \cos(T_1) \text{ at } X_1 = 0, \tag{6.54a}$$

$$H_{01X_1} = 0 \text{ as } x \to \infty, \tag{6.54b}$$

$$O(\alpha^n) : H_{0n} = 0 \text{ at } X_1 = 0, \tag{6.55a}$$
$$H_{0nX_1} = 0 \text{ as } x \to \infty, \tag{6.55b}$$

where $n > 1$.

By again introducing a perturbation around α, we arrive at the following equations for $O(\varepsilon\alpha^n)$,

$$O(\varepsilon\alpha) : 2H_{11T_1} - H_{11X_1X_1} = 0, \tag{6.56a}$$
$$O(\varepsilon\alpha^2) : 2H_{12T_1} - H_{12X_1X_1} = (H_{01}H_{11})_{X_1X_1} - 2\sin(T_1)\cot(\beta)H_{01X_1}, \tag{6.56b}$$
$$O(\varepsilon\alpha^3) : 2H_{13T_1} - H_{13X_1X_1} = (H_{01}H_{12})_{X_1X_1} + (H_{02}H_{11})_{X_1X_1} - 2\sin(T_1)\cot(\beta)H_{02X_1}, \tag{6.56c}$$
$$\vdots \qquad \vdots \qquad \vdots$$
$$O(\varepsilon\alpha^n) : 2H_{1nT_1} - H_{1nX_1X_1} = \sum_{a=1}^{n-1} \left(H_{0a}H_{1(n-a)}\right)_{X_1X_1} - 2\sin(T_1)\cot(\beta)H_{0(n-1)X}. \tag{6.56d}$$

The boundary conditions for these equations are as follows

$$O(\varepsilon\alpha^n) : H_{1n} = 0 \text{ at } X_1 = 0, \tag{6.57a}$$
$$H_{1nX_1} = 0 \text{ as } x \to \infty, \tag{6.57b}$$

for $n \geq 1$.

6.6.2 SEMI-ANALYTICAL APPROACHES

Whilst the benefits of higher order solutions will be shown in the next section, the calculation of these solutions can become very time consuming. To aid in the computation, an algorithm has been developed and implemented using Fortran to compute a semi-analytical solution.

To solve the general form equations (6.53d) and (6.56d), we shall first assume the solution is in the form, based on the previous solutions (Stojsavljevic et al., 2012)

$$H_{in} = \sum_{m=0}^{b} X_1^m \exp(cX_1)\Big\{a_{1m}\cos\left(dT + eX_1\right) + a_{2m}\sin\left(dT + eX_1\right)\Big\}, \tag{6.58}$$

where i denotes the order of shallow water parameter (ε) and n denotes the order of the amplitude parameter (α).

This set form of the solution allows us to compute only the coefficients $a_{1m}, a_{2m}, b, c, d, e$. In addition, the functions within equation (6.58) are easily

differentiable and multipliable and the resulting equation(s) after these operations have been applied can easily be manipulated back into the same form. The right-hand-side of equations (6.53d) and (6.56d) are the source terms of the inhomogeneous diffusion equation. This source term is a function of lower order solutions that have been previously computed. If we have k number of source terms in the form (6.58), we can express the general form (6.53d) for $O(\varepsilon^0\alpha^n)$ as

$$2H_{0nT_1} - H_{0nX_1X_1} = \sum_{i=1}^{k} f_i, \tag{6.59}$$

where f_i is a term in the form (6.58). Using the principle of superposition, we can further simplify this to having k equations to solve.

$$2H_{0niT_1} - H_{0niX_1X_1} = f_i, \tag{6.60}$$

where

$$H_{0n} = \sum_{i=1}^{k} H_{0ni}. \tag{6.61}$$

By substituting H_{0n} on the left-hand-side of equation (6.60) with equation (6.58), all that is required is to differentiate the resulting equation once with respect to T_1 and twice with respect to X_1. It is then a matter of calculating the coefficients $a_{1m}, a_{2m}, b, c, d, e$ and then solving to fit the boundary conditions. This method has been verified by comparing the computed coefficients with the solutions derived by Teo et al. (2003). The coefficients of the solutions up to $O(\varepsilon\alpha^4)$ are given in the appendix (§6.8). The solution for for $O(\varepsilon)$ is obtained by using the same method.

6.6.3 COMPARISONS WITH THE SECOND-ORDER APPROXIMATION

The algorithm briefly presented in Section 6.6.2 can in principal obtain the coefficients of higher-order analytical solutions up to an arbitrary order. However, there is a computational limit. Using a workstation with a 3 GHz processor and 48GB RAM, we were able to compute solutions up to 20th order. Herein, we shall mainly concentrate on the solution of $O(\varepsilon\alpha^8)$ as we are able to show the differences between previously derived lower order solutions and with Teo et al. (2003) solution of $O(\varepsilon^2\alpha^2)$.

Bear (1972) considers the hydraulic conductivity, K, for coastal aquifers of a range between 50 m/day (fine sand) and 1000 m/day (gravel). Tidal wave frequency $\omega = 4\pi$/day and aquifer depth D varying between 4 and 10 metres. With these values, $0.1 < \varepsilon < 0.6$ and $0.1 < \alpha < 0.5$.

Due to the computational nature of the semi-analytical solutions, when compared to the analytical solutions derived by Teo et al. (2003) we see that there is a limited level of accuracy due to the finite precision inherent within computational representations of values. Solutions of $O(\varepsilon^0)$ produce errors at an order of magnitude of 10^{-17} whilst $O(\varepsilon^1)$ produce errors at the order of magnitude of 10^{-9}. The large difference in magnitude between the two orders can be attributed to the poor accuracy

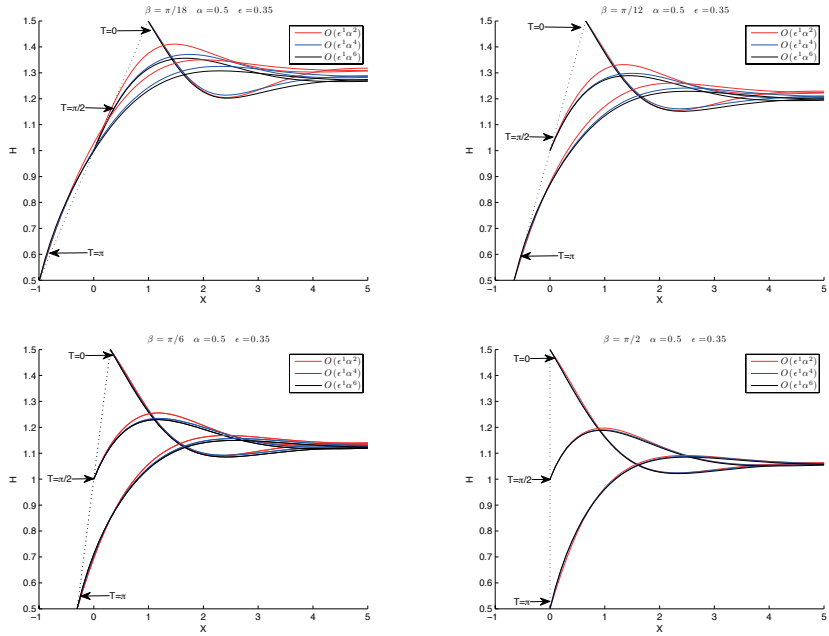

Figure 6.7 Comparisons of tide induced beach water table fluctuations for $\alpha = 0.5$, $\varepsilon = 0.35$ for various slopes of the beach.

of computation of the coefficients that contain the cotangent function, which reduces numerical accuracy to around half precision ($\approx 10^{-8}$).

Figure 6.7 consists of four plots that show the water table fluctuations at different times during the ebbing tide. They differ by showing the fluctuations for various beach slopes. When comparing the new higher order solutions to the previously derived $O(\varepsilon^1\alpha^2)$ solution, we see that there is a very clear over height of the water table approximated by the lower order solution, most prominently near the beach face. This can be attributed to the additional higher order components within the new solutions damping the fluctuations of the water table. These over heights are also of a larger magnitude when the beach slope is shallow ($\pi/18$). This can be explained by the nature of the cotangent function and its effect on the solution. For a vertical beach, the $O(\varepsilon^1)$ components of the solution are removed due to $\cot(\beta/2) = 0$. The relatively small differences in the varying order solutions within Figure 6.7 for the vertical beach are due to the higher order components of $O(\varepsilon^0)$. The plots indicate that the magnitude of coastal aquifer water table fluctuations are strongly linked to the slope of the beach. In addition the relevance of the higher order solutions derived in this study are much more important for shallow beach slopes. Also noticeable in Figure 6.7 is a super-elevation of the water table landward which will be looked at in more detail in section §6.6.5, where we shall examine the non-transient terms of the newly derived solutions.

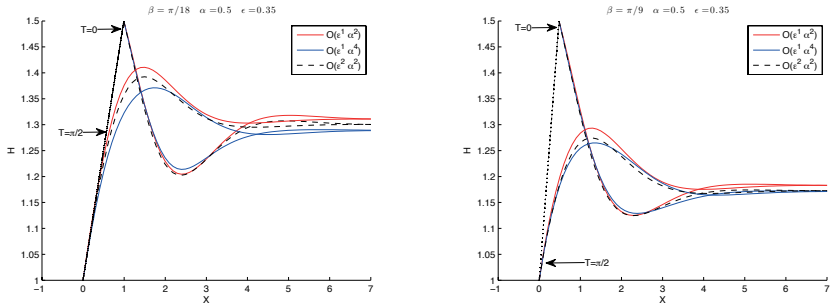

Figure 6.8 Comparisons of tide induced beach water table fluctuations for $\alpha = 0.5$, $\varepsilon = 0.35$ for beach slopes $\pi/18$ and $\pi/9$. New solution $O(\varepsilon\alpha^4)$ compared with previously derived solutions by Teo et al. (2003).

A comparison between $O(\varepsilon\alpha^2)$, $O(\varepsilon\alpha^4)$ and Teo et al. (2003) solution $O(\varepsilon^2\alpha^2)$ is illustrated in Figure 6.8. It can clearly be seen that there is over height in the fluctuations of Teo et al. (2003) solution, similar to $O(\varepsilon\alpha^2)$. As the beach slope increases, Teo et al. (2003) solution becomes close to the new $O(\varepsilon\alpha^4)$ solution. As previously noted, an increase of the steepness of the beach slope causes a decrease in the magnitude of the $O(\varepsilon^1)$ components of the solution resulting in only the $O(\varepsilon^0)$ terms significantly contributing to the solution. This again points to the importance of the beach slope to the water table fluctuations and indicates that the usefulness of the higher order solutions derived in this study are for shallow beach slopes.

6.6.4 EFFECTS OF HIGHER-ORDER COMPONENTS

To quantify the effects of the higher order components, we calculate the relative difference between higher order solutions and the linear solution. We use the following formula,

$$\Delta H_{\max}(\%) = \frac{|H_{O(\varepsilon\alpha^4)} - H_{linear}|}{H_{linear}}\%. \tag{6.62}$$

The relative difference between the solutions is dependent on beach slope β, and the values chosen for α and ε. This is illustrated by Figure 6.9 where, for a shallow beach slope $\beta = \pi/18$ and $\alpha = \varepsilon = 0.4$, the difference between the new high order solution and the linear solution differ by as much as 20%. When the beach slope is fairly steep, $\beta = \pi/4$, the new solution compares favourably with the results for Teo et al. (2003) $O(\varepsilon^2\alpha^2)$ solutions, both showing, at best, a relative difference of approximately 7% in comparison to the linear solution for a beach slope of $\pi/4$.

6.6.5 NON-TRANSIENT COMPONENTS OF SOLUTIONS

Philip (1973) showed that by using the Boussinesq equation for unsteady groundwater flow in a homogeneous porous media, the groundwater level lies

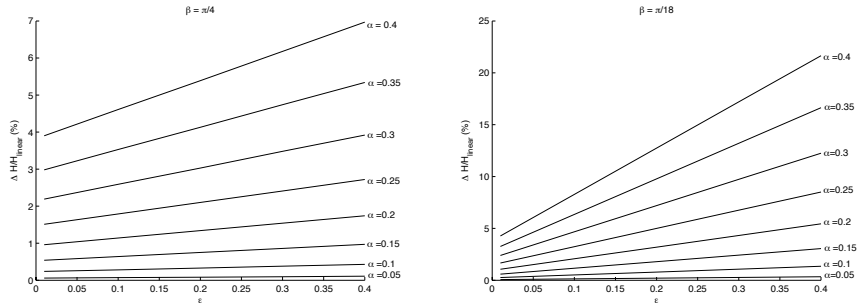

Figure 6.9 Relative difference between $O(\alpha)$ and $O(\varepsilon\alpha^4)$ solutions.

significantly above the mean sea level. Nielsen (1990) field measurements agreed with this and also showed that the beach slope was an influence to this super elevation.

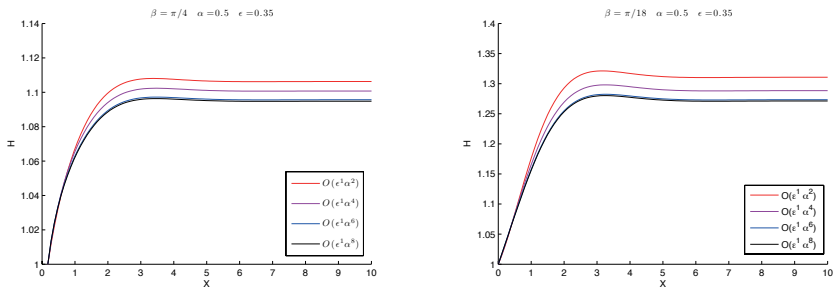

Figure 6.10 Static solution terms for beach slopes $\pi/18$ and $\pi/4$.

Figure 6.10 shows the non-transient components of the solution for two different beach slopes. Whilst in both it can be seen that horizontally the maximum value is reached at around $X = 2.5$, the magnitude is far less for the steeper beach. Also note that whilst the difference between $O(\varepsilon\alpha^2)$ and $O(\varepsilon\alpha^4)$ is large, $O(\varepsilon\alpha^6)$ and $O(\varepsilon\alpha^8)$ are very similar for these chosen values of α and ε.

The inclusion of the non-transient terms causes a large change in the solution. When comparing this to lower order solutions, it can be seen that the non-transient term affects the landward water table height significantly. In addition, this term also increases the magnitude of the exponentially decaying wave as we move closer to the maximum value.

Teo et al. (2003) solution shows an overestimation of the over height comparable to the lower order solutions implying that the higher order components are necessary for an accurate solution when using the perturbation method. A physical explanation of the landward over height can be attributed to the asymmetry of infiltration during the rising tide and ex-filtration, or drainage, during the ebb tide. Shallower beach

slopes seem to produce a larger super-elevation which is in accordance with Nielsen (1990) field observations.

6.7 SUMMARY AND REMARKS

In this chapter, the problem of tidal dynamics in coastal aquifers was considered with the associate boundary value problem. Based on the shallow water expansion, the problem was sorted out with two small parameters, shallow water parameters ($\varepsilon = D/L$) and amplitude parameter ($\alpha = A/D$) by the perturbation technique. Then, analytical solutions for tide-induced water table fluctuations in coastal aquifers were derived, based on the second-order shallow water expansion. Following the framework, a semi-analytical perturbation high-order solution was outlined.

In the new model, two perturbation parameters, the shallow water parameter (ε) and the amplitude parameter (α), were introduced. With these two parameters, the boundary condition at the intersection of ocean and inland is satisfied consistently, and complete higher-order solutions were derived. Furthermore, the new model covers all ranges of beach slope.

The present solution provides complete higher-order components and is compared with previous similar solutions (Nielsen, 1990; Li et al., 2000*b*). The component of $O(\alpha^2)$ plays a dominant role in the estimation of the water table level. A significant difference between the zeroth-order approximation and second-order approximation is found. The relative difference between the two solutions increases as α and ε increase. The considered examples demonstrate the significant influence of beach slope on the tide-induced water table fluctuations. In general, water table level (H) increases as beach slope (β) decreases.

Comparisons with previous solutions demonstrate that for certain cases, the high order solution provides a better prediction of the fluctuations than previously derived solutions. It is most useful for shallow beaches and where α is large. Under these conditions, a significant difference between the linear solution can be seen. This result is comparable with Teo et al. (2003) solution. In addition, for shallow beach slopes, Teo et al. (2003) solution exhibits similar over height issues as with the $O(\varepsilon\alpha^2)$ solution. This is overcome by the new higher order solution.

As observed by Nielsen (1990) and Philip (1973), the super-elevation of the water table landward can also be seen to be attributed to the non-transient components of the solutions. The super-elevation is over-estimated by lower order solutions, and seem to converge to a value as we introduce higher order terms to the solution.

6.8 APPENDIX: COEFFICIENTS FOR THE HIGHER-ORDER SOLUTION FOR TIDAL DYNAMICS IN COASTAL AQUIFERS

The solutions provided in the tables relate to the coefficients present in equation (6.58). The solutions are then constructed using the following equation,

$$\begin{aligned} H = 1 &+ \alpha H_{01} + \alpha^2 H_{02} + \alpha^3 H_{03} + \alpha^4 H_{04} + \varepsilon\alpha H_{11} + \varepsilon\alpha^2 H_{12} \\ &+ \varepsilon\alpha^3 H_{13} + \varepsilon\alpha^4 H_{14} + O(\varepsilon\alpha^5). \end{aligned} \tag{6.63}$$

The algorithm used to derive these coefficients did not solve equations H_{01} and H_{11}. The solutions of these were input into the program and are as follows

$$H_{01} = \exp(-X_1)\cos(T_1 - X_1), \quad \text{and} \quad H_{11} = 0. \tag{6.64}$$

It is noted that the proposed algorithm can obtain the coefficients of any arbitrary order solution. However, due to the limitations of computational capacity, on the workstation with a 3GHz processor and 48GB RAM, we have computed up to $O(\varepsilon^1\alpha^{20})$ solutions. In this appendix, only the coefficients up to $O(\varepsilon\alpha^4)$ are provided in Tables 6.1–6.4.

Table 6.1
Semi-analytical solution coefficients, H_{02} and H_{03}.

Coefficients, H_{02}					
a_1	a_2	b	c	d	e
-0.250000	0	0	-2	0	0
-0.500000	0	0	-2	2	-2
0.250000	0	0	0	0	-0
0.500000	0	0	-1.414214	2	-1.414214
Coefficients, H_{03}					
a_1	a_2	b	c	d	e
0.55	-0.01	0	-3.0	1	-1
0.375	0	0	-3	3	-3
0.125	0.125	1	-1	1	-1
-0.25	0.088388	0	-2.414214	1	-0.414214
-0.515165	0	0	-2.414214	3	-2.414214
-0.3	0.011612	0	-1	1	-1
0.140165	0	0	-1.732051	3	-1.732051

Table 6.2
Semi-analytical solution coefficients, H_{04}.

a_1	a_2	b	c	d	e
-0.0625	0	1	-2	0	0
-0.125	0.125	1	-2	2	-2
0.304115	-0.079436	0	-3.414214	2	-1.414214
-0.070083	0.040462	0	-2.732051	2	-0.732051
-0.151007	0	0	-2.732051	4	-2.732051
-0.677083	0.156250	0	-4	2	-2
-0.368750	0	0	-4	0	0
-0.333333	0	0	-4	4	-4
0.062450	0	0	-3.414214	0	0.585786
0.212500	0	0	-2	0	0
0.425000	-0.011612	0	-2	2	-2
0.281534	-0.129275	0	-3.414214	2	-1.414214
0.187500	0.044194	0	-3.414214	0	-0.585786
0.582447	0	0	-3.414214	4	-3.414214
0.088388	-0.088388	1	-1.414214	2	-1.414214
-0.062500	0	0	-2.828427	0	0
-0.12450	-0	0	-2.828427	4	-2.828427
-0.263483	0.023611	0	-1.414214	2	-1.414214
-0.031250	0	0	-0	0	-0
0.026894	0	0	-2	4	-2

Table 6.3
Semi-analytical solution coefficients, H_{12} and H_{13}.

Coefficients, H_{12}					
a_1	a_2	b	c	d	e
-0.500000 cb[#]	0.500000 cb	0	-1	0	-1
-0.500000 cb	0.500000 cb	0	-1	2	-1
0.500000 cb	0	0	0	0	0
0.500000 cb	-0.500000 cb	0	-1.414214	2	-1.414214
Coefficients, H_{13}					
a_1	a_2	b	c	d	e
0.250000 cb	-0.250000 cb	1	-1	1	-1
-0.515165 cb	0.515165 cb	0	-2.414214	3	-2.414214
-0.161612 cb	0.338388 cb	0	-2.414214	1	-0.414214
0.500000 cb	0	0	-2	1	0
0.500000 cb	-0.500000 cb	0	-2	1	-2
0.500000 cb	-0.500000 cb	0	-2	3	-2
-0.353553 cb	0.353553 cb	0	-1.414214	1	-1.414214
-0.353553 cb	0.353553 cb	0	-1.414214	3	-1.414214
-0.484835 cb	-0.191942 cb	0	-1	1	-1
0.368718 cb	-0.368718 cb	0	-1.732051	3	-1.732051

[#] cb=$\cot\beta$.

Table 6.4
Semi-analytical solution coefficients, H_{14}.

a_1	a_2	b	c	d	e
-0.125 cb[#]	0	1	-2	0	0
-0.25 cb	0.250000 cb	1	-2	2	-2
0.224679 cb	-0.383551 cb	0	-3.414214	2	-1.414214
0.176777 cb	0.176777 cb	0	-2.414214	0	0.414214
-0.397239 cb	0.397239 cb	0	-2.732051	4	-2.732051
-0.077919 cb	0.290799 cb	0	-2.732051	2	-0.732051
-0.312500 cb	-0.312500 cb	0	-3	0	1
0.062500 cb	0.062500 cb	0	-1	0	1
0.367417 cb	0	0	-2	0	0
0.734835 cb	0.191941 cb	0	-2	2	-2
0.152258 cb	-0.410809 cb	0	-3.414214	2	-1.414214
0.582447 cb	-0.582447 cb	0	-3.414214	4	-3.414214
0.205806 cb	0.294194 cb	0	-3.414214	0	-0.585786
0.176777 cb	-0.353553 cb	1	-1.414214	2	-1.414214
-0.125000 cb	0	0	-2.828427	0	0
-0.250000 cb	0.250000 cb	0	-2.828427	4	-2.828427
-0.462500 cb	0.112500 cb	0	-3	0	-1
-0.775000 cb	0.425000 cb	0	-3	2	-1
-0.562500 cb	0.562500 cb	0	-3	2	-3
-0.562500 cb	0.562500 cb	0	-3	4	-3
0	0.125000 cb	1	-1	0	-1
0	0.125000 cb	1	-1	2	-1
0.106694 cb	0.018306 cb	0	-2.414214	0	-0.414214
0.283471 cb	-0.158471 cb	0	-2.414214	2	-0.414214
0.621860 cb	-0.621859 cb	0	-2.414214	2	-2.414214
0.621860 cb	-0.621859 cb	0	-2.414214	4	-2.414214
0.144194 cb	-0.155806 cb	0	-1	0	-1
0.206694 cb	-0.218306 cb	0	-1	2	-1
-0.121386 cb	0.121386 cb	0	-1.732051	2	-1.732051
-0.121386 cb	0.121386 cb	0	-1.732051	4	-1.732051
-0.163388 cb	0	0	0	0	0
-0.686991 cb	0.201369 cb	0	-1.414214	2	-1.414214
0.126820 cb	-0.126820 cb	0	-2	4	-2

[#] cb=$\cot\beta$.

Taylor & Francis
Taylor & Francis Group
http://taylorandfrancis.com

7 Tidal Dynamics in Coastal Aquifers with Capillarity Effects

7.1 INTRODUCTION

In the conventional approach to describing tidal fluctuations in coastal aquifers, it is often assumed that the upper free surface is a sharp boundary between saturated and dry aquifer material. This assumption is an oversimplification in many situations as the upper boundary is not abrupt, but a diffuse transition zone of partially unsaturated material (see Figure 6.1). Parlange and Brutsaert (1987) proposed a capillarity correction to describe the effect of the diffuse transition zone based on the Boussinesq equation. Later, Barry et al. (1996) extended Parlange and Brutsaert (1987) work to order $O(\alpha^2)$, and concluded that the capillarity correction is important at high frequencies. All these investigations considered only the zeroth-order capillarity correction for a vertical beach, not for a sloping beach.

In this chapter, we will discuss a higher-order capillarity correction to free surface flow of groundwater in a sloping beach. First, based on the capillarity correction proposed by Parlange and Brutsaert (1987), a second-order capillarity correction $O(\varepsilon^2)$ is derived. Then, a new definition of the capillarity fringe is proposed for the case of small capillarity number, N_{cap} (defined in (7.15)), and a simplified model is derived. With the two new analytical solutions, the effects of the capillarity correction and sloping beaches on water table fluctuations in coastal aquifers are discussed in detail.

7.2 BOUNDARY VALUE PROBLEM

In this chapter, the flow is assumed to be homogeneous and incompressible in a rigid porous medium. The configuration of the groundwater flow in a coastal aquifer is shown in Figure 6.1. In the figure, $h(x,t)$ is the total tide-induced water table height, D is the thickness of the aquifer, and β is the slope of the beach. Seepage face effects are ignored in this study. Since the fluid is incompressible, the free surface flow of groundwater, satisfying the conservation of mass, leads to Laplace's equation for the hydraulic head (Bear, 1972):

$$\phi_{xx} + \phi_{zz} = 0, \qquad 0 \le z \le h(x,t). \tag{7.1}$$

Equation (7.1) is to be solved subject to the following boundary conditions,

$$\phi_z = 0, \qquad \text{at } z = 0, \tag{7.2a}$$

$$\phi = h, \qquad \text{at } z = h, \tag{7.2b}$$

$$\phi(x_o(t),t) = D(1+\alpha\cos\omega t), \qquad x_o(t) = A\cot\beta\cos\omega t, \tag{7.2c}$$

$$n_e\phi_t = K\left[\phi_x^2 + \phi_z^2\right] + q - (K+q)\phi_z, \qquad \text{at } z = h, \tag{7.2d}$$

$$\phi_x = 0, \qquad \text{as } x \to \infty. \tag{7.2e}$$

Note that the soil properties are defined by the soil porosity (n_e) and hydraulic conductivity (K). In (7.2d), q is the source term representing the rate at which water crosses the saturated surface.

To simplify the mathematical procedure, we introduce the following non-dimensional variables:

$$X = \frac{x}{L} = \frac{\varepsilon x}{D}, \quad Z = \frac{z}{D}, \quad H = \frac{h}{D}, \quad \Phi = \frac{\phi}{D}, \quad \alpha = \frac{A}{D},$$
$$T = \omega t, \quad L = \sqrt{\frac{2KD}{n_e\omega}}, \quad \varepsilon = \frac{D}{L} = \sqrt{\frac{n_e\omega D}{2K}}, \quad q = K\varepsilon^2\Psi. \tag{7.3}$$

Compare the above boundary value problem with those in Chapter 6, the only difference is q, which represents the capillarity source contribution.

Following the same procedure outlined in Chapter 6, we define the new independent variables as (Li et al., 2000*b*; Teo et al., 2003)

$$X_1 = X - X_0(T), \qquad \text{and} \qquad T_1 = T. \tag{7.4}$$

To apply the perturbation technique to the non-linear kinematic boundary condition (7.2d), the water table height (H), potential head (Φ) and capillarity fringe (Ψ) are expressed in powers of the shallow water parameter (ε):

$$H = \sum_{n=0}^{\infty}\varepsilon^n H_n, \qquad \Phi = \sum_{n=0}^{\infty}\varepsilon^n\Phi_n, \quad \text{and} \quad \Psi = \sum_{n=0}^{\infty}\varepsilon^n\Psi_n, \tag{7.5}$$

resulting in the following equations to second-order:

$$O(1): \quad 2H_{0T_1} = (H_0H_{0X_1})_{X_1} + \Psi_0, \tag{7.6a}$$

$$O(\varepsilon): \quad 2[H_{1T_1} + \alpha\sin(T_1)\cot(\beta)H_{0X_1}] = (H_0H_1)_{X_1X_1} + \Psi_1, \tag{7.6b}$$

$$O(\varepsilon^2): \quad 2\left[H_{2T_1} + \alpha\sin(T_1)\cot(\beta)H_{1X_1}\right] = \frac{1}{2}(H_1^2)_{X_1X_1} + (H_0H_2)_{X_1X_1} + \frac{1}{3}(H_0^3H_{0X_1X_1})_{X_1X_1} + \Psi_2 + \Psi_0H_0H_{0X_1X_1}, \tag{7.6c}$$

with boundary conditions

$$H_0(0,T_1) = 1+\alpha\cos(T_1), \qquad H_1(0,T_1) = H_2(0,T_1) = \cdots = 0, \tag{7.7a}$$

$$H_{0X_1}(0,T_1) = H_{1X_1}(0,T_1) = H_{2X_1}(0,T_1) = \cdots = 0, \tag{7.7b}$$

where $\Psi = \Psi_0 + \varepsilon\Psi_1 + \ldots$ are the capillarity source contributions that are derived in the latter section.

7.3 CAPILLARITY CORRECTION

7.3.1 DEFINITION OF CAPILLARITY CORRECTION

Following Parlange and Brutsaert (1987), the capillarity source contribution is defined as:

$$q \simeq -\frac{\partial}{\partial t}\left[\frac{\int_{\theta_r}^{\theta_0}(\theta-\theta_r)Dd\theta}{K+\int_h^{\infty}\frac{\partial\theta}{\partial t}dz}\right], \tag{7.8}$$

where θ_0 is the volumetric water content at saturation and θ_r its residual value. From conservation of mass, we have

$$\int_h^{\infty}\frac{\partial\theta}{\partial t}dz = n_e\frac{\partial h}{\partial t}+q. \tag{7.9}$$

We define the capillarity fringe constant (Parlange and Brutsaert, 1987)

$$B=\int_{\theta_r}^{\theta_o}\frac{(\theta-\theta_r)D}{K}d\theta, \tag{7.10}$$

representing an average suction required to extract water held by capillarity. The importance of capillarity increases with B.

Following Parlange and Brutsaert (1987), (7.8)–(7.10) then give

$$q=-\frac{\partial}{\partial t}\left[\frac{B}{1+(hh_x)_x}\right]. \tag{7.11}$$

Now, we introduce non-dimensional and perturbation parameters given in (7.3) into (7.11),

$$\begin{aligned}\Psi^I &= \frac{q}{K\varepsilon^2} = -\frac{B}{K\varepsilon^2}\frac{\partial}{\partial t}\left[\frac{1}{1+(hh_x)_x}\right]\\ &= -\frac{N_{cap}}{\varepsilon^2}\left\{\frac{\partial}{\partial T_1}\left[\frac{1}{1+\varepsilon^2(HH_{X_1})_{X_1}}\right]\right.\\ &\qquad \left.+\alpha\varepsilon\cot\beta\sin(T_1)\frac{\partial}{\partial X_1}\left[\frac{1}{1+\varepsilon^2(HH_{X_1})_{X_1}}\right]\right\}\\ &= \Psi_0^I+\varepsilon\Psi_1^I+\varepsilon^2\Psi_2^I+O(\varepsilon^3),\end{aligned} \tag{7.12}$$

where $N_{cap}=\omega B/K$ is defined as the *capillarity number*, which the inverse of the form defined by Li et al. (1997*a*). The superscript "I" denotes the definition proposed by Parlange and Brutsaert (1987).

In (7.12), Ψ_0^I, Ψ_1^I and Ψ_2^I are given by

$$\Psi_0^I = N_{cap}(H_0 H_{0X_1})_{X_1 T_1}, \tag{7.13a}$$

$$\Psi_1^I = N_{cap}\left[(H_0 H_1)_{X_1 X_1 T_1} + \alpha \cot\beta \sin(T_1)(H_0 H_{0X_1})_{X_1 X_1}\right], \tag{7.13b}$$

$$\begin{aligned}\Psi_2^I = N_{cap}\Bigg\{&(H_0 H_2)_{X_1 X_1 T_1} + (H_1 H_{1X_1})_{X_1 T_1} - \frac{1}{2}\left[((H_0 H_{0X_1})_{X_1})^2\right]_{T_1} \\ &+\alpha \cot\beta \sin(T_1)(H_0 H_1)_{X_1 X_1}\Bigg\}.\end{aligned} \tag{7.13c}$$

Note that only the zeroth-order component (Ψ_0^I) was presented in Parlange and Brutsaert (1987).

7.3.2 NEW DEFINITION OF CAPILLARITY CORRECTION

Here, we consider the situation when the capillarity source term is much smaller than other terms, i.e., $q << n_e \frac{\partial h}{\partial t}$. Then, (7.9) can be written as

$$\int_h^\infty \frac{\partial \theta}{\partial t} dz = n_e \frac{\partial h}{\partial t}, \tag{7.14}$$

and (7.8) becomes

$$q \simeq = -\frac{\partial}{\partial t}\left[\frac{B}{1 + \dfrac{n_e}{K}\dfrac{\partial h}{\partial t}}\right]. \tag{7.15}$$

Thus,

$$\begin{aligned}\Psi^{II} =& \frac{q}{K\varepsilon^2} = -\frac{B}{K\varepsilon^2}\frac{\partial}{\partial t}\left(\frac{1}{1 + \dfrac{n_e}{K}\dfrac{\partial h}{\partial t}}\right) \\ =& N_{cap}\{2H_{0T_1T_1} \\ &+ \varepsilon[2H_{1T_1T_1} + \alpha \cot\beta(H_{0X_1T_1}\sin T_1 \\ &\quad + H_{0X_1}\cos T_1) + 2\alpha \cot\beta H_{0X_1T_1}\sin T_1)] \\ &+ \varepsilon^2[2H_{2T_1T_1} - 2(H_{0T_1}^2)_{T_1} \\ &\quad + \alpha \cot\beta(H_{1X_1T_1}\sin T_1 + H_{1X_1}\cos T_1) \\ &\quad + 2\alpha \cot\beta \sin T_1(H_{1X_1T_1} + \alpha \sin T_1 \cot\beta H_{0X_1X_1})]\} + O(\varepsilon^3) \\ =& \Psi_0^{II} + \varepsilon\Psi_1^{II} + \varepsilon^2\Psi_2^{II} + O(\varepsilon^3),\end{aligned} \tag{7.16}$$

where

$$\Psi_0^{II} = 2N_{cap}H_{0T_1T_1}, \tag{7.17a}$$

$$\Psi_1^{II} = N_{cap}[2H_{1T_1T_1} + \alpha \cot\beta(H_{0X_1T_1}\sin T_1 + H_{0X_1}\cos T_1)$$

$$+2\alpha\cot\beta H_{0X_1T_1}\sin T_1], \tag{7.17b}$$

$$\Psi_2^{II} = N_{cap}[2H_{2T_1T_1} + \alpha\cot\beta(H_{1X_1T_1}\sin T_1 + H_{1X_1}\cos T_1) - 2(H_{0T_1}^2)_{T_1} + 2\alpha\cot\beta\sin T_1(H_{1X_1T_1} + \alpha\sin T_1\cot\beta H_{0X_1X_1})], \tag{7.17c}$$

in which the superscript "*II*" denotes the new definition.

7.4 APPROXIMATION I: COMPLETE SOLUTION

7.4.1 THE SECOND-ORDER APPROXIMATION

The tide-induced water table fluctuation (H) can be expanded in terms of the shallow water and amplitude parameters (ε and α) as

$$H_{mn} = 1 + \sum_{m=0}^{\infty}\sum_{n=1}^{\infty}\varepsilon^m\alpha^n H_{mn}. \tag{7.18}$$

Following the procedure outline in Chapter 6, H_{mn} can be expressed as

$$H_{01}(X_1,T) = e^{-P_1X_1}\cos\theta_1, \tag{7.19a}$$

$$H_{02} = \frac{1}{4}\left[1-e^{-2P_1X_1}\right] + \frac{1+6N_{cap}^2}{2(1+9N_{cap}^2)}\left(e^{-\sqrt{2}P_2X_1}\cos\theta_2 - e^{-2P_1X_1}\cos 2\theta_1\right) + \frac{N_{cap}}{2(1+9N_{cap}^2)}\left(e^{-\sqrt{2}P_2X_1}\sin\theta_2 - e^{-2P_1X_1}\sin 2\theta_1\right), \tag{7.19b}$$

$$H_{11} = 0, \tag{7.20a}$$

$$H_{12} = \frac{\cot\beta}{(P_1^2+Q_1^2)^2}\{(P_1^2+Q_1^2)Q_1 - A_4 + e^{-P_1X_1}[(-(P_1^2+Q_1^2)P_1 + A_3)\sin(Q_1X_1) + ((P_1^2+Q_1^2)Q_1 + A_4)\cos(Q_1X_1)]\} + \cot(\beta)\{A_1[e^{-P_1X_1}\cos\theta_3 - e^{-\sqrt{2}P_2X_1}\cos\theta_2] - A_2[e^{-P_1X_1}\sin\theta_3 - e^{-\sqrt{2}P_2X_1}\sin\theta_2]\}, \tag{7.20b}$$

$$H_{21} = \frac{X_1}{6}e^{-P_1X_1}(B_1\cos\theta_1 - B_2\sin\theta_1), \tag{7.21a}$$

$$
\begin{aligned}
H_{22} = & \frac{1}{4P_1^3}(B_3 + B_4 P_1)(1 - e^{-2P_1 X_1}) - \frac{1}{4P_1^2} B_3 X_1 e^{-2P_1 X_1} \\
& + e^{-\sqrt{2}P_2 X_1}[(B_9 X_1 - B_7)\cos\theta_2 - (B_{10} X_1 - B_8)\sin\theta_2] \\
& + e^{-2P_1 X_1}[(B_5 X_1 + B_7)\cos 2\theta_1 - (B_6 X_1 + B_8)\sin 2\theta_1],
\end{aligned}
\tag{7.21b}
$$

where

$$
\theta_1 = T_1 - Q_1 X_1,\ \theta_2 = 2T_1 - \sqrt{2}Q_2 X_1, \theta_3 = 2T_1 - Q_1 X_1 \tag{7.22a}
$$

and

$$
\left\{ \begin{array}{c} P_m \\ Q_m \end{array} \right\} = \left[\frac{1}{\sqrt{1 + m^2 N_{cap}^2}} \pm \frac{m N_{cap}}{1 + m^2 N_{cap}^2} \right]^{1/2}, \qquad m = 1, 2. \tag{7.22b}
$$

The various coefficients A_i and B_i are given in the Appendix §7.7

7.4.2 SPECIAL CASES

Three special cases can be easily deduced from the above analytical solutions.

Special case I: Vertical beach without capillarity correction

For the simplest case of a vertical beach without capillarity correction, $\beta = \pi/2$ and $N_{cap} = 0$, when $X_1 = X$, $T_1 = T$ and $\cot\beta = 0$, the solution, combining (7.19a)–(7.21b), becomes

$$
\begin{aligned}
H(X,T) = & \alpha e^{-X}\cos\theta_1 \\
& + \alpha^2 \left\{ \frac{1}{4}(1 - e^{-2X}) + \frac{1}{2}\left[e^{-\sqrt{2}X}\cos(\theta_2) - e^{-2X}\cos(2\theta_1) \right] \right\} \\
& - \frac{\sqrt{2}}{3}\varepsilon^2 \alpha X e^{-X}\cos(\theta_1 - \frac{\pi}{4}) \\
& + \frac{1}{3}\varepsilon^2\alpha^2 \left\{ -1 + \left(1 + \frac{X}{2}\right) e^{-2X} - 2X e^{-\sqrt{2}X}\cos(\theta_2 - \frac{\pi}{4}) \right. \\
& \left. + e^{-\sqrt{2}X}\sin\theta_2 + \sqrt{2}X e^{-2X}\cos(2\theta_1 - \frac{\pi}{4}) - e^{-2X}\sin 2\theta_1 \right\}.
\end{aligned}
\tag{7.23}
$$

Note that (7.23) is identical to the $O(\alpha^2)$ solution for a vertical beach given in Parlange et al. (1984), and to the $O(\varepsilon^2\alpha^2)$ solution for a vertical beach given in (6.52).

Special case II: Vertical beach with capillarity correction

The second special case is for a vertical beach with capillarity correction, i.e., $N_{cap} \neq 0$, $\beta = \pi/2$, when $X_1 = X$, $T_1 = T$ and $\cot\beta = 0$, the solution is

$$\begin{aligned} H(X,T) = {} & \alpha e^{-P_1 X}\cos\theta_1 + \alpha^2\Big[\frac{1}{4}(1-e^{-2X}) \\ & + \frac{(1+6N_{cap}^2)}{2(1+9N_{cap}^2)}(e^{-\sqrt{2}P_2 X}\cos\theta_2 - e^{-2P_1 X}\cos 2\theta_1) \\ & + \frac{N_{cap}}{2(1+9N_{cap}^2)}(e^{-\sqrt{2}P_2 X}\sin\theta_2 - e^{-2P_1 X}\sin 2\theta_1)\Big] \\ & + \varepsilon^2\alpha\frac{X}{6}e^{-P_1 X}\{B_1\cos\theta_1 - B_2\sin\theta_1\} \\ & + \varepsilon^2\alpha^2\Big\{\frac{1}{4P_1^3}(B_3 + B_4 P_1)(1-e^{-2P_1 X}) - \frac{1}{4P_1^2}B_3 X e^{-2P_1 X} \\ & + e^{-\sqrt{2}P_2 X}[(B_9 X - B_7)\cos\theta_2 - (B_{10}X - B_8)\sin\theta_2] \\ & + e^{-2P_1 X}[(B_5 X + B_7)\cos 2\theta_1 - (B_6 X + B_8)\sin 2\theta_1]\Big\}. \end{aligned} \tag{7.24}$$

Note that (7.24) is identical to the solution of $O(\alpha^2)$ for a vertical beach with capillarity corrections given in Barry et al. (1996).

Special case III: Sloping beach without the capillarity correction

The third special case is for a sloping beach with no capillarity correction, i.e., $N_{cap} = 0$, $\beta \leq \pi/2$. From (7.19a)–(7.21b), the solution is:

$$\begin{aligned} H(X_1,T_1) = {} & \alpha e^{-X_1}\cos(\theta_1) \\ & + \alpha^2\Big[\frac{1}{4}(1-e^{-2X_1}) + \frac{1}{2}e^{-\sqrt{2}X_1}\cos(\theta_2) - \frac{1}{2}e^{-2X_1}\cos(2\theta_1)\Big] \\ & + \frac{1}{\sqrt{2}}\cot(\beta)\varepsilon\alpha^2\Big[\frac{1}{\sqrt{2}} - e^{-X_1}\cos(X_1 - \frac{1}{4}\pi) \\ & \quad + e^{-\sqrt{2}X_1}\cos(\theta_2 + \frac{1}{4}\pi) - e^{-X_1}\cos(\theta_3 + \frac{1}{4}\pi)\Big] \\ & - \frac{\sqrt{2}}{3}\varepsilon^2\alpha X_1 e^{-X_1}\cos(\theta_1 - \frac{\pi}{4}) \\ & + \frac{1}{3}\varepsilon^2\alpha^2\Big\{-1 + (1+\frac{X_1}{2})e^{-2X_1} - 2X_1 e^{-\sqrt{2}X_1}\cos(\theta_2 - \frac{\pi}{4}) \\ & \quad + e^{-\sqrt{2}X_1}\sin(\theta_2) + \sqrt{2}X_1 e^{-2X_1}\cos(2\theta_1 - \frac{\pi}{4}) \\ & \quad - e^{-2X_1}\sin(2\theta_1)\Big\}, \end{aligned} \tag{7.25}$$

which is identical to that derived by Teo et al. (2003).

7.4.3 EFFECTS OF HIGHER-ORDER COMPONENTS

As mentioned previously, existing analytical solutions which include the capillarity correction in approximating the tide-induced water table fluctuations in coastal aquifers have been up to $O(\varepsilon^0\alpha^3)$ for a vertical beach (Barry et al., 1996; Teo et al., 2003). Using the new higher-order solutions given here, it is possible to examine directly the effects of higher-order components. A straightforward way to compare orders is to calculate the water table level by using the above approximation. water table levels (H) versus ($T/2\pi$) for various orders are plotted in Figure 7.1. Significant differences between the zeroth-order $O(\alpha)$ and second-order solution ($\varepsilon^2\alpha^2$) are observed.

In Figure 7.1, two different beach slopes are considered, $\beta = \pi/6$ and $\pi/3$. It is observed that a large beach slope will enhance the influence of the higher-order components on the water table height (H). For example, the maximum difference between the linear solution, $O(\alpha)$, and the second-order solution, $O(\varepsilon^2\alpha^2)$, is 2.5% of D (the mean aquifer thickness) with $\beta = \pi/6$, while it is 5% of D with $\beta = \pi/3$. This results implies that non-linear effects are more important for steeper beaches.

7.4.4 EFFECTS OF THE CAPILLARITY CORRECTION

The importance of the capillarity correction is quantified by the capillarity number, $N_{cap}(= \omega B/K)$. The capillarity number increases with the frequency and capillarity fringe length, and as the hydraulic conductivity decreases. In most coastal aquifers, the capillarity fringe constant (B) varies from 0 to 0.4 m and the hydraulic conductivity (K) varies from 10 m/d to 1000 m/d (Bear, 1972). We consider tides, the frequency of which (ω) is 4π d^{-1}. Thus, the capillarity number, N_{cap}, varies between zero and 0.5. Figure 7.2 demonstrates the importance of the capillarity number on the water table fluctuations. This indicates that the influence of the capillarity correction is about 2% of water table level H.

7.5 APPROXIMATION II: SOLUTION WITH NEW DEFINITION OF CAPILLARITY CORRECTIONS

Based on the new definition of capillarity corrections, (7.15), and governing equations outline in Section §7.3.2, we can derive the analytical solution for a sloping beach with new definition of capillarity corrections in this section.

7.5.1 SIMPLIFIED SOLUTION

The simplified solution can be written as

$$H_{01} = e^{-R_1 X_1}\cos\delta_1, \tag{7.26a}$$

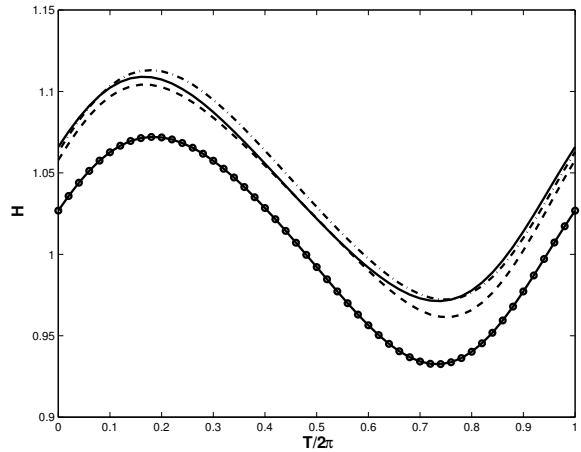

(a) $\beta = \pi/6$

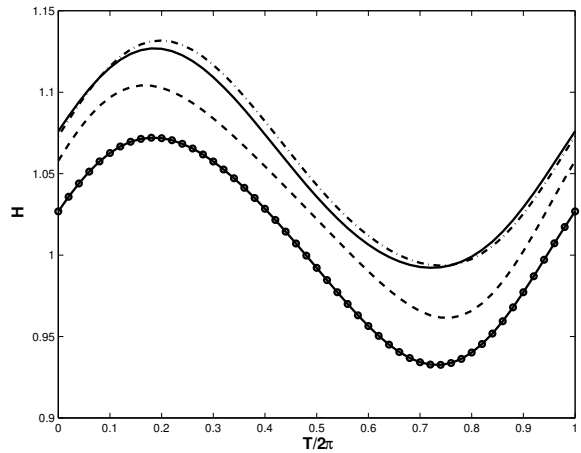

(b) $\beta = \pi/3$

Figure 7.1 Distribution of water table fluctuations (H) versus time ($T/2\pi$) for various order solutions and beach slopes. (a) $\beta = \pi/6$ and (b) $\beta = \pi/3$ ($\varepsilon = \alpha = 0.35$, and $X = 1.5$). $-\bullet-$ is the $O(\alpha)$ solution, - - the $O(\alpha^2)$ solution, - . the $O(\varepsilon\alpha^2)$ solution and $-$ is the $O(\varepsilon^2\alpha^2)$ solution.

$$H_{02} = \frac{1}{4}\left(1 - e^{-2R_1X_1}\right) + \frac{1}{2}\left(e^{-\sqrt{2}R_2X_1}\cos\delta_2 - e^{-2R_1X_1}\cos 2\delta_1\right) + \frac{N_{cap}}{2}\left(e^{-\sqrt{2}R_2X_1}\sin\delta_2 - e^{-2R_1X_1}\sin 2\delta_1\right), \tag{7.26b}$$

$$H_{11} = 0, \tag{7.27a}$$

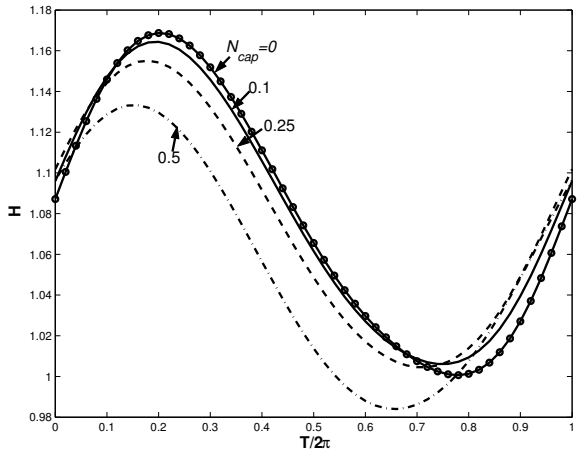

Figure 7.2 Distribution of water table fluctuations (H) versus time ($T/2\pi$) for various values of N_{cap} ($\varepsilon = \alpha = 0.4$, $X = 1.5$, $\beta = \pi/6$).

$$
\begin{aligned}
H_{12} = \frac{\cot\beta}{(R_1^2+S_1^2)}\{S_1 - \frac{N_{cap}}{2}R_1(1+3S_1) \\
- e^{-R_1X_1}[(R_1\sin(S_1X_1)+S_1\cos(S_1X_1)) \\
+ \frac{N_{cap}}{2}(1+3S_1)(S_1\sin(S_1X_1)-R_1\cos(S_1X_1))]\} \\
+ \cot\beta[C_1(e^{-R_1X_1}\cos\delta_3 - e^{-\sqrt{2}R_2X_1}\cos\delta_2) \\
+ C_2(e^{-\sqrt{2}R_2X_1}\sin\delta_2 - e^{-R_1X_1}\sin\delta_3)],
\end{aligned}
\tag{7.27b}
$$

$$
H_{21} = \frac{X_1}{6}e^{-R_1X_1}(D_1\cos\delta_1 + D_2\sin\delta_1), \tag{7.28a}
$$

and

$$
\begin{aligned}
H_{22} = \frac{1}{4R_1^3}(D_3+D_4R_1)(1-e^{-2R_1X_1}) - \frac{1}{4R_1^2}D_3X_1e^{-2R_1X_1} \\
+ e^{-\sqrt{2}R_2X_1}[(D_9X_1-D_7)\cos\delta_2 - (D_{10}X_1-D_8)\sin\delta_2] \\
+ e^{-2R_1X_1}[(D_5X_1+D_7)\cos2\delta_1 - (D_6X_1+D_8)\sin2\delta_1],
\end{aligned}
\tag{7.28b}
$$

where

$$
\delta_1 = T_1 - S_1X_1, \quad \delta_2 = 2T_1 - \sqrt{2}S_2X_1, \quad \delta_3 = 2T_1 - S_1X_1, \tag{7.29a}
$$

$$
\left\{ \begin{array}{c} R_m \\ S_m \end{array} \right\} = \left[\sqrt{1+m^2N_{cap}^2} \pm mN_{cap}\right]^{1/2}. \tag{7.29b}
$$

The various coefficients C_i and D_i are given in Appendix §7.7.

The simplified solution, (7.27a)–(7.28b), can also be reduced to the three special cases through the same procedure as the previous section.

7.5.2 COMPARISON OF TWO SOLUTIONS

The new definition of the capillarity correction, i.e., (7.15), provides a simplified solution compared with that in Parlange and Brutsaert (1987). We now investigate the difference of water table fluctuations calculated from the two solutions. In the example, we vary the two perturbation parameters, the shallow water parameter (ε) and the amplitude parameter (α), between 0 and 0.4, this range being reasonable since they are assumed to be significantly less than unity. In the following sections, the water table level calculated from the first approximation, extended from the definition proposed in Parlange and Brutsaert (1987), is denoted as H^I, whilst the results from the second approximation, the simplified model, is denoted as H^{II}.

To investigate the difference between two solutions H^I and H^{II}, given by (7.11) and (7.15), respectively. We consider the relative difference $|H^I - H^{II}|/H^I = 1.5\%$ as an acceptable accuracy. Figure 7.3(a) illustrates the applicable zone of the simplified model for various ε with a 1.5% relative difference. In the figure, three parameters, ε, α and N_{cap} vary within reasonable physical ranges as discussed above. For cases belonging to Zone A (below the curves), the simplified model can be used, while the original model should be used for parameters in the range above the curves, in Zone B. The figure clearly indicates that the simplified model is applicable for most cases.

Figure 7.3(b) further investigates the applicable zone of the simplified model for various beach slopes. The results swmonstrate that the simplified model is more applicable for larger beach slopes. For a vertical beach, the simplified model can replace the original model for the range up to (ε, α) = (0.5, 0.5).

7.6 SUMMARY

In this chapter, the definition of capillarity correction proposed by Parlange and Brutsaert (1987) was extended to second-order and to sloping beaches. The significant effects of higher-order components on the water table fluctuations are also demonstrated. The results indicate the influence of the capillarity correction may reach 2% of the water table level.

A new definition of capillarity correction was then proposed for the case of small capillarity fringe, and a simplified solution was derived. A comparison of the two solutions indicates that the simplified model can be used in most cases.

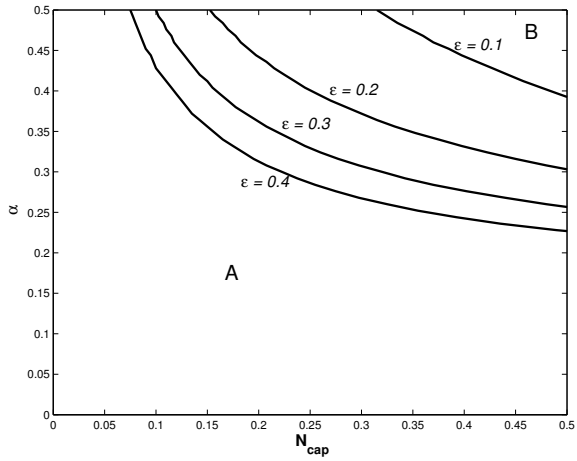

(a) $\beta = \pi/6$

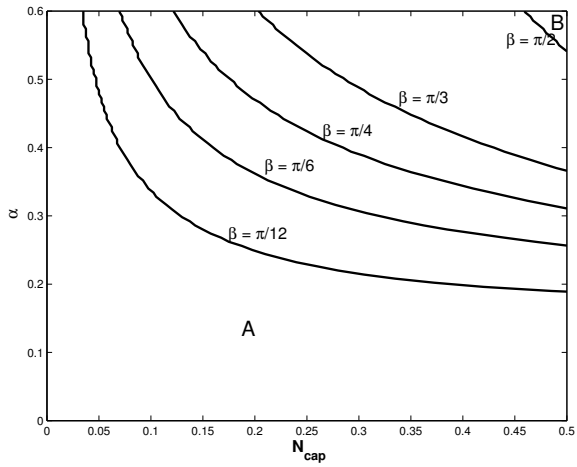

(b) $\varepsilon = 0.3$

Figure 7.3 Applicable zone of the simplified model based on 1.5% of relative differences $(H^I - H^{II})/H^I$. (a) various ε with $\beta = \pi/6$ and (b) various beach slope β with $\varepsilon = 0.3$. ($T = 0$ and $X = 1.5$).

7.7 APPENDIX: LIST OF COEFFICIENTS FOR TIDAL DYNAMICS IN COASTAL AQUIFERS WITH CAPILLARITY EFFECTS

The coefficients A_i and B_i in (7.20a)–(7.21b) are:

$$A_1 = \frac{1}{\Delta}\left\{\left[Q_1 - \frac{N_{cap}}{2}Q_1(Q_1^2 - 3P_1^2)\right]\left[2P_1Q_1N_{cap} - (P_1^2 - Q_1^2)\right] + \left[-P_1 + \frac{N_{cap}}{2}P_1(P_1^2 - 3Q_1^2)\right]\left[4 - 2P_1Q_1 - N_{cap}(P_1^2 - Q_1^2)\right]\right\}, \tag{7.30a}$$

$$A_2 = \frac{1}{\Delta}[(-P_1 + \frac{N_{cap}}{2}P_1(P_1^2 - 3Q_1^2))(2P_1Q_1N_{cap} - (P_1^2 - Q_1^2)) \\ - (Q_1 - \frac{N_{cap}}{2}Q_1(Q_1^2 - 3P_1^2))(4 - 2P_1Q_1 - N_{cap}(P_1^2 - Q_1^2))], \tag{7.30b}$$

$$A_3 = \frac{N_{cap}}{2}P_1(P_1^4 - 10P_1^2Q_1^2 + 5Q_1^4), \tag{7.30c}$$

$$A_4 = \frac{N_{cap}}{2}Q_1(Q_1^4 - 10P_1^2Q_1^2 + 5P_1^4), \tag{7.30d}$$

$$\Delta = [(P_1^2 - Q_1^2) - 2N_{cap}P_1Q_1]^2 + [4 - 2P_1Q_1 - 2N_{cap}(P_1^2 - Q_1^2)]^2, \tag{7.30e}$$

$$B_1 = (P_1^3 - N_{cap}Q_1^3) + 3P_1Q_1(N_{cap}P_1 - Q_1), \tag{7.31a}$$

$$B_2 = -(N_{cap}P_1^3 + Q_1^3) + 3P_1Q_1(P_1 + N_{cap}Q_1), \tag{7.31b}$$

$$B_3 = \frac{1}{3}P_1^2B_1, \tag{7.31c}$$

$$B_4 = \frac{2}{3}P_1^4 - \frac{1}{3}P_1B_1 - 2P_1^2Q_1^2, \tag{7.31d}$$

$$B_5 + iB_6 = \frac{(1 + N_{cap}^2)(1 + 2iN_{cap})(P_1 + iQ_1)^2(B_1 + iB_2)}{12\left[-i(1 + 3N_{cap}^2) + 2N_{cap}\right]}, \tag{7.32a}$$

$$B_7 + iB_8 = \frac{(1 + N_{cap}^2)(B_{11} - 4(B_5 + iB_6)(P_1 + iQ_1)(1 + 2iN_{cap}))}{4\left[-i(1 + 3N_{cap}^2) + 2N_{cap}\right]}, \tag{7.32b}$$

$$B_9 + iB_{10} = \frac{\left[\left(1 + 6N_{cap}^2\right) - iN_{cap}\right]}{3\sqrt{2}(1 + 2iN_{cap})(1 + 9N_{cap}^2)}\left(P_2 + iQ_2\right)^3, \tag{7.32c}$$

$$B_{11} = -\frac{1}{3}(1+2iN_{cap})(P_1+iQ_1)(B_1+iB_2)+2(P_1+iQ_1)^4 - \frac{8\left[\left(1+6N_{cap}^2\right)-iN_{cap}\right]}{3(1+9N_{cap}^2)}(P_1+iQ_1)^4. \tag{7.32d}$$

The coefficients C_i and D_i in (7.27a)–(7.28b) are:

$$C_1 = \frac{1}{2(1+9N_{cap}^2)}\{3N_{cap}[S_1 - \frac{N_{cap}}{2}R_1(1-3S_1)] - [R_1 - \frac{N_{cap}}{2}S_1(1-3S_1)]\}, \tag{7.33a}$$

$$C_2 = \frac{1}{2(1+9N_{cap}^2)}\{-[S_1 - \frac{N_{cap}}{2}R_1(1-3S_1)] + 3N_{cap}[R_1 - \frac{N_{cap}}{2}S_1(1-3S_1)]\}, \tag{7.33b}$$

$$D_1 = R_1(R_1^2-3S_1^2), \quad D_2 = S_1(S_1^2-3R_1^2), \tag{7.34a}$$

$$D_3 = \frac{1}{3}R_1^2D_1, \quad D_4 = \frac{2}{3}R_1^4 - \frac{1}{3}R_1D_1 - 2R_1^2S_1^2 - N_{cap}(R_1^2-S_1^2), \tag{7.34b}$$

$$D_5+iD_6 = \frac{i}{12}(R_1+iS_1)^2(D_1-iD_2), \tag{7.34c}$$

$$D_7+iD_8 = \frac{3iC_4^* + (R_1+iS_1)^3(D_1-iD_2)}{12}, \tag{7.34d}$$

$$D_9+iD_{10} = \frac{(1-iN_{cap})}{3\sqrt{2}}(R_2+iS_2)^3, \tag{7.34e}$$

$$D_{11} = -\frac{1}{3}(R_1+iS_1)(D_1-iD_2)+\frac{1}{3}(-2+8iN_{cap})(R_1+iS_1)^4 - 2N_{cap}^2. \tag{7.34f}$$

8 Tidal Dynamics in Coastal Aquifers in Estuarine Zone

8.1 INTRODUCTION

The evaluation of the tide-induced water table fluctuations in a sandy beach is important for the erosion process, saltwater intrusion, contamination from groundwater discharge and biological activity. Most previous analytical solutions have been limited to the 1D case and included the assumption of a straight coastline. Tidal dynamics in coastal aquifers in a 2D domain, in which alongshore coastline variability is considered, have only recently been investigated. Among these, Sun (1997) developed an analytical model where the tidal fluctuation is modelled in an aquifer is adjacent to an estuary. However, the boundary condition in this model ignored the effects of oceanic tides propagating and attenuating in the estuary. Li et al. (2000*b*) took this into account, and developed a new analytical solution based on the Green's function approach. Their solution demonstrated that interactions between estuarine and oceanic tides on water table fluctuations can be significant. Later, Li et al. (2002*a*) further derived a simplified approximation for the tidal dynamics in an L-shape coastal aquifer. However, all these analyses were limited to a straight coastline.

Recently, Li et al. (2002*b*) proposed a 2D approximation for tide-induced water table fluctuations in a coastal aquifer bounded by rhythmic coastlines, in which both sinusoidal and natural coastlines are considered. However, their solution was based on the linearised Boussinesq equation. As Parlange et al. (1984) pointed out, the solution of non-linear Boussinesq equation could provide better predictions of the groundwater free surface elevation, especially as the amplitude of tidal waves increases. This finding has been further confirmed with a higher-order shallow water expansion (Teo et al., 2003). Therefore, a higher-order solution, which is a direct approximation to the Boussinesq equation, is required to get better insight of the 2D problem. Jeng et al. (2005*a*) was the first attempt considering the tidal dynamic in a coastal aquifer with a sloping beach in 2D estuarine zone. Later, Jeng et al. (2005*e*) further extended the model to the case with capillarity effects.

In this chapter, we extend the aforementioned analytical investigations. A 2D analytical solution for tide-induced water table fluctuations in a sloping beach bounded by rhythmic shorelines will be derived. The solution is based on the second-order governing equation of shallow water expansion. With the new solution, we investigate the effects of beach slope, higher-order components and coastline variation. The second part of this chapter, capillarity effect on the 2D model is considered.

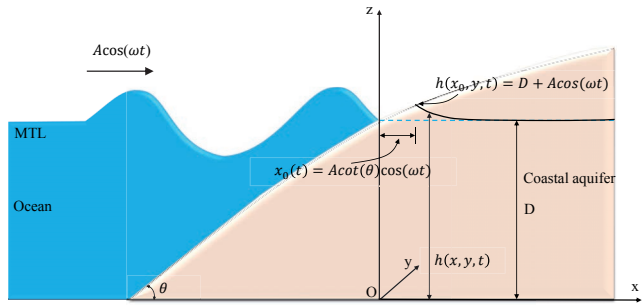

(a) side elevation

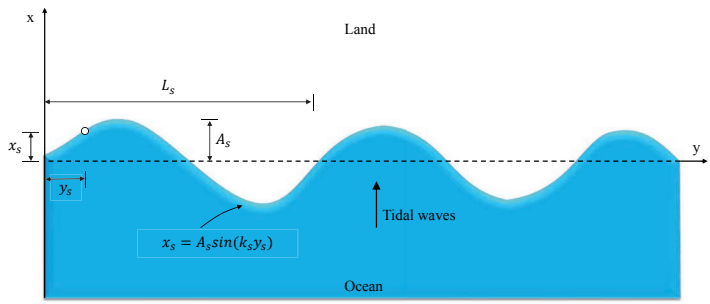

(b) plan view

Figure 8.1 Definition of a 2D coastal aquifer: (a) side elevation; (b) plan view.

8.2 PROBLEM SET-UP

The configuration of the tidal dynamics in coastal aquifers is shown in Figure 8.1. The horizontal x-axis is positive inland from a fixed origin at the mean tidal level (MTL). In the figure, $h(x,y,t)$ is the water table height, and D is the thickness of aquifer. If θ is the slope of the beach, the horizontal extent of the intersection of the sloping beach boundary is

$$x_0(t) = A\cot\theta\cos\omega t, \tag{8.1}$$

where A and ω represent the amplitude and frequency of the tides, respectively. Ignoring the seepage face effects, the condition that the water table heights at the interface of ocean and land (i.e., x_0) are equal to the specified tidal variation, i.e.,

$$h(x_0(t),y_s,t) = D(1+\alpha\cos\omega t) = 0, \quad 0 \le z \le h(x,y,t), \tag{8.2}$$

in which $\alpha(=A/D)$ is the amplitude parameter, representing the ratio of tidal amplitude, A, to the mean thickness of the aquifer, D.

For an incompressible and inviscid fluid in an isotropic and homogeneous porous medium, the potential head $\phi(x,y,z,t) = z + p/\gamma g$, will satisfy the continuity equation which leads to the governing Laplace's equation (Bear, 1972)

$$\frac{\partial^2\phi}{\partial x^2} + \frac{\partial^2\phi}{\partial y^2} + \frac{\partial^2\phi}{\partial z^2}. \tag{8.3}$$

Equation (8.3) can be solved subject to (8.1) and the following boundary conditions:

$$n_e \frac{\partial\phi}{\partial t} = K\left[\left(\frac{\partial\phi}{\partial x}\right)^2 + \left(\frac{\partial\phi}{\partial y}\right)^2 + \left(\frac{\partial\phi}{\partial z}\right)^2\right] - K\frac{\partial\phi}{\partial z}, \quad \text{on } z = h, \tag{8.4a}$$

$$\frac{\partial\phi}{\partial z} = 0, \quad \text{at } z = 0, \tag{8.4b}$$

$$\phi = h, \quad \text{on } z = h, \tag{8.4c}$$

$$\frac{\partial\phi}{\partial z} = 0, \quad \text{as} z \to \infty, \tag{8.4d}$$

where (8.4a) describes the dynamic condition at the free surface, (8.4b) states that vertical flux through the bottom boundary is zero, (8.4c) describes the pressure head at the free surface is zero while (8.4d) states that the tidal influence in the x-direction is eventually negligible. The soil properties in the equations are defined by n_e and K for soil porosity and hydraulic conductivity, respectively. In this study, K is a constant as appropriate for an isotropic and homogeneous material.

A sinusoidal coastline is considered in Figure 8.1(b). The coastline can be described by

$$x_s = A_s \sin(k_s y_s), \tag{8.5}$$

where A_s is the amplitude of the shoreline oscillation, $k_s = 2\pi/L_s$ is its wave number while its wavelength is L_s.

8.3 PERTURBATION APPROXIMATION

8.3.1 NON-DIMENSIONAL PARAMETERS

The horizontal and vertical variables are non-dimensionalised by the tidal decay length (L) and the mean coastal aquifer thickness (D), respectively. These parameters are summarised below.

$$\begin{gathered} X = \frac{x}{L} - \frac{\beta}{\lambda}\sin(\lambda Y) - \alpha\varepsilon\cot\theta\cos T, \\ Y = \frac{Y}{L}, \quad Z = \frac{z}{D}, \quad H = \frac{h}{D}, \quad \Phi = \frac{\phi}{D}, \quad T = \omega t, \\ \varepsilon = \frac{D}{L}, \quad L = \sqrt{\frac{2KD}{n_e\omega}}, \quad \lambda = K_s L, \quad \beta = k_s A_s, \end{gathered} \tag{8.6}$$

where λ is the wave number of coastline fluctuation times the linear decay length and ε is defined as a shallow-water parameter representing the ratio of the mean tidal height to the linear decay length.

8.3.2 PERTURBATION PROCESS

There are three independent parameters defined by the material and the boundary conditions: the shallow water parameter (ε), the mean tidal amplitude parameter (α) and the coastline parameter β). The solution constructed for the problem through a perturbation expansion should be valid for small ε, α and β and a wide range of beach slopes, θ ($0 < \theta \leq \pi/2$).

Both potential head (Φ) and the total water table fluctuation (H) are perturbed with the small parameters ε, α and β.

$$H = 1 + \sum_{m=0}^{1}\sum_{n=1}^{2}\sum_{l=0}^{2} \varepsilon^m \alpha^n \beta^l H_{mnl}, \tag{8.7a}$$

$$\Phi = \sum_{m=0}^{1}\sum_{n=1}^{2}\sum_{l=0}^{2} \varepsilon^m \alpha^n \beta^l \Phi_{mnl}, \tag{8.7b}$$

where the upper limits of the expansion are the first-, second-, and second-order expansion for the shallow-water parameter (ε), amplitude parameter (α) and the coastline parameter (β), respectively.

By introducing the perturbation expansion from (8.7) into the governing equation (8.3) and the boundary conditions (8.4), the following linearised governing equations are obtained;

$$O(\varepsilon^0\alpha^1\beta^0) \quad : \quad 2H_{010T} = \lambda^2 H_{010YY} + H_{010XX}, \tag{8.8a}$$

$$O(\varepsilon^0\alpha^1\beta^1) \quad : \quad 2H_{011T} = \lambda^2 H_{011YY} + H_{011XX} + \lambda \sin(Y) H_{010X} - 2\lambda \cos(Y) H_{010XY}, \tag{8.8b}$$

$$O(\varepsilon^0\alpha^1\beta^2) \quad : \quad 2H_{012T} = \lambda^2 H_{012YY} + H_{012XX} + \lambda \sin(Y) H_{011X} - 2\lambda \cos(Y) H_{011XY} + \frac{1}{2}[1 + \cos(2Y)] H_{010XX}, \tag{8.8c}$$

$$O(\varepsilon^0\alpha^2\beta^0) \quad : \quad 2H_{020T} = \lambda^2 H_{020YY} + H_{020XX} + \frac{1}{2}[1 + \cos(2Y)] H_{010XX}, \tag{8.9a}$$

$$O(\varepsilon^0\alpha^2\beta^1) \quad : \quad 2H_{021T} = \lambda^2 H_{021YY} + H_{021XX} + \lambda \sin(Y) H_{020X} - 2\lambda \cos(Y) H_{020XY} + \frac{1}{2}\lambda \sin(Y)(H_{010}62)_X - \lambda \cos(Y)(H_{010}^2)_{XY} + 2\lambda^2 (H_{010Y} H_{011})_Y$$

$$+H_{010}H_{011YY}+2(H_{010X}H_{011})_X$$
$$+H_{010}H_{011XX}, \tag{8.9b}$$

$$O(\varepsilon^1\alpha^1\beta^0) \quad : \quad 2H_{110T}=\lambda^2H_{110YY}+H_{110XX}, \tag{8.10a}$$
$$O(\varepsilon^1\alpha^1\beta^1) \quad : \quad 2H_{111T}=\lambda^2H_{111YY}+H_{111XX}+\lambda\sin(Y)H_{110X}$$
$$-2\lambda\cos(Y)H_{110XY}, \tag{8.10b}$$

$$O(\varepsilon^1\alpha^2\beta^0) \quad : \quad 2H_{120T}=\lambda^2H_{120YY}+H_{120XX}$$
$$-2\sin(T)\cot(\theta)H_{010X}, \tag{8.11a}$$
$$O(\varepsilon^1\alpha^2\beta^1) \quad : \quad 2H_{121T}=\lambda^2H_{121YY}+H_{121XX}+-\lambda\sin(Y)H_{120X}$$
$$-2\sin(T)\cot(\theta)H_{010X}, \tag{8.11b}$$

The above equations can be solved with the following boundary conditions:

$$H_{010}(0,T)=\cos(T), \quad H_{010X}(\infty,T)=0,$$
$$H_{mnl}(0,T)=0, \quad H_{mnlX}(\infty,T)=0, \tag{8.12}$$
$$m=1,2, \;\; n=0,1,2, \;\; \text{and} \;\; l=0,1,2.$$

8.3.3 ZEROTH-ORDER SHALLOW WATER EXPANSION

By solving the linearised governing equation (8.8) for $O(\varepsilon^0\alpha^1)$ subject to the boundary conditions (8.12), the solutions below are derived;

$$O(\varepsilon^0\alpha^1\beta^0) \quad : \quad H_{010}=e^{iT}\,e^{-k_{010}X}, \tag{8.13a}$$
$$O(\varepsilon^0\alpha^1\beta^1) \quad : \quad H_{011}=\frac{k_{010}}{\lambda}e^{iT}\sin(Y)(e^{-k_{011}X}-e^{-k_{010}X}), \tag{8.13b}$$
$$O(\varepsilon^0\alpha^1\beta^2) \quad : \quad 2H_{012}=\frac{1}{2\lambda}e^{iT}[i\cos(Y)(e^{-k_{012}X}-e^{-k_{010}X})$$
$$+k_{010}k_{011}\cos(2Y)(e^{-k_{011}X}-e^{-k_{012}X})$$
$$+k_{010}k_{011}(e^{-k_{010}X}-e^{-k_{011}X})], \tag{8.13c}$$

where $k_{mn}=\sqrt{2m_i+n^2\lambda^2}$, m,n =0, 1, 2.

The derivations for the higher-order solutions (i.e., $O(\beta^3)$) are laborious. Here, the zeroth-order equation solution is derived up to second-order in β, (8.13). When these solutions are investigated under sandy beach conditions, only minor differences are found in between orders of β^1 and β^2 in terms of water table fluctuations. Therefore, the perturbation solution solved up to first-order in β with higher-order terms in ε and α is considered adequate here.

By solving the linearised governing equation (8.9) for $O(\varepsilon^0\alpha^2)$ subject to the boundary conditions (8.12), the solutions below are derived;

$$O(\varepsilon^0\alpha^2\beta^0) \quad : \quad H_{020} = \frac{1}{4}(1-e^{-2X}) - \frac{1}{2}e^{2iT}(e^{-k_{010}X} - e^{-k_{020}X}), \tag{8.14a}$$

$$\begin{aligned} O(\varepsilon^0\alpha^2\beta^1) \quad : \quad H_{021} = {} & \frac{\lambda}{2(\lambda^2-4)}\sin(Y)(e^{-2X} - e^{-\lambda X}) \\ & -A_{21}\sin(Y)e^{2iT}(e^{-2k_{010}X} - e^{-k_{021}X}) \\ & +A_{22}\sin(Y)e^{2iT}(e^{-2(k_{010}+k_{011})X} - e^{-k_{021}X}) \\ & +\frac{k_{020}}{2\lambda}\sin(Y)e^{2iT}(e^{-k_{020}X} - e^{k_{021}X}). \end{aligned} \tag{8.14b}$$

$$A_{21} = \frac{2k_{010}(k_{010}^2 - k_s^2)}{k_s[4i\lambda^2 - (4k_{010}^2 - k_s^2)]},$$

$$A_{22} = \frac{\lambda k_{010}k_{011}(k_{010}+k_{011})}{4+\lambda^2}.$$

Equations (8.13a) and (8.14a) are identical to those given by Barry et al. (1996) for the shallow flow approximation neglecting capillarity effects (the case considered here).

8.3.4 FIRST-ORDER SHALLOW-WATER EXPANSION

Governing equation (8.10) for the oscillations, $O(\varepsilon\alpha)$, are identical to governing equation (8.8), hence the solutions to the former are zero when the boundary conditions (8.12) are imposed,

$$H_{110} = 0, \quad \text{and} \quad H_{111} = 0. \tag{8.15}$$

The solution derived for (8.11), which are for $O(\varepsilon^1\alpha^2)$, are expressed as:

$$\begin{aligned} O(\varepsilon^1\alpha^2\beta^0) \quad : \quad H_{120} = {} & \frac{\cot\theta}{2}(1+i)[i(1-e^{-k_{010}X}) \\ & +e^{2iT}(e^{-k_{020}X} - r^{-k_{010}X})], \end{aligned} \tag{8.16a}$$

$$\begin{aligned} O(\varepsilon^1\alpha^2\beta^1) \quad : \quad H_{121} = {} & \cot\theta\sin(Y)\left[\frac{i\lambda}{k_{011}^2}\left(e^{-(1-i)X} - e^{-\lambda X}\right)\right. \\ & +\frac{k_{020}k_{010}}{\sqrt{2}\lambda}e^{2iT}\left(e^{-k_{020}X} - e^{-k_{121}X}\right) \\ & \left.+\frac{\lambda(2+i\lambda^2)}{(\lambda^4+4)}e^{2iT}(e^{-k_{121}X} - e^{-k_{010}X})\right]. \end{aligned} \tag{8.16b}$$

Equations (8.13)–(8.16) provide the total solution for water table fluctuations in higher-order form, including real and imaginary oscillations. The solutions derived for different orders can be assembled as a total water table height in the following manner;

$$\begin{aligned} H = 1+ \quad & \alpha(H_{010} + \beta H_{011} + \beta^2 H_{012}) + \alpha^2(H_{020} + \beta H_{021}) \\ & +\varepsilon\alpha(H_{120} + \beta H_{121}). \end{aligned} \tag{8.17}$$

8.3.5 SPECIAL CASES

Equation (8.17) is the new approximation for fluctuations in a 2D coastal unconfined aquifer. Teo et al. (2003) derived the analytical solution for a sloping beach in 1D form. The solution in (8.17) is identical to Teo et al. (2003) when $\beta = 0$. The solution in (8.17) can be further reduced to that for a vertical beach by setting $\theta = \pi/2$. In this case, the solution is identical to that given by Jeng et al. (2005*e*).

8.4 RESULTS AND DISCUSSIONS

8.4.1 COMPARISON WITH EXPERIMENTAL DATA

Since experimental data for 2D case is unavailable, we reduce the present solution to 1D case and compare with recent results (Cartwright et al., 2003, 2004). Details of the experiment can be found in Cartwright et al. (2004). As shown in Figure 8.2, the analytical solution over-all agrees with the experimental results, although a disagreement between all theoretical solutions and experimental data near the ocean wave/inland interface is observed. This disagreement might be caused by the fact that the analytical models ignore the possibility of seepage face effects.

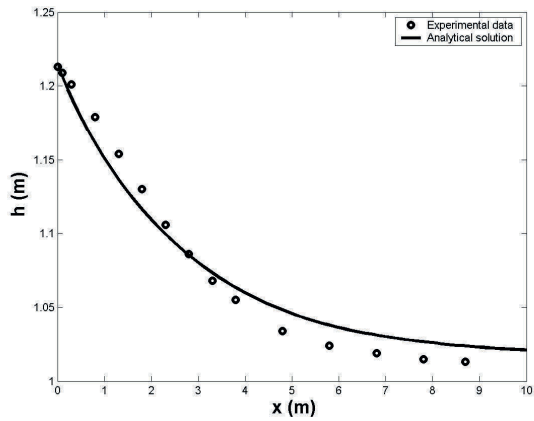

Figure 8.2 Comparison of the present solution and experimental results (Cartwright et al., 2004). Input data: $\varepsilon = 0.469$, $\alpha = 0.202$, $\theta = 11.6°$, $K = 114.5$ m/day.

8.4.2 WATER TABLE FLUCTUATIONS FOR A SANDY BEACH IN A TEMPORAL DOMAIN

The primary aim of this note is to investigate the effect of the higher-order components in the shallow water expansion, beach slopes and the coastline

variability on the fluctuations. The variables used in a prototypical sandy beach is presented are: $K = 20$ m/day, $D = 1.5$ m and $n_e = 0.25$.

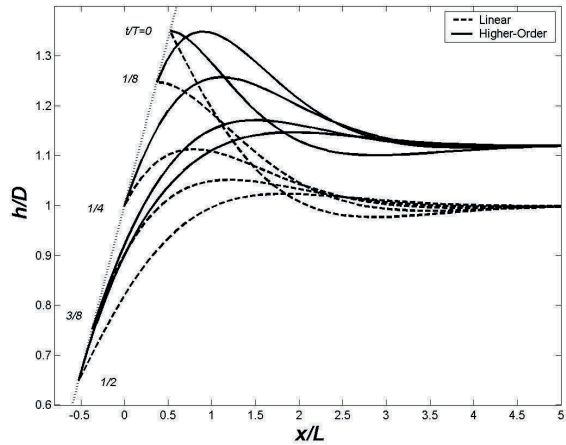

(a) ebb tide

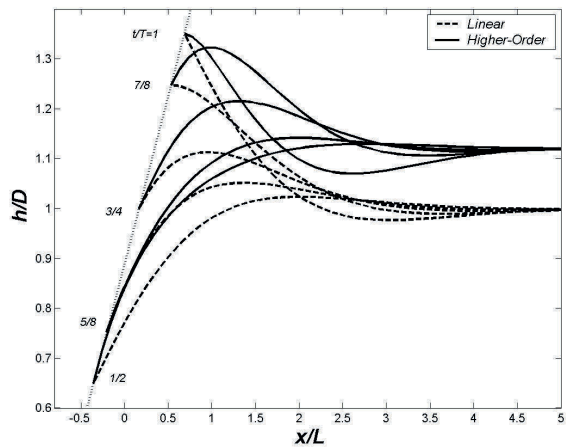

(b) rising tide

Figure 8.3 Effect of water table fluctuations during (a) ebb tide and (b) rising tide ($\varepsilon = 0.4$, $\alpha = 0.35$, $\beta = 0.35$, $\theta = 15^\circ$).

Two sub-graphs in Figure 8.3 are plotted to examine the phenomenon of ebb and rise of the tide. The figures are also plotted in order to compare the linear

and higher-order solutions. The water table at the boundary is affected by the rise and ebb of the mean tide level. In Figure 8.3(a), the water table at the boundary is higher in the early stage of the tide ebb. As the mean tide level reduces further, the water table at the boundary decreases. Away from the boundary, the water table propagates to a constant height where tidal influence is negligible. In Figure 8.3(b), water table fluctuations during tide rise are plotted. The increase of mean tide level at the boundary increases the water table height. Similar decay patterns can be observed for the water table fluctuations during the tide rise. Between the boundary and $x/L = 2.5$, the tidal influence on the water table fluctuations is found to be significant. The plots for linear and higher-order solutions in Figure 8.3 show a relative difference of about 2% at constant water table heights between linear and higher-order solutions.

8.4.3 EFFECTS OF THE RHYTHMIC COASTLINE

Figure 8.4 shows the effect of rhythmic coastlines on water table fluctuations. Recall that β is defined as $k_s A_s$ in (8.6) which in terms of the ratio of coastline length and amplitude is $2\pi A_s/L_s$. For the fluctuation of a rhythmic coastline we typically expect that its wave length (L_s) is much greater than its amplitude (A_s), i.e., $L_s >> A_s$, meaning that relatively low values of β expected. Figure 8.4 shows plots of water table fluctuations with $\beta = 0.1$, 0.3 and 0.5 at the dimensionless distance $x/L = 1$. The figure shows that variations in water table fluctuations result from different coastlines, as represented by β. The variation in different coastlines changes the phase of the fluctuations and amplifies it slightly (Figure 8.4). For example, with the coastline parameter $\beta = 0.1$, the water table height at the peak and trough are found to be approximately 1.0985 and 0.948, respectively. While with coastline parameter of $\beta = 0.5$, the water table height at the peak and through are found to be approximately 1.1065 and 0.927, respectively.

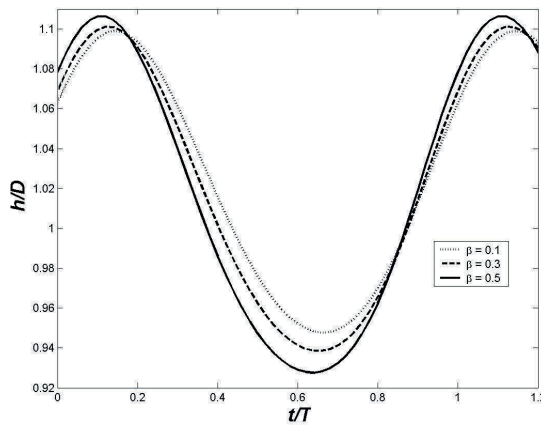

Figure 8.4 Water table fluctuations for different coastline parameters ($\varepsilon = 0.4$, $\alpha = 0.35$, $\theta = 45^\circ$, y/L_s=0.5, x/L=1).

Figure 8.5 displays the effect of coastlines in different order solutions for the water table fluctuations in the x-direction. In the figure, $t/T = 0.3$ with $\beta = 0.1$ and 0.3 for the various solutions. Higher water table heights are produced from lower value of the coastline pa-rameter (i.e., $\beta = 0.1$). The figure also shows the great difference in water table fluctuations between different orders of solutions, reaching about 8% between $O(\varepsilon\alpha^2\beta)$ and $O(\alpha^2\beta)$ and about 11% between $O(\varepsilon\alpha^2\beta)$ and $O(\alpha\beta)$.

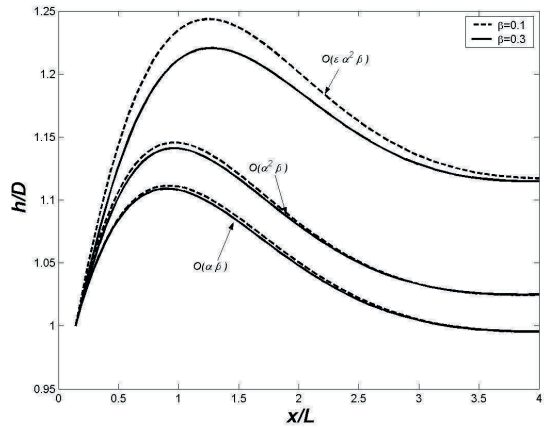

Figure 8.5 Water table fluctuations in the x-direction for various orders of solutions ($\varepsilon = 0.4$, $\alpha = 0.35$, $\theta = 15°$, y/L_s=0.5, t/T=1/4).

8.4.4 EFFECTS OF BEACH SLOPES

The solution derived in this paper considers the sloping beach boundary. The influence of different beach slopes affects the higher-order solution. Figure 6 shows the water table fluctuations for various beach slopes. The water fluctuations vary inversely to the beach slope. A steeper beach slope results in a reduced influence on the water table fluctuations. On the other hand, for a shallowly sloped beach the influence on water table fluctuations will be significant. This phenomenon can be explored with a higher-order solution.

Figure 8.6 show the plots for various beach slopes for different orders of solutions. The values of ε and α adopted in the figures are 0.4 and 0.2, respectively. Greater water table fluctuations can be seen for a beach slope of 30°, especially for the higher-order solution (solid line).

8.5 2D MODEL WITH CAPILLARITY FRINGE

In this section, combing the 2D model for an aquifer in an estarine zone (Jeng et al., 2005*a*) with the solution with capillarity fringe (Jeng et al., 2005*c*), a 2D analytical

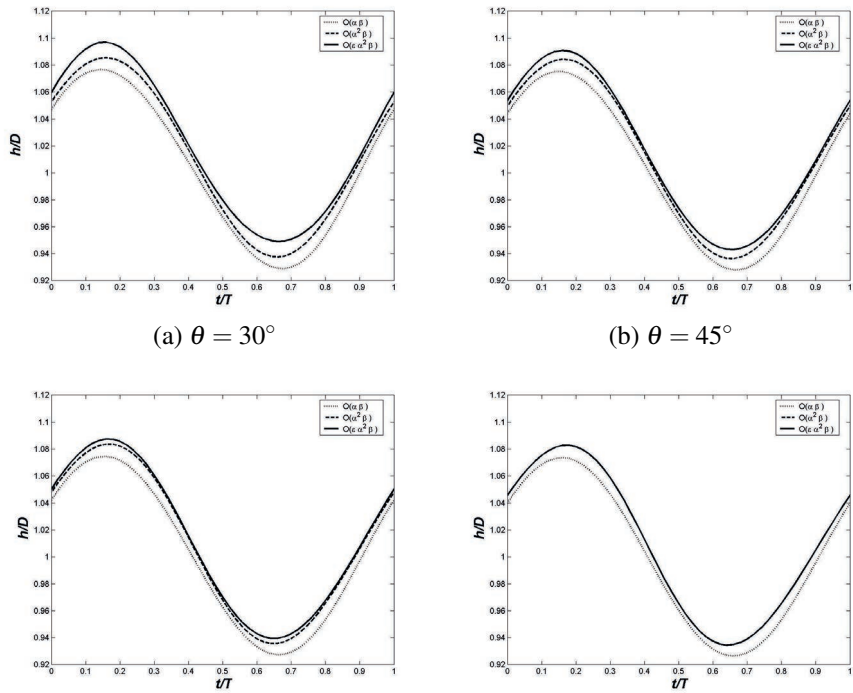

(a) $\theta = 30^\circ$ (b) $\theta = 45^\circ$

(c) $\theta = 60^\circ$ (d) $\theta = 90^\circ$

Figure 8.6 Tide-induced water table fluctuations in various beach slopes (θ) ($\varepsilon = 0.2$, $\alpha = 0.2$, $\beta = 0.1$, y/L_s=0, x/L=1).

solution for tide-induced groundwater fluctuation in a sloping aquifer with capillarity fringe Jeng et al. (2005*e*) will be outlined. Based on parametric study, the effects of the capillarity fringe in 2D case will be discussed.

8.5.1 BOUNDARY VALUE PROBLEMS

Considering tidal fluctuations in a coastal aquifer, as depicted in Figure 8.7, the aquifer is assumed to be homogenous and isotropic. To simplify the problem, only a vertical beach is considered here. The phenomenon is governed by the 2D groundwater flow equation under the Dupuit assumption Bear (1972), with an approximation to account for the capillarity fringe (Parlange and Brutsaert, 1987).

$$n_e \frac{\partial h}{\partial t} = \left(K + B\frac{\partial}{\partial t}\right)\left[\frac{\partial}{\partial x}\left(h\frac{\partial h}{\partial x}\right) + \frac{\partial}{\partial y}\left(h\frac{\partial h}{\partial y}\right)\right], \tag{8.18}$$

where h denotes the water table elevation, n_e is effective porosity, K is hydraulic conductivity, B is the typical capillarity fringe height, and x and y are the cross-shore

and along-shore coordinates, respectively. Note that the capillarity fringe height is small, compared with the thickness of aquifers (Parlange and Brutsaert, 1987).

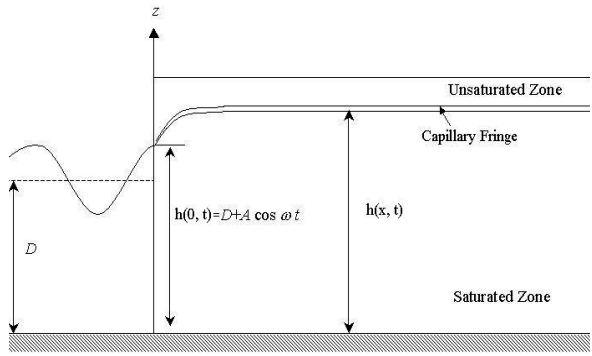

Figure 8.7 Schematic diagrams of a coastal aquifer interacting with tidal signals with a vertical beach.

In this section, a sinusoidal coastline is considered, which can be expressed as that in (8.5) At the boundary along the coastline, the water height is given by the ocean tide fluctuations, that is,

$$h(0,y,t) = D + A\cos(\omega t). \tag{8.19a}$$

Away from the coastline, the water table should be a constant, i.e., zero-gradient of tide-induced water table fluctuations at infinity,

$$\lim_{x\to\infty} \frac{\partial h(x,y,t)}{\partial x} = 0. \tag{8.19b}$$

The other boundary conditions are the same as those given in Section §8.2. The water table elevation, h, in (8.18) is solved subject to the boundary condition (8.19).

8.5.2 ANALYTICAL SOLUTIONS

To obtain the water table elevation (h) in (8.18), a perturbation technique will be used. The principle of a perturbation approximation is to transfer the non-linear differential equations to a set of linear differential equations through the perturbation parameters. In general, the perturbation parameters should be small, which will ensure convergence of the solutions. Since the perturbation parameter is small, the first few terms (or orders) dominate the profile of the solution.

Following the same procedure in Section §8.3.2, with the first perturbation parameter, $\alpha = A/D$, the tide-induced water table fluctuation, h, can be expanded as

$$h = D\left[1 + \alpha h_1 + \alpha^2 h_2 + \alpha^3 h_3 + O(\alpha^4)\right]. \tag{8.20}$$

Then, equation (8.18) can be expanded according to powers of α,

$$O(\alpha): \quad \frac{n_e}{T}\frac{\partial h_1}{\partial t} = \left(1+\frac{B}{K}\frac{\partial}{\partial t}\right)\left(\frac{\partial^2 h_1}{\partial x^2}+\frac{\partial^2 h_1}{\partial y^2}\right), \tag{8.21a}$$

$$\begin{aligned} O(\alpha^2): \quad \frac{n_e}{T}\frac{\partial h_2}{\partial t} = \left(1+\frac{B}{K}\frac{\partial}{\partial t}\right)\Bigg[&\frac{\partial^2 h_2}{\partial x^2}+\frac{\partial^2 h_2}{\partial y^2} \\ &+\frac{\partial}{\partial x}\left(h_1\frac{\partial h_1}{\partial x}\right)+\frac{\partial}{\partial y}\left(h_1\frac{\partial h_1}{\partial y}\right)\Bigg], \end{aligned} \tag{8.21b}$$

where $T = KD$ is the transmissivity of the aquifer.

First-order approximation

Since the boundary condition, (8.5), is not on a straight line, a new coordinate system is introduced with

$$x_1 = x - A_s\sin(k_s y), \quad y_1 = y, \quad t_1 = \omega t. \tag{8.22}$$

With the above transformation, (8.21a) can be rewritten as

$$\begin{aligned} \frac{\omega n_e}{T}\frac{\partial h_1}{\partial t_1} = \left(1+\omega^*\frac{\partial}{\partial t_1}\right)\Big\{&\left(1+\beta^2\cos^2 k_s y_1\right)\frac{\partial^2 h_1}{\partial x_1^2} \\ &-2\beta\cos k_s y_1\frac{\partial^2 h_1}{\partial x_1\partial y_1}+\frac{\partial^2 h_1}{\partial y_1^2}+k_s\beta\sin k_s y_1\frac{\partial h_1}{\partial x_1}\Big\}, \end{aligned} \tag{8.23}$$

where $\omega^* = \omega B/K$ is the inverse of the capillarity number (N_{CAR}, (Li et al., 1997*a*), which is zero when the capillarity effect is ignored.

Now, the second perturbation parameter, β , is introduced to solve (8.23) with the expansion $h_1 = h_{10}+\beta h_{11}+\beta^2 h_{12}+O(\beta^3)$. The solutions of (8.23) for each order of β are given as

$$h_{10} = \mathrm{Re}\{e^{it_1-k_{10}x_1}\}, \tag{8.24a}$$

$$h_{11} = \mathrm{Re}\{\frac{k_{10}}{k_s}\sin k_s y_1 e^{it_1}\left(e^{-k_{11}x_1}-e^{-k_{10}x_1}\right)\}, \tag{8.24b}$$

$$\begin{aligned} h_{12} = \mathrm{Re}\Bigg\{e^{it_1}\Bigg[&\frac{k_{10}^2}{4k_s^2}\cos 2k_s y_1\left(e^{-k_{12}x_1}-e^{-k_{10}x_1}\right) \\ &+\frac{k_{10}k_{11}}{2k_s^2}\cos 2k_s y_1\left(e^{-k_{11}x_1}-e^{-k_{12}x_1}\right) \end{aligned}$$

$$+\frac{k_{10}k_{11}}{2k_s^2}\left(e^{-k_{10}x_1}-e^{-k_{11}x_1}\right)\Bigg]\Bigg\}, \tag{8.24c}$$

where

$$k_{1m}=\sqrt{\frac{in_e\omega}{T(1+i\omega^*)}+m^2k_s^2}, \quad m=0,1,2. \tag{8.24d}$$

Second-order approximation

Since Li et al. (2002*b*) demonstrated that the results up to the order of $O(\alpha\beta)$ and $O(\alpha\beta^2)$ are almost identical for the case of $\alpha \leq 1$, which is the basic requirement of perturbation approximation. Based on this insight, we only derive the solution up to $O(\alpha^2\beta)$ for the second-order approximation.

Substituting (8.22) into the second-order equation, (8.21b), the governing equation becomes,

$$\begin{aligned}\frac{\omega n_e}{T}\frac{\partial h_2}{\partial t_1}=&(1+\omega^*\frac{\partial}{\partial t_1})\{\left(1+\beta^2\cos^2 k_s y_1\right)\frac{\partial^2 h_2}{\partial x_1^2}\\ &-2\beta\cos k_s y_1\frac{\partial^2 h_2}{\partial x_1\partial y_1}+\frac{\partial^2 h_2}{\partial y_1^2}+k_s\beta\sin k_s y_1\frac{\partial h_2}{\partial x_1}\}\\ &+(1+\omega^*\frac{\partial}{\partial t_1})\{\left(1+\beta^2\cos^2 k_s y_1\right)[h_1\frac{\partial^2 h_1}{\partial x_1^2}+(\frac{\partial h_1}{\partial x_1})^2]\\ &-2\beta\cos k_s y_1[h_1\frac{\partial^2 h_1}{\partial x_1\partial y_1}+\frac{\partial h_1}{\partial x_1}\frac{\partial h_1}{\partial y_1}]\\ &+[\frac{\partial^2 h_1}{\partial y_1^2}+(\frac{\partial h_1}{\partial y_1})^2]+h_1\frac{\partial^2 h_1}{\partial x_1\partial y_1}\\ &+k_s\beta\sin k_s y_1 h_1\frac{\partial h_1}{\partial x_1}\}.\end{aligned} \tag{8.25}$$

Proceeding as for the first-order approximation, we obtain the second-order solution (h_{20} and h_{21}):

$$\begin{aligned}h_{20}=&\mathrm{Re}\{\frac{1}{4}[1-\exp(-2k_{10r}x_1)]\\ &+\frac{[-(1+6\omega^{*2})+i\omega^*]}{2(1+9\omega^{*2})}\exp(2i\omega t)\left[\exp(-2k_{10}x_1)-\exp(-k_{20}x_1)\right]\},\end{aligned} \tag{8.26a}$$

$$\begin{aligned}h_{21}=&\mathrm{Re}\{-\frac{k_{10r}\left(4k_{10r}^2+k_s^2\right)}{2k_s\left(4k_{10r}^2-k_s^2\right)}[\exp(-k_s x_1)-\exp(-2k_{10r}x_1)]\sin\left(k_s y_1\right)\\ &+A_{21}\exp(2i\omega t)\sin\left(k_s y_1\right)\left(\exp(-2k_{10}x_1)-\exp(-k_{21}x_1)\right)\end{aligned}$$

$$+A_{22}\exp(2i\omega t)\sin(k_s y_1)\left(\exp(-(k_{10}+k_{11})x_1)-\exp(-k_{21}x_1)\right)$$
$$+A_{23}\sin(k_s y_1)\exp(2i\omega t)(\exp(-k_{20}x_1)-\exp(-k_{21}x_1))\},\tag{8.26b}$$

where

$$k_{2m}=\sqrt{\frac{2in_e\omega}{T(1+2i\omega^*)}+m^2k_s^2},\quad m=0,1,\tag{8.26c}$$

$$A_{21}=\frac{2k_{10}(1+2i\omega^*)\left(k_{10}^2-A_{20}k_s^2\right)}{k_s\left[4i\lambda^2-(1+2i\omega^*)(4k_{10}^2-k_s^2)\right]},\tag{8.26d}$$

$$A_{22}=\frac{k_{10}(1+2i\omega^*)\left(2\left(k_{10}+k_{11}\right)^2-k_s^2\right)}{k_s\left[4i\lambda^2-(1+2i\omega^*)\left((k_{10}+k_{11})^2-k_s^2\right)\right]},\tag{8.26e}$$

$$A_{23}=\frac{(1+2i\omega^*)A_{20}k_sk_{20}}{\left[4i\lambda^2-(1+2i\omega^*)(k_{20}^2-k_s^2)\right]}.\tag{8.26f}$$

8.5.3 COMPARISON WITH PREVIOUS SOLUTIONS

Based on the above analytical solution, the effects of capillarity fringe, higher-order components and the shape of the coastline on the tidal fluctuation in a coastal aquifer will be examined. The input data used in the numerical examples are listed in Table 8.1. The two non-dimensional parameters, α and β, are used in the numerical examples. As noted above, the first parameter, α, represents the effect of non-linearity in the governing equation while the second, β, incorporates the influence of coastline oscillation. Note that the order of the magnitude of α and β could be different, depending on the field data.

Table 8.1
Parameters in numerical examples.

Parameter	Value
n_e	0.25
K	1.8 m/hr
A	1 m or 2 m
D	5 m
ω	0.5236 rad/hr
A_s	1 m or 2 m
L_s	20 m
B	0.25 m or various (0 $\sim$ 2 m)

Since neither experimental nor field data have been available for both capillarity effects and 2D cases, the new solution will be verified by comparing with the following well-known solutions, which are the special cases of the present model.

(1) 2D model without capillarity effects: The analytical solution proposed by Li et al. (2002*b*) is a solution to O(α) without capillarity effects. It is clear that if $\omega^* = 0$ (i.e., capillarity effects are ignored), (8.24a)–(8.24d)) are identical to the solution of Li et al. (2002*b*).

(2) 1D model with capillarity effects: If a straight coastline is considered, i.e., the O($\alpha^2\beta^0$) term and $k_s = 0$, the proposed 2D solution reduces to the 1D solution of Barry et al. (1996).

(3) 1D model without capillarity effects: For a straight coastline and ignoring the capillarity fringe, i.e., $\omega^* = 0$ and O($\alpha^2\beta^0$) term dropped, the present solution is identical to Parlange et al. (1984).

The behaviour of the water table fluctuations, $h - D$, versus time, t, for various order solutions at the embayment centres ($y_1 = y = 5$ m) and at headlands ($y_1 = y =$ 15 m) is illustrated in Figures 8.8 and 8.9, respectively. Four sets of perturbation parameters (α, β) are used to demonstrate the influence of high-order components. The solution proposed by Li et al. (2002) is $O(\alpha\beta^2)$, while the present solution is $O(\alpha^2)$. As shown in the figures, the influence of the higher-order component is important for larger tidal amplitudes, as expected. Figures 8.8 and 8.9 also show the phase shift between solution of different orders of α and β.

The influence of higher-order terms on the approximation is relatively important especially for water table fluctuations at the embayment centre. Fluctuations in this region reduce for the higher-order β solution but increase for the higher-order α solution (Figure 8.8). As a result, the curve computed for $O(\alpha\beta^0)$ appears in between that for $O(\alpha\beta^2)$ and $O(\alpha^2\beta)$. However, both higher-order components of α and β increase the water table fluctuation at the headland centres. This implies that the effects of coastal shape (i.e., β) will enhance the tidal fluctuation at headland centres. The influence of α is expected because the higher-order components of α will certainly become more important for a larger tidal amplitude. However, the difference behaviour of β at the centre of embayments and headlands come from the steady component of the second-order solution, especially the first term in (8.26b).

To examine further the effects of high-order components, the maximum amplitude of the tidal fluctuation ($|h - D|_{max}$) versus the distance inland (x_1) is illustrated in Figure 8.10. As shown there, the amplitude of the water table level decreases with inland distance (x_1). The influence of the second-order component (α^2) can be observed in the figure. Generally speaking, the non-linear effects enhance the water table fluctuations at the centre of the embayment. However, as shown in the figure, the curves calculated from the solution to O($\alpha\beta^2$) (i.e., solid lines) have a rising tail and are lower than the other two solutions. This result comes from the steady term appear in the second-order component, i.e., the first term on the right-hand-side of (8.26a) and (8.26b).

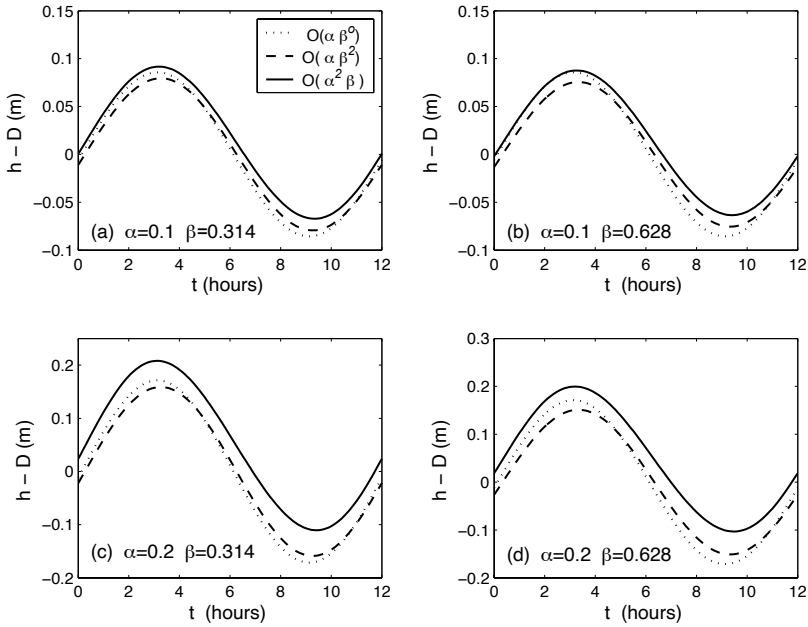

Figure 8.8 Comparison between analytical solutions at centre of embayment with various values of α and β (x_1=20 m, B=0.25 m).

To illustrate the difference between the second-order $O(\alpha^2\beta)$ and first-order $O(\alpha\beta^2)$ components, the difference between the amplitudes of the local water table fluctuation calculated from the two solutions, Li et al. (2002*b*) and the present solution, are plotted in Figure 8.11. The results indicate that the difference between the two solutions varies by up to 5% of the tidal-amplitude.

8.5.4 CAPILLARITY EFFECTS IN 2D CASES

The second objective of this study is to examine the capillarity effects on the tide-induced water table fluctuation in a coastal aquifer. We note that previous analytical approximations on the capillarity correction have been 1D. As shown in the proposed analytical solution, the non-dimensional parameter ω^* ($= \omega B/K$) is an index for capillarity effects.

In general, capillarity effects will be particularly important for the case of high frequency (Li et al., 1997*a*). Typical values of the capillarity fringe height for a sandy beach with coastal tidal forcing would be in the range $B = 0.25 - 0.5$ m, while $B = 2$ m might be appropriate for a lake undergoing seasonal variations with a low permeability aquifer (Bear and Verruijt, 1987; Barry et al., 1996). Thus, the values of $\omega^* = \omega B/K$ vary from 0.0 to 0.145 for a sandy beach with $K = 1.8$ m/hr. In this

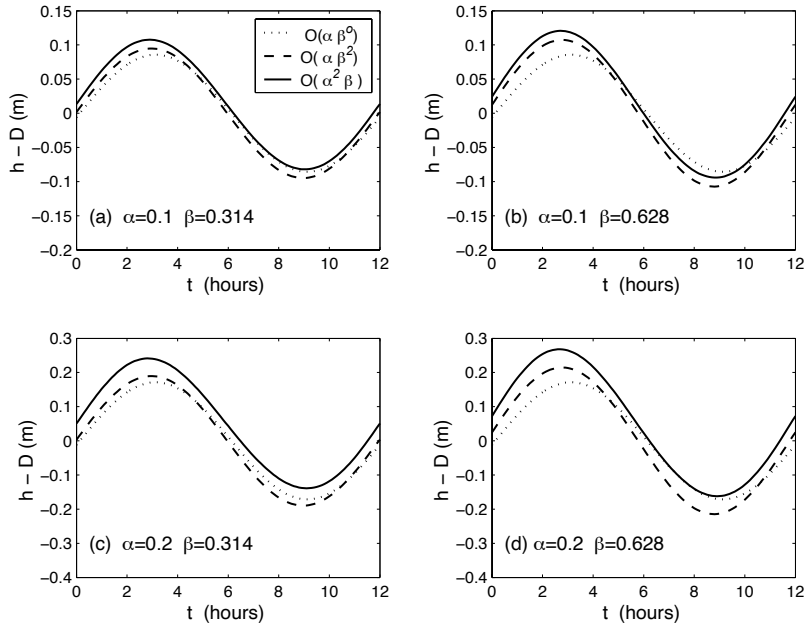

Figure 8.9 Comparison between analytical solutions at centre of headland with various values of α and β. (x_1=20 m, B=0.25 m).

example, we choose the values of ω^* varying between 0 and 0.582 ($B = 0 \sim 2$ m) to cover most of the possible range.

Figure 8.12 illustrates the water table fluctuations in a coastal aquifer for various values of ω^* at embayment and headland centres. As shown in the figure, the capillarity fringe significantly increases the phase lag as ω^* increases (Figure 8.12(a)&(c)). It is also observed that the amplitude of tide-induced water table fluctuations decreases as ω^* increases (Figure 8.12(b)&(d)). It is evident that the capillarity fringe will reduce the magnitude of the tidal fluctuation propagated in the coastal aquifer.

The difference in water table fluctuation between the second-order $O(\alpha^2\beta)$ and first-order $O(\alpha\beta^2)$ components with capillarity effects is plotted in Figure 8.11. Here, the effect of the capillarity fringe on the relative difference between the two solutions is insignificant.

Effects of the shape coastline

The third objective of this study is to examine the effects of the coastline on the tide-induced water table fluctuations. Two parameters are involved: the non-dimensional amplitude of the shoreline oscillations ($\beta = 2\pi A_s/L_s$) and the shape of coastline. The influence of β on the water table fluctuations has been demonstrated in Figures 8.8–8.10. The effect of the coastline shape can be evaluated by examining

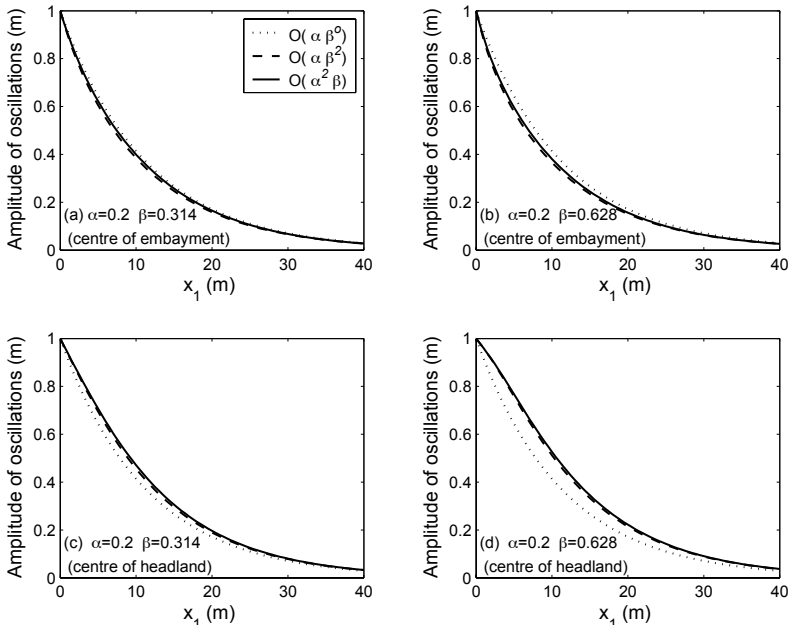

Figure 8.10 Comparison of amplitude of water table fluctuations at centres of embayment (y_1=5 m) and headland (y_1=15 m, B=0.25 m).

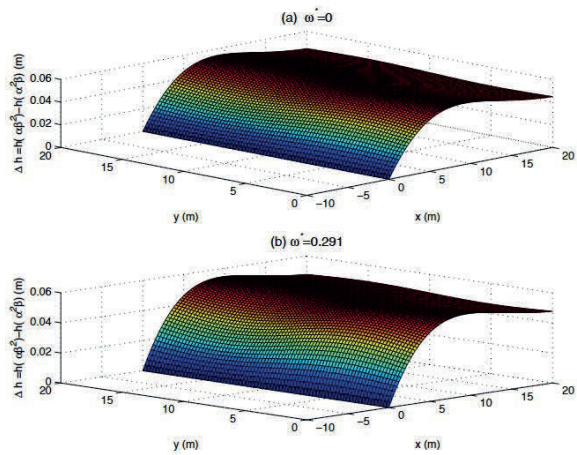

Figure 8.11 Difference in amplitude of the water table based on the present solution and Li et al. (2002*b*). (a) no capillarity effects (ω^*=0); (b) ω^*=0.291.

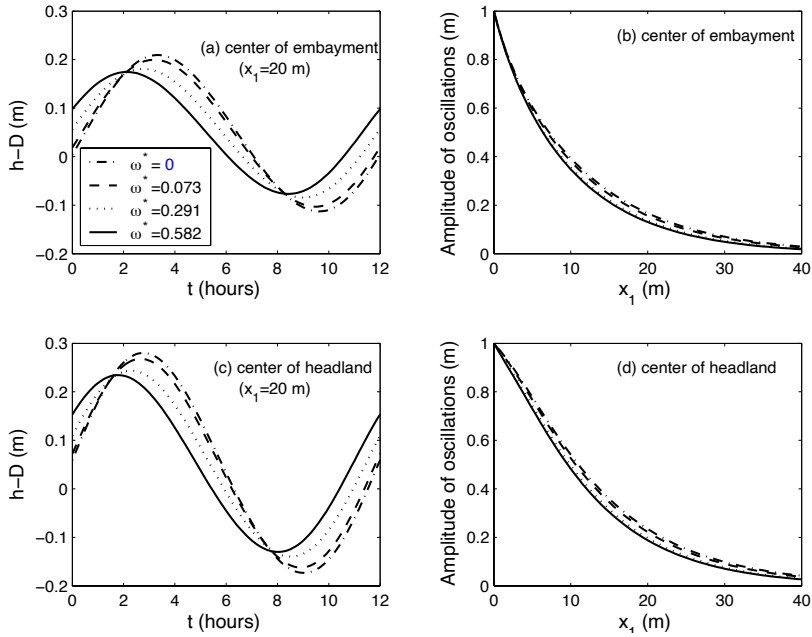

Figure 8.12 Effects of capillarity fringe on the water table fluctuation at centres of embayment (y_1=5 m) and headland (y_1=15 m).

the local damping rate, which is defined by (Li et al., 2002*b*),

$$\kappa_d = -\ln\left[\frac{A(x_1, y_1)}{A(0, y_1)}\right] / x_1. \tag{8.27}$$

Figure 8.13(a) illustrates the effects of high-order components on the local damping rate (k_d). It is clear that the first-order solution, $O(\alpha\beta^2)$, over-estimates the local damping rate. The effect of the capillarity fringe on the local damping rate is illustrated in Figure 8.13(b). The local damping rate significantly increases as ω^* increases, while it decreases as with the distance inland.

8.6 SUMMARY

In this chapter, a new 2D analytical solution for tide-induced water table fluctuations in a sloping beach is derived. In the new solution, the shallow water (ε), amplitude (α) and coastline (β) parameters are used in the perturbation expansion. From the numerical results obtained, the newly derived solution demonstrates that the higher-order components, the beach slopes and the rhythmic coastline are important in the prediction of tide-induced groundwater fluctuations in a coastal aquifer. Conventional analyses of beach water table fluctuations assume a vertical beach and a 1D aquifer. Clearly, in practice, these assumptions will not hold in general, and the analysis presented here permits a mean to quantify departures from that ideal case.

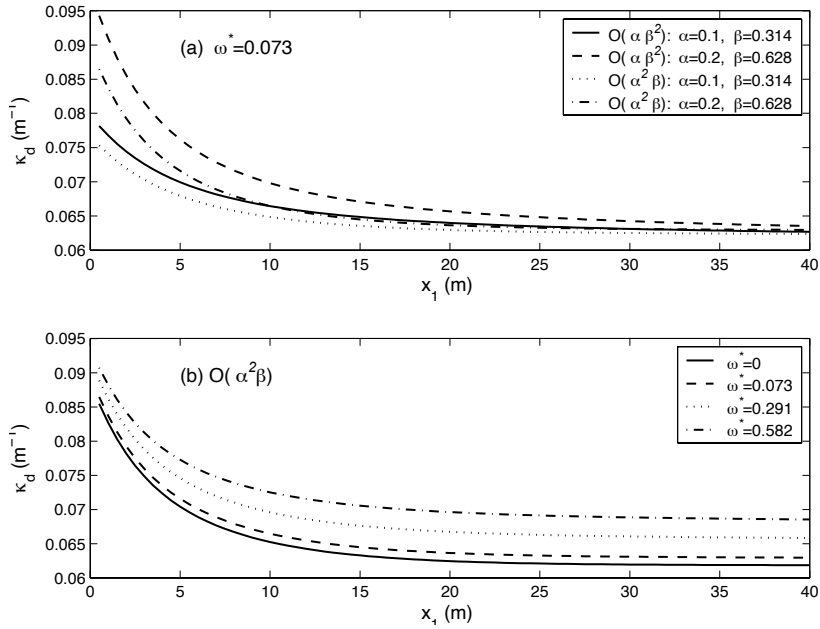

Figure 8.13 Distribution of local damping rate at centre of embayment versus inland distance (x). (a) effects of various order; (b) effects of capillarity fringe.

In the second part of this chapter, the capillarity fringe is included in the 2D model. In general, the capillarity fringe will reduce the tidal fluctuation, as evident in numerical examples. The capillarity fringe also significantly affects the phase of the water table fluctuations. Both the dimensionless amplitude of the coastline oscillation (β) and the local damping rate (k_d) are used to represent the effects of the sinusoidally varying coastline shape on the water table fluctuations. As seen in numerical examples, higher-order components and capillarity effects will reduce the local damping rate.

Taylor & Francis
Taylor & Francis Group
http://taylorandfrancis.com

9 Other Solutions for Tidal Dynamics in Coastal Aquifers

In this chapter, three different cases for tidal dynamics in a coastal aquifer will be discussed. They are:

(1) *Steepness expansion:* The conventional approaches for tidal dynamics in coastal aquifers have been based on the shallow water expansion for both vertical and sloping beaches (Parlange et al., 1984; Nielsen, 1990; Li et al., 2000*b*; Teo et al., 2003; Stojsavljevic et al., 2012). In principle of mathematics, the shallow water expansion is based on perturbation technique, which entirely depends on the perturbation parameters selected. In the shallow water expansion, two perturbation parameters are used: shallow water parameter and amplitude parameter. Therefore, the applicable range of the shallow water expansion will be the limit of these two parameters. Jeng et al. (2005*d*) proposed a new perturbation parameter, steepness parameter, for the tide-induced groundwater fluctuations in coastal aquifers. This approach is named as *steepness expansion*. In this chapter, we will outline this approach.

(2) *Tidal fluctuations in a leaky confined aquifer:* In real coastal aquifers, both phreatic and confined aquifer responses could be co-existed. Most studies treat phreatic and confined aquifers independently, i.e., without leakage effects. However, coupled aquifer systems are commonplace in nature. These aquifers are separated by a thin semi-permeable layer. Where a head difference exists between the unconfined and confined aquifers, leakage through the semi-permeable layer will occur. since the specific yield of the unconfined aquifer is usually several orders of magnitude larger than the confined aquifer's storage coefficient, pressure waves in the confined aquifer tend to propagate much further inland (Erskine, 1991; Farrell, 1994), creating head differences between the aquifers. Consequently, interactions between the confined and unconfined aquifers need to be considered in predicting the tidal oscillations in the aquifers. In this chapter, we will outline the analytical solution for the tidal fluctuations in a leaky confined aquifer.

(3) *Spring-neap tide-induced water table fluctuations:* Most existing studies for tidal dynamics in coastal aquifers focus on single tidal period. However, in reality, tides are more complicated and often bi-chromatic, containing oscillations of at least two different frequencies. For example, in Ardeer,

Scotland, a semi-diurnal solar tide has period $T_1 = 12$ hours, while $T_2 = 12.42$ hours for a semi-diurnal lunar tide (Mao et al., 2006). In this chapter, we will outline the existing studies for Spring-neap tide-induced water table fluctuations.

9.1 STEEPNESS EXPANSION FOR FREE SURFACE FLOW IN COASTAL AQUIFERS

As discussed in Chapter 6, in the shallow-water expansion, the shallow-water parameter ε is defined as the ratio of the mean thickness of the aquifer (D) to a reference length, normally the linear decay length (L) (Teo et al., 2003):

$$\varepsilon = \frac{D}{L} = \sqrt{\frac{n_e \omega D}{2K}}, \quad \text{where} \quad L = \sqrt{\frac{2KD}{n_e \omega}}, \tag{9.1}$$

where n_e is the soil porosity, K the hydraulic conductivity and ω the tidal frequency.

The shallow-water expansion is valid for $\varepsilon << 1$. This assumption will be invalid for conditions such as: high frequencies, deeper aquifers and low hydraulic conductivity. For example, with $D = 5$ m, $T = 0.5$ d (T is the tide period), $\omega = 4\pi$ /d and $n_e = 0.3$, K must satisfy $K > 9.42$ m/day to even satisfy $\varepsilon < 1$. Thus it would be useful to derive a new representation to cover wider ranges of the free surface flow of groundwater.

An alternative parameter that may used to replace the shallow-water parameter is the wave steepness parameter, defined by

$$\xi = \frac{A}{L}, \tag{9.2}$$

where A is the tidal wave amplitude, which is normally much smaller than L, i.e., $\xi << 1$.

In this section, we outline a new analytical solution for tide-induced fluctuations in coastal aquifers, based on the wave steepness ξ (Jeng et al., 2005*d*). The new solution will provide a wider applicable range compared with the conventional shallow-water expansion.

9.1.1 STEEPNESS EXPANSION

Boundary value problem

In this study, the flow is assumed to be homogeneous and incompressible in a rigid porous medium. The flow configuration is shown in Figure 6.1. The effects of seepage through the face are neglected in this study. The boundary value problem is the same as tose presented in (6.3) and (6.4).

It is convenient to introduce the following non-dimensional variables (Teo et al., 2003):

$$\begin{aligned} X &= \frac{x}{L} - \xi \cot(\beta)\cos(\omega t), \quad T = \omega t, \quad Z = \frac{z}{D}, \\ H &= \frac{h}{D}, \quad \Phi = \frac{\phi}{D}, \quad \alpha = \frac{A}{D}. \end{aligned} \tag{9.3}$$

The definitions (9.3) contain two non-dimensional parameters: the steepness (ξ) and the amplitude (α) parameter. The amplitude parameter α, representing the ratio of tidal amplitude (A) to the mean thickness of the aquifer (D), is normally less than unity. The applicable range of the steepness (ξ) has been discussed previously. Thus, there are three independent parameters defined by the material and boundary conditions: ξ, α and β. The approximate solution is constructed assuming that ξ and α are small, and allowing for a large range of β $(0 < \beta < \pi/2)$.

To apply the perturbation technique to the non-linear boundary value problem (6.3) and (6.4), the water table height (H) and potential head (Φ) are expressed in powers of the steepness parameter (ξ):

$$\Phi = \sum_{n=0}^{\infty} \xi^n \Phi_n, \quad \text{and} \quad H = \sum_{n=0}^{\infty} \xi H_n, \tag{9.4}$$

so that to zeroth and first-order:

$$O(1) \quad : \quad 2H_{0T} = (H_0 H_{0X})_X, \tag{9.5a}$$

$$O(\xi) \quad : \quad 2[H_{1T} + \sin(T)\cot(\beta) H_{0X}] = (H_0 H_1)_{XX}, \tag{9.5b}$$

with boundary conditions

$$H_0(0,T) = 1 + \alpha\cos(T), \quad H_1(0,T) = 0, \tag{9.6a}$$

$$H_{0X}(\infty,T) = H_{1X}(\infty,T) = 0. \tag{9.6b}$$

Note that we attempt to solve the water table heights $(h(x,t))$ from the above boundary value problem, not the potential function $(\phi(x,z;t))$ in the interior domain.

Zeroth-order approximation

Since (9.5a) is non-linear, we expand the solution in powers of α, defining H_0 as

$$H_0 = 1 + \sum_{n=1}^{\infty} \alpha^n H_{0n}. \tag{9.7}$$

From equation (9.5a), the equations to be solved for the zeroth-order approximation in ξ are:

$$O(\alpha) \quad : \quad 2H_{01T} = H_{01XX}, \tag{9.8a}$$

$$O(\alpha^2) \quad : \quad 2[H_{02T} = H_{02XX} + (H_{01} H_{01X})_X, \tag{9.8b}$$

$$O(\alpha^3) \quad : \quad 2[H_{03T} = H_{03XX} + (H_{01} H_{02})_{XX}, \tag{9.8c}$$

with boundary conditions

$$H_{01}(0,T) = \cos(T), \quad \text{and} \quad H_{01X}(\infty,T) = 0, \tag{9.9a}$$

$$H_{02}(0,T) = \cos(T), \quad \text{and} \quad H_{02X}(\infty,T) = 0, \tag{9.9b}$$

$$H_{03}(0,T) = \cos(T), \quad \text{and} \quad H_{03X}(\infty,T) = 0. \tag{9.9c}$$

The solution of the zeroth-order boundary value problem can be written as

where

$$H_{01} = e^{-X}\cos(\eta_1), \tag{9.10a}$$

$$H_{02} = \frac{1}{4}\left(1-e^{-2X}\right) + \frac{1}{2}\left[e^{-\sqrt{2}X}\cos(\eta_2) - e^{-2X}\cos(2\eta_1)\right], \tag{9.10b}$$

$$\begin{aligned} H_{03} =& \frac{\sqrt{2}X}{8}\cos\left(\eta_1+\frac{\pi}{4}\right) + \frac{1}{20}\left(e^{-3X}-e^{-X}\right)\left[11\cos(\eta_1)+2\sin(\eta_1)\right] \\ &+ \frac{3+2\sqrt{2}}{8\sqrt{2}}\left[e^{-sqrt3}\cos(\eta_3) - e^{-(\sqrt{2}+1)X}\cos(\eta_4)\right] \\ &+ \frac{1}{4}\left[e^{-X}\cos(\eta_1) - e^{-(\sqrt{2}+1)X}\cos(\eta_5)\right] \\ &+ \frac{1}{8\sqrt{2}}\left[e^{-(\sqrt{2}+1)X}\sin(\eta_5) - e^{-X}\sin(\eta_1)\right] \\ &+ \frac{3}{8}\left[e^{-\sqrt{3}X}\sin(3\eta_1) - e^{-sqrt3X}\sin(\eta_3)\right], \end{aligned} \tag{9.10c}$$

where $\eta_1 = T_X$, $\eta_2 = 2T - \sqrt{2}X$, $\eta_3 = 3T - \sqrt{3}X$, $\eta_4 = 3T - (\sqrt{2}+1)X$, $\eta_5 = T - (\sqrt{2}-1)X$.

First-order approximation

We now consider equation (9.5b). Again, we expand the solution in powers of α, defining H_1 as

$$H_1 = \sum_{n=0}^{\infty} \alpha^n H_{1n}. \tag{9.11}$$

From equation (9.5b), the equations to be solved for the first-order approximation in are:

$$O(\xi\alpha^0) \quad : \quad 2H_{10T} = H_{10XX}, \tag{9.12a}$$

$$\begin{aligned} O(\xi alpha) \quad : \quad & 2[H_{11T} + 2\sin(T)\cot(\beta)H_{01X} \\ & = H_{11XX} + (H_{10}H_{01X})_{XX}, \end{aligned} \tag{9.12b}$$

$$\begin{aligned} O(\xi\alpha^2) \quad : \quad & 2[H_{12T} + 2\sin(T)\cot(\beta)H_{02X} \\ & = H_{12XX} + (H_{01}H_{11} + H_{01}H_{02})_{XX}, \end{aligned} \tag{9.12c}$$

with boundary conditions

$$H_{10}(0,T) = 0, \quad \text{and} \quad H_{10X}(\infty,T) = 0, \tag{9.13a}$$

$$H_{11}(0,T) = \cos(T), \quad \text{and} \quad H_{11X}(\infty,T) = 0, \tag{9.13b}$$

$$H_{12}(0,T) = \cos(T), \quad \text{and} \quad H_{12X}(\infty,T) = 0. \tag{9.13c}$$

The solution of the first-order boundary value problem can be written as

$$H_{10} = 0, \tag{9.14a}$$

$$H_{11} = \frac{1}{\sqrt{2}}\cot(\beta)\left[\frac{1}{\sqrt{2}} - e^{-X}\cos\left(X - \frac{\pi}{4}\right) + e^{-\sqrt{2}X}\cos\left(\eta_2 + \frac{\pi}{4}\right) - e^{-X}\cos\left(\eta_2 + T + \frac{\pi}{4}\right)\right], \tag{9.14b}$$

$$\begin{aligned} H_{12} = \cot(\beta)\Bigg\{ & \frac{1}{2}\left[e^{-2X}\cos(T) - e^{-X}\cos(\eta_1)\right] \\ & + \frac{1}{2}\left[e^{-\sqrt{3}X}\cos\left(\eta_3 + \frac{\pi}{4}\right) - e^{-sqrt2X}\cos\left(T + \eta_2 + \frac{\pi}{4}\right)\right] \\ & + \frac{1}{2}\left[e^{-X}\cos\left(\eta_1 + \frac{\pi}{4}\right) - e^{-\sqrt{2}X}\cos\left(\eta_2 - T + \frac{\pi}{4}\right)\right] \\ & \frac{1}{\sqrt{2}}\left[e^{-2X}\cos\left(\eta_1 - X + \frac{\pi}{4}\right) - e^{-2X}\cos\left(\eta_1 + \frac{\pi}{4}\right)\right] \\ & + \frac{1}{2}\left[e^{-\sqrt{3}X}\cos\left(\eta_3 + \frac{\pi}{4}\right) - e^{-2X}\cos\left(3\eta_1 + X + \frac{\pi}{4}\right)\right] \\ & + \frac{3+2\sqrt{2}}{8}\left[e^{-\sqrt{3}X}\cos\left(\eta_3 + \frac{\pi}{4}\right) - e^{-(\sqrt{2}+1)X}\cos\left(\eta_4 + \frac{\pi}{4}\right)\right] \\ & + \frac{1}{2\sqrt{2}}\left[e^{-X}\cos\left(\eta_3 + \frac{\pi}{4}\right) - e^{-(\sqrt{2}+1)X}\cos\left(\eta_5 + \frac{\pi}{4}\right)\right] \\ & + \frac{1}{4\sqrt{2}}\left[e^{-(\sqrt{2}+1)X}\sin\left(\eta_5 + \frac{\pi}{4}\right) - e^{-X}\cos\left(\eta_1 + \frac{\pi}{4}\right)\right]\Bigg\}. \end{aligned} \tag{9.14c}$$

Note that, from (9.14b) and (9.14c), H_{11} and H_{12} will vanish for the special case, a vertical beach (i.e., $\beta = \pi/2$). As reported in Teo et al. (2003), the solutions for vertical beach only appear in the even-order terms.

9.1.2 RESULTS AND DISCUSSIONS

The major difference between previous shallow-water expansions and the new steepness expansion is the use of a different perturbation parameter, i.e., ξ instead of ε . Figure 9.1 shows an estimate of the applicable ranges corresponding to the two assumptions, $\varepsilon << 1$ and $\xi << 1$, as a function of K. In general, a perturbation parameter should be less than 0.5 (at least), see Kevorkian and Cole (1981), and when the parameter nears unity the expansion will be unreliable. As shown in Figure 9.1, if we choose $\varepsilon = 0.5$ as the critical value, the shallow-water expansion will be invalid when $K < 8$ m/day with $D = 1$ m and $K < 37$ m/day with $D = 5$ m. Clearly the steepness parameter provides a much wider range of applicability for a range of the amplitude parameter, $\alpha = A/D$. Thus using the steepness parameter to replace the shallow-water parameter is a more versatile option.

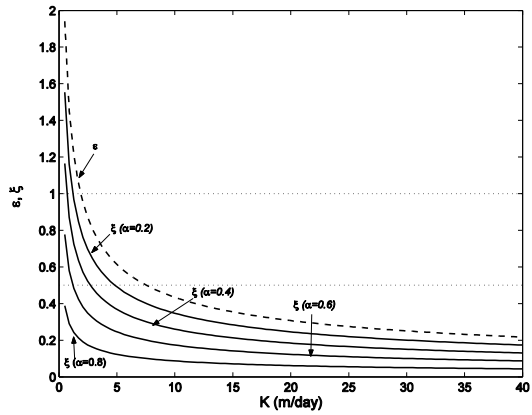

(a) Vertical beach

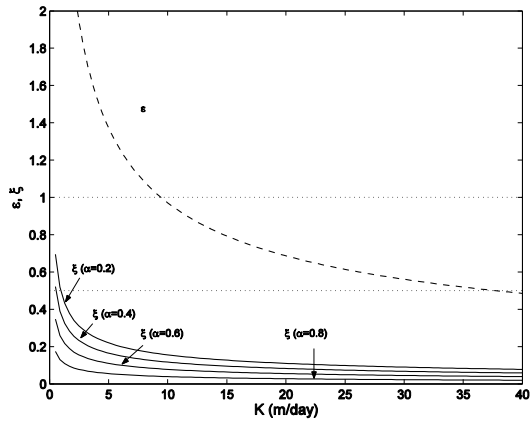

(b) Sloping beach

Figure 9.1 Distribution of the shallow-water parameter (ε) and steepness parameter (ξ) versus hydraulic conductivity (K).

To verify the theoretical models, experimental data from Cartwright et al. (2003, 2004), the shallow-water expansion (Teo et al., 2003) and the present steepness expansion are compared for a vertical beach and a sloping beach with $\beta = 0.202$ (rad). The input data used are shown in Table 9.1 while the results for a vertical beach are illustrated in Figure 9.2(a). The steepness expansion provides a better prediction of the water table level than the shallow-water expansion. Referring to Table 9.1, the shallow-water parameter $\varepsilon = 0.752$, which is close to one, while the steepness parameter $\xi = 0.161$, much less than one. Thus, for this example, the

Table 9.1
Properties of tidal waves and coastal aquifers in experimental work.

Properties	Vertical beach	Sloping beach
Hydraulic conductivity (m/d)	40.6	114
Aquifer thickness (m)	1.094	1.01
Wave period (s)	772	348
Amplitude (m)	0.235	0.204
Shallow-water parameter (ε)	0.752	0.469
Amplitude parameter (α)	0.214	0.202
Steepness parameter (ξ)	0.161	0.095
Slope (β)	$\pi/2$	0.202 (rad)

steepness parameter is a more suitable perturbation parameter than the shallow-water parameter.

The second comparison is for a sloping beach with $\beta = 0.202$. It includes a comparison with the results of Nielsen (1990) and is illustrated in Figure 9.2(b). In this case the steepness expansion provides a slightly better prediction than the shallow expansion, while Nielsen's solution does not fully satisfy the boundary condition at $X = 0$ (Li et al., 2000*b*; Teo et al., 2003). It is also noted that there is a disagreement between all theoretical solutions and the experiments near the ocean wave/inland interface. This may come from the neglect of seepage at the beach face in the models.

Figure 9.3 illustrates the amplitudes of the tide-induced water table fluctuations versus horizontal distance for both expansions. The two expansions give similar results for the case of high hydraulic conductivity (for example $K = 5$ m/day). The difference between the two expansions increases as K decreases. When K is smaller than a particular value, for example $K = 14$ m/d in Figure 9.3, the shallow-water expansion is clearly incorrect. The expansion diverges as X increases because the parameter is greater than one.

9.2 TIDAL FLUCTUATION IN A LEAKY CONFINED AQUIFER

Tidal propagation in coastal aquifers has been subject to numerous studies in recent years (e.g., Baird et al. (1998); Jiao and Tang (1999); Li et al. (1997*b*, 2000*b*); Nielsen (1990); Turner et al. (1997); Turner (1998)). Most studies treat phreatic and confined aquifers independently, i.e., without leakage effects. However, coupled aquifer systems are commonplace in nature. Figure 9.4 shows a representative case of a leaky confined aquifer overlain by a phreatic aquifer (Chen and Jiao, 1999; Li et al., 2001). These aquifers are separated by a thin semi-permeable layer. Where a head difference exists between the unconfined and confined aquifers, leakage through the

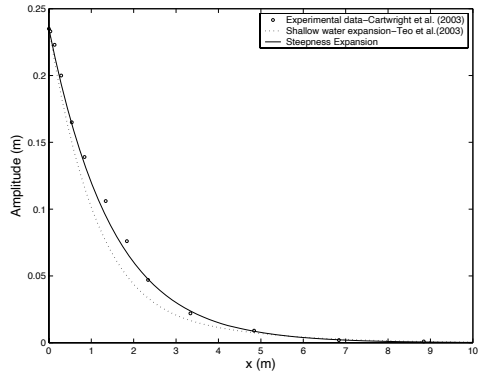

(a) $D = 1$ m

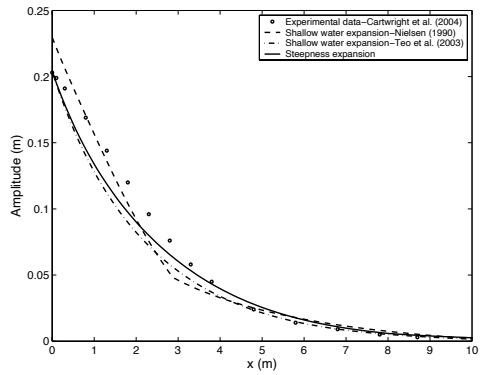

(b) $D = 5$ m

Figure 9.2 Comparison of the two models against experimental data in (a) a vertical beach and (b) a sloping beach.

semi-permeable layer will occur. Note that the aquifer configuration shown in Figure 9.4 will almost certainly give rise to head differences. That is, since the specific yield of the unconfined aquifer is usually several orders of magnitude larger than the confined aquifer's storage coefficient, pressure waves in the confined aquifer tend to propagate much further inland (Chen and Jiao, 1999; Erskine, 1991; Farrell, 1994; Jiao and Tang, 1999), creating head differences between the aquifers. Consequently, interactions between the confined and unconfined aquifers need to be considered in predicting the tidal oscillations in the aquifers.

Jiao and Tang (1999, 2001) presented an analytical solution of tidal fluctuations in a confined aquifer including leakage effects. In their approach, two assumption were made:

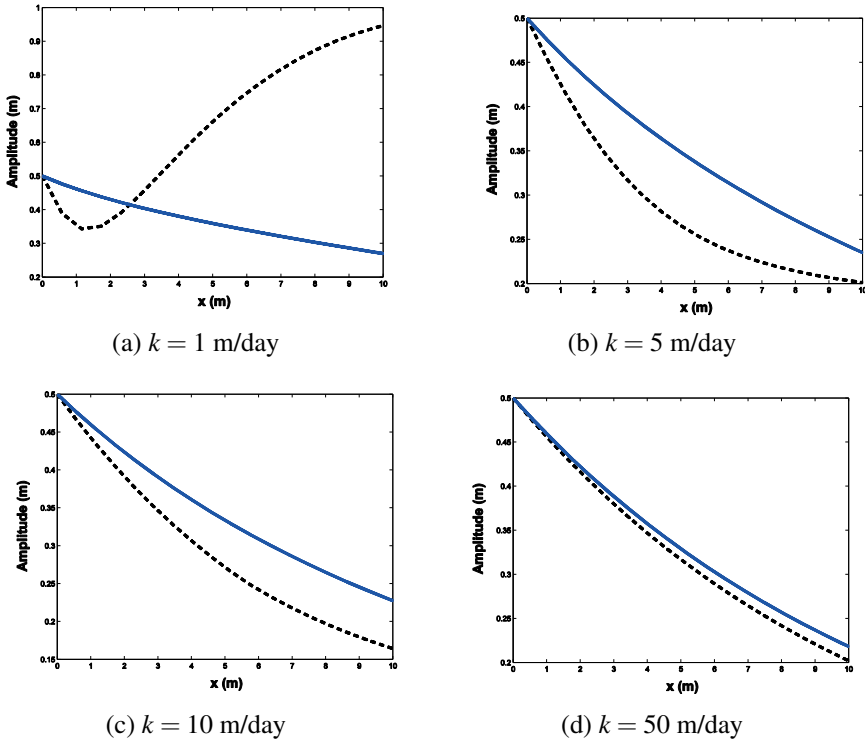

(a) $k = 1$ m/day (b) $k = 5$ m/day

(c) $k = 10$ m/day (d) $k = 50$ m/day

Figure 9.3 Comparison of the two models for various values of K. Solid lines represent steepness expansion and dashed lines denote shallow-water expansion.

(1) The storage of the semi-permeable layer is negligible. As Li and Jiao (2001) reported, this assumption is only valid when the storage ratio of the semi-permeable to the confined aquifers is less than 0.5.

(2) The water table fluctuation in the unconfined aquifer is negligible, leading to a constant head above the semi-permeable layer. Thus, the vertical leakage through the semi-permeable layer is proportional to the difference between the confined aquifer's head and the constant head of the unconfined aquifer. Although the tidal water table fluctuations are likely to be damped quickly in the unconfined aquifer, the effects of these oscillations will still be transmitted to the confined aquifer (Volker and Zhang, 2001). These transmitted oscillations are important, particularly where the semi-permeable layer has a large leakage capacity (Li et al., 2001). Moreover, ignoring transmitted water table fluctuations obviously inhibits detailed studies of the leakage effects on tidal propagation in the unconfined aquifer.

In this section, the closed-form analytical solution for tidal responses in a fully coupled leaky confined and unconfined aquifer system (see Figure 9.4) derived

by Jeng et al. (2002) will be outlined. Because we relax the second assumption of Jiao and Tang (1999), the new solution will provide a closer representation of the reality and enable studies of tidal interactions between a leaky confined and unconfined aquifers. In addition, we compare the exact solution with our earlier approximation (Li et al., 2001). That approximation was derived on the assumption that the semi-permeable layer was such that only perturbations were transmitted between layers. The range of applicability of the perturbation approximation is examined.

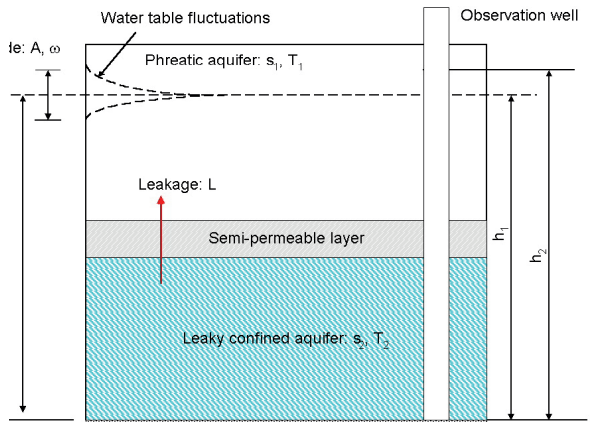

Figure 9.4 Schematic diagram of a leaky confined aquifer with an overlying phreatic aquifer.

9.2.1 BOUNDARY VALUE PROBLEM

We consider tidal fluctuations in both confined and phreatic aquifers, as shown in Figure 9.4. These two homogeneous and isotropic aquifers interact with each other through leakage. The origin of the (horizontal, positive landward) x axis is at the beach face, the slope of which is ignored. The flows in both aquifers are assumed to be essentially horizontal and are governed by (Bear and Verruijt, 1987; Li et al., 2001)

$$s_1 \frac{\partial h_1}{\partial t} = T_1 \frac{\partial^2 h_1}{\partial x^2} + L(h_2 - h_1), \tag{9.15a}$$

$$s_2 \frac{\partial h_2}{\partial t} = T_2 \frac{\partial^2 h_2}{\partial x^2} + L(h_1 - h_2), \tag{9.15b}$$

where h_1 and h_2 are the heads in the confined and the phreatic aquifers, respectively; s_1 and T_1 are the specific yield and transmissivity of the phreatic aquifer, respectively; s_2 and T_2 are the storage coefficient and transmissivity of the confined aquifer, respectively; and L is the specific leakage of the semi-permeable layer. Note that

the equation for the phreatic aquifer, (9.15a), has been linearised. The conditions under which the linearisation is applicable are well known (Bear and Verruijt, 1987).

We recall that h_1 was assumed to be constant in Jiao and Tang (1999)'s solution. Here, we consider h_1 as a variable, reflecting tidal water table fluctuations in the phreatic aquifer. The boundary conditions are,

$$h_1(0,t) = h_2(0,t) = h_M + A\cos\omega t, \tag{9.16a}$$

$$\frac{\partial h_1}{\partial x}|_{x\to\infty} = \frac{\partial h_2}{\partial x}|_{x\to\infty} = 0, \tag{9.16b}$$

where A and ω are the tidal amplitude and frequency, respectively; and h_M is the time-averaged elevation of the mean sea level. Equation (9.16a) represents a single tidal constituent. Multiple tidal constituents can easily be included by superposition of the solution presented below. Note that (9.16b) represents the no-flow lateral boundary conditions.

9.2.2 ANALYTICAL SOLUTION

The governing equations (9.15a) and (9.15b) can be solved directly with the boundary conditions (9.16a) and (9.16b). We first re-organise (9.15a) as

$$h_2 = \frac{1}{L}\left\{ s_1\frac{\partial h_1}{\partial t} - T_1\frac{\partial^2 h_1}{\partial x^2}\right\} + h_1. \tag{9.17}$$

Substitution of (9.17) into (9.15b) yields

$$\begin{aligned}\frac{T_1T_2}{L}\frac{\partial^4 h_1}{\partial x^4} - \left(\frac{s_2T_1}{L}+\frac{s_1T_2}{L}\right)\frac{\partial^3 h_1}{\partial x^2\partial t} - (T_1+T_2)\frac{\partial^2 h_1}{\partial x^2}\\ + \frac{s_1s_2}{L}\frac{\partial^2 h_1}{\partial t^2} + (s_1+s_2)\frac{\partial h_1}{\partial t} = 0.\end{aligned} \tag{9.18}$$

As usual in problems involving a periodic boundary condition, the solution is most easily found by writing the problem in complex form. According to the boundary condition (9.16a), the tidal head fluctuation can be expressed as

$$h_1(x,t) = h_M + \mathbf{Re}\left[H_1 e^{-i\omega t}\right],\quad h_2(x,t) = h_M + \mathbf{Re}\left[H_2 e^{-i\omega t}\right]. \tag{9.19}$$

Then, substituting (9.19) into (9.18), we have

$$\begin{aligned}\frac{T_1T_2}{L}\frac{\partial^4 H_1}{\partial x^4} + \frac{i\omega}{L}(s_2T_1+s_1T_2)\frac{\partial^2 H_1}{\partial x^2} - (T_1+T_2)\frac{\partial^2 H_1}{\partial x^2}\\ + \left[-\omega^2\frac{s_1s_2}{L} - i\omega(s_1+s_2)\right]H_1 = 0.\end{aligned} \tag{9.20}$$

The general solution to the fourth-order ordinary differential equation, (9.20), is of the following form (Pearson, 1983)

$$H_1(x) = \left\{ a_1 e^{\lambda_1 x} + a_2 e^{-\lambda_1 x} + a_3 e^{\lambda_2 x} + a_4 e^{-\lambda_2 x} \right\}, \tag{9.21a}$$

where

$$\lambda_{1,2}^2 = \frac{1}{2}\left[-b \pm \sqrt{b^2 - 4c} \right], \tag{9.21b}$$

$$b = i\omega \left(\frac{s_2}{T_2} + \frac{s_1}{T_1} \right) - L\left(\frac{1}{T_2} + \frac{1}{T_1} \right), \tag{9.21c}$$

$$c = -\frac{\omega^2 s_1 s_2}{T_1 T_2} - \frac{i\omega L}{T_1 T_2}(s_1 + s_2). \tag{9.21d}$$

To satisfy the boundary conditions (9.16b), (9.21a) is reduced to

$$h_1(x,t) = h_M + \mathbf{Re}\left\{ \left[a_2 e^{-\lambda_1 x} + a_4 e^{-\lambda_2 x} \right] \; e^{-i\omega t} \right\}, \tag{9.22}$$

where λ_1 and λ_2 have been chosen so that their real parts are positive. From (9.17), we have

$$\begin{aligned} h_2(x,t) = h_M + \Bigg\{ & \left[(1 - \frac{i s_1 \omega}{L}) - \frac{T_1 \lambda_1^2}{L} \right] a_2 e^{-\lambda_1 x} \\ & + \left[(1 - \frac{i s_1 \omega}{L}) - \frac{T_1 \lambda_2^2}{L} \right] a_4 e^{-\lambda_2 x} \Bigg\} \; e^{-i\omega t}. \end{aligned} \tag{9.23}$$

Then, we can obtain a_2 and a_4 using the boundary conditions (9.16a) as follows

$$a_2 = -\frac{i s_1 \omega + T_1 \lambda_2^2}{T_1(\lambda_1^2 - \lambda_2^2)} A \quad \text{and} \quad a_4 = \frac{i s_1 \omega + T_1 \lambda_1^2}{T_1(\lambda_1^2 - \lambda_2^2)} A. \tag{9.24}$$

To obtain a similar expression for h_2, we re-organise (9.15b) as

$$h_1 = \frac{1}{L}\left\{ s_2 \frac{\partial h_2}{\partial t} - T_2 \frac{\partial^2 h_2}{\partial x^2} \right\} + h_2. \tag{9.25}$$

Substituting (9.19) and (9.25) into to (9.15a), we have

$$\begin{aligned} & \frac{T_1 T_2}{L}\frac{\partial^4 H_2}{\partial x^4} + \frac{i\omega}{L}(s_2 T_1 + s_1 T_2)\frac{\partial^2 H_2}{\partial x^2} - (T_1 + T_2)\frac{\partial^2 H_2}{\partial x^2} \\ & \qquad + \left[-\omega^2 \frac{s_1 s_2}{L} - i\omega(s_1 + s_2) \right] H_2 = 0. \end{aligned} \tag{9.26}$$

Following the foregoing approach, the solution of h_2 can be expressed as,

$$h_2(x,t) = h_M + \mathbf{Re}\left\{ \left[b_2 e^{-\lambda_1 x} + b_4 e^{-\lambda_2 x} \right] \; e^{-i\omega t} \right\}, \tag{9.27a}$$

where

$$b_2 = -\frac{i s_2 \omega + T_2 \lambda_2^2}{T_2(\lambda_1^2 - \lambda_2^2)} A, \qquad b_4 = \frac{i s_2 \omega + T_2 \lambda_1^2}{T_2(\lambda_1^2 - \lambda_2^2)} A. \tag{9.27b}$$

9.2.3 SPECIAL CASE I: CONSTANT HEAD IN THE SEMI-PERMEABLE LAYER

As mentioned previously, Jiao and Tang (1999)'s approximation considered a constant head in semi-permeable layer, i.e., h_1 = constant, which is a special case of the present solution with $s_1 \to \infty$ and $T_1 \to 0$.

To avoid the secular root arising from h_1 components in the present solution, we substitute $T_1/T_2 \to 0$ (i.e., $T_1 << T_2$) into (9.26), leading to

$$\left(\frac{i\omega s_1 T_2}{L} - T_2\right)\frac{\partial^2 H_2}{\partial x^2} - \left[\omega^2 \frac{s_1 s_2}{L} + i\omega(s_1 + s_2)\right] H_2 = 0. \tag{9.28}$$

The root of the above equation is

$$\lambda^2_{h_1=constant} = \frac{\omega^2 s_1 s_2 + i\omega L(s_1 + s_2)}{i\omega s_1 T_2 - T_2 L}. \tag{9.29}$$

When $s_1 >> s_2$ (i.e., $s_1/s_2 \to \infty$), $\lambda_{h_1=constant}$ becomes

$$\lambda^2_{h_1=constant} = \frac{-i\omega s_2}{T_2} + \frac{L}{T_2}, \tag{9.30}$$

which is identical to the λ in Jiao and Tang (1999)'s solution (Note that we use $A\mathbf{Re}\{\exp(-i\omega t)\}$, while Jiao and Tang (1999) uses $A\mathbf{Re}\{\exp(i\omega t)\}$). Thus, the present solution can be reduced to obtain the previous solution (Jiao and Tang, 1999).

9.2.4 SPECIAL CASE II: NO LEAKAGE

For the special case without leakage (i.e., $L = 0$), it is easy to obtain from the present solution the standard solution without leakage. Substitution of $L = 0$ into (9.21b)–(9.21d) gives

$$\lambda_1 = (1-i)\sqrt{\frac{\omega s_1}{2T_1}} \quad \text{and} \quad \lambda_2 = (1-i)\sqrt{\frac{\omega s_2}{2T_2}}. \tag{9.31}$$

Then, we have

$$h_1 = h_M + \mathbf{Re}\left\{A e^{-(\lambda_1 x + i\omega t)}\right\}, \quad \text{and} \quad h_2 = h_M + \mathbf{Re}\left\{A e^{-(\lambda_2 x + i\omega t)}\right\}, \tag{9.32}$$

h_2 in equation (9.32) is identical to Jiao and Tang (1999)'s solution with $L = 0$.

In summary, the present solution is a generalisation of previous solutions. In particular, the water table solution (9.22) includes the leakage effects due to the confined aquifer, which are ignored in the previous solution (Jiao and Tang, 1999). The confined aquifer solution (9.23) incorporates the dynamic effects of the unconfined aquifer. In the following section, we shall examine these effects.

Table 9.2
Input data for the case study.

Quantity	Value
Leakage L	1/day or varying
Transmissivity of unconfined aquifer T_1	2000 m^2/day or varying
Transmissivity of confined aquifer T_2	2000 m^2/day
Non-dimensional transmissivity parameter T	1 or varying
Storativity indexstorativity s_1	0.3
Storativity s_2	0.001
Non-dimensional storativity coefficient s	300 or varying
Amplitude of tide A	0.65 m
Tidal speed ω	2π rad/day
Mean sea level h_M	0

9.2.5 LEAKAGE EFFECTS ON TIDAL FLUCTUATIONS IN THE CONFINED AND PHREATIC AQUIFERS

Aquifer conditions used in the calculations are collected in Table 9.2. The values used in the numerical examples fill in the possible ranges of the parameters reported in the literature (Li et al., 2001). The leakage effects on the amplitude of head fluctuations in the confined aquifer ($|H_2|$) are illustrated in Figure 9.5(a). In the figure, solid lines represent the present solution, and dashed lines are predictions of Jiao and Tang (1999)'s solution. In general, the differences between the two solutions increase as leakage (L) increases. The present solution indicates that Jiao and Tang (1999)'s solution, ignoring the water table fluctuations, over-predicts the damping of tidal head fluctuations in the confined aquifer due to leakage. Figures 9.5(b)–(d) display the head fluctuations over a tidal cycle at $x = 50$ m. The results again demonstrate the differences between the present solution and that of Jiao and Tang (1999). Differences exist in both the amplitude and phase of the head fluctuations.

As mentioned above, the leakage effects of the confined aquifer on the water table fluctuation in the phreatic aquifer were ignored by previous analytical solutions. Based on the present solutions, we shall examine the importance of these effects. Figure 9.6(b) presents the leakage effects on the water table fluctuation in the phreatic aquifer ($|H_1|$). Generally speaking, the amplitude of h_1 increases as leakage (L) increases. The leakage effect on h_1 is considerable although it is less than that on h_2.

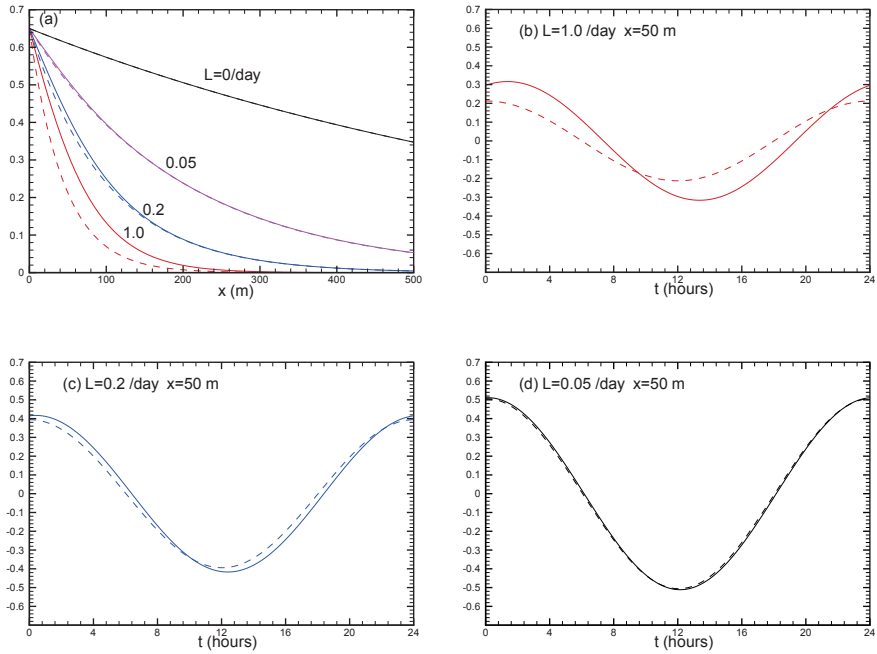

Figure 9.5 Change of groundwater heads in the confined aquifer for various values of leakage, L. Solid lines denote the present solution, dashed lines for Jiao and Tang (1999) ($s = 300$, $T = 1$) .

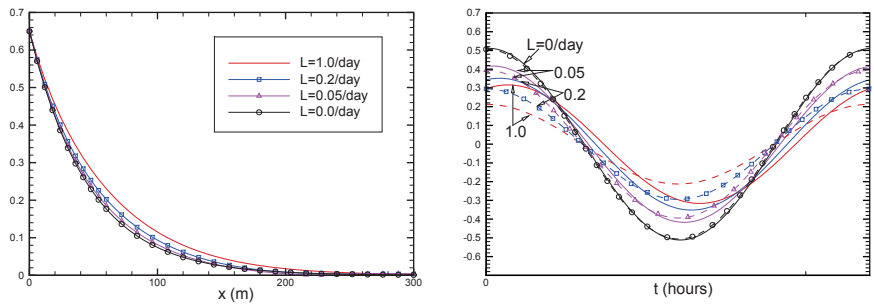

Figure 9.6 Change of groundwater heads in the unconfined aquifer for various values of leakage, L ($s = 300$, $T = 1$).

9.2.6 DYNAMIC EFFECTS OF THE PHREATIC AQUIFER ON TIDAL HEAD FLUCTUATIONS IN THE CONFINED AQUIFER

Dynamic effects of the phreatic aquifer were ignored in Jiao and Tang (1999)'s analytical solution. These effects were examined in our previous study, which was based on an approximate solution using a perturbation technique (Li et al., 2001). Here, we shall re-examine the dynamic effects of the phreatic aquifer. To do so, we introduce non-dimensional ratios for specific yield/storativity ($s = s_1/s_2$) and transmissivity ($T = T_1/T_2$). If the dynamic effect is ignored, $s \to \infty$ and $T \to 0$, giving the special case of Jiao and Tang (1999).

The storativity coefficient is an important parameter in quantifying non-steady flow in an aquifer. Figure 9.7 shows the effects of storativity ratio (s) on the head fluctuation in both the confined and unconfined aquifers. The solution of Jiao and Tang (1999) (i.e., $s \to \infty$) is also included in the figure for comparison. Figure 9.7(a) clearly indicates that the tidal fluctuation in the confined aquifer (h_2) is affected significantly by the magnitude of s. This implies that the dynamic effects on tidal head fluctuations will become more important with a smaller specific yield in the unconfined aquifer. The corresponding behaviour of h_1 under different values of s is shown in Figure 9.7(b). The effects of the storativity ratio s on h_1 are also significant.

Similar effects of the transmissivity ratio $T = T_1/T_2$ on the behaviour of h_1 and h_2 can be observed in Figure 9.8. Generally speaking, groundwater heads h_1 and h_2 increase as T increases. Dynamic effects of the phreatic aquifer are important for large values of T.

To further demonstrate the effects of ignoring leakage and dynamic effects in estimating aquifer parameters, a hypothetical example is used here. In the example, the present solution is assumed to be the"true value" of groundwater-head h_2, the results of ignoring the dynamic effects (Jiao and Tang, 1999), $h_{2(JT)}$ and the results of ignoring leakage, $h_{2(L=0)}$ are estimated. By comparing the "estimated" and the "true" values of the h_2, the error introduced by the neglect of dynamic effects and leakage can be observed.

Based on the input data in Table 9.2, the groundwater head h_2 at $x = 50m$ and $t = 0$ with dynamic effects and leakage can be calculated from (9.23). The true and estimated groundwater heads as well as their relative errors are presented in Table 9.3. In the whole problem, three parameters, L, $s = s_1/s_2$ and $T = T_1/T_2$ will directly affect the groundwater heads. As can be seen in the figure, Jiao and Tang (1999)'s model (i.e., excluding dynamic effects, special case I) underestimated by 65.1%, while ignoring leakage (special case II) overestimated 205%. Several observations have been found in Table 9.3. They are: (1) dynamic effect is more significant as L and T increase, or as s decreases. (2) relative error caused by ignoring leakage increases as L and s increases, but as T decreases.

9.2.7 COMPARISON WITH OUR PREVIOUS APPROXIMATE SOLUTION

We previously studied, based on a perturbation solution, the dynamic effects of the phreatic aquifer on tidal head fluctuations in the confined aquifer (Li et al.,

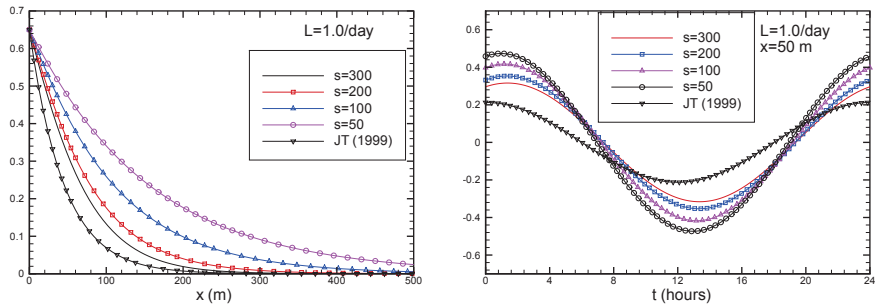

(a) Confined aquifer

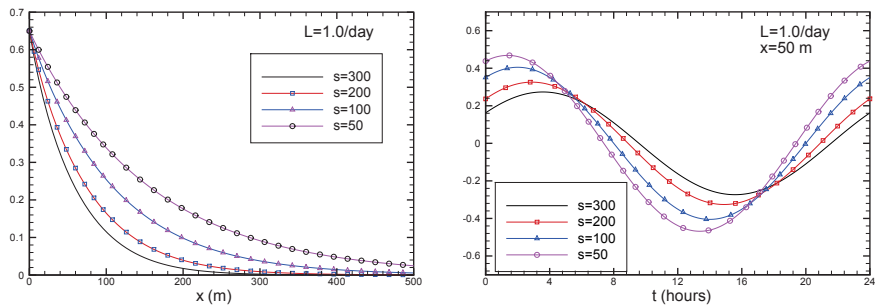

(b) Unconfined aquifer

Figure 9.7 Change of groundwater heads in the (a) confined aquifer and (b) unconfined aquifer for various values of s ($T = 1$).

2001). Here we shall check the accuracy of the perturbation solution against the present exact solution. Figure 9.9 shows the comparison between the two solutions for h_2. As expected, the perturbation solution provides a good approximation of the exact solution for small L (Figure 9.9(a)). For large leakage, the perturbation solution becomes erroneous (Figure 9.9(b)). Nevertheless, both solutions indicate that ignoring the dynamic effects of the phreatic aquifer will lead to over-prediction of leakage-induced amplitude damping for tidal head fluctuations in the confined aquifer, as by Jiao and Tang (1999)'s solution.

9.3 SPRING-NEAP TIDE-INDUCED BEACH WATER TABLE FLUCTUATIONS IN A SLOPING COASTAL AQUIFER

Most analytical solutions are based on the assumption of monochromatic tides, which may oversimplify the tidal wave conditions. In reality, tides are more complicated and often bi-chromatic, containing oscillations of at least two different frequencies. For example, in Ardeer, Scotland, a semi-diurnal solar tide has period

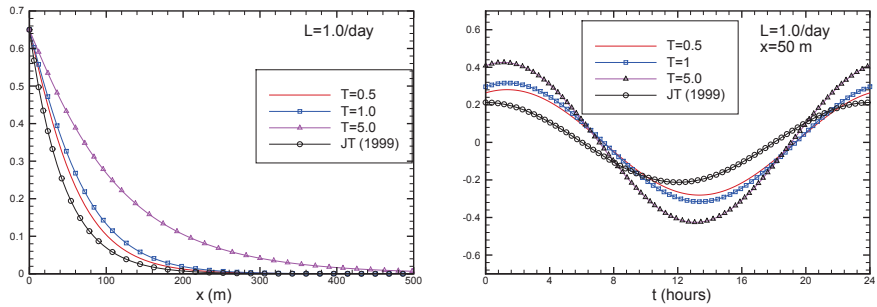

(a) Confined aquifer

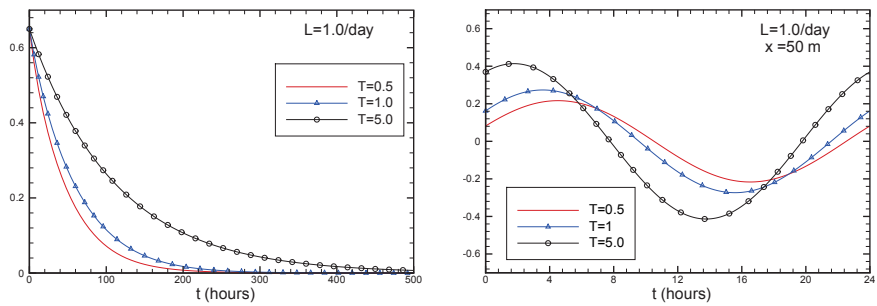

(b) Unconfined aquifer

Figure 9.8 Change of groundwater heads in the (a) confined aquifer and (b) unconfined aquifer for various values of T ($s = 300$).

$T_1 = 12$ hours and frequency $\omega_1 = 0.5236$ rad/h, while $T_2 = 12.42$ hours and $\omega_2 = 0.5059$ rad/h for a semi-diurnal lunar tide (Mao et al., 2006). As a result, the spring-neap cycle (i.e., the tidal envelope) is formed with a longer period, $T_{sn} = 2\pi/(\omega_1 - \omega_2) = 14.78$ days. The nonlinear propagation of the bi-chromatic tides in the aquifer results in low-frequency water table fluctuations over the spring-neap period, as has been measured in the field by Raubenheimer et al. (1999) and demonstrated mathematically by Li et al. (2000*b*). These low frequency water table fluctuations, called spring-neap tidal water table fluctuations hereafter, propagated much further inland than the primary tidal signals (i.e., diurnal and semi-diurnaltides). Such fluctuations have been analyzed recently (Li et al., 2000*b*; Su et al., 2003), with results demonstrating the effects of interacting tidal components. However, these results were based on only the zeroth-order shallow water expansion, i.e., the Bouniessq equation, which may be insufficient for some tidal conditions (Teo et al., 2003).

In this section, we further extend these results by deriving an analytical solution for spring-neap tide-induced water table fluctuations in a sloping sandy beach, based

Table 9.3
Impact of dynamic effects and leakage on groundwater head estimation when they are ignored.

s	h_2	$(h_{2(JT)}-h_2)/h_2$ %	$(h_{2(L=0)}-h_2)/h_2$ %
$L=0.2$/day, T=1.0, $h_{2(JT)}$=0.3942 m, $h_{2(L=0)}$=0.6907 m			
1000	0.3969	-0.68	74.0
300	0.4147	-4.95	66.5
200	0.4263	-7.54	62.0
100	0.4530	-12.98	52.45
50	0.4859	-18.88	42.13
10	0.5592	-29.51	23.51
1	0.6093	-35.30	13.352
$L=1.0$/day, T=1.0, $h_{2(JT)}$=0.2124 m, $h_{2(L=0)}$=0.6907 m			
1000	0.2264	-6.13	205.11
300	0.2961	-28.24	133.24
200	0.3320	-35.99	108.03
100	0.3977	-46.56	73.69
50	0.4580	-53.67	50.60
10	0.5592	-61.78	24.24
1	0.6093	-65.13	13.352
T	h_2	$(h_{2(JT)}-h_2)/h_2$ %	$(h_{2(L=0)}-h_2)/h_2$ %
$L=0.2$/day, s=300, $h_{2(JT)}$=0.3942 m, $h_{2(L=0)}$=0.6907 m			
10^{-6}	0.3946	-0.11	75.01
0.5	0.4034	-2.29	71.19
1	0.4147	-4.95	66.52
5	0.4649	-15.21	48.56
10	0.4940	-20.20	39.81
$L=1.0$/day, s=300, $h_{2(JT)}$=0.2124 m, $h_{2(L=0)}$=0.6907 m			
10^{-6}	0.2265	-6.19	203.49
0.5	0.2636	-19.38	162.04
1	0.2961	-28.24	133.24
5	0.4085	-47.98	69.08
10	0.4601	-53.81	50.12

on a higher-order shallow water expansion. The proposed analytical solution will be compared briefly with field observations from Adreer, Scotland (Mao et al., 2006), and previous analytical solution based on Boussinesq equation (Li et al., 2000*b*). Then, a parametric study to investigate the influence of amplitude ratio,frequency ratio and phases is conducted.

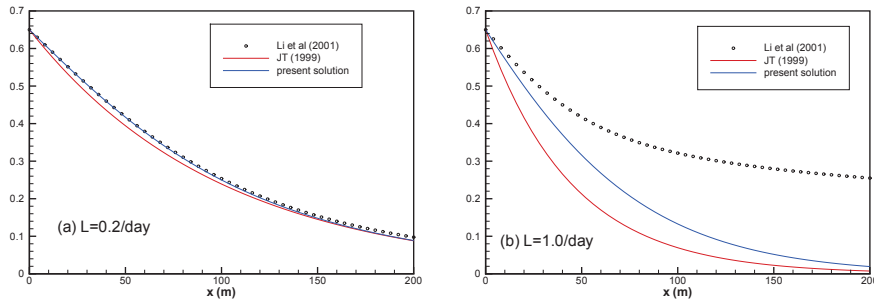

Figure 9.9 Comparison between the present solution and the previous perturbation approximation (Li et al., 2001) for the amplitude of groundwater head fluctuations in the confined aquifers with L = (a) 0.2/day and (b) 1/day (s = 300, $T = 1$). Predictions of Jiao and Tang's solution are also included.

9.3.1 ANALYTICAL SOLUTION

In this study, the flow is assumed to be homogeneous and incompressible in a rigid porous medium. The configuration of the groundwater flow in coastal aquifers is shown in Figure 6.1. In this study, seepage face effects are ignored. The boundary value problem is the same as those listed in Chapter 6, except the boundary condition at $x = x_0$, i.e.,

$$\begin{aligned} h(x_0,t) =& D + A_1\cos(\omega_1 t+\delta_1) + A_2\cos(\omega_2 t+\delta_2), \\ & at \quad x_0 = [A_1\cos(\omega_1 t+\delta_1) + A_2\cos(\omega_2 t+\delta_2)]\cot(\beta). \end{aligned} \tag{9.33}$$

To simplify the mathematical procedure, we introduce the following non-dimensional variables (Teo et al., 2003):

$$X_1 = \frac{x}{L}, \quad H = \frac{h}{D}, \quad \Phi = \frac{\phi}{D}, \quad T = omega_1 t, \tag{9.34}$$

where $L = \sqrt{2KD/n_e\omega_1}$ is the linear decay length.

We further employ a co-ordinate transformation (Li et al., 2000*b*),

$$X = X_1 - \alpha\varepsilon\cot(\beta)\left[\cos(T+\delta_1) + \lambda\cos(\omega T+\delta_2)\right], \tag{9.35}$$

where $\varepsilon = \sqrt{n_e\omega_1 D/2K}$ is the shallow water parameter, $\alpha = A_1/D$ is the amplitude parameter, $\lambda = A_2/A_1$ is the ratio of amplitude of two tidal components, $\omega = \omega_2/\omega_1$ is the ratio of frequencies of two tidal components, and δ_1 and δ_2 are the phase of each component.

Using the shallow water parameter (ε), the non-dimensional water table level (H) and potential head (Φ) can be expanded as:

$$H = H_0 + \varepsilon H_1 + \varepsilon^2 H_2 + \cdots, \quad \text{and} \quad \Phi = \Phi_0 + \varepsilon\Phi_1 + \varepsilon^2\Phi_2 + \cdots, \tag{9.36}$$

Substituting (9.36) into the governing equations and boundary conditions can be sorted in terms of the shallow water parameter as

$$O(1) \quad : \quad 2H_{0T} = (H_0 H_{0X})_X\,, \tag{9.37a}$$

$$O(\varepsilon) \quad : \quad 2\Big\{H_{1T} + \alpha\cot\beta\Big[\sin(T+\delta_1) + \lambda\,\omega\sin(\omega T+\delta_2)\Big]H_{0X}\Big\} = (H_0 H_1)_{XX}\,, \tag{9.37b}$$

$$O(\varepsilon^2) \quad : \quad 2\{H_{2T} + \alpha\cot\beta\,[\sin(T+\delta_1) + \lambda\,\omega\sin(\omega T+\delta_2)]H_{1X}\} = \frac{1}{2}\left(H_1^2\right)_{XX} + (H_0 H_2)_{XX} + \frac{1}{3}\left(H_0^3 H_{0XX}\right)_{XX}\,. \tag{9.37c}$$

Since the above equations are non-linear, the amplitude parameter ($\alpha = A_1/D$) is used to expand the various equations in order to solve them approximately, that is,

$$H_0 = 1 + \alpha H_{01} + \alpha^2 H_{02} + \cdots, \text{ and } H_n = \alpha H_{n1} + \alpha^2 H_{n2} + \cdots \quad (n \geq 1). \tag{9.38}$$

Then, (9.37a)-(9.37c) can be further sorted in terms of the amplitude parameter (α) as

$$O(\alpha) \quad : \quad 2H_{01T} = H_{01XX}, \tag{9.39a}$$

$$O(\alpha^2) \quad : \quad 2H_{02T} = H_{02XX} + \frac{1}{2}\left(H_{01}^2\right)_{XX}, \tag{9.39b}$$

$$O(\varepsilon\alpha) \quad : \quad 2H_{11T} = H_{11XX}, \tag{9.39c}$$

$$O(\varepsilon\alpha^2) \quad : \quad 2H_{12T} = H_{12XX} - 2\cot\beta\Big[\sin(T+\delta_1) + \lambda\,\omega\sin(\omega T+\delta_2)\Big]H_{01X}, \tag{9.39d}$$

$$O(\varepsilon^2\alpha) \quad : \quad 2H_{21T} = H_{21XX} + \frac{1}{3}H_{01XXX}. \tag{9.39e}$$

The above equation (9.39) is solved with the following boundary conditions:

$$H_{01}(0,T) = \cos(T+\delta_1) + \lambda\cos(\omega T+\delta_2), \tag{9.40a}$$

$$H_{02}(0,T) = H_{11}(0,T) = H_{12}(0,T) = H_{21}(0,T) = 0, \tag{9.40b}$$

$$H_{01X}(\infty,T) = H_{02X}(\infty,T) = 0, \tag{9.40c}$$

$$H_{11X}(\infty,T) = H_{12X}(\infty,T) = H_{21X}(\infty,T) = 0. \tag{9.40d}$$

The solution of water table elevation in the above boundary value problem is summarized here:

$$H = 1 + \left(\alpha H_{01} + \alpha^2 H_{02}\right) + \varepsilon\left(\alpha H_{11} + \alpha^2 H_{12}\right) + \varepsilon^2\alpha H_{21}, \tag{9.41a}$$

which is the non-dimensional form of equation. The functions on the righ-hand-side are given by

$$H_{01} = e^{-X}\cos(\theta_1+\delta_1) + \lambda e^{-\sqrt{\omega}X}\cos(\eta_1+\delta_2), \tag{9.41b}$$

$$
\begin{aligned}
H_{02} =& \frac{1}{4}\left(1-e^{-2X}\right)+\frac{\lambda^2}{4}\left(1-e^{-2\sqrt{\omega}X}\right)\\
&+\frac{1}{2}\left[e^{-\sqrt{2}X}\cos(\theta_2+2\delta_1)+\lambda e^{-2X}\cos 2(\theta_1+\delta_1)\right]\\
&+\frac{\lambda^2}{2}\left[e^{-\sqrt{2\omega}X}\cos(\eta_2+2\delta_1)-e^{-2\sqrt{\omega}X}\cos 2(\eta_1+\delta_2)\right]\\
&+\frac{\lambda\left(1+\sqrt{\omega}\right)^2}{4\sqrt{\omega}}\Big[e^{-\sqrt{1+\omega}X}\cos(\eta_3+\delta_1+\delta_2)\\
&\qquad -e^{-(1+\sqrt{\omega})X}\cos(1+\omega)T\Big]\\
&+\frac{\lambda}{2}\Big[e^{-(1+\sqrt{\omega})X}\cos(\theta_1-\eta_1+\delta_1-\delta_2)\\
&\qquad -e^{-\sqrt{1+\omega}X}\cos(\eta_4+\delta_1-\delta_2)\Big]\\
&+\frac{\lambda(1-\omega)}{4\sqrt{\omega}}\Big[e^{-(1+\sqrt{\omega})X}\sin(\theta_1-\eta_1+\delta_1-\delta_2)\\
&\qquad -e^{-\sqrt{1-\omega}X}\cos(\eta_4+\delta_1-\delta_2)\Big],
\end{aligned}
\tag{9.41c}
$$

$$
H_{11}=0, \tag{9.42a}
$$

$$
\begin{aligned}
H_{12} =& \frac{1}{\sqrt{2}}\cot\beta\left\{\frac{1}{\sqrt{2}}-e^{-X}\cos(X-\frac{\pi}{4})\right.\\
&\qquad \left.+\lambda^2\sqrt{\omega}\left[\frac{1}{\sqrt{2}}-e^{-\sqrt{\omega}X}\cos(\sqrt{\omega}X-\frac{\pi}{4})\right]\right.\\
&+\left[e^{-\sqrt{2}X}\cos(\theta_2+2\delta_2+\frac{\pi}{4})-e^{-X}\cos(\theta_3+2\delta_1+\frac{\pi}{4})\right]\\
&+\frac{\lambda^2}{2}\left[e^{-\sqrt{2\omega}X}\cos(\eta_2+2\delta_2)-e^{-2\sqrt{\omega}X}\cos 2(\eta_1+\delta_2)\right]\\
&+\lambda\sqrt{\omega}\left[e^{-\sqrt{1+\omega}X}-e^{-\sqrt{\omega}X}\right]\cos(\eta_3+\delta_1+\delta_2+\frac{\pi}{4})\\
&+\lambda\sqrt{\omega}\Big[e^{-\sqrt{\omega}X}\cos(T-\eta_1+\delta_1-\delta_2-\frac{\pi}{4})\\
&\qquad -e^{-\sqrt{1-\omega}X}\cos(\eta_4+\delta_1-\delta_2-\frac{\pi}{4})\Big]\\
&+\lambda\Big[e^{-\sqrt{1+\omega}X}\cos(\eta_3+\delta_1+\delta_2+\frac{\pi}{4})\\
&\qquad -e^{-X}\cos(\theta_1+\omega T+\delta_1+\delta_2+\frac{\pi}{4})\Big]\\
&+\lambda\Big[e^{-\sqrt{1-\omega}X}\cos(\eta_4+\delta_1-\delta_2+\frac{\pi}{4})
\end{aligned}
$$

$$
\begin{aligned}
&- e^{-X}\cos(\theta_1+\omega T+\delta_1-\delta_2+\frac{\pi}{4})\Big]\\
&+\frac{\lambda\sqrt{\omega}}{\sqrt{2}}\Big[e^{-\sqrt{2\omega}X}\cos(\eta_2+2\delta_2+\frac{\pi}{4})\\
&- e^{-\sqrt{\omega}X}\cos(\theta_1+\omega T+2\delta_2+\frac{\pi}{4})\Big]\Bigg\},
\end{aligned}
\tag{9.42b}
$$

$$
H_{21}=-\frac{\sqrt{2}}{3}\left[Xe^{-X}\cos(\theta_1+\delta_1+\frac{\pi}{4})+\frac{\lambda\omega^2}{\sqrt{\omega}}e^{-\sqrt{\omega}X}\cos\left(\eta_1+\delta_2-\frac{\pi}{4}\right)\right], \tag{9.42c}
$$

where $\theta_1=T-X$, $\theta_2=2T-\sqrt{2}X$, $\theta_3=2T-X$, $\eta_1=\omega T-\sqrt{\omega}X$, $\eta_2=2\omega T-\sqrt{2\omega}X$, $\eta_3=(1+\omega)T-\sqrt{1+\omega}X$, $\eta_4=(1-\omega)T-\sqrt{1-\omega}X$.

The above non-dimensional water table fluctuation H can be rewritten in the dimensional form as

$$
h(x,t)=D[1+(\alpha H_{01}+\alpha^2H_{02})+\varepsilon(\alpha H_{11}+\alpha^2H_{12})+\varepsilon^2\alpha H_{21}]. \tag{9.43}
$$

9.3.2 COMPARISONS WITH FIELD DATA

To test the analytical solutions, field data of water table fluctuations at Ardeer, Scotland, are used as an example. Ardeer is a former industrial site containing a substantial waste deposit. The low-relief estuary adjacent to the site has a mildly sloping sandy beach. Between low and high tide the beach length varies by 180 m. Field monitoring was conducted to characterize the tidal influence on the groundwater dynamics and contaminant migration as well as the saltwater intrusion. Detailed information on the field observations is available elsewhere (Mao et al., 2006).

Analysis on tidal signals shows that the fluctuation amplitude decreases exponentially with distance from the estuary, accompanied by a phase lag, as has been shown by the FFT analysis of the observed data (Mao et al., 2006). FFT analyses of the estuarine tides have shown the dominant frequencies are M2, S2 and O1. To simplify the analytical solution, we only considered M2 and S2 components. The fitted expression modeling the estuarine tides is

$$
\begin{aligned}
h(x,t)=&D+1.1745\cos\left(\omega_1 t-1.6676+\frac{\pi}{2}\right)\\
&+0.08\cos\left(\omega_2 t-1.3377+\frac{\pi}{2}\right),
\end{aligned}
\tag{9.44}
$$

where h is measured in meters, $\omega_1=2\pi/0.52$ rad/d and $\omega_2=4\pi$ rad/d.

The calculated groundwater table fluctuation based on the analytical solution with the above estuarine tide is shown in Figure 9.10 where the damping of the amplitude is compared against observed data. In the development of the analytical solutions, we assume the coastal aquifer is homogeneous with a uniformly sloped

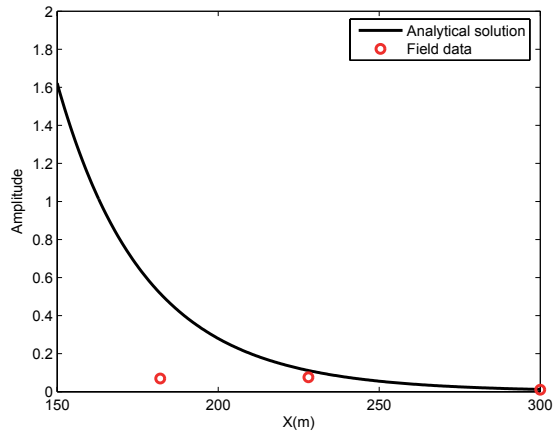

Figure 9.10 Comparison of analytical solution with field data.

beach. However, the real aquifer is multilayered and inhomogeneous in both vertical and horizontal direction near the intersection of the ocean and the aquifer. It has been reported that inhomogeneity will affect water table fluctuations (Trefry, 1999). Furthermore, the variations of beach slope are expected to affect the water table level, but no solution is available yet. In addition, seepage face effects have been ignored. Finally, we consider two main frequencies of tidal waves (M2 and S2) in equation (9.44), based on FFT analysis. The inclusions of other tidal components may improve the prediction of the analytical solutions.

9.3.3 RESULTS AND DISCUSSIONS

The major difference between the present solution and previous solution (Li et al., 2000*b*) is the higher-order component. It is of interesting to examine the effects of higher-order component here. The input data for the comparison are listed in Table 9.4. As seen in Figure 9.11, the previous solution (Li et al., 2000*b*) overestimates the water table elevation.

As shown in analytical solutions, numerous parameters are involved in the solutions. The objective of this parametric study is to investigate three parameters. These are (1) amplitude ratio($\lambda = A_2/A_1$), (2) frequency ratio ($\omega = \omega_2/\omega_1$), and(3) phases ($\delta_1$ and δ_2). Although spring-neap tides normally have the frequencies ration (ω) close to unity, the variation of frequency ration (ω) is also considered here for the general applications of other cases rather than limited to spring-neap tides. Recently, Li et al. (2000*b*) discussed part of the above parameters briefly based on Boussinesq equation, it is worthwhile to reexamine the effects of the above parameters with the new solution. The input data of numerical examples are given in Table 9.4.

The amplitude ratio (λ) is the ratio of the amplitudes of two tidal components (A_2/A_1). Here we allow l to vary from zero (0) to unity (1). $\lambda = 0$ represents the case

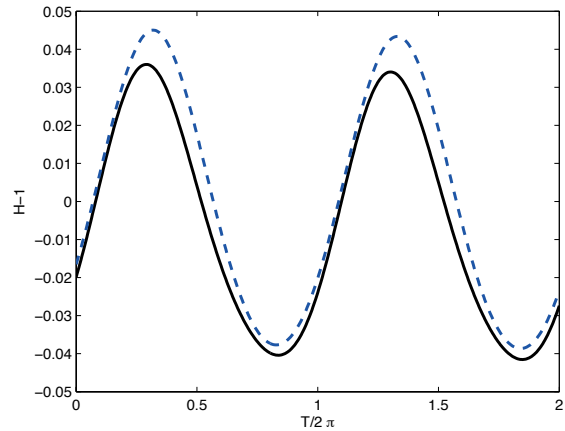

Figure 9.11 Effects of higher-order components on water table fluctuations in coastal aquifers (solid line is from the present solution and dashed line is from Li et al. (2000*b*)). X_1=2, λ =0.5, ω=0.5, and (δ_1, δ_2) =(0, 0).

Table 9.4
Input data for numerical examples.

Soil porosity (n_e)	0.22
Hydraulic conductivity (K) (m/day)	50
Slope of the beach (β) (rad)	0.02
Thickness of aquifer (D) (m)	5
Amplitude of the first tidal wave (A_1) (m)	2
Frequency of the first tidal wave (ω_1)	4π
Amplitude parameter (α)	0.372
Shallow water parameter (ε)	0.2

without the second tidal component, which is the case reported by Teo et al. (2003), while $\lambda = 1$ represents the case of equal weight of two tidal signals.

Figure 9.12(a) illustrates the effects of the amplitude ratio(λ) on the tide-induced water table height above the mean thickness of aquifer at $T = 0$, i.e., $H - 1 = (h - D)/D$. As shown in the figure, the water table height increases as the amplitude ratio (λ) increases, i.e., it increases as the amplitude of the second tidal signal increases.

Besides the amplitude ratio (λ), the frequency ratio(ω) is another factor, which may affect the tide-induced water table fluctuations. The distribution of water table heights versus the horizontal distances (X) for various values of frequency ratio (ω) is

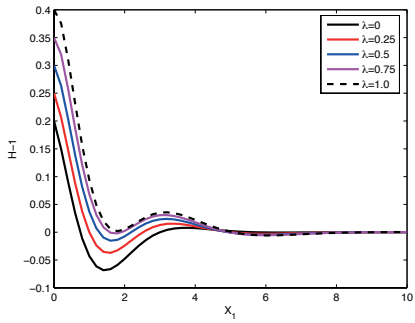

(a) varying λ

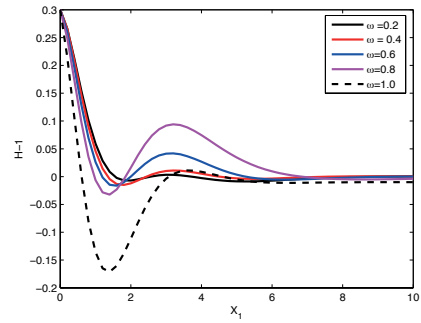

(b) varying ω

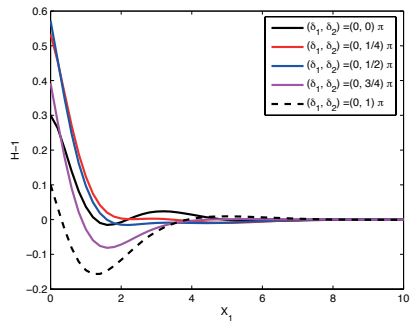

(c) varying (δ_1 and δ_2)

Figure 9.12 Effects of amplitude ratio (λ), frequency ratio (ω) and phases (δ_1 and δ_2) on water table fluctuations in coastal aquifers. Here (a) varying λ with $\omega = 0.5$, $(\delta_1, \delta_2) = (0,0)$, $t = 0$; (b) varying ω with $\lambda = 0.5$, $(\delta_1, \delta_2) = (0,0)$, $t = 0$; and (c) varying (δ_1 and δ_2) with λ =0.5, ω =0.5, $t = 0$.

presented in Figure 9.12(b). As seen in the figure, the water table height decreases as ω increases when $X < 1.8$. When X increases ($X > 1.8$), the influence of w perform an irregular trend, which may require more advanced theories.

Another major difference between the previous solution (Teo et al., 2003) and the present solution is the phase differences between two tidal signals. Figure 9.12(c) illustrates the effects of phase differences of two tidal components on the tide-induced water table heights. To see the influence of phase difference, we fix $\delta_1 = 0$, and vary δ_2 from zero (0) to π. Generally speaking, the phase difference significantly affects the water table height. For example, the water table height decreases as $\delta_2 - \delta_1$ increases.

9.4 SUMMARY

In this chapter, we further investigate three different solutions/cases for tidal dynamics in coastal aquifers. First, a new perturbation parameter, steepness

parameter, the ratio of amplitude (A) to the linear decay length (L), is introduced to replace the shallow water parameter. As demonstrated in numerical examples, the steepness parameter provides a much wider range of applicability for a range of the amplitude parameter. Using the steepness parameter to replace the shallow water parameter is more versatile option.

Second, an analytical solution for tidal fluctuation in a leaky confined aquifer is presented, in which a linear solution is presented. Numerical examples show that the dynamic effects on tidal head fluctuations will become more important with a smaller specific yield in the unconfined aquifer. Furthermore, groundwater heads increases as transmissivity increases. Regarding leakage effect, dynamic effect is more significant as the leakage increases. Meanwhile, the relative error caused by ignoring leakage increases as leakage increases.

Finally, spring-neap tide-induced water table fluctuation in a sloping coastal aquifer is considered. Using Ardeer, Scotland as an example, the analytical solution is compared with the field data. Three parameters, amplitude ratio, frequency ratio and phase difference between two tidal signals, are investigated. All these parameters affect the spring-neap tide-induced groundwater fluctuation in coastal aquifers significantly.

Taylor & Francis
Taylor & Francis Group
http://taylorandfrancis.com

Section III

Fluid-Seabed Interactions around Marine Structures

Taylor & Francis
Taylor & Francis Group
http://taylorandfrancis.com

10 Poro-Elastic Model for Fluid-Seabed Interactions

10.1 INTRODUCTION

An appropriate engineering design of marine infrastructures such as breakwaters, offshore pipelines, platforms, and offshore wind turbine foundations consists of three key components: (1) hydrodynamic loading generated in the marine environment; (2) structural design for infrastructures; and (3) geotechnical design for foundation of infrastructures. Recently, marine geotechnical research has attracted great attentions among coastal and geotechnical engineers due to the growing activities in offshore environments. An appropriate design of foundations of marine infrastructures has been recognised as an one of key factors in the success of offshore engineering projects. Therefore, the evaluation of the wave-induced soil response and its resultant seabed instability is particularly important for engineers involved in the design of marine infrastructures.

In the past few decades, considerable efforts have been devoted to the problem of the wave-soil-structure interactions. The major reason for the growing interest is that a few marine infrastructures have been damaged by the wave-induced seabed instability and its associate failure of the infrastructure rather than construction deficiencies (Christian et al., 1974; Lundgren et al., 1989). Another reason is that the poro-elastic theories for wave-soil interaction have been further applied to field measurements, such as the determination of the wave surface profiles using measured pore pressure in marine sediments (Raubenheimer et al., 1998), determination of the shear modulus of soil (Yamamoto and Trevorrow, 1991), the directional spectra of ocean surface waves (Nye and Yamamoto, 1994), and acoustic wave propagating through porous media (Yamamoto and Turgut, 1988).

It has been well known that dynamic wave pressures on the sea floor will further induce pore pressures and effective stresses within the seabed (Wang et al., 2004). With increase of excess pore pressure and diminishing vertical effective stress, part of the seabed may become unstable or even liquefied. Once liquefaction occurs, the soil particles are likely to be carried away as a heavy fluid by any prevailing bottom current or mass transport owing to the action of hydrodynamic loading.

Two mechanisms of the wave-induced soil response have been reported in the literature, Based on the observations in the laboratory and field measurements (Zen and Yamazaki, 1990*a*; Nago et al., 1993; Sumer and Fredsoe, 2002). They are:

- The first mechanism resulted from the *transient* or *oscillatory* excess pore pressure and is accompanied by attenuation of the amplitude and phase lag in the pore pressure changes (Yamamoto et al., 1978; Madsen, 1978).

This is particularly important for small-amplitude waves and it could only liquefy momentarily in the seabed under wave troughs (Jeng, 2012).

- The second mechanism is termed as the residual pore pressure, which is the build-up of excess pore pressure caused by contraction of the soil under the action of cyclic loading (Seed and Rahman, 1978; Sumer and Fredsoe, 2002). As reported in Jeng (2012), the residual mechanism is more important for large wave loading.

Thus, the wave-induced pore pressure within marine sediments consists of two components: oscillatory and residual mechanisms, as shown in Figure 10.1, which can be expressed as (Sumer and Fredsoe, 2002)

$$p = p_s + u_e, \quad u_e = \frac{1}{T}\int_t^{t+T} p dt, \tag{10.1}$$

where p_s represents the oscillatory pore pressure that leads to momentary liquefaction, while u_e represents the period-averaged pore pressure; and T is the wave period.

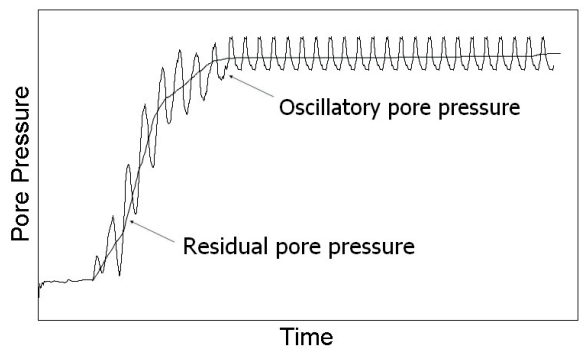

Figure 10.1 Conceptual sketch of two different mechanisms of pore pressure (not in scale).

In this Chapter, basic mechanics of wave-seabed interactions will be introduced first. Some fundamental solutions for the wave-induced seabed response and its application for the prediction of seabed instability will be outlined. Then, the phenomenon of solitary wave over a sloping seabed will be investigated.

10.2 HYDRODYNAMIC MODELS

In this chapter, a soil matrix subjected to a 2D ocean wave system is considered, as depicted in Figure 10.2. Ocean waves propagate in the positive x-direction, whilst the z-axis is positive upward from the *seabed surface*.

In this section, two wave models will be outlined, including the potential flow model and Navier-Stoke model. The linear wave theory, based on the potential

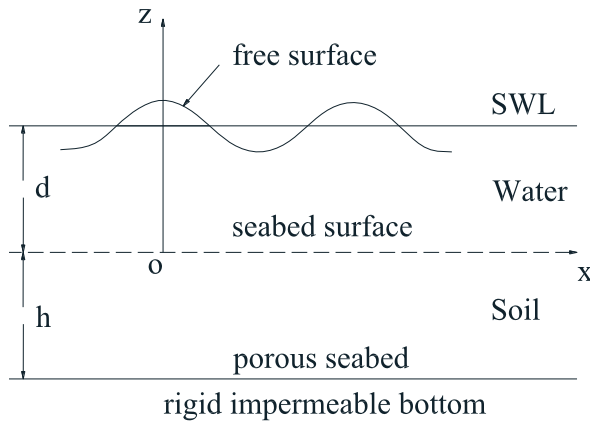

Figure 10.2 The sketch of ocean waves propagating over a porous seabed.

flow, has been commonly used in the previous research in the field of marine geotechnics (Yamamoto et al., 1978). The non-linear wave model is based on the Reynolds-Averaged Navier-Stokes (RANS) equations, which provide more precise prediction of wave characteristics. In this section, only 2D wave models are introduced. These models can be further extended to 3D cases.

10.2.1 LINEAR WAVE THEORY

In general, the linear wave theory has been commonly-used for the wave-seabed interactions in the literature because of its simplicity. Referring to the linear wave theory in 2D (Dean and Dalrymple, 1984), the velocity potential (ϕ) and the free surface elevation η are given as

$$\phi = \frac{gH}{2\omega}\frac{\cosh kz}{\cosh kd}\sin(kx-\omega t), \quad \eta = \frac{H}{2}\cos(kx-\omega t), \tag{10.2}$$

where H is the wave height, k is the wave number ($k = 2\pi/L$, in which L is the wavelength); g is the gravity; t is time and d is the water depth above the seabed surface (referring to Figure 10.2).

The wave frequency ω (= $2\pi/T$, where T is the wave period) satisfies the wave dispersion equation

$$\omega^2 = gk\tanh kd. \tag{10.3}$$

Introducing the velocity potential (ϕ) and the surface elevation (η) into the Bernoulli's equation, the dynamic wave pressure at the seabed surface (P_b) can be expressed as

$$P_b(x,t) = \frac{\gamma_w H}{2\cosh kd}\cos(kx-\omega t) = p_0\cos(kx-\omega t), \tag{10.4}$$

in which γ_w is the unit weight of water; and p_0 is the amplitude of dynamic wave pressures. Noted that the dynamic wave pressure, (10.4), will be used as the external loading for seabed models for one-way coupling model.

10.2.2 REYNOLDS-AVERAGED NAVIER-STOKES (RANS) MODEL

The hydrodynamic model for wave and current is governed by the Volume-Averaged Reynolds-Averaged Navier-Stokes (VARANS) equations for the incompressible and continuous fluid motion. Based on the mass and momentum conservation, the governing equations can be expressed as,

$$\frac{\partial \langle u_i \rangle}{\partial x_i} = 0, \tag{10.5a}$$

$$\frac{\partial \rho \langle u_i \rangle}{\partial t} + \frac{\partial \rho \langle u_i \rangle \langle u_j \rangle}{\partial x_j} = -\frac{\partial \langle p \rangle}{\partial x_i} + \frac{\partial \tau_{ij}}{\partial x_j} + \frac{\partial}{\partial x_j}\left(-\rho \langle u_i' u_j' \rangle\right) + \rho g_i, \tag{10.5b}$$

where ρ is the fluid density, u_i is the fluid velocity, p is the fluid pressure, g_i denotes the acceleration of gravity, i and $j \in [1,2,3]$, which denote the components in the x, y and z direction respectively, and τ_{ij} is the viscous stress that is defined as:

$$\tau_{ij} = 2\mu\sigma_{ij}, \quad \sigma_{ij} = \frac{1}{2}\left(\frac{\partial \langle u_i \rangle}{\partial x_j} + \frac{\partial \langle u_j \rangle}{\partial x_i}\right), \tag{10.6}$$

in which μ is the dynamic viscosity of fluid. As pointed out by Rodi (1993), the Reynolds stress term, $-\rho \langle u_i' u_j' \rangle$, in (10.5b) can be determined by:

$$-\rho \langle u_i' u_j' \rangle = \mu_t \left(\frac{\partial \langle u_i \rangle}{\partial x_j} + \frac{\partial \langle u_j \rangle}{\partial x_i}\right) - \frac{2}{3}\rho \delta_{ij} \kappa, \tag{10.7}$$

where μ_t is the turbulent viscosity, δ_{ij} is the Kronecker delta and κ the turbulence kinetic energy. Substituting (10.6)–(10.7) into (10.5b), we have the following expression:

$$\begin{aligned} \frac{\partial \rho \langle u_i \rangle}{\partial t} + \frac{\partial \rho \langle u_i \rangle \langle u_j \rangle}{\partial x_j} = &-\frac{\partial}{\partial x_i}\left[\langle p \rangle + \frac{2}{3}\rho\kappa\right] \\ &+ \frac{\partial}{\partial x_j}\left[\mu_{eff}\left(\frac{\partial \langle u_i \rangle}{\partial x_j} + \frac{\partial \langle u_j \rangle}{\partial x_i}\right)\right] + \rho g_i, \end{aligned} \tag{10.8}$$

where μ_{eff} is the efficient dynamic viscosity, which is defined as $\mu_{eff} = \mu + \mu_t$.

The $k-\varepsilon$ turbulence model for the closure of the VARANS equations is expressed as follow:

$$\frac{\partial \rho \kappa}{\partial t} + \frac{\partial \rho \langle u_j \rangle \kappa}{\partial x_j} = \frac{\partial}{\partial x_j}\left[\left(\mu + \frac{\mu_t}{\sigma_k}\right)\frac{\partial \kappa}{\partial x_j}\right] + 2\mu_t \sigma_{ij}\frac{\partial u_i}{\partial x_j} - \rho\varepsilon, \tag{10.9a}$$

$$\frac{\partial \rho \varepsilon}{\partial t}+\frac{\partial \rho \langle u_j \rangle \varepsilon}{\partial x_j}=\frac{\partial}{\partial x_j}\left[\left(\mu+\frac{\mu_t}{\sigma_\varepsilon}\right)\frac{\partial \varepsilon}{\partial x_j}\right]+C_{1\varepsilon}\frac{\varepsilon}{\kappa}\left(2\mu_t\sigma_{ij}\right)\frac{\partial u_i}{\partial x_j}-C_{2\varepsilon}\frac{\rho\varepsilon^2}{\kappa}, \quad (10.9b)$$

$$\mu_t=\rho\nu_t=\rho\frac{C_\mu k^2}{\varepsilon}, \quad (10.9c)$$

where κ and ε are the turbulent kinetic energy and its dissipation rate respectively, ν_t is the turbulent viscosity frequency, and C_μ, $C_{1\varepsilon}$, $C_{2\varepsilon}$, σ_k, σ_ε are empirical constants, which are taken as 0.09, 1.44, 1.92, 1.0, 1.3 respectively (Rodi, 1993). The values of these constants have been refined by numerous iterations of consistency checks based on various flow conditions (Versteeg and Malalasekera, 2007) and have been shown useful applications on free-shear layer flows with relatively small pressure gradients (Huang et al., 1997).

In the hydrodynamic model, each cell within the computational domain could be considered as a mixture of two-phases fluid (i.e., water and air). Therefore, one indicator phase function (α) is sufficient to describe the free surface. The α is defined as the quantity proportion of the water in a cell:

$$\alpha=\begin{cases}1 & \text{water}\\ 0 & \text{air}\\ 0<\alpha<1 & \text{free surface,}\end{cases} \quad (10.10)$$

$\alpha=1$ represents the cell is full of water, while $\alpha=0$ means the cell is full of air, and for the value of α between 0 and 1, these cells belong to the free surface. The Volume-Averaged Volume of Fluid (VOF) technique is used to track the movement of phases (Hirt and Nichols, 1981):

$$\frac{\partial \alpha}{\partial t}+\frac{\partial \langle u_i \rangle \alpha}{\partial x_i}=0, \quad (10.11)$$

Manipulation that involves an artificial term $\partial u_{ci}\alpha(1-\alpha)/\partial x_i$ is applied to (10.11) in OpenFOAM to achieve consistent with physical processes, which include keeping the sharp interface and limiting α between 0 and 1 (Higuera et al., 2013). The final expression is:

$$\frac{\partial \alpha}{\partial t}+\frac{\partial \langle u_i \rangle \alpha}{\partial x_i}+\frac{\partial \langle u_{ci} \rangle \alpha(1-\alpha)}{\partial x_i}=0, \quad (10.12)$$

where u_{ci} is defined as $|u_{ci}|=\min[c_\alpha|u_i|,\max(|u_i|)]$, in which c_α is a user adjustable factor for the enhancement of the compression of the interface.

Appropriate boundary conditions are required for the wave model. Regarding the mean flow field, the no-slip boundary condition is imposed on the seafloor surface (u_{fi}=0). The zero-stress condition is adopted on the mean free surface ($\tau_{fij}=0$) while the effect of air flow is neglected. A sponge layer damping method is applied for vertical flow component at both domain ends which are far from the concerned region. Thus, the error induced by the reflecting waves can be neglected.

10.3 SEABED MODELS: OSCILLATORY MECHANISM

Basically, existing studies for the wave-induced oscillatory soil response can be classified into three categories: Quasi-static model, $u-p$ approximation and fully dynamic model. We provide a brief discussion about three different types of models.

- **Quasi-static model**: This is the conventional Biot's consolidation model, in which inertia effects are ignored, based on the assumption of slow propagation of porous flow in the seabed, compare with environmental loading such as waves, currents and earthquakes. This approach has been commonly used for the problem of wave-seabed interaction around a fixed structure. The classic solutions include Yamamoto et al. (1978); Madsen (1978); Hsu and Jeng (1994); Mei and Foda (1981); Okusa (1985) and others.
- $u-p$ **approximation**: In this approach, the the inertial term of solid phase is included, which was first proposed by Zienkiewicz et al. (1980) for earthquake loading and applied to ocean wave-induced soil response by Jeng et al. (1999). More detailed information for $u-p$ approximation can be found in Jeng et al. (1999) for an infinite seabed and Jeng and Rahman (2000) for a seabed of finite thickness.
- **Fully dynamic model**: Both inertial effects of solid and pore fluid phases are considered. This approach was first applied to the problem of wave-seabed interactions by Jeng and Cha (2003) and clarified the applicable range of consolidation models. Later, Ulker et al. (2009) further illustrated the applicable range of three models with a different way.

Regarding *Quasi-static model*, three different approaches have been adopted in the literature. They are: Yamamoto-Madsen model, Okusa model, Boundary-layer approximation. We outline the contribution of several key publications available in the literature here.

(a) **Yamamoto-Madsen model**: Yamamoto et al. (1978) proposed an analytical solution for an infinite seabed with hydraulic isotropy, while Madsen (1978) derived an analytical solution for a similar problem but with hydraulic anisotropy (i.e., permeabilities in all directions are different). Different seabed conditions, such as a seabed of finite thickness Yamamoto (1977) and a layered seabed Yamamoto (1981) were considered. Later, the Y-M model was further extended to more complicated wave conditions such as 3D short-crested wave systems (Hsu et al., 1993; Hsu and Jeng, 1994; Hsu et al., 1995) or various seabed conditions such as cross-anisotropic soil behaviour (Jeng, 1997*a*) or non-homogeneous seabed profile (Jeng and Seymour, 1997; Jeng and Lin, 1996; Kitano and Mase, 2001). Some numerical models have been developed with this framework, which have been reviewed in Jeng (2012)(Chapter 2).

(b) **Okusa model:** Based on the plane stress conditions, Okusa (1985) further reduced the sixth order governing equation in Y-M model to fourth-order governing equation and Laplace equation. He focused on the effects of the

degree of saturation on the phase lag. However, since this model was based on plane stress condition, which cannot further apply to three-dimensional (3D) conditions. Therefore, no further applications of this approach have been attempted in the literature after Okusa (1985).

(c) **Boundary-layer approximation**: Based on the theory of mixture, Mei and Foda (1981) proposed the boundary-layer approximation for the wave-induced soil response. In their study, both seabeds with infinite and finite soil depth were considered, and simplified closed-form analytical solutions were proposed. Based on the same framework, Sakai et al. (1992) further investigated the potential of wave-induced momentary liquefaction in a seabed. Later, based on this approach, Kitano and Mase (1999) re-investigated the case of a seabed with variable permeability.

In this section, we will present the basic governing equations and boundary conditions for quasi-static model first. Then, we outline the analytical solution of three different approaches (Y-M model, Okusa model and Boundary-layer approximation) and compare the results obtained form these model, as well as the laboratory tests.

10.3.1 BIOT'S CONSOLIDATION (QUASI-STATIC) MODEL

To establish the quasi-static model for the wave-seabed interactions problem shown in Figure 10.2, some basic assumptions for the wave and soil properties are necessary. They are:

- The horizontal porous seabed is elastically isotropic, unsaturated, and hydraulically anisotropic. The isotopic soil behavior is an idealized one, which has been normally used as the first approximation, although natural seabed may display certain degree of anisotropy. For the cross-anisotropic seabed, readers can referred to the author's previous work (see Jeng, 2012, Chapter 5).
- The soil skeleton and pore fluid are compressible. The assumption of compressibility of soil skeleton and pore fluid is valid, especially for a sandy bed under an unsaturated condition.
- The inertial effect of sediments is neglected so that the soil skeleton generally obeys Hooke's law. This assumption is acceptable for the problem of porous flow in a sandy seabed. A detailed information for the applicable range of different approaches can be found in Jeng and Cha (2003); Ulker et al. (2009). More detailed discussions for the effects of inertial forces on the wave-induced soil response can be found in the previous work (see Jeng, 2012, Chapter 6).
- The flow in the porous bed obeys Darcy's law. This is a common assumption for a porous flow used in previous studies available literature. Recently, Zhou et al. (2021*b*) proposed a non-Darcy model for the wave-induced oscillatory soil response, which will be discussed in Section §11.3.

- The dynamic wave pressure on the seabed surface is considered as the only external loading force in the wave-seabed interaction, i.e., the effect of boundary layer is ignored in this study. It has been well documented that wave boundary layer only concentrates on a thin layer above the seabed surface. Compared with the order of wave pressure, it may be negligibly small in a laminar boundary layer. The effects of wave bottom boundary layer on the wave-induced oscillatory soil response was discussed in Ye and Jeng (2011).

With the above assumptions, the consolidation equation (Biot, 1941) is generally accepted as those governing the flow of compressible pore fluid in a compressible porous medium. For a 2D problem, and treating the porous bed as hydraulically anisotropic, with permeabilities k_x, and k_z in the x-, and z-directions, respectively, the governing equation can be expressed as

$$\frac{k_x}{k_z}\frac{\partial^2 p_s}{\partial x^2}+\frac{\partial^2 p_s}{\partial z^2}-\frac{\gamma_w n'\beta}{k_z}\frac{\partial p_s}{\partial t}=\frac{\gamma_w}{k_z}\frac{\partial \varepsilon_s}{\partial t}, \tag{10.13}$$

where p_s is the wave-induced oscillatory pore pressure; γ_w is the unit weight of the pore-water; n' (or n_s) is the soil porosity; and ε_s is the volume strain defined by

$$\varepsilon_s=\frac{\partial u_s}{\partial x}+\frac{\partial w_s}{\partial z}, \tag{10.14}$$

where u_s and w_s are the soil displacements in the x- and z-directions, respectively.

The compressibility of the pore fluid (β) is related to the apparent bulk modulus of the pore fluid (K') and the degree of saturation (S_r) such that

$$\beta=\frac{1}{K'}=\frac{1}{K_w}+\frac{1-S_r}{P_{wo}}, \tag{10.15}$$

where K_w is the true bulk modulus of elasticity of water, which may be taken as 1.95×10^9 N/m^2, (Yamamoto et al., 1978); P_{wo} is the absolute water pressure. If the soil skeleton is completely air-free, i.e., fully saturated, then $\beta=1/K_w$, since S_r=1.

The equations for overall equilibrium in a poro-elastic medium, relating to the soil displacements and pore pressure, are given by

$$G\nabla^2 u_s+\frac{G}{(1-2\mu)}\frac{\partial \varepsilon_s}{\partial x}=\frac{\partial p_s}{\partial x}, \tag{10.16a}$$

$$G\nabla^2 w_s+\frac{G}{(1-2\mu)}\frac{\partial \varepsilon_s}{\partial z}=\frac{\partial p_s}{\partial z}, \tag{10.16b}$$

where the shear modulus (G) is related to Young's modulus (E) and the Poisson's ratio (μ) in the form of $E/2(1+\mu)$.

Based on the generalized Hooke's law, the relationships between elastic incremental effective stresses and soil displacements are given by

$$\begin{aligned}\sigma'_{sx} &= 2G\left[\frac{\partial u_s}{\partial x}+\frac{\mu}{1-2\mu}\varepsilon_s\right],\quad \sigma'_{sz}=2G\left[\frac{\partial w_s}{\partial z}+\frac{\mu}{1-2\mu}\varepsilon_s\right],\\ \tau_{sxz} &= G\left[\frac{\partial u_s}{\partial z}+\frac{\partial w_s}{\partial x}\right]=\tau_{szx},\end{aligned} \tag{10.17}$$

where σ'_{sx} and σ'_{sz} are effective normal stresses in the horizontal and vertical directions, respectively; and τ_{sxz} is the shear stress.

It is important to note that the equations of force equilibrium, equations, (10.13), (10.16a)–(10.16b), and the stress-strain relationships, (10.17), are only valid for an isotropic seabed. For a cross-anisotropic seabed, these equations must be modified, as considered in Jeng (2012, Chapter 5).

For a homogeneous soil matrix, mathematical expressions for the wave-induced soil response can be derived, with appropriate boundary conditions. They are:

- **SBC: Boundary conditions at seabed surface ($z=0$):**
  It is commonly accepted that vertical effective normal stresses and shear stresses vanish and the pore pressure is equal to the dynamic wave pressure at the seabed surface,i.e.,

$$\sigma'_{sz}=\tau_{sxz}=0,\quad p_s=P_b(x,t)\ \text{ at }\ z=0, \tag{10.18a}$$

- **BBC: Boundary condition at the bottom ($z=-h$ or $z\to-\infty$):**
  For the soil resting on an impermeable rigid bottom, zero displacements and no vertical flow occur at the horizontal bottom. For a seabed of infinite thickness,

$$u_s=w_s=p_s=0\ \text{ as }\ z\to-\infty, \tag{10.18b}$$

  For a seabed of finite thickness,

$$u_s=w_s=\frac{\partial p_s}{\partial z}=0\ \text{ as }\ z=-h, \tag{10.18c}$$

The boundary value problem, describing the wave-seabed interactions, can be solved, based on the governing equations, (10.13) & (10.16), and boundary conditions, (10.18). The analytical solution for the wave-induced pore pressure and soil displacements can first be obtained, from which the effective stresses can then be found from (10.17).

10.3.2 YAMAMOTO-MADSEN MODEL

The above boundary value problem is for 2D progressive wave-induced soil response in a isotropic homogeneous seabed. the analytical solution was first introduced by Yamamoto et al. (1978) and Madsen (1978) for 2D progressive waves, further

extended to 3D short-crested waves system (Hsu et al., 1993; Hsu and Jeng, 1994; Hsu et al., 1995) for different seabed conditions.

For an infinite seabed, the complete expressions for the soil displacements can be expressed by (Hsu et al., 1993)

$$u_s = \frac{ip_o}{2G}\left[(C_0^\infty + C_1^\infty z)\ e^{kz} + C_2^\infty\ e^{\delta z}\right]\ e^{i(kx-\omega t)}, \tag{10.19a}$$

$$w_s = \frac{p_o}{2G}\left[\left(C_0^\infty - \frac{1+2\lambda^*}{k}C_1^\infty + C_1^\infty z\right)\ e^{kz} + \frac{\delta}{k}C_2^\infty\ e^{\delta z}\right]\ e^{i(kx-\omega t)}, \tag{10.19b}$$

where p_0 is the amplitude of linear wave pressures, defined in (10.4).

The wave-induced pore pressure is given by

$$p_s = \frac{p_o}{1-2\mu}\left[(1-2\mu-\lambda^*)C_1^\infty\ e^{kz} + \frac{\delta^2-k^2}{k}(1-\mu)C_2^\infty\ e^{\delta z}\right]\ e^{i(kx-\omega t)}, \tag{10.19c}$$

and the effective vertical stresses are

$$\begin{aligned}\sigma'_{sx} = -p_o\Bigg\{&\left[k(C_0^\infty + C_1^\infty z) + \frac{2\mu\lambda^*}{1-2\mu}C_1^\infty\right]\ e^{kz}\\ &+\left(k^2 - \frac{\mu(\delta^2-k^2)}{k(1-2\mu)}\right)C_2^\infty\ e^{\delta z}\Bigg\}\ e^{i(kx-\omega t)},\end{aligned} \tag{10.19d}$$

$$\begin{aligned}\sigma'_{sz} = p_o\Bigg\{&\left[kC_0^\infty + C_1^\infty kz - \frac{2\lambda^*(1-\mu)}{1-2\mu}C_1^\infty\right]\ e^{kz}\\ &+\frac{1}{k(1-2\mu)}\left(\delta^2(1-\mu) - k^2\mu\right)C_2^\infty\ e^{\delta z}\Bigg\}\ e^{i(kx-\omega t)},\end{aligned} \tag{10.19e}$$

and the shear stresses are given by

$$\tau_{sxz} = ip_o\left\{[kC_0^\infty + (kz-\lambda^*)C_1^\infty]\ e^{kz} + \delta C_2^\infty\ e^{\delta z}\right\}\ e^{i(kx-\omega t)}, \tag{10.19f}$$

where the δ and λ^* coefficients are defined as

$$\delta^2 = k^2\frac{k_x}{k_z} - \frac{i\omega\gamma_w}{k_z}\left(n'\beta + \frac{1-2\mu}{2G(1-\mu)}\right), \tag{10.20a}$$

$$\lambda^* = \frac{(1-2\mu)\{k^2(1-\frac{k_x}{k_z}) + \frac{i\omega\gamma_w n'\beta}{k_z}\}}{k^2(1-\frac{k_x}{k_z}) + \frac{i\omega\gamma_w}{k_z}(n'\beta + \frac{1-2\mu}{G})}. \tag{10.20b}$$

In equations (10.19), the C_i^∞ coefficients are given by

$$C_0^\infty = \frac{-\lambda^*[\mu(\delta-k)^2 - \delta(\delta-2k)]}{k(\delta-k)(\delta-\delta\mu+k\mu+k\lambda^*)}, \tag{10.21a}$$

$$C_1^{\infty} = \frac{\delta - \delta\mu + k\mu}{\delta - \delta\mu + k\mu + k\lambda^*}, \tag{10.21b}$$

$$C_2^{\infty} = \frac{k\lambda^*}{(\delta - k)(\delta - \delta\mu + k\mu + k\lambda^*)}. \tag{10.21c}$$

Note that there is a typo "missing k" in the expression of σ_x' in Jeng (2012) and Jeng (2018). The original reference (Hsu et al., 1993) is correct and should be referred to.

The above solution is for an infinite seabed, the analytical solution for a seabed of finite thickness can be found in Hsu and Jeng (1994). Following the same procedure, the semi-analytical solution for a layered seabed can be found in Hsu et al. (1995).

10.3.3 OKUSA (1985) MODEL

The consolidation model presented in the last section is based on the plane strain conditions. Based on the *plane stress conditions*, Okusa (1985) derived an analytical solution, which decoupled the consolidation model's sixth order differential equations into one fourth-order differential equation and one second-order differential equation. In this subsection, we only outlined final solution for an infinite seabed. For the detailed derivations, readers can refer to Okusa (1985).

In Okusa (1985), an infinite seabed was considered. The final form of the wave-induced soil response can be expressed as,

$$p_s = p_0 \left\{ B_1' e^{kz} \cos(kx - \omega t) + (1 - B_1') e^{\delta_1 z} \cos(kx - \delta_2 z - \omega t) \right\}, \tag{10.22a}$$

$$\begin{aligned} \sigma_{sx}' = & p_0 \left\{ (1 - B_1') e^{kz} \cos(kx - \omega t) + kz e^{kz} \cos(kx - \omega t) \right. \\ & \left. - \frac{\mu(1 - B_1')}{1 - \mu} e^{\delta_1 z} \cos(kx - \delta_2 z - \omega t) \right\}, \end{aligned} \tag{10.22b}$$

$$\begin{aligned} \sigma_{sz}' = & p_0 \left\{ (1 - B_1') e^{kz} \cos(kx - \omega t) - kz e^{kz} \cos(kx - \omega t) \right. \\ & \left. - (1 - B_1') e^{\delta_1 z} \cos(kx - \delta_2 z - \omega t) \right\}, \end{aligned} \tag{10.22c}$$

$$\tau_{sxz} = p_0 \left\{ kz e^{kz} \sin(kx - \omega t) \right\}, \tag{10.22d}$$

$$\frac{1}{B_1'} = 1 + \frac{3(1 - B)}{2 + (1 + \mu)B} = 1 + \frac{n'\beta}{m_v}, \quad \delta_1 = \delta_2 = \sqrt{\omega / 2c_v}, \tag{10.22e}$$

$$c_v = \frac{K_z B'}{\gamma_w m_v}, \quad m_v = \frac{(1 - 2\mu)}{2G(1 - \mu)}, \tag{10.22f}$$

where B is the Skemption's pore pressure coefficient and c_v is the coefficient of consolidation.

10.3.4 BOUNDARY-LAYER APPROXIMATION: MEI AND FODA (1981)

Based on the mixture theory, Mei and Foda (1981) proposed the *boundary-layer approximation* and further discussed its application to the problem of waves propagating over a porous seabed and proposed a boundary layer approximation. The detailed derivation can be found in Mei (2003, Chapter 13). In this section, we only outline their solutions for both infinite seabed and a seabed of finite thickness.

In principle, Mei and Foda (1981) assumed the soil response in a porous medium can be divided into two components: within the top thin layer $z = O(\delta^*) \ll O(L)$, where L is the wavelength and δ^* is the boundary layer thickness, which will is defined in (10.25). That is

$$(\dots) = (\dots)_{\text{out}} + (\dots)_{\text{b.l.}}, \tag{10.23}$$

For an infinite seabed, the pore pressure and stresses can be expressed as,

$$p = p_0 \left[\frac{1}{1+m} e^{kz} + \frac{m}{1+m} \Gamma \right] e^{i(kx-\omega t)}, \tag{10.24a}$$

$$\sigma'_{sx} = p_0 \left[\left(-\frac{m}{1+m} - kz \right) e^{kz} + \frac{\mu}{1-\mu} \frac{m}{1+m} \Gamma \right] e^{i(kx-\omega t)}, \tag{10.24b}$$

$$\sigma'_{sz} = p_0 \left[\left(-\frac{m}{1+m} + kz \right) e^{kz} + \frac{m}{1+m} \Gamma \right] e^{i(kx-\omega t)}, \tag{10.24c}$$

$$\tau_{sxz} = i p_0 k z e^{kz} \, e^{i(kx-\omega t)}, \tag{10.24d}$$

where

$$\delta^* = \left(\frac{G k_s / \gamma_w \omega}{n' G \beta + \frac{1-2\mu}{2(1-\mu)}} \right)^{1/2}, \quad \Gamma = e^{(1-i)kz/(\sqrt{2}\delta^*)}, \quad m = \frac{n' G \beta}{1-2\mu}. \tag{10.25}$$

Note that there was a typo in the expression of δ^* in Jeng (2018), which is corrected here.

For a seabed of finite thickness, the pore pressure and stresses are given as,

$$p = p_0 \left\{ -\frac{1}{1+m} \left(\Omega_2 \cosh kz - \Omega_1 \sinh kz \right) + \left(1 + \frac{\Omega_2}{1+m} \right) \Gamma^* \right\} e^{i(kx-\omega t)}, \tag{10.26a}$$

$$\begin{aligned} \sigma'_{sx} = p_0 \Bigg\{ & \left[\left(1 + \frac{1+2m}{1+m} \Omega_2 \right) \cosh kz - \frac{m}{1+m} \Omega_1 \sinh kz \right. \\ & \left. + kz \left(\Omega_2 \sinh kz - \Omega_1 \cosh kz \right) \right] + \frac{\mu}{1-2\mu} \left(1 + \frac{\Omega_2}{1+m} \right) \Gamma^* \Bigg\} e^{i(kx-\omega t)}, \end{aligned} \tag{10.26b}$$

$$\sigma'_{sz} = -p_0 \left\{ \left[\left(1+\frac{\Omega_2}{1+m}\right)\cosh kz - \frac{\Omega_1}{1+m}\sinh kz \right.\right. \\ \left.\left. +kz\left(\Omega_2 \sinh kz - \Omega_1 \cosh kz\right)\right] + \left(1+\frac{\Omega_2}{1+m}\right)\Gamma^* \right\} e^{i(kx-\omega t)}, \tag{10.26c}$$

$$\tau_{sxz} = -ip_0\left[(1+\Omega_2)\sinh kz + kz\left(\Omega_2\cosh kz - \Omega_1 \sinh kz\right)\right]\ e^{i(kx-\omega t)}, \tag{10.26d}$$

where

$$\Omega_1 = \frac{4kh + 2(1-4\Gamma^*)\sinh 2kh}{\Lambda},\quad \Omega_2 = \frac{2-2(1-4\Gamma^*)\cosh 2kh}{\Lambda}, \\ \Gamma^* = \frac{\lambda_e + 2G}{2(\lambda_e+G)},\quad \lambda_e = n'\beta + \frac{2G\mu}{1-2\mu}. \tag{10.27}$$

10.3.5 DISCUSSION: COMPARISONS BETWEEN VARIOUS MODELS

In this section, we compare different models presented previously. First, we compare the solutions for infinite seabed. For a fully saturated seabed, with the following treatments,

- $\lambda^* = 0$ in Y-M model in (10.19),
- $B'_1 = 1$ in Okusa (1985) model in (10.22), and
- $m = 0$ in Mei and Foda (1981) model in (10.24),

it is obvious that three solutions are identically. Therefore, we only present the numerical results for an unsaturated seabed for both coarse sand and fine sand in Figure 10.3.

Figure 10.3 illustrates the vertical distribution of the maximum amplitude of the wave-induced soil response versus soil depth (z/L) obtained from three different analytical solutions (Mei and Foda, 1981; Okusa, 1985; Hsu et al., 1993). An unsaturated seabed with $S_r = 0.98$ is considered as an example here. The wave conditions in North Sea used in the example is for a 15 sec progressive wave in a water depth d = 70 m (wavelength L = 311.59 m). Fine and coarse sands are used, with permeability coefficients of $k_s = k_x = k_z = 10^{-4}$ m/sec and 10^{-2} m/sec, respectively. As shown in the figure, both Y-M model and Mei and Foda (1981) model are identical for fine sane, while there are slightly difference for coarse sand. Comparing Okusa (1985) model and Y-M model, slightly difference is observed for both coarse sand and fine sand. However, these differences are insignificant.

To facilitate the second comparison, the results of consolidation model was computed from the analytical solution for a seabed of finite thickness (Hsu and Jeng, 1994), and that of Mei and Foda (1981) from their final equations. For a fully saturated and isotropic seabed of finite thickness, h = 25 m and $G\beta$ = 0, this data set represents soil-wave conditions for the North Sea. The vertical distributions of

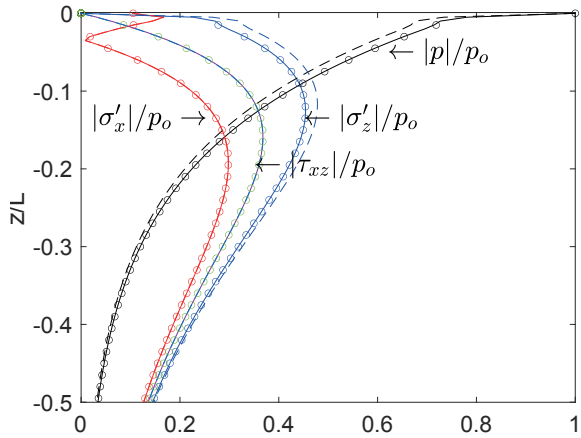

(a) Fine sand ($k_s = 10^{-4}$ m/s)

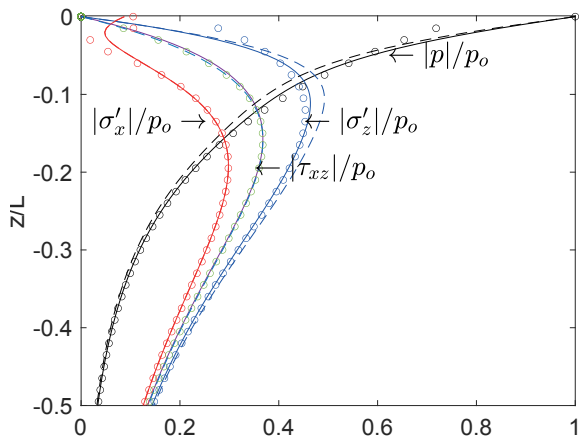

(b) Coarse sand ($k_s = 10^{-2}$ m/s)

Figure 10.3 Vertical distribution of the maximum pore pressure and effective stresses versus z/L for an unsaturated infinite seabed. Notation: Mei and Foda (1981) in "$\circ$", Okusa (1985) in dashed lines, and Y-M model in solid lines. Input data: T=15 sec, d=70 m, L=311.59 m, $G = 10^7$ N/m^2, S_r=0.98, μ =1/3, n'=0.3.

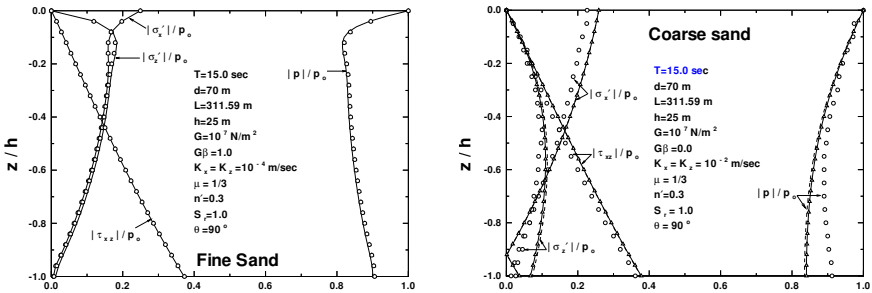

(a) Saturated seabed

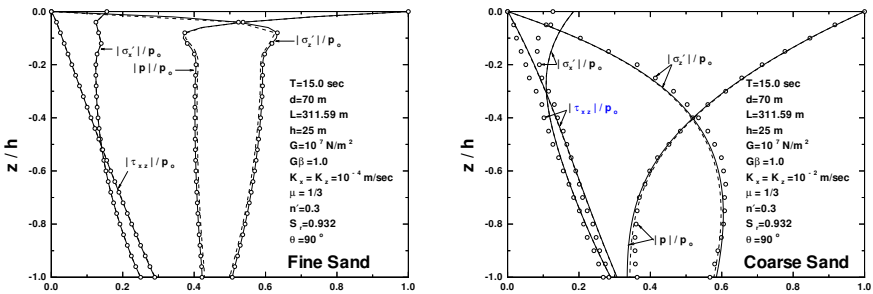

(b) Unsaturated seabed

Figure 10.4 Vertical distribution of the maximum pore pressure and effective stresses versus z/h for a hydraulically isotropic seabed of finite thickness. Notation: Mei and Foda (1981) in "○", Jeng and Lin (1996) in dashed lines, and Y-M model in solid lines.

the non-dimensional pore pressure $|p_s|/p_o$ and effective stresses, $|\sigma'_{sx}|/p_o$, $|\sigma'_{sz}|/p_o$ and $|\tau_{sxz}|/p_o$ are drawn as a function of z/h in Figure 10.4. It also agrees with the computed results of Mei and Foda (1981) for fine sand, but they deviate slightly from it for coarse sand, as shown in Figure 10.4(a)).

For a partially saturated condition at S_r= 0.932 ($G\beta = 1.0$). For fine sand under an unsaturated condition, the normalized pore pressure and effective stresses against z/h from Jeng and Lin (1996) are in almost complete agreement with the analytical solution (Figure 10.4(b)). However, Mei and Foda (1981) results for coarse sand (the circle "○" in Figure 10.4(b)) also deviate slightly from the exact solution, similar to that for a fully saturated condition.

Although the results from the boundary-layer approximation proposed by Mei and Foda (1981) differ slightly from Hsu and Jeng (1994) solution near the seabed bottom, Mei and Foda (1981) solutions provide much simpler expressions than that of Hsu and Jeng (1994). Since the wave-induced seabed instability only occurs near the seabed surface (Jeng, 1997*b*), and the results of boundary-layer approximation are almost identical to the exact solutions in these regions, the solution of Mei and Foda (1981) may be more readily accessible for engineering applications.

In addition to the comparisons between different analytical solutions, comparisons against the results of numerical models are presented in Figure 10.4. The results of a 2D numerical model (finite element method) of Jeng and Lin (1996) are included for saturated fine and coarse sands. Complete agreement was found in the results of the analytical solution and numerical model (FEM) (Jeng and Lin, 1996) for both coarse and fine sand.

10.3.6 DISCUSSION: COMPARISON WITH EXPERIMENTAL DATA

The results of consolidation model (Hsu and Jeng, 1994) is further compared with the recent 1D experimental results (Liu et al., 2015). Figure 10.5 presents a comparison of the wave-induced pore pressure ($|p_s|/p_0$) versus the sandy deposit relative depth (z/h) between the experimental results and the analytical solution. In the figure, p_0 is the amplitude of dynamic wave pressure at the surface of the sandy deposit, which was defined in (10.4).

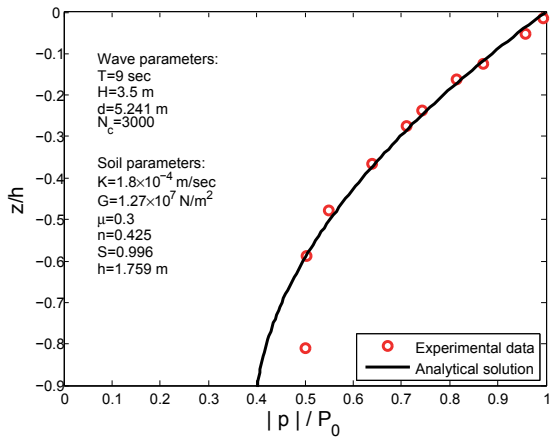

Figure 10.5 Vertical distribution of the maximum amplitudes of wave-induced pore pressure ($|p_s|/p_0$) versus the sandy deposit relative depth (z/h) for comparison between the experimental data (symbols) with analytical solution (solid line).

As shown in Figure 10.5, the analytical solution overall agrees with the experimental results in the upper part of the sandy deposit. However, in the lower part of the sandy deposit, the experimental results and the analytical solution presented some significant differences. One possible explanation is that sandy deposit thickness has been changing during the wave loading, as discussed in Liu et al. (2015). The initial sandy deposit thickness is 1.8 m in the experiment. However, the sandy deposit thickness changed once the deposit became unstable (i.e., liquefaction occurred), the sandy deposit surface will move up and down. Furthermore, the changing of sandy deposit thickness will cause changes in sandy deposit relative depth (z/h), which leads to the changing in maximum amplitudes of wave-induced pore pressures ($|p_s|/p_0$). Since the consolidation model (Hsu and Jeng, 1994) was based on

poro-elastic theory and assumption of small deformation of solid, which was not able to provide precise prediction of the process of large deformation such as liquefaction. Another possible mechanism is that the relative density of the deposit is considerably changed along the depth since the deposit depth is pretty large. Thus, the soil response may be deviated considerably from the analytical curve which assumes constant soil properties all across the soil depth.

10.4 SEABED MODELS: RESIDUAL MECHANISM

Numerous studies for wave-induced residual liquefaction have been carried out since the 1980s. Most models were based on the Seed-Rahman approach (Seed and Rahman, 1978), which was adopted from the earthquake-induced liquefaction. This approach has been widely used because of its simplicity. Later, some poro-elastoplastic models were proposed for post-liquefaction and densification (Sassa et al., 2001; Miyamoto et al., 2004). In this chapter, we outline the Seed-Rahman model and its extended models.

Based on the experimental data, Seed and Rahman (1978) proposed a 1D model for the wave-induced residual pore pressures in a porous seabed. In their approach, the source term in the modified Biot's C equation is derived using a linear relationship between pore pressure ratio (u_g/σ_0') and cyclic ratio (N/N_ℓ). This model has been used by many researchers working in the field of the wave-induced residual liquefaction. Based on the 1D Seed-Rahman model (Seed and Rahman, 1978), McDougal et al. (1989) proposed a set of analytical solutions for wave-induced pore pressure build-up in a uniform layer of soil, based on the assumption of an incompressible soil. To provide a convenient practical result for engineers, McDougal et al. (1989) presented their solutions for the cases of shallow, finite and deep soil depths. Using a similar approach, Cheng et al. (2001) re-examined the analytical solution of McDougal et al. (1989) and proposed a numerical model to investigate the same problem. As pointed out by Cheng et al. (2001), the analytical solution proposed by McDougal et al. (1989) revealed some errors in the formulations. However, after a close examination of both solutions (McDougal et al., 1989; Cheng et al., 2001), Jeng et al. (2007) found numerous errors in both publications and proposed a set of new correct solutions by using Laplace transformation for deep foundation and Fourier transformation for finite and shallow foundations. The analytical solution for infinite seabed is the same as that of Sumer and Fredsoe (2002) with a different form. Based on the analytical solutions, Jeng and Seymour (2007) proposed a simplified approximation for the prediction of wave-induced residual liquefaction in an infinite seabed, which is termed as $J-S$ curve. This model was further extended by Geremew (2013) to include the oscillatory pore pressure in the criterion of residual liquefaction. However, numerous errors was found in his paper (Geremew, 2013), as pointed out by Guo and Jeng (2014). Recently, a modified $J-S$ curve was developed for a seabed of finite thickness (Guo et al., 2014).

In the aforementioned studies for wave-induced residual pore pressures in marine sediments, the source term was considered as time-independent function because the

maximum amplitude of the oscillatory shear stress was used. In fact, this source term was determined by the oscillatory shear stress which should be a time-dependent function. Furthermore, these approaches were 1D model, which may be insufficient to represent the real process. Recently, Jeng and Zhao (2015) re-defined the source term as a time-dependent function with the instant oscillatory shear stress and developed a 2D model for residual soil response in marine sediments. This new residual model has been further applied to various marine infrastructures (Zhao and Jeng, 2015, 2016; Zhao et al., 2017).

10.4.1 1D SEED-RAHMAN MODEL

The residual pore pressure (u_e) in a homogenous, isotropic soil can be derived from the 1D Biot's consolidation equation (Sumer and Fredsoe, 2002)

$$\frac{\partial u_e}{\partial t} = c_v \frac{\partial^2 u_e}{\partial z^2} + f, \tag{10.28}$$

where f is the accumulation pore pressure source term. A detailed derivation of (10.28) can be found in Sumer and Fredsoe (2002). In (10.28), c_v is the coefficient of consolidation, given by

$$c_v = \frac{Gk_s}{\gamma_w} \frac{2(1-\mu)}{(1-2\mu)+2(1-\mu)n_s G\beta_s}. \tag{10.29}$$

To solve (10.28), the following boundary and initial conditions are required:

$$u_e(z,0) = u_e(0,t) = 0, \quad \text{and} \quad \frac{\partial u_e(h,t)}{\partial z} = 0 \ \text{ or } \ u_e(\infty,t) = 0. \tag{10.30}$$

We now investigate the "*source term*" of the pore pressure generation (f), and consider both linear and nonlinear mechanisms of pore pressure generation. The laboratory results from Seed et al. (1975); de Alba et al. (1976) established the relationship between the development of pore pressure and the number of load cycles. It is given by (Seed et al., 1975)

$$\frac{u_g}{\sigma_0'} = \frac{1}{2} + \frac{1}{\pi} \sin^{-1} \left[2 \left(\frac{N}{N_\ell} \right)^{1/\theta} - 1 \right], \tag{10.31}$$

where u_g is the pore pressure generation due to cyclic loading, σ_0' is the effective over burden, θ is the shape factor suggested to be 0.7 (Seed et al., 1975). N is the number of cycles to liquefaction, which is a function of the cyclic shear stress ratio (Seed and Rahman, 1978; Sumer and Fredsoe, 2002),

$$N_\ell = \left[\frac{\tau_m}{\alpha_r \sigma_0'} \right]^{-1/\beta_r}, \tag{10.32}$$

where τ_m is the maximum amplitude of wave-induced shear stress, and α_r and β_r are the functions of the soil type and relative density.

In (10.32), α_r and β_r are obtained by the large-scale simple shear test data corresponding to the relative density (D_r) of the soil as proposed by Seed et al. (1975). The relative density, D_r, is defined as follows:

$$D_r = \frac{e_{max} - e}{e_{max} - e_{min}}, \tag{10.33}$$

where e is the void ratio; and e_{max} and e_{min} are maximum and minimum void ratios, respectively. The coefficients α_r and β_r in (10.36) are defined from the following empirical expressions (Sumer et al., 2012):

$$\alpha_r = 0.34 D_r + 084, \quad \beta_r = 0.37 D_r - 0.46. \tag{10.34}$$

Note that the above empirical expression was firstly proposed by Sumer et al. (2012), based on the laboratory experiments (Seed et al., 1975). Due to limited number of experimental data, the correlation of the above expression is low. However, this is the only relation available in the literature. This relationship could be used as the first approximation.

To simplify the problem, a linear relation of pore pressure generation was proposed (Seed and Rahman, 1978)

$$\frac{u_g}{\sigma_0'} = \frac{N}{N_\ell}, \tag{10.35}$$

from which the source term of pore pressure generation can be expressed as

$$f = \frac{\partial u_g}{\partial t} = \frac{\sigma_0'}{T} \left[\frac{\tau_0}{\alpha_r \sigma_0'} \right]^{1/\beta_r}. \tag{10.36}$$

The linear mechanism of pore pressure generation was first applied to the wave-induced pore pressure build-up in marine sediment by Seed and Rahman (1978). Since then, this relation has been commonly used in various approaches (McDougal et al., 1989; Cheng et al., 2001; Sumer and Fredsoe, 2002; Jeng and Seymour, 2007). After a detailed investigation (Jeng et al., 2007), it is found that the full non-linear relation of pore pressure generation, (10.31), can be ignored, as the linear relation, (10.36), provides close prediction of pore pressures.

In this section, three analytical solutions are presented. First, the general solution for finite soil depth, which cover all ranges of seabed thickness. Second, the special case for shallow soil depth ($h/L \leq 0.1$) is considered. Third, the case of deep soil foundation ($h/L \geq 0.3$) is considered. Detailed derivations can be found in Jeng et al. (2007).

Finite soil model

For the finite soil depth, the amplitude of the oscillatory pore pressure (p_m) and shear stress (τ_m) for a saturated seabed are given for a seabed of finite thickness by (Hsu and Jeng, 1994)

$$p_m = \frac{p_0}{1-2\mu}\Big[(1-2\mu)(C_2e^{-kz} - C_4e^{kz} + (1-\mu)(\delta^2-k^2)(C_5e^{-\delta z} - C_6e^{\delta z})\Big], \tag{10.37a}$$

$$\tau_m = p_0\Big[(C_1+C_2kz)e^{-kz} - (C_3-C_4kz)e^{kz} + k\delta(C_5e^{-\delta z} - C_6e^{\delta z})\Big], \tag{10.37b}$$

where the C_i ($i = 1, \cdots, 6$) coefficients can be found in Hsu and Jeng (1994).

The complete function, (10.36) is required for the source term. Using a Fourier series expansion, the residual pore pressure can be expressed as

$$u_e = \sum_{n=1}^{\infty} a_n\left(1 - e^{-c_v\kappa_n^2 t/h^2}\right)\sin(\frac{\kappa_n z}{h}), \tag{10.38a}$$

$$a_n = \frac{2h}{c_v k_n^2}\int_0^h f(r)\sin\left(\frac{\kappa_n r}{h}\right)dr, \tag{10.38b}$$

where f is given in (10.36), and $\kappa_n = (2n-1)\pi/2$.

Shallow soil model

For relatively shallow soil depth, $h/L \leq 0.1$, we consider the shallow depth approximation, in which the shear stress can be expressed as

$$\tau_m = mp_0z, \tag{10.39}$$

where the value of m can be determined by equating (10.37b) and (10.39), and integrated over the entire soil depth, yielding

$$m = \frac{2}{kh^2}\Big\{-\left(C_1e^{-kh} + C_3e^{kh}\right) + \left(C_2e^{-kh} - C_4e^{kh}\right) + C_1 - C_2 + C_3 + C_4 + kh\left(C_2e^{-kh} + C_4e^{kh}\right) - k^2\left(C_5e^{-\delta h} + C_6e^{\delta h}\right) + k^2(C_5+C_6)\Big\}, \tag{10.40}$$

Then, the source term for shallow soil depth can be further simplified as

$$f = az, \quad a = \frac{(1+2K_0)\gamma'}{3T}\left[\frac{3mp_0}{\alpha_r(1+2K_0)\gamma'}\right]^{1/\beta_r}, \tag{10.41}$$

where $\gamma' = \gamma_s - \gamma_w$, and γ_s is the unit weight of soil. The residual pore pressure can again be given by a Fourier series as

$$u_e = \frac{a}{2c_v}\left[\left(h^2 z - \frac{z^3}{3}\right) - \sum_{n=1}^{\infty} a_n e^{-c_v \kappa_n^2 t/h^2} \sin\left(\frac{\kappa_n z}{h}\right)\right], \tag{10.42a}$$

$$a_n = \frac{2}{h}\int_0^h \left(h^2 r - \frac{r^3}{3}\right) \sin\left(\frac{\kappa_n r}{h}\right) dr. \tag{10.42b}$$

Deep soil model

For soil depth in the range $h/L \geq 0.3$, we consider the deep (infinite) depth approximation, in which the shear stress is given by

$$p_m = p_0 e^{-kz} \quad \text{and} \quad \tau_m = p_0 kz e^{-kz}. \tag{10.43}$$

As shown in (10.43), the wave-induced pore pressure and shear stress in an infinite seabed are independent of soil characteristic.

Based on (10.43). The source term for deep soil can be expressed as

$$f = A^* z e^{-\lambda z}, \quad \lambda = \frac{k}{\beta_r} \text{ and } A^* = \frac{(1+2K_0)\gamma'}{3T}\left[\frac{3p_0 k}{\alpha_r(1+2K_0)\gamma'}\right]^{1/\beta_r}. \tag{10.44}$$

Then, the residual pore pressure is calculated using a Laplace transformation as

$$u_e = \frac{2A^*}{c_v \lambda^3}\left[1 - \left(\frac{\lambda z}{2} + 1\right) e^{-\lambda z} - \frac{1}{\pi}\int_0^\infty \frac{e^{-rc_v\lambda^2 t}}{r(1+r)^2} \sin\left(\sqrt{r}\lambda z\right) dr\right]. \tag{10.45}$$

Sumer and Fredsoe (2002) also obtained an analytical solution in a different form. Jeng and Seymour (2007) proved that (10.45) can be reduced to the solution of Sumer and Fredsoe (2002), but (10.45) provides a much simpler form.

Engineering application of 1D model

For engineering practice, the most important task is to examine where liquefaction will occur and how deep it is. The criterion of residual liquefaction is

$$\frac{u_{e(t\to\infty)}}{\sigma_0'} = 1. \tag{10.46}$$

Based on the solution for an infinite seabed, (10.45), and the above criterion of liquefaction, we have

$$u_{e(t\to\infty)} = \frac{2A}{c_v\lambda^3}\left[1-\left(\frac{\lambda z_L}{2}+1\right)e^{-\lambda z_L}\right] = \sigma_0' = \frac{(1+2K_0)}{3}\gamma' z_L, \tag{10.47}$$

where z_L is the liquefaction depth.

Let

$$B = \frac{(1+2K_0)\gamma' c_v\lambda^2}{6A^*}. \tag{10.48}$$

The relationship of the maximum liquefied depth (z_L) and the parameter B is illustrated in Figure 10.6. For engineering applications, given wave and soil conditions, we can determine the parameter B from (10.48). The maximum liquefied depth can then be easily determined from Figure 10.6. It is noted that the relation presented in Figure 10.6 is universal, applicable to all engineering conditions.

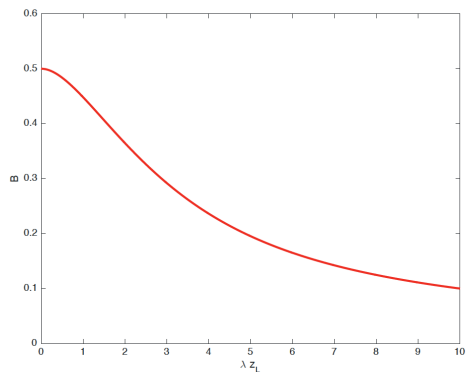

Figure 10.6 Distribution of the maximum liquefied depth (z_L) and parameter B, $J-S$ curve (Jeng and Seymour, 2007).

Herein, we further consider a special case: assuming λz_L is small. With this assumption, if we further expend $\exp(-\lambda z_L)$ with Taylor's expansion and then use the first three terms (Jeng et al., 2007), we have the solution of (10.47) as $z=0$ or

$$z_L = \frac{2}{\lambda}\sqrt{\frac{1}{2}-B}. \tag{10.49}$$

Note that (10.49) is only valid under the condition of $B \le 1/2$. It is noted that $B > 1/2$ will provide an unrealistic solution. Under such a condition, $z_L = 0$ will be the solution (i.e., no liquefaction occurs).

Based on Jeng and Seymour (2007), Geremew (2013) proposed a simplified model to directly adding oscillatory (Hsu and Jeng, 1994) and residual (Jeng and

Seymour, 2007) components to examine the wave-induced residual liquefaction. That is,

$$\frac{2A}{c_v\lambda^3}\left[1-\left(\frac{\lambda z_L}{2}+1\right)e^{-\lambda z_L}\right]+p_0e^{-kz_L}=\frac{(1+2K_0)}{3}\gamma' z_L. \tag{10.50}$$

Unfortunately, numerous mistakes were found in their work, for example, the determination of the wavelength and calculation of the liquefaction depth (Guo and Jeng, 2014). Based on (10.50), the revised $J-S$ curve is is illustrated in Figure 10.7 together with the case presented in Geremew (2013) (B=0.046, λz_L=21.73). Furthermore, based on the input data used in Geremew (2013), the oscillatory component is only 1/70 of the residual component (Guo and Jeng, 2014). In such a condition, the oscillatory mechanism can be ignored.

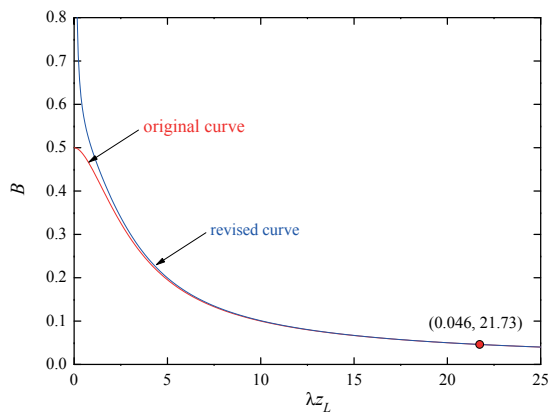

Figure 10.7 The revised $J-S$ curve for the distribution of the maximum liquefied depth (z_L) and parameter B (Guo and Jeng, 2014).

Following the same approach for a deep foundation (Jeng and Seymour, 2007), Guo et al. (2014) further extended the $J-S$ curve (Jeng and Seymour, 2007) to the case of a seabed of finite thickness, and proposed a new relationship between the liquefaction depth ($z_L^*=z_L/h$) and parameter (B^*) as

$$3-z_L^{*2}=B^*,\quad B^*=\frac{2(1+2K_0)\gamma' c_v}{ah^2}, \tag{10.51}$$

which is the modified $J-S$ curve and plotted in Figure 10.8. More detailed parametric study in regarding the effects of soil parameters on the wave-induced residual liquefaction can be found in Guo et al. (2014).

It is noted that z_L^* is positive and less than 1.0 ($0\le z_L^*\le h$). Figure 10.8 illustrates the relationship of the maximum liquefied depth z_L^* versus the parameter (B^*). With given wave and soil conditions, this chart provides a simple and visualized evaluation

of the liquefied depth in engineering practice. If B^* is greater than 3, no liquefaction appears; for $B^* \leq 2$, the shallow seabed will be totally liquefied. When B^* lies between 2 and 3, the liquefied depth can be directly determined from this chart with given wave and seabed characteristics.

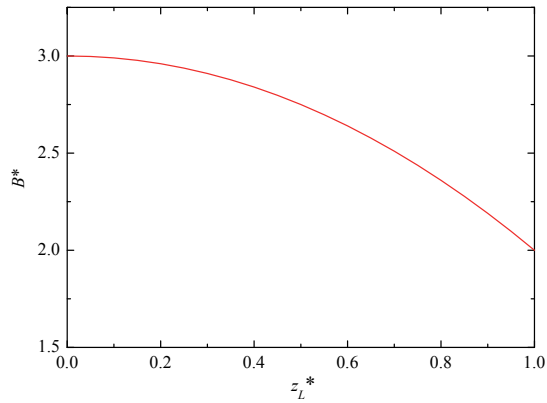

Figure 10.8 Distribution of the maximum liquefied depth (z^*) and parameter B^* in a seabed of finite thickness.

10.4.2 2D SEED-RAHMAN MODEL

The previous 1D model is re-derived to 2D by Jeng and Zhao (2015) as

$$c_{v2}\left(\frac{\partial^2 u_e}{\partial x^2}+\frac{\partial^2 u_e}{\partial z^2}\right)u_e=\frac{\gamma_w c_v(1+n'\beta)}{k_s}\frac{\partial u_e}{\partial t}+f(x,z,t),$$
$$c_{v2}=\frac{Gk_s}{\gamma_w(1-2\mu)}, \tag{10.52}$$

where c_{v2} is the coefficient of consolidation in 2D

In (10.52), the source term ($f(x,z,t)$) for the new model is defined as

$$f(t)=\frac{\partial u_g}{\partial t}=\frac{\sigma_0'}{T}\left[\frac{|\tilde{\tau}_{ins}(x,z,t)|}{\alpha_r\sigma_0'}\right]^{-1/\beta_r}, \tag{10.53}$$

It is noted that the governing equation used in the new model (10.52), which is different from the previous 1D model (Sumer and Fredsoe, 2002; Jeng and Seymour, 2007). In addition, the source term used in the previous models was generated by the maximum amplitude of transient shear stresses over a wave period, which is a simplified calculation method. While the the instant absolute oscillatory shear stress are considered as the source of pore pressure generation in this new model. This new model will reflect the effects of instant oscillatory shear stresses on the pore pressure build-up, which will become a time-dependent function, as shown in (10.53).

10.4.3 DISCUSSION: ROLE OF OSCILLATORY AND RESIDUAL MECHANISMS

In Jeng and Seymour (2007), a question was raised up "Under what conditions, residual mechanism is more important than oscillatory mechanism?" They defined the scale factor (ε_1) as the ratio of equilibrium residual pore pressure ($u_e(z,\infty)$, to the amplitude of the oscillatory pore pressure ($|p_{osc}|$). that is,

$$\varepsilon_1 = \frac{u_e(z,\infty)}{|p_{osc}|} = \frac{2A\left[1-\left(\frac{\lambda z}{2}+1\right)e^{-\lambda z}\right]}{c_v\lambda^3 p_0 e^{-kz}}. \tag{10.54}$$

Based on (10.54), Jeng and Seymour (2007) plot Figure 10.9(a) to indicating the range where each mechanism dominate the development of the pore pressures. That is, when should we can consider residual or oscillatory mechanism or both mechanisms. $\varepsilon_1 = 1$ is used as a critical value. However, when we investigate the problem closely, it is found that ε_1 is impossible to achieve for any wave and soil conditions. Therefore, using ε_1 and Figure 10.9(a), reproduced from Jeng and Seymour (2007), is incorrect for the scaling analysis. Note that the original figure in Jeng and Seymour (2007) seems incorrect, it was re-plotted in Figure 10.9(a) with the same input data here.

Referring to the criteria for liquefaction for both oscillatory and residual mechanisms, the above definition is inappropriate and cannot present the scaling analysis for realistic condition. Here, we re-defined the scaling factor as

$$\varepsilon_2 = \frac{u_e(z,\infty)}{p_0 - |p_{osc}|} = \frac{2A\left[1-\left(\frac{\lambda z}{2}+1\right)e^{-\lambda z}\right]}{c_v\lambda^3 p_0(1-e^{-kz})}. \tag{10.55}$$

Herein, $(p_0 - |p_{osc}|)$ represents the excess pore pressure for oscillatory mechanism, which is part of liquefaction criterion of liquefaction (Zen and Yamazaki, 1990*a*; Jeng, 1997*b*).

To clarify the range of residual mechanism with an appropriate index, we plot the critical line of $\varepsilon_2 = 1$ with wave steepness and relative water depth at $z = 5$ m in Figure 10.9(b). The lines represent the critical relationship of H/L and d/L with given a consolidation coefficient c_v. The region below the curve denotes conditions when the oscillating mechanism dominates, while the region above the curve denotes conditions when the residual mechanism dominates. The critical curve will move up as the consolidation coefficient c_v increases.

To further compare the difference between the results of ε_1 and ε_2, the results of $c_v = 0.01$ and $c_v = 0.001$ are plotted in Figure 10.9(c). As shown in the figure, using $\varepsilon = 1$ in the scaling analysis will over-estimate the role of oscillatory mechanism, as the curves move up. Although both criteria of ε_1 and ε_2 provide similar trends, it is more appropriate to use $\varepsilon_2 = 1$ as the criterion to determine the role of both mechanisms.

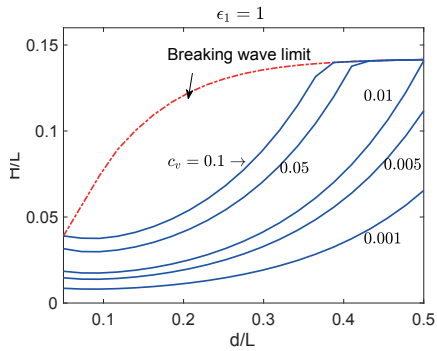

(a) $\varepsilon_1 = 1$

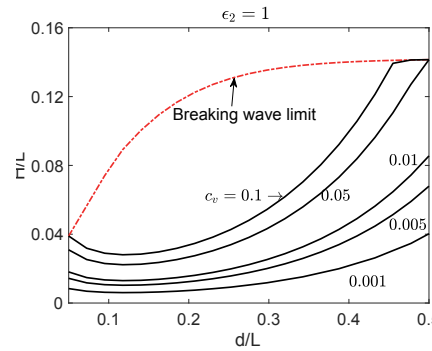

(b) $\varepsilon_2 = 1$

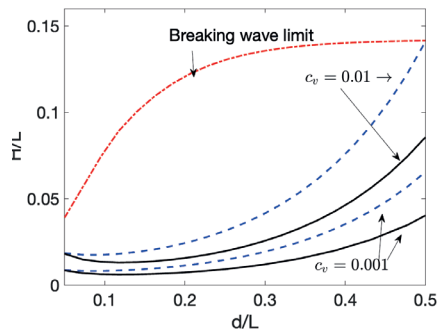

(c) ε_2 (solid lines) and ε_1 (dash lines)

Figure 10.9 Distribution of critical wave steepness (H/L) versus relative water depth (d/L) for various values of consolidation coefficient (c_v) with criteria of ε_1 andε_2. Input data: T=10 sec, $\alpha_r = 0.246$, $\beta_r = 0.25$, $z = 5$ m.

10.4.4 DISCUSSION: COMPARISON BETWEEN 1D AND 2D SEED-RAHMAN MODELS

The major differences between the new 2D model (Jeng and Zhao, 2015) and previous 1D models (Sumer and Fredsoe, 2002; Jeng and Seymour, 2007) is the definition and numerical simulation method for the source term. As shown in (10.36) for the 1D model, the source term is a function of z and being time-independent in the maximum model, while it's a time-dependent function in the new 2D model, as shown in (10.53).

The previous experimental data reported in Sumer et al. (2012) are used to validate the residual mechanism of the present numerical model. The numerical

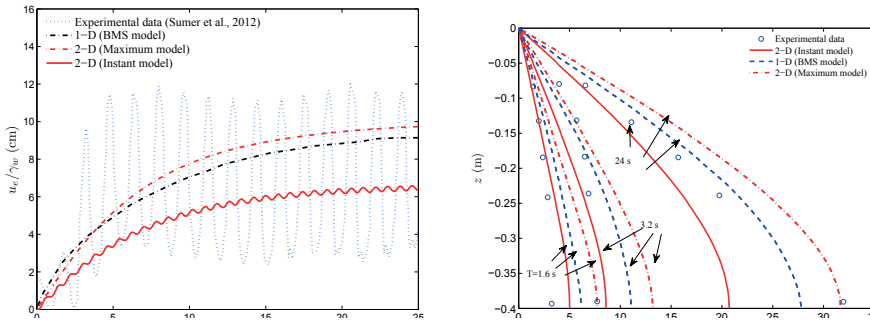

(a) (x,z)=(0,-0.085) m (b) (x,z)=(0,-0.24) m

Figure 10.10 Comparison of model results and experimental data (Sumer et al., 2012). Input data: H=0.18 m, T=1.6 s, d=0.55 m, $k_s = 1.5\times10^{-5}$ m/s, n'=0.51, $G = 1.92\times10^6$N/m^2, h=0.4 m, μ=0.29, $c_v = 0.0127$ m^2/s, D_r=0.28.

results are observed in Figure 10.10. In the figure, 1D analytical solutions developed by Sumer and Fredsoe (2002) are also included in the comparison. As shown in the figure, the overall trend of the residual pore pressure of the present 2D instant model can capture the experimental data extremely well, and the value of the build-up pore pressure agrees quite well with the experimental data plotted in the figure, which provides much better prediction than the 2D maximum model. There is a little difference of the trend of the build-up pore pressure between the instant 2D model with the 1D model (Sumer and Fredsoe, 2002; Jeng et al., 2007), but the final residual pore pressure is acceptable. This comparison validate the new model and demonstrate the significant improvement of the prediction of the wave-induced residual pore pressures in marine sediment with the new definition of the source term in our new 2D model.

10.4.5 DISCUSSION: DEVELOPMENT OF LIQUEFACTION ZONES

The source term for the residual pore pressure generation is re-defined as a time-dependent function in the new 2D model. This new feature will directly affect the pattern of the liquefaction zone. It is well-known that liquefaction occurs when the excess pore pressure reaches the initial effective stress, i.e., $u_e = \sigma_0'$. The source term for the residual pore pressure generation is 2D and time-dependent function in the present model. This feature directly affects the pattern of the liquefaction zone. Figure 10.11(a) shows the resulting variations of wave-induced residual liquefaction zones versus the wave cycle (t/T) for various types of wave loads. As shown in the figure, the liquefaction zone under progressive waves occurs as a 2D pattern during the first wave period after liquefaction ($t/T = 90$ in this example). The reason there is a 2D liquefaction zone in the first liquefaction wave period may be from the 2D phase-resolved shear stress used as the source of the pore pressure. The region where the 2D pattern occurs is related to the initial incidence of the wave phases. As the

progressive wave loading continues, the nature of the liquefaction zone changes from 2D pattern to 1D pattern after one wave period. The 1D pattern travels with the wave and reaches a constant value after several wave cycles.

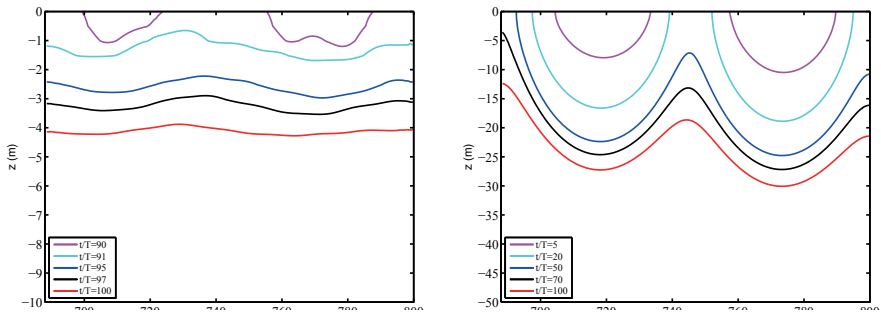

(a) progressive wave (b) standing waves

Figure 10.11 Time histories of the development of the liquefaction zone and pore pressure accumulations along the x-direction under (a) progressive waves and (b) standing waves. Input data: H=5 m, T=10 s, d=16 m, $k_s = 10^{-4}$ m/s, n'=0.425, $G = 5 \times 10^6$N/m^2, h=50 m, μ=0.35, $c_v = 0.1699$ m^2/s, D_r=0.2, α_r=0.246 and β_r=0.165.

For the case of a standing wave system, as shown in Figure 10.11(b), the liquefaction zone will occur initially in the region where the shear strains are most significant, then this liquefied zone extends laterally and vertically. Finally even the soil at the antinode section will be liquefied after certain wave cycles. This phenomenon coincide well with what has been discussed by Sassa et al. (2001).

10.5 TWO-WAY COUPLING MODEL

Most existing theoretical models (both analytical solutions and numerical simulations) for wave-seabed interactions have based on one-way coupling (or named as integrated) process (Jeng et al., 2013). In these approaches, the flow domain is solved by either potential flow (Yamamoto et al., 1978; Hsu and Jeng, 1994) or Navier-Stokes model (Jeng et al., 2013; Yang and Ye, 2017; Li et al., 2018, 2020), which assumed that an impermeable seabed as the bottom boundary condition, as shown in Figure 10.12(a). Based on the flow model for wave motion with (or without) currents, the dynamic wave pressures along the seabed surface can be obtained and used as the external loading for the seabed domain, which is a porous medium. There is an obvious contradiction between the physical process and theoretical models in the existing approaches. That is, the assumption of the impermeable seabed for flow model contradicts the porous seabed model. Another drawback of the one-way coupling or integrated models is that wave motion will not be affected by the seabed characteristics such as deformation and seepage, although it may not always be significant for certain types of seabeds.

To overcome the above contradiction between physical process and theoretical models, two methods can be adopted. The first approach is to solve flow and seabed

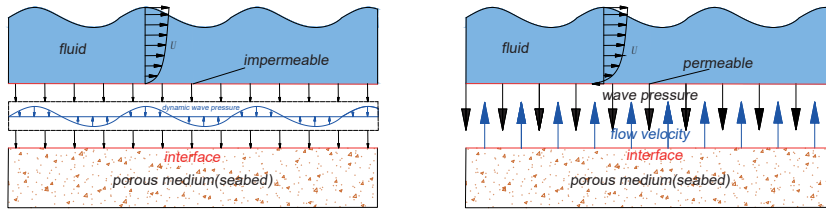

(a) Concept of one-way coupling model (b) Concept of two-way coupling model

Figure 10.12 Concepts of coupling models. (a) one-way coupling concept and (b) two-way coupling concept.

at the same time in one model, which ensures fluid and solid domains neither detach nor overlap during deformation (Zhang and Hisada, 2001). However, the method requires a large system equation consist of discrete equations of fluid and seabed domains, which would likely cause the instability of the numerical results due to the large difference of fluid and seabed stiffness. Meanwhile, the method requires the same mesh along the interface of wave and seabed, which is difficult in practice due to the same accuracy usually requiring larger mesh size of fluid domain comparing with the seabed fluid (Wang et al., 2004). Another approach is to solve flow and seabed separately, but the data exchange the boundary conditions at the interface of wave and seabed domains would be bidirectional rather than one-way. This could avoids the demerits of the first method and allowed the spatial distributions of nodes along the interface and the time-step size in different sub-domains.

Most previous studies have adopted the one-way coupling approach (or named integrated model). To date, only a few researchers attempted the two-way coupling approach to understand in the effects of seabed characteristics on the wave motion, such as wave damping effects. For example, Jeng (2000) adopted the analytical solution for the seabed model (Hsu and Jeng, 1994) with the concept of complex wave number to examine the wave damping process. However, his approach was based on the linear wave theory and potential flow theory. This approach was further extended to wave-seabed interaction in a Coulomb-damped seabed (Lee et al., 2002). Wang et al. (2004) proposed a weak coupling algorithm for the wave-seabed interaction, based on the error integration over a time interval and space along fluid–seabed interfaces. Their model exchanged the pressure and normal velocity at the seabed surface but ignored the velocity in other direction. In their study (Wang et al., 2004), the fluid domain was solved by FVM, while the seabed was solved by meshfree model. Later, Karunarthna and Lin (2006) proposed a two-way coupling algorithm for both wave and seabed fields by the N-S equation for wave field and Biot's QS equations for the pore pressures in the seabed domain. However, in their model, the seabed was regarded as a porous medium as fluid seepage through, but they ignored the effective stress and soil displacements.

Recently, Zhai and Jeng (2022) developed a new two-way coupling model for the wave-induced oscillatory soil response. They rewrite the existing OpenFOAM model, olaFlow, by release the boundary condition at the seabed surface for the flow model. They introduced the concept of continuity of velocity at the seabed surface, in addition to the continuity condition of pressures, as shown in Figure 10.12(b). Unlike previous flow-sub model (Higuera et al., 2013; Liang et al., 2020; Liang and Jeng, 2021), the bottom boundary condition of flow sub-model treated as permeable wall with the fixed value, which is obtained from the combined seepage velocity and soil displacement induced velocity:

$$\mathbf{u}_f = -\frac{k_s}{\gamma_w}\nabla p_s + \frac{\partial \mathbf{u_s}}{\partial t}, \quad \text{at} \quad z = 0. \tag{10.56}$$

Note that the above boundary condition is similar to those in Jeng (2000) and Wang et al. (2004). However, Wang et al. (2004) missed out a negative sign in the first-term of the right-hand-side, which could be a typo.

In the two-way coupling model, the whole loop from one time step to the next time step for the two-way coupling algorithm in Figure 10.13 is divided into four steps:

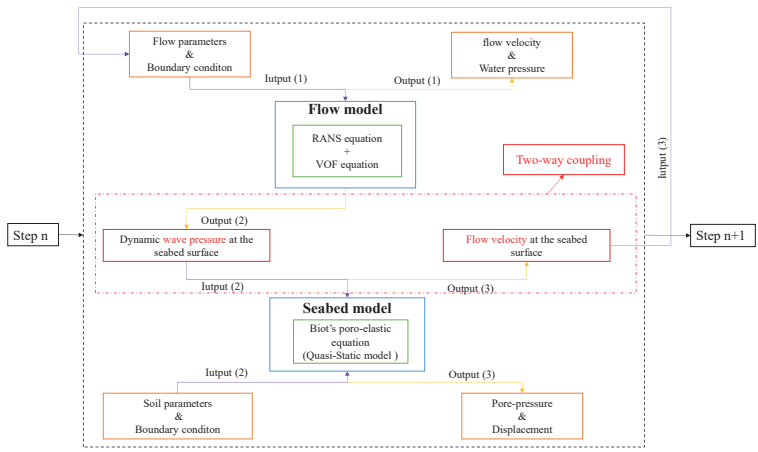

Figure 10.13 Flow chart of the numerical model.

- **Steps 1**: The flow parameters and boundary conditions are imported into flow model to solve the water pressure and flow velocity of the whole computational domain. Then, the dynamic wave pressure of the interface is imported as the external loading for the seabed model. Note that this step is the one-way coupling process, which is same as the previous model (Liang et al., 2020; Liang and Jeng, 2021). This is aim to obtain the initial

condition for the flow domain, based on the assumption of impermeable seabed.

- **Steps 2**: With soil parameters and dynamic wave pressures from the wave model in Step 1, the pore pressures, stresses and soil displacements obtained in the porous seabed model.
- **Steps 3**: Now, we replace the boundary condition at the interface for the flow model by (10.56), in which the pore pressures and soil displacements are obtained from the seabed model in Step 2. In this boundary condition, the flow velocity caused by the combination of seepage velocity and movement of soil particle induced velocity at the interface is added as the boundary condition of flow model. Then, the fluid domain will be updated after running flow model.
- **Steps 4**: The updated dynamic wave pressures will be used as the new external loading for the seabed model, and go to Step 2.

Noted that the at the beginning of the model ($n = 1$ in Figure 10.13), the flow velocity at the interaction of fluid and seabed surface are set up as zero by setting the boundary conditions as "fixedValue" of zero. Hence, the numerical process of two-way coupling model is same as the one-way coupling model at the first time step. Then, the flow velocities at the interface are calculated and input to the flow model as boundary condition at the end of the first time step. Then, the two-way coupling process as Figure 10.13 start from the second time step.

As seen in Figure 10.13, With the output(3) from the seabed model, we can obtain the combined velocity due to seepage and soil particle at the fluid-seabed interface as Input(3) for the flow model. This will affect the flow domain at each time step. In the previous one-way coupling model, there is no Input(3) in the flow model, which cannot include the effects of soil properties in the flow model.

10.5.1 COMPARISON WITH EXPERIMENTAL DATA

Herein, we compare the wave-induced pore pressure along with the seabed depth (z/h) for two coupling models with the experimental data (Liu et al., 2015) and analytical solution (Hsu and Jeng, 1994). The compared results of the maximum wave-induced pore pressure ($|p_s|/p_0$) within the seabed with depth (z/h) were displaced in Figure 10.14, in which p_s denotes the maximal pore pressure. It is obvious from the figure that the results of the present model for one-way and two-way coupling algorithms all have the same trend with the analytical results of Hsu and Jeng (1994). However, the $|p_s|/p_0$ of present model obtained by one-way and two-way coupling algorithms all larger than the analytical solutions near the seabed surface, which was due to the given wave beyond the range of linear wave but Hsu and Jeng (1994) still used the linear wave theory. Meanwhile, the solution of the present model agree well with the experimental data (Liu et al., 2015), but the results of two-way coupling model closer to the experimental results comparing with the present one-way coupling model.

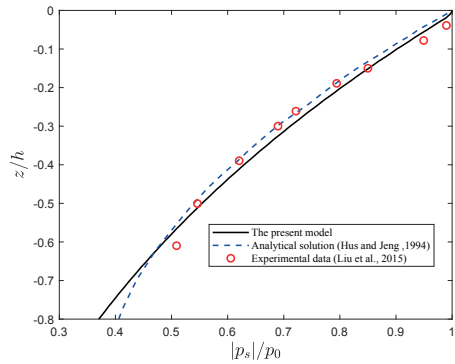

Figure 10.14 Comparisons of the present results (two-way coupling concept) with the experimental data (Liu et al., 2015) and the analytical solution with one-way coupling concept (Hsu and Jeng, 1994).

10.5.2 COMPARISON BETWEEN TWO-WAY AND ONE-WAY COUPLING MODELS FOR 2D WAVE-SEABED INTERACTIONS

In the section, we will compare the flow and seabed characteristics by using two-way with one-way coupling algorithms and clarify the condition when the two-way coupling model is necessary. In the computing domain, The length of computational domain (L_s) is set as three times linear wavelength (L_0) and the input parameters for numerical examples are given in Table 10.1.

Table 10.1
Input data for numerical examples.

Characteristics	Value	Unit
Wave characteristics		
Wave height (H)	3.0	[m]
Wave period (T)	8	[s]
Water depth (d)	10	[m]
Water density (ρ_w)	1000	[kg/m^3]
Bulk modulus of elasticity of water (K_w)	2.0×10^9	[N/m^2]
Seabed characteristics		
Permeability (k_s)	5×10^{-2}	[m/s]
Poisson's ratio (μ_s)	0.3	–
Porosity (n)	0.448	–
Degree of saturation (S_r)	0.98	-
Shear modules (G_s)	5×10^6	[N/m^2]
Density of soil (ρ_s)	2679	[kg/m^3]
Seabed thickness (h)	30	[m]]

The essential difference between the one-way and two-way coupling algorithm is the different assumption for the interface between fluid and seabed (i.e., the seabed surface). The interface of fluid and seabed is assumed as slip and impermeable in one-way coupling model, from which the flow velocity at the seabed surface is regarded as zero. This is common assumption used in the existing models for wave–seabed interactions (Yamamoto et al., 1978; Hsu and Jeng, 1994; Ye et al., 2014; Tang et al., 2015; Elsafti and Oumeraci, 2016). However, this assumption contradicts to the physical phenomena for waves over a porous seabed. Therefore, the two-way coupling model combines seepage velocity and soil displacement induced flow velocity as the flow velocity at the interface of fluid and seabed. According to the essential difference of the two coupling algorithms, the flow velocity at the interface of fluid and seabed in the $x-$ and $z-$ direction (u_f and w_f) are plotted in Figures 10.15(a) & (b). In the figure, the subscript "1" denotes the results from one-way coupling model, while "2" is for the results of two-way coupling model. It is clear that the maximal flow velocity is about 2 mm/s in the x- direction and 30 mm/s in the z- direction for the two-way coupling algorithm. Furthermore, the flow velocity in the $z-$ direction is one-magnitude-order larger than flow velocity in the x-direction, while they are zeros with the one-way coupling model. Although the flow velocity at the interface of fluid and seabed are small, it will cause the impacts to the flow and seabed characteristics, which will be discussed in the following sections.

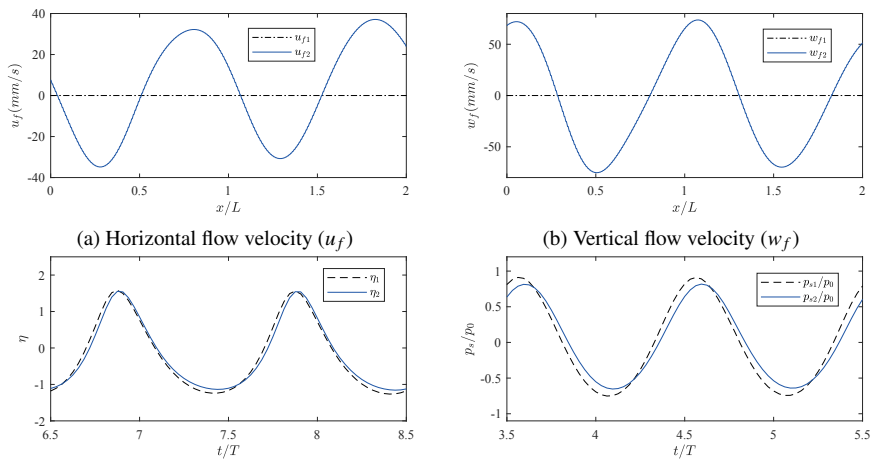

(a) Horizontal flow velocity (u_f)

(b) Vertical flow velocity (w_f)

(c) Free water surface elevation (η)

(d) Dynamic wave pressure (p_s/p_0) at $z = 0$

Figure 10.15 Comparison of flow velocity at the seabed surface ($z = 0$) for different coupling algorithms: (a) variation of horizontal flow velocity at the seabed surface (u_f), (b) variation of vertical flow velocity at the seabed surface (w_f), (c) free water surface elevation (η) and (d) dynamic wave pressure (p_s/p_0) at $z = 0$. Note: subscript "1" is the results of one-way coupling model and "2" is for two-way coupling model.

The free water surface elevation (η) is one of important wave parameters in the hydrodynamic analysis. The influence of different coupling algorithms on free

water surface elevation (η) is illustrated in Figure 10.15(c). As shown in the figure, one-way coupling algorithm may slightly overestimated the amplitude of wave compared with the results of two-way coupling model. However, the difference of water surface elevation caused by one-way coupling and two-way coupling algorithm is insignificant in Figure 10.15(c). To further clarify their difference, we check $\frac{\Delta\eta}{H/2}$ along with time (graph not shown, referring to Zhai and Jeng (2022)), in which $\Delta\eta$ ($=\eta_2 - \eta_1$) represents the difference of the water surface elevation obtained by two-way and one-way coupling algorithms. It is that the range of $\frac{\Delta\eta}{H/2}$ is about $\pm$ 12%.

In addition to wave characteristics, different coupling algorithms also affect the wave-induced soil response. Figure 10.16 presents the influence of different coupling algorithms on the pore pressures. As shown in Figure 10.16(a), the maximum of $|\Delta p_s|/p_0$ along with seabed depth quickly reduce with the increased seabed depth and then reach a stable value below one half of seabed depth. The wave-induced soil displacement is another important seabed response parameter. As shown in Figure 10.16(b), the maximal soil displacement calculated by two-way coupling algorithm is little smaller than one-way coupling results in both x- and z- directions. Furthermore, the increased ratio of $\mathbf{\Delta u_s/u_{s1}}$ would reduce in the $z-$ direction and hover around a fixed value about -16.3% in the x-direction.

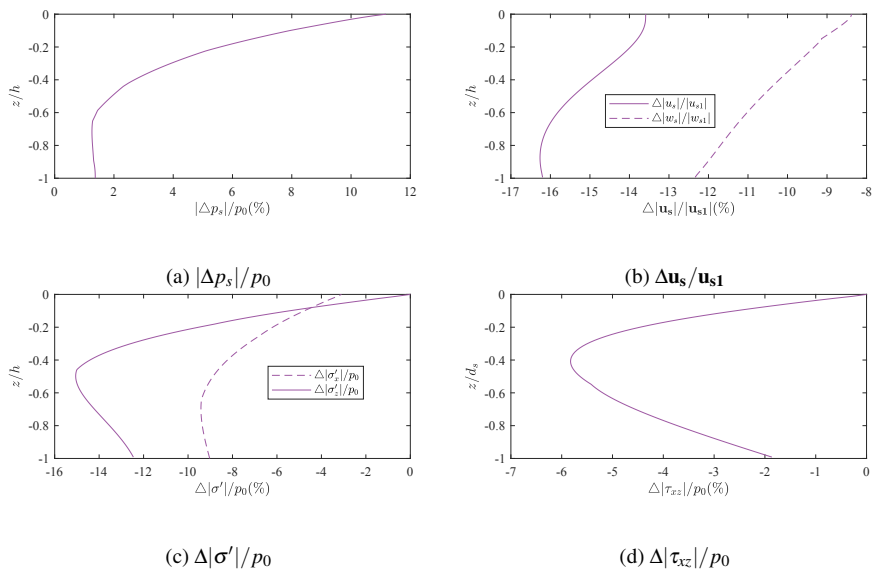

(a) $|\Delta p_s|/p_0$ (b) $\mathbf{\Delta u_s/u_{s1}}$

(c) $\Delta|\sigma'|/p_0$ (d) $\Delta|\tau_{xz}|/p_0$

Figure 10.16 Comparison of relative difference of soil response between one-way and two-way coupling models. (a) $|\Delta p_s|/p_0$ (b) $\mathbf{\Delta u_s/u_{s1}}$, (c) $\Delta|\sigma'|/p_0$, and (d) $\Delta|\tau_{xz}|/p_0$.

The difference of maximal effective normal stresses and shear stress between one-way and two-way coupling algorithms are analysed and the results are plotted in Figures 10.16(c)&(d) . In general, the maximal effective normal stresses and shear stress by two-way coupling model are smaller than that of one-way coupling model.

As shown in the figures, $\Delta|\sigma'|/p_0$ and $\Delta|\tau_{xz}|/p_0$ reduce firstly and then increased with the increased soil depth. The maximal absolute value of the $\Delta|\sigma'_z|/p_0$ can reach to about 15 %, which means the influence of different coupling algorithms on effective normal stress in the z- direction is largest compared with other stresses.

More detailed parametric study regarding the effects of wave and seabed parameters on the relative differences between one-way and two-way coupling models can be found in Zhai and Jeng (2022), in which the application to mono-piles and cofferdams were also examined.

10.6 SUMMARY

In this chapter, several porous models for the wave-induced seabed response in marine sediments were presented. Based on numerical examples presented, the following conclusions can be drawn:

(1) Three existing analytical solutions for the wave-induced oscillatory soil response (Mei and Foda, 1981; Okusa, 1985; Hsu and Jeng, 1994) are presented and compared. Through the numerical comparison between solutions (Mei and Foda, 1981; Hsu and Jeng, 1994) for both saturation and unsaturated seabed ($S_r = 0.932$), although the results from the boundary-layer approximation (Mei and Foda, 1981) are different from the exact solution (Hsu and Jeng, 1994) near the seabed bottom in coarse sand, it provides a good prediction near the seabed surface. The analytical solution (Hsu and Jeng, 1994) overall agrees well with the recent experimental data (Liu et al., 2015).

(2) The 1D Seed-Rahman model has been commonly-used for the prediction of the wave-induced residual liquefaction. Based on the Laplace's transformation and Fourier transformation, three solutions are presented for finite soil layer, deep soil layer and shallow soil layer. The mistake of the scaling analysis in Jeng and Seymour (2007) is pointed out and re-analyzed. A simplified model for the prediction of maximum residual liquefaction depth for both finite and deep foundations are presented, which provide an effective tool for coastal geotechnical engineers as the first approximation.

(3) The Seed-Rahman model was extended to 2D with a time-dependent source term that provides better predictions of residual liquefaction. As shown in the numerical examples, the pattern of liquefied zone for progressive waves gradually changes from 2D to 1D after numerous wave cycles, while the pattern of liquefied zone for standing remains as 2D. This phenomenon can only be predicted by 2D model, rather than 1D model.

(4) A new two-way coupling model for the wave-induced oscillatory seabed response in a porous seabed is presented. This model overcomes the contradiction between physical process and previous theoretical models (since the 1970's). Numerical examples demonstrated the significant differences between two-way coupling and previous one-way coupling model.

Taylor & Francis
Taylor & Francis Group
http://taylorandfrancis.com

11 Ocean Waves over a Porous Seabed with Special Cases

11.1 OVERVIEW

On the basis of Biot's poro-elastic consolidation theory (Biot, 1941), numerous theoretical investigations for wave-induced oscillatory pore-pressure response have been carried out since the 1970s (Yamamoto et al., 1978; Madsen, 1978; Gatmiri, 1990; Hsu and Jeng, 1994; Jeng and Hsu, 1996; Sumer and Fredsoe, 2002; Jeng and Seymour, 2007). These studies provided a solid basis to understand the wave-induced oscillatory soil response, however, they have been limited to homogeneous seabeds. A few researchers further considered layered seabed (Yamamoto, 1981; Hsu et al., 1995), cross-anisotropic seabed (Gatmiri, 1992; Jeng, 1997*a*), variable permeability and shear modulus (Jeng and Lin, 1996, 2000*a*; Sui et al., 2016). Detailed discussion about the aforementioned studies have been discussed in Jeng (2012).

In this chapter, two different cases will be discussed:

- **A non-cohesive seabed with dynamic permeability:** Most previous studies for the wave-seabed interactions have assumed a constant soil permeability, which may lead to non-physical tensile stress in the non-cohesive liquefied zone. Although a few studies considered permeability of other soil properties varying in a spatial domain (normally in the vertical direction), they are limited to static status. That is, the permeability and soil properties is time-independent. Recently, based on the experimental evidence, Zhou et al. (2020) proposed a penalty-like dynamic permeability model, in which the soil permeability is function of pore pressures.
- **A seabed with non-Darcy flow:** Most previous studies applied the linear Darcy model to characterize the porous flow in a seabed. This treatment was found to cause fallacious tensile stresses in a non-cohesive seabed. To overcome such shortcomings of previous models, Zhou et al. (2021*b*) proposed the first non-Darcy flow model for the wave-induced instantaneous liquefaction in a non-cohesive seabed, based on a Karush-Kuhn-Tucker (KKT) condition. In the KKT condition, the primal constraint arises from the fact that the tensile behavior does not exist in a non-cohesive seabed, while the dual condition arises from the physical evidences that the pore-fluid velocity increases during liquefaction.

11.2 A NON-COHESIVE SEABED WITH DYNAMIC PERMEABILITY

A major limitation of the previous studies is that negative effective stresses (i.e., tensile stresses) can be resulted in the instantaneously-liquefied soil. However, tensile behavior is non-physical in a non-cohesive seabed (Qi and Gao, 2018) and can further significantly pollute the overall pore pressure distribution. These non-physical tensile stresses during the instantaneous liquefaction may come from the invariant poro-elastic assumption adopted by existing models (Yamamoto et al., 1978; Hsu and Jeng, 1994). These studies commonly did not consider the variations of physical and mechanical parameters in seabed during liquefaction, such as the soil modulus, permeability, etc. However, some experimental studies and field observations have ever indicated that soil modulus decreases with effective stress by power law at very low effective stress (Haigh et al., 2012), implying a nearly zero-value soil modulus while liquefaction occurs. Some experimental evidences for dramatic increase of soil permeability when effective stresses reduce to zero during soil liquefaction have been reported in the literature (Arulanandan and Sybico Jr, 1992; Ha et al., 2003; Wang et al., 2013; Shahir et al., 2014; Ueng et al., 2017).

In general, there are generally three ways to alleviate or avoid the aforementioned nonphysical tensile stresses in instantaneously-liquefied seabed:

- decreasing the solid-phase resistance (e.g., soil modulus),
- increasing the fluid-phase flow capacity (e.g., soil permeability), and
- a combination of both treatments.

To date, a few studies considering the variation of soil permeability and shear modulus for non-homogeneous seabed (Jeng and Lin, 1996; Jeng and Seymour, 1997; Zhang et al., 2016; Sui et al., 2019). However, these works only considered the variation in a spatial domain and hence fell into the scope of linear fluid flow behavior. Wu and Jeng (2019) was the first considered soil permeability being a function of pore-water pressures in the problem of wave-seabed interactions. This new model introduced a non-linear flow behavior, which is essentially different from the aforementioned spatial-variable permeability. It was recently extended by Wu et al. (2020) to further taken into account dynamic saturation degree for consolidation-induced contaminate transport. However, the dynamic permeability model used in Wu and Jeng (2019) was found to cause an apparent decrease of the soil permeability in the liquefied zone, disagreeing with increased permeability during soil liquefaction observed in existing experiments. Therefore, appropriate approach for wave-seabed interactions with dynamic soil permeability was proposed by Zhou et al. (2020), which will be outlined in this section.

11.2.1 BASIC GOVERNING EQUATIONS

The schematic of the wave-seabed interactions is referring to Figure 10.2. According to the quasi-static consolidation theory by Biot (1941), the governing equations are

summarised here:

$$k\nabla\cdot(k\nabla p)-n_s\beta_s\gamma_w\frac{\partial p}{\partial t}=\gamma_w\frac{\partial(\nabla\cdot\mathbf{u}_s)}{\partial t}, \tag{11.1}$$

$$G_s\nabla^2\mathbf{u}_s+\frac{G_s}{1-2\mu_s}\nabla(\nabla\cdot\mathbf{u}_s)=\nabla p, \tag{11.2}$$

where p is the pore pressure in this chapter, which was denoted as p_s before; n_s is the soil porosity; k is the soil permeability in this chapter; $\mathbf{u}_s$ is the soil displacement vector; G_s is the shear modulus and β_s is the compressibility of the pore fluid, which was defined in (10.15). The boundary conditions are the same as that in Chapter 11, (10.18).

11.2.2 DYNAMIC PERMEABILITY MODELS

The fluid flow in porous media is assumed to obey the generalized Darcy's law, providing the relation between the fluid velocity and pore pressure:

$$\mathbf{v}_w=-\frac{k}{\gamma_w}\nabla(-p_z), \tag{11.3}$$

where $p_z=\gamma_w z$ is the pressure related to position/elevation.

The soil permeability is assumed to be constant or dependent on the spatial location in most previous numerical investigations with respect to wave-induced seabed response (Jeng and Lin, 1996; Jeng and Seymour, 1997). Recently, Wu and Jeng (2019) pointed out that the pore pressure (p) has a significant effect on the soil permeability (k). The dependence of k on p was considered to analyze the seabed response via a $k-p$ relationship originally proposed by Gardner (1956) for the unsaturated moisture flow equation. An apparent decrease of the soil permeability can be seen in the simulated liquefied zone (Wu and Jeng, 2019), showing a disagreement with increased permeability during soil liquefaction observed in recent studies. More detailed information concerning permeability increase during liquefaction will be presented as below.

Mechanism of permeability increase during liquefaction

The theoretical basis of the permeability increase during liquefaction process can be tentatively interpreted by the well-known Kozeny-Carman (KC) equation (Kozeny, 1927; Carman, 1956),

$$k=\frac{\gamma_w}{\mu}\frac{1}{\kappa_0\zeta S_0^2}\frac{e^3}{1+e}, \tag{11.4}$$

with μ is the dynamic viscosity of water, κ_0= the pore shape factor, S_0 is the wetted surface area per unit volume of particles, and e is the void ratio of soil. The tortuosity

factor of the pore-flow, ζ, is generally defined as the ratio of the actual path length of the fluid particles to the shortest path length in the flow direction (Ghassemi and Pak, 2011). The KC equation provides a link between pore-level media attributes and flow resistance in pore channels. When liquefaction occurs due to seismic or ocean wave loading, with increases of pore pressure and loss of grain contacts, there is negligible volume change of the sand in a short time. Therefore, the values of the void ratio of soil and the unit weight of pore-water can be considered approximately constant during liquefaction. However, the values of κ_0 and ζ will remarkably change during liquefaction, as discussed below.

When a seabed is liquefied, the soil particles lose full contact with each other and are in suspension in the pore fluid. This creates an easier and shorter path for the pore-water to readily flow through the liquefied soil without bypassing the grain contacts. The creation of such flow paths reduces the tortuosity (ζ) and the pore shape factor (κ_0) (Shahir et al., 2014; Ueng et al., 2017). Hence the soil permeability becomes larger than its initial value. However, the estimation of κ_0, S_0 and ζ is not straightforward in engineering practice and hence only empirical values are available. A modified KC formula by Liu and Jeng (2019*a*,*b*) can avoid the use of these inconvenient parameters. In their study, only particle geometry parameters and the soil porosity are involved. During soil liquefaction, the particle geometry parameters remains constant but the porosity will increase. According to the modified KC formula, the permeability consequently increases significantly during liquefaction (Liu and Jeng, 2019*a*).

The above theoretical analysis have been supported by numerous experimental evidences in the literature. For example, Arulanandan and Sybico Jr (1992) used resistivity measurement in centrifuge tests to characterize the soil structure during and after liquefaction. It was found that the permeability of saturated sand during liquefaction increased to 6–7 times its initial value. Ha et al. (2003) observed in shaking table tests that the sand permeability during liquefaction increased to 1.4-5 times the initial permeability. Haigh et al. (2012)) fluidized the sand specimen with an upward flow (sand boiling) and then lowered the flow rate to measure the permeability. As the effective stress approached zero, the permeability was found to increase 1.1–5 times the original value. Wang et al. (2013) conducted shaking table tests and concluded that the post-liquefaction behavior can be predicted well if the change of permeability after liquefaction, which is about 4 times its initial value, was considered. Ueng et al. (2017) developed a new experimental approach by combining seepage and liquefaction tests together to directly measure the permeability of a saturated sand specimen during and after liquefaction. It was found that the permeability during liquefaction was about 4–5 times the initial value.

Although the above laboratory tests focused on the saturated sand, the qualitative tendency of the permeability increase can be reasonably shared by unsaturated soil. As aforementioned, the KC equation can be used to explain the physical mechanism of permeability increase in the saturated sand. Chapuis and Aubertin (2003) reported that the KC equation is applicable for an unsaturated sand with a reduction factor. This reduction factor is determined by the degree of saturation. Therefore, when liquefaction occurs in an unsaturated seabed, κ_0 and ζ increase.

Equations for dynamic permeability associated with liquefaction

Several equations have been proposed for dynamic permeability during liquefaction before. In these equations, the dynamic permeability is commonly expressed as a function of excess pore pressure ratio (r_u), which is defined as the ratio between the excess pore pressure and initial confining stress. Haigh et al. (2012) presented a power-law expression of the dynamic soil permeability to fit their experimental results of a series of fluidization tests:

$$k(p) = k_0 (1 - r_u)^c, \tag{11.5}$$

where k_0 is the initial value of the soil permeability and r_u is the excess pore pressure ratio. r_u is defined as the ratio of excess pore pressure to the initial vertical effective stress. The parameter c varies from -0.30 to -0.01 for different potentially liquefiable sands in their experiments. Equation (11.5) results in an infinite permeability for the fluidized sand ($r_u = 1$). However, only the permeability after the soil liquefaction was measured in their tests. Using the fitting results to extrapolate the soil permeability during liquefaction seems lack of evidence.

Later, Shahir et al. (2014) proposed another expression of the dynamic soil permeability to account for the pore pressure evolution during seismic liquefaction:

$$\frac{k(p)}{k_0} = \begin{cases} 1 + (c_1 - 1)e_u^{c_2} & r_u < 1.0 \quad \text{during pore pressure accumulation} \\ c_1 & r_u = 1 \quad \text{at liquefaction state} \\ 1 + (c_1 - 1)e_u^{c_3} & r_u < 1.0 \quad \text{during pore pressure dissipation} \end{cases}, \tag{11.6}$$

where c_1, c_2 and c_3 are model parameters. This equation is an improved version based on their previous work (Shahir et al., 2012). Combining benchmark centrifuge tests, they calibrated the constants as: $c_1 = 10$, c_2=2 and c_3=10.

Equation (11.6) was further modified by Ueng et al. (2017) to fit their experimental data during the pore pressure dissipation phase:

$$k(p) = k_f + (k_L - k_f) r_u^{4.8}, \tag{11.7}$$

where k_f is the permeability after full dissipation of excess pore pressure, and k_L is the permeability at $r_u = 1$, i.e., during liquefaction. It was found that k_L is 4-5 times the initial value k_0. The permeability variation during pore pressure buildup phase was not mentioned. The difference between (11.6) and (11.7) is that k_f is considered in (11.7) rather than the initial permeability k_0 in (11.6).

Based on (11.6) and conducting some modifications to adapt for wave-induced liquefaction, the following permeability equation is proposed:

$$\frac{k(p)}{k_0} = \begin{cases} 1 & r_u \le r_u^{cr} \\ 1 + (c_1 - 1)(r_u - r_u^{cr})^{c_2} & r_u > r_u^{cr} \end{cases}, \tag{11.8}$$

where c_1, c_2 and r_u^{cr} are model parameters. For wave-seabed interaction, the excess pore pressure ratio r_u is defined as (Qi and Gao, 2018):

$$r_u = \frac{(p - P_b)}{\sigma'_{v0}}, \tag{11.9}$$

with P_b is the dynamic wave pressure at the seabed surface. Assuming that seabed surface is a horizontal plane, the initial vertical effective stress of the seabed σ'_{v0} is determined by $\gamma'|z|$, where γ' is the buoyant unit weight of the seabed and z is the soil depth. Note that the above definition of the initial vertical stress is only valid for the case without a structure. For the case with a structure, it needs to consider the pre-consolidation (Jeng et al., 2013).

To provide an intuitive explanation about the modifications of (11.8) from (11.6), the $k/k_0 - r_u$ curves in both equations are plotted (see Figure 11.1). In the figure, the model by Shahir et al. (2014) with $c_1 = 10$, $c_2 = 2$ and $c_3 = 10$ is labelled as DP1 (Dynamic Permeability). The symbols DP1-a and DP1-d denote the pore pressure accumulation and dissipation phases, respectively. Two different groups of model parameters are considered with respect to the model by (11.8): (i) DP2 corresponds to $c_1 = 901$, $c_2 = 2$ and $r_u^{c_2}$=0.9; (ii) DP3 corresponds to $c_1 = 100$, $c_2 = 1$ and $r_u^{c_2}$=1. The value of $c_1 = 901$ in DP2 is chosen to ensure that DP2 and DP1 have an equal value of permeability when soil liquefies ($r_u = 1$). The liquefaction state is indicated by the hollow square in Figure 11.1. Combining with Figure 11.1, the differences between equations (11.6) and (11.8) are discussed as below.

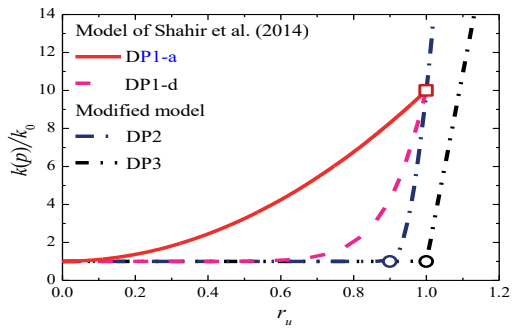

Figure 11.1 Variation of soil permeability versus the excess pore pressure ratio.

(1) The pore pressure accumulation and dissipation phases in (11.6) are not distinguished in (11.8), due to the numerical character. As to be presented in the latter discussion, if c_1 is large enough (e.g., $c_1 \geq 100$) and c2 is reasonably small (e.g., $c_2 leq 2$), the further variations of c1 and c2 will have negligible influences on the numerical results. This is a consequence of the penalty-like treatment by the new dynamic permeability model, as discussed in the end of this subsection.

(2) A controlling point (indicated by hollow circles in Figure 11.1) is added as $r_u = r_u^{cr}$ in (11.8), due to the following two reasons. First, the soil permeability represented by DP1-a starts to increase quickly even the excess pore pressure ratio r_u is relatively low. This behavior disagrees with the experimental data by Haigh et al. (2012) which showed that the permeability increase is not significant unless the effective stress reaches

values below 0.1 kPa. An overall increase in permeability is not realistic (Adamidis and Madabhushi, 2016). Therefore, it is reasonable to set a starting value r_u^{cr} to control when the soil permeability begins to increase. Second, experimental results for instantaneous seabed liquefaction (e.g., Liu et al. (2015)) provide a basis for the numerical tests using dynamic permeability by trial and error. By conducting such numerical tests, $r_u^{cr} = 0.9 \sim 1.0$ was found to agree with the experimental data in a reasonable sense. However, $r_u^{cr} = 1.0$ (corresponding to (11.6) led to a dramatic deviation with the experimental results, as shown in the latter discussion.

(3) The ending point (indicated by the hollow square in Figure 11.1 of the $k/k_0 - r_u$ curves in (11.6)) means that excess pore pressure ratio cannot exceed the upper limit value of $r_u = 1.0$ during liquefaction phase. This restriction conforms to the physical understanding that no tensile stress can be sustained in a non-cohesive seabed. However, to numerically implement zero effective stress requirement in liquefied zone, the ending point needs to be removed and the new dynamic permeability model then becomes conceptually similar to the penalty method or perturbed Lagrange method used for nonlinear contact problems (Wang et al., 2019*b*).

With the above modifications, a new dynamic permeability model expressed by (11.8) is proposed to adapt for wave-seabed interaction. In what follows, the values of r_u^{cr} used in DP2 and DP3 are further discussed in detail.

The value of $r_u^{cr} = 0.9$ in DP2 means that the seabed has reached a disturbed state before liquefaction. The seabed zone satisfying $r_u \geq 0.9$ will have an increased permeability. When the criteria typically requiring $r_u = 1.0$ is used to determine the liquefaction, it is very likely that no liquefaction can be predicted, as shown in the latter section. Therefore, it seems necessary to introduce a concept of "quasi-liquefaction" if $r_u^{cr} = 0.9$ is used. Under this concept, the liquefaction is not a "yes or no" problem anymore. The liquefaction risk, instead of the liquefaction state, should be used. The liquefaction criteria need modifications accordingly. However, "quasi-liquefaction" is not yet an accepted concept. The results with $r_u^{cr} = 0.9$ will be used only for a tentative discussion. The value of $r_u^{cr} = 1.0$ is recommended in this chapter, as adopted by DP3. By using $r_u^{cr} = 1.0$, the permeability will not increase until when the liquefaction state is reached. If no liquefaction occurs, then numerical results by constant and dynamic permeability will be exactly the same. Therefore, the existing liquefaction criteria remain applicable. It can be concluded that, compared with DP2, DP3 minimizes the difficulty of using the new model (11.8) within the classical computational framework for wave-induced seabed response.

Moreover, another concern about the model parameters is clarified here. At first sight, it seems that $r_u^{cr} = 1.0$ cannot reproduce the permeability increase during the liquefaction state. However, the permeability increase is fulfilled here in an approximate way. As aforementioned, the new model is conceptually similar to the penalty method or perturbed Lagrange method. Therefore, $r_u^{cr} = 1.0$ is approximately satisfied. The residual value, $\varepsilon_{ru} = r_u - 1 > 0$, can then be used to reproduce the permeability increase according to (11.8). At the liquefaction state, the pore pressure

is permitted to slightly exceed the initial vertical effective stress of the seabed. Then obviously, ε_{ru} should be controlled to be close to zero, and this can be achieved by "tuning" the two parameters c_1 and c_2.

11.2.3 COMPARISON WITH CYLINDER TESTS UNDER 1D WAVE LOADING

Liu et al. (2015) conducted a series of cylinder tests under 1D wave loading conditions using a 1.8 m thick sandy deposit. The experimental facility enables installing more pore pressure measurement points (10 points) in the soil layer along the vertical direction than conventional wave flume tests (usually 3 or 4 points). Additional static water pressures were added onto the harmonic dynamic wave pressure, allowing for simulating a greater water depth.

Linear elasticity behavior is assumed to the solid phase with material parameters given by: shear modulus $G_s = 1.27 \times 10^7$ Pa, Poisson's ratio $\mu_s = 0.3$. The initial value of the sand permeability is given as $k_0 = 1.8 \times 10^{-4}$ m/s. The water depth h is 5.2 m, taking into account the additional static water pressure added in the tests. Liu et al. (2015) reported 24 experimental tests in total, by changing the soil porosity n_s, soil saturation S_r, wave period T and pressure amplitude p_0. The "Test 20" is used in the following examples (see Liu et al., 2015, Table 2).

Performance of dynamic permeability models: case study

For "Test 20" in Liu et al. (2015), the computational parameters are given by: $n_s = 0.425$, γ'=9.41 KN/m^3, $S_r = 0.996$, $T = 9$ sec and p_0=34.32 kPa. In this section, four numerical tests are conducted, with one using constant permeability and the others using dynamic permeability, as listed in Table 11.1.

Table 11.1
Numerical tests for "Test 20" in Liu et al. (2015).

Case abbreviation	c_1	c_2	c_3	Remarks
CP	-	-	-	Constant permeability
DP1-a	10	2	0	Dynamic permeability
DP2	901	2	0.9	
DP3	100	1	1	

Figure 11.2 presents the variation of the pressure amplitude along with the soil depth. As shown in the figure, the numerical result using constant permeability (CP) achieves a good agreement with the analytical solution by Hsu and Jeng (1994), validating the present model. If the model parameters in Shahir et al. (2014), i.e., DP1-a, are directly used here, a dramatic deviation can be observed between the numerical and experimental results. This implies that an overall increase in the soil permeability is inappropriate for simulating the wave-induced seabed response. In

contrast, the cases using constant permeability (CP), DP2 and DP3 all coincide with the experimental data in a reasonable sense. The permeability variations in DP2 and DP3 result in a decrease in the pressure amplitude, but the decrease is not significant.

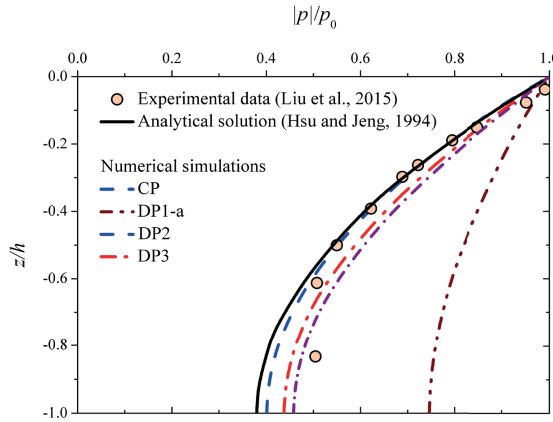

Figure 11.2 The pressure amplitude versus the soil depth.

In the analysis of wave-induced seabed liquefaction, the phase lag is a key character and is found here to have a considerable influence on the location of the maximum liquefaction depth. Two cases CP and DP3 are discussed as below. The discussions for DP2 and DP1-a are similar. Figure 11.3 shows the phase lag effect on the temporal variation of p at different soil depths. It can be seen from the figure that the trough values of p occur when $t \geq 0.5T$. The trough values occur later in deeper position, well corroborated by the general characteristics of wave-induced seabed response.

This phenomenon can be observed more apparently in Figure 11.4 by plotting the vertical distribution of $\sigma'_{v0} - (p - P_b)$ at two representative instants, i.e., $t = 0.45T$ and $t + 0.5T$. The following criterion proposed by Zen and Yamazaki (1990*a*) is hereafter used to determine the wave-induced instantaneous liquefaction:

$$(p - P_b) \geq \sigma'_{v0}, \tag{11.10}$$

As shown in Figure 11.4, the liquefaction depths at $t = 0.5T$ are 0.85 m and 0.46 m for CP and DP3, respectively. However, the instant of $t = 0.45T$ is found to have the maximum liquefaction depths of 1.02 m and 0.67 m for CP and DP3 respectively. It can be concluded that simply investigating the instant when the wave trough arrives ($t = 0.5T$) is not enough. Instead, the temporal variation should be considered. It is also notable that the phase lag would not always cause the "early liquefaction" phenomenon, as further discussed in the lateral section. For all the four cases (CP, DP2, DP3 and DP1-a), Figure 11.5 gives the vertical distributions of $p - P_b$ and $\sigma'_{v0} - (p - P_b)$ when maximum liquefaction depth is observed ($t = 0.45T$).

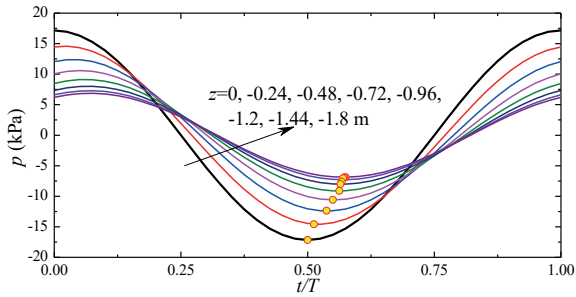

(a) CP model

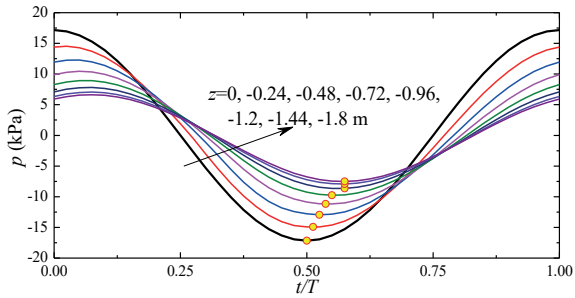

(b) DP3 model

Figure 11.3 The temporal variation of p at different soil depths. (a) CP model and (b) DP3 model.

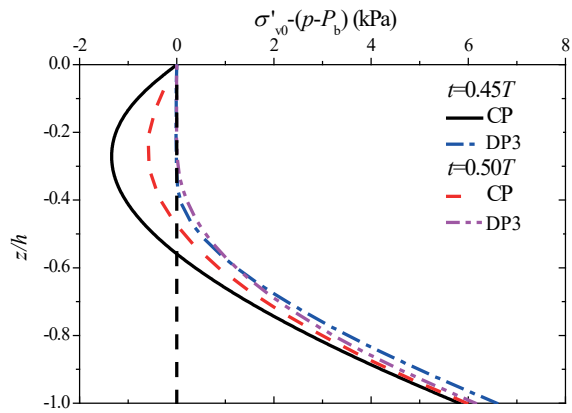

Figure 11.4 Vertical distribution of $\sigma'_{v0} - (p - P_b)$ at two different instants.

In Figure 11.5(a), the wave-induced pore pressure by constant permeability (CP) exceeds the initial vertical effective stress (i.e., $r_u > 1$) in the liquefaction zone. This leads to tensile stresses observed in Figure 11.5(b), which should never appear in a non-cohesive sandy seabed. In contrast, DP2 and DP3 remarkably ease this nonphysical behavior. However, no liquefaction is observed in DP2. Noting that r_u^{cr}=0.9 is used in DP2, the criterion by equation (11.10) is tentatively modified here as $p - P_b \geq 0.9\sigma'_{v0}$ to determine a zone with high liquefaction risks instead of liquefaction state. The corresponding depth is determined as 0.85 m. It is notable that this type of modification cannot work for DP1-a because $r_u^{cr} = 0$ is used in this case.

Based on the above observations, it was found that DP1-a is not suitable for simulating wave-induced seabed response, while DP2 leads to some additional difficulties in determining the liquefaction zone. Therefore, the results by DP2 and DP1-a will not be discussed hereafter. Instead, DP3 is recommended when dynamic permeability is considered.

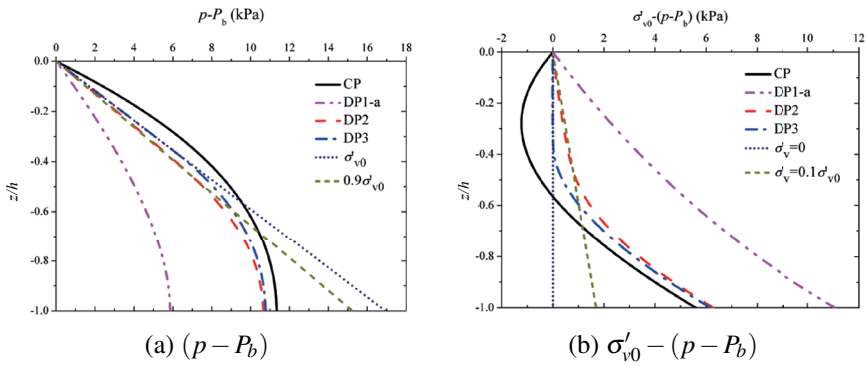

(a) $(p - P_b)$ (b) $\sigma'_{v0} - (p - P_b)$

Figure 11.5 Vertical distributions of (a) $(p - P_b)$ and (b) $\sigma'_{v0} - (p - P_b)$.

Comparison with cylinder tests using proposed dynamic permeability model

The above discussions show that the dynamic permeability model proposed in this paper can improve the numerical performance. In order to further validate the improvement, this section conducts a comparison with more experimental tests, shown in Figures 11.6 & 11.7. Three values of wave pressure amplitude p_o are considered, i.e., 12.10 kPa, 24.52 kPa and 34.32 kPa.

In Figures 11.6(a1) & (b1), all the numerical results generally coincide with the experimental data in a reasonable sense. It seems that the improvement of using dynamic permeability is not significant for sands with high saturation ($S_r = 0.996$). This is mainly due to the fact that the tensile stress in case CP is under a relatively low magnitude, as shown in Figures 11.6(a2) & (b2). Therefore, the difference between constant and dynamic permeability is not apparent in the vertical distribution of the pressure amplitude $|p|$. For the experimental tests under 12.10 kPa and 24.52 kPa

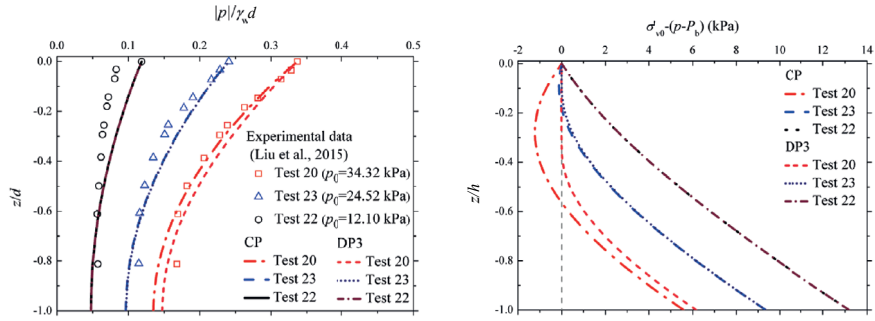

(a1) $|p|/\gamma_w d$ (a2) $\sigma'_{v0} - (p - P_b)$

(a) Loose sand with high saturation

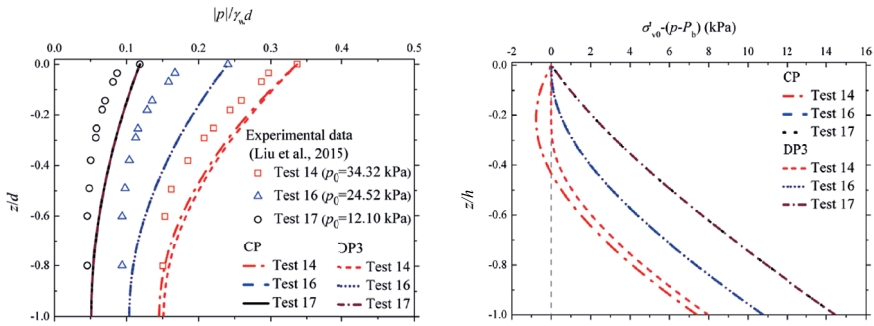

(b1) $|p|/\gamma_w d$ (b2) $\sigma'_{v0} - (p - P_b)$

(b) Dense sand with high saturation

Figure 11.6 Vertical distributions of pressure amplitude $|p|/\gamma_w h$; and $\sigma'_{v0} - (p - P_b)$ in different seabed. Notation: Loose sand : $n = 0.425$, γ'=9.41 kN/m^3; Dense sand: $n = 0.387$, γ'=10.0 kN/m^3; high saturation: S_r=0.996.

(i.e., tests 22-23 in Figures 11.7(a) and tests 16-17 in Figures 11.7(b)), the numerical results by CP and DP3 even stay almost the same.

The numerical performance for sands with low saturation ($S_r = 0.951$) can be greatly improved by using the dynamic permeability model proposed in this paper. As shown in Figures 11.7(a1) & (b1), the conventional model using constant permeability (CP) leads to a dramatic discrepancy with the experimental results. This is a consequence of the abnormally large negative values (tensile stresses) shown in Figures 11.7(a2) & (b2) (close to -11 kPa in Test 2). These abnormal tensile stresses are greatly eased by adopting DP3. Meanwhile, DP3 obtains acceptable agreements with the experimental data, especially the overall experimental tendency is well reproduced. Discrepancy between the numerical and experimental results mainly appears near the seabed surface. The discrepancy can be primarily attributed to the dynamic movement pattern of the soil particles near the sample surface. It is not surprise that this type of dynamic behaviors in the liquefied zone cannot

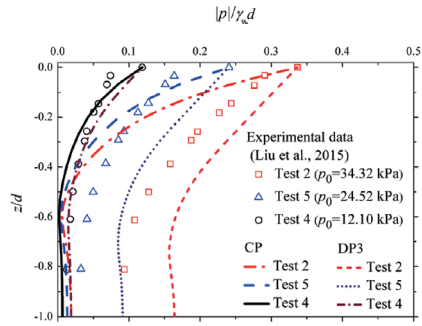

(a1) $|p|/\gamma_w d$

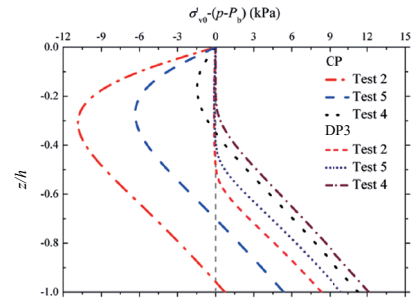

(a2) $\sigma'_{v0} - (p - P_b)$

(a) Loose sand with low saturation

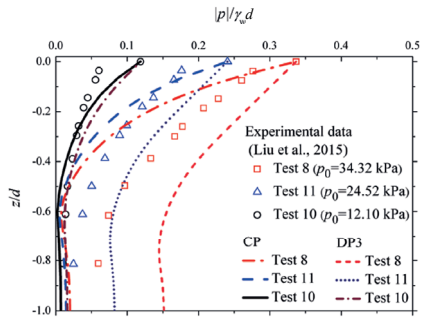

(b1) $|p|/\gamma_w d$

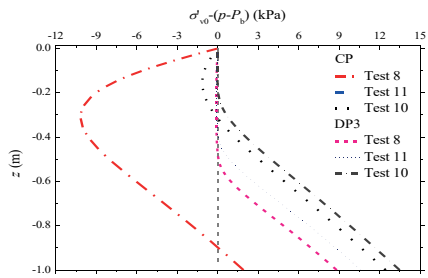

(b2) $\sigma'_{v0} - (p - P_b)$

(b) Dense sand with low saturation

Figure 11.7 Vertical distributions of pressure amplitude $|p|/\gamma_w h$; and $\sigma'_{v0} - (p - P_b)$ in different seabed. Notation: Loose sand : $n = 0.425$, γ'=9.41 kN/m^3; Dense sand: $n = 0.387$, γ'=10.0 kN/m^3; low saturation: S_r=0.951).

be reproduced by quasi-static numerical simulations under the assumption of porous medium. Nevertheless, the dynamic permeability model provides a solid improvement to existing computational framework in a convenient way.

For all the above tests, the maximum liquefaction depths predicted by CP and DP3 are given in Table 11.2. The last column in Table 11.2 is the ratio of the liquefaction depth by CP to the value by DP3. The symbol "-" means that no liquefaction is found. It can be seen that the liquefaction depth by CP is 1.52-2.00 times the value by DP3. The dynamic permeability has a significant influence on the liquefaction estimation.

In Figures 11.6 & 11.7, the distributions of $\sigma'_0 - (p - P_b)$ correspond to the instant when the negative peak value of $\sigma'_0 - (p - P_b)$ occurs or the maximum liquefaction depth emerges (if there is any liquefaction). Again, the phase lag effect of causing the "early liquefaction" phenomenon is considered. Here the "Test 2" (low saturation) is discussed by observing four instants. As shown in Figures 11.8,

Table 11.2
Maximum liquefaction depths predicted by different models.

Remarks	Test no.	p_0 (kPa)	n	γ' (kN/m^3)	S_r	Liquefaction depth (m) CP	DP3	Ratio
Loose sand	20	34.32				1.02	0.67	1.53
with high	23	24.52	0.425	9.41	0.996	0.33	0.21	1.60
saturation	22	12.10				-	-	-
Dense sand	14	34.32				0.78	0.50	1.56
with high	17	24.52	0.387	10.0	0.996	-	-	-
saturation	16	12.10				-	-	-
Loose sand	2	34.32				1.72	0.87	2.00
with low	5	24.52	0.425	9.41	0.951	1.27	0.75	1.70
saturation	4	12.10				0.63	0.38	1.67
Dense sand	8	34.32				1.67	0.86	1.89
with low	11	24.52	0.387	10.0	0.996	1.19	0.74	1.62
saturation	10	12.10				0.57	0.36	1.57

the maximum liquefaction depth occurs when the wave trough arrives ($t = 0.5T$). This observation implies that the "early liquefaction" phenomenon does not always appear, but depends on the computational parameters.

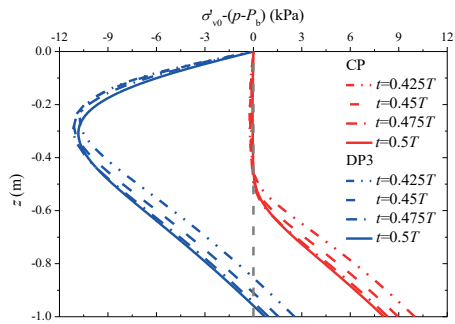

Figure 11.8 Vertical distributions of $\sigma'_{v0} - (p - P_b)$ at four different instants in "Test 2".

Effects of model parameters

As discussed in the last section, when constant permeability is used, "Test 2" has much larger tensile stresses than other tests. Therefore, "Test 2" is chosen here to investigate the effects of model parameters by adopting four groups of c_1 and c_2 while keeping $r_u^{cr} = 1$.

First, the model parameter $c_2 = 1$ is fixed. By using c_1 = 10, 100 and 1000, the minimum values of $\sigma'_0 - (p - P_b)$ are reduced to -1.546, -0.135 and -0.012 kPa,

respectively. With the increase of c_1 , the tensile stresses approach zero gradually. If $c_1 = 10$ is used, apparent tensile stresses can still occur, as shown in Figure 11.9(a). Nevertheless, it already obtains a considerable improvement over CP. The results by $c_1 = 100$ and 1000 are almost the same and the tensile stresses become unapparent. These results imply that c_1= 100 is large enough to obtain a good numerical performance.

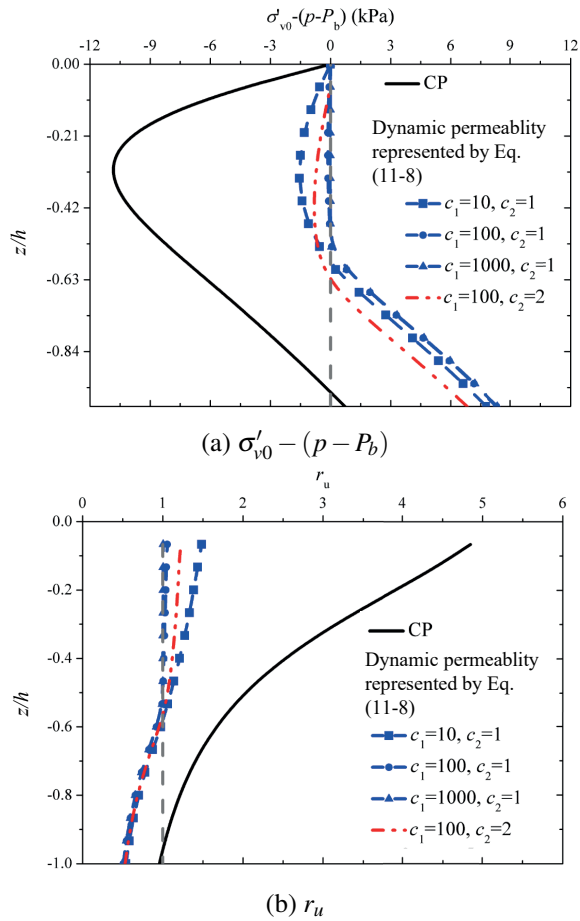

Figure 11.9 Vertical distributions of (a) $\sigma'_{v0} - (p - P_b)$ and (b) r_u for various values of c_1 and c_2.

Then, the model parameter c_1 = 100 is fixed. Two values of c_2 = 1 and 2 are compared. The k/k_0–r_u curves are shown in Fig 11.10(a), according to Equation (11.8). It can be seen that c_2=1 has a sharper increase than c_2=2 until r_u=2. Figure 11.9(b) already showed that the maximum values of r_u obtained by dynamic permeability never exceed 2. This is to say, c_2=1 can provide a larger permeability increase to correct the tensile stress during the nonlinear iterative

procedure. Therefore, c_2=1 can obtain a better performance than c_2=2, as shown in Figure 11.9(a).

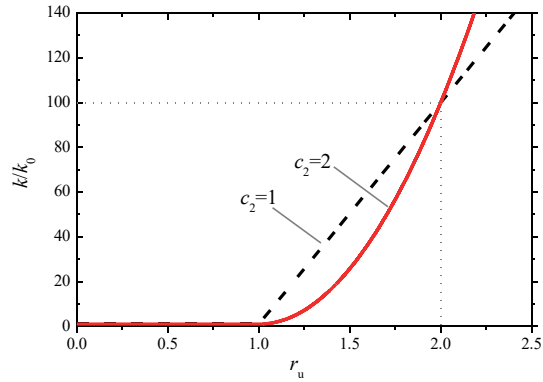

(a) k/k_0 versus r_u

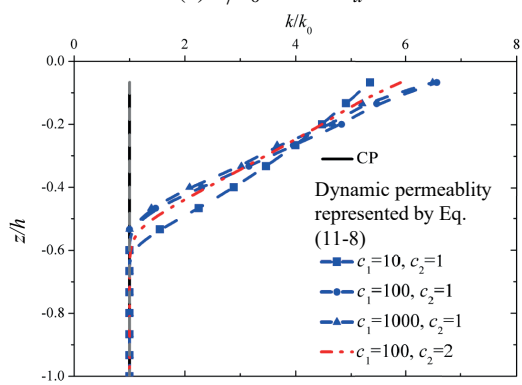

(b) k/k_0 versus z/h

Figure 11.10 Parametric study: (a) k/k_0–r_u curves by using C_2= 1 and 2; (b) the vertical distribution of soil permeability k/k_0 versus z/h for various values of c_1 and c_2.

Figure 11.10(b) further shows the vertical distribution of the soil permeability. It can be seen that the shallow position of the seabed has the maximum permeability when using dynamic permeability. The reason is that r_u is rather large by constant permeability (CP) at the shallow position (see Figure 11.9(b)), where greater permeability is needed to correct the unreasonable behavior of $r_u > 1$. Once the correction is accomplished by the iterative nonlinear procedure, all the four parameter groups are found to have a similar permeability distribution. It is more interesting that the two values of c_1 = 100 and 1000 have almost the same permeability. This implies that the increase of c_1 will give a converged result, making the dynamic permeability model somehow a parameter-free treatment. More precisely, once is large enough (i.e., 100), the further variation of will have a negligible influence on the numerical result. This performance is similar to the

penalty method within the constrained variational principle (Zhou et al., 2018; Wang et al., 2019*b*).

11.3 A NON-DARCY FLOW MODEL FOR A NON-COHESIVE SEABED

Despite that complicated factors have been considered for instantaneous liquefaction, Qi and Gao (2015, 2018) found that existing works can lead to tensile behavior in the liquefied zone. This phenomenon should not occur in a non-cohesive seabed and can lead to a consequence that the liquefaction depths predicted by different liquefaction criteria depart from each other (Qi and Gao, 2015, 2018). Once this topic is taken into discussion, one can reasonably argue that the porous-medium theory for liquefied soil should be replaced by micro-mechanical discontinuum-based models (Scholtés et al., 2014; Fukumoto and Ohtsuka, 2018; Narsilio et al., 2009; Martin et al., 2020) and then the continuum-based framework for instantaneous liquefaction should be rebuilt.

The dynamic permeability model (Zhou et al., 2020), Section §11.2,poses difficulties in nonlinear convergence. Numerical divergence can even occur when using large model parameters or fine computational mesh or simulating the seabed under 2D wave loading, making the application limited. To address this issue, Zhou et al. (2021*a*) modeled the instantaneous liquefaction problem in physics as a nonlinear complementarity problem (NCP) in mathematics. The improvements over the dynamic permeability model (Zhou et al., 2020) are apparent. Within the NCP treatment (Zhou et al., 2021*a*), a Karush-Kuhn-Tucker (KKT) condition is constructed specified for instantaneous liquefaction. It is treated by the Lagrange multiplier method and the primal–dual active set strategy (PDASS) (Kunisch and RöSch, 2002). For the saddle-point system arising from the Lagrange multiplier method, the Direct delta function is used to interpolate the multipliers which can therefore be statically condensed to guarantee the computational efficiency.

To minimize the implementation effort and at the same time obtain numerical performances close to the NCP treatment (Zhou et al., 2021*a*), a non-Darcy flow model specified for instantaneous liquefaction is established by Zhou et al. (2021*b*), on the basis of physical evidences (e.g., micro mechanisms, laboratory experiments and field trials). In order to avoid any unnecessary misleading of the existing non-Darcy models determining the limits of Darcy's law validity by means of Reynolds number (e.g. Forchheimer model (Girault and Wheeler, 2008), Hansbo model (Hansbo, 2001)), it is clarified here that the present model is derived based on a new concept, wherein the liquefaction criterion is revised as a primal constraint based on micro-scale simulations and field observations. The primal constraint is first imposed by the Lagrange multiplier method to make clear the physical meaning of the Lagrange multiplier, so as to find a dual complementarity condition to check and then correct the assumed liquefied zone. The primal-dual pair forms a Karush-Kuhn-Tucker (KKT) condition, removing the requirement that the liquefied zone should be predetermined (Towhata et al., 1992). The difficulties of the dynamic permeability model (Zhou et al., 2020) in nonlinear convergence are also well addressed by the new non-Darcy model.

11.3.1 NONLINEAR COMPLEMENTARITY PROBLEM ARISING FROM INSTANTANEOUS LIQUEFACTION

Basis of wave-seabed interactions and liquefaction criteria

Figure 11.11 shows the wave-seabed interactions and associated seabed liquefaction, wherein the seabed thickness, water depth and wave height are denoted by d, h and H, respectively. The coordinate z equals to zero at the seabed surface and all the other positions in seabed correspond to positive values of z. Note that the wave is shown as linear in Figure 11.11. If large waves in shallow water are involved, then Stokes wave (Gao et al., 2003*b*) or cnoidal wave (Zhou et al., 2014) should be applied to account for the nonlinear effect. For simplicity, the linear wave theory (Dean and Dalrymple, 1984) is applied in this study.

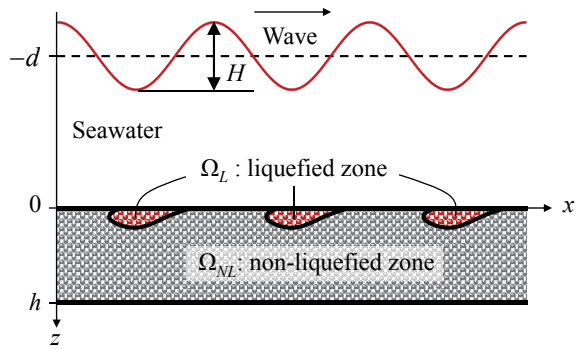

Figure 11.11 Schematic of the wave-seabed interactions involving instantaneous liquefaction.

When instantaneous liquefaction occurs, the considered seabed domain Ω is decomposed into two non-overlapping sub-domains:

$$\Omega = \Omega_L \cup \Omega_{NL}, \quad \Omega_L \cap \Omega_{NL} = \varnothing. \tag{11.11}$$

where Ω_L and Ω_{NL} denote the instantaneously liquefied and non-liquefied zones, respectively.

The liquefied zone (Ω_L) can be determined by several criteria, among which two criteria widely applied in ocean engineering are as follows (Qi and Gao, 2018):

$$p - P_b \geq \gamma' z, \tag{11.12a}$$

$$j_z \geq \gamma', \tag{11.12b}$$

where p is the wave-induced excessive pore pressure. Its gradient along the vertical direction is denoted by $j_z = \partial p / \partial z$. γ' is the buoyant unit weight of the seabed and can be determined by: $\gamma' = (G_s - 1)(1 - n)\gamma_w$, where G_s is the specific gravity of

sand particles and n is the sand porosity. The porosity n has a relation with the void ratio e (the ratio of the void volume to the volume of solid particles): $n = e/(1+e)$.

The criterion by (11.12a) was deduced by Zen and Yamazaki (1990*a*), based on the force analysis on the vertical soil column. When wave trough arrives, the excess pore pressure p and the wave pressure P_b become both negative. Instantaneous liquefaction occurs when the difference $p - P_b$ exceeds the overburden seabed pressure $\gamma' z$. The extension of this criterion to 3D scenarios was presented by Jeng (1997*b*).

The criterion by (11.12b) was proposed by Bear (1972) from the perspective of soil-element scale. The positive value of j_z can be interpreted as the upward seepage force. If the upward seepage force exceeds the critical value (usually chosen as γ'), the soil layer will reach a instantaneously-liquefied state.

Revising the liquefaction criterion as a primal constraint

Generally, the liquefied zones determined by the above two criteria can be different. This issue was recently discussed by Qi and Gao (2018) and was found to be caused by the tensile behavior occurring in Ω_L. This phenomenon was stated as nonphysical (Qi and Gao, 2018), according to the evidences shown in Figure 11.12.

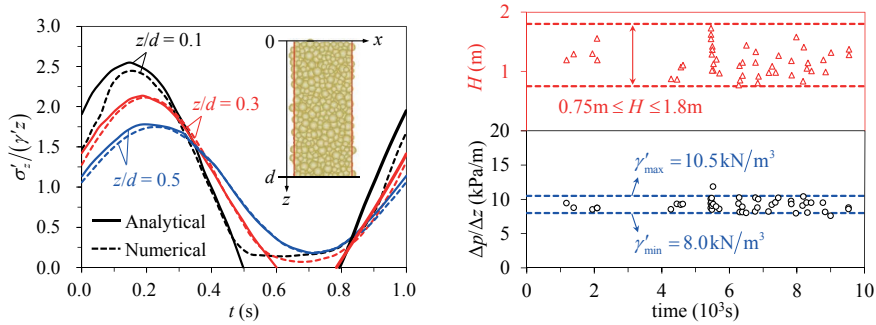

(a) DEM–PFV simulations (b) Field trials

Figure 11.12 Evidences for the primal constraints: (a) DEM–PFV simulations (Scholtés et al., 2014); (b) field trials (Mory et al., 2007).

The first evidence is the temporal effective stress obtained by the simulations using the discrete element method (DEM) coupled with a pore-scale finite volume (PFV) scheme (Scholtés et al., 2014), as presented in Figure 11.12(a). The effective stress by the numerical simulations stays non-negative even liquefaction occurs. The micro-mechanical investigation of liquefaction of granular media by cyclic DEM tests (Martin et al., 2020) produces similar conclusions. This motivates revising the liquefaction criterion by (11.12a) as the following primal constraint:

$$p - P_b = \gamma' z \quad \text{in} \quad \Omega_L. \tag{11.13}$$

The second evidence is the field trials by Mory et al. (2007) wherein 47 instantaneous liquefaction events were observed, as shown in Figure 11.12(b). Despite that the wave height varies from 0.75 m to 1.8 m, the upward seepage force (j_z) generally approximates to a threshold value, i.e. the buoyant unit weight (γ'). A further increase of wave height could not induce higher seepage force in the liquefied zone. This motivates revising the liquefaction criterion by (11.12b) as the following primal constraint:

$$j_z = \gamma' \quad \text{in} \quad \Omega_L. \tag{11.14}$$

Equation (11.13) has been numerically handled by Zhou et al. (2021*a*). This study focuses on dealing with the primal constraint by (11.14) in a numerical manner. With (11.14) as an additional constraint, the boundary value problem can be given as:

$$\nabla \cdot \left(\boldsymbol{\sigma}' - p\mathbf{I}_{2\times 2}\right) + \mathbf{b} = 0 \quad \text{in} \quad \Omega, \tag{11.15a}$$

$$\frac{\partial \varepsilon_v}{\partial t} + n\beta \frac{\partial p}{\partial t} - \nabla \cdot \left(\frac{k_s}{\gamma_w} \nabla p\right) = 0 \quad \text{in} \quad \Omega, \tag{11.15b}$$

$$j_z = \gamma' \quad \text{in} \quad \Omega_L, \tag{11.15c}$$

$$\mathbf{u} = \hat{\mathbf{u}} \quad \text{on} \quad \Gamma_u, \tag{11.15d}$$

$$\boldsymbol{\sigma} \cdot \mathbf{n}_\sigma = \hat{\mathbf{t}} \quad \text{on} \quad \Gamma_\sigma, \tag{11.15e}$$

$$p = \hat{p} \quad \text{on} \quad \Gamma_p, \tag{11.15f}$$

$$\mathbf{v}_w \mathbf{n}_v = \hat{v}_w^n \quad \text{on} \quad \Gamma_v. \tag{11.15g}$$

where the former two equations, (11.15a) and (11.15b), arise from the poro-elastic theory (Biot, 1941) and represent the equilibrium of the solid-fluid mixture and the conservation of mass, respectively. In (11.15a), $\boldsymbol{\sigma}'$ is the effective stress, $\mathbf{I}_{2\times 2}$ is a second-order unit tensor and $\mathbf{b}$ is the body force per unit volume. In (11.15b), ε_v is the volumetric strain, t denotes time, β is the pore fluid compressibility and k_s is the Darcy's coefficient of permeability.

The last four equations in (11.15) represent the boundary conditions. Γ_u and Γ_σ are Dirichlet and Neumann boundaries of the solid phase, respectively. In (11.15d),

$\mathbf{u}$ is the displacement vector and $\hat{\mathbf{u}}$ is the constrained displacement. In (11.15e), $\boldsymbol{\sigma}$ is the total stress tensor, $\mathbf{n}_\sigma$ is the outward unit normal vector of Γ_σ and $\hat{\mathbf{t}}$ is the boundary traction. Γ_p and Γ_v are Dirichlet and Neumann boundaries of the fluid phase, respectively. In (11.15f), $\hat{p}$ is the constrained pore pressure. In (11.15g), $\mathbf{v}_w$ is the pore-fluid velocity vector, $\mathbf{n}_v$ is the outward unit normal vector of Γ_v and $\hat{v}_w^n$ denotes the boundary Darcy velocity.

11.3.2 FINDING THE DUAL CONDITION COMPLEMENTARY TO THE PRIMAL CONSTRAINT

The primal constraint in (11.15) is still insufficient to obtain expected results, because the liquefied zone Ω_L is undetermined as well as time-dependent. Therefore, a dual condition is needed to check and then correct Ω_L. To this end, the Lagrange multiplier method is used to impose the primal constraint, with the Lagrange multiplier λ introduced as an additional unknown field. The trial and weighting spaces are defined as:

$$\mathscr{V}_u = \left\{ \mathbf{u} \in \left[H^1(\Omega)\right]^3 \middle| \, \mathbf{u}|_{\Gamma_u} = \hat{\mathbf{u}} \right\}, \quad \mathscr{V}_\Phi = \left\{ \Phi \in \left[H^1(\Omega)\right]^3 \middle| \, \Phi|_{\Gamma_u} = \mathbf{0} \right\}, \tag{11.16a}$$

$$\mathscr{V}_p = \left\{ p \in \left[H^1(\Omega)\right] \middle| \, p|_{\Gamma_p} = \hat{p} \right\}, \quad \mathscr{V}_\phi = \left\{ \phi \in \left[H^1(\Omega)\right] \middle| \, \phi|_{\Gamma_p} = 0 \right\}, \tag{11.16b}$$

$$\mathscr{V}_\lambda = \left\{ \lambda \in \left[H^1(\Omega)\right] \middle| \, \lambda|_{\Omega_{NL}} = 0 \right\}, \quad \mathscr{V}_w = \left\{ w \in \left[H^1(\Omega)\right] \middle| \, w|_{\Omega_{NL}} = 0 \right\}, \tag{11.16c}$$

where H^1 is a Sobolev space of degree one. Φ, ϕ and w are variations of $\mathbf{u}$, p and λ, respectively.

The weak form can therefore be stated as finding $(\mathbf{u}, p, \lambda) \in \mathscr{V}_u \times \mathscr{V}_p \times \mathscr{V}_\lambda$ such that there holds:

$$\int_\Omega \nabla\Phi : \left(\boldsymbol{\sigma}' - p\mathbf{I}_{2\times 2}\right) \mathrm{d}\Omega + \int_\Omega \Phi \cdot \mathbf{b}\, \mathrm{d}\Omega + \int_{\Gamma_\sigma} \Phi \cdot \hat{\mathbf{t}}\, \mathrm{d}\Gamma = 0, \tag{11.17a}$$

$$\int_\Omega \phi \left(\frac{\partial \varepsilon_v}{\partial t} + n\beta \frac{\partial p}{\partial t} \right) \mathrm{d}\Omega + \int_\Omega \frac{k_s}{\gamma_w} \nabla\phi \cdot \nabla p \, \mathrm{d}\Omega + \int_{\Gamma_v} \phi \hat{v}_w^n \, \mathrm{d}\Gamma + \int_{\Omega_L} \frac{\partial \phi}{\partial z} \lambda \, \mathrm{d}\Omega = 0, \tag{11.17b}$$

$$\int_{\Omega_L} w \left(\frac{\partial p}{\partial z} - \gamma' \right) \mathrm{d}\Omega = 0, \tag{11.17c}$$

for all $(\Phi, \phi, w) \in \mathscr{V}_\Phi \times \mathscr{V}_\phi \times \mathscr{V}_w$.

Equation (11.17c) is the weak form of the primal constraint (11.14) and (11.14) further introduces another additional variational term into the weak form, i.e. the last term in (11.17b). This term represents the virtual work in the liquefied zone contributed by the Lagrange multiplier (λ), whose physical meaning can therefore be presented as a fictitious pore-fluid velocity. Existing works found that soil liquefaction can speed up the pore-fluid flow and regarded this phenomenon as the permeability increase. Among these, Arulanandan and Sybico Jr (1992) reported that the sand permeability during liquefaction increased to 6-7 times its initial value. The permeability was observed by Haigh et al. (2012) to increase 1.1-5 times the original value, as the effective stress approached zero. Other studies indicated the ratio of permeability during liquefaction to its initial value as 1.4-5 (Ha et al., 2003), 4 (Wang et al., 2013), or 4-5 (Ueng et al., 2017), etc. This motivates constructing the dual complementary condition as follows:

$$\lambda \geq 0 \quad \text{in} \quad \Omega_L. \tag{11.18}$$

The above equation means that the additional pore-fluid velocity (λ) should be non-negative in the liquefied zone, so as to help the excessive pore pressure decreasing appropriately in an implicit manner such that tensile behavior never occurs. Now that the primal constraint ($j_z = \gamma'$) and its dual condition ($\lambda \geq 0$) have been obtained for the liquefied zone, the KKT condition for instantaneous liquefaction can therefore be given as:

$$j_z \leq \gamma', \quad \lambda \geq 0, \quad \left(j_z - \gamma'\right)\lambda = 0, \quad \text{in} \quad \Omega, \tag{11.19}$$

11.3.3 WEAK FORM BY USING THE PENALTY METHOD

The penalty method (Meng and Yang, 2010) is another classic technique for imposing the KKT condition. Compared with the Lagrange multiplier method, the penalty method imposes the constraints in an approximate manner but is more convenient for numerical implementation. With the use of this method, a penalty factor κ is introduced to build a connection between the primal and dual variables. The KKT condition by (11.19) is then rewritten as a penalized form:

$$\lambda = \kappa\left(j_z - \gamma'\right), \quad \text{with} \quad \kappa = \begin{cases} 0, & \text{if } j_z < \gamma' \\ \kappa_\infty, & \text{if } j_z \geq \gamma' \end{cases}, \tag{11.20}$$

where κ_∞ is the penalty parameter used in the liquefied zone. If κ_∞ equals to ∞, (11.20) is equivalent to (11.19). However, ∞ is not possible to achieve during the numerical procedure and hence κ_∞ is usually chosen as a large value. (11.20) is an approximate version of (11.19). The subscript ∞ is used here to keep in mind that κ_∞ should be large enough to make the original KKT condition be approximated with satisfactory accuracy.

By using the primal-dual relationship given by (11.20), the weak form by using the Lagrange multiplier method, (11.17), can then be rewritten as:

$$\int_\Omega \nabla\Phi : \left(\boldsymbol{\sigma}' - p\mathbf{I}_{2\times 2}\right) \mathrm{d}\Omega + \int_\Omega \Phi \cdot \mathbf{b}\, \mathrm{d}\Omega + \int_{\Gamma_\sigma} \Phi \cdot \hat{\mathbf{t}}\, \mathrm{d}\Gamma = 0, \tag{11.21a}$$

$$\int_\Omega \phi\left(\frac{\partial \varepsilon_v}{\partial t}+n\beta\frac{\partial p}{\partial t}\right)\mathrm{d}\Omega+\int_\Omega \frac{k_s}{\gamma_w}\nabla\phi\cdot\nabla p\,\mathrm{d}\Omega+\int_{\Gamma_v}\phi\hat{v}_w^n\,\mathrm{d}\Gamma + \int_\Omega \kappa\frac{\partial\phi}{\partial z}\left(\frac{\partial p}{\partial z}-\gamma'\right)\mathrm{d}\Omega=0. \tag{11.21b}$$

It can be found that the primal constraint explicitly represented as (11.17c) by using the Lagrange multiplier method is now implicitly determined here by the penalty factor κ.

11.3.4 REFORMULATING THE NONLINEAR COMPLEMENTARITY PROBLEM AS A NON-DARCY FLOW MODEL

In the above section, either (11.17) or (11.21) can be adopted to find the solution $(\mathbf{u}, p)$. However, the constrained variational principle may lead to barriers for numerical implementation and future extensions, because it is neither standard nor modular within the finite element framework. In order to provide a numerical formulation easier to be reproduced, this section reformulates the above penalty formulation ((11.21)) as an equivalent non-Darcy flow model.

Weak form with nonlinear flow

If nonlinear relation between the velocity and the pressure gradient is considered, then the mass conservation equation, (11.15b), must be modified as:

$$\frac{\partial \varepsilon_v}{\partial t}+n\beta\frac{\partial p}{\partial t}+\nabla\cdot\mathbf{v}_w=0 \quad \text{in} \quad \Omega. \tag{11.22}$$

The weak form by using nonlinear flow is then given as follows:

$$\int_\Omega \nabla\Phi:\left(\boldsymbol{\sigma}'-p\mathbf{I}_{2\times 2}\right)\mathrm{d}\Omega+\int_\Omega \Phi\cdot\mathbf{b}\,\mathrm{d}\Omega+\int_{\Gamma_\sigma}\Phi\cdot\hat{\mathbf{t}}\,\mathrm{d}\Gamma=0, \tag{11.23a}$$

$$\int_\Omega \phi\left(\frac{\partial \varepsilon_v}{\partial t}+n\beta\frac{\partial p}{\partial t}\right)\mathrm{d}\Omega-\int_\Omega \nabla\phi\cdot\mathbf{v}_w\,\mathrm{d}\Omega+\int_{\Gamma_v}\phi\hat{v}_w^n\,\mathrm{d}\Gamma=0. \tag{11.23b}$$

Non-Darcy flow model arising from the nonlinear complementarity problem

Keeping in mind that the non-Darcy model is a variationally equivalent version of the penalized KKT condition, (11.23b) should be identical to (11.21b). That is, the second term in (11.23b) should equal to the sum of second and last terms in (11.21b). This equivalence provides the following function to determine the pore-fluid velocity $\mathbf{v}_w$:

$$v_{wx}=-\frac{k_s}{\gamma_w}\frac{\partial p}{\partial x}, \quad v_{wz}=-\frac{k_s}{\gamma_w}\frac{\partial p}{\partial z}-\kappa\left(\frac{\partial p}{\partial z}-\gamma'\right), \tag{11.24}$$

where v_{wx} and v_{wz} are the two components of $\mathbf{v}_w$ in the horizontal and vertical directions, respectively. In (11.24), the Darcy's law still holds in the horizontal direction, while an apparent non-linearity arising from the penalty factor κ appears in the vertical direction.

According to (11.20), it is known that the second term in v_{wz} in (11.24) is the Lagrange multiplier λ. Therefore, the actual pore-fluid velocity in Ω_L contains two parts, with one coming from the conventional Darcy's law and the other λ. This makes clear again that the Lagrange multiplier λ means the additional pore-fluid velocity added into Ω_L. Noting that the pressure gradient has a relation to the hydraulic gradient ($\Delta p = \gamma_w \mathbf{i}$), v_{wz} can be rewritten in terms of i_z:

$$v_{wz} = -k_s i_z - \kappa (i_z - i_{\mathrm{cr}}) = \begin{cases} -k_s i_z, & \text{if } i_z < i_{\mathrm{cr}} \\ -k_s i_{\mathrm{cr}} - (k_s + \kappa_\infty \gamma_w)(i_z - i_{\mathrm{cr}}), & \text{if } i_z \geq i_{\mathrm{cr}} \end{cases}, \quad (11.25)$$

where i_{cr} equals to γ'/γ_w and represents the critical value determining whether liquefaction occurs or not. The above equation is illustrated in the v_{wz}-i_z space by Figure 11.13, which appears clearly as a non-Darcy flow model.

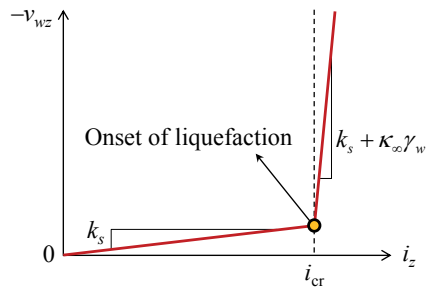

Figure 11.13 Schematic of the non-Darcy flow model.

Previous studies also observed the nonlinear v_{wz}-i_z relationships when seepage failure occurs, as shown in Figure 11.14. Fukumoto and Ohtsuka (2018) reported a 3D direct particle-fluid simulation model for the seepage failure of granular soils. This model couples DEM and LBM (Lattice Boltzmann Method). The interaction between the soil particles and the seepage flow was also considered. The failure process induced by the seepage flow was captured with no macroscopic assumptions. The obtained evolution of inflow velocity was plotted as a function of the hydraulic gradient, as shown in Figure 11.14(a). The piping experiments by Skempton and Brogan (1994) provides another evidence for the nonlinear v_{wz}-i_z relationship during seepage failure, as presented in Figure 11.14(b). These evidences indicate that the pore-fluid velocity can increase significantly if liquefaction occurs, which is reproduced by the non-Darcy model, (11.25).

Figure 11.15 provides an intuitive comparison between the permeability increase and the non-Darcy flow model by using an imaginary test. If the data from real laboratory experiments is used, the following discussion can be also conducted. As

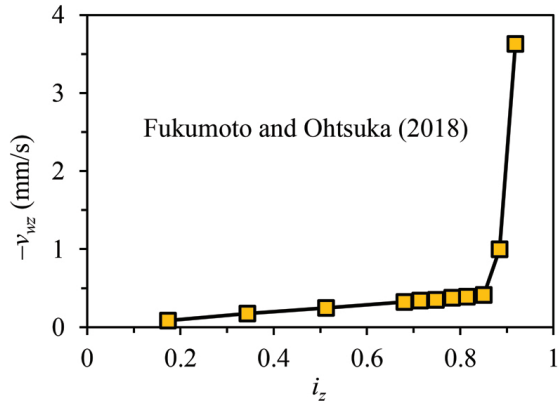

(a) Numerical evidence

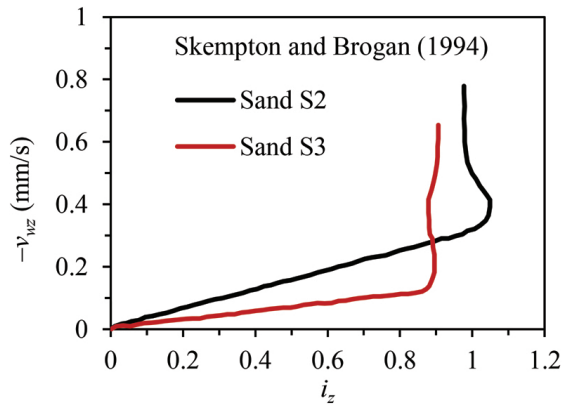

(b) Experimental evidence

Figure 11.14 Evidences for the dual condition: (a) numerical results of non-cohesive granular soils with upward seepage flow (Fukumoto and Ohtsuka, 2018); (b) experimental results on piping in sandy gravels (Skempton and Brogan, 1994).

shown in Figure 11.15(a), when the liquefied state is not taken into account, a linear Darcy model with constant permeability can be obtained by fitting the points under the non-liquefied state. If the liquefied state is considered and the Darcy model with dynamic permeability (denoted by k_d here) is applied, see Figure 11.15(b), k_d will be calculated as the slope from the coordinate origin (0,0) to each data point, because $v_{wz} = -k_d i_z$ is adopted. It is assumed that seven data points are measured during liquefaction. Then, seven values of k_d will be obtained, e.g. k_d/k_s = 1,2,3,4,5,6,7 in Figure 11.15(b). Note that one may obtain more data points (or less) under the liquefaction state in real laboratory experiments. The point number of seven as well as the specific values of k_d are just used here for an instance and dose not affect the conceptual comparison.

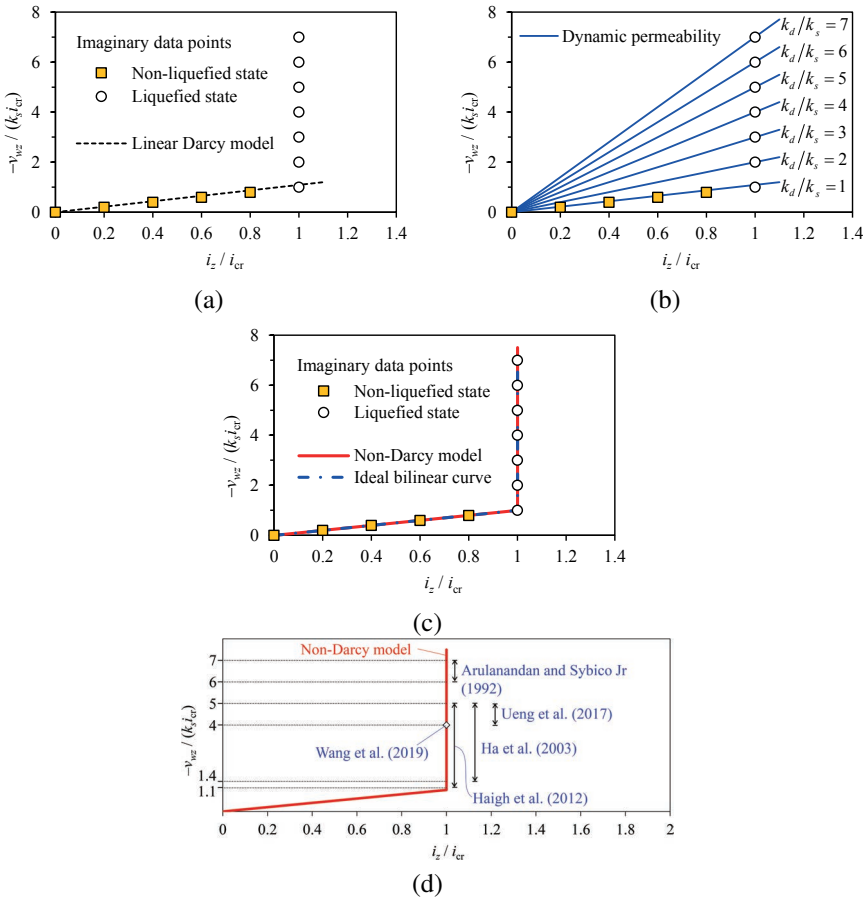

Figure 11.15 Conceptual comparison of different models by an imaginary test: (a) conventional Darcy model with constant permeability; (b) Darcy model with dynamic permeability; (c) non-Darcy model; (d) reconsidering permeability increase as non-Darcy flow.

If all the data points are connected by a continuous curve, then a bi-linear function can be obtained, as shown in Figure 11.15(c). According to the primal constraint (11.14), the hydraulic gradient i_z should not exceed the limit value i_{cr}. Therefore, for the bi-linear curve in Figure 11.15(c), the first stage has a slope of 1 (i.e. $v_{wz} = -k_s i_z$) and the second stage has a slope of ∞. As aforementioned, the non-Darcy model is based on the penalty method, which fulfills the primal constraint in an approximate manner by taking the penalty parameter κ_∞ as large values. In Figure 11.15(c), $\kappa_\infty = 10^6 \, k_s/\gamma_w$ is applied for an instance. It can be found that this value of κ_∞ can reproduce the ideal bi-linear curve with a sufficient accuracy. we will further examine the influence of different values of κ_∞ on the numerical results as

well as the nonlinear convergence later. Therefore, as shown in Figure 11.15(d), the reported permeability increases during liquefaction can be rearranged in the v_{wz}-i_z space and can then be regarded as the increase of pore-fluid velocity, acting as additional evidences for the non-Darcy model, (11.25).

11.3.5 CYLINDER TESTS UNDER 1D WAVE LOADING

In this section, the present model is used to reproduce the cylinder tests (Liu et al., 2015). Among their 24 tests, twelve of these tests were simulated by Zhou et al. (2020). It was reported that removing tensile behavior in numerical method provided a better agreement with the experimental results. Zhou et al. (2021*a*) investigated six tests by Liu et al. (2015) and obtained a similar conclusion. It is therefore not necessary to repeat comparing numerical results with that much tests. In this study, two tests (i.e. "Test 2" and "Test 20" (Liu et al., 2015)) are considered. During the simulation, four numerical treatments are investigated: CP (the conventional Darcy model using **Constant Permeability**), DP (**Dynamic Permeability** model (Zhou et al., 2020)), NCP (**Nonlinear Complementarity Problem** using the Lagrange multiplier method (Zhou et al., 2021*a*)) and ND (**non-Darcy** model presented in this study). DP model uses the parameters $c_1 = 100$, $c_2 = 1$ and $r_u^{\mathrm{cr}} = 1$, which are recommended by Zhou et al. (2020). ND model takes the penalty parameter as $\kappa_\infty = 10^6\, k_s/\gamma_w$. Note that NCP (Zhou et al., 2021*a*) is a parameter-free treatment.

Pore pressure and corresponding liquefaction analysis

First, the "Test 20" (Liu et al., 2015), where liquefaction was observed, is simulated. Figure 11.16 gives the vertical distribution of pressure amplitude as well as the computational parameters. CP model is found to achieve a good agreement with the analytical solution (Hsu and Jeng, 1994), validating the in-house code developed in this study. Other three numerical models (DP, NCP and ND) obtain nearly identical results, which also coincide with the experimental data in a reasonable sense. The difference between these four numerical models in the pressure amplitude is not significant, but can become apparent by comparing other results, e.g., Figure 11.17.

Figure 11.17(a) gives the liquefaction depths determined by the criterion (11.12a). The liquefaction depths by DP, NCP and ND are almost the same and smaller than that by CP. For a typical instant of $0.425T$ shown in Figure 11.17(a), Figure 11.17(b) and Table 11.3 further provides the vertical effective stress $\gamma' z - (p - P_b)$. The maximum tensile stress by CP model is -1367.30 Pa. This tensile stress is nonphysical in a non-cohesive seabed (Qi and Gao, 2018) and is reduced by DP, NCP and ND to -12.59 Pa, 0 and -0.0023 Pa, respectively. From an engineering point of view, the error by ND is negligible. If higher accuracy is required, larger penalty parameter κ_∞ is suggested. Note that large parameters in DP will lead to numerical instability (Zhou et al., 2020). Therefore, only NCP and ND are promising.

Then, the "Test 2" (Liu et al., 2015), where the saturation degree S_r equals to 0.951, is simulated. The only difference from "Test 20" ($S_r = 0.996$) is the saturation. As illustrated in Figure 11.18, the results by DP, NCP and ND are still close to

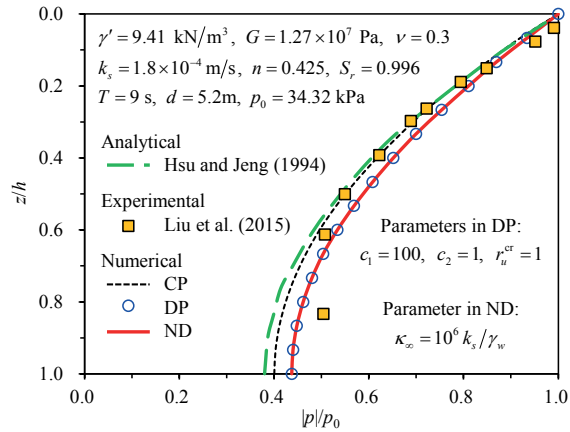

Figure 11.16 The pressure amplitude $|p|/p_0$ versus the soil depth z/h of "Test 20".

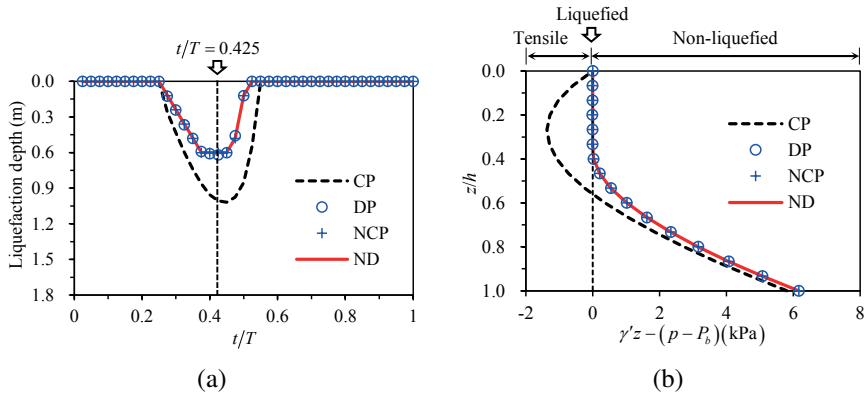

Figure 11.17 Liquefaction analysis of "Test 20" by the criterion (11.12a): (a) temporal liquefaction depth; and (b) vertical distribution of $\gamma' z - (p - P_b)$ at the instant of $0.425T$.

each other. The liquefaction depth by CP is overestimated, because abnormally large tensile stress occurs. As shown in Table 11.4, the maximum tensile stress by CP reaches to -11240.89 Pa, which is reduced by DP, NCP and ND to -199.46 Pa, 0 and -0.0392 Pa, respectively. Although the tensile value (-0.0392 Pa) by ND here in "Test 2" is larger than that in "Test 20" (-0.0023 Pa), it is still close to zero and hence can be also neglected.

Hydraulic gradient and corresponding liquefaction analysis

The above liquefaction analysis is conducted based on using the criterion (11.12a). In this subsection, another criterion (11.12b) is investigated and compared with

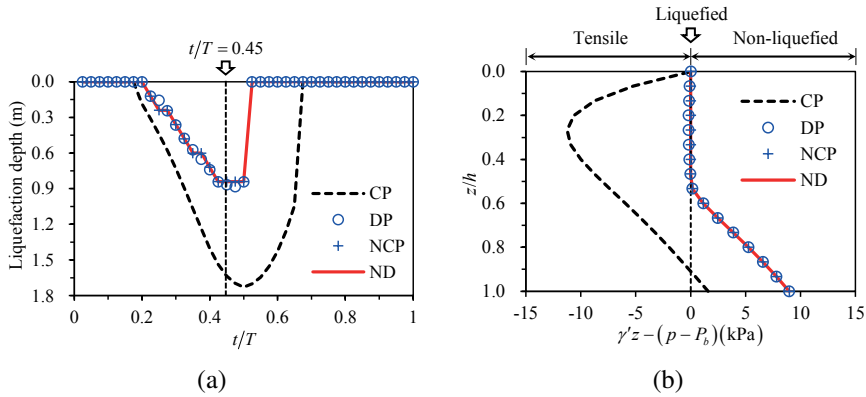

Figure 11.18 Liquefaction analysis of "Test 2" by the criterion (11.12a): (a) temporal liquefaction depth; and (b) vertical distribution of $\gamma' z - (p - P_b)$ at the instant of $0.45T$.

Table 11.3
Vertical effective stress at $t = 0.425T$ (Test 20).

z (m)	z/d	$\gamma' z - (p - P_b)$ (Pa)			
		CP	DP	NCP	ND
0.00	0.00	0	0	0	0
0.12	0.07	-596.54	-7.93	0	-0.0008
0.24	0.13	-1022.96	-10.74	0	-0.0014
0.36	0.20	-1278.54	$\boxed{-12.59}$	0	-0.0019
0.48	0.27	$\boxed{-1367.30}$	-8.85	0	-0.0022
0.60	0.33	-1296.75	-3.97	0	$\boxed{-0.0023}$
0.72	0.40	-1076.81	21.79	24.98	24.97
0.84	0.47	-718.78	206.93	209.44	209.43
0.96	0.53	-234.60	542.73	544.68	544.68
1.08	0.60	363.83	1017.74	1019.27	1019.27
1.20	0.67	1065.25	1619.57	1620.79	1620.79
1.32	0.73	1859.42	2336.12	2337.12	2337.12
1.44	0.80	2737.55	3156.53	3157.37	3157.37
1.56	0.87	3692.52	4071.77	4072.51	4072.51
1.68	0.93	4719.11	5075.15	5075.83	5075.83
1.80	1.00	5814.12	6162.53	6163.19	6163.19
Liquefaction depth (m)		1.007	0.618	0.600	0.600

Table 11.4
Vertical effective stress at $t = 0.45T$ (Test 2).

z (m)	z/d	$\gamma' z - (p - P_b)$ (Pa)			
		CP	DP	NCP	ND
0.00	0.00	0	0	0	0
0.12	0.07	-5212.26	-93.87	0	-0.0100
0.24	0.13	-8733.08	-151.41	0	-0.0185
0.36	0.20	-10637.49	-192.80	0	-0.0256
0.48	0.27	$\boxed{-11240.89}$	$\boxed{-199.46}$	0	-0.0312
0.60	0.33	-10914.84	-179.65	0	-0.0353
0.72	0.40	-9996.78	-127.28	0	-0.0380
0.84	0.47	-8751.18	-43.47	0	$\boxed{-0.0392}$
0.96	0.53	-7362.50	150.94	162.63	162.61
1.08	0.60	-5945.02	1136.63	1145.28	1145.27
1.20	0.67	-4559.45	2463.49	2472.71	2472.70
1.32	0.73	-3230.09	3873.81	3884.12	3884.11
1.44	0.80	-1959.72	5254.20	5265.26	5265.25
1.56	0.87	-740.78	6566.01	6577.46	6577.45
1.68	0.93	436.83	7802.55	7814.16	7814.15
1.80	1.00	1580.87	8966.55	8978.20	8978.19
Liquefaction depth (m)		1.007	0.618	0.600	0.600

(11.12a). Considering that (11.12b) is given in terms of the hydraulic gradient, a finer mesh with z-directional element size of 0.01 m is used here to guarantee the accuracy. With this mesh, DP and NCP models are not considered, due to the following two considerations. First, DP model was found to cause numerical instability in this fine mesh, as demonstrated previously. Second, the above results have clearly shown that the difference between ND and NCP is not significant. Therefore, only CP and ND models are discussed in this subsection.

As presented in Figure 11.19(a), if CP model is used, (11.12b) obtains apparently smaller liquefaction depth than (11.12a). In contrast, when ND model is used, the liquefaction depths determined by the two criteria become unified. For the instant of $0.425T$, Figure 11.19(b) provides the vertical distributions of $\gamma' z - (p - P_b)$ and $\gamma' - j_z$, where the negative values mean the tensile stresses induced in the volumetric soil element or across the surface of the vertical soil column. This nonphysical behavior is nearly removed by ND model. Figure 11.20 shows the numerical results of "Test 2". For seabed under lower saturation, CP model leads to larger discrepancy between the two criteria which are unified again by ND model presented in this study.

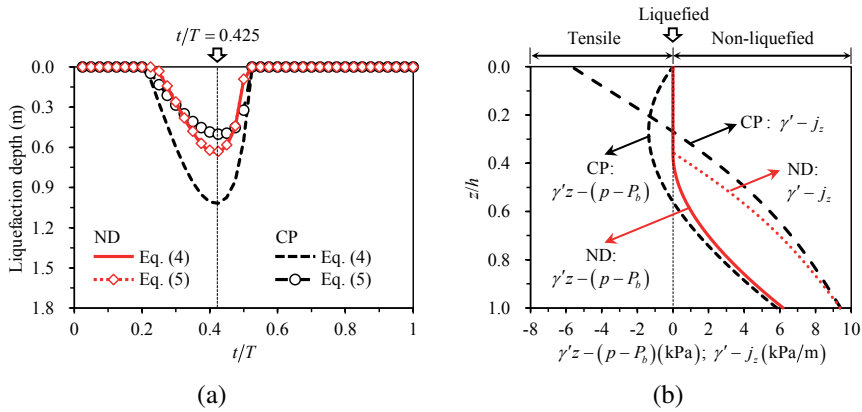

Figure 11.19 Liquefaction analysis of "Test 20" by the criteria Eqs. (11.12a) and (11.12b): (a) temporal liquefaction depth; and (b) vertical distributions of $\gamma' z-(p-P_b)$ and $\gamma'-j_z$ at the instant of $0.425T$.

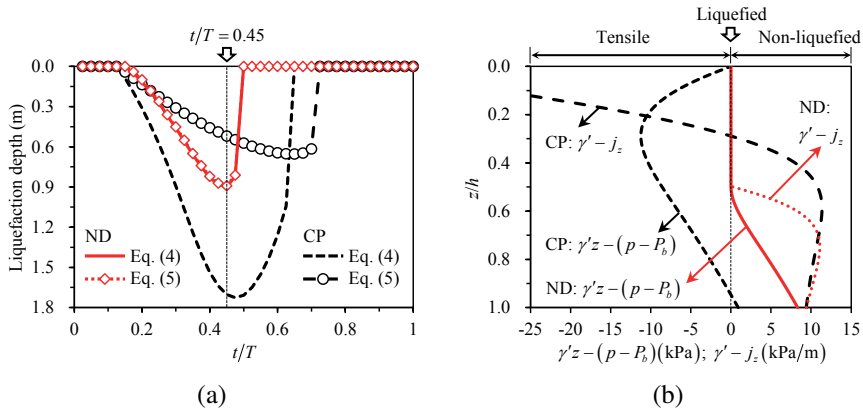

Figure 11.20 Liquefaction analysis of "Test 2" by the criteria Eqs. (11.12a) and (11.12b): (a) temporal liquefaction depth; and (b) vertical distribution of $\gamma' z-(p-P_b)$ and $\gamma'-j_z$ at the instant of $0.45T$.

Parametric study on the instantaneous liquefaction depth

According to the above discussions, CP model generally leads to tensile stresses in the liquefied zone. To improve the prediction accuracy, a concise suggestion is presented for the engineering applications as below. First, CP model is used to determine whether there is liquefaction or not. If there is no liquefaction, ND model will provide identical results with CP model and therefore is not needed. If liquefaction occurs, then ND model is required to remove the unreasonable tensile stresses. In this subsection, the effects of ND model on the liquefaction depths are investigated by conducting a parametric study.

During the parametric study, the computational model of the cylinder test is adopted and a benchmark test is set. The computational parameters of the benchmark test are listed in Table 11.5. Four soil parameters (Young's modulus E, permeability coefficient k_s, saturation degree S_r and soil porosity n) and three wave parameters (wave period T, water depth h and wave height H) are tested. The seabed thickness d is also tested. Note that the buoyant unit weight γ' changes with n and is determined by: $\gamma' = (G_s - 1)(1 - n)\gamma_w$, with G_s given as 2.67 in this paper. In the benchmark test, γ' equals to 9.41 kN/m^3 and the Poisson's ratio ν is taken as 0.3. It is also notable that the wave parameters herein may be beyond the linear wave theory. The influence of wave non-linearity will be included in our future works.

Table 11.5
The computational parameter of the benchmark test in the parametric study.

Parameter	E (MPa)	k_s (m/s)	S_r (-)	n (-)	T (s)	h (m)	H (m)	d (m)
Value	50	1×10^{-4}	0.99	0.425	9	5	3.5	1.8

Considering that the criterion by (11.12a) is the most widely applied one for seabed liquefaction, this section uses (11.12a) to determine the liquefaction depths for both CP and ND models. As shown in Figure 11.21, the liquefaction depth increases with the increase of E, n, T and H but decreases with the increase of k_s, S_r and h. These tendencies are well corroborated by the general characteristics of wave-seabed interactions (Jeng, 2018). Moreover, when the liquefaction depth is larger, the difference between the CP and ND models becomes more apparent. It is notable that the influence of seabed thickness d on the liquefaction depth is insignificant in the parametric study presented here but can become significant under some 2D wave conditions (Jeng, 2018).

The liquefaction depths predicted by the two models are then plotted in Figure 11.22, wherein all the results of Figure 11.21 are collected together. In Figure 11.22, the abscissa z_{CP} denotes the liquefaction depth by CP model. The ordinate z_{ND} denotes the liquefaction depth by ND model. A linear relationship is found to fit well with the numerical results. The correlation coefficient is $R^2 = 0.94$. The instantaneous liquefaction depth by ND model is roughly 0.73 times the value by CP model. This relationship can be used as a quick reference for engineering practice because the analytical solution for CP model is available in the literature (Hsu and Jeng, 1994) and commonly used in offshore geotechnical engineering industry. It should be noted that this quick estimation is obtained herein for a sandy seabed in shallow marine settings under the assumption of linear waves. If more general scenarios need to be considered, systematical studies are required to include more factors, or alternatively, one can use our non-Darcy model to conduct numerical simulations for specific applications.

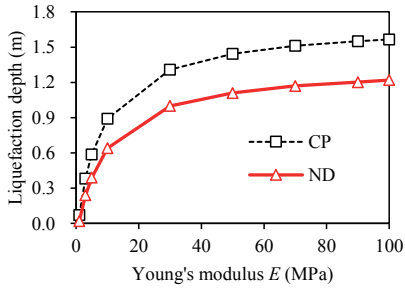

(a) Young's modulus E

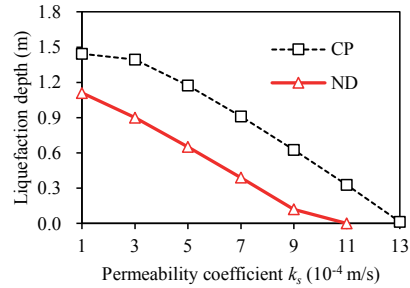

(b) permeability coefficient k_s

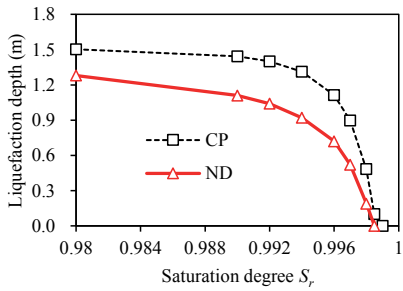

(c) saturation degree S_r

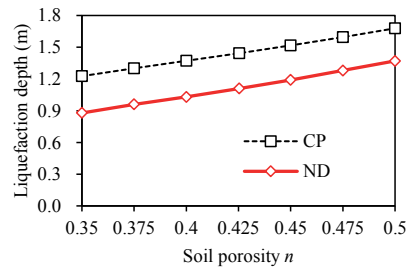

(d) soil porosity n

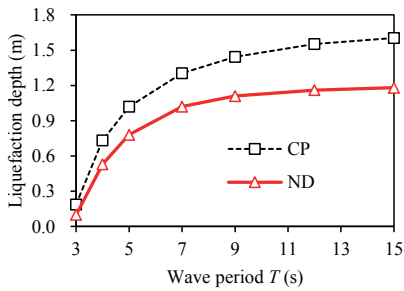

(e) wave period T

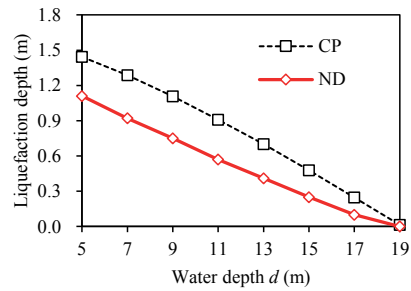

(f) water depth d

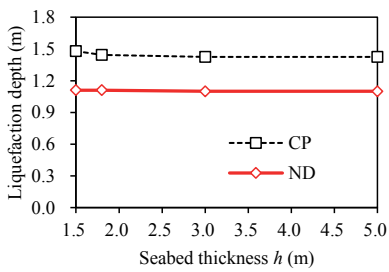

(g) wave height H

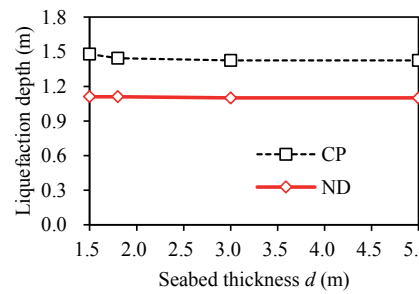

(h) seabed thickness h

Figure 11.21 Liquefaction depths versus (a) Young's modulus E; (b) permeability coefficient k_s; (c) saturation degree S_r; (d) soil porosity n; (e) wave period T; (f) water depth h; (g) wave height H; (h) seabed thickness d.

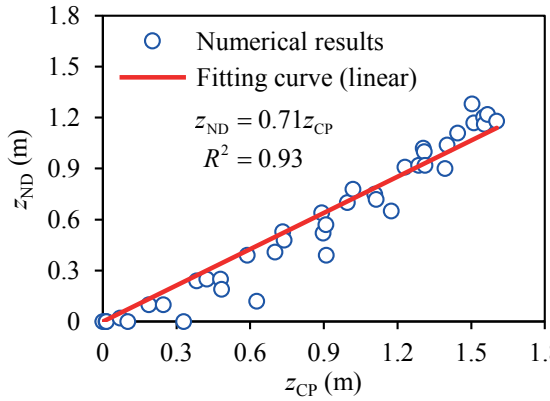

Figure 11.22 Relationship of the liquefaction depths by CP and ND models.

11.3.6 2D WAVE-SEABED INTERACTIONS

This section applies the present non-Darcy flow model to analyze the 2D wave-seabed interactions. The computational parameters are the same to those in "Test 2" (Liu et al., 2015). The penalty parameter in ND model is taken as $\kappa_\infty = 10^6 \, k_s / \gamma_w$. CP, DP and NCP models are used in the simulation for comparative study. The DP parameters ($c_1 = 10$, $c_2 = 1$, $r_u^{cr} = 1$) used in 2D simulation by (Zhou et al., 2020) are also applied here in the DP model. NCP model needs no additional parameters.

The seabed thickness is taken as 100 m, which is larger than the wavelength ($L \approx 61.4$ m here). This setup can be used to simulate a seabed with infinite thickness (Yamamoto et al., 1978; Hsu et al., 1993). The seabed length is set as three times of the wavelength L (Ye and Jeng, 2012) to minimize the influence of the x-directional boundary and meanwhile minimize the computational effort.

The liquefaction analysis focuses on a region around $x = 1.5L$, where the wave trough arrives at $t = T$. Therefore, the numerical results are given at the instant of $t = T$. Figure 11.23 presents the contours of the vertical effective stress $\gamma' z - (p - P_b)$ obtained by three models. Their vertical distributions along the line of $x = 1.5L$ are given by Figure 11.24, wherein the results by CP model agrees exactly with the analytical solution (Yamamoto et al., 1978). This again validates the numerical code.

As shown in Figures 11.23 and 11.24, the tensile behavior by CP model is considerable. It is eased by DP model but still non-negligible. Larger values of c_1 are expected theoretically to further reduce the tensile behavior. Unfortunately, the numerical algorithm may diverge when using large c_1 (Zhou et al., 2020). In contrast, both NCP and ND models are free of nonphysical tensile phenomenon as well as numerical instability. Noting that large penalty parameter κ_∞ in ND model is the key to remove the tensile behavior, the nonlinear performance becomes another important concern, as addressed in the next subsection.

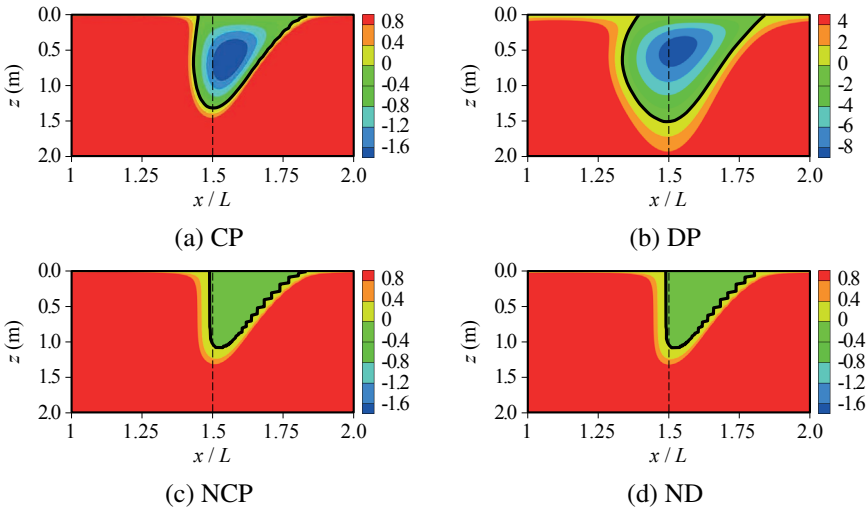

Figure 11.23 The vertical effective stress $\gamma' z-(p-P_b)$ (kPa) by: (a) CP; (b) DP with parameters of $c_1 = 10$, $c_2 = 1$ and $r_u^{\mathrm{cr}} = 1$; (c) NCP; (d) ND with penalty parameter of $\kappa_\infty = 10^6\, k_s/\gamma_w$.

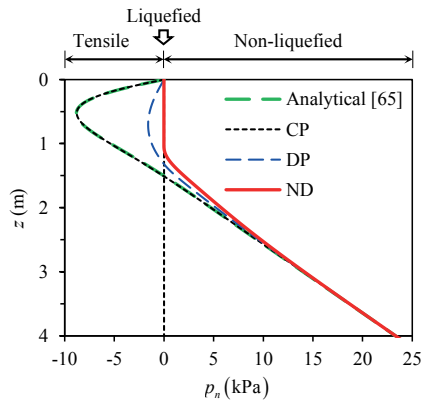

Figure 11.24 Vertical distribution of the vertical effective stress $\gamma' z-(p-P_b)$ along the line of $x = 1.5L$. Note: the analytical solution: Yamamoto et al. (1978).

By finding the isoline of $\gamma' z-(p-P_b)=0$ (i.e. the black lines in Figure 11.23), the liquefied zones can be determined by (11.12a) and are further compared in Figure 11.25. NCP and ND models are found to obtain nearly the same results and can be referred to the accurate estimation. Hence, the comparison indicates that CP model overestimates the liquefaction potential. The liquefaction estimation by DP can be regarded as an intermediate result from CP towards the accurate one, due to that the parameter c_1 is not large enough. A close view of the liquefied zone shows

that non-smoothness occurs in both NCP and ND models. This issue was discussed in Zhou et al. (2021*a*) and can be addressed to some extent by using finer computational meshes.

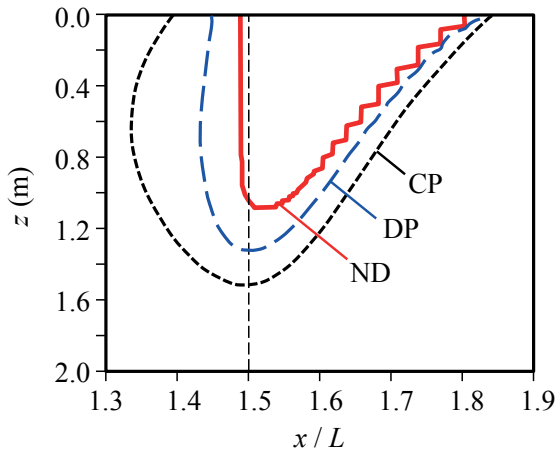

Figure 11.25 The liquefied zones determined by (11.12a) in the 2D simulation.

Although the DP and ND models both introduce additional parameters, the difference is that the penalty parameter κ_∞ used in ND model can be taken as large enough and meanwhile do not destroy the numerical algorithm. To validate this performance, four values of κ_∞ are tested, i.e. 10, 10^2, 10^4 and 10^6 times of k_s/γ_w. The results by using $\kappa_\infty = 10^6\, k_s/\gamma_w$ have been discussed in the above subsection and are compared here with the other three cases by Figure 11.26(a) in the vertical effective stress $\gamma' z - (p - P_b)$ and by Figure 11.26(b) in the liquefied zone. In these two comparisons, the results by CP model are provided as a reference.

As shown in Figure 11.26(a), if the penalty parameter κ_∞ is not large enough (e.g. $\kappa_\infty = 10\, k_s/\gamma_w$ or $10^2\, k_s/\gamma_w$), the tensile stresses cannot be removed. For the case of $\kappa_\infty = 10\, k_s/\gamma_w$, the tensile stresses are still apparent despite the apparent improvement over CP model. The value of $\kappa_\infty = 10^2\, k_s/\gamma_w$ can make the tensile stresses at a much lower value but still not close to zero. The residuals of tensile stresses have a significant influence on the liquefaction zones shown in Figure 11.26(b). In contrast, large penalty parameters (e.g., $\kappa_\infty = 10^4\, k_s/\gamma_w$ and $10^6\, k_s/\gamma_w$) provide a satisfactory accuracy in removing the tensile stresses. The results by these two values are almost the same. This implies that the increase of κ_∞ will achieve a converged result, making ND model somehow a parameter-free treatment. More precisely, once κ_∞ is large enough (e.g., $10^4\, k_s/\gamma_w$), the further variation of κ_∞ will have a negligible influence on the numerical results. The above performance is a common consequence of the penalty method within the constrained variational principle. In this study, the value of $\kappa_\infty = 10^6\, k_s/\gamma_w$ is used as a conservative choice.

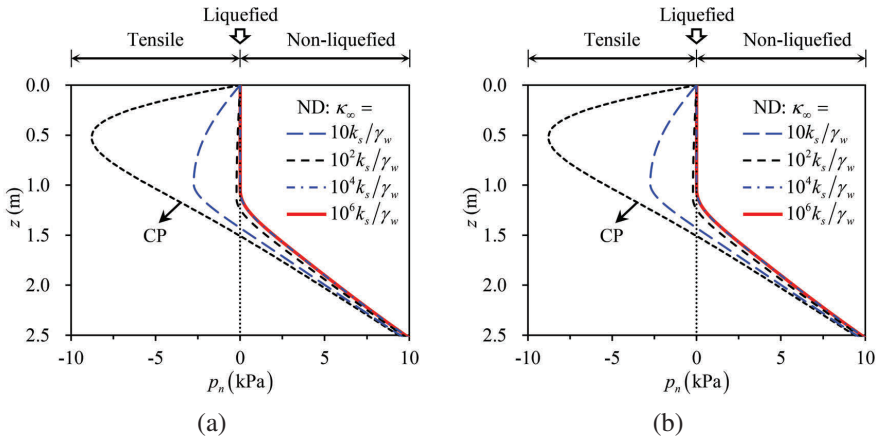

Figure 11.26 Parametric study of the penalty parameter κ_∞: (a) vertical distribution of the vertical effective stress $\gamma' z - (p - P_b)$ along the line of $x = 1.5L$; (b) liquefied zones determined by (11.12a).

11.4 SUMMARY

In this chapter, two special cases for the wave-induced oscillatory soil response are considered. First, a model considering dynamic soil permeability as a function of pore pressure is proposed. Second, a non-Darcy flow model is proposed to deal with the instantaneous liquefaction in a non-cohesive seabed. Based on numerical examples presented, the following conclusions can be drawn.

(1) A new relation of soil permeability and pore pressure is established and applied to the problem of wave-seabed interactions. Numerical examples demonstrates significant influence of dynamic soil permeability on the wave-induced soil liquefaction, compared with the conventional model with constant soil permeability.

(2) Compared with the Darcy model with constant permeability, the non-Darcy model reproduces the pore-fluid velocity increase during liquefaction as well as eliminates the fallacious tensile behavior in a non-cohesive seabed. Moreover, two instantaneous liquefaction criteria widely applied in ocean engineering are unified by the present model. According to the parametric study, the liquefaction depth by the present model is found to be roughly 0.73 times of the value predicted by constant permeability.

(3) Compared with the dynamic permeability model (Zhou et al., 2020), the present non-Darcy model overcomes the difficulties in the nonlinearity treatment and achieves superior convergences. The penalty parameter introduced by the new model is found to have slight influence on the nonlinear convergence, indicating that the additional computational efforts of using larger penalty

values are negligible in spite of their stronger non-linearities. Therefore, the penalty parameter can be chosen large enough so that the tensile behavior can be sufficiently eliminated.

12 Liquefaction around Marine Structures: Breakwaters

12.1 OVERVIEW: FLUID-SEABED-STRUCTURE INTERACTIONS

The phenomenon of wave-seabed interactions and the associated seabed instability such as liquefaction, shear failure and scour around marine infrastructures has a major bearing on this issue and is central to the design of coastal structures such as breakwaters, pipelines and platforms. A large number of investigations and research projects for the wave-seabed-structures interactions have been carried out since the 1970s. The 3 year EU project (2002-2004), LIMAS (Liquefaction around Marine Structures), led by Professor BM Sumer at DTU (Denmark University of Technology) is an example. the research outcomes were published in two special issues in the ASCE journal (Sumer, 2006, 2007).

Breakwaters are commonly adopted to protect and enhance the utility of coastlines. For example, the total length of all breakwaters in Japan is 4,143 km – one fifth of its coastline (Hsu et al., 2000). In most countries such as the UK and Japan, coastline protection is a national priority. The constructions of new breakwaters and the expansions of existing breakwaters involve major investment. Worldwide, the combined costs for building new breakwaters and maintaining the existing ones are in the order of tens of billions of pounds a year.

Breakwaters are vulnerable to the liquefaction of the seabed foundation, a process that can often lead to significant degradations of the foundation in as little as a few years after construction and sometimes even result in total collapse (Zen et al., 1985; Lundgren et al., 1989; Franco, 1994; Zhang and Ge, 1996; Sumer and Fredsoe, 2002; Chung et al., 2006; Zhang et al., 2012*b*). An inappropriate design or maintenance of breakwaters can lead to catastrophic coastal disaster. A recent example of coastal tragedy due to failure of breakwaters is that of New Orleans during Hurricane Katrina, which caused deaths and personal and economic chaos (Travis, 2005).

Among the previous studies for wave-seabed structure interactions, breakwaters including vertical seawalls, composite breakwaters and submerged breakwaters have been intensively studied. Based on the boundary-layer approximation (Mei and Foda, 1981), Mynett and Mei (1982); Tsai et al. (1990) derive analytical solutions for the wave-induced soil response around a caisson-type breakwater. Numerous numerical models have been proposed for the wave-induced soil response and liquefaction in the vicinity of a breakwater with different wave loading (Mase et al., 1994; Mizutani et al., 1996; Mizutani and Mostafa, 1998; Mostafa et al., 1999; Jeng et al., 2001; Mostafa and Mizutani, 2002; Ulker et al., 2010, 2012). All these have been limited to 2D conditions.

Regarding a simple breakwater such as a vertical seawall in a 3D, a short-crested wave system is formed in the vicinity of a vertical wall. The seabed response in a

homogeneous isotropic seabed in front of a vertical seawall have been studied by analytical solutions (Hsu et al., 1993; Hsu and Jeng, 1994; Jeng and Hsu, 1996; Hsu et al., 1995; Tsai, 1995). Later, More complicated wave and seabed conditions such as nonlinear wave loading, cross-anisotropic soil behaviour and non-homogeneous seabeds have been carried out by either analytical approximation or numerical modeling (Jeng, 1997*a*; Jeng and Seymour, 1997; Jeng and Lee, 2001; Jeng, 2001). All these relevant studies have been reviewed in Jeng (2003) and two previous books (see Jeng, 2012, Chapter 2) and (see Jeng, 2018, Chapter 1).

In this chapter, we will outline the numerical model (PORO-FSSI) first. Then, we focus on the The phenomenon of wave-seabed interactions around following types of breakwaters: Composite breakwaters, submerged breakwaters, breakwater heads at the river mouth and offshore detached breakwaters. The first two cases are 2D, while the last two cases are 3D.

12.2 NUMERICAL MODEL: PORO-FSSI MODEL

Recently, a framework model (PORO-FSSI, Porous model for Fluid-Seabed-Structure Interactions) was developed to integrate various wave loading, seabed models for different marine infrastructures. This integrated numerical model consists of two sub-models: flow and seabed models. The flow model is used for generating waves and currents and describing their propagation in a viscous fluid. The seabed model is used to determine the seabed responses to the waves, including the pore pressure, soil displacements and effective stresses. An one-way integrating algorithm is adopted to integrate both models together. In the seabed model, Quasi-static, $u-p$ and full dynamic models are included as well as an-isotropic soil behaviour and non-homogeneous seabed profiles. More information about the governing equations for the flow and seabed models can be found in Chapter 10.

Figure 12.1 illustrates the procedure of a typical numerical study using PORO-FSSI model, including three parts: pre-processing, numerical simulation and post-processing. The integrated process between the flow and seabed sub-models is reflected in the content framed by the dotted box, in which a one-way coupling algorithm is adopted through the pressure continuity on the common waves-seabed interfaces. As shown in Figure 12.1, the work flow of this integrated model is:

- In the pre-processing stage, the integral 3D numerical model is established by configuring the computational domain, dividing the mesh grids, setting the time interval scheme, determining the initial fields and inputting various model parameters.
- After accomplishing the process of pre-processing, the fluid motion that interacted with the structure are solved by the VARANS equations along with the $k-\varepsilon$ turbulence model. At each time step, the hydrodynamic pressure at the waves-seabed interface is extracted from the flow sub-model and applied to the soil model.
- Using the hydrodynamic pressure at the seabed surface as the boundary condition, the soil model solves the governing equations, depending on the different constitutive models.

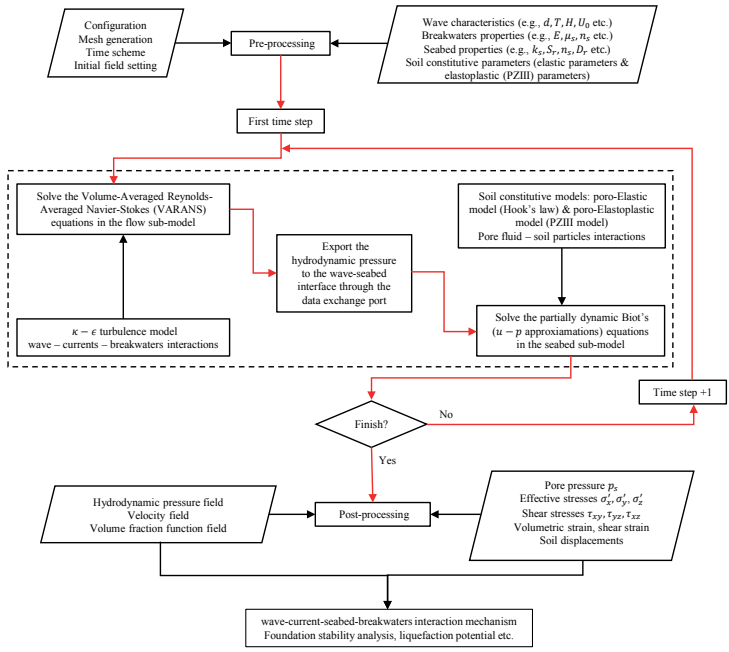

Figure 12.1 The coupling process of the numerical model.

- The simulation finishes when the time step reaches the prescribed total simulation time and we can obtain the main outputs include: the hydrodynamic pressure field, velocity field and volume fraction function field in the fluid domain and pore pressures, effective stresses, volumetric strain and soil displacements etc. in the solid domain.
- By post-processing these results, we can try to understand the mechanism of wave-current-seabed-breakwaters interactions and evaluate the liquefaction potential in the vicinity of the structure.

12.3 VALIDATION OF THE MODEL

To validate the proposed numerical model, four sets of previous experiments available in the literature are used. They are:

(A) Lu (2005) wave experiments for progressive waves over a porous seabed.
(B) Tsai and Lee (1995) wave experiments for a standing wave system in from of a vertical wall.
(C) Mizutani and Mostafa (1998) wave experiment for regular waves over a submerged breakwater.
(D) Mostafa et al. (1999) wave experiments for a composite breakwater.
(E) Cho et al. (2004) wave experiments for multiple submerged breakwaters.

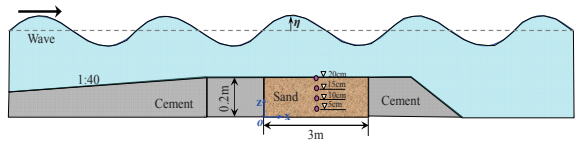

(a) Lu (2005) experiment: fifth-order wave and Cnoidal wave

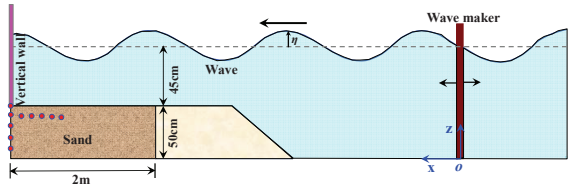

(b) Tsai and Lee (1995) experiment-Standing wave

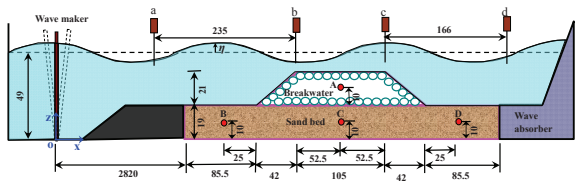

(c) Mizutani and Mostafa (1998) experiment-Submerged breakwater

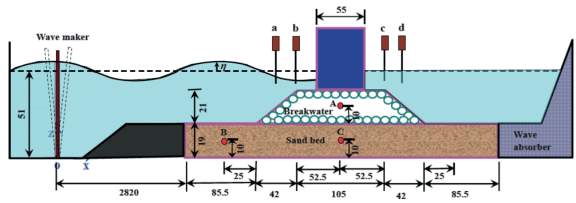

(d) Mostafa et al. (1999) experiment-Composite breakwater

Figure 12.2 Experiment setup of previous wave tank experiments for the validation of the present model.

The experimental set-up of these experiments are given in Figure 12.2. The input data of all experiments are tabulated in Table 12.1.

A. Comparison with experiments for progressive waves (Lu, 2005)

Lu (2005) conducted a series of laboratory experiments for the wave-induced dynamic response of sand bed in a wave flume, which is 60 m long, 1.5 m wide and 1.8 m high. The waves generated in the wave flume include regular progressive waves and cnoidal waves. The periods of wave vary from 1.0 to 1.8 seconds and the wave heights vary from 8 to 16 cm. The experimental setup is shown in Figure 12.2(a). The pore pressure at the four points on the mid-line of sand bed are measured in experiments. In the present model, the 5^{th}-order Stokes wave theory is adopted for the generation of the regular progressive wave (H=12 cm, d=0.4 m, T=1.2 s).

Table 12.1
Soil properties and wave characteristics in verification cases.

Properties[1]	Lu [2]	T&L	M&M	Mostafa
Wave type	5^{th}-order	2^{nd}-order	linear	2^{nd}-order
H (cm)	12	5.‘	3	5
d (m)	0.4	0.45	0.3	0.32
T (sec)	1.2	1.5	1.4	2.2
G_s (N/m^2)	10^7	2.64×10^7	5×10^8	5×10^8
G_b (N/m^2)	-	-	10^9	10^9
μ_s	0.3	0.3	0.33	0.33
μ_b	-	-	0.24	0.24
k_s (m/s)	10^{-3}	1.2×10^{-4}	2.2×10^{-3}	2.3×10^{-3}
k_b (m/s)	-	-	1.8×10^{-1}	1.6×10^{-1}
n_s	0.3893	0.38	0.3	0.3
n_b	-	-	0.33	0.33
d_{s50} (mm)	0.44	0.187	1.0	0.8
d_{b50} (mm)	-	-	30	27
S_r (sand)	0.98	0.98	0.99	0.98
S_r (breakwater)	-	-	0.99	0.99

[1] The subscript “s”=properties of seabeds, and “b”=properties of breakwaters.
[2] Lu=Lu (2005); T&L=Tsai and Lee (1995); M&M=Mizutani and Mostafa (1998); Mostafa =Mostafa et al. (1999)

As illustrated in Figure 12.3, the numerical prediction of the wave-induced pore pressures overall agrees well with experimental data (Lu, 2005).

B. Comparison with experiments for a standing wave in front of a vertical seawall (Tsai and Lee, 1995)

Another set of experiment for the validation was conducted by Tsai and Lee (1995) in a wave flume for a standing wave system. As shown in Figure 12.2(b), the wave generated by the wave maker propagates into the sand bed region, and to the vertical smooth wall, from which a perfect reflection of wave occurs. In the sandy bed, the wave-induced pore pressure at 9 points were measured (shown in Figure 12.2(b)). Among these, five measurements are taken on the left-end-side of the sand bed, four are on the line parallel with the seabed surface, and the distance to the seabed surface is 10 cm. The intervals between the ten points are 10 cm. As shown in Figures 12.4, the present model overall agrees with the experimental data. Some differences for the minimum pore pressure between the present model and experimental data are observed at the upper four points on the left-end-side of sand bed (Figure 12.4).

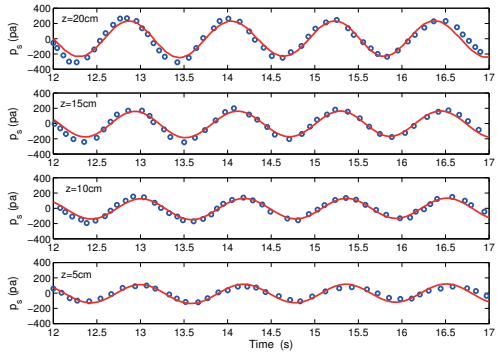

Figure 12.3 Comparisons of wave-induced dynamic pore pressures on the midline of sand bed between the numerical results and the experimental data in Lu (2005) experiments. —: numerical results; ○: experimental data.

Regarding the results for the left four points on the line parallel with sand bed surface, the readers can refer to Jeng et al. (2013).

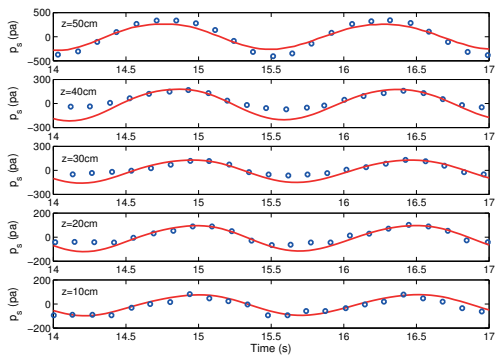

Figure 12.4 Comparisons of the standing wave-induced dynamic pore pressure in the sand bed (the left-end-side of bed ($x = 0$)) in Tsai and Lee (1995) experiment. —: numerical results, ○: experimental data.

C. Comparison with experiments for a submerged breakwater (Mizutani and Mostafa, 1998)

The third set of comparison is with Mizutani and Mostafa (1998), in which a series of wave flume tests was conducted to investigate the interaction between the regular wave, submerged breakwater and sand bed. The experimental setup is shown in Figure 12.2(c). In the experiment, a submerged breakwater is constructed on the

sand bed. Four wave gauges are installed at points a, b, c and d to monitor the wave profile. Four pressure sensors are installed at point A, B, C and D to record the pore pressure. The properties of the sand bed and breakwater, and the wave characteristics provided by Mizutani and Mostafa (1998) are listed in Table 12.1. Due to the fact that the wave steepness is 0.0143, the linear wave model is sufficient to accurately simulate the generation and propagation of the wave in the wave flume.

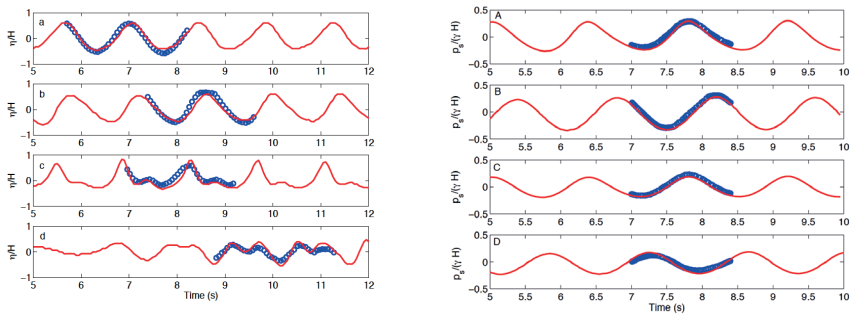

(a) wave profile (b) pore pressure

Figure 12.5 Comparison of the PORO-FSSI model and the experimental data in Mizutani and Mostafa (1998). - - -: numerical results; ○: experimental data.

The comparisons for the wave profile and the wave-induced dynamic pore pressure in a sand bed and rubble mound breakwater between the numerical results predicted by the present model and the experiment data are shown in Figure 12.5. As illustrated in the figure, the agreements for the wave profile at a and b are good, while some little differences are observed at points c and d that locate at the behind of the breakwater (Figure 12.5a). Furthermore, the agreements for the wave-induced dynamic response at A, B, C and D are all excellent (Figure 12.5b). The comparison clearly demonstrates that the integrated model PORO–FSSI is applicable for the FSSI problem.

D. Comparison with experiments for a composite breakwater (Mostafa et al., 1999)

Based on the experiments conducted by Mizutani and Mostafa (1998), Mostafa et al. (1999) further conducted a series of experiments in the same wave flume to investigate the interaction between the wave, composite breakwater and sand bed, as shown in Figure 12.2(d). In the experiments, a wooden box (the width is 55 cm) is placed on the breakwater to form a composite breakwater in the wave flume. Four wave gauges are installed at points a, b, c and d to monitor the wave profile; two of them are in front of the composite breakwater, while the other two are behind of the composite breakwater. Three pressure sensors are installed at points A, B and C to record the pore pressure. The properties of the sand bed and breakwater, and the wave characteristics provided by Mostafa et al. (1999) are listed in Table 12.1.

Here, the wave model with the wave maker of second-order Stoke wave is adopted to simulate the generation, propagation, reflection and interference of wave.

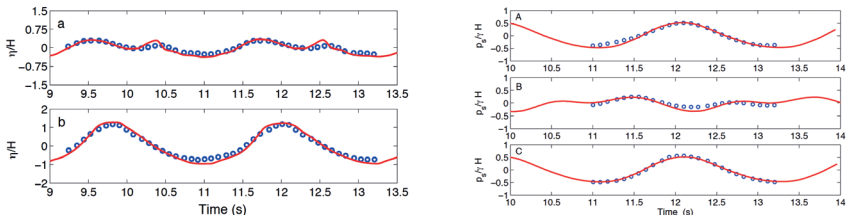

(a) wave profile (b) pore-water pressure

Figure 12.6 Comparison of (a) wave profile and (b) pore-water pressure between the PORO-FSSI model and the experimental data in Mostafa et al. (1999) for the wave profile. —: numerical results; ○: experimental data.

The comparisons for the wave profile and the wave-induced dynamic pore pressure in sand bed and the rubble mound between the numerical results predicted by PORO-FSSI and the experiment data are shown in Figure 12.6. Due to the blocking effect of the impermeable wooden box, only little water can flow into and out the right side of the composite breakwater through the rubble mound. Therefore, the amplitude of wave behind the composite breakwater is very small. In Figure 12.6(a), only the wave profiles of points a and b are used to make the comparison between numerical results and experiment data. Figure 12.6(b), it can be seen that the numerical results obtained by the present model agree well with the experiment data both for wave profile and wave-induced dynamic pore pressure.

E. Comparison with experiments for multiple submerged breakwaters (Cho et al., 2004)

Cho et al. (2004) performed a series of laboratory experiments to investigate the strong reflection of regular water waves over a train of permeable submerged breakwaters in a wave flume of 1 m wide, 2 m deep and 56 m long. To numerically reproduce their experiments, the parameters of numerical experiments are defined as follows: still water depth d =0.8 m, wave height H_w =0.04 m, structure height $h = 0.5d$ =0.4 m, bottom width $w_b = 2d$ =1.6 m, crown width $w_t = 0.5d$ =0.4 m, adjacent distance $L_s = 2.5d$ =2 m, porosity n =0.5 and equivalent mean diameter d_{50} =0.076 m. Periods of incident water waves are $1.14 \leq T \leq 3.73$ s, leading to the relative wave numbers of $0.5 \leq kd \leq 2.5$. It is noted that the experiments were conducted on an impermeable seabed (i.e., no seabed response is considered) (Cho et al., 2004). Therefore, in this comparison, an impermeable seabed is used in the PORO-FSSI numerical model.

The computational domain covers $-50 \leq x \leq 50$ m and $0 \leq z \leq 1.2$ m. In the vertical direction, Δz =0.005 m is uniformly distributed. To better fit the shape of the trapezoidal breakwater, a non-uniform grid system is applied in the x-direction. Δx =0.01 m is used in the breakwater region ($0 \leq x \leq 8.8$ m), while Δx =0.05 m

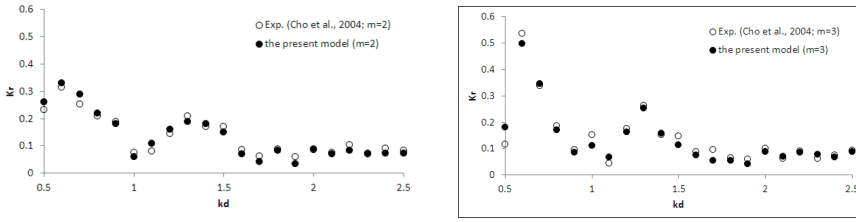

(a) $N = 2$ (b) $N = 3$

Figure 12.7 Comparisons of computed reflection coefficients with experimental measurements (Cho et al., 2004). (a) $N = 2$ and (b) $N = 3$.

is used in other regions. The internal wave-maker is located at the cross-section x =-20 m. The numerical sponge layer (having a length of twice the wavelength of the surface wave) is applied to reduce the wave reflection at the two side boundaries. When waves propagate into the sponge layer region, their velocities are gradually and artificially reduced by multiplying an absorption function. To obtain computational stability, the time interval (Δt) is automatically adjusted at each time step to satisfy Cournat-Friedrichs-Lewy condition and the diffusive limit condition (Liu et al., 1999).

Figure 12.7 shows the comparison of the simulated reflection coefficients and experimental measurements. In this example, the reflection coefficient (K_r, a ratio of reflected wave height to incident wave height) is determined by the model of Goda and Suzuki (1976). The simultaneous water elevation levels are taken at two adjacent locations placed in front of the submerged breakwaters, and the amplitudes of Fourier components are analyzed by the FFT technique. The amplitudes of incident and reflected wave components are estimated from the Fourier components. Overall, there is a good agreement between simulation and measurements. The results show that the reflection coefficient K_r is highly dependent on wave period (in term of kd) and it reaches a maximum value when $kd = 0.6$ in both cases: two breakwaters ($N = 2$) and three breakwaters ($N = 3$). It is noted that N represents the total numbers of breakwaters. The maximum reflection coefficient of three breakwaters ($K_r = 0.52$, the average of measurement and simulation) is obviously higher than that of two breakwaters ($K_r = 0.32$). This implies that more incident wave energy can be reflected back to the sea with the presence of one more breakwater. In the other words, both wave period and the number of breakwaters (N) have a significant impact on the wave motion. As seabed response is mainly dominated by the wave motion, these two parameters may also affect the wave-induced seabed response.

12.4 SEABED RESPONSE AROUND A COMPOSITE BREAKWATER UNDER OCEAN WAVE LOADING

In this section, the present model (PORO-FSSI) is applied to investigate the response of seabed and a composite breakwater under wave loading in real offshore

environments. In the examples, we consider a composite breakwater consisting of a permeable rubble mound and an impermeable caisson, sitting on a porous seabed. The thickness of seabed is 30 m, and the horizontal computational length of seabed is chosen as 250 m, which is much greater than the horizontal dimension of the composite breakwater. The dimensions and position of composite breakwater are shown in Figure 12.8. In the range z=27 m to z=30 m, the vertical size of elements varies from 0.1 m to 0.3 m. In other range $z \leq 27$ m, the vertical size of elements is 0.8 m to 2.0 m. The horizontal size of elements in the whole domain is set as 0.5 m to 2.0 m. In the wave model, the horizontal and vertical size of grids is 0.3 m and 0.06 m, respectively.

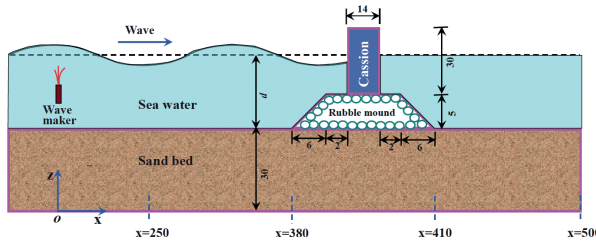

Figure 12.8 Sketch of wave-seabed interaction around a composite breakwater (Unit: m).

12.4.1 DYNAMIC RESPONSE OF A SEABED

In natural offshore environments, the seabed generally has experienced the consolidation process under the seawater loading and self-gravity in the geological history. In addition, after the composite breakwater is constructed, the seabed in the vicinity of the composite breakwater will be compressed and deform due to the static loading. The seabed will then reach a new balanced state, based on the previous consolidation state under dead loading. To correctly simulate the interactions between the ocean waves, a seabed and marine structures, the initial consolidation state of seabed due to static loading has to be determined before the ocean wave loading is applied in the numerical model. In this section, the initial consolidation state of seabed is calculated by using the present model (PORO-FSSI) with the static loading, including the static water pressures and weight of the composite breakwater. The properties of seabed soil, rubble mound and caisson are listed in Table 12.2.

Once the initial consolidation state of seabed is determined under the static water pressure and weight of composite breakwater, it will be taken as the initial stress state when determining the dynamic response of seabed under dynamic ocean wave loading. As shown in the procedure (see Figure 12.1), the seabed and rubble mound are considered as porous medium, while the caisson is considered as impermeable structure in wave model. The full pressure acting on sea floor and composite breakwater is transmitted to the soil model to predict the response of seabed and the composite breakwater. The predicted seabed responses induced by the full pressure

Table 12.2
Properties of seabed soil, rubble mound and caisson adopted in large-scale model.

Medium	G (kN/m^2)	μ_s	k_s m/s	n_s	d_{50} (mm)	S_r
Seabed soil	10^5	0.33	0.0001	0.25	0.5	98%
Rubble mound	5.0×10^5	0.33	0.2	0.35	400	98%
Caisson	10^7	0.25	0.0	0.0		0%

are considered as full response, and the wave-induced dynamic response can be determined from the difference between full response and initial consolidation state.

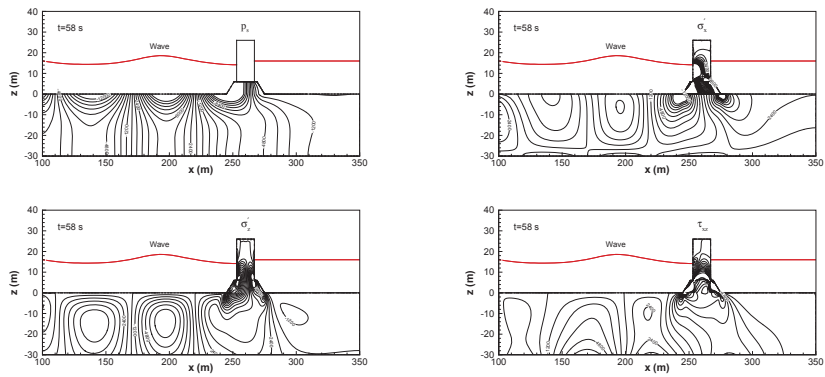

Figure 12.9 The dynamic response of the seabed and composite breakwater under the ocean wave loading at t=73.6 s. Wave characteristics: T=10 s, H=3 m, d=20 m.

In this example, the wave characteristics are chosen as: wave period T=10 s, wave height H=3 m, water depth d=20 m. Figure 12.9 shows the distributions of dynamic effective stresses and pore pressure in the seabed and composite breakwater at t=73.6 s under dynamic wave loading. At the right-hand-side of composite breakwater, the effect of the ocean wave is limited in a range which does not excess x=450 m due to the blocking of breakwater. In the region far away from the composite breakwater, the effect of ocean wave basically disappears. At time t=73.6 s, as shown in Figures 12.9, the seabed near the rubble mound is likely to be liquefied when the wave trough is propagating on it, and the dynamic effective stresses and pore pressure are negative, which would lead to the collapse of the composite breakwater.

Before the ocean wave arrives at the structure, the composite breakwater gradually moves downward to the seabed due to its weight and reaches the initial consolidation state. Figure 12.10 shows the development of horizontal and vertical displacements of the upper left corner of the caisson. The results indicate that the

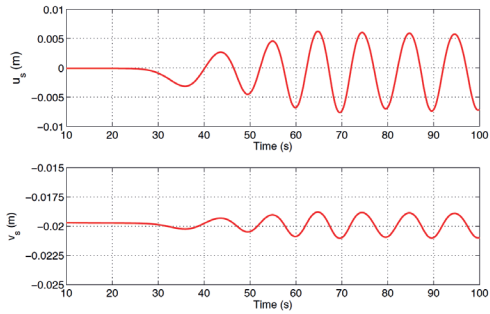

Figure 12.10 The variation of horizontal and vertical displacements of the left corner of the impermeable caisson under ocean wave. Negative value of "u_s" means moving toward left, negative value of "v_s" means moving toward down.

structure vertically subsides about 19 mm during $0< t <25$ s. After the ocean wave reaches the caisson ($t >25$ s), the caisson begins to vibrate vertically and horizontally with a small amplitude. After the full interaction between the waves and structures ($t >60$ s), the breakwater subjects to a periodical wave force and its induced vibration.

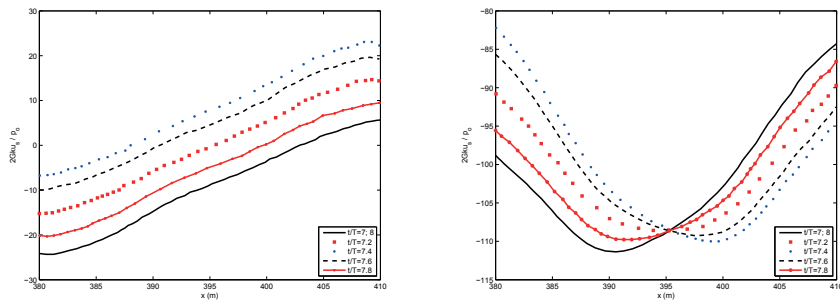

(a) Horizontal soil displacements (b) Vertical soil displacements

Figure 12.11 Distributions of the (a) horizontal and (b) vertical soil displacements at the bottom of rubble mound at different time under ocean wave loading.

Figure 12.11 illustrate the distributions of the horizontal and vertical displacements around the bottom of rubble mound at different time levels after the standing wave system is fully developed. It is found (graphs not shown) that the horizontal and vertical displacements at the bottom of rubble mound are both symmetric in the first two wave periods. There is no further movement before the ocean wave reaches the composite breakwater. After the 4^{th} wave crest arriving, the horizontal and vertical displacements at the bottom of rubble mound begin to gradually increase with a small magnitude due to the loading of ocean wave. When

the interaction between ocean wave and composite breakwater becomes much more intensive, the displacements at this plane start to increase (see Figure 12.11).

Figure 12.12 shows that distribution of pore pressure around the bottom of rubble mound after the standing wave system is fully developed. The numerical results show that the pore pressure beneath rubble mound is a little higher than that outside of the rubble mound in the 2^{nd} period. In the 4^{th} period, the pore pressure begins to vary due to the wave motion around composite breakwater. When the wave crest arrives at the composite breakwater, the pore pressure on the bottom of rubble mound increases; while the pore pressure decrease with the wave tough above. The impact of wave motion on pore pressure near the right end of the bottom of rubble mound (x=407∼410 m) becomes negligible, indicating that the breakwater can efficiently protect the offshore seabed and coastline from the erosion by ocean wave.

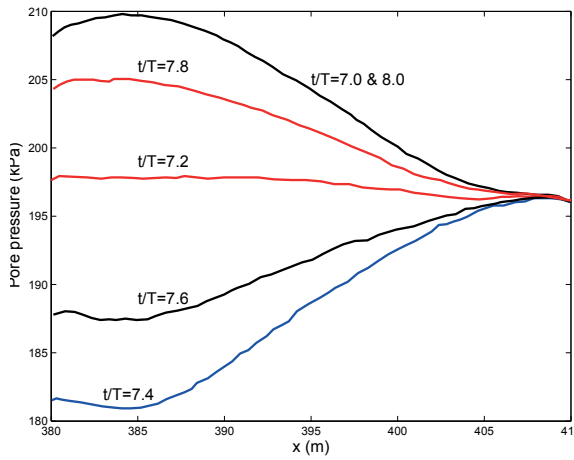

Figure 12.12 The distributions of the pore pressure at the bottom of rubble mound at different time under ocean wave loading.

12.4.2 WAVE-INDUCED MOMENTARY LIQUEFACTION

As mentioned previously, two mechanisms of the wave-induced soil response, oscillatory and residual, have been observed in the laboratory and field measurements, depending on the manner that the pore pressure is generated (Zen and Yamazaki, 1990*b*). In this section, we focus on the former mechanism–oscillatory soil response, which will lead to the momentary liquefaction. Some examples for such a liquefaction have been reported in the literature. For example, laboratory experiments (Zen and Yamazaki, 1990*b*) have been conducted to confirm the existence of the momentary liquefaction of sand bed under wave loading. A

long-term field measurements (Mory et al., 2007) also indicated the occurrence of the wave-induced momentary liquefaction near coastal structures.

In general, the momentary liquefaction is directly related to the magnitude and direction of the seepage force. The seabed is likely to be liquefied when the seepage force is upward because it will decrease the contact effective stresses between soil particles. In contrast, the seabed will absolutely not be liquefied when the seepage force is downward because it will increase the contact effective stresses of soil particles.

To investigate the liquefaction properties in a seabed under ocean wave loading, the liquefaction criterion proposed by Okusa (1985) are adopted by considering the initial effective stress due to pre-consolidation (Jeng et al., 2013), which can be expressed as,

$$|(\sigma_z')_{initial}| \leq \sigma_z', \tag{12.1}$$

where the $(\sigma_z')_{initial}$ is the vertical effective stress at the initial consolidation state.

Figure 12.13 The three liquefaction zones in seabed under ocean wave at time t=73.6 s and t=76.8s.

Figure 12.13 shows the liquefaction zones in the seabed under the ocean wave loading at the time t=73.6 s and t=76.8 s, in which the modified liquefaction criterion (12.1) are adopted. As illustrated in Figure 12.13, there are two liquefaction zones in the region near the seabed surface at time t=73.6 s; they are located at the range of 250< x <290 m (Zone I) and 370< x <380 m (Zone III), respectively. There is only one liquefaction zone in the region near the seabed surface at time t=76.8 s, which is located at the range of 310< x <350 m (Zone II). Zones II and III are very close to the foundation of breakwater, and they may have a large impact on the foundation stability. Therefore, we will further investigate the (depth, width and area) development of these two liquefaction zones.

Figure 12.14 illustrates the variations of liquefaction potential of Zones II and III under the ocean wave loading (T=10 s, H=3 m, d=20 m), respectively. It can be seen from Figure 12.14(a) that the liquefaction potential of Zone II is very small, when the first wave trough passing through, but it increases largely during the second wave trough. After the interaction between wave and structure develops, the liquefaction depth, width and area of Zone II further increase. The maximum liquefaction depth, width and area are about 1.4 m, 41.0 m and 38.5 m^2 (which occur at t=79 s), respectively. As shown in Figure 12.14(b), the liquefaction potential of Zone III has a similar development process as that of Zone II. The maximum liquefaction depth, width and area of Zone III are about 0.46 m, 11.5 m and 3.85 m^2 (which occur at

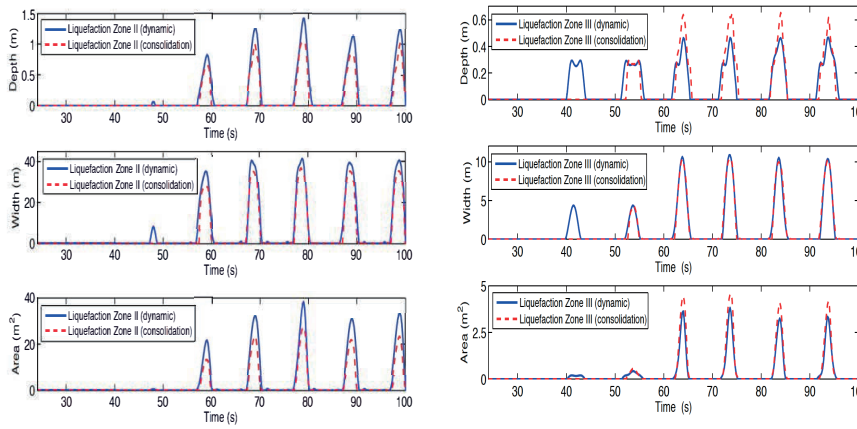

(a) Liquefaction Zone II (b) Liquefaction zone III

Figure 12.14 The liquefaction properties (depth, width and area) in (a) liquefaction Zones II and (b) liquefaction Zones III.

t=74 s), respectively. The liquefaction potential of Zone III are much smaller than that of Zone II, which can be ascribed to that the weight of composite breakwater significantly increases the vertical effective stress of initial consolidation state in Zone III.

Although the liquefaction potential in Zone III is small compared to that in Zone II, more attentions need to be paid to the Zone III as it is next to the foundation of composite breakwater. The soil liquefaction may lead to a collapse of composite breakwater. In engineering applications, some methods, such as a replacement of the fine sand with gravel materials, need to be adopted to protect the structure foundations.

The influence of the inertial terms associated with the accelerations of the pore-water and soil particles on the wave-induced dynamic pore pressures and effective stresses in the previous work (Jeng and Cha, 2003; Ulker and Rahman, 2009; Ulker et al., 2009). It is of interest to examine the effects of inertial term on the liquefaction potential. In Figure 12.14(a) , the predictions of liquefaction zone by the conventional consolidation model are also included as dashed lines. As shown in the figure, the predictions of the consolidation model are slightly greater than that of the dynamic model.

It is well known that the wave characteristics, including the wave height (H), wave period (T) and water depth (d) have an impact on the seabed liquefaction. Generally, the seabed is most likely to be liquefied under the long wave with a high wave height propagating in shallow water. In this part, the effect of wave characteristics on the liquefaction potential is numerically investigated. Only the Zone III is considered here, as this zone is close to the structure foundation and may lead to the instability of foundation. As reported by Jeng et al. (2013), the wave

height, wave period and water depth have great impact on the maximal liquefaction potential in Zone III. A longer wave period, higher wave height or shallower water depth will lead to a larger liquefaction potential. This mainly due to that the long wave or the wave with high height carries more energy, leading to a more intensive WSSI. Meanwhile, a deep water could effectively reduce the wave-induced dynamic pressure acting on seabed, and consequently results in the liquefaction potential of seabed. More detailed parametric study regarding the effect of wave characteristics on the liquefaction properties (including maximum liquefaction depth, width and area) of liquefaction Zone III can be found in Jeng et al. (2013).

12.5 WATER WAVES OVER PERMEABLE SUBMERGED BREAKWATERS WITH BRAGG REFLECTION

In recent years, permeable submerged breakwaters have become increasingly attractive to coastal engineers, as these structures have significant advantages in

- reflecting efficiently incident wave energy,
- dissipating wave energy due to the flow friction within the porous media,
- reducing the impact that structures have on water quality, nearby ecosystem and also visual impacts (as the crowns of the structures are under the sea surface).

Water waves propagating from offshore to near-shore zones will strongly interact with such marine structures, and part of the incident wave energy is reflected. The reflection by the multiple submerged structures can be amplified when the incident waves are twice as long as the structure spacing, which is called as Bragg reflection. This mechanism is due to the constructive interference of reflected waves from successive structure crests, and it plays a significant role in the evolution of surface waves and in the formulation of offshore ripples (Davies and Heathershaw, 1984; Mei and Liu, 1993; Yu and Mei, 2000). The construction of such kind of marine structures may largely interact with ocean waves and seabed soil. As the seabed response (such as pore fluid pressure, effective stress of soil and liquefaction potential) is mainly dominated by the wave pressure and shear stress at the sea floor, it can be significantly affected by the Bragg reflection of incident waves.

Although the Bragg reflection of water waves over impermeable obstacles have been extensively studied (Davies and Heathershaw, 1984; Liu and Cho, 1993; Liu and Yue, 1998; Cho and Lee, 2000; Cho et al., 2001; Hsu and Wen, 2001; Hsu et al., 2007; Tang and Huang, 2008), the knowledge related to permeable structures is limited. Among these, Mase et al. (1995) developed a time-dependent wave equation to describe a wave propagating over permeable ripple beds taking into account of the effects of porous medium, based on two assumptions: (i) the mean water depth and the thickness of porous layer slowly varying compared to the wavelength of surface wave and (ii) the spatial scale of ripples being the same as the wavelength of surface waves. Cho et al. (2004) experimentally and Jeon and Cho (2006) numerically investigated the strong reflection of regular

waves over a train of submerged breakwaters, and both studies concluded that the reflection coefficients of permeable submerged breakwaters are less than those of impermeable breakwater as wave energy is additionally dissipated due to porous structures. later, Lan et al. (2009) developed an analytical solution based on linear wave theory and Biot's poro-elastic theory to predict the Bragg scattering of waves propagating over a series of poro-elastic submerged breakwaters. Their results indicated that the elasticity, permeability and the breakwater height of the series of poro-elastic submerged breakwaters have a significant impact on Bragg reflection. All aforementioned researches mainly have focused on the wave-structure interaction, and did not consider the wave-induced seabed response around the permeable submerged structures until Zhang et al. (2012*b*); Cui and Jeng (2018)

In this section, the Bragg reflection and seabed response due to water waves over multiple permeable submerged breakwaters will be examined. The $u - p$ approximation is used for the seabed model and only oscillatory mechanism is considered in this section.

12.5.1 NUMERICAL EXAMPLE CONFIGURATION

The trapezoidal permeable submerged breakwaters are considered in this study, as they are recommended for engineering applications providing a good balance of reflecting capacity and overall performance (Cho et al., 2004; Tang and Huang, 2008). A schematic sketch of trapezoidal shape of permeable submerged breakwaters is shown in Figure 12.15. Up to three breakwaters ($N = 1$, $N = 2$ and $N = 3$, N denotes the submerged breakwater number) are considered, and each one has bottom width w_b, crown width w_t and height h. Porosity n and equivalent mean diameter d_{50} are the characteristic parameters of permeable material of breakwaters. The distance between two adjacent breakwaters is defined as L_S. The origin of the Cartesian coordinate system is located at the left-bottom corner of the first breakwater ($N = 1$). Regular waves with still water depth d, wave period T and wave height H_w are generated at the left-hand-side of breakwaters.

The seabed of finite thickness (H_s =10 m) is considered, and its soil properties are fixed as follows: soil porosity n_s =0.3, soil permeability $K = 10^{-3}$ m/s, the degree of saturation S =1.0, soil shear modulus $G = 10^7$ N/m^2, Poisson's ratio μ_s =1/3 and the unit weight of soil $\gamma_s = 2.65\gamma_w$. In this section, a series of numerical simulations are carried out to model the laboratory experiments of Cho et al. (2004), and the simulated reflection coefficients are compared with the measurements. Then, the wave field and seabed response (in terms of pore fluid pressure and effective stress) due to Bragg reflection of water waves over permeable submerged breakwaters are numerically investigated.

12.5.2 PORE FLUID PRESSURES

The pore fluid pressures in a porous seabed are mainly dominated by the wave pressures along the sea floor. A variation of wave motion consequently results in a change of pore fluid pressure. Figures 12.16(a) & (b) display the distribution of

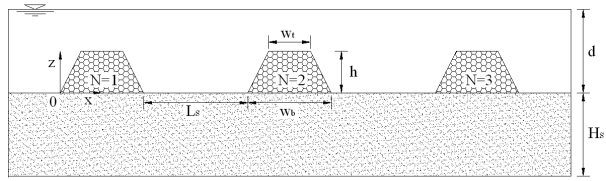

Figure 12.15 A schematic sketch of trapezoidal shape of permeable submerged breakwaters.

wave-induced pore fluid pressures $p/(0.5\gamma_w H_w)$ around breakwaters with a wave period of T =3.16 s at different time levels. As a result of wave-seabed-structure interactions, the existence of structures has a significant impact on the distribution of wave-induced pore pressure. It is noted that the impact of wave motion on pore fluid pressure is negligible in the region below $z/H_s < -0.5$.

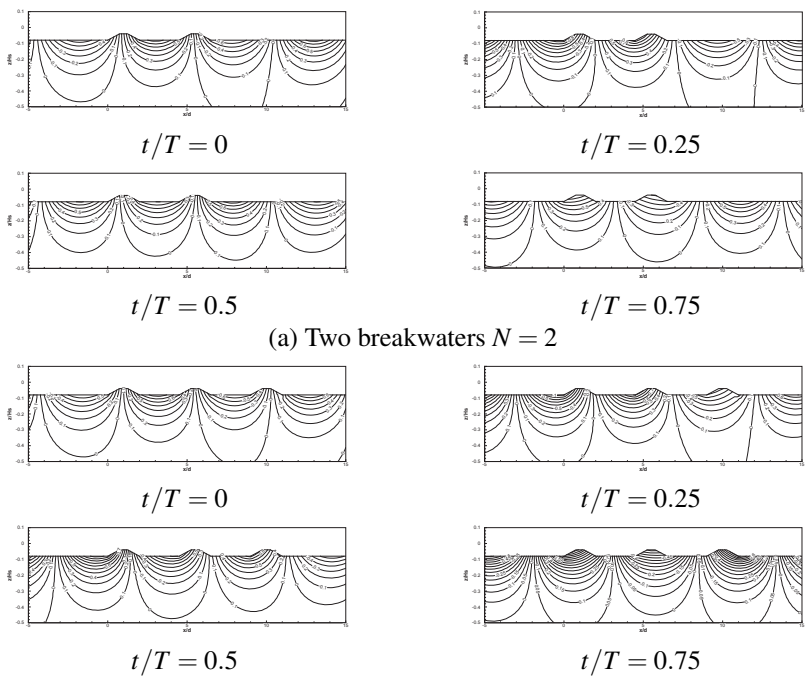

Figure 12.16 Distribution of the wave-induced pore fluid pressure $p/(0.5\gamma_w H_w)$ around (a) two breakwaters ($N = 2$) and (b) three breakwaters ($N = 3$) with a wave period of T =3.16 s at different times.

Figure 12.17 gives the vertical distributions of maximum wave-induced pore pressures $|p|_{max}/(0.5\gamma_w H_w)$ versus z/H_s below the toe of breakwaters where

the seabed liquefaction is most likely to take place. The results show that $|p|_{max}/(0.5\gamma_w H_w)$ at the cross-section $x/d = 0$ (the toe of the first breakwater) is greater than those at other cross-sections. $|p|_{max}/(0.5\gamma_w H_w) > 1$ at the point, $(x/d = 0,\ z/H_s = 0)$ indicates that the height of wave crest is increased in front of the first breakwater due to the Bragg reflection. $|p|_{max}/(0.5\gamma_w H_w) < 1$ at other points, $(x/d = 4.5,\ z/H_s = 0)$ and $(x/d = 9,\ z/H_s = 0)$ shows that the transmitted wave energy can be significantly reduced by Bragg reflection and friction dissipation of permeable breakwaters.

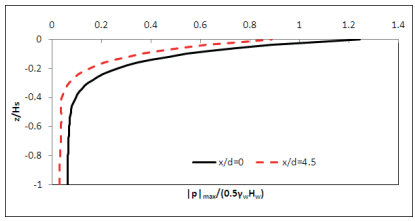

(a) Two breakwaters $N = 2$

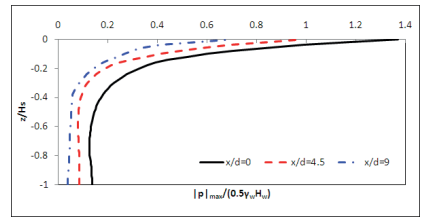

(b) Three breakwaters $N = 3$

Figure 12.17 Vertical distribution of the maximum magnitude of wave-induced pore pressure $|p|_{max}/(0.5\gamma_w H_w)$ versus z/H_s below the toe of breakwaters. (a) two breakwaters $N = 2$ and (b) three breakwaters $N = 3$.

The case with $N = 3$ is taken as an example to study the impact of the strength of Bragg reflection on wave-induced pore pressure. The source of the Bragg reflection is due to constructive interference of incident and reflected waves and is well known in x-ray diffraction by crystalline materials. When the wavelength of the surface wave becomes closer to the twice of wavelength of bottom undulation, the phenomenon of Bragg reflection becomes stronger (Mei et al., 2005). Three different values of wave period ($T = 3.16$, 2.76 and 2.46 s), leading to three different reflection coefficients ($K_r = 0.50$, 0.35 and 0.17), are considered here (see Figure 12.18). The strength of Bragg reflection has an important impact on the $|p|_{max}/(0.5\gamma_w H_w)$ in front of first breakwater. For instance, a stronger Bragg reflection (such as the case with wave period of T =3.16 s) results in a larger value of $|p|_{max}/(0.5\gamma_w H_w)$, implying more chance for the seabed liquefaction. This is because a higher wave crest takes place in front of structures when the wave reflection becomes stronger. However, the impact of Bragg reflection on $|p|_{max}/(0.5\gamma_w H_w)$ decreases at cross-section $x/d = 4.5$ and becomes negligible at cross-section $x/d = 9$.

12.5.3 VERTICAL EFFECTIVE NORMAL STRESSES

Figures 12.19(a)&(b) show the distribution of vertical effective stress $\sigma'_z/(0.5\gamma_w H_w)$ around the foundation. The wave period is T =3.16 s in the example. It can be seen that the value of $\sigma'_z/(0.5\gamma_w H_w)$ below the breakwaters is different from those away from the structures, as the magnitude of $\sigma'_z/(0.5\gamma_w H_w)$ is increased due to the weight of structures. Positive and negative values of $\sigma'_z/(0.5\gamma_w H_w)$ within the porous seabed

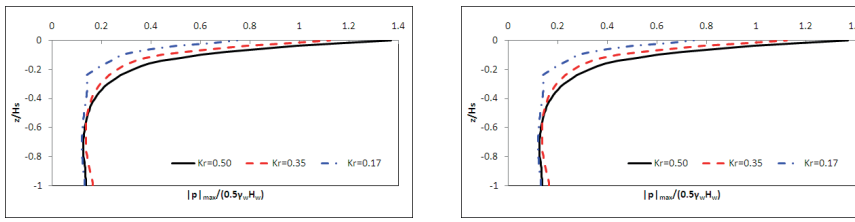

(a) cross-section $x/d = 0$ (b) cross-section $x/d = 4.5$

Figure 12.18 Effect of strength of Bragg reflection on $|p|_{max}/(0.5\gamma_w H_w)$ at different cross-section in the case $N = 3$. (a) cross-section $x/d = 0$, and (b) cross-section $x/d = 4.5$.

are induced by the wave trough and wave crest, respectively. The magnitudes of $\sigma'_z/(0.5\gamma_w H_w)$ increase at the toe of breakwaters.

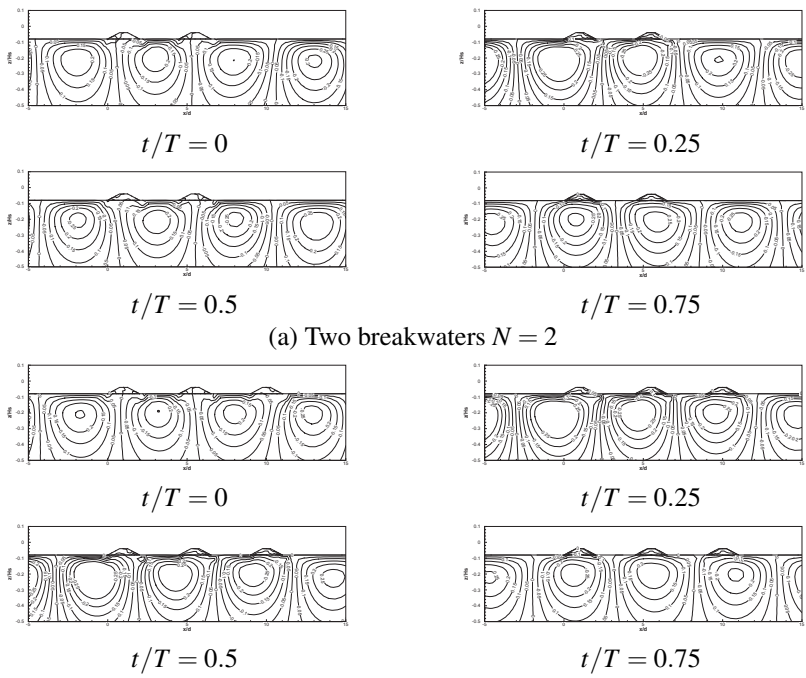

$t/T = 0$ $t/T = 0.25$

$t/T = 0.5$ $t/T = 0.75$

(a) Two breakwaters $N = 2$

$t/T = 0$ $t/T = 0.25$

$t/T = 0.5$ $t/T = 0.75$

(b) Three breakwaters $N = 3$

Figure 12.19 Distribution of vertical effective stress $\sigma'_z/(0.5\gamma_w H_w)$ around (a) two breakwaters ($N = 2$) and (b) three breakwaters ($N = 3$) with a wave period of T =3.16 s at different time.

Comparison of Figures 12.19(a) & (b) indicates that an additional breakwater ($N = 3$) also has an impact on the $\sigma'_z/(0.5\gamma_w H_w)$. In the upper region of seabed ($z/H_s > 0.4$), the values of $\sigma'_z/(0.5\gamma_w H_w)$ at cross-sections $x/d = 0$ and $x/d = 4.5$

when $N = 3$ are larger than those when $N = 2$. The resulted crest height in the case N=3 is larger than that in the case $N = 2$, and it will cause higher wave pressure on the structure. Part of the wave pressure on marine structure will be passed into the soil skeleton and increase the vertical effective stress. Generally speaking, a change of configuration/number of arrayed breakwaters leads to a variation of the overall interaction of the whole wave-seabed-structure system resulting from the incoming wave, and consequently induces different seabed response.

12.5.4 LIQUEFACTION POTENTIAL

Soil liquefaction is an extreme form of seabed instability, which may lead to a vertical movement of sediment. Seabed liquefaction may take place when the wave-induced effective stress is equal to the initial effective stress. The wave-induced maximum liquefaction areas around different numbers of breakwater are given in Figure 12.20. A liquefaction depth (1.52 m) in the case $N = 2$ is higher than that (1.4 m) in the case $N = 3$. The construction of the third breakwater also has a significant impact on the distribution of maximum liquefaction depth within the range of $x/d < 8.0$.

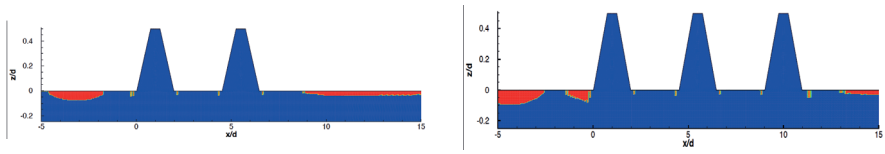

(a) Two breakwaters ($N = 2$) (b) Three breakwaters ($N = 3$)

Figure 12.20 Effect of the number of breakwaters on wave-induced maximum liquefaction areas: (a) two breakwaters ($N = 2$) and (b) three breakwaters ($N = 3$).

12.6 3D MODEL FOR SEABED RESPONSE AROUND BREAKWATER HEADS

Recently, coastal zones have been in increasingly strong demands for human activities such as port trade, marine transport, tourism and fishery production, etc. While bringing immeasurable economic benefits, these demands also directly lead to the rapid development of the coast, and the shoreline protection and management become an important concern for coastal engineers. Breakwaters have been commonly constructed in coastal zones with various purposes. Sometimes, breakwaters are deployed at estuaries as an extension of river banks towards the sea. One of example is the Southport Spit at Gold Coast, Queensland, Australia (https://haveyoursay.dsdmip.qld.gov.au/the-spit), as shown in Figure 12.21.

Most previous studies were limited to 2D conditions, in which only the trunk section of breakwaters under perpendicular incident waves can be studied. However, in the natural environment, there are situations that involve much more complicated flow-structure-seabed interactions. For example, the Southport Spit at Gold Coast

Figure 12.21 The Southport Spit, Gold Coast, QLD, Australia (Figure retrieved from https://haveyoursay.dsdmip.qld.gov.au/the-spit).

(Figure 12.21). Two paralleled breakwaters are constructed at the Southport, Nerang River mouth to provide a stable navigation channel for the ships entering and leaving the Pacific Ocean. In this condition, the incident waves are oblique with the breakwaters, causing the reflected waves in front of breakwaters and diffracted waves behind the breakwaters. Meanwhile, the river currents coming out of the river mouth meet all components of the waves, which cause the complicated interactions in the vicinity of breakwater heads. Therefore, to understand these 3D effects in the evaluation of the seabed foundation stability, a 3D model is required. Only a few studies of wave-seabed-breakwater interaction employed 3D models (Jeng, 1996; Li and Jeng, 2008; Liao et al., 2018; Ye et al., 2017; Li and Jeng, 2023). However, most researches only considered the wave-induced oscillatory pore pressure and momentary liquefaction (Jeng, 1996; Li and Jeng, 2008; Liao et al., 2018). In Ye et al. (2017)'s model, the structure is a single caisson breakwater and the effect of current has not been considered.

In this section, the 3D engineering condition as shown in Figure 12.21 will be examined. Two soil constitutive models are adopted to simulate the transient soil responses in a poro-elastic seabed foundation and the residual soil responses in a poro-elastoplastic seabed foundation, respectively. More detailed information can be found in Cui and Jeng (2021).

12.6.1 NUMERICAL MODEL SET-UP

Figure 12.22(a)&(b) illustrates the computational domain and the cross-section of the breakwater for examples presented in this section. As shown in Figure 12.22(a), two breakwaters with different lengths are built over the seabed foundation at an angle of 45 degree to the negative $x-$ axis. A rigid pavement with 4 m width and 1 m height is placed on top of the breakwater. The form of such breakwaters are

very similar to form of groins, which are usually deployed perpendicularly to the coastline. The seabed foundation is considered as the porous medium, whose length (L_x), width (L_y) and thickness (L_z) are 130 m, 90 m and 15 m, respectively. Two parallel breakwaters 60 m (L_{bre1}) and 40 m (L_{bre2}) long, respectively, have been reproduced in the numerical tests.

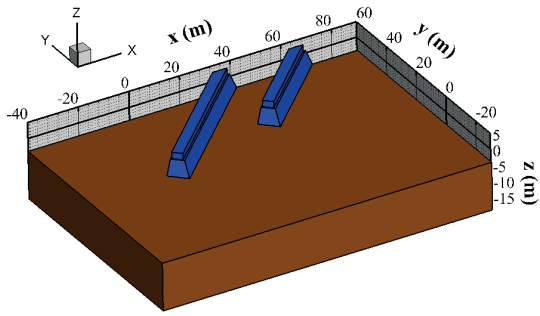

(a) The 3D view

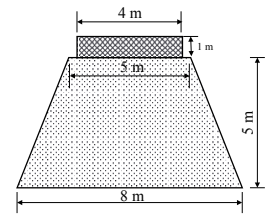

(b) Breakwater cross-section

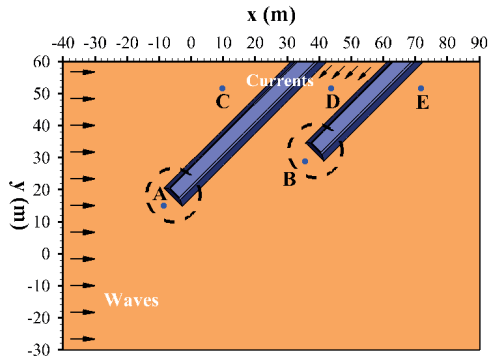

(c) The top-view of computational domain

Figure 12.22 The configuration of the problem.

It can be seen from the top-view of computational domain in Figure 12.22(c) that the ocean waves propagate along the positive direction of the *x*- axis while the river currents flow from the inland into the ocean via two breakwaters and meet the propagating waves. Five typical locations, including two points that are near to the breakwater heads (location A and B) and three points that locate in front of, between and behind the middle part of the breakwaters (location C, D and E) respectively, are selected as the references points to monitor the flow properties and seabed foundation responses, such as water profiles and dynamic pore pressure, etc. In addition, in order to specifically study the dynamic seabed foundation responses around two breakwater heads under the 3D wave/current loading, two circles with a radius of 10 m that centred in two breakwater heads respectively are selected as the study areas, as indicated by the dashed lines.

The following boundary conditions are applied in the numerical simulation:

(1) At the seabed surfaces, the pore pressure is equivalent to the wave induced pressure obtained from flow model. The effective normal stresses and shear stresses are negligible at the seabed surface.

$$p_s = p_b, \quad \boldsymbol{\sigma}' = \boldsymbol{\tau} = 0. \tag{12.2a}$$

(2) For the bottom of the porous seabed foundation, a rigid and impermeable boundary is adopted. Zero displacements occur at the bottom of seabed foundation ($z = -L_z$):

$$u_s = v_s = w_s = 0 \quad \text{and} \quad \frac{\partial p_s}{\partial z} = 0. \tag{12.2b}$$

(3) For the four lateral boundaries of the computational domain, the degrees of freedom in $x-$ direction are restricted for the x =-40 m and x =90 m planes, and for the planes at y =-30 m and y =60 m, the degrees of freedom in $y-$ direction are restricted, therefore, the displacements are fixed in the corresponding directions:

$$u_s = 0 \quad \text{at } x \text{ =-40 m and } x \text{ =90 m}, \tag{12.2c}$$

$$v_s = 0 \quad \text{at } y \text{ =-30 m and } y \text{ =60 m}. \tag{12.2d}$$

The input parameters of the numerical simulations are listed in Table 12.3. In this study, two soil constitutive models, poro-elastic model and poro-elastoplastic model (Pastor-Zienkiewicz mark III model), are adopted to analyse the 3D behaviour of seabed foundation around breakwaters under combined wave and current loading. Parameters for both constitutive models are given in the table. For the PZIII model, two sets of parameters are presented, representing the dense soil and loose soil, respectively. These two sets of parameters were obtained from Zienkiewicz et al. (1999) for Nevada sand. In addition, it is noted that a relatively large value (i.e., 0.5) of breakwater porosity is adopted in this study. In the existing literature, various practical values of porosity in porous coastal structures have been proposed. For example, Karim et al. (2009) suggested that the porosity for porous structure varies from 0.3 to 0.6 at most in general. Choosing a large porosity within the reasonable range has following advantages: more decrease of wave transmission due to more energy dissipation caused by friction inside the porous structure; lower wave force on the structure due to the increase of wave energy dissipation; less expensive for construction due to decrease of material costs. At last, in this section, unless otherwise stated, the default values that are in bold in Table 12.3 are used for the results discussion in this section.

Table 12.3
Input parameters used in the numerical study.

Wave characteristics		
Wave period (T)		**6.0 s**, 5.0 s or 4.0 s
Wave height (H)		**2.0 m**, 1.0 m or 2.5 m
Still water level (d)		**4.0 m**, 3.0 m or 5.0 m
River currents velocity (U_0)		**1.0 m/s**, 0.8 m/s, 0.6 m/s or 0.0 m/s
Breakwater characteristics		
	Caisson	**Rubble mound**
Young's modulus (E)	1.0×10^{10} Pa	1.0×10^{8} Pa
Poisson's ratio (μ_s)	0.25	0.33
Permeability (k_s)	-	8.9×10^{-2} m/s
Porosity (n_s)	-	0.5
Seabed foundation properties		
Permeability (k_s)		**10^{-5} m/s**, 10^{-7} m/s or 10^{-3} m/s
Porosity (n_s)		0.3
Degree of saturation (S_r)		**98 %**, 95% or 93%
Relative density (D_r)		**40 %** or 60%
Elastic parameters		
Young's modulus (E)		2.0×10^{7} Pa
Poisson's ratio (μ_s)		0.333
Parameters for PZIII Model		
	dense sand	**loose sand**
M_g	1.32	**1.15**
M_f	1.3	**1.035**
α_f	0.45	**0.45**
α_g	0.45	**0.45**
K_{evo}	2000.0 kPa	**770.0 kPa**
G_{eso}	2600.0 kPa	**1155.0 kPa**
β_0	4.2	**4.2**
β_1	0.2	**0.2**
p'_0	4.0 kPa	**4.0 kPa**
H_0	750.0	**600.0**
H_{U0}	40000.0 kPa	**40000.0 kPa**
γ_u	2.0	**2.0**
γ_{DM}	4.0	**0.0**

12.6.2 HYDRODYNAMIC PROCESS AROUND BREAKWATERS

An accurate simulation of the wave/current-breakwater interactions is the prerequisite for correctly assessing the seabed foundation stability around the structure. Therefore, the hydrodynamic characteristics of the flow field will be firstly examined.

A. Wave profile

Figure 12.23 shows the development of free surface elevation around the breakwaters in one wave period (from t =300 s to t =306 s) under the wave condition of T =6 s, H =2 m, d =4 m, and U_0= 1 m/s. Four typical slices along the y- axis are selected (y =50 m, 25 m, 0 m and -30 m) to illustrate the 3D wave-current-breakwaters interactions. It can be seen from the figures that four main zones are formed as the propagating waves approaching obliquely on the breakwaters:

(1) in front of the first breakwater with the standing waves;
(2) the zone between two breakwaters with the diffracted waves and river currents;
(3) the zone near to the breakwater heads with the progressive waves and the river currents; and
(4) the zone behinds the second breakwater.

As shown in Figure 12.23, incident waves are reflected by the first breakwater and interact with the subsequent incident waves, which forms the standing wave with a larger wave height in the first zone. For the second and third zones, the incident waves, reflected waves, diffracted waves and the river currents exist simultaneously. Due to the effect of the breakwaters, the water surface in the fourth zone is more stable. It is also worth noting that, comparing the slice No.3 and No.4, a slight difference in the wave shape could be observed between two breakwaters where the river current comes out. It indicates that the currents from the river might have an impact on the wave transformation.

To have a more intuitive and quantified illustration, the time series of water profiles at five locations (A, B, C, D and E, referring to Figure 12.22(c)) are plotted in Figure 12.24. The case without river currents between the breakwaters is also presented. It can be seen from the figures that for the locations near to the breakwater heads, the water profile oscillation near the first breakwater (location A) is larger than that near the second breakwater (location B), the amplitude ratio is more than twice, especially for the case without currents, the water profile oscillation at B is even smaller. Furthermore, the non-linearity of the wave shape at these two locations can be observed, which, on the one hand, could be caused by the interactions among the incident, reflected, diffracted waves, currents and breakwater heads. On the other hand, the shallow water depth (i.e., 4 m) considered in this study could also be one of the reasons for causing the non-linearity of wave profiles. For the locations in front of, between and behind the breakwaters (location C, D and E), the largest water profile oscillation occurs at location in front of the first breakwater (location C),

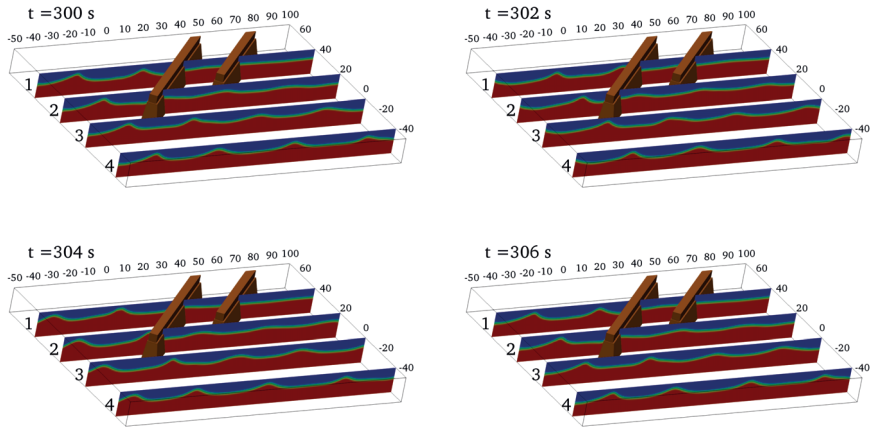

Figure 12.23 The free surface around the breakwaters at t =300 s, 302 s, 304 s and 306 s under the wave condition of T =6 s, H =2 m, d =4 m, and U_0= 1 m/s.

where the momentary liquefaction is more likely to occur due to the large oscillatory amplitude. In addition, comparing Figure 12.24, it can be found that the presence of the river currents makes the water profile oscillation increase at all locations. At the same time, it increases the non-linearity of the wave shape, making the wave crest sharper. Generally, the presence of the river currents will make the flow field more complicated and severe and therefore has a potential to further affect the breakwater foundation stability.

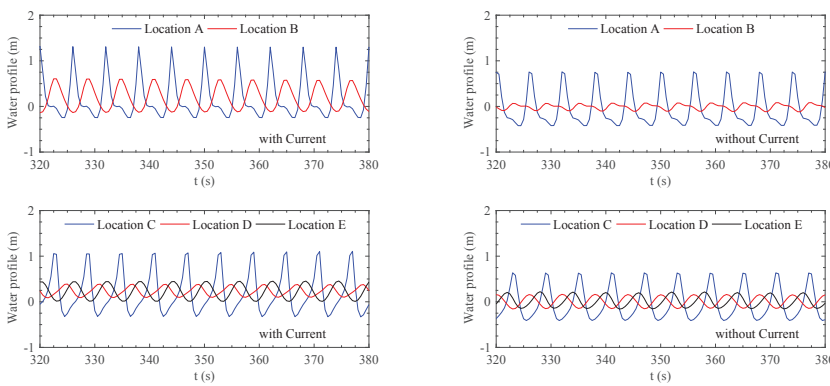

(a) waves with river currents (b) wave loading only

Figure 12.24 Time series of water profiles at location A, B, C, D and E in the case: (a) with river currents when T =6 s, H =2 m, d =4 m, and U_0= 1 m/s and (b) without river currents when T =6 s, H =2 m, d =4 m, and U_0= 0 m/s.

B. Velocity field

Figure 12.25 illustrates the velocity field in the x- and y-directions around breakwaters at the free water surface. A total of 400 s simulation time was performed

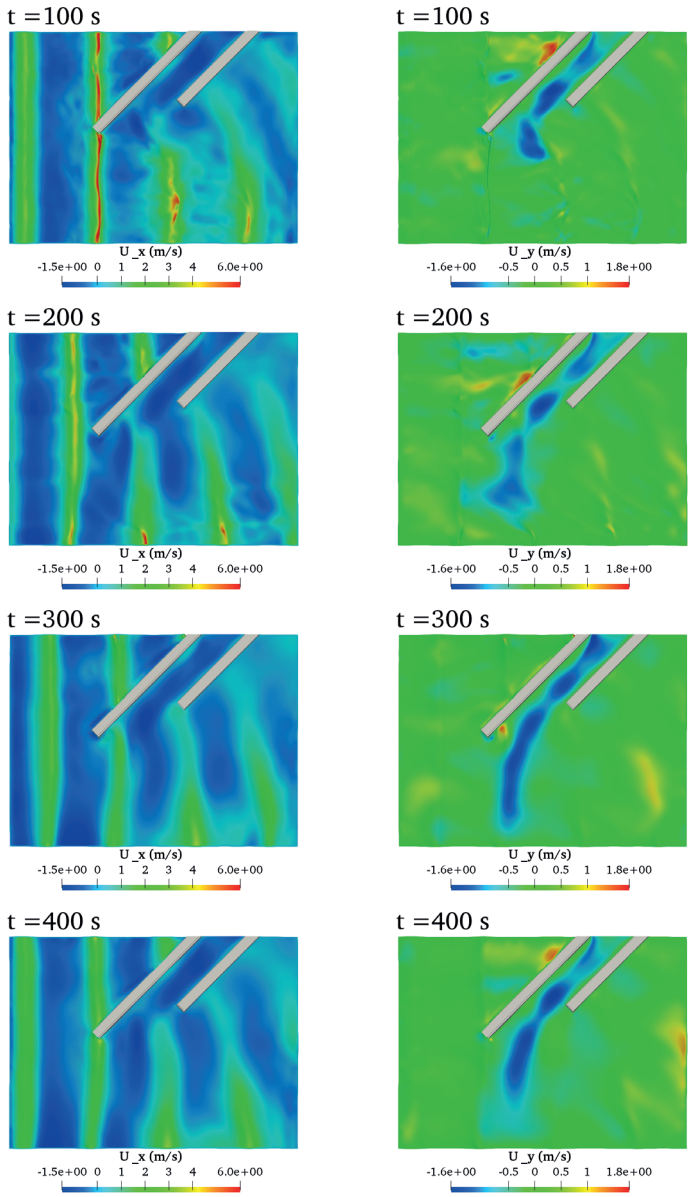

(a) The $x-$ direction (b) The $y-$ direction

Figure 12.25 The velocity field around breakwaters at t =100 s, 200 s, 300 s and 400 s when T =6 s, H =2 m, d =4 m, and U_0= 1 m/s.

in order to achieve a relative stable condition within the flow domain, in which four typical moments (t =100 s, 200 s, 300 s and 400 s) are selected to demonstrate the historic changes of the velocity field. In this study, the backside of the computational domain between two breakwaters was set as the inlet of the river current. A constant current velocity was given at this inlet, which was simply assumed not change along the water depth as the friction from the seabed surface was ignored. Figure 12.25(a) shows that the breakwater can significantly reduce U_x between and behind the breakwaters, in which human activities may be threatened. The diffracted wave components can be observed at the region behind the first breakwater head and near the second breakwater head.

It can be observed from Figure 12.25(b) that river currents are coming out via two breakwaters. During the waves-currents interactions, river currents tend to deflect along the direction of wave propagation meanwhile have an influence on wave transformation. As mentioned previously, the river currents are treated as the steady uniform currents, the velocity of currents is considered as one of the variables affecting the seabed foundation stability. It is noted that some positive U_y values have been observed in front of the flank of first breakwater and behind the first breakwater head. This is because when waves encounter the front flank of the first breakwater, a part of waves will travel upward along the breakwater, while the one at the head of the first breakwater is caused by the wave diffraction.

C. Hydrodynamic pressures

Due to the pressure continuity between two sub-models, the interaction effects of the wave-current-breakwaters is basically reflected in the form of hydrodynamic pressure that transmitted from flow sub-model to the seabed sub-model. Figure 12.26 illustrates the hydrodynamic pressure in a wave cycle from t =300 s to t =306 s. It can be seen that the distribution pattern is related to the water surface elevation. The pattern moves along with waves propagation and is distributed by the alternatively positive and negative variations. The maximum hydrodynamic pressure appears in front of the first breakwater and near to the first breakwater head, the minimum occurs behind and between the breakwaters, which is the results of protection effects of the breakwaters. Therefore, the first breakwater faces a greater hazard of instability compared with the second breakwater. Meanwhile, it is found that the hydrodynamic pressure distribution is not uniform due to the presence of reflected waves and diffracted waves. In particular, the hydrodynamic pressure zones formed behind the breakwaters present the more dispersed distribution feature.

12.6.3 DYNAMIC SOIL RESPONSES IN THE SEABED FOUNDATION

The seabed foundation around the breakwaters undergoes a long-term consolidation process under the hydro-static pressure and the self-weight. The consolidation is actually a process of dissipating the excess pore pressure within the seabed foundation, shrinking the soil skeleton and increasing the soil bearing capacity.

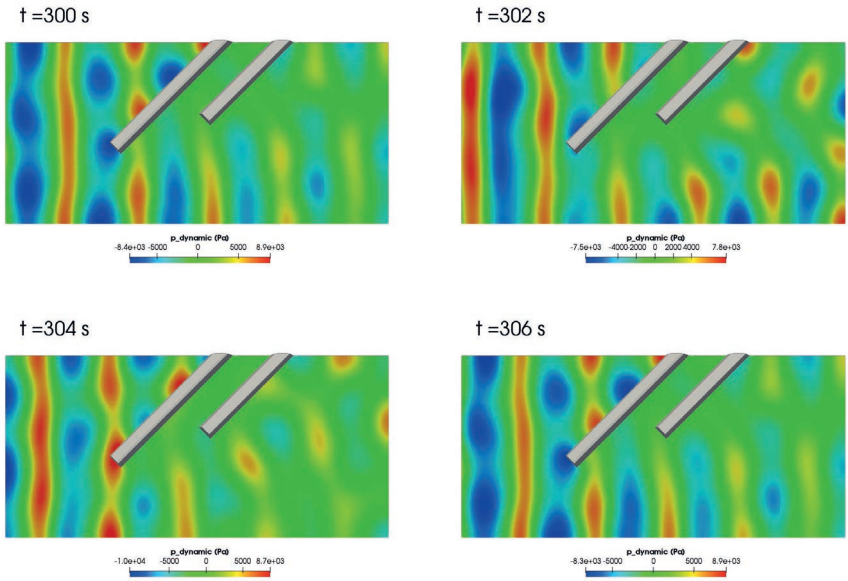

Figure 12.26 The hydrodynamic pressures acting on the seabed surface around breakwaters at t =300 s, 302 s, 304 s and 306 s when T =6 s, H =2 m, d =4 m, and U_0= 1 m/s.

Figure 12.27 illustrates the distribution of pore pressures (p_s), effective normal stresses (σ'_x, σ'_y and σ'_z) and shear stresses (τ_{xy}, τ_{yz} and τ_{zx}) on a plane (y =30 m) after the completion of consolidation process. It can be seen from the first figure that the pore pressure layered uniformly from top to the bottom, which indicates that there is no excess pore pressure remained and the consolidation process has completed. The stress state in the region below or near the breakwaters has been significantly affected. Due to the compression effect of the breakwater, the effective stresses all obviously increase under each breakwater and appear as the layered structure, especially the effective normal stress, the magnitude can reach up to 800 kPa. For the shear stresses, τ_{xy} and τ_{zx} concentrate at two side of each breakwater while τ_{yz} appears as a whole region at the bottom of the seabed just below two breakwaters. Comparing the three shear stresses, τ_{zx} is the dominant stress whose magnitude can reach up to 250 kPa, while the magnitude of τ_{xy} is very small which is less than 700 Pa.

Once the pre-consolidation process has been completed, the new stress state will be used as the initial condition for the dynamic analysis of seabed response under the wave/current loading. When the waves propagate over the seabed surface, a complex change of pore pressures, effective normal stresses and displacements within the seabed foundation is caused by the cyclic wave loading, especially for the areas with strong 3D interactions. The extreme situation is the soil liquefaction, which usually directly leads to the instability failure of the upper structures. Therefore, a clear

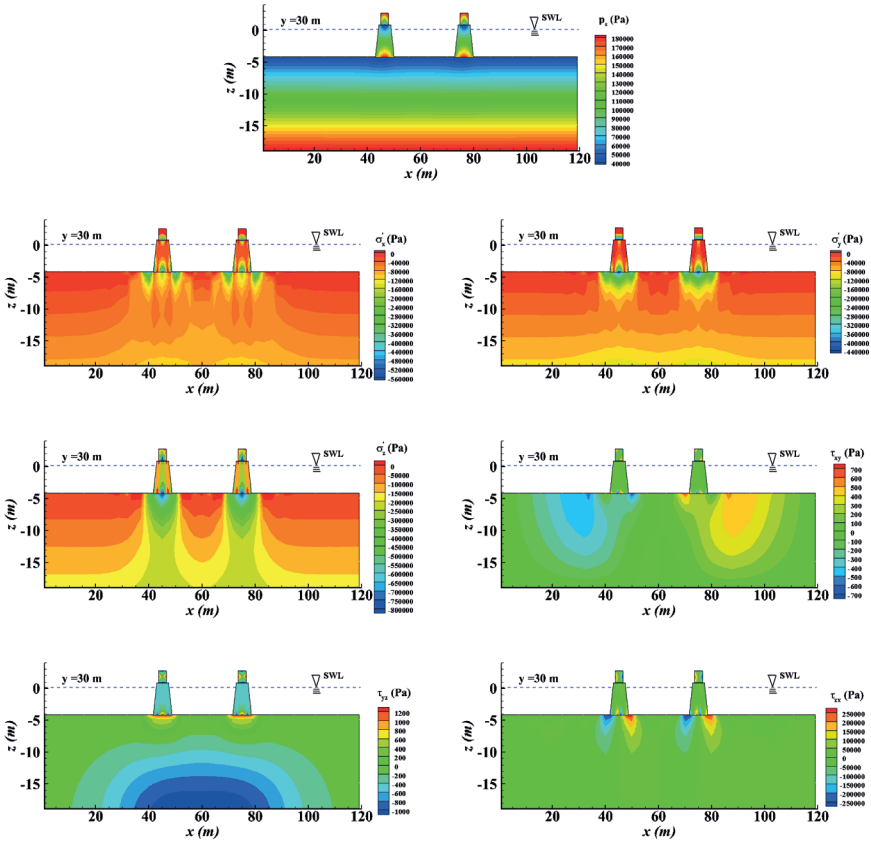

Figure 12.27 Distribution of pore pressure (p_s), effective stresses (σ_x', σ_y' and σ_z') and shear stresses (τ_{xy}, τ_{yz} and τ_{zx}) on plane y =30 m after consolidation process.

understanding of seabed response mechanism is the precondition for assessing the foundation stability. In this section, the dynamic soil response under combined wave and current loading will be investigated. The results predicted using the different constitutive models under the same condition will be compared to further understand the different mechanisms of dynamic soil response.

A. Time series of dynamic soil responses

Figure 12.28 demonstrates the time series of dynamic soil response, including pore pressures (p_s), effective normal stresses (σ_x', σ_y' and σ_z') and shear stresses (τ_{xy}, τ_{yz} and τ_{zx}), at the breakwater head (locations). Both residual soil response (red line) and oscillatory soil response (blue line) are presented in the figures. The difference between the residual soil response predicted by the poro-elastoplastic model and the

oscillatory soil response predicted by poro-elastic model is obvious. The residual soil response consists of two parts: periodic oscillatory part and residual part. While the oscillatory soil response only has the oscillatory component. For different kind of soils, with different expected results, it is very important to use a more appropriate constitutive model for the simulation.

In Figure 12.28, the residual pore pressure (red line) at location near to the breakwater head (location A) continues to increase until it remains at a stable value after around t =260 s. The accumulative amount of pore pressure reaches 25 kPa. While the oscillatory pore pressure (blue line) only oscillates around the initial value. For the residual effective stresses, they reduce from the initial compressive state and approach zero. According to the definition of soil liquefaction, location A has been liquefied at t =260 s after the effective stress become zero. σ_z' has the largest initial value which is at around 23 kPa compared to σ_x' and σ_y' at around 11 kPa. Since the wave is propagating along the $x-$ direction, the oscillatory component of σ_y' is quite small. For the shear stress, the dominant factor is τ_{zx}, while τ_{xy} and τ_{yz} have relative small amplitude and basically oscillate near zero. The residual τ_{zx} has increased at the beginning then decreased to zero as approaching to the soil liquefaction. This kind of trend also reflects the mechanism of residual soil response: at the initial stage, the shear force gradually increased due to the cyclic wave/current loading, making the soil skeleton compressed. However, when the soil is liquefied, the soil loses its strength and appears as a liquid state, hence the shear stress disappears. Meanwhile, the oscillatory τ_{zx} predicted by the poro-elastic model has no such trend, only oscillating around zero which represents the feature of an elastic seabed foundation.

For the location D (between the two breakwaters, see Figure 12.22(c)), due to the protection effect from breakwaters, it is far from the liquefaction status (graph not shown). The non-linearity of the soil response at this point is also more obvious. With the pore pressure build-up, the seabed foundation at this point is becoming more and more unstable undoubtedly. However, it has not been liquefied since the effective stress still remains a relative large value, for example, σ_z' remains over 14 kPa after t =400 s. Also, τ_{zx} keeps accumulating without an attenuation appears. In summary, the numerical analysis (1) explained the historic curves of dynamic soil response at different locations around breakwaters; (2) compared the differences between two mechanism obtained from two constitutive models; (3) revealed the relations between different dynamic responses with seabed foundations; (4) concluded that location A has been first liquefied. More detailed analysis for the variations of pore pressures at different locations can be found in Cui and Jeng (2021).

Figure 12.29 shows the wave/current induced soil displacements (u_s, v_s and w_s) at locations A and C within the poro-elastoplastic seabed and poro-elastic seabed. The poro-elastoplastic seabed presents sway in the corresponding direction at both locations as the cyclic loading acting on the seabed surface. The displacement in the z-direction is obviously the dominant one, whose magnitude is about 40 mm at location A and 25 mm at location C. It is observed that there is a clear accumulation of positive u_s and negative w_s in the poro-elastoplastic seabed, which can both reach up to 40 mm. This indicates that the first breakwater has settled downwards and tilted

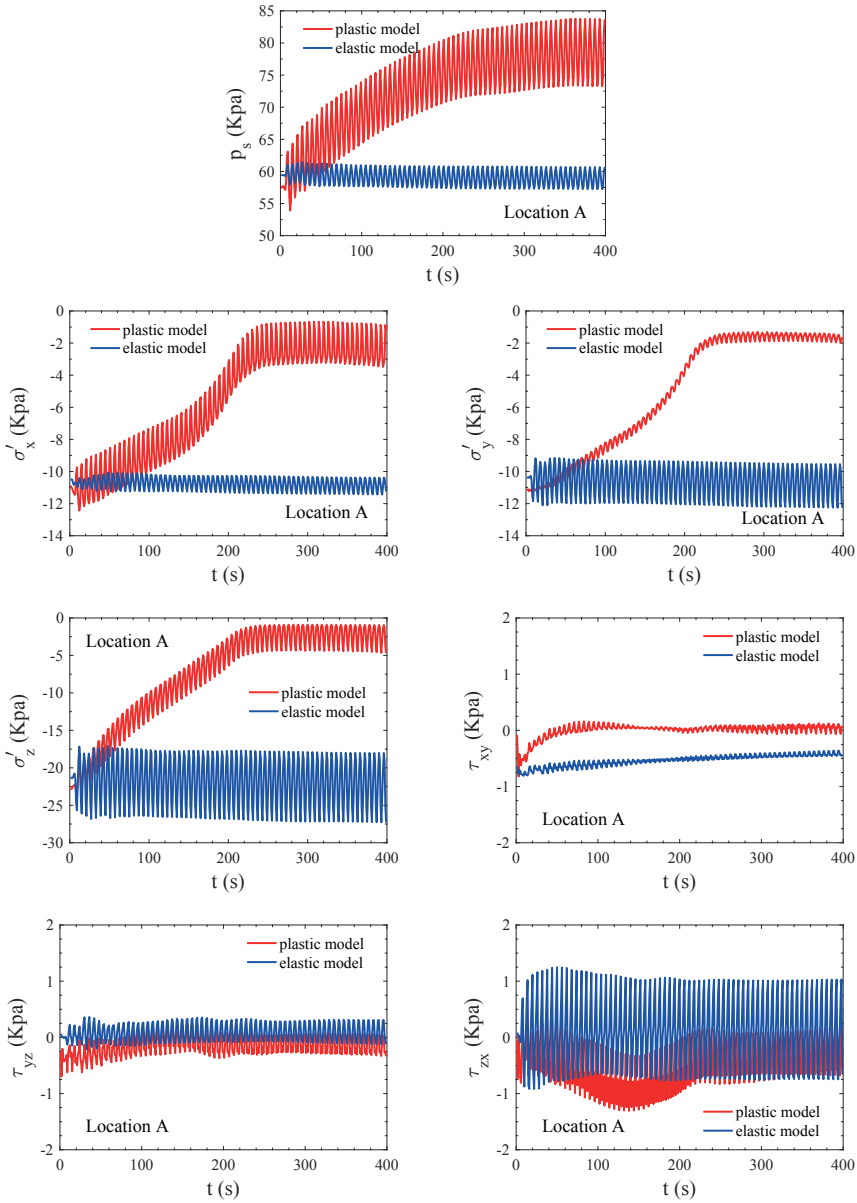

Figure 12.28 Time series of the dynamic soil responses, including pore pressure (p_s), effective stresses (σ_x', σ_y' and σ_z') and shear stresses (τ_{xy}, τ_{yz} and τ_{zx}) at location A (x =-10 m, y =15 m, z =-6 m) near to first breakwater head when T =6 s, H =2 m, d =4 m, U_0= 1 m/s, k_s =$10^{-5}m/s$, S_r =98%, D_r =40%.

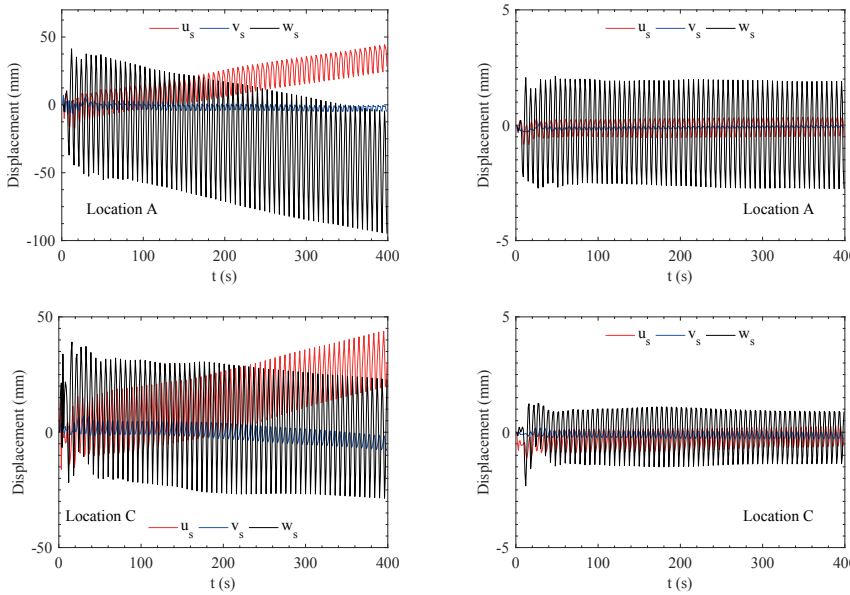

(a) poro-elastoplastic seabed foundation (b) poro-elastic seabed foundation

Figure 12.29 Time series of displacements in $x-$ direction (u_s), $y-$ direction (v_s) and $z-$ direction (w_s) at location A (x =-10 m, y =15 m, z =-6 m) and C (x =10 m, y =52 m, z =-6 m) when T =6 s, H =2 m, d =4 m, U_0= 1 m/s, k_s =$10^{-5}m/s$, S_r =98%, D_r =40%.

rightwards permanently under the wave/current loading, which has huge impacts on its stability. For the y-direction displacement (v_s), the amplitude is small and there is almost no accumulated value. Comparing with the results in the poro-elastoplastic seabed, the displacement response mechanism in the poro-elastic seabed foundation is totally different. First of all, there is no accumulative displacements in the elastic seabed, each point only vibrate at its original position. It shows that the elastic seabed foundation does not undergo any permanent deformation. Secondly, the displacement response in the poro-elastic seabed foundation is much weaker than that in the poro-elastoplastic seabed foundation, the amplitude ratio of displacement in elastic and plastic seabed foundation is only 10%.

B. Spatial distribution of dynamic soil responses

Figure 12.30 illustrates the spatial distribution of the oscillatory pore pressures and stress field within an elastic seabed foundation around the breakwaters at t = 300 s. It can be seen that the propagating wave trough reaches to the front of the first breakwater at t = 300 s, which causes a large negative pore pressure in this region. The corresponding upward-directed seepage force in this area causes the pore fluid to move upwards, thereby weakening the contact force between the soil skeleton. When the seepage force is greater than the initial effective stress, the

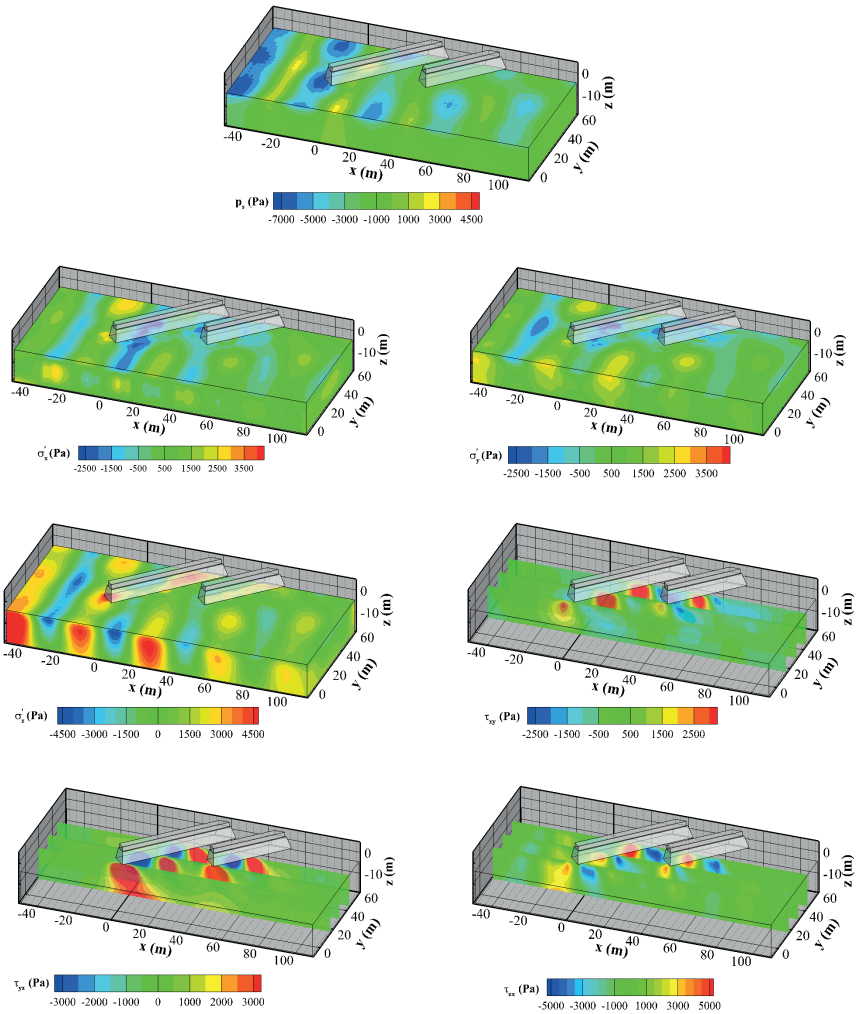

Figure 12.30 Spatial distribution of oscillatory pore pressure (p_s) and stress field (effective stresses: σ'_x; σ'_y; σ'_z and shear stresses: τ_{xy}; τ_{yz}; τ_{zx}) within an elastic seabed foundation around the breakwaters at t =300 s when T =6 s, H =2 m, d =4 m, U_0= 1 m/s, k_s =$10^{-5}m/s$, S_r =98%.

momentary liquefaction happens. If the momentary liquefaction zone is just below the breakwater, it poses a threat to the stability of the breakwater. From another point of view, the same conclusion can be drawn based on the spatial distribution of the dynamic effective stress. In the soil under the wave trough, the effective stresses show large positive values (the negative value is assumed as compression in this study). When the positive dynamic effective stress is greater than the initial effective stress, the momentary liquefaction occurs. For the areas under the wave crest, as the pore

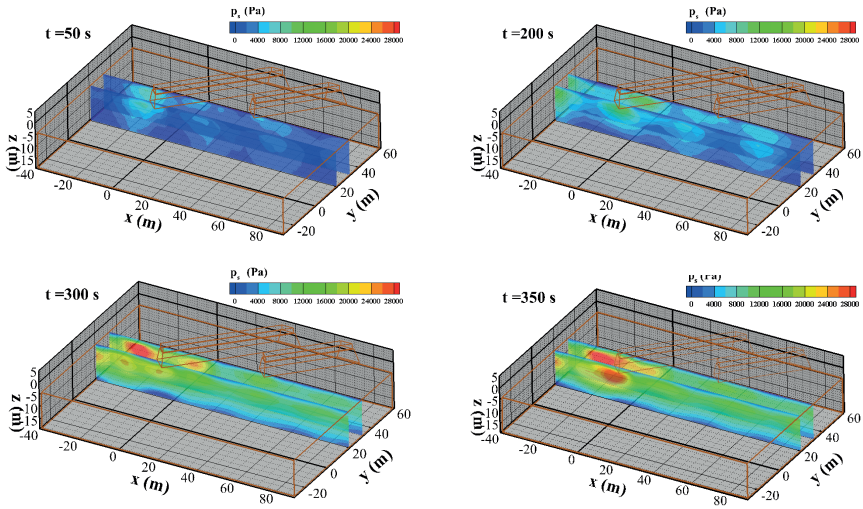

Figure 12.31 Accumulation of the residual pore pressure within a poro-elastoplastic seabed foundation at t =50 s, 200 s, 300 s and 350 s when T =6 s, H =2 m, d =4 m, U_0= 1 m/s, k_s =$10^{-5}m/s$, S_r =98%, D_r =40% of the loose sand.

pressure is positive, the seepage force is downward-directed, the dynamic effective stress is in compression, the momentary soil liquefaction is unlikely to happen.

The wave induced shear stresses (τ_{xy}, τ_{yz} and τ_{zx}) appear on two sides of each breakwater. Comparing all shear stresses, τ_{zx} is the dominant one, whose magnitude reaches up to 5 kPa. The wave induced cyclic shear stress could also be one of the failure factor for the stability of breakwaters. Another phenomenon that is easy to be observed is that the amplitude of dynamic response in the areas in font of and near to the breakwaters is greater than that behind the breakwaters. This is due to the reflection and diffraction effects of the breakwater on the wave transformation. It proves that the breakwaters can effectively block the wave and protect the seabed foundation behind the breakwaters.

Different from the oscillatory soil response, the residual soil response within the poro-elastoplastic seabed is usually manifested as the build-up of pore-water pressures. The process of pore pressure build-up involves the permanent deformation of the seabed foundation, which cannot be solved properly by poro-elastic model. Figure 12.31 shows the accumulation of the residual pore pressure within a poro-elastoplastic seabed foundation under the long-term cyclic wave/current loading from t =50 s to t =350 s. It is clearly seen from the figures that the wave/current induced pore pressures (p_s) at location in front of the first breakwater (the upper slice) and near to the first breakwater head (the lower slice) is increasing and accumulating significantly, from less than 8 kPa at t =50 s to over 28 kPa at t =350 s. It can also be found that the accumulation of the pore pressure in front of the breakwater is more rapid, intense and obvious than that near to the breakwater head,

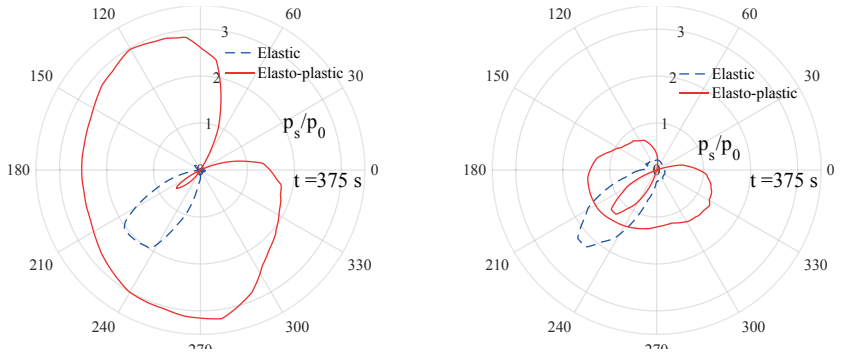

Figure 12.32 Distribution of the dynamic pore pressure on a circular area around two breakwater heads at t =375 s when T =6 s, H =2 m, d =4 m, U_0= 1 m/s, k_s =$10^{-5}m/s$, S_r =98%, D_r =40%.

which indicates that the area in front of the breakwater is more likely to be liquefied. Since these potential liquefaction zones are close to the breakwater foundation, they may pose greater threats to the breakwater stability.

The pore pressure distribution around two breakwater heads should be the most complex, meanwhile because of the persistence of the cyclic shear stress, the possibility of instability of the breakwater heads is high. Figure 12.32 demonstrates the distribution of the pore pressure on a circular area around two breakwater heads at t =375 s. These circles, as shown in Figure 12.22(c), reach out from the centre of the breakwater heads ((-5.67, 17.67, -6) and (38.47, 31.81, -6)) with a radius of 10 m, whose vertical depth is 2 m from the seabed surface (z =-6 m). Likewise, both residual and oscillatory pore pressure are presented in the figure, indicated by the red solid line and blue dashed line, respectively. It can be observed from the figures that two mechanisms of the dynamic pore pressure response are different. For the oscillatory pore pressure (the blue dashed lines), at t =375 s, the largest value appears at point right in front of two breakwater heads at around 225 degree, which is around twice p_0. Then, the oscillatory pore pressure gradually decreased to almost zero starting from this point to the point located just beneath the breakwater heads.

The residual pore pressure in the poro-elastoplastic seabed around the first breakwater is about three times of p_0, which is significantly larger than the value around the second breakwater head whose value is just over p_0. This is due to the protection effect from the first breakwater since the second breakwater head is located behind the first breakwater. The larger residual pore pressure mainly distributes on two sides of the each breakwater head with rapid reduce to the point beneath breakwater heads. There is even a negative value in the range of 20 to 75 degree, which indicates that the dissipation rate is greater than the accumulation rate in this range, so it is unlikely that the soil liquefaction occurs here. It can be concluded from this figure that the liquefaction is more likely to occur at two sides of the breakwater head in the poro-elastoplastic seabed, which may cause the tilt of the breakwater heads.

12.6.4 SOIL LIQUEFACTION IN THE SEABED FOUNDATION

The previous section mainly focuses on the dynamic responses and their spatial/temporal distribution characteristics within the seabed foundation around the breakwaters, including the pore pressures, effective normal stresses, shear stresses and displacements. Based on these results, the instability of the seabed foundation will be further understood by studying the liquefaction conditions around the breakwaters.

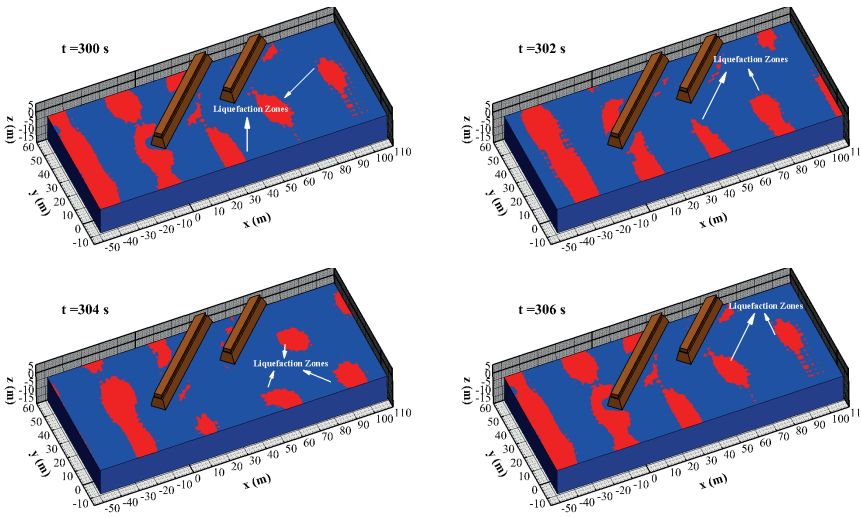

Figure 12.33 The predicted momentary liquefaction zones around the breakwaters in a typical wave period from t =300 s to t =306 s, based on Tsai (1995)'s liquefaction criterion when T =6 s, H =2 m, d =4 m, U_0= 1 m/s, k_s =$10^{-5} m/s$, S_r =98%.

A. Momentary liquefaction

Figure 12.33 shows the momentary liquefaction zones within an elastic seabed foundation around the breakwaters in a wave cycle from t =300 s to t =306 s, which is the same wave period chosen to demonstrate the hydrodynamic pressure shown in Figure 12.26. It can be seen in the figures that the momentary liquefaction mainly occurs on the seabed surface where the pore pressure gradient is large. The liquefaction depth in an elastic seabed foundation is quite small, which is less than 0.5 m. Comparing with the distribution of hydrodynamic pressure shown in Figure 12.26, it is found that the momentary liquefaction zones can only occur in the region where the hydrodynamic pressure is negative (i.e., under the wave troughs), where the upward seepage force is generated in these regions. For the areas where the hydrodynamic pressure is positive (i.e., under the wave crests), the vertical seepage force is downward, the soil in these areas will not liquefy.

Due to the interactions of the wave/current and breakwaters, the liquefaction zones behind the breakwaters are significantly reduced, however, there are still a few scattered pieces caused by the diffracted waves. The liquefaction zones are moving as the movement of the wave trough. When the liquefaction zones move to the region near to the breakwater foundation, the stability of the breakwater will be greatly affected. For example, at t =300 s, a large liquefied area appears around the first breakwater head, which is likely to cause the breakwater head instability or even collapse.

B. Residual liquefaction

The development mechanism of residual liquefaction zones in the plastic seabed foundation is quite different from the momentary liquefaction in the elastic seabed foundation. As mentioned previously, the residual liquefaction within a poro-elastoplastic seabed foundation does not occur instantaneously. As the excess pore-water pressure increases, the stability of the seabed foundation gradually decreases until the excess pore-water pressure reaches the mean initial effective stress value when the residual liquefaction happens. In order to describe such a process of gradual reduction in seabed stability, a variable named liquefaction potential ($L_{potential}$) has been introduced to assess the possibility of occurrence of residual liquefaction can be expressed as Cui and Jeng (2021),

$$L_{potential} = \frac{p_{excess}}{\frac{1}{3}(|\sigma'_{x0}| + |\sigma'_{y0}| + |\sigma'_{z0}|)}, \tag{12.3}$$

in which p_{excess} is the dynamic residual pore pressure caused by the cyclic wave/current loading; σ'_{x0}, σ'_{y0} and σ'_{z0} are the initial effective stresses in x-, y- and z-directions, respectively, which is determined after the consolidation process. When $L_{potential}$ is equal or greater than 1, the residual soil liquefaction occurs.

Figure 12.34 illustrates the time series of residual liquefaction potential at locations (A, B, C, D and E) around the breakwaters. It can be found that the residual liquefaction potential $L_{potential}$ gradually increases with different increasing rate and the accumulated value at different locations, indicating that the stability at these locations are different. Location A, B and C have a faster increasing rate and larger accumulated value of liquefaction potential. All these locations have been liquefied as time goes on. Especially for location A and C, as indicated in blue line and green line, $L_{potential}$ reaches 1 at around t =100 s and t = 160 s, respectively, indicating that residual liquefaction has occurred. However, due to the protection of the breakwaters, $L_{potential}$ at the point located between two breakwaters (D) and behind the breakwaters (E) only reaches around 0.8 and 0.65, respectively. It is far away from 1 which demonstrates that there is no liquefaction occurs at point D and E, whereas it still can be seen from the development trend that the stability of the seabed foundation at these two locations is decreasing, especially at point D.

Figure 12.35 shows the vertical distribution of $L_{potential}$ within a poro-elastoplastic seabed and a poro-elastic seabed at t =350 s. In the poro-elastoplastic seabed foundation, the liquefaction potential is zero on the bottom of seabed. Along the

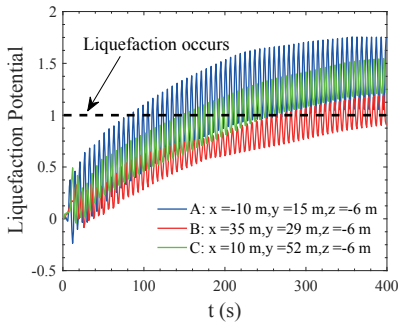

(a) Location A, B and C

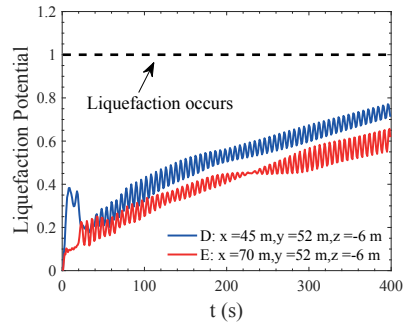

(b) Location D and E

Figure 12.34 Time series of residual liquefaction potential at location A, B, C, D and E within the poro-elastoplastic seabed foundation around the breakwaters when T =6 s, H =2 m, d =4 m, U_0= 1 m/s, k_s =$10^{-5}m/s$, S_r =98%, D_r =40%.

upward-direction of the seabed depth, the liquefaction potential gradually increases until $L_{potential}$ reaches a maximum value at the seabed surface. It is found that liquefaction occurs at locations A and C as $L_{potential}$ exceeds the critical value for the liquefaction ($L_{potential} = 1$) and the liquefaction depths for location A and C at t =350 s reach almost 30% and 10% of the seabed thickness, respectively. While locations B, D and E are not liquefied. In contrast, in the poro-elastic seabed foundation, the liquefaction potential at all locations within the bottom 70% of the seabed is zero, showing that no liquefaction happens there. The liquefaction potential only begin to change on the upper layer of seabed. Only $L_{potential}$ at point A has exceeded 1, indicating that point A is under the wave trough at this moment at t =350 s and the momentary liquefaction occurred here. For locations B, C and D, $L_{potential}$ is negative, which means that these locations are under the wave crest at t =350 s. The soil is under compression and liquefaction is impossible. Although location E has a positive $L_{potential}$ (i.e., under the wave trough), it does not liquefy (i.e., $L_{potential}$ less than 1) since it is located behind the breakwaters. From this figure, it can be seen again that the liquefaction development and distribution trends in the elastic seabed foundation and plastic seabed foundation are totally different. Under the same wave/current loading condition, the residual liquefaction phenomenon in the plastic seabed foundation usually is more serious.

12.7 SEABED RESPONSE IN THE VICINITY OF OFFSHORE DETACHED BREAKWATERS

Offshore detached breakwaters have been widely constructed as one of the coastal management facilities to protect shorelines from wave invasion. The segmented, emerged form of offshore detached breakwaters is usually utilised in practical engineering sites to provide a shelter for the coastline. During the service period

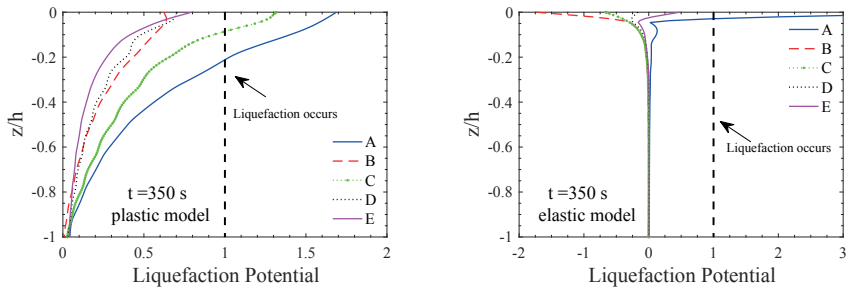

(a) poro-elastoplastic seabed (b) poro-elastic seabed

Figure 12.35 Vertical distribution of the wave/current induced liquefaction potential at location A, B, C, D and E within (a) poro-elastoplastic seabed foundation; and (b) poro-elastic seabed foundation at t =350 s when T =6 s, H =2 m, d =4 m, U_0= 1 m/s, k_s =$10^{-5}m/s$, S_r =98%, D_r =40%.

of these breakwaters, the interactions among waves, currents, seabeds and the breakwaters may lead to the increase of pore pressures that is responsible for the weakening of seabed stiffness, and subsequently even result in fatal failures of the foundation such as intolerable deformation and liquefaction (Oumeraci, 1994).

In this section, we further investigate the dynamic response and stability of offshore detached breakwater foundations composed of loose sand soil, whose mechanical properties are poor and vulnerable to the long-term ocean loading. The effects of a perpendicular longshore current on the flow regime and subsequent liquefaction potential of seabed foundation are considered.

12.7.1 CONFIGURATION OF THE BREAKWATERS AND INPUT PARAMETERS

Figure 12.36 shows the configuration of the computational domain for the present study. This includes: a seabed foundation is 95 m × 80 m × 12 m; three breakwaters that are paralleled to the shoreline sit on the middle of the seabed foundation with width equals to 5 m and height equals to 5.6 m. The length of the breakwaters on two sides is 10 m and 20 m for the middle breakwater. The gap between the breakwaters is 20 m. The stability of the porous seabed foundation in the vicinity of the offshore detached breakwaters is examined using a 3D numerical model, which consists of two sub-models and a one-way integrated module.

Figure 12.37 illustrates the computational domain. The waves are generated at the left boundary and propagate rightward to the breakwaters. Currents that travel at right angle to the incident waves (in negative y- axis direction) are to simulate the longshore currents, which commonly exist in the near shore zones. Three main zones can be identified in this study, which contain different wave/current components. Zone I is in front of the breakwaters including incident waves, reflected waves and longshore currents, zone II is between the breakwaters including only the incident

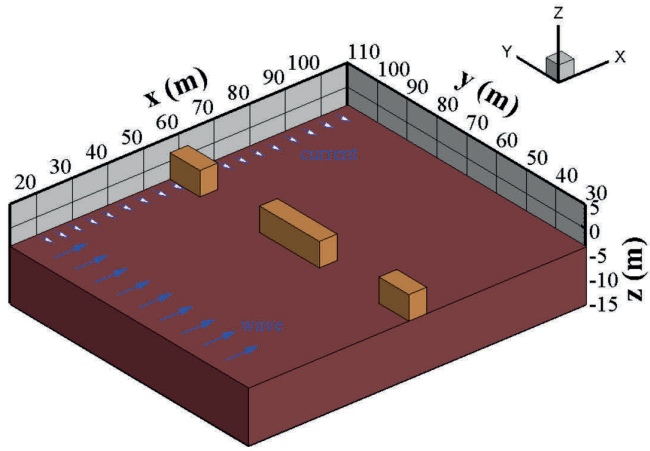

Figure 12.36 The computational domain of the present study for offshore detached breakwaters.

and diffracted waves, while zone III is behind the breakwaters including part of the incident waves, diffracted waves and currents. Due to the different wave/current impacts, the soil behaviours should be different from zone to zone. Hence, four reference points (A, B, C and D) are selected in corresponding zones to monitor the hydrodynamic process caused by wave/current-structure interactions and soil behaviour within the seabed foundation.

The computational procedure of the numerical model is illustrated in Figure 12.1, including three parts: pre-processing, numerical simulation and post-processing. The integrated process between the flow and seabed sub-models is reflected in the content framed by the dotted box, in which a one-way coupling algorithm is adopted through the pressure continuity on the common waves-seabed interfaces.

The seabed foundation is treated as both poro-elastic material and poro-elastoplastic material, which is simulated by the elastic and plastic constitutive models, respectively. The input parameters of the wave characteristics, properties of the breakwaters and porous seabed foundation are listed in Table 12.4.

12.7.2 HYDRODYNAMICS AROUND OFFSHORE DETACHED BREAKWATERS

Figure 12.38 illustrates the impact of longshore currents to flow field around breakwaters. The velocity vectors around the offshore detached breakwater at water depth of -2 m are presented. The longshore currents commonly exist in the nearshore zone that move parallel to the shoreline. It is clear that the presence of currents has a significant impact on the velocity field. At the beginning of the simulation when the first wave has not reached the breakwater (e.g., t =4.5 s), a steady lateral velocity field has formed within the whole region under the condition where currents are

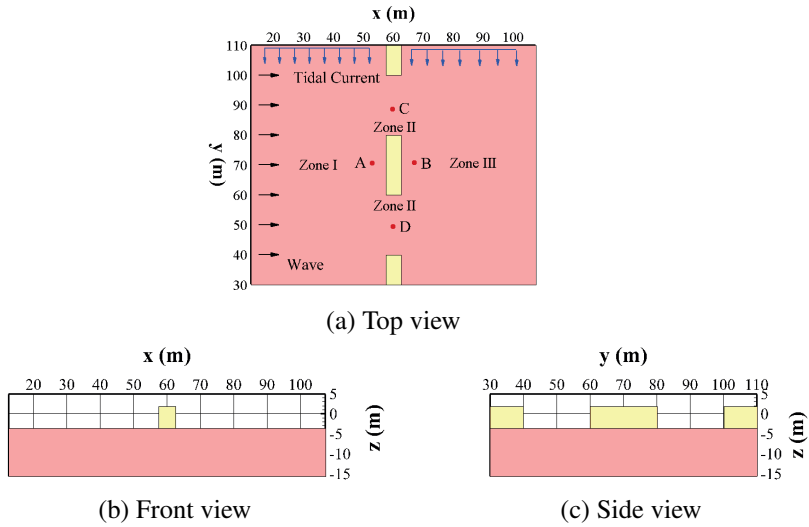

Figure 12.37 The computational domain: (a) top view, (b) front view, and (c) side view.

existing (Figures 12.38 a&c). The averaged velocity for two cases are 0.164 m/s and 0.632 m/s, respectively. The presence of the longshore currents significantly increase the velocity field in the vicinity of breakwaters. When time reaches 100 s, the impact is even more obvious, as shown in Figures 12.38 b&d. For the condition with wave loading only (Figures 12.38 a&b), the pattern of flow field is close to symmetry due to symmetry of computational domain. The waves in front of the three breakwaters have a higher velocity because of the superimposition of the reflected waves. Non-linear interactions between the fluid and the structures can be clearly observed, some symmetrical vortexes form behind the breakwater gaps. While for the condition with perpendicular longshore currents, the turbulent wave motion is more obvious. The velocity of the waves tend to be accelerated in the whole domain and the direction of the waves tend to be push to the downward by the lateral currents.

Figure 12.39 illustrates the time series of water surface elevation at locations A, B, C and D (refer to Figure 12.37) in different zones for case with longshore currents and case with waves only. Figures show that, for the wave height, location A in zone I is the largest, followed by location C & D in Zone II and location B in zone III. It is because of the blockage effect of the breakwaters, the incident and reflected waves were superposed in front of the breakwaters, while there are only diffracted waves behind the breakwaters. The surface elevations at location C & D are completely coincident in the case with only waves due to the symmetry. However, the presence of the currents can change this situation, it makes the wave crest at location D more sharp and a deviation of free water surface elevation between location C and D can be observed. The same effects can be observed at location A & B, the shape of the waves is altered by longshore current. This may further has impacts on the soil response in the seabed foundation and structure stability.

Table 12.4
The input parameters.

Wave characteristics		
Wave period (T)		4.5 s, 4.0 s or 3.5 s
Wave height (H)		2.4 m, 2.05 m or 1.7 m
Still water level (d)		3.6 m, 4.6 m or 5.6 m
Longshore current velocity (U_0)		0.6 m/s, 0.3 m/s or 0.0 m/s
Breakwater characteristics		
Young's modulus (E)		2.48×10^9 Pa
Poisson's ratio (μ_s)		0.24
Permeability (k_s)		1.0×10^{-3} m/s
Porosity (n_s)		0.49
Seabed foundation properties		
Permeability (k_s)		10^{-6} m/s, 10^{-4} m/s or 10^{-8} m/s
Porosity (n_s)		0.425
Degree of saturation (S_r)		99 %, 98 % or 97 %
Relative density (D_r)		40 % or 60 %
Elastic parameters		
Young's modulus (E)		1.35×10^7 Pa
Poisson's ratio (μ_s)		0.35
Parameters for PZIII Model		
	dense sand	**loose sand**
M_g	1.32	1.15
M_f	1.3	1.035
α_f	0.45	0.45
α_g	0.45	0.45
K_{evo}	2000.0 kPa	770.0 kPa
G_{eso}	2600.0 kPa	1155.0 kPa
β_0	4.2	4.2
β_1	0.2	0.2
p'_0	4.0 kPa	4.0 kPa
H_0	750.0	600.0
H_{U0}	40000.0 kPa	40000.0 kPa
γ_u	2.0	2.0
γ_{DM}	4.0	0.0

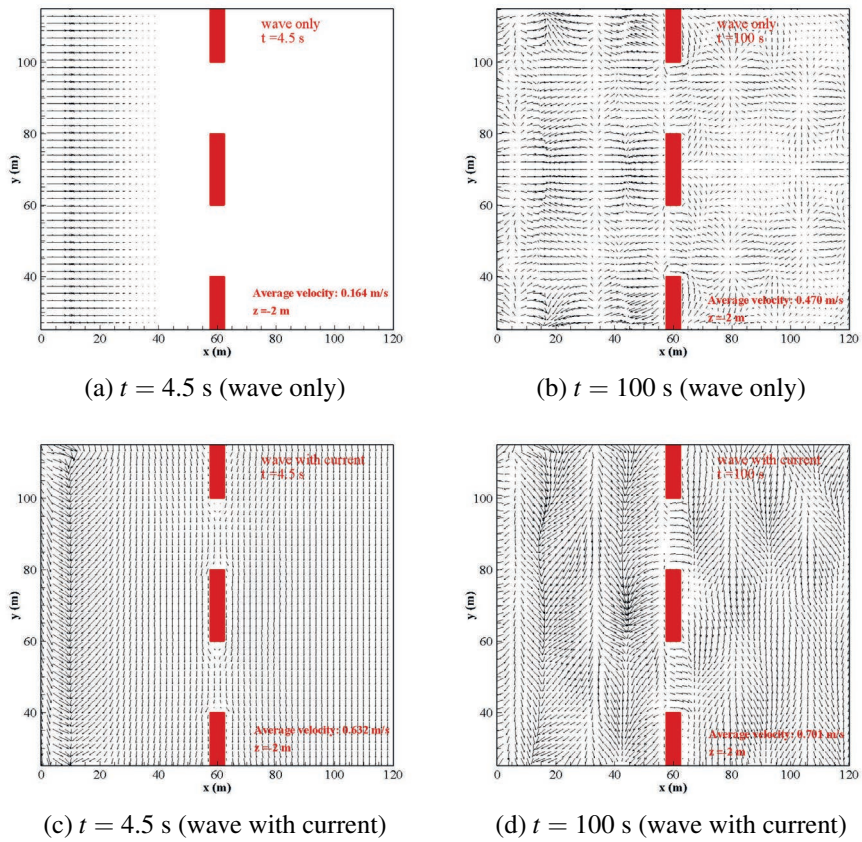

(a) $t = 4.5$ s (wave only) (b) $t = 100$ s (wave only)

(c) $t = 4.5$ s (wave with current) (d) $t = 100$ s (wave with current)

Figure 12.38 The distribution of the velocity vector of flow field around breakwaters under conditions without currents and with currents at (a) & (b) t =4.5 s and (c) & (d) 100 s.

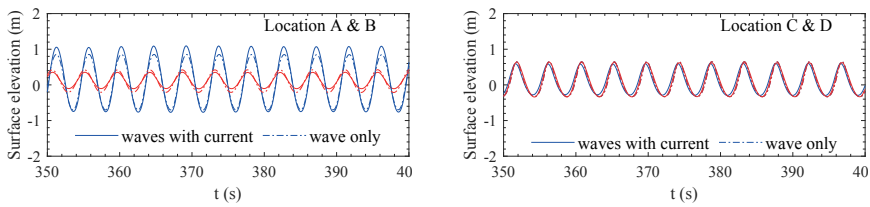

Figure 12.39 The surface elevation along time at location A, B, C & D in the cases with currents and without currents.

12.7.3 DYNAMIC SOIL RESPONSES AROUND THE OFFSHORE DETACHED BREAKWATERS

Different from the elastic soil, the behaviour of elastoplastic soil depends not only on the initial and final stress state, but also on the path it has gone through to reach the

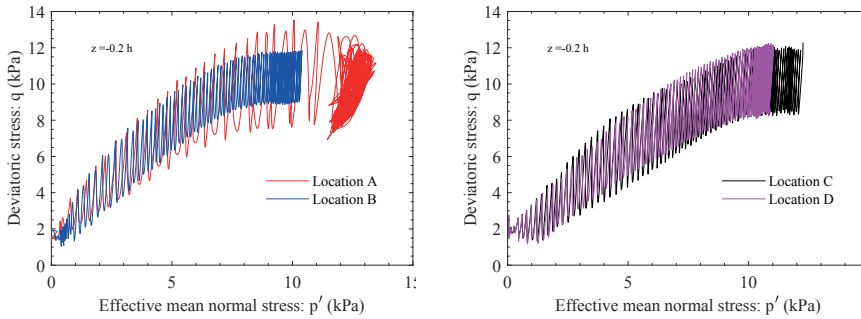

Figure 12.40 Effective stress paths at locations A, B, C and D subjected to wave and current loading.

final state. The stress path can effectively describe the mechanical properties of the elastoplastic seabed under the long-term cyclic waves, thus reflecting the strength variation and the possibility of liquefaction of the seabed. Figure 12.40 shows the effective stress paths at four reference points (location A, B, C & D in Figure 12.37) at depth of $0.2h$ in the seabed foundation under cyclic waves. It is found that the mean effective stress p' and the deviatoric stress q both drop quickly at all locations until p' reaches zero and the seabed foundation liquefies. It indicates that the liquefaction of a elastoplastic seabed foundation does not occur instantaneously, but a progressive process that the soil gradually lose its strength under the cyclic loading. At location A, the seabed foundation can maintain a relatively stable strength in the early stage, then followed by a high rate of decrease in p' and q until the seabed liquefies. The stability of seabed foundation decrease uniformly at other locations under the action of waves and currents and the non-linearity is not very obvious. However, they all reach the liquefaction state.

12.7.4 LIQUEFACTION AROUND THE OFFSHORE DETACHED BREAKWATERS

The liquefaction condition in the seabed foundation is evaluated based on the liquefaction criterion proposed by Jeng and Zhao (2015), which is calculated as follow:

$$\frac{1}{3}(|\sigma'_{x0}| + |\sigma'_{y0}| + |\sigma'_{z0}|) \leq p_{excess}, \tag{12.4}$$

where the left-hand-side denotes the initial mean effective stress and the right-hand-side represents the excess pore pressure caused by the wave loading. Since the residual liquefaction is caused by the weakening in the contact force between the soil particles due to the build-up of the pore pressure, p_{excess} should be considered as the accumulative value of the pore pressure induced by wave loading.

Figure 12.41 displays the residual liquefaction zones in the vicinity of breakwaters within a loosely packed poro-elastoplastic seabed foundation from

t =250 s to t =350 s. Three cross-sections at typical locations are selected: x =54 m which is located in front of the breakwaters, x =60 m which is just beneath the breakwaters and x =66 m which is behind the breakwaters. It is found from the figure that the soil in front of and beneath the breakwaters is most severely liquefied, while the liquefaction of soil behind the breakwaters is relatively less severe due to the protection from the breakwaters, only small areas of liquefaction appeared which concentrate on the gap region between breakwaters. For example, at t =350 s, the largest liquefaction depth in the slice of x =54 m is around 30 % of foundation thickness and less than 20 % in the slice of x =66 m. It is also found that liquefaction depth beneath the breakwaters is even larger, which brings great threat to the stability of the structure. In terms of time span, the liquefaction zones keep expanding, but the rate of expansion is slowing down.

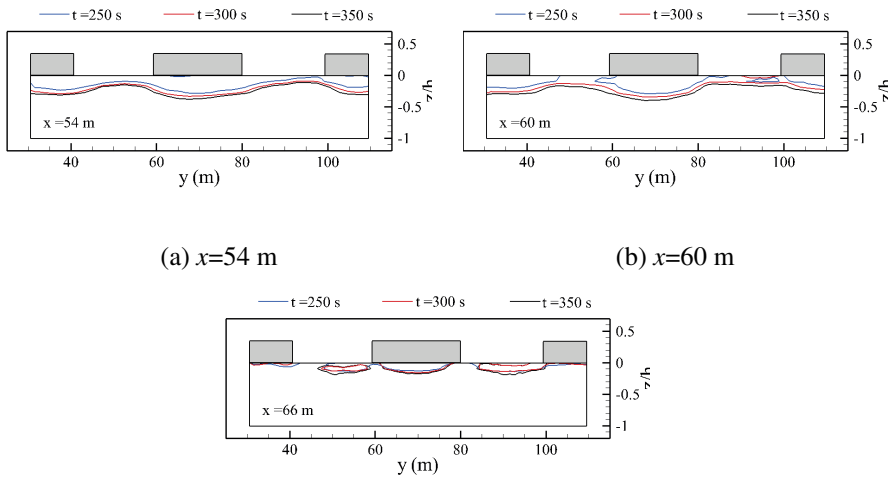

(a) x=54 m (b) x=60 m

(c) x=66 m

Figure 12.41 Liquefaction zones within a loosely packed poro-elastoplastic seabed foundation around breakwaters at t =250, 300 and 350 s for three typical slices: (a) x =54, (b) x =60 and (c) x =66 m.

Figure 12.42 illustrates the liquefaction depth (L_{depth}) within the seabed foundation at t =300 s. The 3D effect of wave/current loading around the structures can be clearly observed from the figure. From the figure, the largest L_{depth} occurs in front of the middle breakwater, which is over 2 m. This is because the strong non-linear interactions between the incident waves, reflected waves and longshore current makes this area more active comparing to other regions. The segmented coast-paralleled breakwaters can partly provide shelter area behind the breakwater, however, due to that the waves can pass through the gaps between the breakwaters and the existence of diffracted waves, there will still be a certain degree of liquefaction behind the breakwaters after a long period of cyclic loading. However,

the liquefaction zones behind the breakwaters are relatively shallow and distributed dispersively.

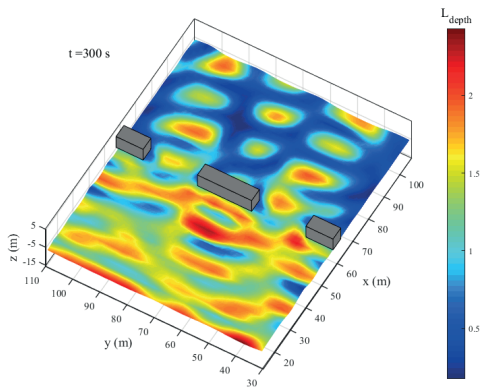

Figure 12.42 The liquefaction depth within a seabed foundation at t =300 s.

12.7.5 PARAMETRIC STUDY

To quantify the susceptibility of the *poro-elastoplastic* seabed foundation to liquefaction, a parameter $L_{potential}$ (liquefaction potential) can be obtained by performing a simple operation on (12.4):

$$L_{potential} = \frac{p_{excess}}{\frac{1}{3}(|\sigma'_{x0}| + |\sigma'_{y0}| + |\sigma'_{z0}|)}. \tag{12.5}$$

Differently, the pore pressure in the *poro-elastic* seabed foundation is periodic without accumulation, hence, we use parameter $L_{potential(max)}$ instead to evaluate the possibility of a poro-elastic seabed to be liquefied. $L_{potential(max)}$ depends on the maximum wave-induced dynamic effective stresses within the whole simulation period, which is calculated as (12.6) based on the liquefaction criteria proposed by Tsai (1995):

$$L_{potential(max)} = \frac{\frac{1}{3}(\sigma'_{xd} + \sigma'_{yd} + \sigma'_{zd})}{\frac{1}{3}(|\sigma'_{x0}| + |\sigma'_{y0}| + |\sigma'_{z0}|)}, \tag{12.6}$$

where the numerator represents the mean value of the wave-induced dynamic effective stresses (i.e., the increase of the effective stresses caused by the wave cyclic loading); the denominator represents the initial mean effective stresses.

From the definitions, the higher the $L_{potential}$, the closer the seabed foundation is to liquefaction. In order to investigate the effects of various parameters on the stability of the seabed foundation around detached breakwaters when subject to

waves and longshore currents loading, the liquefaction potential along the depth of the seabed foundation at location A (Zone I) & B (Zone III) will be discussed for both the poro-elastoplastic and the poro-elastic seabed foundation.

A. Effect of seabed properties

Among the soil parameters, the permeability of soil (k_s) and degree of saturation (S_r) are usually the sensitive parameters. k_s is an important parameter for measuring the drainage capacity of the soil, which has a great impact on the accumulation rate of the pore-water pressure. When soil permeability (k_s) is large, the drainage performance of the soil is good and the pore-water pressure build-up rate is low; otherwise, the drainage capacity is bad and the pore-water pressure build-up rate is high. The degree of saturation (S_r) is another soil parameter that might affect the seabed foundation response. Although most seabed foundations have degrees of saturation close to fully saturated, the full saturation condition is rare in the real environment, it is common to find air within the seabed soil (Okusa, 1985).

Figure 12.43 and Figure 12.44 illustrate the effect of soil permeability (k_s) and degree of saturation (S_r) on the vertical distribution of liquefaction potential ($L_{potential}$ or $L_{potential(max)}$) at location A and B in the poro-elastoplastic and poro-elastic seabed foundation. The figures show that k_s has a more significant impact on the foundation stability compared to S_r. As been displayed by Figure 12.43, the liquefaction condition is more severe in the seabed foundation with low k_s. An interesting finding is that $L_{potential}$ increases as k_s decreases from 10^{-4} m/s to 10^{-8} m/s in the poro-elastoplastic seabed foundation, however, the effect of k_s on the foundation stability becomes less sensitive as it reaching 10^{-6} m/s and continuing to decrease. This might indicate that the soil liquefaction does not deteriorate indefinitely with the decrease of k_s. When k_s is low to a certain extent, the liquefaction condition reaches its worst case. For the influence of degree of saturation (S_r) in the poro-elastoplastic seabed foundation, there are no significant differences between different cases, which indicates that S_r has little effect on the stability of poro-elastoplastic seabed foundation. Therefore, it can be concluded that in the poro-elastoplastic seabed foundation, the key influence factor among the soil properties on the foundation stability is the soil permeability (k_s).

To see the difference between poro-elastic model and poro-elastoplastic model, we also consider the poro-elastic seabed, which only have oscillatory liquefaction rather than residual liquefaction. It is observed that the liquefaction potential in the poro-elastic seabed foundation is much smaller than that in the poro-elastoplastic seabed foundation under the same wave/current loading, the value of $L_{potential}$ of the former foundation is only about 10 % of the latter foundation. For example, in the case of seabed with k_s =10^{-4} m/s, $L_{potential_{max}}$ is less than 0.25, indicating that the poro-elastic seabed foundation is not liquefied under such condition. Different from that in poro-elastoplastic seabed foundation, S_r has quite an impact on the stability of poro-elastic seabed foundation. It is observed that $L_{potential_{max}}$ increases as S_r decreases, and $L_{potential_{max}}$ reduces swiftly as S_r becomes 100 %. In summary, compared to the poro-elastoplastic seabed foundation, the liquefaction has minor

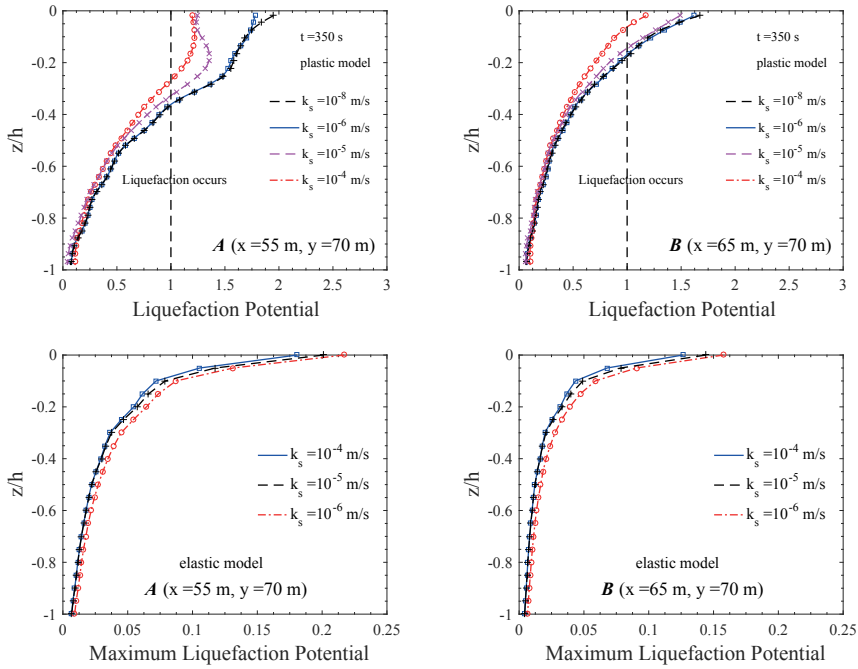

Figure 12.43 Vertical distribution of the liquefaction potential for various soil permeability ($k_s = 10^{-4}$ m/s, $k_s = 10^{-5}$ m/s, $k_s = 10^{-6}$ m/s and $k_s = 10^{-8}$ m/s) at location A (x =55 m, y =70 m) and B (x =65 m, y =70 m) within the poro-elastoplastic and poro-elastic seabed foundation (T =4.5 s, H =2.4 m, d =3.6 m, U_0 =0.6 m/s).

effects on the structure stability in a poro-elastic seabed foundation. However, the liquefaction may still deteriorate the scouring around breakwaters and affect the stability of coastal structures. Comparing among the different locations, location A has a deeper liquefaction depth (L_{depth}) than location B. For example, in the case of seabed foundation with $k_s = 10^{-4}$ m/s, L_{depth} at location A reaches over 20 % of foundation thickness. Due to the protection from the middle breakwater, location B only has a L_{depth} of 5 % of foundation thickness. It is also found from the figures that the liquefaction potential is smallest at seabed bottom ($L_{potential} = 0$) and gradually increases along the depth to the seabed surface, in other words, the closer to the seabed surface, the greater the liquefaction potential value.

Two sets of PZIII constitutive model parameters, representing the loose deposited poro-elastoplastic seabed foundation with relative density (D_r) equals to 40 % and the dense deposited poro-elastoplastic seabed foundation with D_r equals to 60 %, are used to study the foundation stability around the breakwaters. Figure 12.45 shows the vertical distribution of $L_{potential}$ in these two types of seabed foundation at t =350 s. It can be seen from the figure that L_{depth} in loose sand is almost twice as deep as in dense sand at each location. For instance, L_{depth} at location behind the middle

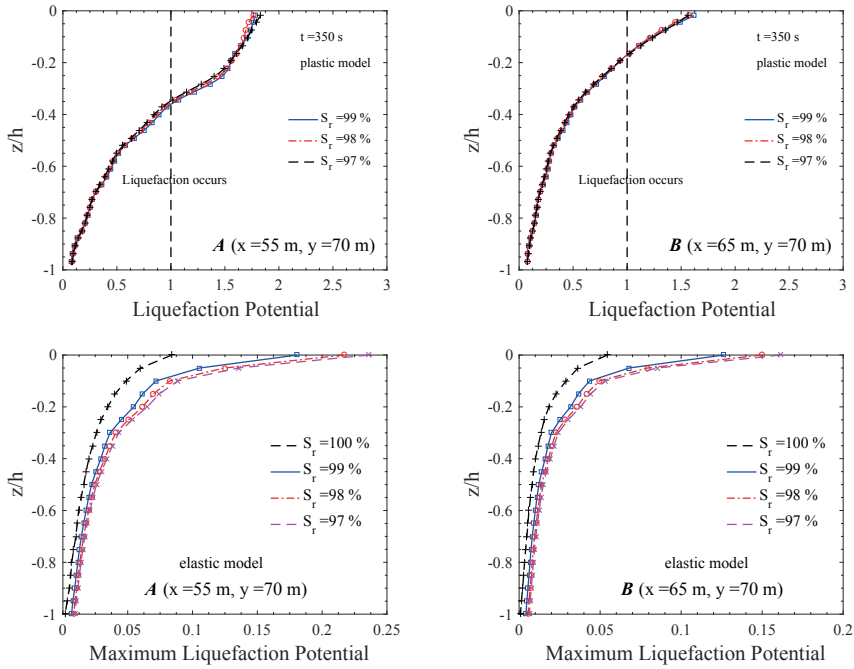

Figure 12.44 Vertical distribution of the liquefaction potential for various degree of saturation (S_r =99%, S_r =98% and S_r =97%) at location A (x =55 m, y =70 m) and B (x =65 m, y =70 m) within the poro-elastoplastic and poro-elastic seabed foundation (T =4.5 s, H =2.4 m, d =3.6 m, U_0 =0.6 m/s).

breakwater (i.e., location B (x =65 m, y =70 m)) reaches nearly 10 % and 20 % of the seabed thickness in dense foundation and loose seabed foundation, respectively. This suggests that there is a higher chance to severe liquefaction in loose seabed foundation with small D_r because loose sand is easier to be contracted under cyclic loading and causes greater pore pressure accumulation.

B. Effect of wave characteristics

Figure 12.46 represents the vertical distribution of $L_{potential}$ and $L_{potential_{max}}$ for various combination of waves and longshore currents (U_0 =-0.6 m/s, U_0 =0 m/s & U_0 =-0.3 m/s) in poro-elastoplastic seabed foundation and poro-elastic seabed foundation, respectively. As illustrated in the figures, the presence of the perpendicular longshore currents increase the liquefaction potential along the depth of seabed foundation and it becomes larger as the magnitude of velocity becomes larger. The influence is mainly reflected in the shallow soil layer near the seabed surface, while the influence on the deep soil is relatively small, especially in the poro-elastoplastic seabed foundation. Therefore, it can be concluded that the effect

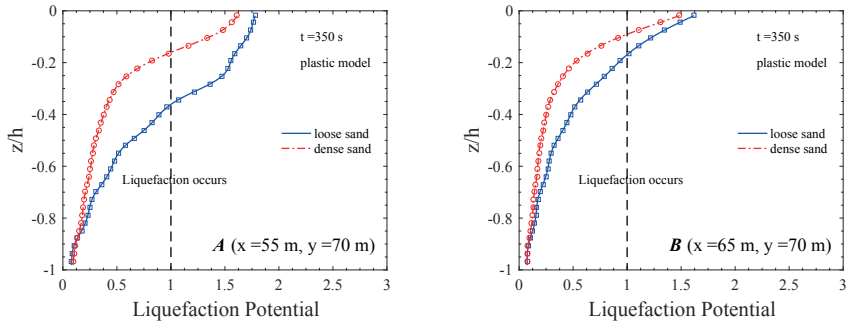

Figure 12.45 Vertical distribution of the liquefaction potential ($L_{potential}$) at location A (x =55 m, y =70 m) and B (x =65 m, y =70 m) within the loosely deposited poro-elastoplastic seabed foundation and densely deposited poro-elastoplastic seabed foundation at t =350 s (T =4.5 s, H =2.4 m, d =3.6 m, U_0 =0.6 m/s).

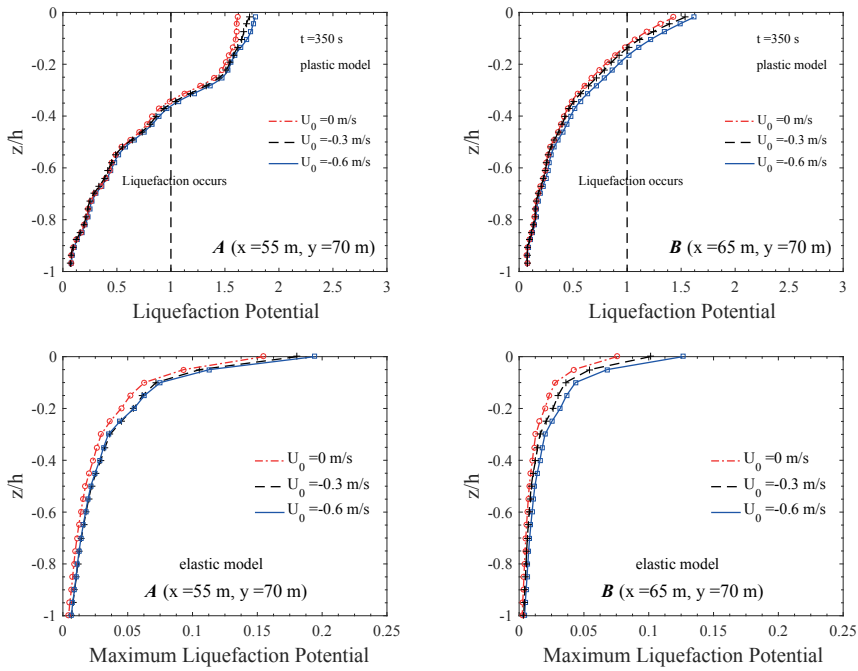

Figure 12.46 Vertical distribution of the liquefaction potential for various longshore currents conditions (U_0 =-0.6 m/s, U_0 =0 m/s and U_0 =-0.3 m/s) at location A (x =55 m, y =70 m) and B (x =65 m, y =70 m) within the poro-elastoplastic and poro-elastic seabed foundation (T =4.5 s, H =2.4 m, d =3.6 m).

of wave-current interaction is more significant in the upper seabed layer with stronger longshore currents and the current has little effect on the deeper seabed stability.

Among the wave parameters, in addition to the ocean currents, wave height (H) and wave period (T) can also affect the stability of the foundation. As illustrated in Figures 12.47, the vertical distribution of liquefaction potential in the poro-elastoplastic and poro-elastic seabed foundation increases as the increase of H and T. It implies that waves with larger height and longer period can pose more threats on foundation stability around the structures than a smaller height and shorter period wave under the same soil condition. As an example, at location A which is in front of the middle breakwater, the liquefaction depth (L_{depth}) is about 25 % of foundation thickness for H =1.7 m, and reaches 35 % of foundation thickness for H =2.4 m; and the difference of L_{depth} between the case with T =3.5 s and T =4.5 can reach up to 20 %. This may be explained by the fact that the wave steepness (H/L) becomes larger for a larger H and the relative water depth (d/L) becomes smaller for a longer T in the same water depth.

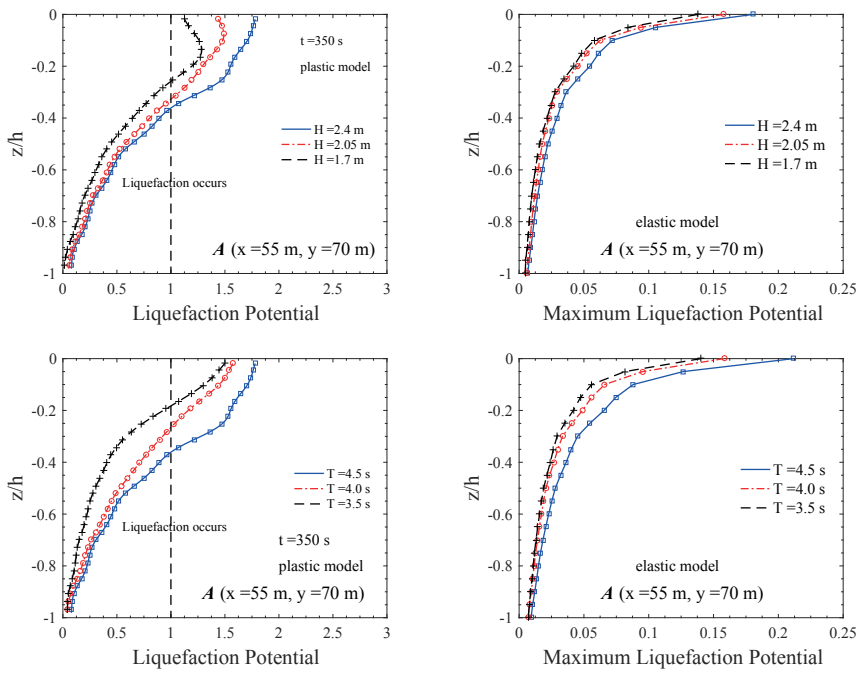

Figure 12.47 Vertical distribution of the liquefaction potential for various wave height (H =2.4 m, H =2.05 m and H =1.7 m) and wave period (T =4.5 s, T =4.0 s and T =3.5 s) at location A (x =55 m, y =70 m) within the poro-elastoplastic and poro-elastic seabed foundation (d =3.6 m, U_0 =0.6 m/s).

12.8 SUMMARY

In this chapter, wave/current-induced seabed liquefaction around breakwaters are discussed. Both 2D and 3D cases are considered as well as poro-elastic and poro-elastoplastic seabed models. Four different types of breakwaters, including composite breakwaters, submerged breakwaters, breakwater head at river mouth and offshore detached breakwaters are considered. Based on the numerical results, the following conclusions can be drawn.

(1) numerical model (PORO-FSSI) have been validated with the existing experimental data for various conditions available in the literature. The validations demonstrate the capacity of PORO-FSSI model.

(2) PORO-WSSI is adopted to investigate the interaction between the wave, composite breakwater and seabed foundation. Intensive fluid exchange takes place in the region close to the seabed surface, where the upward seepage force under wave trough makes the effective stresses decrease, putting the seabed foundation at the risk of liquefaction. When the liquefaction zones are close to the breakwater, they may have significant impact on the foundation stability.

(3) The 3D effect of Fluid-Structure-Seabed Interactions can be intense and cannot be ignored, whose simulation requires a sufficient 3D numerical model. The simulation results of the 3D cases (i.e., breakwater at the river mouth, and offshore detached breakwater) also reveal that the development of liquefaction within the poro-elastoplastic and poro-elastic seabed is different, the liquefaction in the former seabed is much more severe than that in the latter under the same wave load.

(4) Parametric studies show that the wave characteristics and soil properties significantly affect the liquefaction potential of the seabed foundation in the vicinity of the structure. A longer wave period, a higher wave height, shallow water depth or lower soil permeability will lead to a larger liquefaction potential. Additionally, the presence of currents, for example, longshore current and river current, will also exacerbate the wave field and increase the risk of liquefaction of seabed foundation.

13 Liquefaction around Marine Structures: Pipelines

To meet the demand of the new sources of energy and minerals, coastal engineers must work at the frontiers of known technology to ensure the long-term stability of offshore pipelines which are critical in the development of subsea hydrocarbon resources. As reported in the literature, considerable damage caused by anchors and other installations can be attributed to a combination of local indentation and large-scale bending of unburied pipelines, especially in busy shipping lanes and congested port approaches (Palmer, 1986). Subsea pipelines that are buried in a porous seabed can be subject to variations of local-liquefied soil due to storm wave and current action, which can cause pipelines to be exposed to the ocean (Gerwick Jr, 2007). Thereafter, sections of subsea pipelines may be described as being in a sinking or floating status, eventually leading to fatigue. In addition, the negative impact of the snagging (or hooking) of fishing gear and trawler on the pipelines cannot be ignored (Bai and Bai, 2014). Therefore, trenching is recommended to better protect submarine pipelines from fishing activities and exposure in shallow water due to storm waves and ocean currents changing the level of the seabed (Palmer and King, 2008; Fredsoe, 2016).

Construction of trenches in deep water or intermediate water leads to an exceptionally high cost. In this circumstance, offshore pipelines can be directly laid on the seafloor and penetrate into the seabed through its self-burial. However, the geological activities on the seabed induced by the storm surge also trigger the movement of the seabed soil, which in turn causes the pipeline to be exposed to the marine environment. Hence, the technology of using the Articulated Concrete Mattresses (ACMs) to cover both sides of the pipe as a secondary stabilisation measure has been introduced since the early 1980s, which are made up of a matrix of concrete blocks interconnected with wires or ropes (Crowhurst, 1982).

In this chapter, two different methodologies for pipeline protection will be discussed, including pipelines in a trench layer and Articulated Concrete Mattresses. Possible design methodology will be proposed for the design of pipeline protection.

13.1 WAVE-SEABED INTERACTIONS IN THE VICINITY OF PIPELINES IN A TRENCH

Research on trenches can be traced back to the end of the 1970s. More specifically, these studies can be divided into two categories, including hydrodynamic studies in the trenches, and the development and stability of backfill materials in the trenches. Among these, Jacobsen et al. (1989) experimentally studied the reduction coefficients of hydrodynamic loading for partially buried pipelines, and for pipelines

in an open and shallow trench. Their results indicated the reduction coefficients depend on a certain extent on the flow parameters, the KC number and the ratio of the currents. A similar experimental study was conducted by Jo et al. (2002), addressing the stability of various trench conditions in terms of mean amplitudes of oscillating lift and drag force with reduction factors. Regarding the stability of backfill materials in trenches, Fredsoe, (1979) developed a mathematical model to estimate the amount of natural backfilling into a trench, by considering the influence of currents, waves, bed materials, shapes of the trench and water depths. Later, Clukey et al. (1989) conducted a field study to assess the time required to produce a dense, non-liquefiable backfill material under natural conditions. To sum up, the focus of the aforementioned studies involving trenched structures changed from the aspects of hydrodynamics to dynamic sedimentation processes and stability of the backfilling material.

Recently, research on the instability of the pipeline caused by seabed liquefaction has also attracted the attention of coastal engineers (Damgarrd et al., 2006). Using the advantages of a numerical approach by involving the Biot's consolidation equations (Biot, 1941), a series of models have been proposed to estimate the oscillatory pore-water pressure around a pipeline constructed in a full-trenched layer (Wang et al., 2000; Gao et al., 2003*b*,*a*; Gao and Wu, 2006; Luan et al., 2008; Wen et al., 2012; Zhao et al., 2014).

As for the trenching requirement, it has been a common industrial practice in the North Sea to trench or cover all pipelines less than 0.2 m (Dongen, 1983). The newly released guideline DNVGL-RP-F114 has been widely adopted for the on-bottom stability assessments of the pipeline. As suggested in DNVGL-RP-F114, seabed liquefaction is one of the factors that affect the on-bottom stability assessment results, leading to instability of the pipeline. However, there is limited guidance on the stability of the trench design and protection. As a matter of fact, the key issue for designing a trenched pipeline is to determine the burial depth, which depends on various variables such as wave, current, sediment properties, and the liquefaction potential (Sumer and Fredsoe, 2002). Therefore, the issue of backfill thickness of trenched pipelines needs to be addressed through continuous theoretical works, then the advantages of trenching can be utilised.

More advanced numerical programs were proposed by integrating numerical wave generation rather than using analytical solutions for wave pressures. In particular, some studies further evaluated the liquefaction potential around a trenched pipeline in terms of momentary liquefaction (Lin et al., 2016; Duan et al., 2017; Wang et al., 2019*c*; Liang et al., 2020; Liang and Jeng, 2021) and residual liquefaction (Zhao and Jeng, 2016; Chen et al., 2019), respectively. Recently, the seabed liquefaction in the vicinity of two tandem pipelines in a trench have been studied through the PORO–FSSI model (Chen and Jeng, 2022*a*,*b*; Chen, Jeng and Liang, 2022). In addition to the numerical studies, only a few experimental investigations of the wave-induced seabed response around a trenched pipeline were carried out by (Zhai et al., 2018; Sun et al., 2019; Zhai et al., 2022) recently. Among these, Zhai et al. (2018); Sun et al. (2019) considered a single pipe in a trench layer, while Zhai et al. (2022) focused on two tandem pipelines.

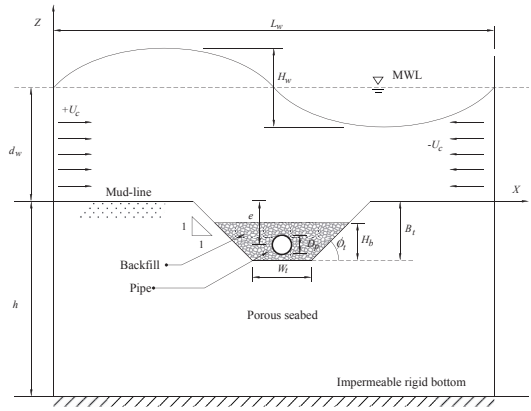

Figure 13.1 Sketch of the wave-current-seabed interactions around a trenched pipeline.

13.1.1 THEORETICAL MODEL

The problem of fluid-seabed-pipeline interactions with a trench layer considered in this study is depicted in Figure 13.1. In the numerical simulation, PORO-FSSI-FOAM model (Liang et al., 2020) will be adopted. The fifth-order Stokes wave theory (Skjelbreia and Hendrickson, 1960) is used for wave generation with fixed water depth (d_w), and the waves propagation. In addition, an uniform current $(\pm U_c)$ is generated prior to wave generation when the influence of ocean currents is considered. Apart from the fluid domain, a trench with a fixed slope (ϕ_t) is considered; the depth of the trench is B_t, the width of its bottom is W_t. An offshore pipeline is placed in the middle of the channel, covered by refilling soil with a specific thickness (H_b); and e is the burial depth which is defined as the distance between the middle of the pipe and the mud-line.

In the seabed model, several boundary conditions are employed at the boundary of the seabed domain and the surface of the submarine pipeline for accurately evaluating the wave-current-seabed-structure interactions (WCSSI). In addition to the boundary condition at the seabed surface and bottom, additional boundary conditions are required for pipe surface. The pipeline is simulated as a rigid impermeable object in which the no-flow boundary condition is applied to its surface:

$$\frac{\partial p_s}{\partial \mathbf{n}} = 0, \tag{13.1}$$

13.1.2 MODEL VALIDATIONS

In this section, the proposed model will be systematically validated using published laboratory experimental results available in the literature. The experiment set-up for

the validations are given in Figure 13.2. The wave and soil parameters considered in the numerical simulations for verification, unless specified, are the same as those used in the laboratory experiments (Table 13.1). The following validations will be presented.

- Validation #1: Comparison with the wave flume experiments for the near-bed fluid velocities around a offshore pipeline (Mattioli et al., 2012).
- Validation #2: Comparison with Turcotte et al. (1984)'s experimental data for the wave-driven soil response in the surrounding of a fully buried pipeline in a trench layer, together with the numerical simulation (Cheng and Liu, 1986).
- Validation #3: Comparison with Sun et al. (2019)'s experimental data for the wave-driven soil response in the surrounding of a partially buried pipeline in a trench layer.
- Validation #4: Comparison with Zhai et al. (2022)'s experimental results for the wave-induced soil response around twin pipelines in a sandy seabed.

Validation #1: Comparison with Mattioli et al. (2012)'s flume observations of wave-pipeline interactions

A series of investigations were carried out by Mattioli et al. (2012), referring to examining the near-bed dynamics around a submarine pipeline lying on different seabed types. Within this validation, only the case of a rigid bed was used to compare the experimental and simulation data. The present model should be simplified to the case of wave-pipeline interactions to ensure the sketch is completely consistent with the experimental set-up in Mattioli et al. (2012). The laboratory set-up is shown in Figure 13.2(a). The wave flume was 50 m long, 1.3 m high and 1 m in width. Specifically, the piston-type wave-maker was located at one end to generate the regular wave and propagate undefined the model section. A plexiglass pipe with a diameter of 0.05 m and a length of 1.0 m was placed on the flume wall, normal to the wave direction, with an initial embedment of $e/D = 0$, within the model section. Furthermore, PTV measurements are used to record the flow around the pipeline, and they are combined with Acoustic Doppler Velocimetry (ADV) for calibration and validation. The input data of this example are listed in Table 13.1. Figure 13.3 illustrates the profiles of the dimensionless horizontal fluid velocity ($u^* = u/(H_w/T_w)$) through the pipeline's centre (z/D) for various wave phases from 0° to 180° with a 45° degree increment, where u defines the horizontal velocity. It is evident that the numerical results generally agree with their experimental counterparts. This comparison shows the flow model can simulate the interactions between waves and a submerged pipeline.

Validation #2: Comparison with the Turcotte et al. (1984)'s laboratory experiment for a fully buried pipeline.

In the first validation, the present model is compared with the laboratory experiments of Turcotte et al. (1984), in which the wave-induced soil response around a fully

Table 13.1 Input parameters of fluid and solid domains for model validation.

Flow characteristics				**Solid characteristics**							
H_w (m)	T_w (s)	d_w (m)	U_c (m/s)	k_s (m/s)	n_s	μ_s	S_r	G_s (N/m^2)	h_s (m)	D_p (m)	e (m)
Mattioli et al. (2012)											
0.1	2.0	0.3	[-]	[-]	[-]	[-]	[-]	[-]	[-]	0.05	[-]
Turcotte et al. (1984)											
0.0524	0.9	0.533	[-]	1.1×10^{-3}	0.42	0.33	0.95	6.4×10^{5}	0.826	0.168	0.167
0.143	1.75	0.533	[-]	1.1×10^{-3}	0.42	0.33	0.95	6.4×10^{5}	0.826	0.168	0.167
0.0302	2.3	0.533	[-]	1.1×10^{-3}	0.42	0.33	0.95	6.4×10^{5}	0.826	0.168	0.167
Sun et al. (2019)											
0.14	1.4	0.4	[-]	3.56×10^{-5}	0.396	0.32	0.999	10^{7}	0.58	0.1	0.15
0.12	1.6	0.4	[-]	3.56×10^{-5}	0.396	0.32	0.999	10^{7}	0.58	0.1	0.05
Zhai et al. (2022)											
0.1	1.2	0.4	[-]	3.56×10^{-5}	0.369	0.3	1.0	8.28×10^{6}	0.58	0.12	[-]
0.1	1.2	0.4	[-]	3.56×10^{-5}	0.369	0.3	1.0	8.28×10^{6}	0.58	0.14	[-]

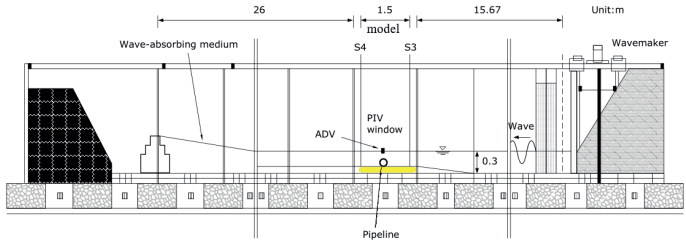

(a) Mattioli et al. (2012)'s wave flume tests

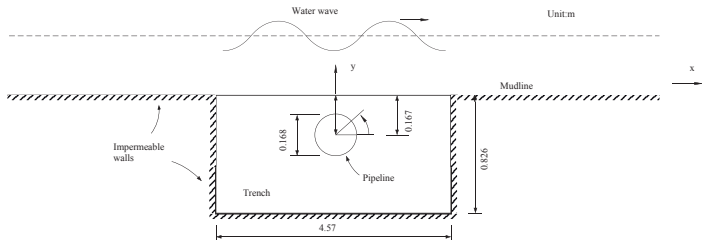

(b) Turcotte et al. (1984)'s experiment

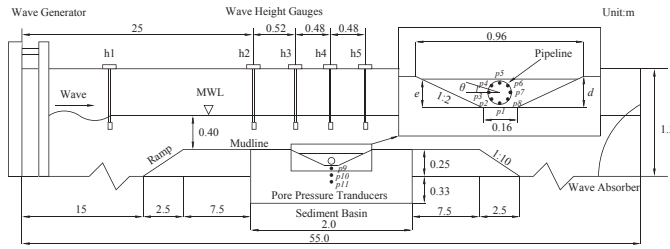

(c) Sun et al. (2019)'s laboratory experiment

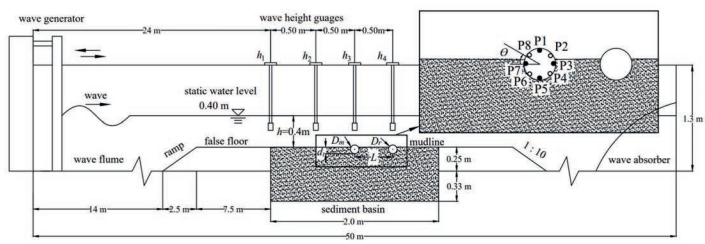

(d) Zhai et al. (2022)'s wave flume

Figure 13.2 The experimental setup of (a) Mattioli et al. (2012)'s wave tests for the wave-pipeline interactions; (b) Turcotte et al. (1984)'s experiments of waves propagating over a partially fully pipeline in a trench layer; (c) Sun et al. (2019)'s flume observations of waves propagating over a partially buried pipeline in a trench layer; (d) Zhai et al. (2022)'s laboratory experiment of wave-induced seabed response around twin pipelines in sandy seabed.

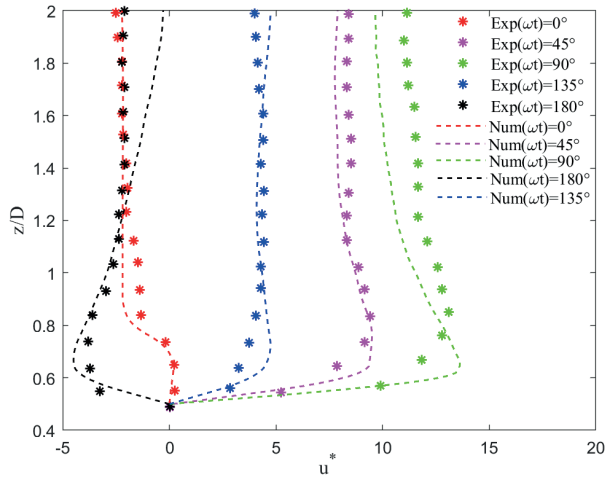

Figure 13.3 Comparison of the vertical distribution of the dimensionless horizontal fluid velocity ($u^* = u/(H_w/T_w)$) along the vertical line through the center of the pipeline (z/D) for different wave phases (ωt) between the measured data of Mattioli et al. (2012) and numerical results of present model.

buried pipeline based on wave tank tests was explored. The tests were carried out in a 16 m long, 0.76 m wide wave tank (see Figure 13.2(b). At the mid-length of the wave tank, a PVC pipe (D_p= 0.168 m) was fully buried (e=0.107 m) within an impermeable trench (4.57 m long and 0.826 m deep). In their experiments, the centre of the pipe was less than 0.167 m below the mud-line. The numerical results (Cheng and Liu, 1986) by applying the Boundary Integral Equation Method(BIEM) is also included in the comparison.

Figure 13.4 illustrates the distribution of the wave-induced maximum pore pressure ($|p_s|/p_0$) along the outer surface of the pipeline (θ) for three wave conditions: (a) T_w=0.9 s, L_w=1.25 m, and H_w=0.0524 m; (b) T_w=1.75 s, L_w=3.54 m, and H_w=0.143 m; and (c) T_w=2.3 s, L_w=4.91 m, and H_w=0.0302 m. Overall, the present model captures the essential features of the laboratory experiments (Turcotte et al., 1984) and numerical solutions (Cheng and Liu, 1986).

Validation #3: Comparison with the experimental data around a trenched pipeline (Sun et al., 2019)

Sun et al. (2019) conducted a series of comprehensive laboratory experiments in a wave flume to study the pore pressure caused by waves around partially embedded pipes in the trench layer. The experiments were carried out in a wave flume that was 55.0 *m* in length, 1.3 *m* in height and 1.0 *m* in width at the laboratory of Hohai University, China. A piston-type wave generator at the upstream end and a sponge-type wave absorber at the downstream end dissipated the incident wave energy and eliminated wave reflection. A sediment basin was located at a distance

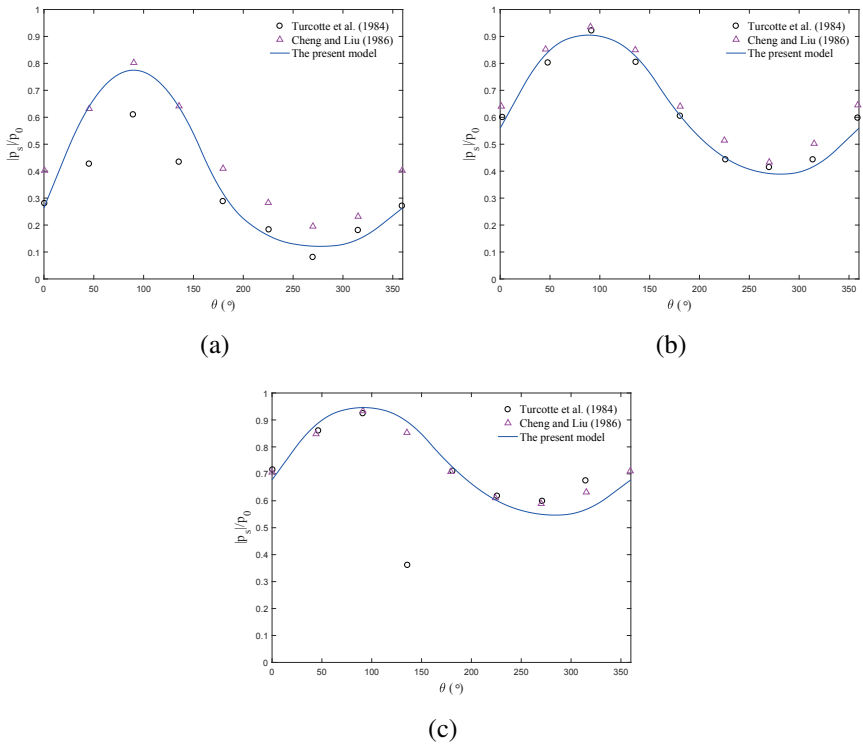

Figure 13.4 Comparisons of numerical results of wave-induced maximum pore pressure ($|p_s|/p_0$) along the periphery of the pipeline (θ) with the experimental data (Turcotte et al., 1984) and the numerical solutions (Cheng and Liu, 1986) for three different wave conditions:(a) T_w=0.9 s, L_w=1.25 m, and H_w=0.0524 m; (b) T_w=1.75 s, L_w=3.54 m, and H_w=0.143 m; and (c) T_w=2.3 s, L_w=4.91 m, and H_w=0.0302 m.

of 25 m away from the wave maker, and its thickness was maintained at 0.58 m. The PMMA pipe with a diameter of 0.10 m was used to model the submarine pipelines located at the bottom of a trenched layer. During the experiments, eight sets of pore pressure transducers were set-up around the pipeline circumference with an interval of $\pi/4$, and others were fixed along the central line just below the trench at three different depths (z=-0.23 m, -0.27 m and -0.40 m), as indicated in Figure 13.2(c).

In the fourth validation, the present model is compared with the flume experiments of Sun et al. (2019), in which the process of the wave-induced transient pore pressure around a trenched pipeline with partial sediment backfilling was investigated. As shown in Figure 13.2(c), the experiment was processed within a wave flume of 55 m in length, 1.3 in depth and 1 m in width, while the sketch for different depths of the trench layer for test 10 and test 49 are displayed. The parameters for the comparison of Sun et al. (2019)'s experiment can be referred to

Table 13.1. Concerning the data obtainment, eight sets of pore pressure transducers were fixed along the periphery of the pipeline circumference with an interval of $\pi/4$.

Figure 13.5 presents the comparison between the simulated and measured maximum amplitudes of the pore-water pressure ($|p_s|/p_0$) around the outer surface of the submarine pipeline for Test No.10 and No.49. More specifically, a pipeline was fully buried in a trench with depth (d_t)= 0.15 m and covered by the backfill with thickness (d_b)= 0.15 m in Test No.10. Test 49 involved a partially buried pipeline in a trench where d_t=0.2 m and d_b=0.05 m. The wave characteristics of the two tests (No.10 and No.49), including wave height and wave period, were 0.14 m at 1.4 s and 0.12 m at 1.6 s, respectively. As can be seen from the figures, the difference between the experimental data and the simulation results is relatively large at the bottom of the pipe. The difference may be due to the boundary set-up near the surface of the seabed in the hydrodynamic model with **u**= 0. In fact, in an actual experimental environment, a non-zero value of flow velocity can be obtained near the junction between the bottom of the pipe and the surface of the seabed.

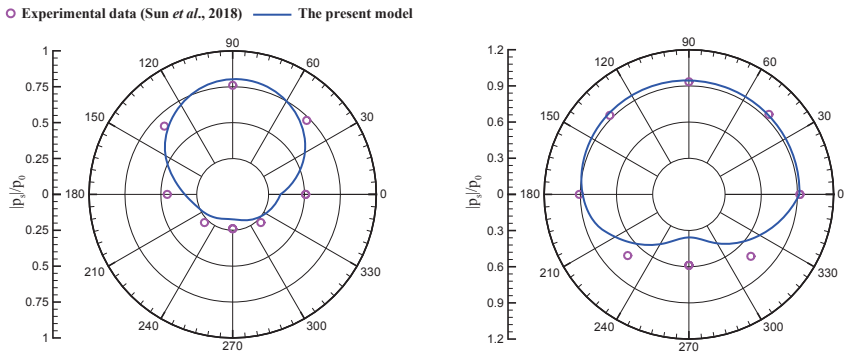

(a) Test 10 ($d_t = d_b = 0.15$ m) (b) Test 49 (d_t=0.2 m; d_b=0.05 m)

Figure 13.5 Comparison of the experimental data (Sun et al., 2019) for the wave-driven transient pore pressure along the periphery of a fully buried pipeline versus a partially buried pipeline with results from the present model. ○: the experimental results, ——: the present model.

Validation #4: Comparison with the experimental data in the proximity of twin pipelines (Zhai et al., 2022)

The experimental work related to the wave-induced seabed response around twin pipes is applied to validate the present model. Recently, a series of experiments were conducted by Zhai et al. (2022) for wave-induced excess pore pressure around two tandem pipelines, especially considering the buried depths and the gap conditions. It is noted that this is the only experimental data for the soil response around twin pipelines available in the literature. As shown in Figure 13.2(d), the

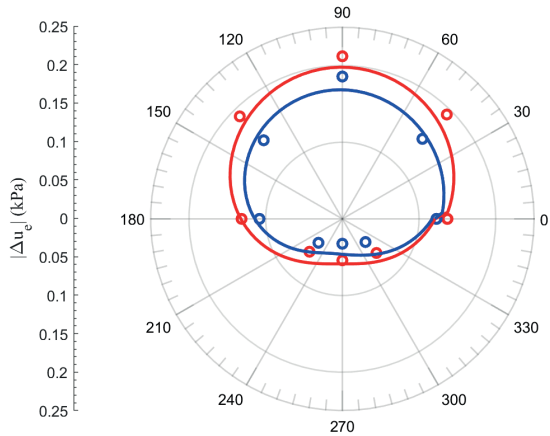

Figure 13.6 Comparison between the experimental data (Zhai et al., 2022) and the present model of the excess pore pressure amplitude ($|\Delta u_e|$) around the pipeline for a single pipe and the upstream pipe for twin pipelines in a fully buried condition. ○ and ——: measured and numerical results of a single pipeline; ○ and ——: measured and numerical results of the upstream pipe for two pipelines in tandem.

experiment was conducted in a wave flume of 50 m in length, 1.3 in depth and 1 m in width. A piston-type wave generator was installed at the wave flume in their experiment, and two porous and sloping wave absorbers were used at both ends to eliminate wave reflection. The sediment basin was located in the middle portion of the flume with dimensions of 2 m long, 1 m width and 0.58 m deep. Two PMMA (poly-methyl-methacrylate) pipes with the same diameter were used to model the offshore pipes. Concerning the data obtainment, eight sets of pore pressure transducers were fixed along the periphery of the upstream pipeline circumference with an interval of $\pi/4$ (see Figure 13.2(d)).

In a fully buried condition, Figure 13.6 shows the comparison of the measured results (Zhai et al., 2022) and corresponding simulated data for the excess pore pressure amplitude ($\Delta u_e = p_s - p_w$) along the periphery of a single pipe and the upstream pipe for the pipelines in tandem. More specifically, the two parallel pipelines have the same diameter (D_m=D_r = 0.12 m), while the distance between the two pipes is 0.24 m. It is apparent that $|\Delta u_e|$ around the upstream pipeline for twin pipelines is larger than that in the vicinity of a single pipeline. In addition, the author and her co-workers assessed the effect of the relative buried depth (d_t/D_m) on the soil response around the upstream pipeline for the two tandem pipelines (D_m=D_r = 0.14 m), where the distance between the two pipes is 0.28 m. The comparison of $|\Delta u_e|/p_0$ profiles with respect to d_t/D_m at three test points (P4–P6) among the experimental data (Zhai et al., 2022) and the present model is illustrated in Figure 13.7. To effectively analyse the relationship between the buried depth and the pore-water pressure distribution, ten conditions of d_t/D_m were simulated with an interval of

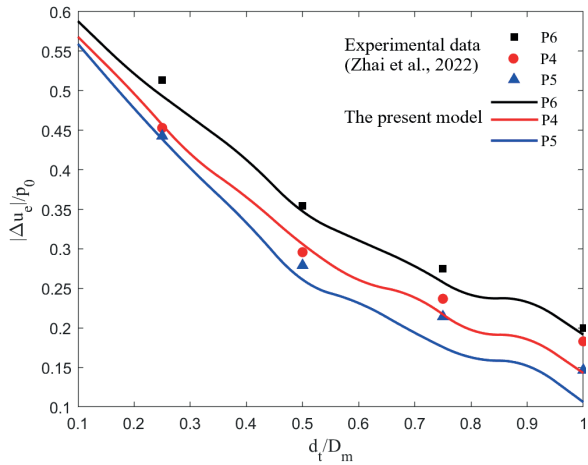

Figure 13.7 Comparison of excess pore pressure amplitude with different buried depths (d_t/D_m) at different points between the numerical results of the present model and Zhai et al. (2022)'s experimental data.

0.1. The value of $|\Delta u_e|/p_0$ decreases with increasing embedment depth, as shown in the figure. The maximum value of $|\Delta u_e|/p_0$ is found at P6, and the minimum value is observed at P5. It is also found that $|\Delta u_e|/p_0$ attenuates more at the smaller buried depth than in the case of the larger buried depth, which may be due to the effect of permeability and deformation properties of the soil. Overall agreement between the observed data and simulation results proves that the integrated model is reliable for predicting seabed response around two parallel pipelines.

13.1.3 HYDRODYNAMIC PROCESS IN THE VICINITY OF THE TRENCHED PIPELINE

The focus of the present study is to investigate the stability of trench pipelines through the proposed numerical model. A series of parametric study will be presented to show the effects of various wave and seabed characteristic as well as trench layer configuration. Based on the parametric study, the design graphs for trenched pipelines, which are based on utilizing different backfill materials, are proposed as an engineering practice. The input data including wave, current and soil characteristics used in the numerical examples are listed in Table 13.2.

The distribution of the maximum amplitude of the flow velocity (i.e. $u = \sqrt{u_x^2 + u_z^2}$, where u_x and u_z are the horizontal and vertical velocities of fluid, respectively) in the proximity of the trenched pipeline under different ocean current loading is shown in Figure 13.8. The case with $U_c = 0$ represents only a wave loading without a current, while $U_c > 0$ means that the wave travels in the direction of the current, and $U_c < 0$ means that the wave travels against the current. It is noted that the

Table 13.2
Input data for studying wave-current-seabed-trenched pipeline interactions.

Characteristics	Value	Unit
Wave characteristics		
Incident wave height (H_w)	2 or various	[m]
Mean water depth (d_w)	8 or various	[m]
Wave period (T_w)	10 or various	[s]
Wave length (L_w)	83.79 or various	[m]
Ocean current characteristics		
Current velocity (U_c)	1 or -1	[m/s]
Seabed characteristics		
Permeability (k_s)	1.0×10^{-4}	[m/s]
Poisson's ratio (μ_s)	0.33	–
Porosity (n_s)	0.425	–
Degree of saturation (S_r)	98.4	%
Shear modules (G_s)	10^7	[N/m^2]
Seabed thickness (h)	15	[m]
Seabed length (L_s)	$2L_w$	[m]
Submerged specific weight of soil (γ_s')	10.71	[kN/m^3]
Pipeline characteristics		
Young's modulus (E_p)	2.09×10^{11}	[Pa]
Pipeline diameter (D_p)	1.0	[m]
Burial depth (e)	2.3	[m]
Poisson's (μ_p)	0.32	–
Submerged specific weight of pipeline (γ_p')	15	[kN/m^3]
Trench & Backfill soil characteristics		
Permeability (k_s)	1.0×10^{-2} or various	[m/s]
Poisson's ratio (μ_s)	0.33	–
Porosity (n_s)	0.425	–
Degree of saturation (S_r)	98.4	%
Shear modules (G_s)	10^7	[N/m^2]
Trench width (W_t)	$3D_p$	[m]
Trench depth (B_t)	$3D_p$	[m]
Trench slope angle (ϕ_t)	45 or various	[deg]
Backfill thickness (H_b)	0.2 or various	[m]

reference time length for obtaining the maximum value of u is three times the wave period (T_0, the linear wave period without any existence of ocean current). The first phenomenon can be observed from the figure is the maximum value of flow velocity in the trench layer (u_1) is relatively smaller than that above the mud-line (u_2), where the ratio of u_2/u_1 is more pronounced when there is a following current. In addition,

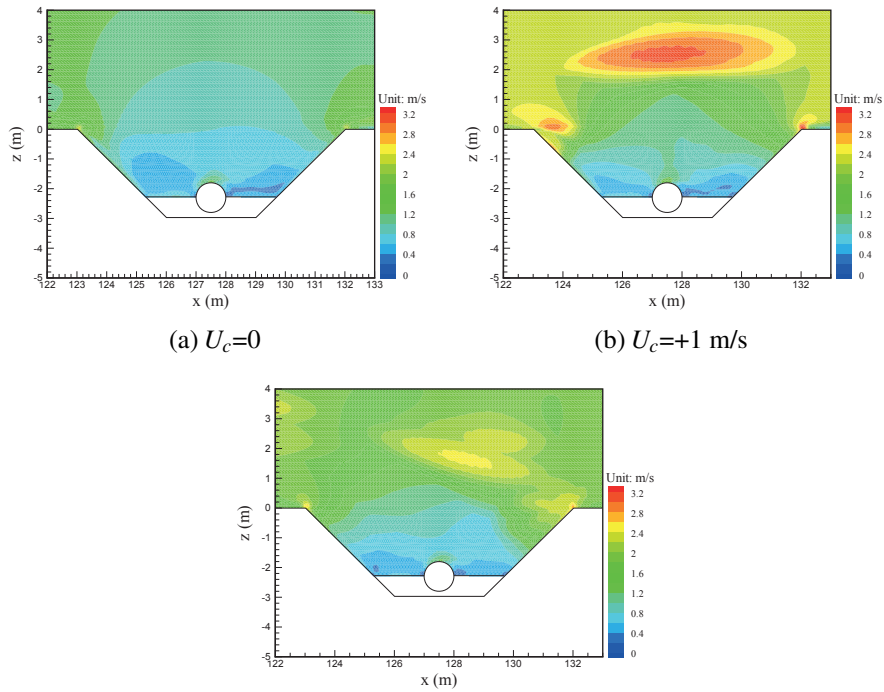

(a) U_c=0 (b) U_c=+1 m/s

(c) U_c=-1 m/s

Figure 13.8 Distributions of the maximum amplitude of the flow velocity (u) around a partially buried pipeline with different U_c during three times wave period. These results are for the cases in which H_w=2 m, T_w=10 s, d_w=8 m, H_b=0.5 m.

the distribution of flow velocity along the surface of the pipe is continuously kept constant. More specifically, it is observed that the value of u on both sides of the pipe is not higher than 0.8 m/s. However, a larger u value can be obtained near the middle of the pipe (θ ranging from 60° to 120°). As such, the flow velocity can be greatly reduced by a trench layer, but the velocity fluctuation will be more significant when a following current is involved. This rapid fluctuation is believed to associate with the oscillation of pore-water pressure in the porous seabed, which will further generate the seepage force upon the trench pipeline resulting in a non-negligible impact on the vertical stability of the pipe (Gao and Wu, 2006).

13.1.4 LIQUEFACTION AROUND A TRENCH PIPELINE

Based on the modified criterion defined in (11.10), the potential for wave-induced liquefaction around an offshore pipeline can be assessed using the developed model. Previous numerical studies have revealed soil liquefaction distributions near pipes

in a partially or fully trenched layer. In other words, the factors affecting pipeline instability in most previous studies were limited to wave, current and soil properties (Wang et al., 2000; Gao and Wu, 2006; Wen et al., 2012; Duan et al., 2017). Nevertheless, the configuration of the trench layer and the self-weight of pipe are also vital, but their influences have not been well documented in the literature. Therefore, when discussing the interactions between ocean currents and waves with different parameters, the effects of ditches and pipe weights will be considered in this section. Besides, the potential of soil liquefaction near the trenched pipeline will be further explored by presenting the flow field at the same time.

Note that when discussing the development of soil liquefaction in cases involving the ocean currents, the soil permeability (k_s) of seabed is all 10^{-4} m/s unless specified, while the k_s of backfill materials can vary from 5.0×10^{-5} to 5.0×10^{-4} m/s. At the same time, when studying the effects of ocean currents on the various wave, soil and trench parameters, the ocean currents are defined as co-currents with a velocity of 1 m/s. In the following section, we first discuss the effects of each variable on the distribution of both flow field and liquefaction zone without considering the pipe's self-weight. Finally, the assessment of the influence of the pipe's self-weight on preventing soil liquefaction from around the foundation will be discussed.

A. Effect of hydrodynamic parameters

Herein, the soil permeability (k_s) of the seabed and the backfill materials are equal to 10^{-4} m/s. Figure 13.9 presents the distribution of the flow field around the partially buried pipeline under three current velocities (U_c= -1 m/s, 0, 1 m/s). As shown in the figure, a significant vortex may exist in the lateral sides of the partially buried pipeline due to the steady current leading to a larger pressure gradient. As seen, more intense hydraulic loads can penetrate the backfill layer under the combined interaction of the propagating wave and the following current. However, a wave propagating against the current could prevent this kind of penetration. Furthermore, the liquefaction depth in the vicinity of the offshore pipeline is more significant under the combined wave and the following current. While the opposing current can prevent the marine structure from wave damage, it also maintains its stability. Note that: the solid pink line indicates the condition by considering the effect of the pipe's self-weight, while the purple dashed line indicates the influence of the pipe's self-weight is exclusive.

In general, it is important to predict the seabed stability around a buried pipeline by the on-site wave characteristics (Jeng and Lin, 1999). More specifically, the wave height (H_w) can directly affect the wave forces on the seabed, and the water depth (d_w) and wave period (T_w) can affect the pore-water pressure and effective stresses in the seabed by affecting the wavelength (L_w). As shown in Figure 13.10, the liquefaction depth around the partially trenched pipeline increases as both H_w and T_w increase, while there is a negative relationship between the liquefaction depth and d_w.

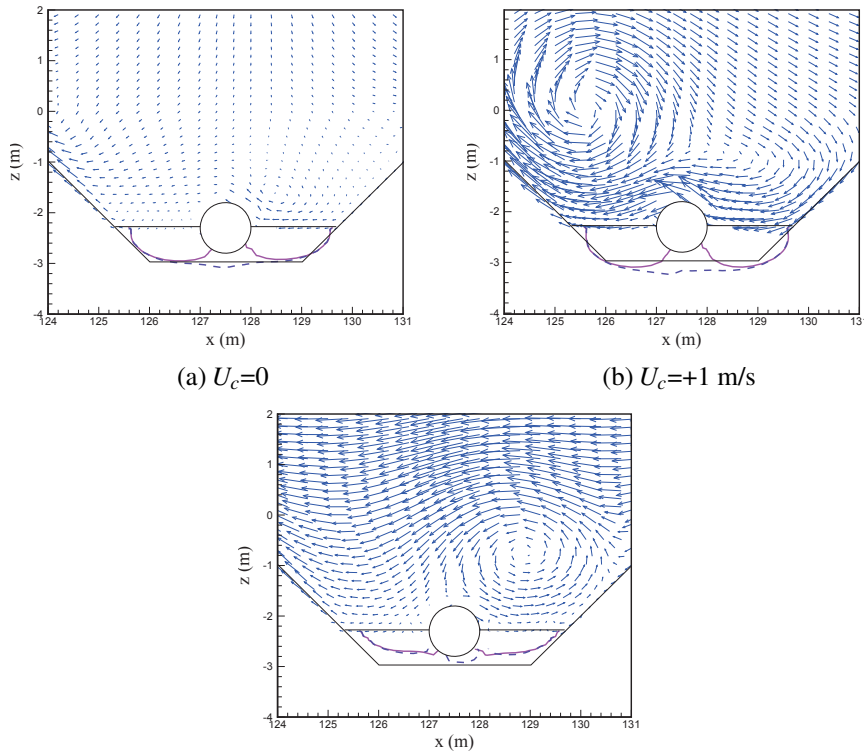

Figure 13.9 Variations of the flow field and the liquefaction depth around a partially buried pipeline with different U_c near the wave troughs at t/T_w= 4.06, 3.92 and 4.28, respectively. These results are for the cases in which H_w=2 m, T_w=10 s, d_w=8 m, k_s=1.0×10^{-4} m/s, S_r=0.984, H_b=0.5 m.

B. Effect of property of backfill sand

In engineering practice, offshore pipelines are designed to be trenched and buried with coarser materials for reducing hydrodynamic loads, especially in shallow water. Besides, the backfill materials can be selected from cut materials. Their properties are the same as that of the seabed foundation when the trench is cut by the mechanical digging chains. Alternatively, the trenches along the pipeline route can be filled by the natural accretion soon after completion of the trenching under harsh environmental conditions. In this case, the backfill material is considered to be fine sand, its mass is relatively lighter, and the coefficient soil permeability between the particles is generally small. As shown in Figure 13.11, the liquefaction depth increases with the decrease of both k_s and S_r. Notably, as the value of k_s rise from 5×10^{-5} to 5×10^{-4} m/s, the development of soil liquefaction zone is reduced markedly. Likewise, the influence of S_r on such a tendency is at a slower rate. This

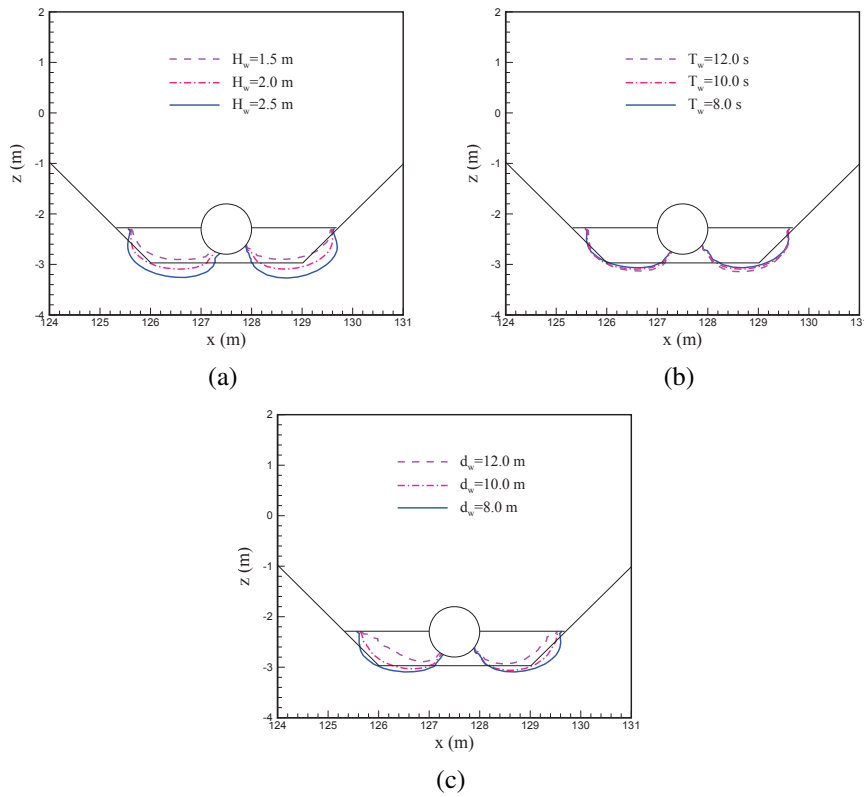

Figure 13.10 Distributions of the liquefaction depth with the effect of pipe's self-weight around a partially buried pipeline for various values of (a) wave height (H_w); (b) wave period, (T_w) and (c) water depth (d_w) under the combined wave and steady current (U_c=1 m/s) loading near the wave troughs at the specific time step.

means that the variation of k_s has less impact on the generation of soil liquefaction than does the S_r around an offshore pipeline constructed not only on the seafloor but also in a trenched layer.

Apart from the soil permeability and degree of saturation, the geometry of the trench pipeline is also considered as an important factor for coastal engineers. In this study, the backfilled thickness of trench (H_b) and the trench slope (ϕ_t) are examined here to understand their influence on the seabed stability as shown in Figures 13.12 and 13.13, respectively. Based on simulation results, the vortex within the trench becomes more intense with the decrease of the H_b. In other words, the amplitude of velocity is inversely proportional to the decreasing H_b. Moreover, the liquefaction depth extends approximately to a depth of up to about $1D_p$ without the influence of the pipe's self-weight. As for ϕ_t, it was unexpectedly observed that due to the reduced protection of the open trenches, there are non-negligible eddy currents on both sides

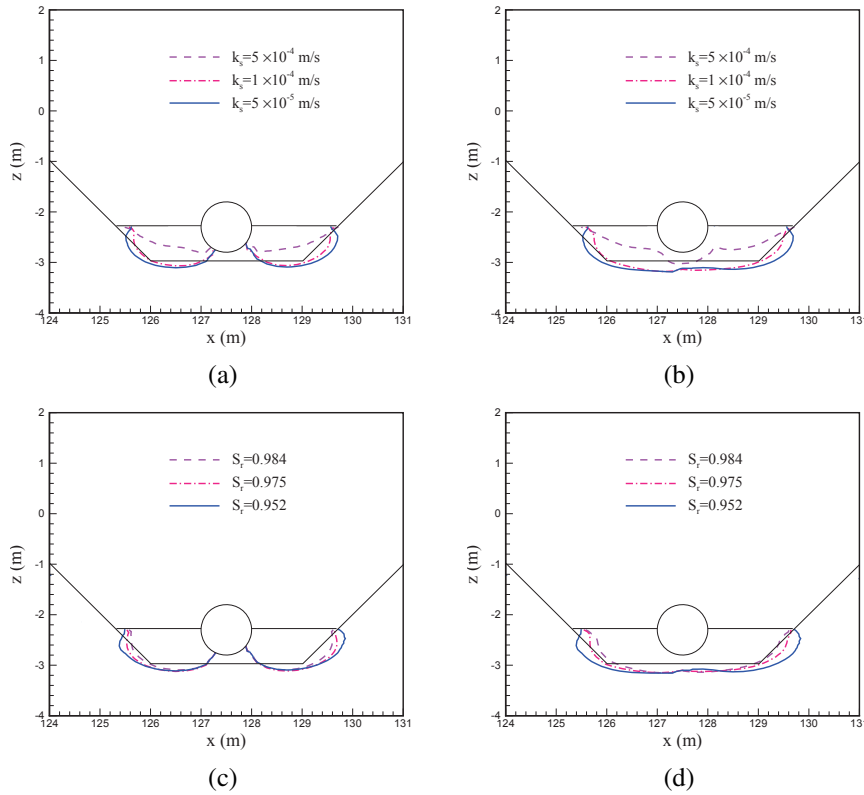

Figure 13.11 Distributions of the liquefaction depth around a partially buried pipeline for different soil conditions: (a)&(b) soil permeability, k_s; (c)&(d) degree of saturation, S_r under the combined wave and steady current (U_c=1 m/s) loading near the wave troughs at the specific time step. Note that: the diagram on the left (i.e., (a) & (c)) indicates the effect of considering the self-weight of the pipe on the liquefaction development, while the diagram on the right (i.e., (b) & (d)) shows the liquefaction depth without the impact of self-weight of the pipe.

of the pipe, since ϕ_t is reduced. It is also interesting to note that the mentioned eddy currents only accumulate above the pipe. Besides, the velocity amplitude within the area between the top of the pipe and the backfill surface is very small. Consequently, the liquefaction depth is reduced with an increase of ϕ_t, and its distribution on both sides is more symmetrical when ϕ_t is equal to 30°.

C. Effect of self-weight of pipe

As reported in the literature (Christian et al., 1974), the self-weight of the pipeline has a positive protective effect on the inhibition of soil liquefaction near the pipeline foundation. Similarly, this benefit of offshore pipelines in the trench layer can also be obtained to some extent. In other words, the greater amplitude of H_w, T_w and the

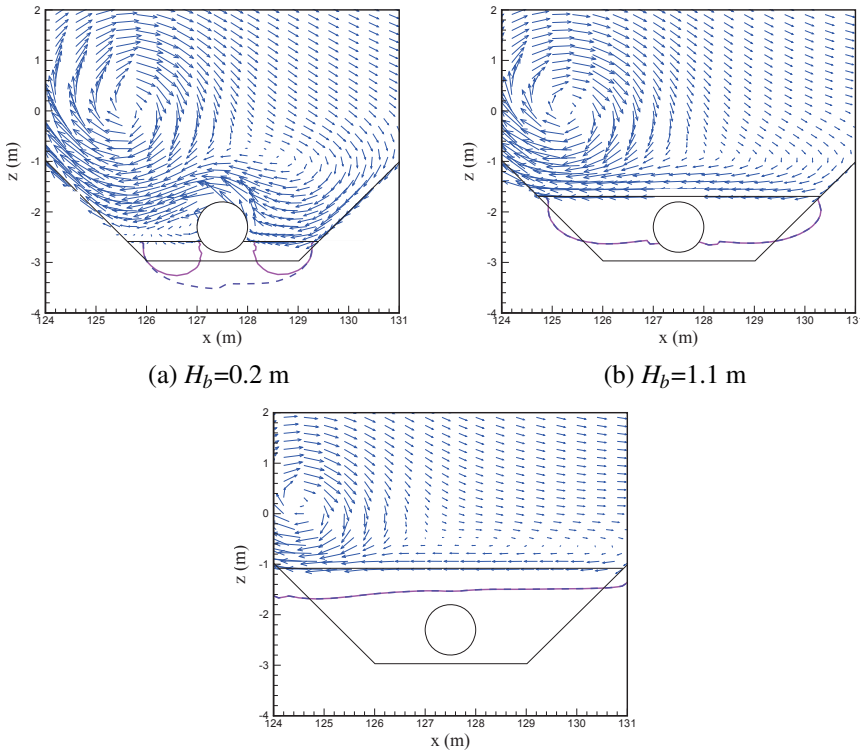

(a) H_b=0.2 m (b) H_b=1.1 m

(c) H_b=1.7 m

Figure 13.12 Distributions of the liquefaction depth around a partially buried pipeline for different trench thickness (H_b) under the combined wave and steady current (U_c=1 m/s) loading near the wave troughs at the specific time step. Note that: the solid pink line indicates the effect of the pipe's self-weight, while the purple dashed line indicates that the pipe's self-weight is not considered.

smaller amount of d_w, k_s and S_r leads to a greater depth of soil liquefaction, which can be offset by the weight of the pipe. However, as the ϕ_t increases, the effect of the pipe's self-weight will gradually become insignificant. In addition, when the H_b is smaller than $0.5D_p$, the pipe with a relatively large specific weight will sink due to the occurrence of soil liquefaction. Nevertheless, when the H_b is greater than $1D_p$, the effect of the pipe's self-weight is negligible because the backfill's own weight provides adequate protection to the bottom of the pipe.

In addition, the pipelines can sink into seabed when its specific weight is larger than that of nearby liquefied deposit (Sumer et al., 1999, 2006). A larger liquefaction depth can be obtained at lateral sides of the pipe with less thickness of backfill. This is exemplified in Figure 13.10(a) when H_w equals 2.5 m, indicating a limited area between the pipe surface and foundation is under temporary stabilization. In fact,

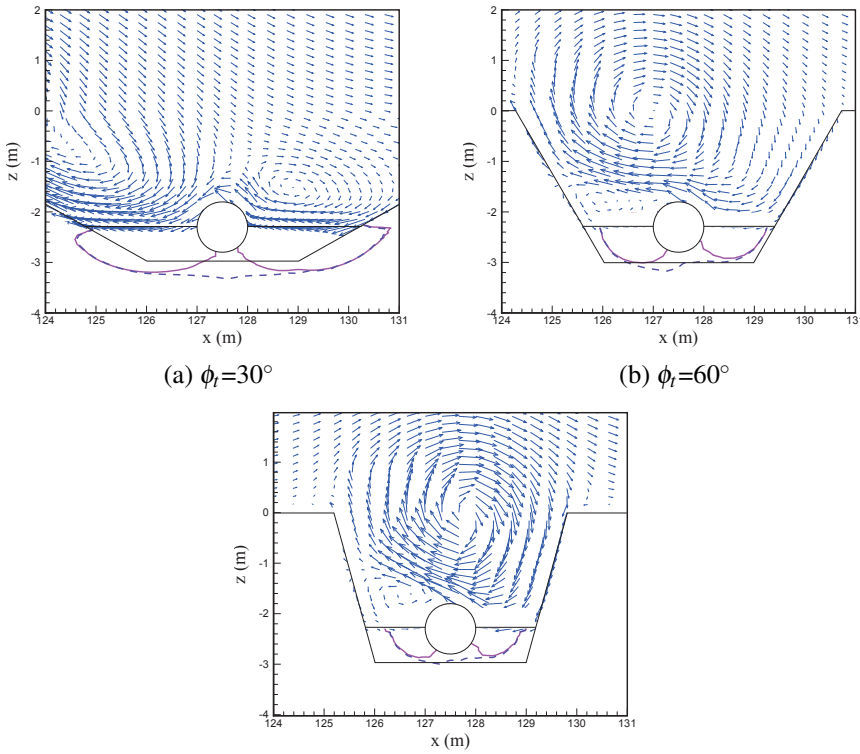

Figure 13.13 Distributions of the liquefaction depth around a partially buried pipeline for different trench slope (ϕ_t) under the combined wave and steady current (U_c=1 m/s) loading near the wave troughs at the specific time step. Note that: the solid pink line indicates the effect of the pipe's self-weight, while the purple dashed line indicates that the pipe's self-weight is not considered.

further serious hazard, namely, shear failure, can be triggered in this area due to the static loading of pipe and the cyclic combined loading of waves and currents.

Note that the above discussions are based on the momentary liquefaction around a pipeline in a trench layer. For the residual liquefaction, readers can refer to Zhao et al. (2022).

13.1.5 DESIGN OF A TRENCH LAYER

To provide sufficient protection against potential damage from trawler nets and anchors, and to allow for the expected variations at seabed levels owing to sand movement, the pipelines are fully/partially trenched into the seabed. Therefore, two feasible options for engineers are chosen:

- *Option(1)*: A fully trenched layer with gravel covers the pipeline
- *Option(2)*: A partial backfill in a trench layer covers the pipeline

Notably, the advantage of using gravels is that its material is highly permeable so that the pore-water pressure in it induced by the waves and currents will be dissipated rapidly. Also, the region beneath the pipe is less likely to be liquefied, which can benefit from the self-weight pressure of the upper part of the gravel. For the purpose of reducing the amount of construction work, the trench is usually backfilled with the excavated material or the in-situ sediment. However, such a method often does not protect the pipeline from liquefaction due to the quality of excavated material. More specifically, the sediment which is in a loose state, may be susceptible to liquefaction under waves and currents.

Herein, we focus on the stability of pipeline in a trenched layer where momentary liquefaction may occur due to the waves and currents. From the preceding review and parametric study, the questions for engineers are: (1) What kind of backfill material is more economical to be applied to the construction site? (2) What is the critical backfill thickness which should be obtained to protect the bottom of the pipe from liquefaction by using different backfill material?

Based on the above parametric study, the critical backfill thickness (H_{bc}) is related to the flow characteristics and soil properties. Along with these parameters, the wave height (H_w), the wave period (T_w), the current velocity (U_c), the backfill permeability (k_s) and the degree of seabed saturation (S_r) are all sensitive factors that control the distributions of the liquefaction depth under the partially buried pipeline; nevertheless, the numerical results indicate that the wave height (H_w) is the dominant factor.

In addition, when a smaller backfill thickness is required, the influence of the pipe's self-weight can additionally increase its stability. In other words, when the trenched pipeline is under severe weather conditions, maintaining its stability can increase the backfill thickness, not just rely on its self-weight. On the other hand, offshore pipelines should use materials with lower density whenever possible in engineering applications, thereby reducing construction difficulty and budget. Therefore, the influence of the pipe's self-weight is excluded in the following discussion about the design of the critical backfill thickness.

To determine H_{bc} under given external loading, a regression method with the least-squares algorithm is applied to provide a method of estimating the critical backfill thickness. However, compared to the previous studies (Zhao and Jeng, 2016; Duan et al., 2017), a quadratic function including two coefficients, namely, a_t and b_t, are employed as designing curve in this paper. In other words, it is more physically relevant to a real engineering practice that no requirement for H_{bc} when H_w equals to 0. Thereby, c_t equalling 0 is considered here.

A. Momentary liquefaction

Herein, we consider the momentary liquefaction around a partial buried pipeline in a trench layer. As shown in the above numerical examples, the relationship between the critical backfill thickness (H_{bc}/D_p) and the wave steepness (H_w/L_0) for various

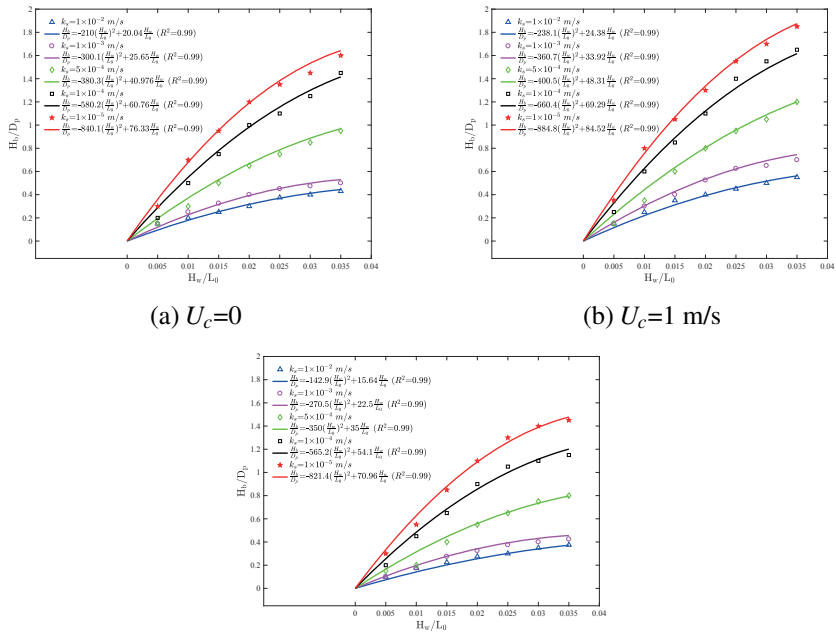

(a) U_c=0 (b) U_c=1 m/s

(c) U_c=-1 m/s

Figure 13.14 Distributions of the critical backfill thickness (H_{bc}/D_p) versus wave steepness (H/L_0) for soil permeability (k_s) under various wave and current conditions.

current velocities based on the numerical results of this study is illustrated in Figure 13.14, and can be expressed as

$$\frac{H_{bc}}{D_p} = a_t \left(\frac{H_w}{L_0}\right)^2 + b_t \left(\frac{H_w}{L_0}\right), \tag{13.2}$$

in which L_0 is the linear wavelength without a current.

The coefficients a_t and b_t for various soil permeability are plotted in Figure 13.15, in which the critical backfill thickness is linked to the soil properties. Therefore, the design process of the critical backfill thickness for a specific offshore pipeline in a trench layer can be estimated in the following steps:

(1) Under the ocean current conditions (U_c) and the selection of feasible backfill materials (k_s), the two coefficients (a_t and b_t) can be determined from the Figure 13.15;
(2) With the coefficients (a_t and b_t) obtained in step (1), the relationship between H_{bc}/D_p and H_w/L_0 can be obtained from (13.2);
(3) Substituting the values of H_w/L_0 and H_{bc}/D_p, the critical backfill thickness (H_{bc}) can be obtained by choosing different backfill materials. Thereby,

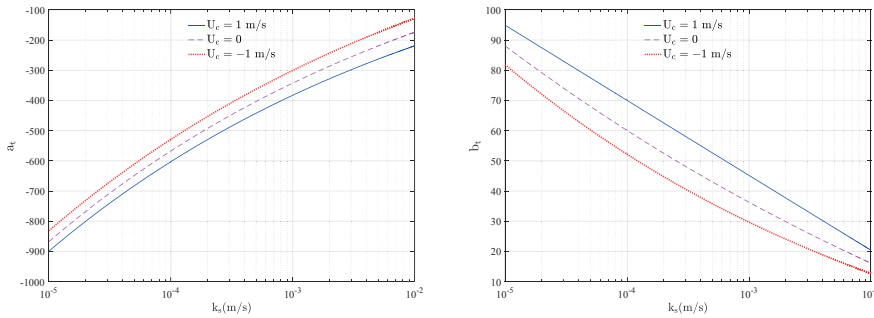

(a) Coefficient a_t (b) Coefficient b_t

Figure 13.15 Coefficients a_t and b_t for different soil permeabilities (k_s) from 1×10^{-5} m/s to 1×10^{-2} m/s in a specific increment.

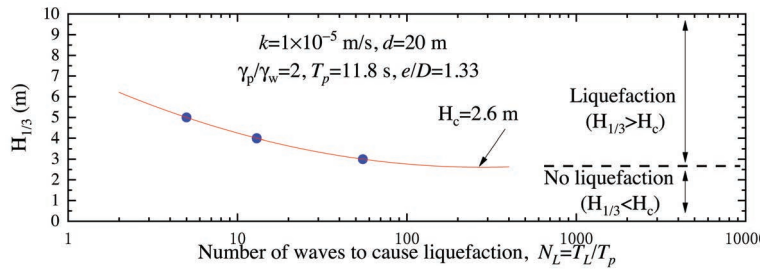

Figure 13.16 The number of waves needed to cause liquefaction at the pipe bottom as a function of wave height.

coastal engineers can propose the most suitable backfill material to protect the trenched pipeline based on site conditions and environmental factors.

B. Residual liquefaction

Herein, based on the parametric study presented in Zhao et al. (2022), we proposed a methodology of the design of a trench layer for the residual liquefaction.

Figure 13.16 shows the number of waves required to initiate liquefaction at the pipe bottom as a function of wave height. Obviously, the smaller the waves, the less cyclic shear stress will be generated in the seabed soil, and the longer duration of ocean storms is needed to cause liquefaction. As with the experimental findings of de Alba et al. (1976) and Sumer et al. (1999), as the number of irregular waves increases, the wave height that affects the shear stress to cause liquefaction tends to be an asymptotic value below which liquefaction no longer occurs. Remember that the pipe specific gravity may vary according to operational requirements. Figure 13.17 shows how the normalised specific gravity of pipe (γ_p/γ_w), the normalised burial depth (e/D), and the drainage condition of backfilling material (k), will affect

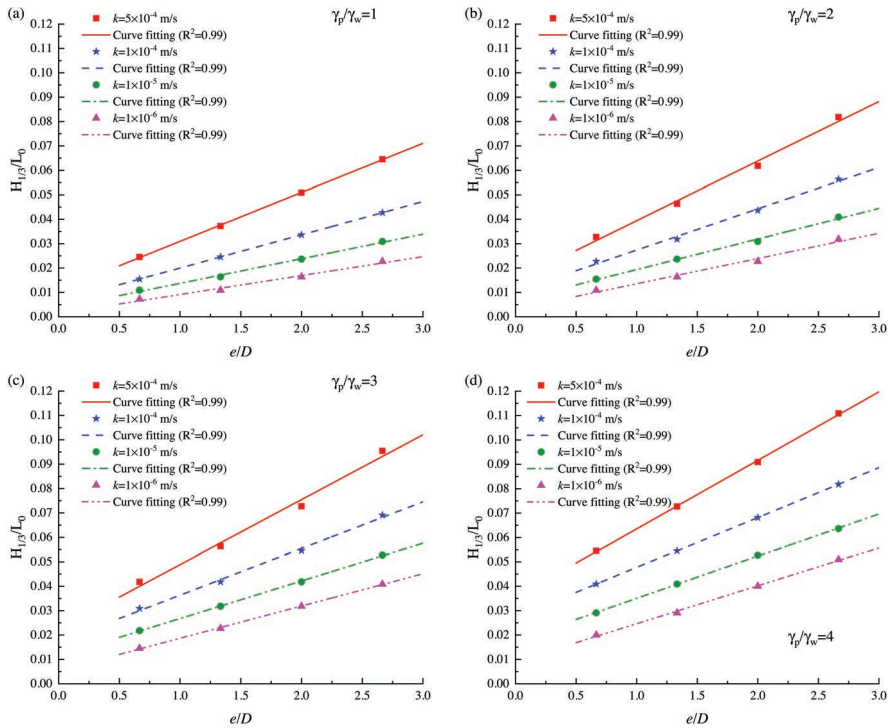

Figure 13.17 The relationship between normalised critical wave height and normalised pipe burial depth.

the normalised critical value of wave heights (H_c/L_0) that are large enough to trigger liquefaction. It is predicted that for each value of γ_p/γ_w or k there is an almost linear relationship between H_c/L_0 and e/D with a regression coefficient that is higher than 0.99. On this basis, an empirical formulation is proposed herein

$$\frac{H_c}{L_0} = a_d\left(\frac{e}{D}\right) + b_d \tag{13.3}$$

The coefficients a_d and b_d in (13.3) for various operational pipe specific gravity and drainage conditions of a trench layer are plotted in Figure 13.18. With this design chart and the empirical formulation, (13.3), pipe engineers are able to design a trench layer by controlling the drainage condition of the backfilling material with the following procedures:

1. For specific operational pipe gravity, select feasible backfilling material and then determine the two coefficients (a_d and b_d) from the design chart (Figure 13.18).
2. With these coefficients, the relationship between H_c/L_0 and e/D can be determined from (13.3).

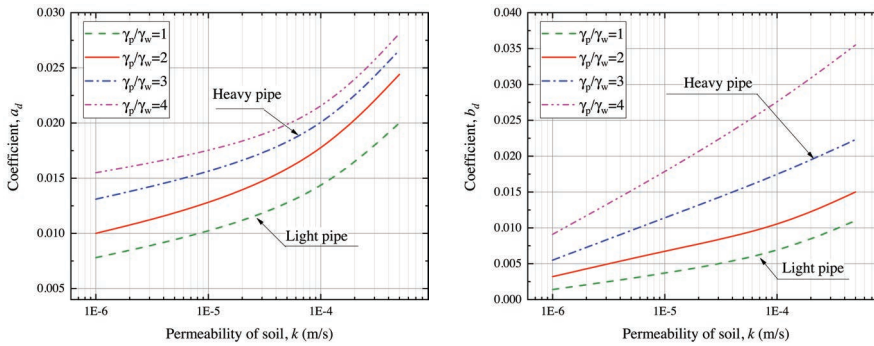

Figure 13.18 Design graphs for determining the coefficients in the empirical formulation.

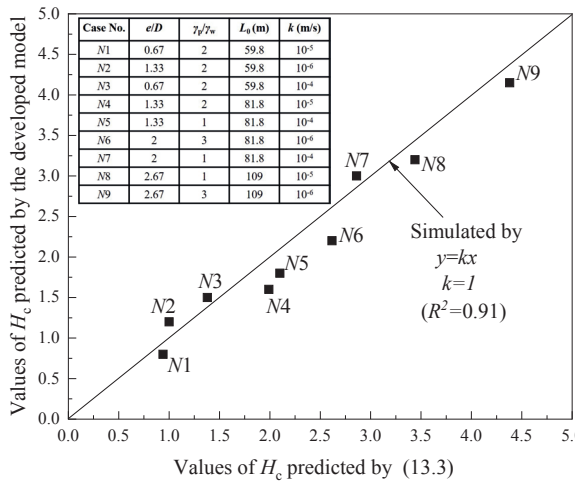

Figure 13.19 H_c predicted by (13.3) versus H_c predicted by the developed model.

3. By substituting the designed value of burial depth e/D, the critical wave steepness (H_c/L_0) needed to cause liquefaction can be determined.
4. Compare the calculated H_c/L_0 against the storm wave conditions on the candidate site to verify that the selected backfill material is capable of protecting the pipeline based on site conditions and operational requirements.

Figure 13.19 shows the relationship between empirical and numerical predictions of the critical wave height (H_c) for nine different cases with a combined variations of e/D, γ_p/γ_w, L_0 and k. It can be seen that the points of H_c predicted by (13.3) and that predicted by the developed model are basically in a straight line at an inclination of 1. This indicates that the proposed empirical equation is applicable to various site and operational conditions in predicting the critical wave steepness to meet the design requirement.

13.2 ARTICULATED CONCRETE MATTRESSES (ACMS) FOR OFFSHORE PIPELINE PROTECTION

In the last section, the effectiveness of trenches in protecting pipelines is discussed and provides valuable guidance for engineering applications. Herein, we discuss another methodology for the pipeline protection.

One of the main potential uses of concrete mattresses for pipe stabilisation is to enhance the existing weight coating system or replace the weight coating that has peeled off (Miller, 1986). At present, relevant research reports are mainly about ACMs' actual engineering cases and their hydrodynamic properties. Among them, Gaeta et al. (2011) conducted a series of small scale physical experiments to analyse the hydrodynamic coefficients for uses in determining stability analyses for the entire mattress. McLaren et al. (2016) investigated the hydrodynamic stability of ACMs with different block sizes in the fluid flow of varying incident angles. Godbold et al. (2002) reported that the primary failure mechanism for submerged concrete mattresses is due to edge lift, resulting in a catastrophic rolling.

In addition, placing the designed ACMs on the pipeline can reduce the degree of pipeline walking, which mainly occurs when there are thermal transients along the pipeline during the start-up and shutdown stages; or when the pipeline has fewer anchor points in the middle. Recently, Frankenmolen et al. (2017) reported the application of a Pipe-Clamping Mattresses (PCMs) to stop the pipeline walking in the Malampaya flowline, where the mattresses were placed on the optimum restraint location and increased the soil resistance to cyclic axial pipe movements. However, the stability of the ACMs/PCMs-Pipeline system can be reduced by the nearby flow-induced seabed scour and liquefaction. Specifically, when the pipeline alone or together with the mattress sinks into the seabed to a certain depth, the protection benefit of the concrete mattresses on the pipeline will change. Thereby, it is necessary to analyze the functional stability of the location of the ACMs-Pipeline system from the perspective of hydrodynamics and seabed conditions.

In engineering practices, there are currently several mattress stability standards, such as DNV-RP-E305 and DNV-RP-F109, which provide a reasonable method for analysing anti-erosion stability. In fact, the aforementioned code uses estimated coefficients from other marine structures to analyse hydrodynamic stability. However, due to the uncertainty in these hydrodynamic coefficients, larger safety coefficients are often chosen for mattress stability analysis, leading to unnecessary costs and inefficient designs. In addition, the analysis of seabed dynamics near ACMs under different hydrodynamic conditions is also particularly important for evaluating the effectiveness of pipeline protection. Nevertheless, none of aforementioned studies has further considered the influence of seabed response on the stability of ACMs.

In this section, we will explore the application of ACMs in the 3D wave-current-seabed-pipeline interactions (WCSPI) through theoretical analysis based on the established model (Liang and Jeng, 2021). The operating conditions are that the pipeline is laid directly on the seabed surface in deep water but is not yet ready to sink and buried into the seabed. We focus on oscillatory soil response and

the resulting instantaneous seabed liquefaction, which can occur near wave troughs, and most of the time is highly related to the seepage and sediment incipient motion (Qi and Gao, 2014; Guo et al., 2019). Thereby, this research aims to fill the current research gap of ACMs design for engineering practice by analysing the instability characteristics of the seabed foundation in the vicinity of the protected pipeline in the system mentioned above.

13.2.1 ENGINEERING PROBLEM CONSIDERED

Based the established 3D integrated numerical model (Liang and Jeng, 2022), we investigate the seabed instability around the ACMs-Pipe system. In this section, the combined effects of the wave, current and seabed together with the configuration of the marine structure on the pore-water pressure around the buried pipeline are examined. All wave and current characteristics, as well as properties of the sandy seabed and offshore pipeline, are given in Table 13.3.

This study focuses on the following contents:

(1) The WCSPI involving the concrete blocks and seabed dynamics of the nearby seafloor foundation under different environmental conditions;
(2) The stability of the seafloor foundation near the ACMs-Pipe system with different spacings under the complex environmental loadings;
(3) The effective range of ACMs for the entire system compared to the case without pipeline protection.

In the following analysis, two scenarios based on the number of layers used in the design are considered: the Single ACMs-Pipe System (SAPS) and Dual ACMs-Pipe System (DAPS), respectively. In addition, to quantify the development of seafloor liquefaction along the pipeline, several sets of dimensionless liquefaction indexes are proposed for data analysis and discussion:

- d_L and d_{LU}, are proposed to indicate the seafloor liquefaction depth of particular reference locations under the ACMs protection and unprotected conditions, respectively.
- Δd_{L12} represents the difference of d_L between the front (ACM#1) and rear (ACM#2) concrete mattresses in the dual ACMs-Pipe system (e.g., the subscript 1 and 2 represent the ACM#1 and ACM#2, respectively).
- Δd_{LU01} and Δd_{LU02} represent the difference in seafloor liquefaction depth under the protected and unprotected conditions around the two ACMs, respectively. (e.g., the subscript 0 represents unprotected condition; 1 and 2 represent the ACM#1 and ACM#2, respectively).

More importantly, dealing with a 3D numerical problem in this study, several reference arcs (O'_1 and O'_2) and planes (RP_{11}, RP_{12}, RP_{13}, RP_{14}, RP_{21}, RP_{22}, RP_{23}) are selected to evaluate the depth of seabed liquefaction (d_L and d_{LU}) at those selected locations (see Figure 13.20), which are further applied to obtain the dimensionless liquefaction indexes (including Δd_{L12}, Δd_{LU01} and Δd_{LU02}) as mentioned above.

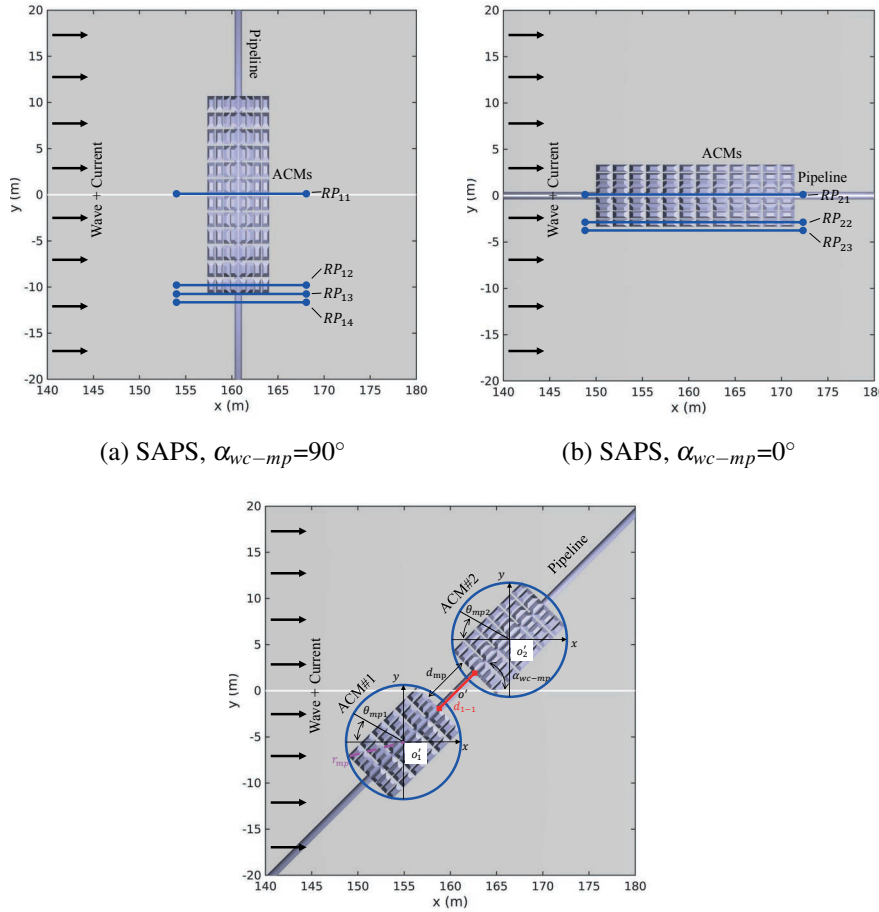

(a) SAPS, α_{wc-mp}=90°

(b) SAPS, α_{wc-mp}=0°

(c) DAPS, α_{wc-mp}=0° ∼ 90°

Figure 13.20 Computational domain with reference points and planes.

SINGLE ACMS-PIPELINE SYSTEM (SAPS)

Generally speaking, artificial concrete mattresses (ACMs) can be lowered to the seabed surface by lifting and handling devices under dynamic sea conditions one by one. Due to its high degree of flexibility, the individual concrete mattress can closely follow the contours of the pipeline or its nearby uneven seabed, forming a single ACMs-pipeline system (SAPS). For better deployment of ACMs, the assessment of the seafloor stability is conducted by concerning the SAPS firstly in the following section.

Figure 13.21 shows the distribution of combined flow field and pore pressure in the vicinity of the ACMs-pipeline system over a typical wave cycle with different

Table 13.3
Input data for studying flow-seabed-pipeline-mattress interactions.

Characteristics	Value	Unit
Fluid characteristics		
Wave height (H_w)	4, 5, 6	[m]
Water depth (d)	20	[m]
Wave period (T_w)	8, 9, 10	[s]
Current velocity (U_c)	0, 1, 2	[m/s]
Wave-current angle (α_{wc})	0	[°]
Interaction angle (α_{wc-mp})	0, 22.5, 45, 67.5, 90	[°]
Seabed characteristics		
Permeability (k_s)	10^{-4}, 5×10^{-5}, 10^{-5}	[m/s]
Poisson's ratio (μ_s)	0.33	–
Porosity (n_s)	0.425	–
Degree of saturation (S_r)	95.2, 97.5, 98.4	%
Shear modules (G_s)	10^7	[N/m2]
Submerged weight of soil (γ_s')	10.71	[kN/m^3]
Seabed thickness (h)	15	[m]
Seabed length (L_s)	100	[m]
Seabed width (W_s)	80	[m]
Mattress characteristics		
Upper length (L_{m1})	0.8	[m]
Middle length (L_{m2})	1.6	[m]
Upper width (W_{m1})	0.4	[m]
Middle width (W_{m2})	0.8	[m]
Height (H_m)	0.4	[m]
Number of block perpendicular to pipe axis (n_1)		
Number of block along pipe axis (n_2)	6, 12	[-]
Spacing (d_{mp})	4.8, 9.8, 14.4	[m]
Submerged specific weight of concrete (γ_c')	13.744	[kN/m^3]
Pipeline characteristics		
Young's modulus (E_p)	2.09×10^{11}	[Pa]
Pipeline diameter (D_p)	0.8	[m]
Burial depth (e)	0.4	[m]

time steps along the reference plane RP_{11} (see Figure 13.20(a)). It is noted that the direction of the arrow represents the movement of the fluid, and the flow velocity is displayed in different colours within the range of 0 to 1.2 m/s. As shown in Figure 13.21(a)–(e), the velocity of the near-bottom fluid is evenly distributed along the wave propagation direction, and the velocity will not increase until it encounters an obstacle in the concrete mattress. In this time step, more significant flow rates can be distributed in the front, middle, and rear ACMs, with the most significant increase in the flow rate above the pipe. On the other hand, when the crests and troughs appear alternately, the flow velocity near the ACMs will decrease. At the same time, eddy currents of different sizes will be generated in the gap between the adjacent mattress,

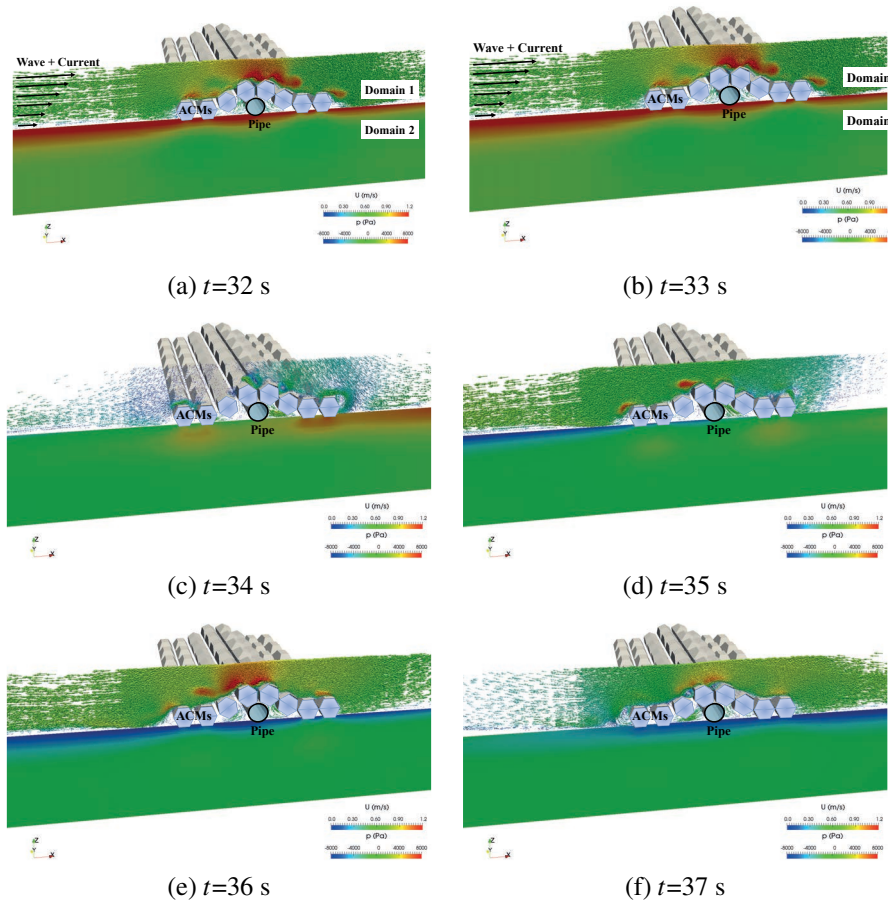

Figure 13.21 The spatial distributions of the combined flow (U_m) and pore-water pressure (p_s) fields around the ACMs-pipeline system over time (H_w=4 m, T_w=10 s, d=20 m, U_c=0 m/s, k_s=10^{-4} m/s, S_r=0.984 and α_{wc-mp}=90°).

as shown in Figure 13.21(c)-(f). As far as the variation of pore pressure is concerned, it can be observed that the vertical range is distributed about one times the depth of the pipe diameter (D_p).

Figure 13.22 shows the simulation results from the fluid and seabed sub-models, specifically showing the flow field near the ACMs as well as the seabed liquefaction depth beneath the seabed foundation under different ocean current velocities. Note that the solid lines of different colours are used to indicate the d_L at three various planes (including RP_{12}, RP_{13} and RP_{14} as shown in Figure 13.20(a)) along the propagating direction of the combined wave and current loading. Also, the cover range of ACMs along the $y-$ axis is between -10.1 m and 10.1 m. In particular, the xz planes at y= -9.9 m is located precisely in the middle of the edge unit block,

whereas the xz planes at y= -10.9 m and -11.9 m are areas away from the edge of the concrete mattress.

As seen in Figure 13.22, three main findings are obtained.

- The direction of wave velocity is offshore when the trough passes. Whiles the velocity direction gradually changes to shoreward as the ocean current velocity (U_c) increases.
- Under the protection of ACMs, the instantaneous liquefaction depth beneath the foundation gradually increases vertically and horizontally as it moves away from its covering position, and this trend becomes more significant with a larger value of U_c.
- The difference in terms of the variation of d_L around a pipeline without any protection (the black dashed line in the figure) and that of RP_{14} (blue solid line) is relatively close at a lower ocean current velocity, while the difference between these two cases can reach 50% under high-velocity conditions (i.e., U_c=2 m/s).

Therefore, it can be expected that the seafloor stability of ACMs will gradually decrease with the increase of ocean current velocity, and the first will begin to lose stability from the edge area.

Notably, there is a different scenario of wave-current-induced seafloor instability along the axis of the pipeline (i.e., α_{wc-mp}=0°). Concerning this, the combined flow field and the instantaneous seabed liquefaction depth around the ACMs-pipeline system in the specific reference planes along or in parallel with the axis of the pipeline are presented in Figure 13.20(b). Similarly, the places including the central axis of the pipeline (RP_{21}) and the concrete unit block at the edge of the protective layer (RP_{22}), as well as the lateral side away from its edge (RP_{23}) are chosen as the reference planes. By comparing, the configuration of the ACMs-pipeline system has less impact on the variation of the flow field compared to previous cases with α_{wc-mp} equalling 90° as shown in Figure 13.22. Nevertheless, the formation of vortices is observed at both ends of the lateral protective layer, and its size becomes more pronounced as the thickness of the stone protective layer increases at the RP_{21} at y=0.

Regarding the instantaneous seabed liquefaction depth, it can be evaluated into two sections located on the lateral sides of the ACMs-pipeline system (i.e., the upstream and downstream ends) and the area covered by the ACMs (in the range between 150.6 m $< x <$ 171 m). As seen, no instantaneous liquefaction occurs in the inner area protected by the ACMs, whereas only a limited scope of liquefaction occurs at both ends of the wave direction. As it moves away from the central axis (namely y= 0), the d_L gradually increases and further develops along the bottom of the ACMs-pipeline system. As a result, the row of concrete block units near their edges will sink further. Overall, the disturbance of the protective layer to the nearby flow field is relatively low when α_{wc-mp}=90°. Other than that, the difference of d_L near the edge of the ACMs and along the axis of pipeline under the unprotected working condition is relatively smaller even at high ocean current velocities in the case with α_{wc-mp}=0°.

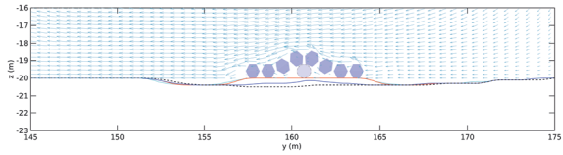

(a) U_c=0

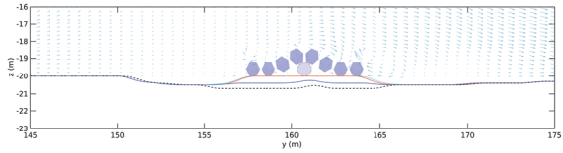

(b) U_c=1 m/s

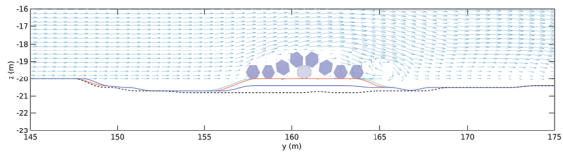

(c) U_c=2 m/s

Figure 13.22 Distributions of the flow field and the depth of instantaneous seabed liquefaction (d_L and d_{LU}) for ACMs-pipeline system with various ocean currents at four reference planes (RP_{11}, RP_{12}, RP_{13} and RP_{14} referred to Figure 13.20(a)). —: with ACMs, RP_{12}, y=-9.9 m; —: with ACMs, RP_{13}, y=-10.9 m; —: with ACMs, RP_{14}, y=-11.9 m; - - -: unprotected, RP_{11}, y=0 m. (H_w=4 m, T_w=8 s, d=20 m and α_{wc-mp}=90°).

13.2.2 DUAL ACMS-PIPELINE SYSTEM (DAPS)

To be more economically, sections of the offshore pipeline are protected by ACMs, forming a dual ACMs-pipeline system rather than designed to cover the entire pipeline longitudinally. From another point of view, sections of the pipeline which are out of the shield from ACMs may still undergo a status of the unprotected condition, generating a high potential of seafloor liquefaction. As the spacing increases, the liquefaction depth under the unprotected pipeline varies. Therefore, the pipelines at different locations will form free spans with various depths due to seabed erosion. Under the coupling interaction of different hydrodynamic conditions, vortex-induced vibration will be further induced, which will endanger the structural safety of the pipeline. In other words, the stability of the pipeline itself can be regarded as a function of the liquefaction depth and the mattress spacing along the axis of the pipeline. Therefore, it is also necessary to design proper mattress spacing to avoid excessive dangling of the pipeline and triggering vortex-induced vibration; and suppress the flow-induced lateral movement of the pipeline. For a better understanding of the influence of mattress spacing (d_{mp}) on the development of seafloor liquefaction, three different d_{mp} (ranges from 3 to 9 m with an interval of 3 m) are selected to evaluate in the following discussion.

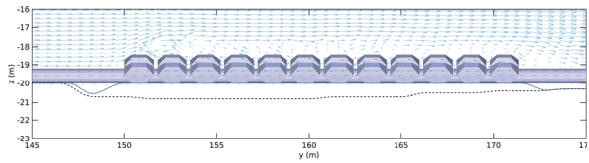

(a) RP_{21}, y=0 m

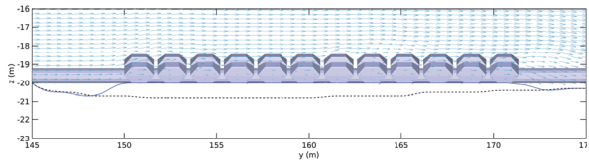

(b) RP_{22}, y=-2.95 m

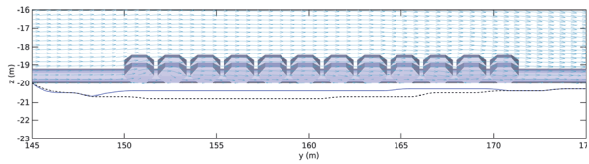

(c) RP_{23}, y=-3.85 m

Figure 13.23 Distributions of the flow field and the depth of instantaneous seabed liquefaction (d_L and d_{LU}) for ACMs-pipeline system at three reference planes (RP_{21}, RP_{22} and RP_{23} referred to Figure 13.20(b)). —: with ACMs; - - -: unprotected. (H_w=4 m, T_w=8 s, d=20 m, U_c=2 m/s and α_{wc-mp}=0°).

Figure 13.24 shows the distribution of instantaneous seabed liquefaction depth (d_L) for various mattress spacing (d_{mp}) over four different time steps. At the same time, the d_{LU} of the cases without any protection under the same hydrodynamic and seabed conditions are also added for comparison. Through data analysis, it can be observed that after the d_L reaches its maximum value at a certain moment, its distribution curve and the boundary of the seabed surface form a closed inverted trapezoid shape. At other subsequent time steps, the curve of d_L showed a bumpy oscillation distribution near the mattresses, which may be attributed to the influence of the lateral individual mattress on the alteration of the nearby flow field. In addition, the effect of ACMs on inhibiting the occurrence of seafloor liquefaction beneath the seabed foundation near the pipeline weakens significantly as the d_{mp} increases. Specifically, the distribution of d_L after being more than two times the pipe diameter (D_p) from the mattress is constant, and the corresponding d_L is the same as the d_{LU} which is obtained from the case without protection.

Figure 13.25 presents the maximum dimensionless seabed liquefaction depth (d_L/D_p) with different mattress spacings and environmental conditions. Specifically, the dimensionless value of d_L/D_p is evaluated at the reference point in the center of the ACMs-pipeline system (i.e., O'=(160.7 0 -20)). As seen, the d_L/D_p gradually

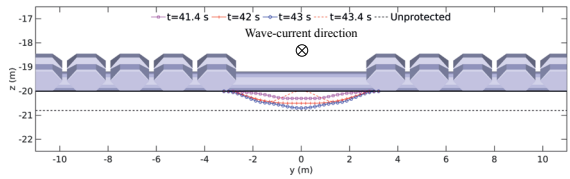

(a) d_{mp}=6D_p

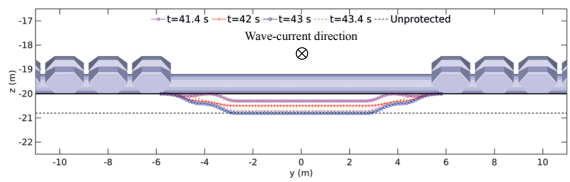

(b) d_{mp}=12D_p

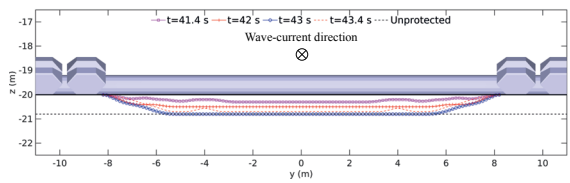

(c) d_{mp}=18D_p

Figure 13.24 Distributions of the instantaneous seabed liquefaction depth along the axis of pipeline under ACM protection (d_L) and unprotected condition (d_{LU}) at the yz plane with various d_{mp} at four time steps (when H_w=4 m, T_w=8 s, d=20 m, U_c= 2 m/s, α_{wc}=0°, α_{wc-mp}=90°, S_r=0.984 and k_s=10^{-4} m/s). Note: the propagating direction of wave-current is perpendicular to the plane of the figure.

increases as the mattress spacing increases. Roughly until the spacing distance is equalling 18D_p, the d_L/D_p is the same as the unprotected case, indicating that the mattress spacing has a certain protection range for the underlying pipeline. By comparing the impact of changes in various environmental factors on seabed liquefaction, it can also be observed that the influence of wave height and soil permeability on the changes of d_L/D_p is greater than that of the other two factors (ie, wave period and saturation). To be more specific, the value of d_L/D_p varies significantly as the H and k_s change separately from 4 m to 6 m and 10^{-4} m/s to 10^{-5} m/s for carious mattress spacings. However, when d_{mp} is equal to 12D_p, the change of d_L/D_p remains roughly unchanged for different wave periods and saturation. In engineering practice, it can be concluded that the wave height and soil permeability can be regarded as two of dominant factors in the stability design of the ACMs-piping system on the sandy seabed.

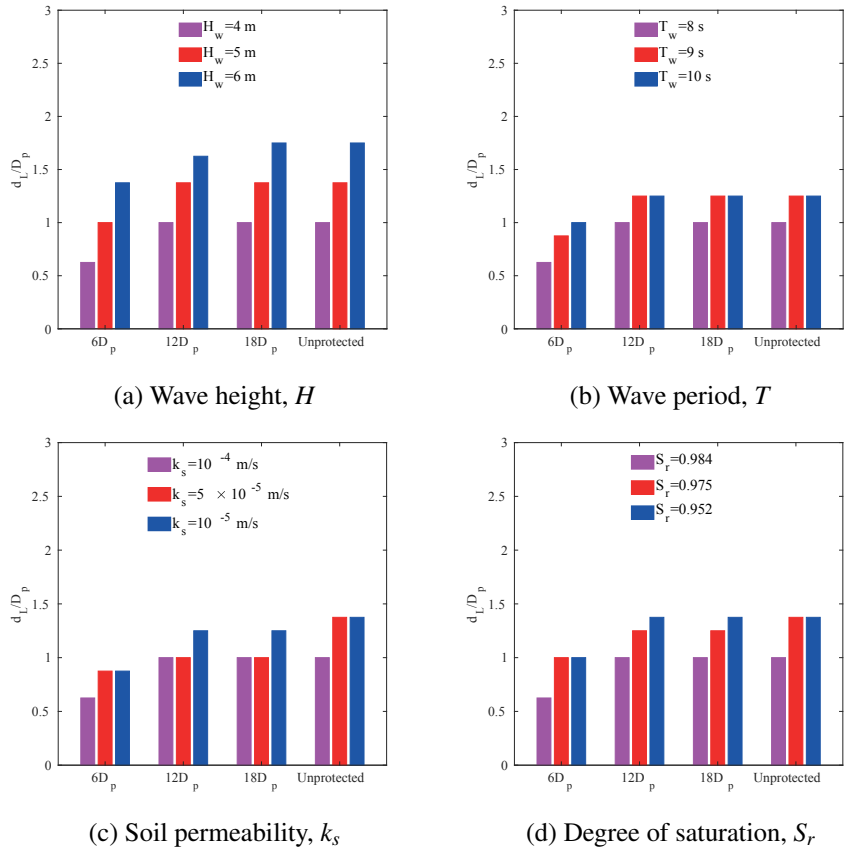

(a) Wave height, H

(b) Wave period, T

(c) Soil permeability, k_s

(d) Degree of saturation, S_r

Figure 13.25 Distributions of the dimensionless flow-induced seabed liquefaction depth (d_L) against various mattress spacings (d_{mp}) at the reference point O'= (160.4 0 -20) of a dual ACMs-pipe system for various environmental conditions (U_c=2 m/s, d=20 m, α_{wc}=0°, and α_{wc-mp}=90°).

13.2.3 EFFECTS OF VARIOUS INTERACTION ANGLES ON THE SEABED LIQUEFACTION

Figure 13.26 displays the spatial distribution of instantaneous seabed liquefaction depth around a dual ACMs-pipeline system with d_{mp}=6D_p under various interaction angles (α_{wc-mp} ranging from 22.5° to 90°) at t=49 s. For a better illustration, a white solid line is provided in each sub-figure of Figure 13.26. With this, the interaction angle (α_{wc-mp}) can be illustrated as the intersection angle between the above-mentioned reference line and the axis of the pipeline, which increases anticlockwise. As shown, the existence of the ACMs-pipeline system obviously alters its nearby spatial distribution of instantaneous seabed liquefaction depth to various degrees under different α_{wc-mp}. Notably, the positive influence of concrete

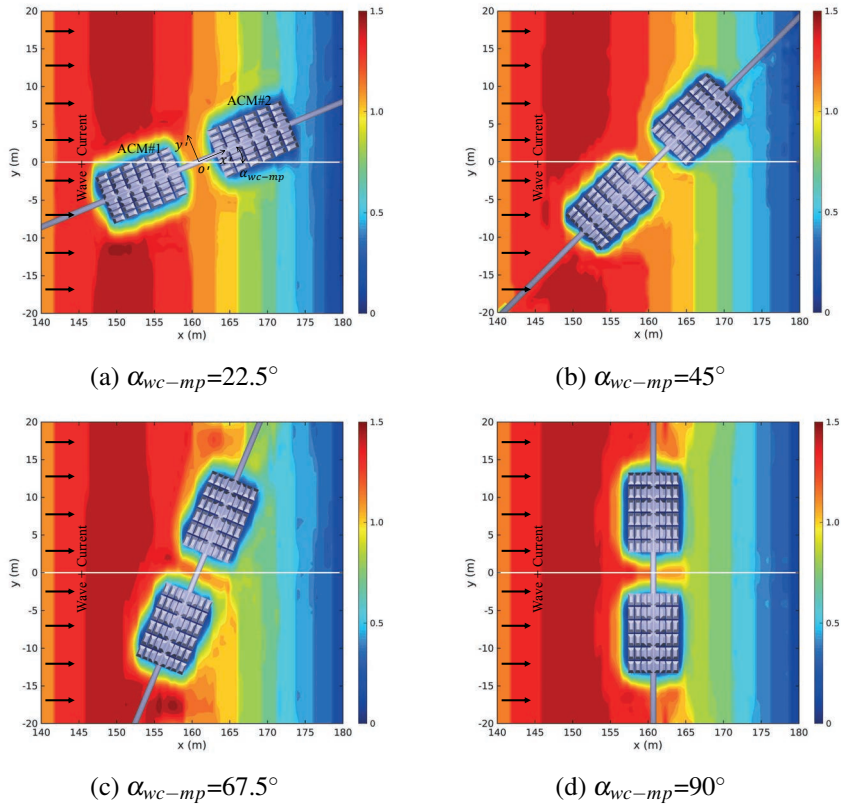

Figure 13.26 Spatial distributions of the the flow-induced seabed liquefaction depth (d_L) near a dual ACMs-pipeline system with a fixed mattress spacing (d_{mp}=6D_p) for various interaction angles (α_{wc-mp}) when H_w=6 m, T_w=8 s, U_c= 2 m/s and d=20 m.

mattresses on the inhabitation of seafloor liquefaction can be attributed to its self-weight on stabilization as well as its perturbation on the passing flow. The latter phenomenon can be clearly observed in the lateral edges of the front mattress when α_{wc-mp} less than 45°. On the other hand, when α_{wc-mp} equalling to 90°, the contour lines of the seabed liquefaction depth at the far end of the left and right individual mattresses are gradually be distributed as an arc. In addition, even if the inner uncover area is in a liquefaction state, the contour line of seabed liquefaction depth at the upstream of the whole system is still roughly distributed in a straight vertical line owing to smaller d_{mp}.

Figure 13.27 illustrates the distributions of maximum dimensionless seabed liquefaction depth (d_L/d_{LU}) along with the axis of pipeline against various interaction angles (α_{wc-mp}) for different mattress spacing (d_{mp}). Note that the pipeline axis rotates around the fixed middle point, which is located at (160.7, 0, -20) in the ranges from 22.5° to 90°. When $d_L/d_{LU} = 1$, the influence of concrete mattresses

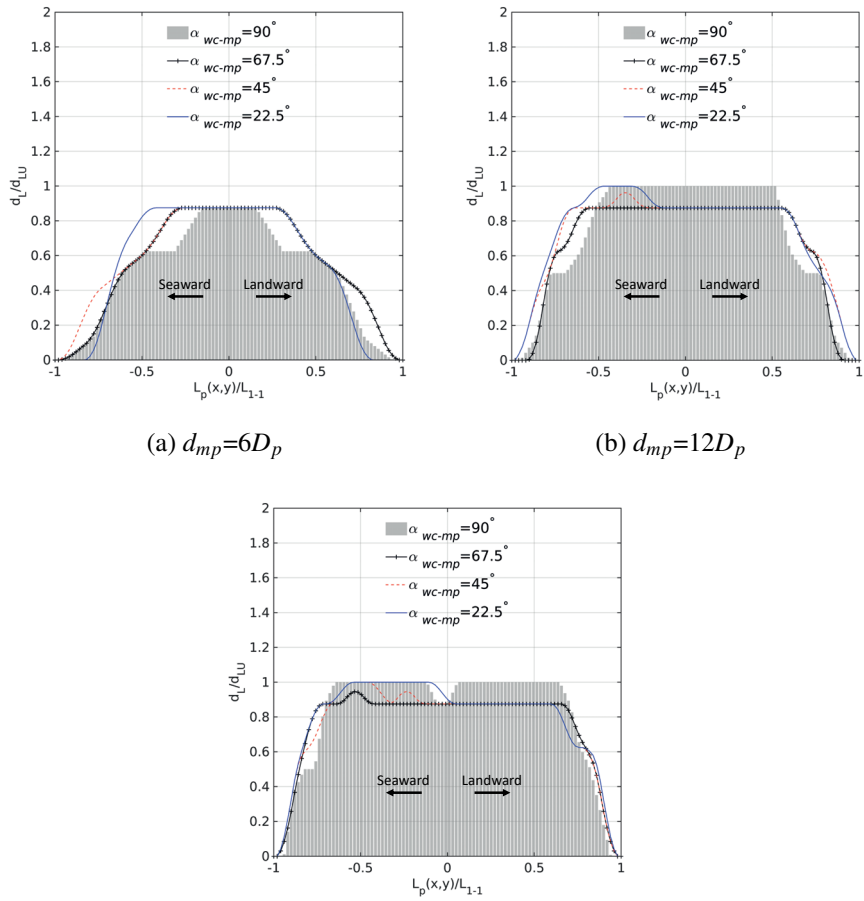

(a) d_{mp}=6D_p (b) d_{mp}=12D_p

(c) d_{mp}=18D_p

Figure 13.27 Distributions of the dimensionless flow-induced seabed liquefaction depth (d_L/d_{LU}) along with the reference axis of pipeline ($L_p(x,y)/L_{1-1}$) of a dual ACMs-pipeline system against various interaction angles (α_{wc-mp}) for different mattress spacing (d_{mp}), where H_w=4 m, T_w=8 s, d=20 m, U_c= 2 m/s, α_{wc}=0°, S_r=0.984 and k_s=10^{-4} m/s.

on the nearby uncovered sections of the pipeline is ignorable. Besides, the specific location of each reference point along the axis of pipeline is defined as $L_p(x,y)$. In other words, as the waves and currents propagate from left to right, the point where the value of $L_p(x,y)$ is less than 0 is located in the section of pipeline seaward, while the opposite ones belong to the section of pipeline landward. Based on this, a greater value of d_L/d_{LU} can be observed along the seaward side of the pipeline. When α_{wc-mp} equals to 22.5° and, d_L/d_{LU} along the seaward section of pipeline

increases from 0.85 to 1 as mattress spacing increases. Meanwhile, the range of this increment expands between -0.5 $< L_p(x,y)/L_{1-1} <$ 0, where L_{1-1} is defined to represent half the distance between the two adjacent bottom ends of these two ACMs (see Figure 13.20(c)). Except for the cases with α_{wc-mp} equalling 90°, the variation of d_L/d_{LU} along the landward section of pipeline is consistent for three mattress spacings. However, when α_{wc-mp} equalling 90°, d_L/d_{LU} increase from 0.85 to 1 as the mattress spacing increase from $6D_p$ to $12D_p$. In short, the variation of interaction angle affects the spatial development of d_L of a dual ACMs-pipeline system very differently from one another. This can be explained by the existence of the front mattress alters the downstream flow field, generating remarkable flow vortices towards the rear mattress. Thereby, the distribution of d_L along the pipeline axis varies non-linearly based on the relative location between these mattresses.

The evaluation of seabed liquefaction around the front and rear mattresses are also worth conducting in the actual design of the protective layer project. To this end, two reference circles (closed arcs) centered on O_1' and O_2' are selected to evaluate the peripheral changes of the front and rear mattress d_L (see Figure 13.20(c)). In this case, the seabed liquefaction depth can be considered as a function of interaction angle, mattress spacing and circle angle, namely $d_L(\alpha_{wc-mp}, d_{mp}, \theta_{mp})$. Note that the θ_{mp} is the angle between the line connecting any point on the reference arc to O_1' (or O_2') and the x-axis. It is zero when it coincides with the negative $x-$ axis, and it rotates counter-clockwise.

The variation of the index Δd_{L12} around a dual ACMs-pipeline system under various interaction angles and mattress spacing is illustrated in Figure 13.28. The index Δd_{L12} is defined as $\frac{d_{L2}}{d_{L1}}$. In other words, it indicates that the seabed liquefaction depth around the rear mattress (ACM#2) is smaller than that of the front one (ACM#1) when the value of $\frac{d_{L2}}{d_{L1}}$ is less than 1. Basically, it can be seen from the figure that the minimum index value is about 0.7, and it is mainly concentrated in the area near the two ends of the protective layer along the pipeline, and the index value of the area at the edge of the protective layer parallel to the pipeline axis is 1. Therefore, it can be inferred that the front row of concrete blocks have a certain degree of locality in inhibiting the liquefaction of the rear row, effectively reducing the depth of seabed liquefaction by 30%. However, there are other exceptions where the value of d_{L12} is greater than 1. For example, as the d_{mp} increases from $6D_p$ to $12D_p$, the ratio of seafloor liquefaction depth on the seaward side of the ACM#2 and ACM#1 (i.e., α_{wc-mp}=45° and θ_{mp}=22.5°) is reduced from 1.4 to 1.2. Whereas d_{mp} increases to $18D_p$, the impact of disturbance on the ACM#2 vanishes, as in most of the cases, the index Δd_{L12} is less than 1 for θ_{mp}= 0 to 360 °. This can be explained by the fact that the shear flow near the seafloor increases due to the disturbance of the front mattress, which intensifies the development of seafloor liquefaction around the rear one under a specific interaction angle (i.e., α_{wc-mp}=45°). In other words, to a certain interaction angle, there is a minimum mattress spacing for laying ACMs. If the rear mattress is laid below this critical value, its stability of seafloor foundation can be accelerated then loosened in the end. Therefore, it is necessary to avoid such design defects in actual engineering applications.

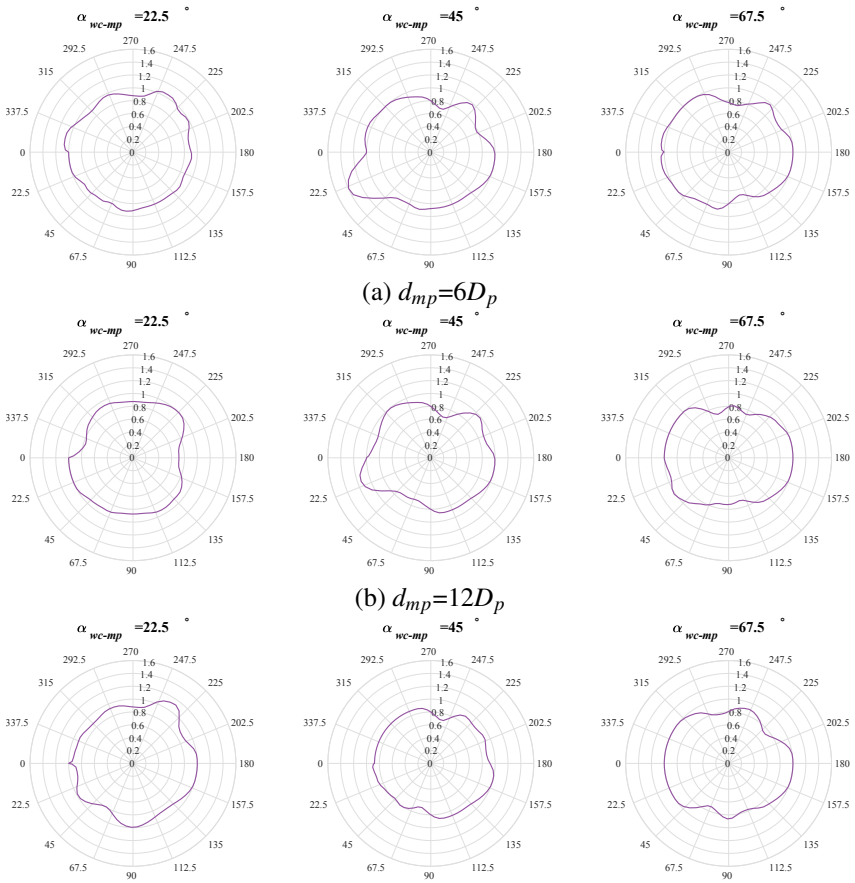

(a) d_{mp}=6D_p

(b) d_{mp}=12D_p

(c) d_{mp}=18D_p

Figure 13.28 The variation of the dimensionless liquefaction index (Δd_{L12}) around a dual ACMs-pipeline system (θ_{mp}= 0 to 360°) under various interaction angles (α_{wc-mp}) and mattress spacing (d_{mp}).

The differences in seafloor liquefaction depth under the protected and unprotected conditions around the front and rear mattress are separately illustrated in Figure 13.29. For instance, taking the front mattress (ACM#1) as the object of analysis, the value of Δd_{LU01} is defined as $\frac{d_{L1}}{d_{LU0}}$, where d_{L1} and d_{LU0} are the seafloor liquefaction depth around ACM#1 (i.e., Figure 13.20(c)) with and without ACM protection, respectively. This definition also works for the dimensionless liquefaction index of the rear mattress (ACM#2), $\Delta d_{LU02} = d_{L2}/d_{LU0}$. As seen in Figure 13.29, the variation of the dotted red line is basically within the closed region formed by the solid blue line. It can be inferred that the use of the concrete mattresses for covering offshore pipelines can effectively reduce the development of seafloor liquefaction (d_L), especially for the area (θ_{mp}= 45° to 67.5° and 247.5° to 270°) covered by

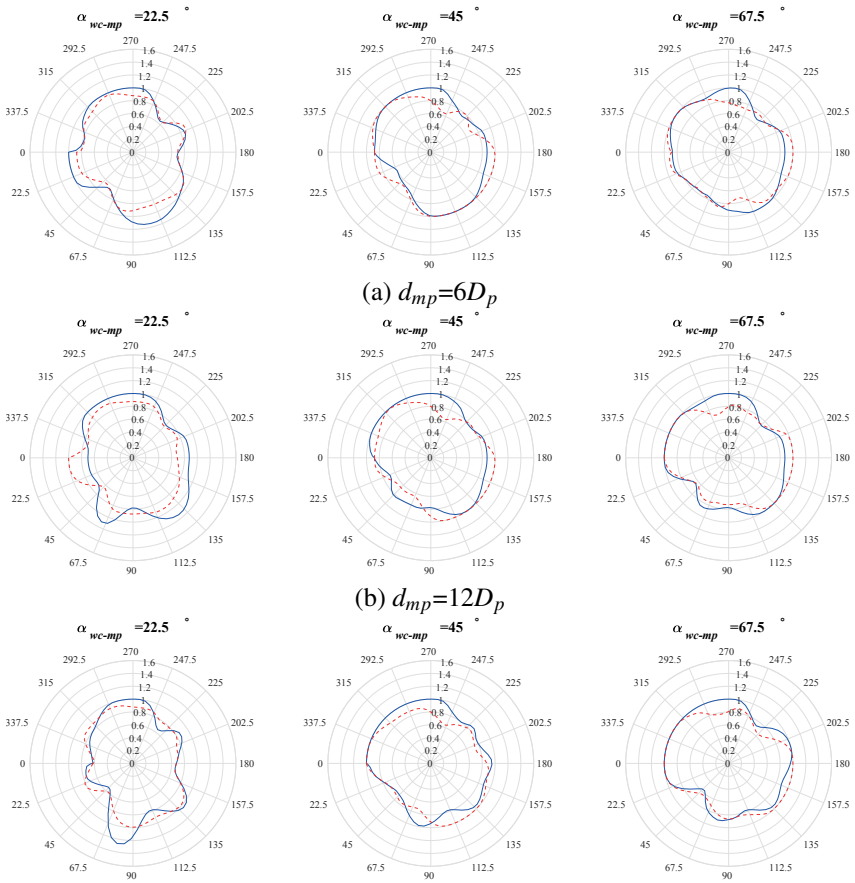

(a) d_{mp}=6D_p

(b) d_{mp}=12D_p

(c) d_{mp}=18D_p

Figure 13.29 The variation of the dimensionless liquefaction indexes (Δd_{LU01} and Δd_{LU02}) in a dual ACMs-pipeline system with various interaction angles (α_{wc-mp}) and mattress spacings (d_{mp}). Note: —: ACM#1; - - -: ACM#2.

the rear mattress when α_{wc-mp}=45° and d_{mp}=12D_p to 18D_p, which can effectively reduce the d_L by up to 40%. At the same time, there is another situation that the parts of the region with the value of Δ_{LU01} and Δ_{LU02} are larger than 1. For example, when α_{wc-mp}=22.5°, d_{mp}=18D_p and θ_{mp}= 67.5° to 90°, this phenomenon can be clearly observed that the maximum value of Δ_{LU01} can be up to nearly 1.4. Interestingly, this indicates that the existence of concrete mattresses inversely aggregates the process of seabed erosion. However, it mainly occurs in the area on both sides of the concrete mattress parallel to the pipeline. Nevertheless, such negative influence can be avoided as the d_{mp} decreases and α_{wc-mp} increases. Thus, the actual engineering design should also avoid the negative effect of the usage of ACMs to increase the depth

of seabed liquefaction. Optimizing the flow characteristics of the ACMs geometry can be an effective means to solve such problems.

13.3 SUMMARY

In this chapter, a theoretical model is proposed for the fluid-seabed-pipeline interactions first. Then, the model is verified with the experimental results from four sets of wave flume tests. By adopting the proposed model, two types of protection measures for subsea pipeline are discussed, including pipeline in a trench layer and Articulated Concrete Mattresses. Note that only regular wave loading is considered in this chapter. For the random wave-induced soil response around a pipeline in a trench layer, readers can refer to Liang and Jeng (2021). The key conclusions of this chapter are listed as following:

(1) Based on a series of parametric studies, design graphs for the critical backfill thickness of trenched pipelines are proposed for engineering practice based on utilizing different backfill materials. These graphs can provide guidance to coastal engineers for proposing the most suitable backfill material to protect pipeline in a trench layer based on site conditions.

(2) Furthermore, design charts and empirical formulations for the design of a pipeline in a trench layer for the residual liquefaction are proposed based on parametric studies. With this methodology, the critical wave steepness to meet the design requirement can be predicted and a trench layer can be designed by controlling the drainage condition of the backfilling material.

(3) Another methodology for the deep water pipeline protection, namely Articulated Concrete Mattresses (ACMs), is evaluated for the fluid-seabed-structure interaction problem using the proposed 3D numerical model.

14 Liquefaction around Marine Structures: Pile-type foundation

Pile-type foundations (e.g., single piles or group piles and jacket support structure, etc.) have been commonly used as the foundation of many marine infrastructures, such as the long-spanning bridges, offshore wind farms, oil platforms, etc. With the surge in demand for the offshore wind farm, many mono-pile with a diameter of up to 6 m have been built to meet more giant turbines. According to the European Wind Energy Association, mono-pile remain the most installed foundation, with 4,258 units (81%) up to date (Ramirez et al., 2021). However, the mono-pile has its limitation to the water depth. therefore, Jacket-type structure is adopted for the offshore wind turbine foundation for deep areas. Most previous studies available in the literature focused on the hydrodynamic performance of these structures. only a few research consider the seabed stability in the vicinity of the structures.

In this chapter, we will discuss two different structures that have been used in oil and gas industry for different purposes and regions. They are: (1) mono-pile for offshore wind turbine foundation, and (2) Jacket-type support structures for offshore wind turbine foundation. Possible potential methodology for the protection of foundation around these structures will be discussed.

14.1 SEABED STABILITY AROUND A SINGLE MONO-PILE

Generally speaking, the application range of mono-pile foundation is the sea area with water depth less than 30 m. Under the combined action of waves and currents, horseshoe vortice and wake vortice will form near the pile foundation, causing turbulence in the water flow, reflection and scattering of waves, wave breaking. Through the change of the flow state, once the drag force of soil particles on the seabed surface exceeds the resistance, the phenomenon of on-site sour and seabed erosion are triggered. However, recent experiments indicated that the development of the seabed motility might relate to the wave(current)-induced pore pressures and associate soil response (Qi and Gao, 2014). To a certain extent, the upward seepage force onto the sand grains under the series of wave troughs could have a visible influence on the local scouring process (Guo et al., 2019; Li et al., 2020; Zhai et al., 2021*b*,*a*).

Regarding wave-structure interactions around a pile-like structure, Ma et al. (2001*a*,*b*) applied the FEM model to analyse the fully non-linear and 3D interactions between the waves and the fixed cylinders. Cao and Wan (2017) examined the relationship between the wave run-up amplitude and the wave parameters on the

different numbers of cylinders. Jiang et al. (2019) investigated the tsunami-like solitary wave interaction with a row of piles on a sloping beach and proposed an empirical equation accounting for the slamming coefficient. Recently, Tang et al. (2020) investigated the effects of different types of breaking waves, such as spilling and plunging waves, on the wave run-up, pressure distribution and horizontal wave force of a large diameter mono-pile.

Based on the consideration of the seabed instability of the single pile foundation resulting from ocean wave-induced seafloor liquefaction, numerous numerical investigations have been carried out recently. Among these, Li et al. (2011) considered the dynamic seabed responses around a single pile by developing a FEM model, in which the nonlinear wave theory was used to provide the wave loading around a single pile. However, the reflection and diffraction phenomenon after the wave encountering the pile foundation was ignored. Chang and Jeng (2014) proposed a FEM seabed model within COMSOL Multiphysics with FVM model for wave motion to study the wave-induced seabed responses of the offshore wind turbine foundation in the East China Sea offshore wind farm. Tong et al. (2017) proposed a FDM-FEM integrated model to examine the pile-group effect on seabed response near a twin-pile group. By integrating both seabed and wave models within the same working platform, a series of FVM models were established to assess the transient instability near the single pile foundation under the wave loading (Lin et al., 2017; Sui et al., 2017) and wave plus current loading (Duan et al., 2019). In addition to numerical simulation methods, numerous experimental studies have been carried out recently. Their wave flume tests include regular wave, irregular wave, and their combined loading with currents(Qi and Gao, 2014; Wang et al., 2019*a*; Zhang et al., 2020; Chen et al., 2020; Chen, Zhai, Wang, Zhang, Wang, Duan and Jeng, 2022).

In terms of the FSSI involving the pile group, Zhang et al. (2017) numerically investigated the behaviour of a pile foundation under wave-only loading, and showed that as the dimensionless pile distance increases, the influence of the shadow from the upstream side pile on the downstream side pile is reduced. Tong et al. (2018) proposed a FDM-FEM integrated model to access the wave-induced seabed response around the three-pile group and revealed the upstream pile's blockage effect on the region between piles is significantly related to the wave obliquity and pile diameter. More recently, Lin et al. (2020) applied their previous model (Lin et al., 2017) to analyse storm wave-cylinder interaction's near-trapping effect on soil response around a cylinder array and pointed out that the upstream cylinders provide good protection from momentary liquefaction for downstream cylinders. However, the studies above considered the environmental loading of pure waves, ignoring other loadings such as currents. Therefore, it is not yet clear how the strong nonlinear influence of wave-current on the interaction between the pile group and the seabed foundation. Recently, based on the 3D numerical model (PORO-FSSI-FOAM), Liang et al. (2022) further investigate the run-up process of the water surface around the pile foundation in a complex marine environment and the liquefaction potential within complex pile foundations under combined wave and current loading. they also discuss the protection of pile foundations. The key findings will be discussed in this section.

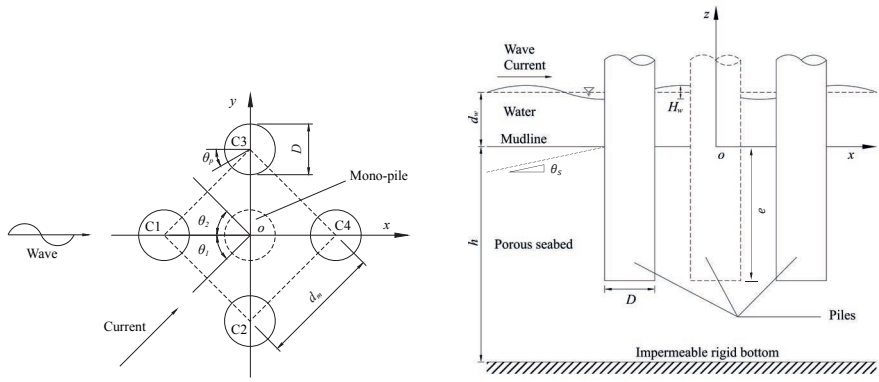

Figure 14.1 Schematic diagram of numerical model. left: plane view; right: section view.

14.1.1 THEORETICAL MODELS (PORO-FSSI-FOAM)

The problem of fluid–seabed–pile interactions considered in this study is depicted in Figure 14.1. In this study, an appropriate wave theory is used for wave generation with a fixed water depth (d_w), based on Le Méhauté (1976). As shown in Figure 14.1(a), the waves are propagating from the left to the right, while the positive z-axis is upward from the seabed surface. In addition, a uniform crossing current (U_c) is generated with an interaction angle (θ_1) to the incoming wave. A mono-pile is placed in the middle of the channel with the specific diameter (D) and embedment (e). The layout of the group pile consists of four single piles above, numbered in a specific order from C1 to C4, with a constant centre-to-centre spacing (d_m). Another parameter (θ_2) is defined as the interaction angle between the normal direction of the line connecting the centre of the front row of piles and the wave direction. Moreover, the seabed slope (θ_s) is modified to generate a depth-limited breaking wave. For the convenience of discussions, the position of reference points along the pile surface (θ_p) starts from the left and goes counter-clockwise (0 to 360°). The above definitions of the structure parameters are indicated in Figure 14.1.

In the flow domain, a no-slip boundary condition is imposed for velocities at the fluid-seabed interface. The Static Boundary Method (SBM) is chosen for the wave generation where there is Dirichlet condition by given values of $U(x,t)$ and $\eta(x,t)$ in the inlet boundary. A newly updated active wave absorption boundary (ER-AWA) is adopted at the outlet to eliminate the reflective waves. Details of the wave generation and absorption can be found in Higuera et al. (2013) and Higuera (2020). In the seabed domain, the lateral and bottom boundaries of the seabed are considered as impermeable and rigid, in which the displacements of the seabed and the normal gradient of pore pressure are zero (u_s=0, $\partial p_s/\partial n$=0, where n is the unit normal on the boundaries). At the seabed surface, the pore pressure is equal to the dynamic wave pressure from the flow sub-model (p_s=p_w), and the vertical effective stress and shear stresses vanish at the seabed surface. Additionally, the pile-type structure

is simulated as a rigid impermeable object, where the slip boundary and no-flow boundary ($\partial p_s/\partial n$=0, where n is the unit normal on the pile surface) conditions are applied at its surfaces in the flow and seabed domain, respectively. In terms of the computational domain's scope, the flow domain's length is set as 3 times the wavelength (L_w), and its width equals 16 times the pile diameter (D). Likewise, the length and width of the seabed domain are $2L_w$ and $10D$, respectively. For all simulation cases, the centre of the pile-type foundation is located in the middle of the computational domain.

14.1.2 MODEL VALIDATION

To validate the present model before being applied to assess the stability of the mono-pile structure, three cases were conducted against the previous experimental data. More specifically, the measured data in previous laboratory experiments, including the velocity profiles, water surface elevations, and soil responses around a mono-pile under different ocean wave loading were compared with the present model.

Validation #1: A large-diameter mono-pile under the combined waves and current loading (Qi and Gao, 2014)

Qi and Gao (2014) experimentally analyzed the local scour development around a large-diameter mono-pile under combined wave and current conditions. The wave flume is 52 m long, 1 m wide, and 1.5 m high in its experimental set-up. Additionally, a specially designed large soil box of 2.0 m $\times$ 0.5m $\times$ 1.0 m was attached at the bottom of the wave flume. The flume was filled with water to a given depth equal to 0.5 m. Two Perspex cylindrical model piles with diameters D= 0.20 m and 0.08 m were used, respectively. The undisturbed flow velocity was measured by an Acoustic Doppler Velocimetry (ADV) located above the sand-bed at a distance of 20 m apart from the pile centre. Figure 14.2 shows a comparison of the simulated and the measured flow velocity at the level of $1.0D$ above the sand-bed under various wave heights. By contrast, the flow velocity periodically enlarges as waves are superimposed onto the following current, which is in good agreement with the experimental data.

Validation #2: Hydrodynamics on offshore wind turbine foundations (Zang et al., 2010)

Zang et al. (2010) conducted a series of experiments for regular waves and focused wave groups hitting a surface-piercing vertical cylinder in the DHI shallow water basin (35 m $\times$ 25 m) with a water depth of 0.505 m. A cylinder of diameter 0.25 m was located at 7.52 m from the paddles. For measuring the total horizontal hydrodynamic force on the cylinder and its nearby wave field, four load cells and 19 wave gauges were adopted, respectively. Figure 14.3 presents the comparison of the simulated and experimental hydrodynamic forces on the cylinder, showing a good capacity for capturing the nonlinear wave-pile interactions.

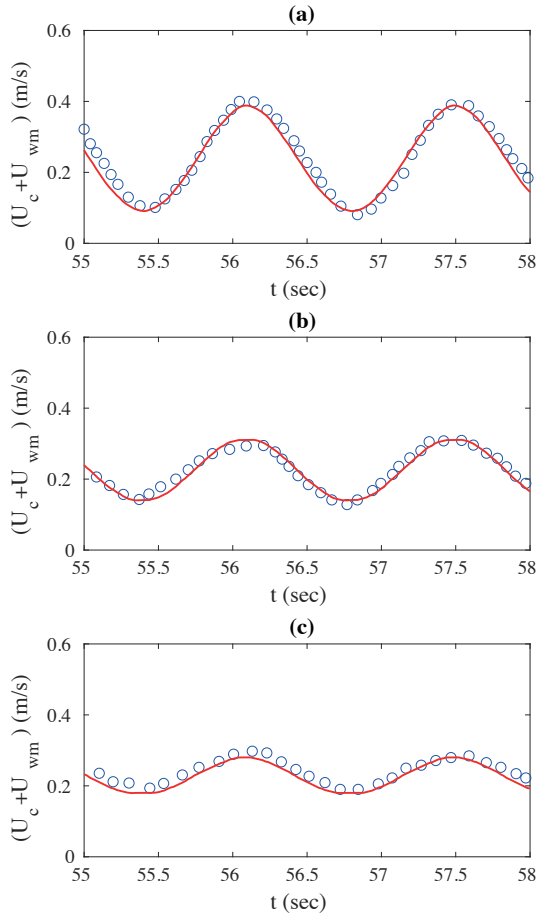

Figure 14.2 Comparisons of the measured velocity at the level of 1.0D above the sand-bed for various wave height. —: the present model, ○: Qi and Gao (2014). Input data: U_c=0.23 m/s, T_w=1.4 s, d_w=0.5 m, D=0.20 m, (a) H_w=0.085 m; (b) H_w=0.052 m; (c) H_w=0.026 m.

Validation #3: Pore-water pressures around a mono-pile under regular waves (Wang et al., 2019*a*)

The research team from the Southwest Jiaotong University in China conducted a series of wave flume tests in the specially-designed flume (60.0 m in length, 1.8 m in width, and 2.0 m in depth). A soil-box of 7.0 m × 1.8 m × 1.0 m is attached at the bottom of the wave flume, where an embedded mono-pile of 0.3 m diameter was installed 0.6 m below the seabed surface (see Figure 14.4). For recording the time-varying distribution of specific variables, five wave gauges (including gauges 551-555) were placed in front of the inlet and in the vicinity of the mono-pile for measuring the wave height and wavelength. In addition to using

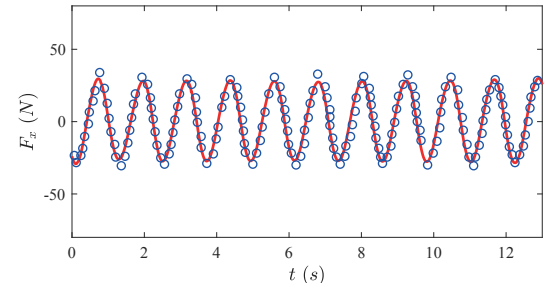

(a) Case R1

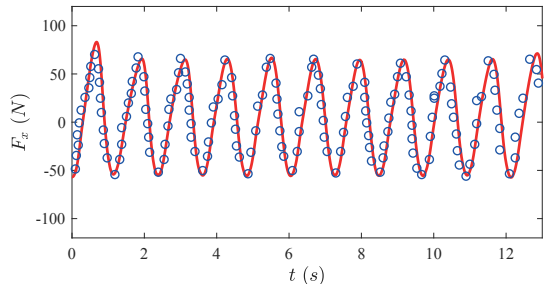

(b) Case R2

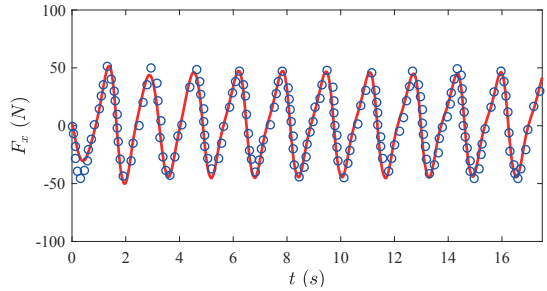

(c) Case R3

Figure 14.3 Time series of horizontal forces on the cylinder for all the three regular wave cases. (a) Case R1, (b) case R2 and (c) case R3. —: the present model, ○: Zang et al. (2010). Input data: H_w= 0.14 m, d_w= 0.505 m, T_w= 1.22 s, D= 0.25 m.

four pore-pressure transducers (i.e. gauges 20-23) to measure the instantaneous wave pressure, the pore-pressure transducers were mounted to measure the excess pore wave-induced pore-pressure nearby the structure in the soil box. Furthermore, an ADV was mounted at 0.3 m above the bottom of the wave flume to measure the undisturbed flow velocity.

Figure 14.5 shows a comparison of the water surface elevation at four wave gauges (i.e. 552-555) concerning the wave alone case (Wang et al., 2019*a*). Besides, Figure 14.6 compares the simulated and experimental wave-induced pore-water

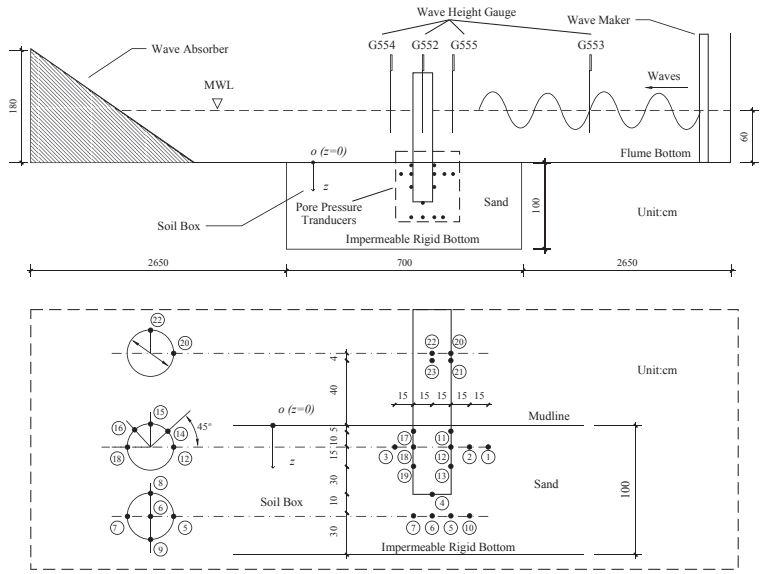

Figure 14.4 Schematic diagram of experimental set-up (Wang et al., 2019*a*).

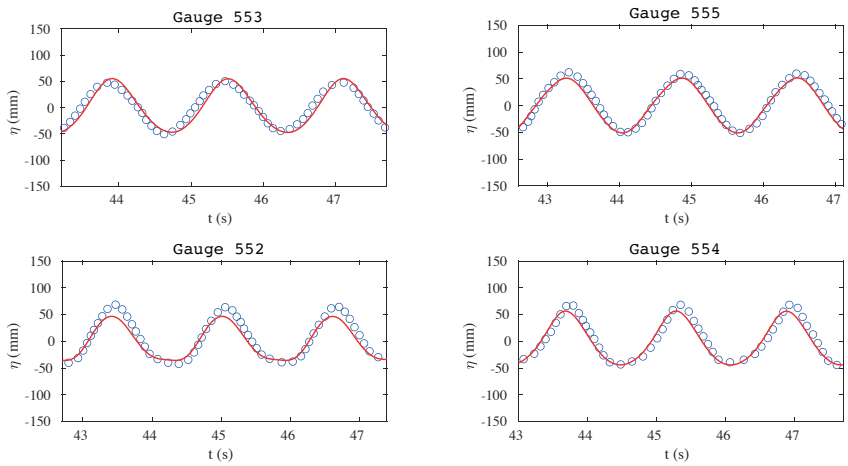

Figure 14.5 Time series of wave profiles measured at wave gauge 552-554. —: the present model, ○: (a) left column: T_w=1.6 s, H_w=0.1 m and d_w=0.6 m (Wang et al., 2019*a*).

pressure in the vicinity of the cylinder. In general, the numerical results predicted by the model are in good agreement with the experimental data.

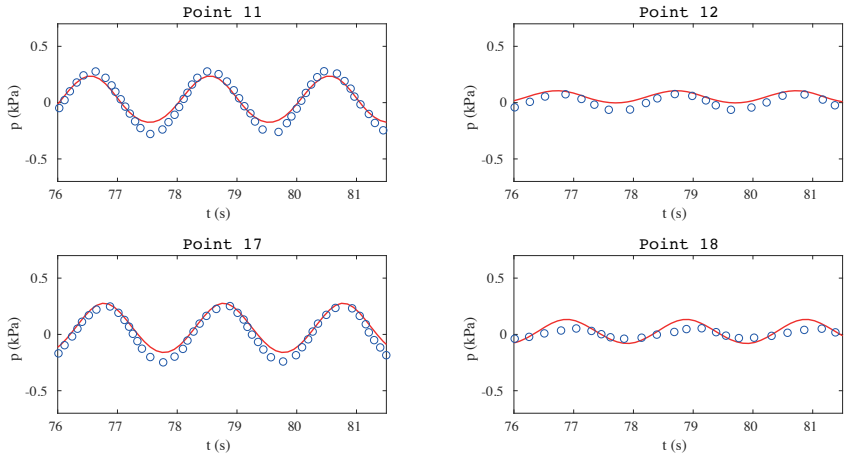

Figure 14.6 Time histories of wave-induced excess pore-water pressures around the mono-pile. —: the present model, ○: Test 43: T_w=2.0 s, H_w=0.1 m and d_w=0.6 m (Wang et al., 2019*a*).

14.1.3 WAVE RUN-UP ON A SINGLE MONO-PILE

The focus of the present study is to investigate the seafloor liquefaction potential near the mono-pile and pile group structure through the proposed numerical model. The input data, including wave, current, and soil characteristics used in the numerical examples, are listed in Table 14.1. Unless otherwise specified, in the following discussion, the black and red arrows in the figures represent the directions of ocean waves and crossing currents, respectively.

Figure 14.7 shows the water surface elevation near a mono-pile with the incident wave plus the crossing current (T_w=8 s, H_w=4 m, U_c=2 m/s, θ_1=45°, θ_s=0). As seen in the figure, the wave diffraction around the pile can be clearly observed. It is manifested that the water is blocked in front of the pile and then runs up along the pile, resulting in the largest wave run-up height. Furthermore, a visible process of wave run-up can be captured on the rear side of the pile. In addition, Figure 14.8 shows the relationship between the maximum run-up ratio η/A and the radial directional angle near the pile surface, where $A = H_w/2$ is the incoming wave amplitude. As shown in the figure, the distribution of η/A is seen as symmetrical along the x-axis when the U_c decreases. On the other hand, it can be observed at 45° as U_c increases, which is exactly the interaction angle between the ocean current and the incident wave. However, a larger amplitude of η/A can be obtained with a smaller value of U_c. This can be explained as the increase of the flow velocity leads to a decrease in the wave height of the incident wave, and the waveform is relatively flat rather than sinusoidal (Qi et al., 2019). Similarly, η/A increases significantly with the increase of H_w, which can reach twice the initial wave amplitude in the area near the front side of the mono-pile. In terms of the water depth and wave period,

Table 14.1
Parameters for the numerical simulation.

Ocean characteristics	
Wave height, H_w (m)	2, 3, 4
Wave period, T_w (s)	7, 8, 9
Water depth, d_w (m)	5.13, 12, 14, 16
Current velocity, U_c (m/s)	1, 1.5, 2
Current-wave angle, θ_1 (°)	45
Structure-wave angle, θ_2 (°)	0, 22.5, 45
Seabed characteristics	
Soil permeability, k_s (m/s)	10^{-3}
Porosity, n_s	0.425
Poisson's ratio, μ_s	0.4
Seabed thickness, h_s (m)	38
Shear modulus, E_s (Pa)	10^7
Degree of saturation, S_r	0.97
Slope, θ_s	0 and 1/15
Mono-pile characteristics	
Diameter, D (m)	6
Spacing, d_m (m)	$2D$, $3D$, $4D$
Embedment depth, e (m)	20
Protection layer characteristics	
Diameter, R_r (m)	4 and 6
Thickness, D_r (m)	2.5 and 4

these factors can directly affect the wavelength. However, η/A increases positively as T_w increases and d_w decreases, respectively. This may reveal that the wave run-up around the pile is also affected by the cyclic incident wave loading frequency.

14.1.4 DEVELOPMENT OF THE WAVE AND CURRENT-INDUCED INSTANTANEOUS LIQUEFACTION AROUND THE PILE

In this section, the presence of the pile can affect the initial stress of the nearby seabed foundation, which was considered in the liquefaction analysis (Zen and Yamazaki, 1990*a*; Jeng, 2018):

$$\sigma_0' - (p_s - p_b) \leq 0, \tag{14.1}$$

in which p_s= pore pressures and p_w= dynamic wave pressures of seafloor; and σ_0'= the mean initial effective stresses after pre-consolidation, which can be defined as

$$\sigma_0' = \frac{\sigma_{0x}' + \sigma_{0y}' + \sigma_{0z}'}{3}, \tag{14.2}$$

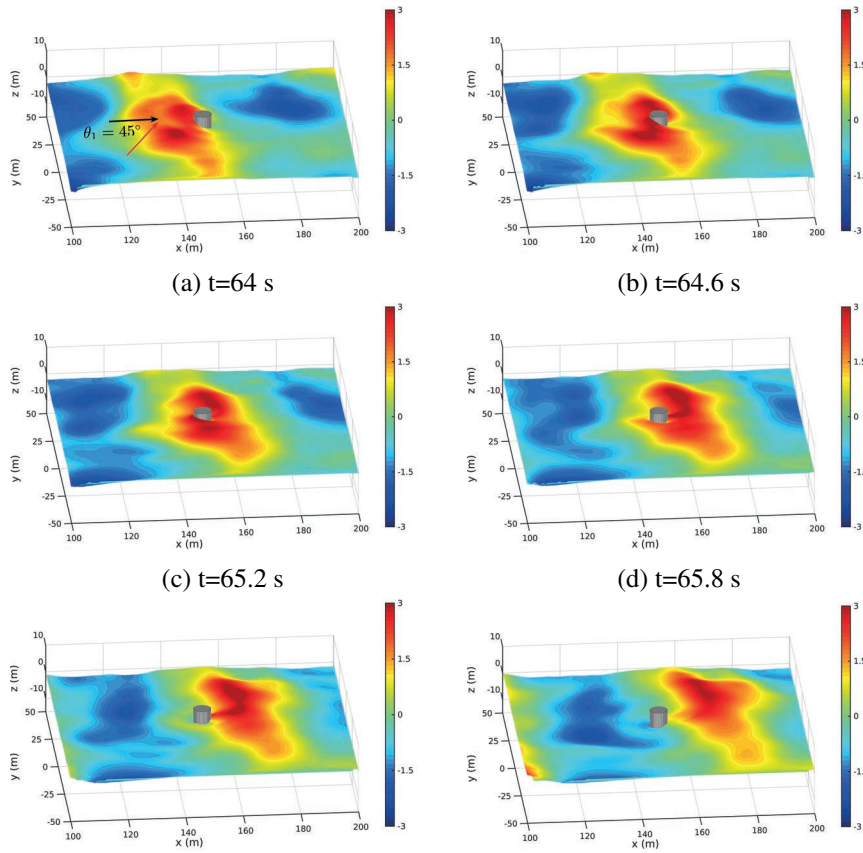

(a) t=64 s (b) t=64.6 s

(c) t=65.2 s (d) t=65.8 s

(e) t=66.4 s (f) t=67 s

Figure 14.7 Snapshots of the wave elevation (η) near the mono-pile under the combined wave-current loading (T_w=8 s, H_w=4 m, U_c=2 m/s, d_w=12 m, θ_1=45°, θ_s=0). The free surface level is shaded from blue to red (Unit: m).

where σ'_{0x}, σ'_{0y} and σ'_{0z} are the initial effective stresses in the x-, y- and z- directions, respectively.

Figure 14.9 displays the spatial distribution of combined wave and current-induced seabed liquefaction around mono-pile at four typical times. To demonstrate the liquefaction development, the viewing angles in this figure are from the front (a & b) and back (c & d) of the pile, respectively. When the wave trough propagates to the pile, the liquefaction area is concentrated significantly in the range of 0 to 90 degrees. After the wave trough passes through the pile, the seabed liquefaction mainly occurs in the area of θ_p ranging from 180 to 270 degrees. In other words, the maximum liquefaction depth develops along a straight line at a fixed angle to the incident wave. In addition, the liquefaction depth on the lateral sides of the pile is smaller than that

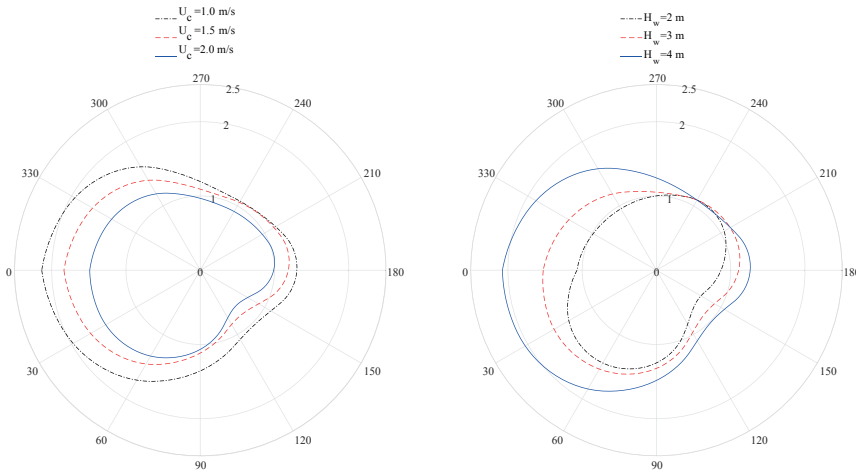

(a) various oblique current (U_c) (b) various wave height (H_w)

(c) various water depth (d_w) (d) various wave period (T_w)

Figure 14.8 Maximum wave run-up ratio at the probes close to the cylinder surface for various (a) oblique current, U_c; (b) wave height, H_w; (c) water depth, d_w; (d) wave period, T_w.

at the front and back of the pile, which can be attributed to the blocking effect of the pile.

To investigate the possible threat from the instantaneous liquefaction to scour protection, maximum potential liquefaction depth near the mono-pile foundation over a typical wave period for various wave and current characteristics is presented in Figure 14.10. It can be observed that maximum liquefaction depth is located in the zone near the mono-pile foundation, with θ_p approximately ranging from 30° to 60°. In contrast, while minimum potential liquefaction depth occurs at two specific areas

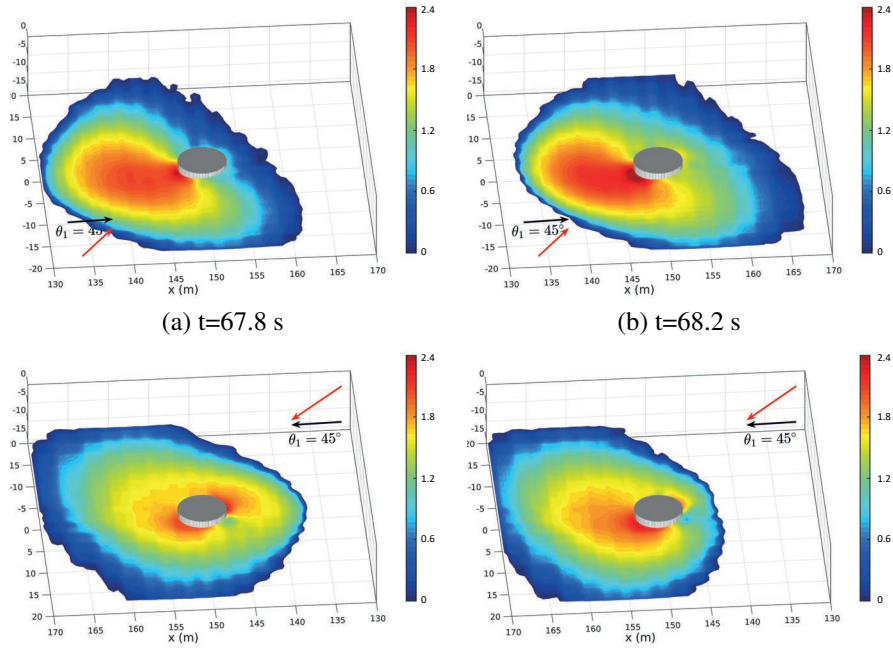

(a) t=67.8 s (b) t=68.2 s

(c) t=68.6 s (d) t=69 s

Figure 14.9 Snapshots of the instantaneous liquefaction development (d_L) around a mono-pile under the combined wave-current loading at several moments (T_w=8 s, H_w=4 m, U_c=2 m/s, d_w=12 m, θ_1=45°, θ_s=0). The free surface level is shaded from blue to red (Unit: m).

of mono-pile foundation, where θ_p is in the range of 120° to 150° and 300° to 330°, respectively. This phenomenon in terms of the instantaneous liquefaction differs from that reported by the previous study (Lin et al., 2017) for the wave-only loading. To some extent, the velocity of ocean current relative to that of waves will alter the distribution of liquefaction depth near the pile, which can be visually explained by the development path of d_L as revealed in Figure 14.9. In general, the parametric study here indicates that d_L increase positively as U_c, H_w, T_w increase except for d_w. However, there is an interesting phenomenon that d_L is inversely proportional to U_c within the range of 270° to 345° around the pile, which may be affected by the wake vortex around the pile and the boundary layer of the fluid domain above the seafloor in this area.

14.1.5 COMBINED BREAKING WAVE AND CURRENTS-INDUCED INSTANTANEOUS LIQUEFACTION AROUND THE PILE

In engineering practice, the damage of fractured waves to the stability of offshore structures built on the porous seabed is much more significant than that of

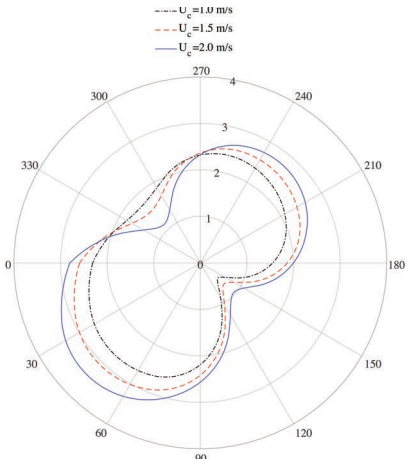

(a) various oblique current (U_c)

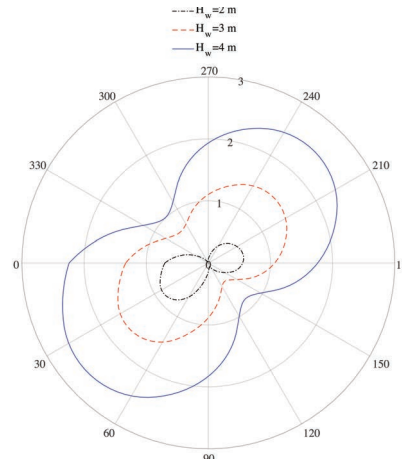

(b) various wave height (H_w)

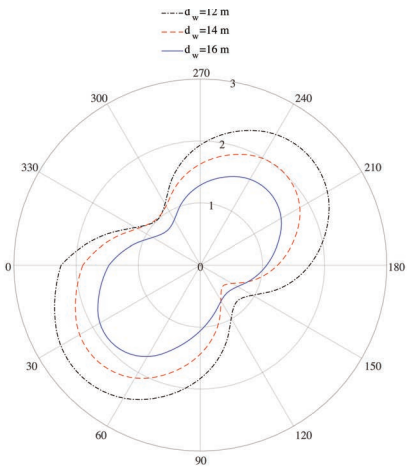

(c) water depth (d_w)

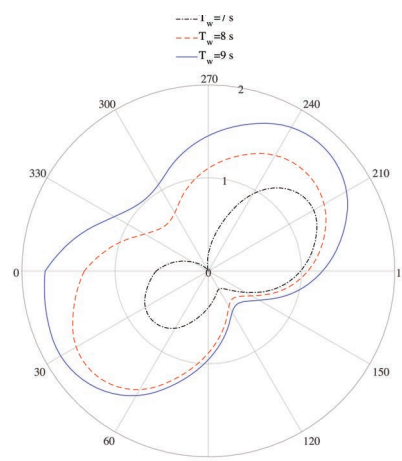

(d) wave period (T_w)

Figure 14.10 Maximum instantaneous liquefaction depth (d_L) around a mono-pile for various (a) oblique current, U_c; (b) wave height, H_w; (c) water depth, d_w; (d) wave period, T_w (Unit: m).

non-fractured waves in offshore areas. Recently, more attention has been paid to the interactions between breaking waves, seabed and marine structures. To demonstrate the impact of breaking waves, four cases are simulated to reproduce the interactions between combined breaking wave with ocean current, seabed and mono-pile with oblique flow velocities ranging from 1 m/s to 2 m/s with a fixed interaction angle equalling to 45°.

To simulate the breaking wave conditions, an impermeable slope (θ_s=1/15) is placed in the front of the mono-pile. Specifically, the water depth (d_w) and wave height (H_w) are 12 m and 4 m, respectively. After that, the d_w decreases to 5.13 m. In this case, H_w/d_w=0.78, resulting in wave breaking. Based on the criterion of Battjes (1974), the surf similarity parameter or Iribarren parameter can be calculated: $\xi = \theta_s/\sqrt{H_w/L_w} = 0.33$, where the breaker is spilling (ξ ¡0.4). First of all, the spatial distributions of the wave elevation under the cycling loading of pure breaking wave (left column) and the combined breaking wave-current (right column, U_c=2 m/s, θ_1=45°) are separately displayed in Figure 14.11. As seen, the wave crest line remains parallel to the y-axis without the influence of crossing ocean currents until after interacting with the mono-pile. Similarly, a wave run-up occurs near the structure when the breaking wave fully touches the mono-pile. Afterwards, the wave crest line is gradually segmented, and the amplitude of wave height decreases significantly. In the case of combined wave breaking and crossing ocean current, the above-mentioned WSSI process is more intense, indicating that the area with an enormous wave run-up continues to expand laterally. After interacting with the mono-pile, the wave crests on both sides (i.e., θ_p=90° and 270°) overlapped not far behind the structure, forming a secondary wave wrest.

In addition, Figure 14.12 illustrates the periphery distribution of the maximum potential liquefaction depth near the mono-pile foundation over a typical wave period for various crossing currents with a fixed current-wave angle equalling to 45°. As seen, the maximum liquefaction depth (d_L) can be obtained up to 2.25 m on both lateral sides of the structure. As the velocity of crossing current (U_c) increases, the shape of the periphery distribution of d_L gradually rotates clockwise. Notably, on the one hand, the maximum liquefaction depth is mainly distributed in the range of $0 < \theta_p < 45°$. On the other hand, a larger d_L can be achieved at θ_p=0° when U_c equals 2 m/s. Based on this, it can conclude that the breaking wave-induced maximum liquefaction depth can be obtained on both lateral sides of the pile, followed by front and rear sides, respectively. In terms of the case with combined breaking wave and current, the d_L in front of the pile increases significantly as the U_c increases compared to other structure locations. This can be explained as the increase of the U_c directly affects the interaction direction of the combined breaking wave-current on the pile; the U_c component along the Y-axis direction limits the development of d_L on the lateral sides of the pile to a certain extent, and such effect is particularly pronounced when U_c increases. Therefore, the primary focus is to reduce the liquefaction depth of the seabed foundation in front of piles under the combined loading of breaking waves and ocean currents.

14.2 SEABED INSTABILITY AROUND THE PILE GROUP

In this section, the dynamic seabed response and liquefaction in the vicinity of a multi-cylinder foundation under the combined crossing ocean current & wave conditions are examined (T_w=8 s, H_w=4 m, U_c=2 m/s, d_w=12 m, θ_s=0). The cylinders are numbered in a specific order from C1 to C4 in the following discussion. The

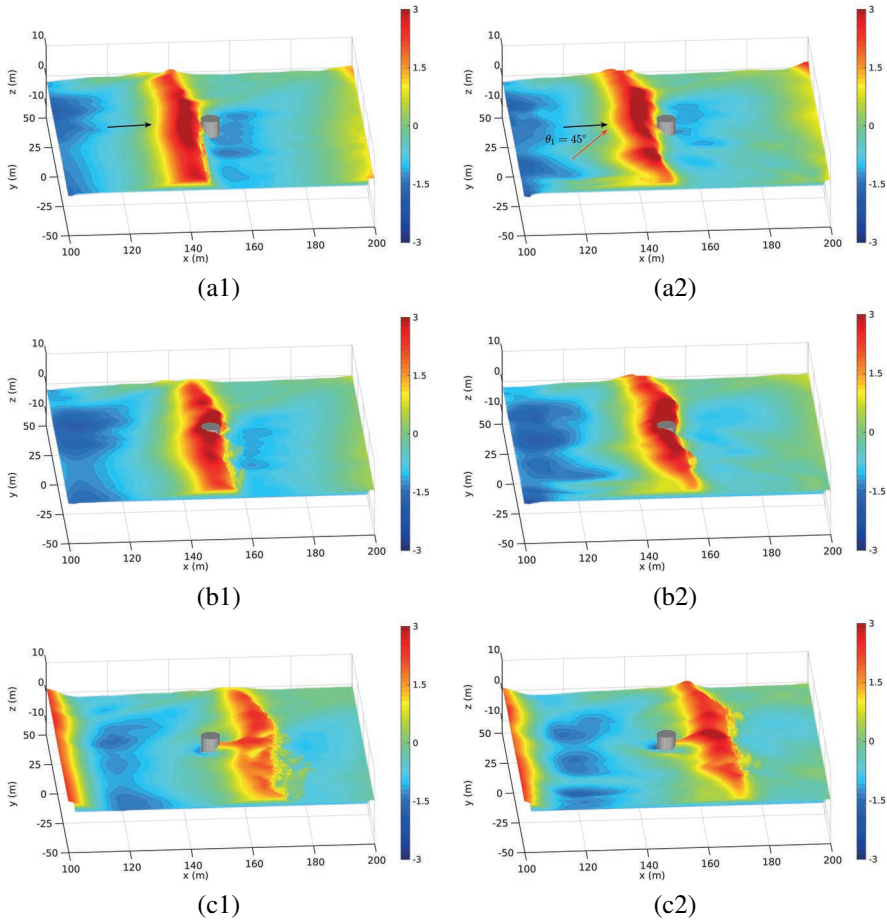

Figure 14.11 Snapshots of the wave elevation (η) near the mono-pile under the combined breaking wave-current loading: (a1&a2) t=64.8 s; (b1&b2) t=65.8 s; (c1&c2) t=67.8 s (T_w=8 s, H_w=4 m, U_c=2 m/s, d_w=12 m, θ_1=45°, θ_s=1/15). The free surface level is shaded from blue to red (Unit: m).

centre-to-centre distance between two adjacent cylinders is defined as d_m, which is equal to $3D$ by default unless otherwise specified.

Figure 14.13 presents the dimensionless wave elevation (η/A) near the pile group when the propagation of wave trough with different wave headings (θ_2=0 to 45°) under the fixed crossing ocean current (θ_1= 45°). It is noted that the left-hand side (a1-c1) and right-hand side (a2-c2) of Figure 14.13 indicate the time step when the propagation of wave crest and tough through the pile group, respectively. As the wave crests propagate, the value of η/A increases up to 2 at circumferential positions facing the inner domain of C2 and C3. This can be explained by the occurrence of the

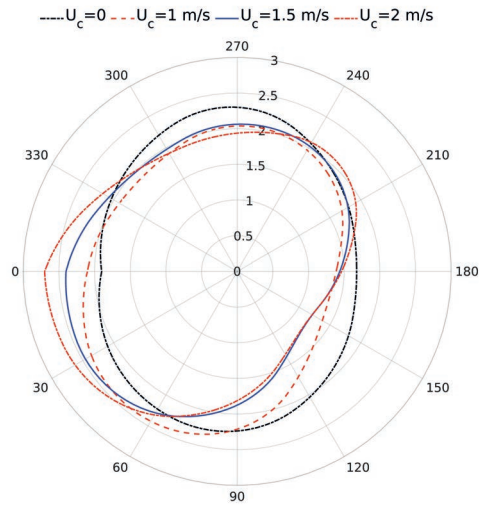

Figure 14.12 Maximum instantaneous liquefaction depth (d_L) around a mono-pile under the combined breaking wave and various oblique currents (Unit: m).

near-trapping effect, compared with the case with a mono-pile where the maximum water elevation is 3 (i.e., η/A=1.5) during the wave crests passing through (see Figure 14.7). With the increase of θ_2, this trend is more prominent and the area where the trend appears gradually becomes larger, indicating a significant wave run-up in the internal field of the pile group. In contrast, the largest amplitude of η/A mainly appears upstream of C1 and C4 when the trough passes. However, as θ_2 increases, the region near C1 with a significant amplitude of η/A will expand to a certain extent, and its absolute value will increase to 1.6. In other words, the near-trapping phenomenon in the pile group also reduces the water surface elevation significantly when the wave though passes, but this effect only appears significantly near a certain cylinder. This can be attributed to the presence of oblique flow, which changes the flow pattern in combination with incident waves during the interaction with the pile group. In summary, the above simulation results indicate that during the combined wave and current loading in one period, C1 & C4 and C2 & C3 from the pile group will experience different dynamic responses, which need to be treated separately for the structural safety and foundation stability.

To estimate the potential risk of seabed instability near the pile group, Figure 14.14 presents the spatial distribution of instantaneous seabed liquefaction around the pile group for various values of θ_2 near the wave trough propagation. Generally speaking, when the θ_2 equals 0, the liquefaction depth (d_L) is distributed symmetrically on both sides of the $x-$ axis. To be precise, due to the impact of crossing ocean currents on the negative side of the $y-$ axis, the d_L on this side is

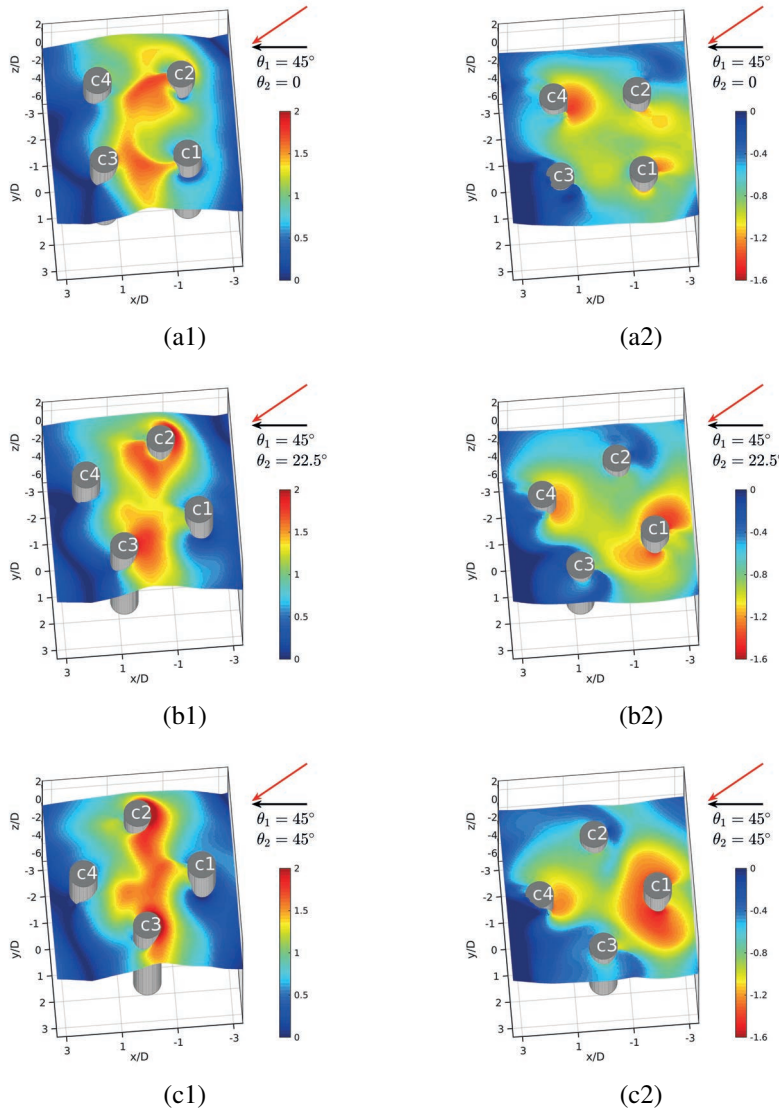

Figure 14.13 Snapshots of the instantaneous distribution of the dimensionless wave elevation (η/A) around a pile-group under the combined wave-current loading for various wave-structure angles and spaces: (a1&a2) θ_2=0; (b1&b2) θ_2=22.5°; (c1&c2) θ_2=45°. (T_w=8 s, H_w=4 m, U_c=2 m/s, d_w=12 m, d_{mp}=3D, θ_1=45°, θ_s=0).

greater than that on the positive side of the $y-$ axis. With the increase of θ_2 from 0 to 45°, d_L near C1 increases significantly, especially on the lee-side of the pile, which can reach 2.4 m. This may be due to the apparent near-trapping phenomenon

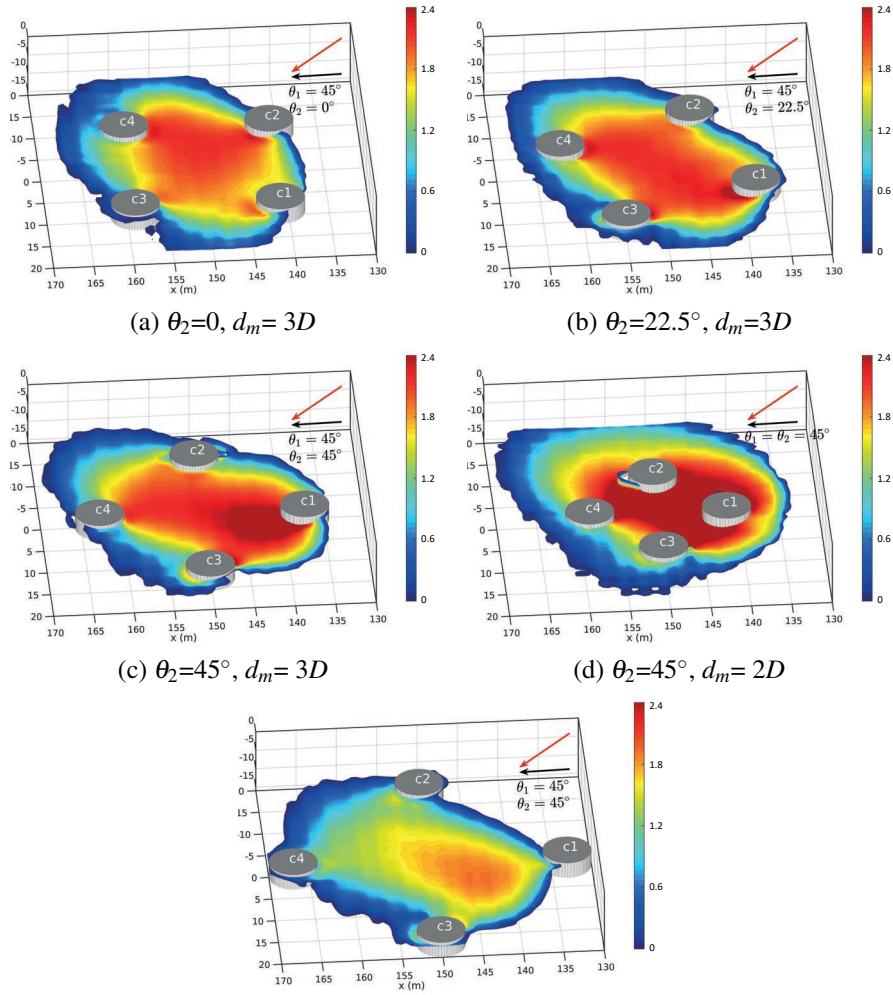

(a) θ_2=0, d_m= 3D (b) θ_2=22.5°, d_m=3D

(c) θ_2=45°, d_m= 3D (d) θ_2=45°, d_m= 2D

(e) θ_2=45°, d_m= 4D

Figure 14.14 Snapshots of the instantaneous liquefaction distribution (d_L) around a pile-group under the combined wave-current loading for various wave/current-structure angle: (a) θ_2=0, d_m= 3D; (b) θ_2=22.5°, d_m= 3D; (c) θ_2=45°, d_m= 3D; (d) θ_2=45°, d_m= 2D; (e) θ_2=45°, d_m= 4D. The interface of liquefaction occurrence is shaded from blue to red. (Unit: m).

in the flow field above the seabed, as its effect on the time-dependent variation of η near C1 is particularly pronounced. Furthermore, Figures 14.14(d) & (e) illustrate the influence of spacing between neighbour piles (d_m) on the development of d_L in the inner region of the pile group. Based on the simulation results, it can be observed that the reduction of the distance between the piles (d_m) leads to a strong seabed

response, which causes the liquefaction potential of the seabed foundation of the overall system to rise sharply. On the contrary, the increase of the d_m significantly reduces the liquefaction potential. Roughly speaking, the d_L decreased from 2.3 m to 1.5 m. This is because that the pile group effect gradually disappears as the d_m increases, indicating a similar variation trend of d_L around a mono-pile as well as a single pile of the pile group structure. Notably, the distribution of d_L inside the pile group is highly correlated with the pile group layout under the given conditions of the ocean environment.

14.3 APPLICATION OF PROTECTION MATTRESS AROUND THE PILE GROUP

In this section, the seabed protection method used here includes replacing the existing layer with suitable materials, among which other parameters are H_w=4 m, T_w =8 s, d_w=12 m, U_c=2 m/s, $\theta_1=\theta_2=45°$, θ_s=0. In terms of the dimension of the protection layer, four cylindrical trenches with D_r in height and R_r in the radius are excavated surrounding each pile and filled with coarse sand. More specifically, the values of D_r and R_r are separately various from 3.5 m to 4 m and 2.5 m to 3 m, increasing at an interval of 0.5 m. In addition, the permeability of the original seabed (fine sand) and replaced soil (coarse sand) is considered as $k_{s1}=10^{-3}$ m/s and $k_{s2}=10^{-2}$ to 10^{-1} m/s, respectively. To clearly discuss the simulation results, Figure 14.15 displays the schematic diagram of the pile group structure using the protective layer design. In the figure, the blue z-plane represents the surface of the seabed, and the protective layer is sleeved on the corresponding single pile, and its designed maximum elevation is consistent with the bed surface.

Figure 14.16 shows the spatial distribution of the instantaneous seabed liquefaction depth (d_L) around a pile group with a fixed θ_2 and various replaced layers. Intuitively, the pile group system with the protective layer can effectively suppress the development of the seabed liquefaction zone, whether it is from the horizontal or vertical direction. Specifically, the positive effect of seabed liquefaction protection on the front row of piles (i.e., C1 & C2) is particularly prominent. In short, by adopting the replaced soil of $k_{s2}=10^{-2}$ m/s, one feasible solution is increasing the radius (R_r) and depth (D_r) of the protective layer. On the other hand, the specific protection layer can be replaced by stones with a greater permeability coefficient ($k_{s2}=10^{-1}$ m/s), on the whole, further restraining the tendency of liquefaction to spread to the bed surface of every single pile due to the near-trapping effect.

For the safety design of the seabed foundation of the pile group, the distribution of the maximum dimensionless instantaneous liquefaction depth (d_L/D) around a pile group for various protection layers over a specific wave period is illustrated in Figure 14.17. It clearly shows that the size of the liquefaction area near the pile group is larger without a protective layer. More specifically, the larger d_L/D appears near C1, C2, and C4, indicating that the liquefaction trend gradually developed from the inner side of the pile group to its lateral sides and downstream. Applying a protective layer with a larger size and a permeability coefficient can effectively concentrate the area where the seabed is seriously under liquefaction in the smaller

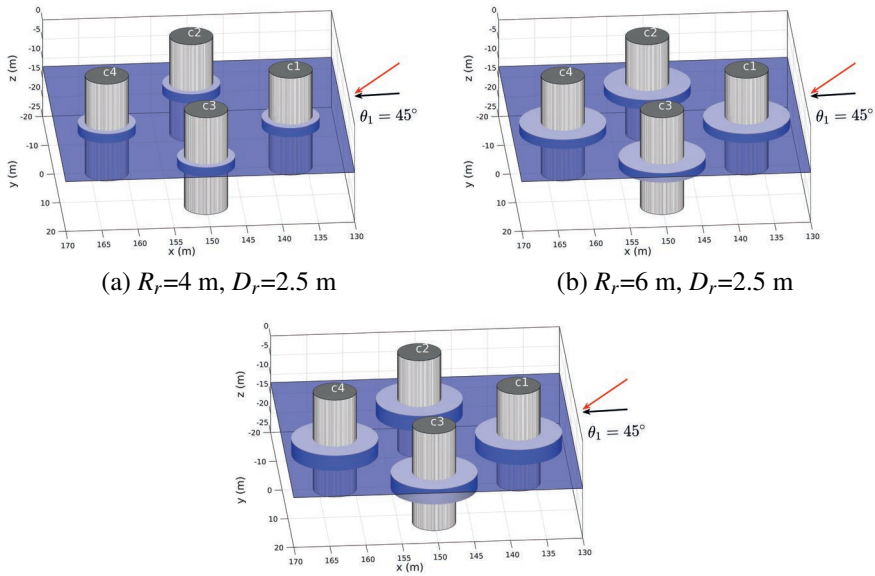

(a) R_r=4 m, D_r=2.5 m (b) R_r=6 m, D_r=2.5 m

(c) R_r=6 m, D_r=4 m

Figure 14.15 Schematic diagram of the pile-group system with different replaced/protection layers: (a) R_r=4 m, D_r=2.5 m; (b) R_r=6 m, D_r=2.5 m; (c) R_r=6 m, D_r=4 m.

region inside the pile group, forming a "rhombus" shape. Quantitatively speaking, the d_L inside the pile group can reach 0.35 times the pile diameter. Regarding this, the soil in the above-mentioned rhombus-like area has tremendous potential for weakening. In addition to the seabed liquefaction, the trend of on-site scour will also be significant. With the development of liquefaction and scouring, the edge stability of the protective layer also requires additional attention.

14.4 SEABED LIQUEFACTION AROUND A JACKET SUPPORT OFFSHORE WIND TURBINE FOUNDATION

Offshore wind turbine foundations, such as gravity-based foundations, suction caissons, mono-pile, multiple-footing foundations, and floating turbines with a mooring system, are an important part of an offshore wind energy system. Of these foundations, mono-pile are most widely used when the water depth is less than 30 m (Bhattacharya, 2014). The jacket foundation is one of the trends for the development of offshore wind farms in the future, due to its operability, practicality, and simple construction process. Yang et al. (2007) analyzed the dynamic response process for the jacket platform considering the wave-current co-action. Sha (2014), Chang (2018) and Xu (2019) further investigated the related subjects about the dynamic characteristics of the jacket structure itself. Jiang et al. (2012) implemented

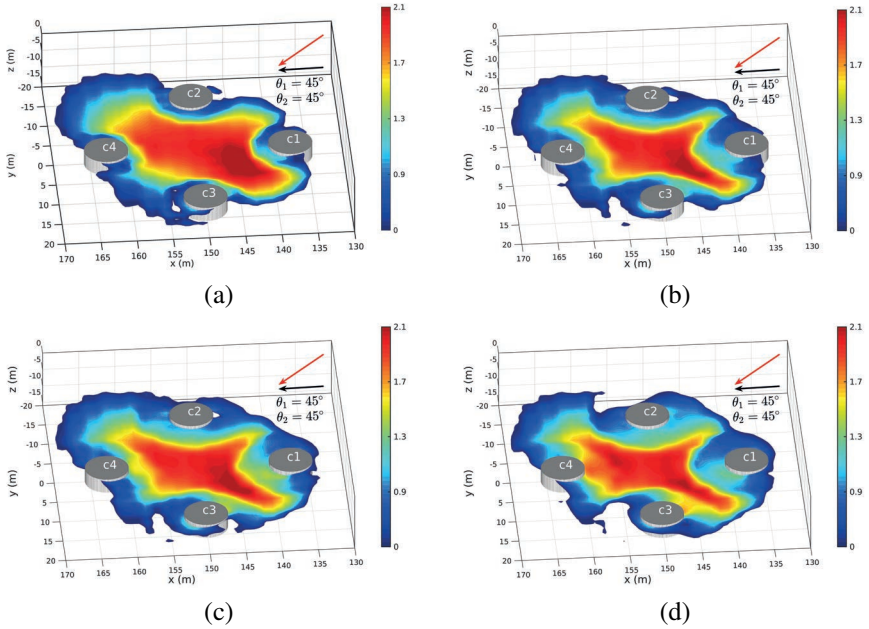

Figure 14.16 Snapshots of the instantaneous liquefaction depth (d_L) around a pile-group for various protection layers when θ_1 and θ_2 equals 45° near the propagation of wave trough: (a) R_r=4 m, D_r=2.5 m, k_{s2}=10^{-2} m/s; (b) R_r=6 m, D_r=2.5 m, k_{s2}=10^{-2} m/s; (c) R_r=6 m, D_r=4 m, k_{s2}=10^{-2} m/s; (d) R_r=6 m, D_r=2.5 m, k_{s2}=10^{-1} m/s. The interface of liquefaction occurrence is shaded from blue to red (Unit: m).

a model experiment to analyze the influence elements of scour depth around the jacket platform foundation. Although the above studies on dynamic response lies in structure itself, the wave-induced seabed response in the vicinity of the jacket is still rare, let alone in the cases of wave-current interaction. It is well-recognized that, the seafloor stability directly affects the stability of the jacket, which in turn affects the structures on the platform. Thus, this study aimed to fill the gaps of the existing research.

The Porous-Fluid-Seabed-Structure Interactions-FOAM (PORO-FSSI-FOAM) is composed of flow and seabed sub-models to simulate the dynamic seafloor response under the wave and current combination around the jacket foundation. Figure 14.18 displays the layout of numerical wave tanks and the location of offshore structures. The dimension of the computational field is set to be $L \times B$, where L is the seabed length ($L = 2L_w$ with L_w denoting the wavelength) and B is the seabed width. As reported in Ye and Jeng (2012), the computing domain with at least two or three times of wavelength is sufficient to avoid the influence of lateral boundary if the concerned structure is located in the middle of the domain. Therefore, two times of wavelength was selected for this study. The origin of Cartesian coordinates (i.e.,

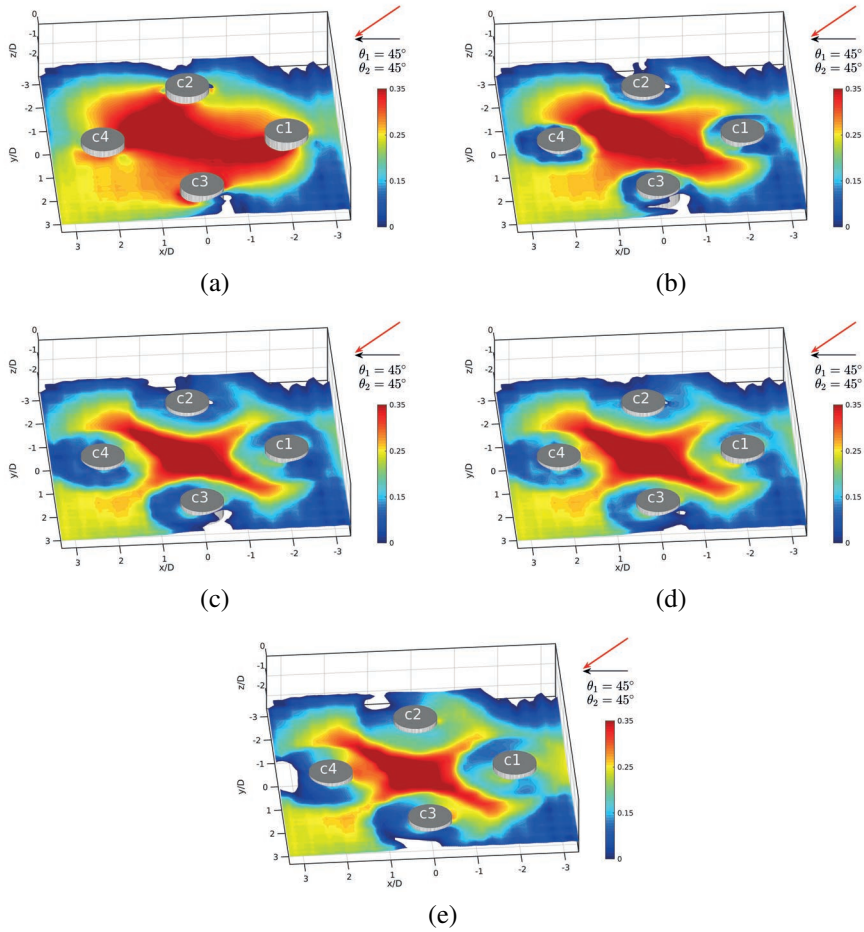

Figure 14.17 Snapshots of maximum dimensionless instantaneous liquefaction distribution (d_L/D) around a pile-group for various protection layers when θ_1 and θ_2 equals 45° during a specific wave period: (a) no protection layer; (b) R_r=4 m, D_r=2.5 m, k_{s2}=10^{-2} m/s; (c) R_r=6 m, D_r=2.5 m, k_{s2}=10^{-2} m/s; (d) R_r=6 m, D_r=4 m, k_{s2}=10^{-2} m/s; (e) R_r=6 m, D_r=2.5 m, k_{s2}=10^{-1} m/s. The interface of liquefaction occurrence is shaded from blue to red.

O) is located in the core of the front and rear piles of the jacket and on the surface of the porous seabed.

14.4.1 HYDRODYNAMIC PROCESS

Figure 14.19 illustrates the variations of free water surface elevation around a jacket structure in an entire wave cycle. The input parameters used in this study are listed in Table 14.2. It is obvious that the wave–structure interactions obviously affected the

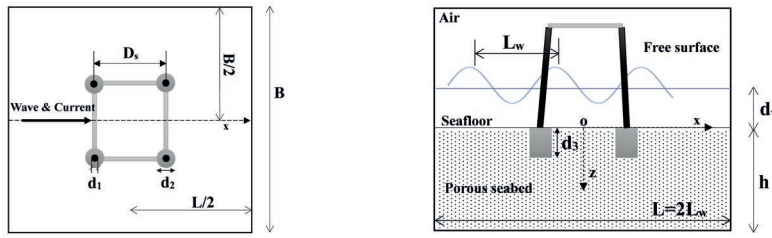

(a) plan view (b) side view

Figure 14.18 Schematic layout of computational domain (D_s: Column spacing, d_1:Column diameter, d_2: Foundation diameter; d_3: Inserted depth).

Table 14.2
Input data of the numerical simulation.

Sub-module	Parameter	Value
Wave-Current	Wave period (T_w)	8 s or various
	Wave height (H_w)	4 m or various
	Wavelength (L_w)	75.8 m or various
	Water depth (d_w)	12 m
	Current velocity (U_c)	-1, 0 and 1 m/s
Seabed	Seabed thickness (h)	28 m
	Seabed length (L)	$2L_w$
	Seabed width(B)	L_w
	Permeability (k_s)	10^{-3} m/s
	Degree of saturation (S_r)	0.97
	Porosity (n_s)	0.425
	Poisson's ratio (ν)	0.4
	Shear modulus(G)	10^7 Pa
Jacket	Foundation diameter (d_2)	6 m
	Inserted depth (d_3)	8 m
	Column diameter (d_1)	2 m
	Column spacing (D_s)	24 m or various
	Interaction angle	45° or various

free water surface distribution. In particular, the amplification effect and the climbing phenomenon were occurred in front of the jacket. This is because that the interaction of the incident and reflected wave and partial fluid kinetic energy changed to potential energy. Meanwhile, the diffracted wave was formed on the lateral side and back of the jacket due to the structural obstruction.

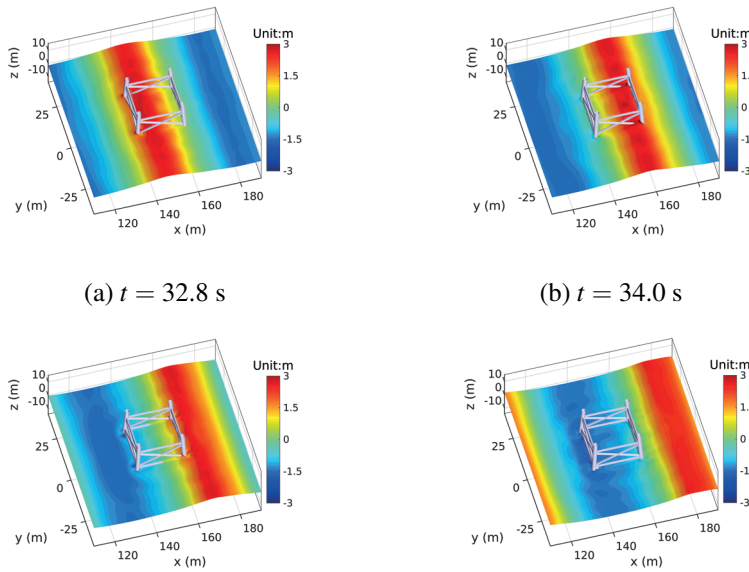

(a) $t = 32.8$ s (b) $t = 34.0$ s

(c) $t = 35.2$ s (d) $t = 36.4$ s

Figure 14.19 Variation of free water surface around a jacket structure throughout one wave period.

14.4.2 DYNAMIC SEABED RESPONSE

This section mainly focused on the transient seabed response around the jacket under the action of wave and current. As illustrated in Figures 14.20 and 14.21, the maximal pore pressure occurs at the wave crest (at t =35.2 s) and minimal value occurs at the wave trough (at t =37.6 s). On the contrary, the negative value of the pore pressure reached its minimum after the wave pressure at the seabed surface achieved its minimum at the trough. In addition, Figure 14.20 shows that the pore pressure near the jacket was irregularly distributed in the presence of the structure. This was because of the hindrance of jacket on flow field and the flow characteristics was changed around the jacket, which further alternated the wave pressure at the seabed surface. In combination with Figure 14.19, it was found that the pore pressure corresponding to the high wave height was also high, and vice versa. It should be noted that the seabed dynamic response weakened with increasing depth, and it was the most prominent within 10 m under the seabed surface.

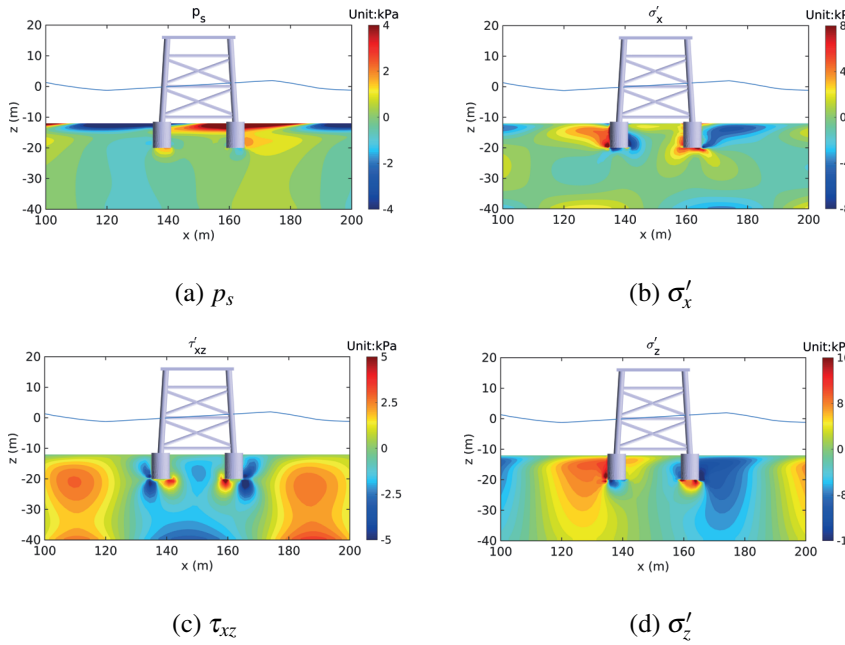

(a) p_s (b) σ'_x

(c) τ_{xz} (d) σ'_z

Figure 14.20 Distribution of wave-induced dynamics of seabed foundation and jacket structure at t =35.2 s.

14.4.3 SEABED INSTABILITY AROUND JACKET STRUCTURE

A. Distribution of seabed liquefaction with time

Figure 14.22 shows the distribution of transient liquefaction depth (d_L) in the vicinity of a jacket foundation under wave-only loading at four different time steps. It was found that the liquefaction range between the four piles at $t = 35.2$ s was obviously smaller than that at other moments. However, the liquefaction depth reached a maximum value of approximately 1.5 m at $t = 37.0$ s. This was because the negative excess pore pressure was produced at the wave trough. This can be attributed to the seabed instability in the proximity of marine structures under the action wave trough. On the other hand, it should be noted that the depth and range of the liquefaction area increased first and then declined gradually as the wave propagated forward. In addition, the jacket platform influenced the morphology of the liquefaction region, which can be observed in Figure 14.22.

B. Effect of wave and currents

In this section, the combined effects of waves and currents on the transient soil response were examined. The distribution of wave- and current-induced transient liquefaction depth near a jacket foundation around different current velocities (U_c)

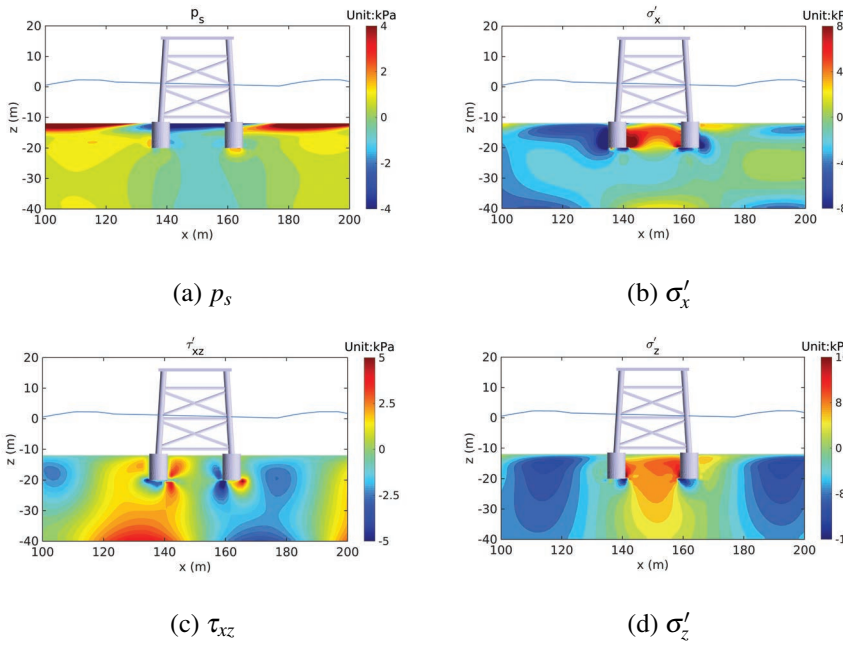

(a) p_s (b) σ'_x

(c) τ_{xz} (d) σ'_z

Figure 14.21 Distribution of wave-induced dynamics of seabed foundation and jacket structure at t =37.6 s.

are represented in Figure 14.23. As shown in the figure, the influence on the liquefaction distribution is more complex when the current exists. The liquefaction depth and range were greater at the action of wave and positive current than those at $U_c = 0$, while the influence of reverse current and wave on the liquefaction distribution around the jacket foundation was less obvious than that in the condition of wave-only loading. In this case, the structure was more prone to stability. On the other hand, the downstream piles were comparatively safe in comparison with the upstream piles, which means that relevant safety precautions should be applied at upstream piles.

The influence of incident angles (θ_s) on the distribution of combined wave- and current-induced transient liquefaction depth near a jacket foundation is displayed in Figure 14.24. Clearly, the incident angle hardly impact the seabed liquefaction in terms of its size and scope. The liquefaction zone in the middle of the jacket structure remained invariant when the incident angle varied from 45° to 67.5° at $t = 37$ s. Thus, the influence of the incident angle on the seabed response could be negligible. Moreover, it can be inferred that the blocking effect of jacket structure is not prominent when the pile spacing is large enough in this study.

In general, wave and current parameters affect the wave pressure at the seabed surface and further alter the transient seabed response. In this section, the effects of wave height (H_w), wave period (T_w), and current velocity (U_c) on the maximum

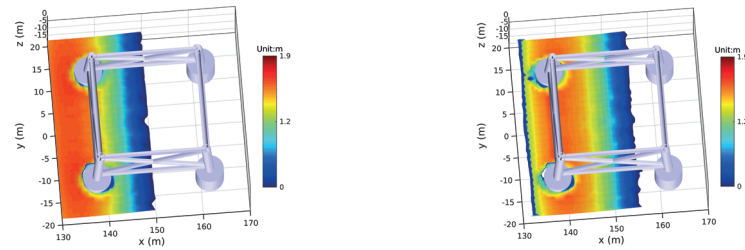

(a) $t = 35.2$ s (b) $t = 35.8$ s

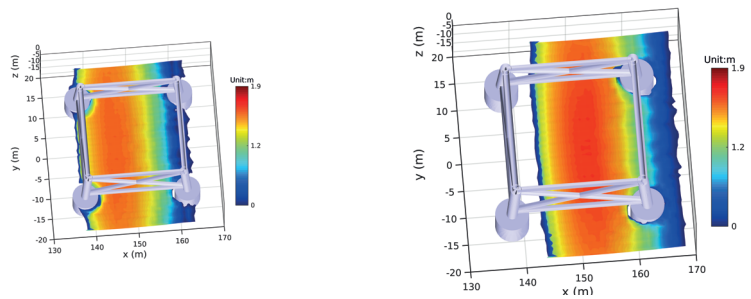

(c) $t = 36.4$ s (d) $t = 37.0$ s

Figure 14.22 Distribution of transient liquefaction depth (d_L) around a jacket foundation under wave loading at various time steps.

liquefaction depth were examined. Different values of H_w (2.0 m,3.0 m, and 4.0 m), T_w (8 s, 10 s, and 12 s), and U_c (1 m/s, 0 m/s, and -1 m/s) were chosen. The maximum d_L around the front and rear piles of the jacket structure under different hydrodynamic parameters are shown in the left and right columns of Figure 14.25, respectively. As seen from Figure 14.25, d_L increased 1.2 m when the wave height increased from 3 m to 5 m. This was because that the change in wave height affected the wave energy and further affected the wave excitation acting on the seabed. On the other hand, d_L also increased with the wave period (Figure 14.25(b)), which indirectly altered the wave pressure on the seabed surface by changing the wavelength. However, the magnitude of this increment was not as significant as that of wave height.

As shown Figure 14.25(c), d_L increased as the current velocity increased from -1 m/s to 1 m/s with H_w and T_w remaining constant. The presence of currents may not adversely affect d_L in comparison with the case of $U_c = 0$. To be more specific, when the direction of the wave and the current are opposite, the development of d_L was inhibited. However, when the directions of the wave and the current were the same, the development of d_L was accelerated. Furthermore, Figure 14.25(c) indicates that d_L around the front piles was greater than that of the rear piles when the current velocity were 1 m/s and 0 m/s, except for the case with U_c=-1 m/s. In particular, the black closed curve shown in Figure 14.25(c) was elliptical when U_c=-1 m/s,

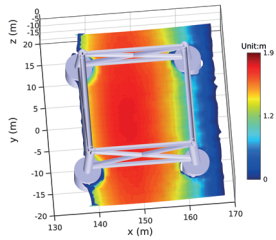

(a) $U_c = 1$ m/s and $t = 35$s

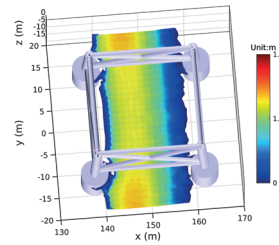

(b) $U_c =$ -1 m/s and $t = 37.2$ s

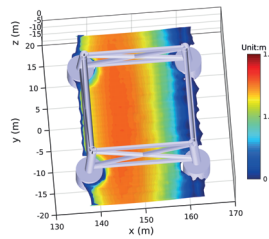

(c) $U_c = 0$ and $t = 36.4$ s

Figure 14.23 Distribution of combined wave- and current-induced transient liquefaction depth (d_L) around a jacket foundation under distinct current velocities.

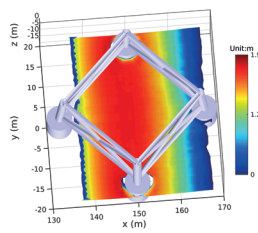

(a) $\theta_s = 45^\circ$

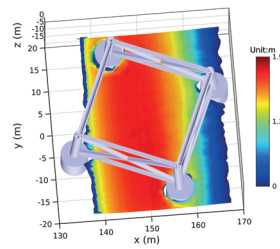

(b) $\theta_s = 67.5^\circ$

Figure 14.24 Distribution of combined wave- and current-induced transient liquefaction depth (d_L) around a jacket foundation with different interaction angles at $t = 37$ s.

indicating that the distribution of seabed liquefaction around the downstream piles was strongly nonlinear.

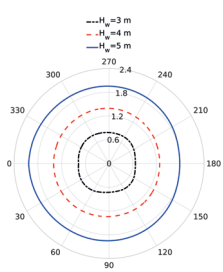

Front piles

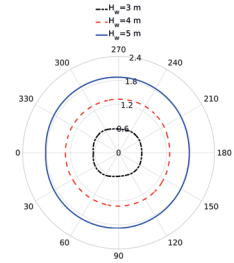

Rear piles

(a) Effect of H_w

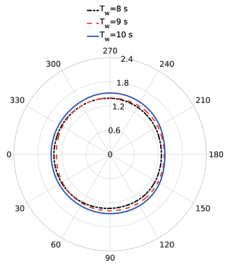

Front piles

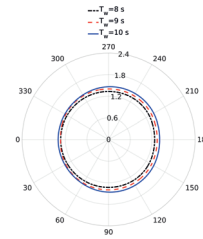

Rear piles

(b) Effect of T_w

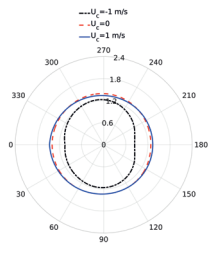

Front piles

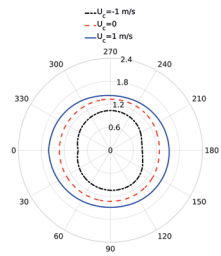

Rear piles

(c) Effect of U_c

Figure 14.25 Distribution of maximum d_L around front and back columns of a jacket structure under different hydrodynamic conditions (units: m/s).

14.5 SUMMARY

In this chapter, pile-type foundations have bee used for marine infrastructures like cross-sea bridges, offshore wind farms and oil/gas industry are considered, as well as possible potential protection measures for the foundation of these structures. Three kinds of pile-type foundations, including mono-pile, group piles and jacket support structure are investigated in the problem of fluid-seabed-structure interaction.

Foundation instability (e.g., seabed liquefaction) of these structure is evaluated base on which to propose a countermeasure that protect pile-type foundations. Based on the numerical results, the following key findings are summarized.

(1) The characteristics of wave run-up and the development of seabed liquefaction around a mono-pile under the combined waves and oblique current loading are investigated. Meanwhile, the investigation regarding the near-trapping effect and seabed instability in various layouts of pile groups is carried out. Studies show that the near-trapping phenomenon inside the pile group is related to the the wave-pile group interaction angle and the oblique ocean current is proven to be a critical factor in the development of the above-mentioned phenomenon.

(2) The numerical results reveal that replacing the existing soil layer around piles with a soil with high permeability can effectively suppress the occurrence of seabed liquefaction in the nearby region. Furthermore, additional gravel can be thrown to compact the seabed and increase the effective stress in place inside the pile group in order to prevent the weakening of the soil in this area.

(3) The presence of ocean current could have significant impact on the liquefaction around the jacket support offshore wind turbine foundation, numerical results show that the direction of ocean current can determine not only the depth of liquefaction, but also the area around the structure where more severe liquefaction occurs.

Bibliography

Acar, Y. B. and Haider, L. (1990), 'Transport of low-concentration contaminants in saturated earthen barriers', *Journal of Geotechnical Engineering, ASCE* **116**(7), 1031–1052.

Adamidis, O. and Madabhushi, G. (2016), 'Post-liquefaction reconsolidation of sand', *Proceedings of Royal Society, Series A* **472**, 20150745.

Al-Tabbaa, A. and Wood, D. M. (1987), 'Some measurements of the permeability of kaolin', *Géotechnique* **37**(4), 499–514.

Alonso, E. E., Battle, F., Gens, A. and Lloret, A. (1988), Consolidation analysis of partially saturated soils-application to earth dam construction, *in* 'Proc., 6th International Conference of Numerical Methods Geomechanics', Innsbruck, pp. 1303–1308.

Alshawabkeh, A. N. and Rahbar, N. (2006), 'Parametric study of one-dimensional solute transport in deformable porous media', *Journal of Geotechnical and Geoenvironmental Engineering, ASCE* **132**(8), 1001–1010.

Alshawabkeh, A. N., Rahbar, N. and Sheahan, T. (2005), 'A model for contaminant mass flux in capped sediment under consolidation', *Journal of Contaminant Hydrology* **78**(3), 147–165.

Alshawabkeh, A. N., Rahbar, N., Sheahan, T. C. and Tang, G. (2004), Volume change effects in solute transport in clay under consolidation, *in* 'Advances in Geotechnical Engineering with Emphasis on Dams, Highway Materials, and Soil Improvement', Vol. 1, pp. 105–115.

Anderson, M. (1984), Movement of contaminants in groundwater: Groundwater transport-advection and dispersion, *in* 'Groundwater Contamination, Studies in Geophysics', National Academy Press, Washington, DC., pp. 37–45.

Arega, F. and Hayter, E. (2008), 'Coupled consolidation and contaminant transport model for simulating migration of contaminants through the sediment and a cap', *Applied Mathematical Modelling* **32**(11), 2413 –2428.

Arulanandan, K. and Sybico Jr, J. (1992), Post-liquefaction settlement of sand, *in* 'The Wroth Memorial Symposium', pp. 94–110.

Azad, F. M., El-Zein, A., Rowe, R. K. and Airey, D. W. (2012), 'Modelling of thermally induced desiccation of geosynthetic clay liners in double composite liner system', *Geotextiles and Geomembranes* **34**, 28–38.

Bai, Q. and Bai, Y. (2014), *Subsea pipeline design, analysis, and installation*, Gulf Professional Publishing.

Baird, A. J., Mason, T. and Horn, D. P. (1998), 'Validation of a boussinesq model of beach groundwater behaviour', *Marine Geology* **148**, 55–69.

Barbour, S. L., Lim, P. C. and Fredlund, D. G. (1996), 'A new technique for diffusion testing of unsaturated soil', *American Society for Testing and Materials* **19**(3), 247–258.

Barry, D. A. (1990), 'Supercomputers and their use in modeling subsurface solute transport', *Reviews of Geophysics* **28**, 277–295.

Barry, D. A. (1992), Modelling contaminant transport in the subsurface: Theory and computer programs, *in* H. Ghadiri and C. W. Rose, eds, 'Modelling Chemical Transport in Soil: Natural and Applied Contaminants', Lewis Publishers, Boca Raton, Florida, USA, pp. 105–144.

Barry, D. A., Barry, S. J. and Parlange, J.-Y. (1996), Capillary correction to periodic solution of the shallow flow approximation, *in* C. B. Pattiaratchi, ed., 'Mixing Process in Estuaries and Coastal Seas', AGU, pp. 496–510.

Barry, D. A. and Sposito, G. (1988), 'Application of the convection-dispersion model to solute transport in finite soil columns', *Soil Science Society of America Journal* **52**, 3–9.

Barry, D. A. and Sposito, G. (1989), 'Analytical solution of a convection-dispersion model with time-dependent transport coefficients', *Water Resources Research* **25**, 2407–2416.

Barry, D., Lockington, D., Jeng, D.-S., Parlange, J.-Y., Li, L. and Stagnitti, F. (2007), 'Analytical approximations for flow in compressible, saturated, one-dimensional porous media', *Advances in water resources* **30**(4), 927–936.

Battjes, J. A. (1974), Surf similarity, *in* 'Coastal Engineering (ICCE1974)', ASCE, pp. 466–480.

Bear, J. (1972), *Dynamics of Fluids in Porous Media*, Elsevier Scientific Publishing Company, New York.

Bear, J. and Cheng, A. H. D. (2010), *Modeling Groundwater Flow and Contaminant Transport*, Springer, Heidelberg.

Bear, J. and Verruijt, A. (1987), *Modeling groundwater Flow and Pollution*, D. Reidel Publ. Co.

Bhattacharya, S. (2014), 'Challenges in design of foundations for offshore wind turbines', *Engineering & Technology Reference* **1**, 922.

Biot, M. A. (1941), 'General theory of three-dimensional consolidation', *Journal of Applied Physics* **12**(2), 155–164.

Bird, G. (1994), 'Molecular gas dynamics and the direct simulation monte carlo of gas flows', *Clarendon, Oxford* **508**, 128.

Bogner, J. E., Chanton, J. P. and Blake, D. (2010), 'Effectiveness of a florida landfill biocover for reduction of ch4 and nmhc emissions', *Environmental Science and Technology* **44**(4), 1197–1203.

Booker, J. R., Quigley, R. M. and Rowe, R. K. (1997), *Clayey Barrier Systems for Waste Disposal Facilities*, Spon Press, London.

Boso, F., Bellin, A. and Dumbser, M. (2013), 'Numerical simulations of solute transport in highly heterogeneous formations: A comparison of alternative numerical schemes', *Advances in Water Resources* **52**, 178–189.

Boyd, J. L. and Sivakumar, V. (2011), 'Experimental observations of the stress regime in unsaturated compacted clay when laterally confined', *Géotechnique* **61**(4), 345–363.

Cann, D., Stiver, W. and Zytner, R. (2004), Correlating gas phase dispersion and moisture content in undisturbed and disturbed unsaturated soils, *in* 'RemTech 2004 Proceedings', Environmental Services Association of Alberta (ESAA).

Cao, H. and Wan, D. (2017), 'Benchmark computations of wave run-up on single cylinder and four cylinders by naoe-foam-sjtu solver', *Applied Ocean Research* **65**, 327–337.

Carman, P. C. (1956), *Flow of Gases Through Porous Media*, Butterworth Scientific Publications.

Cartwright, N., Neilsen, P. and Dunn, S. (2003), 'Watertable waves in an unconfined aquifer: experiments and modeling', *Water Resources Research* **39**, WR002185.

Cartwright, N., Neilsen, P. and Li, L. (2004), 'Experimental observations of water table waves in an unconfined aquifer with a sloping boundary', *Advances in Water Resources* **27**, 991–1004.

Challa, J., Skoff, D. and Quirus, F. J. (1997), 'Landfill gas as source of vocs in ground water', *Practice Periodical of Hazardous, Toxic, and Radioactive Waste Management* **1**(2), 61–75.

Chang, J andYu, H. F. (2018), 'Static analysis of jacket foundation of offshore riser station under wave and current', *China Water Transport* **18**(6), 205–207 (in Chinese).

Chang, K.-T. and Jeng, D.-S. (2014), 'Numerical study for wave-induced seabed response around offshore wind turbine foundation in donghai offshore wind farm, shanghai, china', *Ocean Engineering* **85**, 32–43.

Chapuis, R. P. (2004), 'Predicting the saturated hydraulic conductivity of sand and gravel using effective diameter and void ratio', *Canadian Geotechnical Journal* **41**(5), 787–795.

Chapuis, R. P. and Aubertin, M. (2003), 'On the use of the Kozenya–Carman equation to predict the hydraulic conductivity of soils', *Canadian Geotechnical Journal* **40**, 616–628.

Chen, C. X. and Jiao, J. J. (1999), 'Numerical simulation of pumping tests inmultiplayer wells with non-darcian flow in the wellbore', *Ground Water* **37**, 465–474.

Chen, L., Zhai, H., Wang, P., Jeng, D.-S., Zhang, Q., Wang, S., Duan, L. and Liu, Y. (2020), 'Physical modeling of combined waves and current propagating around a partially embedded monopile in a porous seabed', *Ocean Engineering* **205**, 107307.

Chen, L., Zhai, H., Wang, P., Zhang, Q., Wang, S., Duan, L. and Jeng, D.-S. (2022), 'Experimental study on the irregular wave (current)-induced pore-water pressures around a monopile', *Journal of Coastal Research* **38**(1), 114–132.

Chen, R., Wu, L., Zhu, B. and Kong, D. (2019), 'Numerical modelling of pipe-soil interaction for marine pipelines in sandy seabed subjected to wave loadings', *Applied Ocean Research* **88**, 233–245.

Chen, X. and Jeng, D.-S. (2022*a*), Combined wave-current induced oscillatory seabed responses around two pipelines in tandem, *in* 'The 31st International Ocean and Polar Engineering Conference (ISOPE2022)', Shanghai, China, pp. 1568–1575.

Chen, X. and Jeng, D.-S. (2022*b*), 'Oscillatory seabed responses around two pipelines in tandem under combined wave and current loading', *International Journal of Offshore and Polar Engineering* **31**(3), 321–329.

Chen, X., Jeng, D.-S. and Liang, Z. D. (2022), 'Numerical analysis of seabed liquefaction in the vicinity of two tandem pipelines in a trench', *Ocean Engineering* **266**, 112656.

Cheng, A. H. D. (2016), *Poroelasticity*, Springer Nature.

Cheng, A. H. D. and Liu, P. L.-F. (1986), 'Seepage force on a pipeline buried in a poroelastic seabed under wave loading', *Applied Ocean Research* **8**(1), 22–32.

Cheng, L., Sumer, B. M. and Fredsoe, J. (2001), 'Solution of pore pressure build up due to progressive waves', *International Journal for Numerical and Analytical Methods in Geomechanics* **25**, 885–907.

Cho, Y. S. and Lee, C. (2000), 'Resonant reflection of waves over sinusoidally varying topographies', *Journal of Coastal Research* **16**, 870–876.

Cho, Y.-S., Lee, J.-I. and Kim, Y.-T. (2004), 'Experimental study of strong reflection of regular water waves over submerged breakwaters in tandem', *Ocean Engineering* **31**, 1325–1335.

Cho, Y.-S., Yoon, S. B., Lee, J.-I. and Yoon, T.-H. (2001), 'A concept of beach protection with submerged breakwater', *Journal of Coastal Researc* **34**, 671–678.

Christian, J. T., Taylor, P. K., Yen, J. K. C. and Erali, D. R. (1974), Large diameter underwater pipeline for nuclear power plant designed against soil liquefaction, *in* 'Proceeding of Offshore Technology Conference', Houston, Texas, pp. 597–606.

Chung, S. G., Kim, S. K., Kang, Y. J., Im, J. C. and Prasad, K. N. (2006), 'Failure of a breakwater founded on a thick normally consolidated clay layer', *Géotechnique* **56**(3), 393–409.

Civan, F., Rai, C. S. and Sondergeld, C. H. (2011), 'Shale-gas permeability and diffusivity inferred by improved formulation of relevant retention and transport mechanisms', *Transport in Porous Media* **86**(3), 925–944.

Clukey, E. C., Vermersch, J. A., Koch, S. P. and Lamb, W. C. (1989), Natural densification by wave action of sand surrounding a buried offshore pipeline., *in* 'Proceedings of the 21st Annual Offshore Technology Conference', Houston, Texas, pp. 291–300.

COMSOL (2010), *COMSOL Multiphysics, 3rd Edition*.

Craig, J. R. and Rabideau, A. J. (2006), 'Finite difference modeling of contaminant transport using analytic element flow solutions', *Advances in Water Resources* **29**(7), 1075–1087.

Crowhurst, A. (1982), Wave forces on solid and perforated caisson breakwaters: comparison of field and laboratory measurements, *in* 'Coastal Engineering (ICCE1982)', pp. 2403–2417.

Cui, L. and Jeng, D.-S. (2018), 'Numerical study for soil response around submerged breakwaters with bragg reflection', *International Journal of Ocean and Coastal Engineering* **1**(04), 1850005.

Cui, L. and Jeng, D.-S. (2021), 'Seabed liquefaction around breakwater heads at a river mouth: An integrated 3D model', *Ocean Engineering* **242**, 110036.

Dagan, D. (1967), 'Second-order theory of shallow free-surface flow in porous media', *Quarterly Journal of Mechanics and Applied Mathematics* **20**(4), 517–526.

Dagan, D. and Zeitoun, D. (1998), 'Seawater–freshwater interface in a stratified aquifer of random permeability distribution', *Journal of Contaminant Hydrology* **29**(3), 185–203.

Damgarrd, J. S., Sumer, B. M., Teh, T. C., Palmer, A., Foray, P. and Osorio, D. (2006), 'Guidelines for pipeline on-bottom stability on liquefied noncohesive seabeds', *Journal of Waterway, Port, Coastal, and Ocean Engineering, ASCE* **132**(4), 300–309.

Danckwerts, P. V. (1953), 'Continuous flow systems : Distribution of residence times', *Chemical Engineering Science* **2**, 1–13.

Davies, A. G. and Heathershaw, A. D. (1984), 'Surface-wave propagation over sinusoidally varying topography', *Journal of Fluid Mechanics* **144**, 419–443.

de Alba, P., Seed, H. B. and Chan, C. K. (1976), 'Sand liquefaction in large-scale simple shear tests', *Journal of Geotechnical Division, ASCE* **102**, 909–928.

Dean, R. and Dalrymple, R. A. (1984), *Water wave mechanics for engineers and scientists*, World Scientific.

Dongen, F. (1983), 'Het ingraven van onderzeese leidingen', *Civiele en bouwkundige techniek* **7**, 22–26.

Duan, L., Jeng, D.-S. and Wang, D. (2019), 'PORO-FSSI-FOAM: Seabed response around a mono-pile under natural loadings', *Ocean Engineering* **184**, 239–254.

Duan, L., Liao, C., Jeng, D.-S. and Chen, L. (2017), '2D numerical study of wave and current-induced oscillatory non-cohesive soil liquefaction around a partially buried pipeline in a trench', *Ocean Engineering* **135**, 39–51.

Edil, T. B. (2003), 'A review of aqueous-phase voc transport in modern landfill liners', *Waste Management* **23**, 561–571.

Ellsworth, T. R. and Jury, W. A. (1991), 'A three-dimensional field study of solute transport through unsaturated, layered, porous media: 2. characterization of vertical dispersion', *Water Resources Research* **27**(5), 967–981.

Elsafti, H. and Oumeraci, H. (2016), 'A numerical hydro-geotechnical model for marine gravity structures', *Computers and Geotechnics* **79**, 105–129.

Erskine, D. (1991), 'The effect of tidal fluctuation on a coastal aquifer in the U.K.', *Ground Water* **29**, 556–562.

Farrell, E. R. (1994), 'Analysis of groundwater flow through leaky marineretaining structures.', *Géotechnique* **44**, 255.

Fen, C.-S., Liang, W., Hsiesh, P. and Huang, Y. (2011), 'Knudsen and molecular diffusion coefficients for gas transport in unconsolidated porous media', *Soil Science Society of America Journal* **75**(2), 456–467.

Fityus, S. G., Smith, D. W. and Booker, J. R. (1999), 'Contaminant transport through an unsaturated soil liner beneath a landfill', *Canadian Geotechnical Journal* **36**(2), 330–354.

Foose, G. J. (2002), 'Transit-time design for diffusion through composite liners', *Journal of Geotechnical and Geoenvironmental Engineering, ASCE* **128**(1), 590–601.

Foose, G. J., Benson, C. H. and Edil, T. B. (2002), 'Comparison of solute transport in three composite liners', *Journal of Geotechnical and Geoenvironmental Engineering, ASCE* **128**(5), 391–403.

Fox, P. (2007*a*), 'Coupled large strain consolidation and solute transport. i: Model development', *Journal of Geotechnical and Geoenvironmental Engineering, ASCE* **133**(1), 3–15.

Fox, P. (2007*b*), 'Coupled large strain consolidation and solute transport.ii: Model verification and simulation results', *Journal of Geotechnical and Geoenvironmental Engineering, ASCE* **133**(1), 16–29.

Fox, P. and Lee, J. (2008), 'Model for consolidation-induced solute transport with nonlinear and nonequilibrium sorption', *International Journal of Geomechanics, ASCE* **8**(3), 188–198.

Franco, L. (1994), 'Vertical breakwaters: the italian experience', *Coastal Engineering* **22**(1-2), 31–55.

Frankenmolen, S., Ang, S., Peek, R., Carr, M., MacRae, I., White, D. and Rimmer, J. (2017), Pipe-clamping mattress to stop flowline walking, *in* 'Offshore Technology Conference', pp. OTC–27815.

Fredlund, D. G. and Rahardjo, H. (1993), *Soil Mechanics for Unsaturated Soils*, Wiley.

Fredsoe,, J. (1979), 'Natural backfilling of pipeline trenches', *Journal of Petroleum Technology* **31**, 1223–1230.

Fredsoe, J. (2016), 'Pipeline-seabed interaction', *Journal of Waterway, Port, Coastal and Ocean Engineering, ASCE* **142**(6), 03116002.

Fukumoto, Y. and Ohtsuka, S. (2018), '3-d direct numerical model for failure of non-cohesive granular soils with upward seepage flow', *Computational Particle Mechanics* **5**(4), 443–454.

Fuller, E., Schettler, P. and Giddings, J. (1966), 'A new method for prediction of binary gas-phase diffusion coefficients', *Industrial and Engineering Chemistry* **58**, 18–27.

Gaeta, M., Lamberti, A., Ricchieri, F. and Zurlo, M. (2011), Articulated concrete mattress for submarine pipeline protection: evaluation of the wave-induced forces and stability analysis, *in* 'Coastal Structures 2011', pp. 1116–1125.

Gallipoli, D., Wheeler, S. and Karstunen, M. (2003), 'Modelling the variation of degree of saturation in a deformable unsaturated soil.', *Géotechnique.* **53**(1), 105–112.

Gao, F., Gu, X. and Jeng, D.-S. (2003*a*), 'Physical modeling of untrenched submarine pipeline instability', *Ocean Engineering* **30**(10), 1283–1304.

Gao, F., Jeng, D.-S. and Sekiguchi, H. (2003*b*), 'Numerical study on the interaction between non-linear wave, buried pipeline and non-homogenous porous seabed', *Computers and Geotechnics* **30**(6), 535–547.

Gao, F.-P. and Wu, Y.-X. (2006), 'Non-linear wave induced transient response of soil around a trenched pipeline', *Ocean Engineering* **33**, 311–330.

Gardner, W. R. (1956), 'Mathematics of isothermal water conduction in unsaturated soils', *Highway Research Board Special Report* **40**, 78–87.

Gardner, W. R. (1958), 'Some steady-state solutions of the unsaturated moisture flow equation with application to evaporation from a water table', *Soil Science* **85**(4), 228–232.

Gatmiri, B. (1990), 'A simplified finite element analysis of wave-induced effective stress and pore pressures in permeable sea beds', *Géotechnique* **40**(1), 15–30.

Gatmiri, B. (1992), 'Response of cross-anisotropic seabed to ocean waves', *Journal of Geotechnical Engineering, ASCE* **118**(9), 1295–1314.

Geiges, A. (2009), Examination of the assumption of thermal equilibrium on the fluid distribution and front stability, PhD thesis, Institut fur Wasserbau, Universitat Stuttgart.

Genuchten, M. T. V. (1980), 'A closed form equation for predicting the hydraulic conductivity of unsaturated soils', *Soil Science Society of America Journal* **44**, 892–898.

Geremew, A. M. (2013), 'Pore-water pressure development caused by wave-induced cyclic loading in deep porous formation', *International Journal of Geomechanics, ASCE* **13**(1), 65–68.

Gerwick Jr, B. (2007), *Construction of Marine and Offshore Structures*, CRC Press.

Ghassemi, A. and Pak, A. (2011), 'Pore scale study of permeability and tortuosity for flow through particulate media using lattice boltzmann method', *International Journal of Numerical and Analytical Methods in Geomechanics* **35**(8), 886–901.

Girault, V. and Wheeler, M. (2008), 'Numerical discretization of a darcy-forchheimer model', *Numerische Mathematik* **110**(2), 161–198.

Giroud, J. and Bonaparte, R. (1989), 'Leakage through liners constructed with geomembranes. part i. geomembrane liners. part ii. composite liners.', *Geotextiles and Geomembranes* **8**, 27–68.

Goda, Y. and Suzuki, Y. (1976), Estimation of incident and reflected waves in random wave experiments, *in* 'Proceedings of the 15th International Conference on Coastal Engineering (ICCE1976)', Hawaii, USA, pp. 828–845.

Godbold, J., Sackmann, N. and Cheng, L. (2002), Stability design for concrete mattresses, *in* 'Proceedings of the Twenty-fourth (2014) International Ocean and Polar Engineering Conference (ISOPE2004)', pp. 302–308.

Grant, U. (1948), 'Influence of the water table on beach aggradation and degradation', *Journal of Marine Research* **7**(3), 655–660.

Guerrero, J. and Skaggs, T. (2010), 'Analytical solution for one-dimensional advection-dispersion transport equation with distance-dependent coefficients', *Journal of Hydrology* **390**(1-2), 57–65.

Guo, Z. and Jeng, D.-S. (2014), 'Discussion of "pore-water pressure development caused by wave-induced cyclic loading in deep porous formation" by africa m. geremew', *International Journal of Geomechanics, ASCE* **14**, 326–328.

Guo, Z., Jeng, D.-S. and Guo, W. (2014), 'Simplified approximation of wave-induced liquefaction in a shallow porous seabed', *International Journal of Geomechanics, ASCE* **14**(4), 06014008.

Guo, Z., Jeng, D.-S., Zhao, H., Guo, W. and Wang, L. (2019), 'Effect of seepage flow on sediment incipient motion around a free spanning pipeline', *Coastal Engineering* **143**, 50–62.

Ha, I., Park, Y. and Kim, M. (2003), Dissipation pattern of excess pore pressure after liquefaction in saturated sand deposits, *in* 'Geology and Properties of Earth Materials 2003: Soils, Geology, and Foundations', pp. 59–67.

Haigh, S. K., Eadington, J. and Madabhushi, S. P. G. (2012), 'Permeability and stiffness of sands at very low effective stresses', *Géotechnique* **62**(1), 69–75.

Hamamoto, S., Perera, M. S. A., Resurreccion, A., Kawamoto, K., Hasegawa, S., Komatsu, T. and MÃ¸ldrup, P. (2009), 'The solute diffusion coefficient in variably compacted, unsaturated volcanic ash soils', *Soil Science Society of America* **8**(4), 942–952.

Hansbo, S. (2001), 'Consolidation equation valid for both darcian and non-darcian flow', *Géotechnique* **51**(1), 51–54.

Higuera, P. (2020), 'Enhancing active wave absorption in rans models', *Applied Ocean Research* **94**, 102000.

Higuera, P., Lara, J. L. and Losada, I. J. (2013), 'Realistic wave generation and active wave absorption for navier-stokes models: Application to openfoam', *Coastal Engineering* **71**, 102–118.

Hillel, D. (1998), *Environmental Soil Physics: Fundamentals, Applications, and Environmental Considerations*, Elsevier.

Hills, R., Hudson, I. P. and Wierenga, P. J. (1989), 'Modeling one-dimensional infiltration into very dry soils', *Water Resources Research* **25**, 1271–1282.

Hirt, C. W. and Nichols, B. D. (1981), 'Volume of fluid (vof) method for the dynamics of free boundaries', *Journal of Computational Physics* **39**(1), 201–225.

Hodgson, A., Garbesi, K., Sextro, R. and Daisey, J. (1992), 'Soil-gas contamination and entry of volatile organic compounds into a house near a landfill', *Air and Waste Management* **42**, 277–283.

Hsu, J. R. C.and Jeng, D.-S. (1994), 'Wave-induced soil response in an unsaturated anisotropic seabed of finite thickness', *International Journal for Numerical and Analytical Methods in Geomechanics* **18**(11), 785–807.

Hsu, J. R. C., Jeng, D.-S. and Lee, C. (1995), 'Oscillatory soil response and liquefaction in an unsaturated layered seabed', *International Journal for Numerical and Analytical Methods in Geomechanics* **19**(12), 825–849.

Hsu, J. R. C., Jeng, D.-S. and Tsai, C. P. (1993), 'Short-crested wave-induced soil response in a porous seabed of infinite thickness', *International Journal for Numerical and Analytical Methods in Geomechanics* **17**(8), 553–576.

Hsu, J. R. C., Uda, H. and Silvester, R. (2000), *Shoreline protection methods–Japanese experience*, Vol. 923, McGraw-Hill, pp. 9.1–9.77.

Hsu, T.-W., Hsiao, S.-C., Ou, S.-H., Wang, S.-K., Yang, B.-D. and Chou, S.-E. (2007), 'An application of boussinesq equations to bragg reflection of irregular waves', *Ocean Engineering* **34**, 870–883.

Hsu, T.-W. and Wen, C.-C. (2001), 'A parabolic equation extended to account for rapidly varying topography', *Ocean Engineering* **28**, 1479–1489.

Huang, P. G., Bardina, J. and Coakley, T. (1997), 'Turbulence modeling validation, testing, and development', *NASA Technical Memorandum* **110446**, 147.

Hunt, A. G. and Ewing, R. P. (2003), 'On the vanishing of solute diffusion in porous media at a threshold moisture content', *Soil Science Society of America Journal* **67**, 1701–1702.

Ishihara, K. (1993), At-rest and compaction-induced lateral earth pressures of moist soils, PhD thesis, Civil engineering.

Jacobsen, V., Bryndum, M. and Bonde, C. (1989), Fluid loads on pipelines: sheltered or sliding, *in* 'Proceedings of the 21st Annual Offshore Technology Conference', pp. OTC–6056.

Jeng, D.-S. (1996), 'Wave-induced liquefaction potential at the tip of a breakwater: an analytical solution', *Applied Ocean Research* **18**(5), 229–241.

Jeng, D.-S. (1997*a*), 'Soil response in cross-anisotropic seabed due to standing waves', *Journal of Geotechnical and Geoenvironmental Engineering, ASCE* **123**(1), 9–19.

Jeng, D.-S. (1997*b*), 'Wave-induced seabed instability in front of a breakwater', *Ocean Engineering* **24**(10), 887–917.

Jeng, D.-S. (2000), 'On calculating the length of a short-crested wave over a porous seabed', *Applied Ocean Research* **22**(2), 63–73.

Jeng, D.-S. (2001), 'Mechanism of the wave-induced seabed instability in the vicinity of a breakwater: a review', *Ocean Engineering* **28**(5), 537–570.

Jeng, D. S. (2003), 'Wave-induced sea floor dynamics', *Applied Mechanics Review* **56**(4), 407–429.

Jeng, D.-S. (2012), *Porous Models for Wave-Seabed Interaction*, Springer.

Jeng, D.-S. (2018), *Mechanics of Wave-Seabed-Structure Interactions: Modelling, Processes and Applications*, Cambridge University Press.

Jeng, D.-S., Barry, D. A., Seymour, B., Dong, P. and Li, L. (2005*a*), 'Two-dimensional approximation for tide-induced watertable fluctuations in a sloping sandy beach', *Advances in Water Resources* **28**(10), 1040–1047.

Jeng, D.-S. and Cha, D. (2003), 'Effects of dynamic soil behavior and wave non-linearity on the wave-induced pore pressure and effective stresses in porous seabed', *Ocean Engineering* **30**(16), 2065–2089.

Jeng, D.-S., Cha, D., Lin, Y.-S. and Hu, P. (2000), 'Analysis on pore pressure in an anisotropic seabed in the vicinity of a caisson', *Applied Ocean Research* **22**(6), 317–329.

Jeng, D.-S., Cha, D., Lin, Y.-S. and Hu, P. (2001), 'Wave-induced pore pressure around a composite breakwater', *Ocean Engineering* **28**(10), 1413–1435.

Jeng, D.-S. and Hsu, J. (1996), 'Wave-induced soil response in a nearly saturated sea-bed of finite thickness', *Géotechnique* **46**(3), 427–440.

Jeng, D.-S. and Lee, T. (2001), 'Dynamic response of porous seabed to ocean waves', *Computers and Geotechnics* **28**(2), 99–128.

Jeng, D.-S., Li, L. and Barry, D. (2002), 'Analytical solution for tidal propagation in a coupled semi-confined/phreatic coastal aquifer', *Advances in Water Resources* **25**(5), 577–584.

Jeng, D.-S. and Lin, Y.-S. (1996), 'Finite element modelling for water waves-soil interaction', *Soil Dynamics and Earthquake Engineering* **15**(5), 283–300.

Jeng, D.-S. and Lin, Y.-S. (1999), 'Wave–induced pore pressure around a buried pipeline in gibson soil: finite element analysis', *International Journal for Numerical and Analytical Methods in Geomechanics* **23**(13), 1559–1578.

Jeng, D.-S. and Lin, Y.-S. (2000*a*), 'Poroelastic analysis of the wave–seabed interaction problem', *Computers and Geotechnics* **26**(1), 43–64.

Jeng, D.-S. and Lin, Y.-S. (2000*b*), 'Response of inhomogeneous seabed around buried pipeline under ocean waves', *Journal of Engineering Mechanics, ASCE* **126**(4), 321–332.

Jeng, D.-S., Mao, X., Enot, P., Barry, D. and Li, L. (2005*b*), 'Spring-neap tide-induced beach water table fluctuations in a sloping coastal aquifer', *Water Resources Research* **41**(7), W07026.

Jeng, D.-S. and Ou, J. (2010), '3D models for wave-induced pore pressures near breakwater heads', *Acta Mechanica* **215**(1-4), 85–104.

Jeng, D.-S. and Rahman, M. (2000), 'Effective stresses in a porous seabed of finite thickness: Inertia effects', *Canadian Geotechnical Journal* **37**(6), 1383–1392.

Jeng, D.-S., Rahman, M. and Lee, T. (1999), 'Effects of inertia forces on wave-induced seabed response', *International Journal of Offshore and Polar Engineering* **9**(04), 307–313.

Jeng, D.-S. and Seymour, B. (1997), 'Response in seabed of finite depth with variable permeability', *Journal of Geotechnical and Geoenvironmental Engineering, ASCE* **123**(10), 902–911.

Jeng, D.-S. and Seymour, B. (2007), 'Simplified analytical approximation for pore-water pressure buildup in marine sediments', *Journal of Waterway, Port, Coastal, and Ocean Engineering, ASCE* **133**(4), 309–312.

Jeng, D.-S., Seymour, B., Barry, D., Li, L. and Parlange, J.-Y. (2005*c*), 'New approximation for free surface flow of groundwater: capillarity correction', *Advances in Water Resources* **28**(10), 1032–1039.

Jeng, D.-S., Seymour, B., Barry, D., Parlange, J.-Y., Lockington, D. and Li, L. (2005*d*), 'Steepness expansion for free surface flows in coastal aquifers', *Journal of Hydrology* **309**(1-4), 85–92.

Jeng, D.-S., Seymour, B. and Li, J. (2007*a*), 'A new approximation for pore pressure accumulation in marine sediment due to water waves', *International Journal for Numerical and Analytical Methods in Geomechanics* **31**(1), 53–69.

Jeng, D.-S., Seymour, B. R., Gao, F. and Wu, Y. X. (2007*b*), 'Ocean waves propagating over a porous seabed: Residual and oscillatory mechanisms', *Science in China Series E: Technological Sciences* **50**(1), 81–89.

Jeng, D.-S., Teo, H., Barry, D. and Li, L. (2005*e*), 'Two-dimensional approximation for tidal dynamics in coastal aquifers: capillarity correction', *Journal of Engineering Mechanics, ASCE* **131**(5), 534–541.

Jeng, D.-S., Ye, J.-H., Zhang, J.-S. and Liu, P.-F. (2013), 'An integrated model for the wave-induced seabed response around marine structures: Model verifications and applications', *Coastal Engineering* **72**, 1–19.

Jeng, D.-S. and Zhao, H. Y. (2015), 'Two-dimensional model for accumulation of pore pressure in marine sediments', *Journal of Waterway, Port, Coastal, and Ocean Engineering, ASCE* **141**(3), 04014042.

Jeon, C.-H. and Cho, Y.-S. (2006), 'Bragg reflection of sinusoidal waves due to trapezoidal submerged breakwaters', *Ocean Engineering* **33**, 2067–2082.

Jiang, C., Liu, X., Yao, Y. and Deng, B. (2019), 'Numerical investigation of solitary wave interaction with a row of vertical slotted piles on a sloping beach', *International Journal of Naval Architecture and Ocean Engineering* **11**(1), 530–541.

Jiang, S., Li, Z., Duan, M., Qi, J. and Ma, D. (2012), 'Experimental study of the pile foundation scouring of jacket platform under the effect of wave and current', *China Petroleum Machinery* **40**(9), 57–61 (in Chinese).

Jiao, J. J. and Tang, Z. H. (1999), 'An analytical solution of groundwater responseto tidal fluctuations in a leaky confined aquifer', *Water Resources Research* **35**, 747–751.

Jiao, J. and Tang, Z. H. (2001), 'Reply to R E Volker and Q Zhang's comments on "an analytical solution of groundwater response to tidal fluctuations in a leaky confined aquifer"', *Water Resources Research* **37**, 187–188.

Jo, C., Lee, S., Shin, Y., Hong, S. and Min, K. (2002), 'Numerical and experimental study of offshore pipeline stability in trench', *Journal of Waterway, Port, Coastal, and Ocean Engineering, ASCE* **128**, 258–270.

Jury, W. A., Russo, D., Streile, G. and El-Abd, H. (1990), 'Evaluation of volatilization by organic chemicals residing below the soil surface', *Water Resource Research* **26**, 13–20.

Karim, M., Tanimoto, K. and Hieu, P. (2009), 'Modelling and simulation of wave transformation in porous structures using VOF based two-phase flow model', *Applied mathemtical Modelling* **33**, 343–360.

Karunarthna, K. and Lin, P. (2006), 'Numerical simulation of wave damping over porous seabeds', *Coastal Engineering* **53**(10), 845–855.

Kay, B. D. and Groenevelt, P. H. (1974), 'On the interaction of water and heat in frozen and unfrozen solids: I. basic theory-the vapor phase', *Soil Science Society of America* **38**, 395–400.

Kevorkian, J. and Cole, J. D. (1981), *Perturbation Methods in Applied Mathematics*, Springer-Verlag.

Kim, J. Y. (1997), 'Migration of volatile organic compounds from the landfill liner systems', *Environmental Engineering Research* **2**(4), 233–243.

Kitano, T. and Mase, H. (1999), 'Boundary-layer theory for anisotropic seabed response to sea waves', *Journal of Waterway, Port, Coastal, and Ocean Engineering, ASCE* **125**(4), 187–194.

Kitano, T. and Mase, H. (2001), 'Wave-induced porewater pressure in a seabed with inhomogeneous permeability', *Ocean Engineering* **28**, 279–296.

Klett, N., Edil, T. B., Benson, C. H. and Connelly, J. (2005), Evaluation of volatile organic compounds in wisconsin landfill leachate and lysimeter samples, Technical report, Department of Civil and Environmental Engineering, University of Wisconsin-Madison, Madison, USA.

Kozeny, J. (1927), 'Uber kapillare leitung der wasser in boden', *SItzurngsber Akad. Wiss, Wien* **136**(2a), 271–306.

Kumar, P. and Dodagoudar, G. (2010), 'Meshfree analysis of two-dimensional contaminant transport through unsaturated porous media using efgm', *International Journal for Numerical Methods in Biomedical Engineering* **26**(12), 1797–1816.

Kunisch, K. and RöSch, A. (2002), 'Primal-dual active set strategy for a general class of constrained optimal control problems', *Siam Journal on Optimization* **13**(2), 321–334.

Lan, Y.-J., Hsu, T.-W., Lai, J.-W., Chang, C.-C. and Ting, C.-H. (2009), Bragg scattering of waves propagating over a series of poro-elastic submerged breakwaters, *in* 'Proceedings of the Nineteenth (2009) International Offshore and Polar Engineering Conference (ISOPE2009)', Osaka, Japan, pp. 1180–1187.

Le Méhauté, B. (1976), *Introduction to Hydrodynamics and Water Waves*, Springer-Verlag, New York.

Lee, T., Tsai, C. and Jeng, D.-S. (2002), 'Ocean waves propagating over a coulomb-damped poroelastic seabed of finite thickness: An analytical solution', *Computers and Geotechnics* **29**(2), 119–149.

Leij, F. and Van Genuchten, M. T. (1995), 'Approximate analytical solutions for solute transport in two-layer porous media', *Transport in Porous Media* **18**(1), 65–85.

Lewis, T. W., Pivonka, P. and Smith, D. W. (2009), 'Theoretical investigation of the effects of consolidation on contaminant transport through clay barriers', *International Journal For Numerical and Analytical Methods In Geomechanics* **33**, 95–116.

Li, H. and Jiao, J. J. (2001), 'Analytical studies of groundwater-head fluctuation in a coastal confined aquifer overlain by a semi-permeable layer with storage', *Advances in Water Resources* **24**, 565–573.

Li, H., Jiao, J. J., Luk, M. and Cheung, K. (2002*a*), 'Tide-induced groundwater level fluctuation in coastal aquifers bounded by l-shaped coastlines', *Water Resources Research* **38**(3), 6–1–6–8.

Li, J. and Jeng, D.-S. (2008), 'Response of a porous seabed around breakwater heads', *Ocean Engineering* **35**(8-9), 864–886.

Li, L., Barry, D. A., Parlange, J.-Y. and Pattiaratchi, C. B. (1997*a*), 'Beach water table fluctuations due to wave run-up: Capillarity effects', *Water Resources Research* **33**(5), 935–945.

Li, L., Barry, D. A. and Pattiaratchi, C. B. (1997*b*), 'Numerical modelling of tide induced beach water table fluctuations', *Coastal Engineering* **30**, 105–123.

Li, L., Barry, D., Cunningham, C., Stagnitti, F. and Parlange, J.-Y. (2000*a*), 'A two-dimensional analytical solution of groundwater responses to tidal loading in an estuary and ocean', *Advances in Water Resources* **23**(8), 825–833.

Li, L., Barry, D. and Jeng, D.-S. (2001), 'Tidal fluctuations in a leaky confined aquifer: dynamic effects of an overlying phreatic aquifer', *Water Resources Research* **37**(4), 1095–1098.

Li, L., Barry, D., Stagnitti, F., Parlange, J.-Y. and Jeng, D.-S. (2000*b*), 'Beach water table fluctuations due to spring–neap tides: moving boundary effects', *Advances in Water Resources* **23**(8), 817–824.

Li, L., Dong, P. and Barry, D. A. (2002*b*), 'Tide-induced water table fluctuations in coastal aquifers bounded by rhythmic shorelines', *Journal of Hydraulic Engineering, ASCE* **128**(10), 925–933.

Li, S. and Liu, Y. (2006), Application of fractal models to water and solute transport in unsaturated soils, *in* 'Advances in Unsaturated Soil, Seepage, and Environmental Geotechnics (GSP 148), Proceedings of Sessions of GeoShanghai 2006'.

Li, X., Gao, F., Yang, B. and Zang, J. (2011), 'Wave-induced pore pressure response and soil liquefaction around pile foundation', *International Journal of Offshore and Polar Engineering* **21**(3), 233–239.

Li, Y.-C. and Cleall, P. J. (2011), 'Analytical solutions for advective–dispersive solute transport in double-layered finite porous media', *International Journal for Numerical and Analytical Methods in Geomechanics* **35**(4), 438–460.

Li, Y., Ong, M. C. and Fuhrman, D. R. (2020), 'CFD investigations of scour beneath a submarine pipeline with the effect of upward seepage', *Coastal Engineering* **156**, 103624.

Li, Y., Ong, M. C. and Tang, T. (2018), 'Numerical analysis of wave-induced poro-elastic seabed response around a hexagonal gravity-based offshore foundation', *Coastal Engineering* **136**, 81–95.

Li, Z. and Jeng, D.-S. (2023), 'Dynamic soil response around two-layered detached breakwaters: Three-dimensional OpenFOAM model', *Ocean Engineering* **268**, 113582.

Liang, Z. D. and Jeng, D.-S. (2021), 'PORO–FSSI–FOAM model for seafloor liquefaction around a pipeline under combined random wave and current loading.', *Applied Ocean Research* **107**, 102497.

Liang, Z. D. and Jeng, D.-S. (2022), 'The instantaneous seabed liquefaction around offshore pile-type foundation and seabed protection under combined wave and current loading', *Ocean Engineering* **257**, 111649.

Liang, Z. D., Jeng, D.-S., Liu, J. W. and Zhang, J. (2022), 'Numerical study of articulated concrete mattresses (acms) for offshore pipeline protection', *Ocean Engineering* **255**, 111467.

Liang, Z., Jeng, D.-S. and Liu, J. (2020), 'Combined wave–current induced seabed liquefaction around buried pipelines: Design of a trench layer', *Ocean Engineering* **212**, 107764.

Liao, C., Tong, D., Jeng, D.-S. and Zhao, H. (2018), 'Numerical study for wave-induced oscillatory pore pressures and liquefaction around impermeable slope breakwater heads', *Ocean Engineering* **157**, 364–375.

Lin, J.-S. and Hildemann, L. M. (1995), 'A nonsteady-state analytical model to predict gaseous emissions of volatile organic compounds from landfills', *Journal of Hazardous Materials* **40**, 271–295.

Lin, Y.-S. and Jeng, D.-S. (2000), 'Short-crested wave-induced liquefaction in porous seabed', *Journal of Geotechnical and Geoenvironmental Engineering, ASCE* **126**(5), 481–494.

Lin, Z., Dubravka, P., Guo, Y., Liao, C. and Tang, T. (2020), 'Near-trapping effect of wave-cylinders interaction on pore water pressure and liquefaction around a cylinder array', *Ocean Engineering* **218**, 108947.

Lin, Z., Guo, Y., Jeng, D.-S., Liao, C. and Rey, N. (2016), 'An integrated numerical model for wave–soil–pipeline interactions', *Coastal Engineering* **108**, 25–35.

Lin, Z., Pokrajac, D., Guo, Y., Jeng, D.-S., Tang, T., Rey, N., Zheng, J. and Zhang, J. (2017), 'Investigation of nonlinear wave-induced seabed response around mono-pile foundation', *Coastal Engineering* **121**, 197–211.

Liu, B., Jeng, D.-S., Ye, G. L. and Yang, B. (2015), 'Laboratory study for pore pressures in sandy deposit under wave loading', *Ocean Engineering* **106**, 207–219.

Liu, C., Ball, W. P. and Ellis, J. H. (1998), 'An analytical solution to the one-dimensional solute advection-dispersion equation in multi-layer porous media', *Transport in Porous Media* **30**(1), 25–43.

Liu, P. L.-F. and Cho, Y.-S. (1993), 'Bragg reflection of infragravity waves by sandbars', *Journal of Geophysics Research Oceans* **98**, 22733–22741.

Liu, P. L.-F., Lin, P., Chang, K. A. and Sakakiyama, T. (1999), 'Numerical modelling of wave interaction with porous structures', *Journal of Waterway, Port, Coastal and Ocean Engineering, ASCE* **125**(6), 322–330.

Liu, W. W. (2007), Thermal Analysis of Landfill, PhD thesis, Graduate School of Wayne State University, Detroit, Michigan.

Liu, Y. and Jeng, D.-S. (2019*a*), 'Pore scale study of the influence of particle geometry on soil permeability', *Advances in Water Resources* **129**, 232–249.

Liu, Y. and Jeng, D.-S. (2019*b*), 'Pore structure of grain-size fractal granular material', *Materials* **12**(13), 2053.

Liu, Y. and Yue, D. K. P. (1998), 'On generalized bragg scattering of surface wave by bottom ripples', *Journal of Fluid Mechanics* **356**, 297–326.

Lloret, A. and Alonso, E. E. (1985), State surfaces for partially saturated soils, *in* 'Proc. 11th I.C.S.M.F.E.', Vol. 2, San Francisco, pp. 557–562.

Lu, H. B. (2005), The Research on Pore Water Pressure Response to Waves in Sandy Seabed, PhD thesis, Changsha University of Science & Technology, Changsha Hunan China.

Luan, M., Qu, P., Jeng, D.-S., Guo, Y. and Yang, Q. (2008), 'Dynamic response of a porous seabed–pipeline interaction under wave loading: soil–pipeline contact effects and inertial effects', *Computers and Geotechnics* **35**(2), 173–186.

Lundgren, H., Lindhardt, J. H. C. and Romold, C. J. (1989), Stability of breakwaters on porous foundation, *in* 'Proceeding of 12th International Conference on Soil Mechanics and Foundation Engineering', Vol. 1, pp. 451–454.

Ma, W., Wu, G. X. and Taylor, R. E. (2001*a*), 'Finite element simulation of fully non-linear interaction between vertical cylinder and steep waves. part 1: Methodology and numerical procedure.', *International Journal for Numerical Methods in Fluids* **36**(3), 265–285.

Ma, W., Wu, G. X. and Taylor, R. E. (2001*b*), 'Finite element simulation of fully non-linear interaction between vertical cylinder and steep waves. part 2: Numerical results and validation.', *International Journal for Numerical Methods in Fluids* **36**(3), 287–308.

Madsen, O. S. (1978), 'Wave-induced pore pressures and effective stresses in a porous bed', *Géotechnique* **28**(4), 377–393.

Mao, X., Enot, P., Barry, D., Li, L., Binley, A. and Jeng, D.-S. (2006), 'Tidal influence on behaviour of a coastal aquifer adjacent to a low-relief estuary', *Journal of Hydrology* **327**(1-2), 110–127.

Martin, E., Thornton, C. and Utili, S. (2020), 'Micromechanical investigation of liquefaction of granular media by cyclic 3D DEM tests', *Géotechnique* **70**(10), 906–915.

Mase, H., Oki, S.-I. and Takeba, K. (1995), 'Wave equation over permeable ripple bed and analysis of bragg scattering of surface gravity waves', *Journal of Hydraulic Research* **36**, 789–812.

Mase, H., Sakai, T. and Sakamoto, M. (1994), 'Wave-induced porewater pressure and effective stresses around breakwater', *Ocean Engineering* **21**(4), 361–379.

Mathur, S. and Jayawardena, L. P. (2008), 'Thickness of compacted natural clay barriers in msw landfills', *Practice Periodical of Hazardous, Toxic, and Radioactive Waste Management* **12**(1), 53–57.

Mattioli, M., Alsina, J. M., Mancinelli, A., Miozzi, M. and Brocchini, M. (2012), 'Experimental investigation of the nearbed dynamics around a submarine pipeline laying on different types of seabed: The interaction between turbulent structures and particles', *Advances in Water Resources* **48**, 31–46.

McArdle, S. and McLachan, A. (1991), 'Dynamics of the swash zone and effluent line on sandy beaches', *Marine Ecology Progress Series* **79**, 91–99.

McDougal, W. G., Tsai, Y. T., Liu, P. L.-F. and Clukey, E. C. (1989), 'Wave-induced pore water pressure accumulation in marine soils', *Journal of Offshore Mechanics and Arctic Engineering, ASME* **111**(1), 1–11.

McLaren, R., Chin, C., Weber, J., Binns, J., McInerney, J. and Allen, M. (2016), Articulated concrete mattress block size stability comparison in omni-directional current, *in* 'OCEANS 2016 MTS/IEEE Monterey', pp. 1–16.

Means, R. and Parcher, JV. (1964), *Physical Properties of Soils*, Constable and Company Ltd., London.

Mei, C. C. (2003), *Applied Dyanmics of Ocean Surface Waves*, World Scientific.

Mei, C. C. and Foda, M. A. (1981), 'Wave-induced response in a fluid-filled poro-elastic solid with a free surface-a boundary layer theory', *Geophysical Journal of the Royal Astronomical Society* **66**, 597–631.

Mei, C. C. and Liu, P. L.-F. (1993), 'Surface waves and coastal dynamics', *Annual Review of Fluid Mechanics* **25**, 215–240.

Mei, C. C., Stiassnie, M. and Yue, D. K.-P. (2005), *Theory and Applications of Ocean Surface Waves*, World Scientific, New York.

Meng, K. and Yang, X. (2010), 'Optimality conditions via exact penalty functions', *SIAM Journal on Optimization* **20**(6), 3208–3231.

Miller, K. (1986), Use of concrete mattresses, *in* 'Submersible Technology. Advances in Underwater Technology, Ocean Science and Offshore Engineering', Springer, pp. 297–304.

Milly, P. (1984), 'A simulation analysis of thermal effects on evaporation from soil', *Water Resource Research* **20**, 1087–1098.

Milly, P. C. D. (1982), 'Moisture and heat transport in hysteretic, inhomogeneous porous media: A matric heat-based formulation and a numerical model', *Water Resource Research* **18**, 48–498.

Mitchelll, J. K. (1993), *Fundamentals of Soil Behaviour*, Wiley, New York.

Miyamoto, J., Sassa, S. and Sekiguchi, H. (2004), 'Progressive solidification of a liquefied sand layer during continued wave loading', *Géotechnique* **54**(10), 617–629.

Mizutani, N., McDougal, W. G. and Mostafa, A. M. (1996), Bem-fem combined analysis of non-linear interaction between wave and submerged breakwater, *in* 'The 25th International Conference on Coastal Engineering (ICCE1996)', pp. 2377–2390.

Mizutani, N. and Mostafa, A. M. (1998), 'Nonlinear wave-induced seabed instability around coastal structures', *Coastal Engineering Journal* (2), 131–160.

Moo-Young, H., Myers, T., Tardy, B., Ledbetter, R., Vanadit-Ellis, W. and Kim, T.-H. (2003), 'Centrifuge simulation of the consolidation characteristics of capped marine sediment beds', *Engineering Geology* **70**(3-4), 249– 258.

Morel-Seytour, H. J., Meyer, P. D., Touma, J., van Genuchten, M. T. and Lenhard, R. J. (1996), 'Parameter equivalence for the brooks-corey and van genuchten soil characteristics: Preserving the effective capillary drive', *Water Resources Research* **32**(5), 1251–1258.

Mory, M., Michallet, H., Bonjean, D., Piedra-Cueva, I., J M Barboud, P. F., Abadie, S. and Breul, P. (2007), 'A field study of moentary liquefaction caused by waves around coastal structure', *Journal of Waterways, Port, Coastal and Ocean Engineering, ASCE* **133**(1), 28–38.

Mostafa, A. M. and Mizutani, N. (2002), Nonlinear wave forces on a marine pipeline buried in a sand seabed, *in* 'The 12th International Conference on Offshore and Polar Engineering (ISOPE2002)', Vol. 2, pp. 68–75.

Mostafa, A. M., Mizutani, N. and Iwata, K. (1999), 'Nonlinear wave, composite breakwater and seabed dynamic interaction', *Journal of Waterway, Port, Coastal, and Ocean Engineering, ASCE* **125**(2), 88–97.

Mynett, A. E. and Mei, C. C. (1982), 'Wave-induced stresses in a saturated poroelastic seabed beneath a rectangular caisson', *Géotechnique* **32**, 235–248.

Nago, H., Maeno, S., Matsumoto, T. and Hachiman, Y. (1993), Liquefaction and densification of loosely deposited sand bed under water pressure variation, *in* 'Proceeding of the 3rd international offshore and Polar Engineering Conference (ISOPE1993)', Vol. I, pp. 578–584.

Narsilio, G., Buzzi, O., Fityus, S., Yun, T. and Smith, D. (2009), 'Upscaling of navier-stokes equations in porous media: Theoretical, numerical and experimental approach', *Computers and Geotechnics* **36**(7), 1200–1206.

Nassar, I. and Horton, R. (1999), 'Transport and fate of volatile organic chemicals in unsaturated, nonisothermal, salty porous media:: 1. theoretical development', *Journal of Hazardous Materials* **69**(2), 151–167.

Nassar, I. N. and Horton, R. (1997), 'Heat, water, and solution transfer in unsaturated porous media: I -theory development and transport coefficient evaluation', *Transport in Porous Media* **27**, 17–38.

Nassar, I., Ukrainczyk, L. and Horton, R. (1999), 'Transport and fate of volatile organic chemicals in unsaturated, nonisothermal, salty porous media: 2. experimental and numerical studies for benzene', *Journal of Hazardous Materials* **69**(2), 169–185.

Nguyen, T.-B., Lim, J., Choi, H. and Stark, T. D. (2011), 'Numerical modeling of diffusion for volatile organic compounds through composite landfill liner systems', *KSCE Journal of Civil Engineering* **15**(6), 1033–1039.

Nielsen, P. (1990), 'Tidal dynamics of the water table in beaches', *Water Resource Research* **26**, 2127–2134.

Nye, T. and Yamamoto, T. (1994), 'Field test of buried ocean-wave directional spectrometer system', *Journal of Waterway, Port, Coastal, and Ocean Engineering, ASCE* **120**(5), 451–466.

Okusa, S. (1985), 'Wave-induced stress in unsaturated submarine sediments', *Géotechnique* **35**(4), 517–532.

Ong, S.-K. (2006), Solid/gas partitioning, *in* C. K. Ho and S. W. Webb, eds, 'Gas Transport in Porous Media', Springer, pp. 47–54.

Othman, M. A., Bonaparte, R. and Gross, B. A. (1997), 'Preliminary results of composite liner field performance study', *Geotextiles and Geomembranes* **15**(4-6), 289 – 312.

Oumeraci, H. (1994), 'Review and analysis of vertical breakwater failures—lessons learned', *Coastal Engineering* **22**, 3–29.

Palmer, A. (1986), Trenching and burial of submarine pipelines, *in* 'Submersible Technology', Springer, pp. 305–311.

Palmer, A. C. and King, R. A. (2008), *Subsea Pipeline Engineering*, PennWell Corporation.

Parlange, J.-Y. and Brutsaert, W. (1987), 'A capillarity correction for free surface flow of groundwater', *Water Resources Research* **23**(5), 805–808.

Parlange, J.-Y., Stagnitti, F., Starr, J. and Baddock, R. (1984), 'Tidal dynamics of the water table in beaches', *Journal of Hydrology* **70**, 251–263.

Pearson, C. E. (1983), *Handbook of Applied Mathematics*, Van Nostrand Reinhold.

Peters, G. P. and Smith, D. W. (2001), 'Numerical study of boundary conditions for solute transport through a porous medium', *International Journal for Numerical and Analytical Methods in Geomechanics* **25**(7), 629–650.

Peters, G. P. and Smith, D. W. (2002), 'Solute transport through a deforming porous medium', *International Journal for Numerical and Analytical Methods in Geomechanics* **26**(7), 683–717.

Peters, G. P. and Smith, D. W. (2004), 'The influence of advective transport on coupled chemical and mechanical consolidation of clays', *Mechanics of Materials* **36**(5-6), 467–486.

Petersen, L. W., Moldrup, P., EI-Farhan, Y., Jacobsen, O. H., Yamaguchi, T. and Rolston, D. E. (1995), 'The effect of moisture and soil texture on the adsorption of organic vapors', *Journal of Enviromental Quality* **24**, 752–759.

Philip, J. (1973), 'Periodic nonlinear diffusion: Integral relation and its physical consequences', *Australian Journal of Physics* **26**(4), 513–519.

Philip, J. and de Vries, D. (1957), 'Moisture movement in porous materials under temperature gradients', *Transactions American Geophysical Union* **38**, 222–232.

Philip, J. R. (1969), Theory of infiltration, *in* 'Advances in Hydroscience', Vol. 5, Elsevier, pp. 215–296.

Pierson, P. and Barroso, M. (2002), 'A pouch test for characterizing gas permeability of geomembranes', *Geosynthetics International* **9**(4), 345–372.

Pollock, L. W. and Hummon, W. D. (1971), 'Cyclic changes in interstitial water content, atmospheric exposure and temperature in a marine beach', *Limnology Oceanography* **16**, 522–535.

Porter, L., Kemper, W., Jackson, R. and Stewart, B. (1960), Chloride diff usion in soils as infl uenced by moisture content, *in* 'Soil Science Society of America Proceeding', 24, pp. 460–463.

Potter, L. J., Savvidou, C. and Gibson, R. E. (1994), Consolidation and pollutant transport associated with slurried mineral waste disposal, *in* '1st International Conference on Environmental Geotechnics', Edmonton, Canada, pp. 525–530.

Poulsen, T. G., Massmann, J. W. and Moldrup, P. (1996), 'Effects of vapor extraction on contaminant flux to atmosphere and ground water', *Journal of Enviromental Engineering* **122**(8), 700–706.

Poulsen, T. G., Moldrup, P., Yamaguchi, T., Massmann, J. W. and Hansen, J. A. (1998), 'Voc vapor sorption in soil: soil type dependent model and implications for vapor extraction', *Journal of Environmental Engineering* **124**(2), 146–155.

Prunty, L. (2002), Spatial distribution of heat of wetting in porous media, *in* '2002 ASAE Annual International Meeting / CIGR XVth World Congress', Sponsored by ASAE and CIGR, Chicago, Illinois, USA.

Pu, H. and Fox, P. J. (2015), 'Model for coupled large strain consolidation and solute transport in layered soils', *International Journal of Geomechanics, ASCE* **16**(2), 2725–2734.

Pu, H. and Fox, P. J. (2016), Consolidation-induced contaminant transport in multi-layer soils, *in* S. El-Badawy, D. Cheng and M. Arab, eds, 'Geo-China 2016', ASCE, pp. 1–8.

Qi, W.-G. and Gao, F. P. (2014), 'Physical modeling of local scour development around a large-diameter monopile in combined waves and current', *Coastal Engineering* **83**, 72–81.

Qi, W.-G. and Gao, F.-P. (2015), 'A modified criterion for wave-induced momentary liquefaction of sandy seabed', *Theoretical & Applied Mechanics Letters* **5**(1), 20–23.

Qi, W.-G. and Gao, F.-P. (2018), 'Wave induced instantaneously-liquefied soil depth in a non-cohesive seabed', *Ocean Engineering* **153**, 412–423.

Qi, W.-G., Li, C.-F., Jeng, D.-S., Gao, F.-P. and Liang, Z. (2019), 'Combined wave-current induced excess pore-pressure in a sandy seabed: Flume observations and comparisons with theoretical models', *Coastal Engineering* **147**, 89–98.

Rahman, M. S., El-Zahaby, K. and Booker, J. (1994), 'A semi-analytical method for the wave-induced seabed response', *International Journal for Numerical and Analytical Methods in Geomechanics* **18**, 213–236.

Ramirez, L., Fraile, D. and Brindley, G. (2021), 'Offshore wind in europe: Key trends and statistics 2020', *Wind Europe* .

Raubenheimer, B., Elagr, S. and Guza, R. T. (1998), 'Estimating wave heights from pressure measured in sand bed', *Journal of Waterway, Port, Coastal and Ocean Engineering, ASCE* **124**(3), 151–154.

Raubenheimer, B. R., Guza, T. and Elgar, S. (1999), 'Tidal water table fluctuations in a sandy beaches', *Water Resources Research* **35**, 2313–2320.

Reid, R., Prausintz, J. and Poling, B. (1987), *The Properties of Gases and Liquids*, McGraw-Hill, New York.

Rodi, W. (1993), *Turbulence Models and their Application in Hydraulics-State-of-The-Art Review*, Balkema, Rotterdam, The Netherland.

Rolle, M., Hochstetler, D., Chiogna, G., Kitanidis, P. K. and Grathwohl, P. (2012), 'Experimental investigation and pore-scale modeling interpretation of compound-specific transverse dispersion in porous media', *Transport in Porous Media* **93**(3), 347–362.

Rowe, R. K. (2005), 'Long-term performance of contaminant barrier systems', *Géotechnique* **55**(9), 631–678.

Rowe, R. K. and Badv, K. (1996), 'Advective-diffusive contaminant migration in unsaturated sand and gravel', *Journal of Geotechnical Engineering, ASCE* **122**(12), 965–975.

Rowe, R. K. and Booker, J. R. (1985), '1-D pollutant migration in soil of finite depth', *Journal of Geotechnical Engineering* **111**, 479–499.

Sakai, T., Hatanaka, K. and Mase, H. (1992), 'Wave-induced effective stress in seabed and its momentary liquefaction', *Journal of Waterway, Port, Coastal and Ocean Engineering, ASCE* **118**(2), 202–206.

Sassa, S., Sekiguchi, H. and Miyamamoto, J. (2001), 'Analysis of progressive liquefaction as moving-boundary problem', *Géotechnique* **51**(10), 847–857.

Scanlon, B. and Milly, P. (1994), 'Water and heat fluxes in desert soils, 2. numerical simulations', *Water Resources Research* **30**, 721–733.

Scheutz, C., Bogner, J., Chanton, J., Blake, D. and Morcet, M. (2008), 'Atmospheric emissions and attenuation of non-methane organic compounds in cover soils at a french landfill', *Waste Management* **28**(10), 1892–1908.

Scholtés, L., Chareyre, B., Michallet, H., Catalano, E. and Marzougui, D. (2014), 'Modeling wave-induced pore pressure and effective stress in a granular seabed', *Continuum Mechanics and Thermodynamics* **27**(1-2), 305–323.

Schuetz, C., Bogner, J. and Chanton, J. (2003), 'Comparative oxidation and net emissions of methane and selected mon-methane organic compounds in landfillcover soils', *Environmental Science and Technology* **37**(22), 5150–5158.

Seed, H. B., Martin, P. O. and Lysmer, J. (1975), The generation and dissipation of pore water pressure during soil liquefaction, Technical report, College of Engineering, University of California, Berkeley, California.

Seed, H. B. and Rahman, M. S. (1978), 'Wave-induced pore pressure in relation to ocean floor stability of cohesionless soils', *Marine Geotechnology* **3**(2), 123–150.

Sha, X. (2014), Dynamic Response Analysis of Offshore Wind Turbines' support structure with four piles, PhD thesis, Ocean University of China (in Chinese).

Shahir, H., Mohammadi-Haji, B. and Ghassemi, A. (2014), 'Employing a variable permeability model in numerical simulation of saturated sand behavior under earthquake loading', *Computers and Geotechnics* **55**, 211–223.

Shahir, H., Pak, A., Taiebat, M. and Jeremić, B. (2012), 'Evaluation of variation of permeability in liquefiable soil under earthquake loading', *Computers and Geotechnics* **40**, 74–88.

Shan, C. and Stephens, D. B. (1995), 'An analytical solution for vertical transport of volatile chemicals in the vadose zone', *Journal of Contaminant Hydrology* **18**(4), 259–277.

Sharma, P., Sawant, V., Shukla, S. K. and Khan, Z. (2014), 'Experimental and numerical simulation of contaminant transport through layered soil', *International Journal of Geotechnical Engineering* **8**(4), 345–351.

Sivakugan, N. (1990), 'Inadequacy in the classification of coarse-grained soils', *Geotechnical Testing Journal* **13**(2), 134–137.

Skempton, A. and Brogan, J. (1994), 'Experiments on piping in sandy gravels', *Géotechnique* **44**(3), 449–460.

Skjelbreia, L. and Hendrickson, J. A. (1960), Fifth order gravity wave theory, *in* 'Proceedings of 7th International Conference on Coastal Engineering (ICCE60)', pp. 184–196.

Sleep, B. E. (1998), 'Modeling transient organic vapor transport in porous media with the dusty gas model', *Advances in Water Resources* **22**(3), 247–256.

Smith, D. W. (2000), 'One-dimensional contaminant transport through a deforming porous medium : theory and a solution for a quasi-steady-state problem', *International Journal for Numerical and Analytical Methods in Geomechanics* **24**(8), 693–722.

Smith, J. E. and Gillham, R. W. (1994), 'The effect of concentration-dependent surface tension on the flow of water and transport of dissolved organic compounds: a pressure head-based formulation and numerical model', *Water Resource Research* **30**, 343–354.

Soltani-Ahmadi, H. (2000), A review of the literature regarding non-methane and volatile organic compounds in municipal solid waste landfill gas, Technical report, Department of civil enviromental engineering, University of Delaware.

Stark, T. D. and Choi, H. (2005), 'Methane gas migration through geomembranes', *Geosynthetics International* **12**(2), 120–126.

Staudinger, J. and Roberts, P. V. (2001), 'A critical compilation of henry's law constant temperature dependence relations for organic compounds in dilute aqueous solutions', *Chemosphere* **44**, 561–576.

Stojsavljevic, J. D., Jeng, D.-S., Seymour, B. R. and Pokrajac, D. (2012), 'Higher order analytical solutions of water table fluctuations in coastal aquifers', *Ground Water* **50**(2), 301–307.

Su, N., Liu, F. and Anh, V. (2003), 'Tides as phase-modulated waves inducingperiodic groundwater flow in coastal aquifers overlaying a slopingimpervious base', *Environmental Modelling Software* **18**, 937–942.

Sui, T., Jin, Y., Wang, Z., Zhang, C. and Shi, J. (2019), 'Effects of the soil property distribution gradient on the wave-induced response of a non-homogeneous seabed', *Journal of Marine Science and Engineering* **7**, 281.

Sui, T., Zhang, C., Guo, Y., Zheng, J., Jeng, D.-S., Zhang, J. and Zhang, W. (2016), 'Three-dimensional numerical model for wave-induced seabed response around mono-pile', *Ships and Offshore Structures* **11**(6), 667–678.

Sui, T., Zheng, J., Zhang, C., Jeng, D.-S., Zhang, J., Guo, Y. and He, R. (2017), 'Consolidation of unsaturated seabed around an inserted pile foundation and its effects on the wave-induced momentary liquefaction', *Ocean Engineering* **131**, 308–321.

Sumer, B. M. (2006), 'Special issue on liquefaction around marine structures', *Journal of Waterway, Port, Coastal, and Ocean Engineering, ASCE* **132**(4), 225–226.

Sumer, B. M. (2007), 'Special issue on liquefaction around marine structures: Miscellaneous', *Journal of Waterway, Port, Coastal, and Ocean Engineering, ASCE* **133**(1), 1–2.

Sumer, B. M. (2014), *Liquefaction around Marine Structures*, World Scientific, New Jersey.

Sumer, B. M. and Fredsoe, J. (2002), *The Mechanics of Scour in the Marine Environment*, World Scientific.

Sumer, B. M., Fredsoe, J., Christensen, S. and Lind, M. T. (1999), 'Sinking/floatation of pipelines and other objects in liquefied soil under waves', *Coastal Engineering* **38**(2), 53–90.

Sumer, B. M., Hatipoglu, F., Fredsoe, J. and Hansen, N.-K. O. (2006), 'Critical flotation density of pipelines in soils liquefied by waves and density of liquefied soils', *Journal of Waterway, Port, Coastal, and Ocean Engineering, ASCE* **132**(4), 252–265.

Sumer, B. M., Kirca, V. S. O. and Fredsoe, J. (2012), 'Experimental validation of a mathematical model for seabed liquefaction under waves', *International Journal of Offshore and Polar Engineering* **22**, 133–141.

Sun, H. (1997), 'A two-dimensional analytical solution of groundwater response to tidal loading in an estuary', *Water Resource Research* **33**, 1429–1435.

Sun, K., Zhang, J., Gao, Y., Jeng, D.-S., Guo, Y. and Liang, Z. (2019), 'Laboratory experimental study of ocean waves propagating over a partially buried pipeline in a trench layer', *Ocean Engineering* **173**, 617–627.

Tang, H.-J. and Huang, C.-C. (2008), 'Bragg reflection in a fully nonlinear numerical wave tank based on boundary integral equation method', *Ocean Engineering* **35**, 1800–1810.

Tang, T., Hededal, O. and Cardill, P. (2015), 'On finite volume method implementation of poroelasto- plasticity soil model', *International Journal for Numerical and Analytical Methods in Geomechanics* **39**(13), 1410–1430.

Tang, Y., Shi, W., Ning, D., You, J. and Michailides, C. (2020), 'Effects of spilling and plunging type breaking waves acting on large monopile offshore wind turbines', *Frontiers in Marine Science* **7**, 427.

Tavenas, F., Jean, P., Leblond, P. and Leroueil, S. (1983), 'The permeability of natural soft clays. part ii: Permeability characteristics', *Canadian Geotechnical Journal* **20**(4), 645–660.

Teo, H. T., Jeng, D.-S., Seymour, B. R., Barry, D. A. and Li, L. (2003), 'A new analytical solution for water table fluctuations in coastal aquifers with sloping beaches', *Advances in Water Resource* **26**, 1239–1247.

Terzaghi, K. (1925), *Erdbaumechanik auf Bodenphysikalischer Grundlage*, Leipzig u. Wien, F. Deuticke, Vienna, Deuticke.

Thimus, J. F., Abousleiman, Y., Cheng, A. H. D., Coussy, O. and Detournay, E. (1998), *Poromechanics–a tribute to Maurice A, Biot*, Balkema, Rotterdam/Brookfield.

Thomas, H., He, Y., Sansom, M. and Li, C. (1996), 'On the development of a model of the thermo-mechanical-hydraulic behaviour of unsaturated soils', *Engineering Geology* **41**(1-4), 197 – 218.

Thomas, H. R. and Ferguson, W. J. (1999), 'A fully coupled heat and mass transfer model incorporating contaminant gas transfer in an unsaturated porous medium', *Computers and Geotechnics* **24**, 65–87.

Thomas, H. R. and He, Y. (1997), 'A coupled heat-moisture transfer theory for deformable unsaturated soil and its algorithmic implementation', *International Journal for Numerical Methods in Engineering* **40**, 3421–3441.

Thomas, H. R. and King, S. D. (1994), 'A non-linear, two-dimensional, potential based analysis of coupled heat and mass transfer in a porous medium', *Int. J. Numer. Meth. Engng* **37**, 3707–3722.

Thomas, H. R. and Sansom, M. R. (1995), 'Fully coupled analysis of heat, moisture and air transfer in unsaturated soil', *Journal of Engineering Mechanics, ASCE* **121**, 392–405.

Tong, D., Liao, C., Jeng, D.-S. and Wang, J. (2018), 'Numerical study of pile group effect on wave-induced seabed response', *Applied Ocean Research* **76**, 148–158.

Tong, D., Liao, C., Jeng, D.-S., Zhang, L., Wang, J. and Chen, L. (2017), 'Three-dimensional modeling of wave-structure-seabed interaction around twin-pile group', *Ocean Engineering* **145**, 416–429.

Towhata, I., Sasaki, Y., Tokida, K.-I., Matsumoto, H., Tamari, Y. and Yamada, K. (1992), 'Prediction of permanent displacement of liquefied ground by means of minimum energy principle', *Soils and Foundations* **32**(3), 97–116.

Travis, J. (2005), 'Hurricane katrina: Scientists–fears come true as hurricane floods new orleans', *Science* **309**(5741), 1656–1659.

Trefry, M. G. (1999), 'Periodic forcing in composite aquifers', *Advances in Water Resource* **22**, 645–656.

Tsai, C. P. (1995), 'Wave-induced liquefaction potential in a porous seabed in front of a breakwater', *Ocean Engineering* **22**(1), 1–18.

Tsai, C. P. and Lee, T. L. (1995), 'Standing wave induced pore pressure in a porous seabed', *Ocean Engineering* **22**(6), 505–517.

Tsai, T.-L., Chang, K.-C. and Huang, L.-H. (2006), 'Body force effect on consolidation of porous elastic media due to pumping', *Journal of Chinese Institute of Engineers* **29**(1), 75–82.

Tsai, Y. T., McDougal, W. G. and Sollitt, C. K. (1990), 'Response of finite depth seabed to waves and caisson motion', *Journal of Waterways, Port and Coastal and Ocean Engineering, ASCE* **116**, 1–20.

Tuckermann, R. (2007), 'Surface tension of aqueous solutions of water-soluble organic and inorganic compounds', *Atmospheric Environment* **41**(29), 6265–6275.

Tuckermann, R. and Cammenga, H. K. (2004), 'The surface tension of aqueous solutions of some atmospheric water-soluble organic compounds', *Atmospheric Environment* **38**(36), 6135–6138.

Turcotte, B. R., Liu, P. L.-F. and Kulhawy, F. H. (1984), Laboratory evaluation of wave tank parameters for wave-sediment interaction, Technical report, Joseph F. Defree Hydraulic Laboratory, School of Civil and Environmental Engineering, Cornell University.

Turner, I. L. (1998), 'Monitoring groundwater dynamics in the littoral zoneat seasonal, storm, tide and swash frequencies', *Coastal Engineering* **35**, 1–16.

Turner, I. L., Coates, B. P. and Acworth, R. I. (1997), 'Tides, waves and the superelevationgroundwater at the coast', *Journal of Coastal Research* **13**, 46–60.

Ueng, T.-S., Wang, Z.-F., Chu, M.-C. and Ge, L. (2017), 'Laboratory tests for permeability of sand during liquefaction', *Soil Dynamics and Earthquake Engineering* **100**, 249–256.

Ulker, M. B. C., Rahman, M. S. and Guddati, M. N. (2012), 'Breaking wave-induced response and instability of seabed around caisson breakwater', *International Journal for Numerical and Analytical Methods in Geomechanics* **36**(3), 362–390.

Ulker, M. B. C., Rahman, M. S. and Jeng, D.-S. (2009), 'Wave-induced response of seabed: various formulations and their applicability', *Applied Ocean Research* **31**(1), 12–24.

Ulker, M. and Rahman, M. S. (2009), 'Response of saturated and nearly saturated porous media: Different formulations and their applicability', *International Journal for Numerical and Analytical Methods in Geomechanics* **33**(5), 633–664.

Ulker, M., Rahman, M. S. and Guddati, M. N. (2010), 'Wave-induced dynamic response and instability of seabed around caisson breakwater', *Ocean Engineering* **37**, 1522–1545.

Vaughan, P. R. (2003), 'Observations on the behaviour of clay fill containing occluded air bubbles', *Géotechnique* **53**(2), 265–272.

Verruijt, A. (1969), Elastics storage of aqifers, *in* R. J. M. De Wiest, ed., 'Flow through Porous Media', Academic Press, pp. 331–376.

Versteeg, H. K. and Malalasekera, W. (2007), *An Introduction to Computational Fluid Dynamics: the Finite Volume Method*, Pearson education.

Volker, R. E. and Zhang, Q. (2001), 'Comments on "an analytical solution of groundwater responseto tidal fluctuations in a leaky confined aquifer"', *Water Resources Research* **37**, 185–186.

Wallace, G. B. and Otto, W. C. (1964), 'Differential settlement at selfridge air force base', *Journal of the Soil Mechanics and Foundations Division, ASCE* **90**(5), 197–220.

Wang, B., Zen, K., Chen, G. Q., Zhang, Y. B. and Kasama, K. (2013), 'Excess pore pressure dissipation and solidification after liquefaction of saturated sand deposits', *Soil Dynamics and Earthquake Engineering* **49**, 157–164.

Wang, H. F. (2000), *Theory of linear poroelasticity with applications to Geomechanics and Hydrology*, Princeton University Press.

Wang, J. G., Nogami, T., Dasari, G. R. and Lin, P. Z. (2004), 'A weak coupling algorithm for seabed-wave interaction analysis', *Computer Methods in Applied Mechanics and Engineering* **193**(36), 3935–3956.

Wang, L. H., Zhang, J. F., Jeng, D.-S., Zhang, Q. and Chen, T. (2023), 'Experimental study on the dynamic response of a silty seabed under waves', *Ocean Engineering* **269**), 113554.

Wang, Q. and Zhan, H. (2015), 'On different numerical inverse Laplace methods for solute transport problems', *Advances in Water Resources* **75**, 80–92.

Wang, S., Wang, P., Zhai, H., Zhang, Q., Chen, L., Duan, L., Liu, Y. and Jeng, D.-S. (2019*a*), 'Experimental study for wave-induced pore-water pressures in a porous seabed around a mono-pile', *Journal of Marine Science and Engineering* **7**(7), 237.

Wang, W., Zhou, M., Zhang, B. and Peng, C. (2019*b*), 'A dual mortar contact method for porous media and its application to clay-core rockfill dams', *International Journal for Numerical and Analytical Methods in Geomechanics* **43**(9), 1744–1769.

Wang, X., Jeng, D.-S. and Lin, Y.-S. (2000), 'Effects of a cover layer on wave-induced pore pressure around a buried pipe in an anisotropic seabed', *Ocean Engineering* **27**(8), 823–839.

Wang, X. X., Jeng, D.-S. and Tsai, C.-C. (2019*c*), 'Meshfree model for wave-seabed interactions around offshore pipelines', *Journal of Marine Science and Engineering* **7**(4), 87.

Welty, J., Wicks, C. and Wilson, R. E. (1984), *Foundamentals of Momentum, Heat, and Mass Transfer*, Wiley, chapter 24.

Wen, F., Jeng, D.-S., Wang, J. and Zhou, X. (2012), 'Numerical modeling of response of a saturated porous seabed around an offshore pipeline considering non-linear wave and current interaction', *Applied Ocean Research* **35**, 25–37.

Workman, J. P. (1993), Interpretation of leakage rates in double-liner systems, *in* R. M. Koerner and R. F. Wilson-Fahmy, eds, 'Geosynthetic liner systems: Innovations, concerns, and designs', Industrial Fabrics Association International, pp. 95–112.

Wu, L. and Zhang, L. M. (2009), 'Analytical solution to 1d coupled water inflitration and deformation in unsaturated soils', *International Journal for Numerical and Analytical Methods in Geomechanics* **33**(6), 773–790.

Wu, S. and Jeng, D.-S. (2017), 'Numerical modeling of solute transport in deformable unsaturated layered soil', *Water Science and Engineering* **10**(3), 184–196.

Wu, S. and Jeng, D.-S. (2019), 'Effects of dynamic soil permeability on the wave-induced seabed response around a buried pipeline', *Ocean Engineering* **186**, 106132.

Wu, S., Jeng, D.-S. and Seymour, B. (2020), 'Numerical modelling of consolidation-induced solute transport in unsaturated soil with dynamic hydraulic conductivity and degree of saturation', *Advances in Water Resources* **135**, 103466.

Xu, P. X. (2019), Dynamic response analysis and reliability study of deepwater jacket platform structure, PhD thesis, Southwest Petroleum University (in Chinese).

Yamamoto, T. (1977), Wave induced instability seabed, *in* 'Proceedings A.S.C.E. Special Conference, Coastal Sediments'77', pp. 898–913.

Yamamoto, T. (1981), 'Wave-induced pore pressures and effective stresses in inhomogeneous seabed foundations', *Ocean Engineering* **8**, 1–16.

Yamamoto, T., Koning, H., Sellmeijer, H. and Hijum, E. V. (1978), 'On the response of a poro-elastic bed to water waves', *Journal of Fluid Mechanics* **87**(1), 193–206.

Yamamoto, T. and Trevorrow, M. (1991), Experimental verifications of bottom shear modulus profiler (bsmp) method, *in* 'Proceedings of the International Conference on Geotechnical Engineering for Coastal Development–Theory and Practice on Soft Ground (Geot–Coastal 91)', Vol. 1, pp. 123–128.

Yamamoto, T. and Turgut, A. (1988), 'Acoustic wave propagation through porous media with arbitrary pore size distributions', *Journal of Acoustical Society of America* **83**(5), 1744–1751.

Yang, G. and Ye, J. H. (2017), 'Wave & current-induced progressive liquefaction in loosely deposited seabed', *Ocean Engineering* **142**, 303–314.

Yang, J. H., Zhang, H., Liu, J. K. and He, F. (2007), 'The dynamic analysis of deepwater jacket platform based on abaqus/aqua', *China Offshore Platform* **22**(6), 29–33 (in Chinese).

Ye, J. and Jeng, D.-S. (2011), 'Effects of bottom shear stresses on the wave-induced dynamic response in a porous seabed: Poro-wssi (shear) model', *Acta Mechanica Sinica* **27**(6), 898–911.

Ye, J. and Jeng, D.-S. (2012), 'Response of seabed to natural loadin:: waves and current', *Journal of Engineering Mechanics, ASCE* **138**(6), 601–613.

Ye, J., Jeng, D.-S., Chan, A. H. C., Wang, R. and Zhu, Q. C. (2017), '3D integrated numerical model for fluid-structures-seabed interaction (fssi): Loosely deposited seabed foundation', *Soil Dynamics and Earthquake Engineering* **92**, 239–252.

Ye, J., Jeng, D.-S., Wang, R. and Zhu, C. (2013), 'Validation of a 2-D semi-coupled numerical model for fluid–structure–seabed interaction', *Journal of Fluids and Structures* **42**, 333–357.

Ye, J., Zhang, Y., Wang, R. and Zhu, C. (2014), 'Nonlinear interaction between wave, breakwater and its loose seabed foundation: A small-scale case', *Ocean Engineering* **91**, 300–315.

Yong, R., Mohamed, A. and Warkentin, B. (1992), *Principles of contaminant transport in soils*, Elsevier Science, New York.

Yu, J. and Mei, C. C. (2000), 'Do longshore bars shelter the shore?', *Journal of Fluid Mechanics* **404**, 251–268.

Yule, D. F. and Gardner, W. R. (1978), 'Longitudinal and transverse dispersion coefficients in unsaturated plainfield sand', *Water Resource Research* **14**(4), 582–588.

Zang, J., Taylor, P., Morgan, G., Orszaghova, J., Grice, J., Stringer, R. and Tello, M. (2010), Steep wave and breaking wave impact on offshore wind turbine foundations-ringing re-visited, *in* 'Proceeding 25th International Workshop on Water Waves and Floating Bodies', pp. 1–4.

Zen, K., Umehara, Y. and Finn, W. D. L. (1985), A case study of the wave-induced liquefaction of sand layers under damaged breakwater, *in* 'Proceeding 3rd Canadian Conference on Marine Geotechnical Engineering', pp. 505–520.

Zen, K. and Yamazaki, H. (1990*a*), 'Mechanism of wave-induced liquefaction and densification in seabed', *Soils and Foundations* **30**(4), 90–104.

Zen, K. and Yamazaki, H. (1990*b*), 'Oscillatory pore pressure and liquefaction in seabed induced by ocean waves', *Soils and Foundations* **30**(4), 147–161.

Zhai, H. and Jeng, D.-S. (2022), 'Two-way coupling model for wave-induced oscillatory soil response in a porous seabed', *Ocean Engineering* **249**, 10791.

Zhai, H., Jeng, D.-S., Guo, Z. and Sui, T. (2021*a*), 'Modified shields number for sediment incipient motion around a pile with impact of three-dimensional seepage in a porous seabed', *Applied Ocean Research* **117**, 102896.

Zhai, H., Jeng, D.-S., Guo, Z. and Liang., Z. D. (2021*b*), 'Impact of two-dimensional seepage flow on sediment incipient motion under waves', *Applied Ocean Research* **108**, 102510.

Zhai, Y., He, R., Zhao, J., Zhang, J., Jeng, D.-S. and Li, L. (2018), 'Physical model of wave-induced seabed response around trenched pipeline in sandy seabed', *Applied Ocean Research* **75**, 37–52.

Zhai, Y., Zhang, J., Guo, Y., Tang, Z. and Zhang, T. (2022), 'Study of wave-induced seabed response around twin pipelines in sandy seabed through laboratory experiments and numerical simulations', *Ocean Engineering* **244**, 110344.

Zhan, T. L. and Ng, C. W. (2004), 'Analytical analysis of rainfall infiltration mechanism in unsaturated soils', *International Journal of Geomechanics, ASCE* **4**(4), 273–284.

Zhang, C., Sui, T., Zheng, J., Xie, M. and Nguyen, V. T. (2016), 'Modelling wave-induced 3D non-homogeneous seabed response', *Applied Ocean Research* **61**, 101–114.

Zhang, F. G. and Ge, Z. J. (1996), 'A study on some causes of rubble mound breakwater failure', *China Ocean Engineering* **10**(4), 473–481.

Zhang, H., Jeng, D.-S., Barry, D. A., Seymour, B. R. and Li, L. (2013*a*), 'Migration of volatile organic contaminations (vocs) through a deforming clay liner', *Advances in water resources* **59**, 66–81.

Zhang, H., Jeng, D.-S., Barry, D. A., Seymour, B. R. and Li, L. (2013*b*), 'Solute transport in nearly saturated porous media under landfill clay liners: A finite deformation approach', *Journal of Hydrology* **479**, 189–199.

Zhang, H., Jeng, D.-S., Seymour, B., Barry, D. A. and Li, L. (2012*a*), 'Solute transport in partially-saturated deformable porous media: Application to a landfill clay liner', *Advances in Water Resources* **40**, 1–10.

Zhang, J.-S., Jeng, D.-S., Liu, P.-F., Zhang, C. and Zhang, Y. (2012*b*), 'Response of a porous seabed to water waves over permeable submerged breakwaters with bragg reflection', *Ocean Engineering* **43**, 1–12.

Zhang, L. and Szeri, A. (2005), 'Transport of neutral solute in articular cartilage: effects of loading and particle size', *Proceedings of the Royal Society A–Mathematical Physical and Engineering Sciences* **461**(2059), 2021–2042.

Zhang, Q. and Hisada, T. (2001), 'Investigations of the coupling methods for FSI analysis by FEM', *Trans. Japan. Soc. Mech. Eng.* **67**(662), 1555–1562.

Zhang, Q., Zhai, H., Wang, P., Wang, S., Duan, L., Chen, L., Liu, Y. and Jeng, D.-S. (2020), 'Experimental study on irregular wave-induced pore-water pressures in a porous seabed around a mono-pile', *Applied Ocean Research* **95**, 102041.

Zhang, Q., Zhou, X. L., Wang, J. H. and Guo, J. J. (2017), 'Wave-induced seabed response around an offshore pile foundation platform', *Ocean Engineering* **130**, 567–582.

Zhao, H., Jeng, D.-S., Liao, C. and Zhu, J. (2017), 'Three-dimensional modeling of wave-induced residual seabed response around a mono-pile foundation', *Coastal Engineering* **128**, 1–21.

Zhao, H.-Y. and Jeng, D.-S. (2015), 'Numerical study of wave-induced soil response in a sloping seabed in the vicinity of a breakwater', *Applied Ocean Research* **51**, 204–221.

Zhao, H. Y. and Jeng, D.-S. (2016), 'Accumulated pore pressures around submarine pipeline buried in trench layer with partial backfills', *Journal of Engineering Mechanics, ASCE* **142**(7), 04016042.

Zhao, H.-Y., Jeng, D.-S., Guo, Z. and Zhang, J.-S. (2014), 'Two-dimensional model for pore pressure accumulations in the vicinity of a buried pipeline', *Journal of Offshore Mechanics and Arctic Engineering, ASME* **136**(4), 042001.

Zhao, H. Y., Liu, X.-L., Jeng, D.-S., Zheng, J. H., Zhang, J. S. and Liang, Z. D. (2022), 'Numerical investigation into the vulnerability to liquefaction of an embedded pipeline exposed to ocean storms', *Coastal Engineering* **172**, 104056.

Zhao, M., Vaidya, S., Zhang, Q. and Cheng, L. (2015), 'Local scour around two pipelines in tandem in steady current', *Coastal Engineering* **98**, 1–15.

Zhou, M., Liu, H., Jeng, D.-S., Qi, W. and Fang, Q. (2021*a*), 'Modelling the wave-induced instantaneous liquefaction in a non-cohesive seabed as a nonlinear complementarity problem', *Computers and Geotechnics* **137**, 104275.

Zhou, M.-Z., Jeng, D.-S. and Qi, W.-G. (2020), 'A new model for wave-induced instantaneous liquefaction in a non-cohesive seabed with dynamic permeability', *Ocean Engineering* p. 107597.

Zhou, M. Z., Qi, W. G., Jeng, D.-S. and Gao, F. P. (2021*b*), 'A non-darcy flow model for wave-induced instantaneous liquefaction in a non-cohesive seabed', *Ocean Engineering* **239**, 109807.

Zhou, M., Zhang, B. and Peng, C. (2018), 'Numerical evaluation of soft inter-slab joint in concrete-faced rockfill dam with dual mortar finite element method', *International Journal for Numerical and Analytical Methods in Geomechanics* **42**(5), 781–805.

Zhou, X.-L., Zhang, J., Wang, J.-H., Xu, Y.-F. and Jeng, D.-S. (2014), 'Stability and liquefaction analysis of porous seabed subjected to cnoidal wave', *Applied Ocean Research* **48**, 250–265.

Zhou, Y. and Rajapakse, R. K. N. D. (1998), 'Coupled heat-moisture-are transport in deformable unsaturated media', *Journal of Engineering Mechanics, ASCE* **24**(10), 1090–1099.

Zhou, Y. and Rowe, R. K. (2003), 'Development of a technique for modelling clay liner desiccation', *International Journal for Numerical and Analytical Methods in Geomechanics* **27**, 473–493.

Zhou, Y. and Rowe, R. K. (2005), 'Modeling of clay liner desiccation', *International Journal of Geomechanics, ASCE* **5**(1), 1–9.

Zienkiewicz, O. C., Chan, A. H. C., Pastor, M., Schrefler, B. A. and Shiomi, T. (1999), *Computational Geomechanics with Special Reference to Earthquake Engineering*, John Wiley and Sons, England.

Zienkiewicz, O. C., Chang, C. T. and Bettess, P. (1980), 'Drained, undrained, consolidating and dynamic behaviour assumptions in soils', *Géotechnique* **30**(4), 385–395.

Index